

Xuzhu Dong  
Li Cai *Editors*

The Proceedings of 2023  
4th International  
Symposium  
on Insulation and  
Discharge Computation  
for Power Equipment  
(IDCOMPU2023)

Volume IV

# Lecture Notes in Electrical Engineering

## Volume 1103

### Series Editors

Leopoldo Angrisani, Department of Electrical and Information Technologies Engineering, University of Napoli Federico II, Napoli, Italy  
Marco Artega, Departament de Control y Robótica, Universidad Nacional Autónoma de México, Coyoacán, Mexico  
Samarjit Chakraborty, Fakultät für Elektrotechnik und Informationstechnik, TU München, München, Germany  
Jiming Chen, Zhejiang University, Hangzhou, Zhejiang, China  
Shanben Chen, School of Materials Science and Engineering, Shanghai Jiao Tong University, Shanghai, China  
Tan Kay Chen, Department of Electrical and Computer Engineering, National University of Singapore, Singapore, Singapore  
Rüdiger Dillmann, University of Karlsruhe (TH) IAIM, Karlsruhe, Baden-Württemberg, Germany  
Haibin Duan, Beijing University of Aeronautics and Astronautics, Beijing, China  
Gianluigi Ferrari, Dipartimento di Ingegneria dell'Informazione, Sede Scientifica Università degli Studi di Parma, Parma, Italy  
Manuel Ferre, Centre for Automation and Robotics CAR (UPM-CSIC), Universidad Politécnica de Madrid, Madrid, Spain  
Faryar Jabbari, Department of Mechanical and Aerospace Engineering, University of California, Irvine, CA, USA  
Limin Jia, State Key Laboratory of Rail Traffic Control and Safety, Beijing Jiaotong University, Beijing, China  
Janusz Kacprzyk, Intelligent Systems Laboratory, Systems Research Institute, Polish Academy of Sciences, Warsaw, Poland  
Alaa Khamis, Department of Mechatronics Engineering, German University in Egypt El Tagamoa El Khames, New Cairo City, Egypt  
Torsten Kroeger, Intrinsic Innovation, Mountain View, CA, USA  
Yong Li, College of Electrical and Information Engineering, Hunan University, Changsha, Hunan, China  
Qilian Liang, Department of Electrical Engineering, University of Texas at Arlington, Arlington, TX, USA  
Ferran Martín, Departament d'Enginyeria Electrònica, Universitat Autònoma de Barcelona, Bellaterra, Barcelona, Spain  
Tan Cher Ming, College of Engineering, Nanyang Technological University, Singapore, Singapore  
Wolfgang Minker, Institute of Information Technology, University of Ulm, Ulm, Germany  
Pradeep Misra, Department of Electrical Engineering, Wright State University, Dayton, OH, USA  
Subhas Mukhopadhyay, School of Engineering, Macquarie University, NSW, Australia  
Cun-Zheng Ning, Department of Electrical Engineering, Arizona State University, Tempe, AZ, USA  
Toyooki Nishida, Department of Intelligence Science and Technology, Kyoto University, Kyoto, Japan  
Luca Oneto, Department of Informatics, Bioengineering, Robotics and Systems Engineering, University of Genova, Genova, Italy  
Bijaya Ketan Panigrahi, Department of Electrical Engineering, Indian Institute of Technology Delhi, New Delhi, Delhi, India  
Federica Pascucci, Department di Ingegneria, Università degli Studi Roma Tre, Roma, Italy  
Yong Qin, State Key Laboratory of Rail Traffic Control and Safety, Beijing Jiaotong University, Beijing, China  
Gan Woon Seng, School of Electrical and Electronic Engineering, Nanyang Technological University, Singapore, Singapore  
Jochaim Speidel, Institute of Telecommunications, University of Stuttgart, Stuttgart, Germany  
Germano Veiga, FEUP Campus, INESC Porto, Porto, Portugal  
Haitao Wu, Academy of Opto-electronics, Chinese Academy of Sciences, Haidian District Beijing, China  
Walter Zamboni, Department of Computer Engineering, Electrical Engineering and Applied Mathematics, DIEM—Università degli studi di Salerno, Fisciano, Salerno, Italy  
Junjie James Zhang, Charlotte, NC, USA  
Kay Chen Tan, Department of Computing, Hong Kong Polytechnic University, Kowloon Tong, Hong Kong

The book series *Lecture Notes in Electrical Engineering* (LNEE) publishes the latest developments in Electrical Engineering—quickly, informally and in high quality. While original research reported in proceedings and monographs has traditionally formed the core of LNEE, we also encourage authors to submit books devoted to supporting student education and professional training in the various fields and applications areas of electrical engineering. The series cover classical and emerging topics concerning:

- Communication Engineering, Information Theory and Networks
- Electronics Engineering and Microelectronics
- Signal, Image and Speech Processing
- Wireless and Mobile Communication
- Circuits and Systems
- Energy Systems, Power Electronics and Electrical Machines
- Electro-optical Engineering
- Instrumentation Engineering
- Avionics Engineering
- Control Systems
- Internet-of-Things and Cybersecurity
- Biomedical Devices, MEMS and NEMS

For general information about this book series, comments or suggestions, please contact [leontina.dicecco@springer.com](mailto:leontina.dicecco@springer.com).

To submit a proposal or request further information, please contact the Publishing Editor in your country:

#### **China**

Jasmine Dou, Editor ([jasmine.dou@springer.com](mailto:jasmine.dou@springer.com))

#### **India, Japan, Rest of Asia**

Swati Meherishi, Editorial Director ([Swati.Meherishi@springer.com](mailto:Swati.Meherishi@springer.com))

#### **Southeast Asia, Australia, New Zealand**

Ramesh Nath Premnath, Editor ([ramesh.premnath@springernature.com](mailto:ramesh.premnath@springernature.com))

#### **USA, Canada**

Michael Luby, Senior Editor ([michael.luby@springer.com](mailto:michael.luby@springer.com))

#### **All other Countries**

Leontina Di Cecco, Senior Editor ([leontina.dicecco@springer.com](mailto:leontina.dicecco@springer.com))

**\*\* This series is indexed by EI Compendex and Scopus databases. \*\***

Xuzhu Dong · Li Cai  
Editors

The Proceedings of 2023 4th  
International Symposium  
on Insulation and Discharge  
Computation for Power  
Equipment (IDCOMP2023)

Volume IV

 Springer

*Editors*

Xuzhu Dong  
School of Electrical Engineering  
and Automation  
Wuhan University  
Wuhan, China

Li Cai  
School of Electrical Engineering  
and Automation  
Wuhan University  
Wuhan, China

ISSN 1876-1100

ISSN 1876-1119 (electronic)

Lecture Notes in Electrical Engineering

ISBN 978-981-99-7412-2

ISBN 978-981-99-7413-9 (eBook)

<https://doi.org/10.1007/978-981-99-7413-9>

© Beijing Paiké Culture Commu. Co., Ltd. 2024

This work is subject to copyright. All rights are solely and exclusively licensed by the Publisher, whether the whole or part of the material is concerned, specifically the rights of translation, reprinting, reuse of illustrations, recitation, broadcasting, reproduction on microfilms or in any other physical way, and transmission or information storage and retrieval, electronic adaptation, computer software, or by similar or dissimilar methodology now known or hereafter developed.

The use of general descriptive names, registered names, trademarks, service marks, etc. in this publication does not imply, even in the absence of a specific statement, that such names are exempt from the relevant protective laws and regulations and therefore free for general use.

The publisher, the authors, and the editors are safe to assume that the advice and information in this book are believed to be true and accurate at the date of publication. Neither the publisher nor the authors or the editors give a warranty, expressed or implied, with respect to the material contained herein or for any errors or omissions that may have been made. The publisher remains neutral with regard to jurisdictional claims in published maps and institutional affiliations.

This Springer imprint is published by the registered company Springer Nature Singapore Pte Ltd.

The registered company address is: 152 Beach Road, #21-01/04 Gateway East, Singapore 189721, Singapore

Paper in this product is recyclable.

# Contents

<b>A New Grounding Mode for Suppressing Circulating Currents of Submarine Cables</b> .....	1
Xi Qin, Wenjun Zhou, Ming Lv, Zhongjiang Chen, Lifeng Qiu, Runze Cai, and Shiyong Yang	
<b>Preparation and Anti-icing Properties of Chemically Etched Superhydrophobic Aluminum Surface</b> .....	15
Dayou Liu, Jiakuan Han, and Haiyun Jin	
<b>Research on High Voltage Pulse Ice-Breaking Technology</b> .....	29
Yue Yu, Jiakuan Zheng, Mingxin Zhang, and Zhiye Du	
<b>Design and Implementation of Electric Field-Induction Based Energy Harvesting System for High Voltage Power Transmission Lines</b> .....	41
Yan Jiang, Zheng Zhou, Zhifeng Sun, Wentao Liu, Lei Tao, Xuanan Song, and Xingran Gao	
<b>Defect Identification Method Based on Casing Internal Temperature Variation</b> .....	57
Jingling Sun, Xiaowen Wu, Wei Xiao, and Ping Peng	
<b>Influence of Main Shield Voltage Distribution Configuration on the Post-arc Sheath Development of Vacuum Interrupters</b> .....	71
Hui Chen, Xian Cheng, Guowei Ge, and Shuai Du	
<b>Simulation Study on Spatial Distribution Characteristics of Partial Discharge UHF Signal in Transformer Outlet Device</b> .....	83
Yuntian Guo, Hao Liu, Guoming Ma, Zhenxing Fan, Dan Zhou, and Shicong Zhai	

<b>Temperature Field Simulations of Three-Layer Extrusion in 110 kV Grafted Polypropylene Power Cables</b> .....	91
Ji Wu, Shangshi Huang, Xin Yu, Haihan Cheng, Shihu Yu, Shixun Hu, Qi Li, and Jinliang He	
<b>The Electrical-Thermal Coupling Simulation of Grafted Polypropylene Used in High-Voltage Direct Current Cables</b> .....	101
Yazhou Fan, Wenjia Zhang, Xiangyang Peng, Shangshi Huang, Yingge Li, Shixun Hu, Qi Li, and Jinliang He	
<b>Optimization Technology of Finite Element Stepper Motor Based on Parametric Modeling</b> .....	113
Jiaxin Chen, Houlong Chen, Xiaoming Zhou, and Ji Zheng	
<b>Research on Several Key Technologies for the Development of Power Analyzer</b> .....	123
Jiaxin Chen, Xiaoming Zhou, and Hua Hua	
<b>Experimental and Simulation Verification of the Effects of Different Metal Particle Impurities on the Electrical Properties of Alumina/Epoxy Composites for GIL Insulators</b> .....	133
Hang Yuan, Sijia Zhu, Shuang Yan, Dingxin Wei, Zishi Yang, Yutong Zhang, Peng Liu, and Zongren Peng	
<b>Research on 10 kV Nonlinear Materials Terminal Accessories for Polypropylene-Insulated Cables</b> .....	147
Zhiwen Huang, Qinghao Yang, Yifan Zhou, and Jun Hu	
<b>Mechanism of Surface Charge Regulation with Nonlinear Conductivity Coating in C<sub>4</sub>F<sub>7</sub>N/CO<sub>2</sub> Mixture</b> .....	157
Peng Sun, Jinshu Li, Junhong Chen, Wei Yin, Junbo Deng, Jianben Liu, and Yan Liu	
<b>Prediction Model of Strong Electromagnetic Effect Phenomenon Based on Complement Naive Bayes</b> .....	167
Zhihao Liu, Xuan Cao, Mengxue Li, and Haipeng Wang	
<b>Evaluation and Optimization Schemes of Eddy Current Loss on Structural Components for High Voltage Converter Transformer</b> .....	179
Min Shen, Penghong Guo, Yanling Wang, Youliang Sun, and Xiangdong Yu	
<b>Simulation Study on Spread Characteristics of Wildfire Near Transmission Lines</b> .....	191
Jun Xu, Chaoying Fang, Shiyun Cao, and Shengwen Shu	

**Modeling and Simulation of the Dynamic Characteristics of Vacuum Arc in DC Interruption Based on Artificial Current Zero When the Current is Close to Zero** ..... 201  
 Jing Jiang, Lulin Kuang, Guoqing Wang, Zhongxi Liang, Yu Zhang, Le Du, Qianyi Liang, and Jinwei Lu

**Design and Simulation Analysis of a New Cylindrical Permanent Magnet Linear Motor for Vortex-Induced Vibration Ocean Current Power Generation** ..... 213  
 Liguofan, Guoqiang Liu, Xianjin Song, Wenwei Zhang, Tongyang Jin, Lipeng Wu, and Hui Xia

**3D Pic-Mcc Simulation of Particles Expansion for Straight Curved Contact and Butt Contact in the Post-arc Phase** ..... 225  
 Tong Ziang, Wu Shengxiu, Qin Enyao, Shen Zhengbin, Wu Jianwen, Shi Shengsheng, Zhang Liyan, and Sun Weili

**The Electric-Thermal Characteristics of 110 kV Transformer RIP Bushings Based on Electromagnetic-Thermal-Fluid Analysis** ..... 235  
 Sirui Zhao, Hao Yang, Wenxiu Hu, Jinpeng Chen, and Yimeng Duan

**Simulation Analysis of Mechanical Properties of Grafted Polypropylene Cable** ..... 247  
 Xinhua Dong, Yuxiao Zhou, Changlong Yang, Huajun Wu, Weigang Zheng, Tao Li, Xuchen Lu, and Jinliang He

**Analysis on Surge Characteristics and Protection for Wind Turbines Based on ATP-EMTP Simulation** ..... 257  
 Haoen Li, Ruanming Huang, Fei Fei, Shenhui Hua, Jiafeng Gu, and Zhenyu Pang

**Study on the Influence of Crosslinking By-Products on XLPE Breakdown Performance in XLPE Cables Based on the First-Principles and Band Gap Theory** ..... 265  
 Qiannan Zhao, Jin Liu, Yifei You, Shicheng Gao, and Wei Wang

**Simulation Study on the Motion of Dust Particles in Traveling Wave Electric Curtain Photovoltaic Panel** ..... 273  
 Long Long Wang and Hai Jin

**Study on the Influence of Wildfire on Streamer Discharge in Transmission Line Gap** ..... 285  
 Maoqiang Bi, Shijun Zhang, Chenshihao Jiang, Xiong Wang, Shaolan Lei, and Tianyan Jiang

**Influence of AC Voltage Frequency on Partial Discharge of Oil-Pressboard Insulation and Its Mechanism** ..... 297  
 Shuqi Li, Xinyi Sui, Mingsheng Wang, Penghong Guo, Yongwei Xu, Guodong Gu, Liangkai Wang, and Qingquan Li



<b>Study of Electrical Characteristics of Epoxy Resin Under Different Environmental Conditions of Condensation</b> .....	305
Zhangang Yang, Yongguang Ji, Xiao Ma, Haonan Tan, Xiao Rao, and Maoqiang Bi	
<b>Transformer Health Condition Assessment Method Based on Full Life Cycle Data</b> .....	317
Linhong Xie, Zihao Jiang, Longji Feng, Chengbo Chu, Zhiyong Huang, and Xiaotian Liu	
<b>Effect of Positive Temperature Coefficient Materials on the AC Breakdown Strength and Dielectric Properties of Epoxy Composites</b> .....	327
Chenyuan Teng, Shuo Li, Yuanxiang Zhou, Ling Zhang, Yunxiao Zhang, and Meng Huang	
<b>Stage Recognition of Surface Discharge in Oil-Impregnated Paper Based on Convolutional Neural Network</b> .....	337
Yuanxiang Zhou, Jianning Chen, and Yongyin Li	
<b>Dynamic Behavior of Suspended Bubbles in Insulating Oil Correlation with Flow Field Distribution</b> .....	347
Ning Zhang, Jian Hao, Shili Liu, Junyi Zhang, Houhe Chen, and Ruijin Liao	
<b>Study on the External Insulation Characteristics of Epoxy Resin After Corona Aging Under Hygrothermal Coupling Effect</b> .....	357
Yongliang Ji, Zhangang Yang, Liang Xie, Xiao Rao, Haonan Tan, and Maoqiang Bi	
<b>Design and Optimization of 6.5 kV SiC MOSFET Device Termination</b> .....	367
Chuxuan Ma, Zhaocheng Liu, Xuebao Li, Zhibin Zhao, and Peng Sun	
<b>Research on Factors Affecting Audible Noise of 500 kV Double-Circuit Straight-Line Tower AC Transmission Line</b> .....	379
Xiaosen Zhou and Shengsuo Niu	
<b>Transmission Ampacity Improvement of EHV Submarine Cable</b> .....	387
Hao Zhang, Guoqing Ma, Pengfei Li, Youcong Huang, Tongtong He, and Yuesheng Zheng	
<b>Multi-Physics Field Simulation Analysis of GIS Disconnect Switch Contact Temperature Considering Contact Anomalies</b> .....	397
Ziqi Zhang, Jiangjun Ruan, Shengwen Shu, Qiaofeng Chen, Chen Zhang, and Yongqing Deng	

**Finite Element Analysis of Physical Properties of New Transformer Core Materials** ..... 407  
 Dong Zhao, Yang Wang, Yonggang Jia, Yan Du, Qingdong Zhu, and Bo Zhang

**Research on Current Limiting Protection Method of Short Circuit Faults in Medium Voltage DC Integrated Power Systems** ..... 417  
 Beibei Wang

**Structural, Magnetic, Relaxor Ferroelectric and Magnetoelectric Coupling Properties in Aurivillius Phase  $\text{Bi}_6\text{La}_3\text{Ti}_3\text{Fe}_5\text{O}_{27}$**  ..... 427  
 Maosong Wu, Long Xiao, Feng Deng, and Shengquan Zheng

**Electric Field Optimization of Optical Fiber Insulator Based on Random Focus Search Algorithm** ..... 437  
 Yanjie Cui, Wenhao Lu, Qian Chen, Yang Feng, Liang Liu, Shengtao Li, Wei Xiao, and Senlin Zhao

**Research on the Influence of Safety Film on the Thermal Field Distribution of Metallized Film Capacitors** ..... 447  
 Yanjie Cui, Yong Sun, Wenhao Lu, Cheng Yao, and Chunhong Zhou

**Research on Post-arc Recovery Characteristics of Sheath in Long-Gap Vacuum Circuit Breaker** ..... 457  
 Ying Feng, Dege Li, Jintao Zhang, Ziang Tong, and Jianwen Wu

**Effect of Different Grounding Schemes on the Circulating Current of Gas-Insulated Transmission Lines** ..... 467  
 Zhiren Tian, Junqiang Gong, Zhen Xiang, Gen Li, and Yu Zheng

**Research on Digital Twin Analysis Technology of Electric Field in the Near Area of DC Grounding Electrode** ..... 475  
 Lei Jun, Li Xiaojuan, Li Shaoyu, Qi Weijian, Cao Bibo, and Xie Yankai

**Coupling Simulation and Experimental Verification of Partial Discharge Sound Field and External Optical Fiber in Insulation Air Gap of Cable Joint** ..... 483  
 Guo Tengjun, Qin Weiqi, Zhang Xiaolong, Wang Sihan, Hu Jing, and Ma Guoming

**Analysis of Safety for UAV Inspection of Electric Field in 220 kV Substation** ..... 493  
 Duanjiao Li, Ying Zhang, Yun Chen, Wenxing Sun, Ziran Jia, Wensheng Li, Lin Yi, and Yingyi Yang

**Research on Electric Field Safety Distance of High-Voltage Equipment in Substations Inspected by UAV** ..... 505  
 Ying Zhang, Duanjiao Li, Yun Chen, Gao Liu, Daoqing Fan, Wensheng Li, Liqiang Zhong, and Xiaoming Mai

**Performance of Annual Flashover Rate at Individual Poles in a Distribution Network Due to Indirect Lightning** ..... 515  
 Jinxin Cao, Jianguo Wang, Yaping Du, Amedeo Andreotti, Yuxuan Ding, Li Cai, Yadong Fan, and Mi Zhou

**Analysis of Induced Voltage of a Single-Point Grounded OPGW in 35 kV Distribution Lines** ..... 525  
 Yufei Chen, Jinxin Cao, Yong Wei, Xianchun Wang, Jiaju Zhang, Yadong Fan, Wenhao Zhang, and Jianguo Wang

**Research on Pre-synchronization Control Strategy for the Integration of Individual Microgrid into Microgrid Clusters** .... 535  
 Peng Yu, Rong Fu, Lihong Ma, Zaishun Feng, Mingjun Chen, Jinsong Li, and Xiangtao Zhuan

**Fault Identification of MOA Based on Infrared Thermal Imaging** ..... 547  
 Cheng Guokai, Weng Donglei, Zhou Qibo, Jiang Jiong, Zhang Rongwei, Sun Long, Shen Houming, and Wei Zhen

**Research on Key Technologies of Intelligent Defect Image Detection for Substation Equipment in Complex Scenes** ..... 555  
 Ning Yang, Lihua Li, Yang Yang, Jiayun Zhu, and Wentong Shang

**Calculation Analysis of Fast Motorised Crossing Devices for Transmission Line Erection** ..... 569  
 Wenzhuo Chen, Kai Li, Qiyun Han, Xianfeng Zhu, and Bo Tang

**Application of Portable Tower Arc Sag Observer in Transmission Line Engineering** ..... 577  
 Yushan Yao, Xianfeng Zhu, Kai Li, Jian Jiao, Bo Tang, and Qiyun Han

**Self-learning Diagnosis of Transmission Line Fault Type Based on Deep Forest and SMOTE** ..... 585  
 Xiao Tan, Guoji Chang, Gang Qiu, Jinjin Shi, Jie Chen, and Qiwei Wu

**Chemical Trap Orbital Analysis of Styrene-Grafted Polypropylene for HVDC Cable Insulation** ..... 595  
 Yuxiao Zhou, Changlong Yang, Shixun Hu, Huajun Wu, Weigang Zheng, Tao Li, Shangshi Huang, Xuchen Lu, Qi Li, and Jinliang He

**Numerical Simulation of Transient Temperature Rise on 110 kV/40 MVA Vehicle-Mounted Mobile Transformer** ..... 603  
 Zhijia Feng, Jinxin Cao, Hongling Zhou, Zhenpeng Tang, Jianguo Wang, Yadong Fan, Li Cai, and Mi Zhou

**Calculation of Distributed Photovoltaic Hosting Capacity in Distribution Network** ..... 613  
 Junwen Yang, Lei Shang, Xuzhu Dong, Huaimin Xia, Haiyan Zeng, Qing Duan, and Jie Zhao

**Analysis of Induced Current of OPGW in 750 kV Transmission Lines** ..... 631  
 Yufei Chen, Yong Wei, Xianchun Wang, Jiaju Zhang, Wenzhao Liu, Xianglong Meng, Jinxin Cao, and Jianguo Wang

**Analysis of Electromagnetic Field Distribution of Aircraft Lightning Strike** ..... 641  
 Qin Feng, Duan Denglei, Chen Jiaer, Wang Tong, Zhou Mi, Cai Li, Wang Jianguo, and Fan Yadong

**Study of the Effect of Oblique Photography Route Overlap Rate on 3D Reconstruction** ..... 651  
 Cong Hu, Fuhua Xie, Xian Zhou, Li Cai, Xin Yang, Jianguo Wang, and Yadong Fan

**Design and Thrust Output Analysis of Linear Induction Motor for Electromagnetic Ejection of Fixed-Wing UAV** ..... 659  
 Xijun Liu, Xianchun Huang, and Peifeng Zhao

**A Variable Frequency Voltage Injection Method for Modular Multilevel Converter in Variable Speed Driver** ..... 669  
 Guanlong Jia, Mingshuo Li, Dawei Feng, Binhao Shi, Xiaoming Liu, and Jun Huang

**A 24-Pulse Aviation Rectifier Based on Auto-Fed Half-Bridge Auxiliary Circuit** ..... 679  
 Wenhao Tu, Yongshuai Wang, Hongjuan Ge, Yichen Pan, and Yanbo Shi

**Study on Analysis Method of Zinc Oxide Line Arrester Fracture** ..... 691  
 Qi Yang, Yang Tian, Haixiang Chen, Lei Gao, Zhiyong Deng, and Zhuohong Pan

**Multiphysics Coupling Simulation and Analysis of Influencing Factors on Temperature Rise Characteristics of Tri-Post Insulator GIL** ..... 703  
 F. F. Wu, S. Y. Xie, X. Lin, M. H. Chen, and C. H. Zhang

**Influence Mechanism of Hot-Press Setting Time and Winding Tension on the Performance of Metallized Film Capacitors** ..... 713  
 Huize Cui, Zhaoliang Xing, and Chong Zhang

**Multivariate Model Predictive Control for High Permeability Photovoltaic Microgrid** ..... 723  
 Jipeng Gu, Binjie Wang, Sheng Zheng, Xuguang Wu, Youbing Zhang, and Weijie Zhang

# A New Grounding Mode for Suppressing Circulating Currents of Submarine Cables



Xi Qin, Wenjun Zhou, Ming Lv, Zhongjiang Chen, Lifeng Qiu, Runze Cai, and Shiyu Yang

**Abstract** The usually used grounding mode of submarine cables, e.g., the two-ends grounding mode or the multi-spots grounding mode, can often generate significant circulating currents in the metal sheaths and armors, limiting the allowable ampacity of submarine cables. As a solution, this paper proposes a new grounding mode that mitigates the circulating currents and upgrades the allowable ampacity. The detailed structure and requirements of the proposed grounding mode for single-circuit, double-circuit and triple-circuit transmission lines (TL) are firstly described. The numerical calculation model is then constructed to compare the ampacities and circulating currents in different grounding modes. The numerical results show that the proposed grounding mode can dramatically suppress the circulating currents and upgrade the ampacity by approximately 20%, compared with the traditional grounding method. Further research reveals a high terminal voltage performance of this new method. Therefore, the proposed new method can only be used within the certain laying length which is dependent on the insulation grade. This new grounding mode is a promising solution to upgrade the ampacity of submarine cables.

**Keywords** Submarine cable · Grounding mode · Circulating current · Ampacity

## 1 Introduction

The increasing demand for marine energy has led to constructions of offshore wind farms and oil drilling platforms. These facilities are usually located several kilometers away from the mainland, which paved the way for extensive utilization of

---

X. Qin · W. Zhou · M. Lv · Z. Chen · L. Qiu  
Zhejiang Huayun Electric Power Engineering Design and Consultation Co., Ltd,  
Hangzhou 310014, China

R. Cai · S. Yang (✉)  
College of Electrical Engineering, Zhejiang University, Hangzhou 310027, China  
e-mail: [eesyyang@zju.edu.cn](mailto:eesyyang@zju.edu.cn)

© Beijing Paiké Culture Commu. Co., Ltd. 2024  
X. Dong and L. Cai (eds.), *The Proceedings of 2023 4th International Symposium on Insulation and Discharge Computation for Power Equipment (IDCOMPU2023)*, Lecture Notes in Electrical Engineering 1103, [https://doi.org/10.1007/978-981-99-7413-9\\_1](https://doi.org/10.1007/978-981-99-7413-9_1)

submarine cables to transmit electrical power in both directions. The power transmission capacity is an important index of the TLs. Insufficient power transmission capacity will decrease the operational efficiency of the oil platforms and waste the energy produced by the wind farms. There is a close relationship between the power transmission capacity and the ampacity of the cables under certain voltage levels. Consequently, upgrading the ampacity under a limited number of submarine cables becomes a demanding issue [1, 2].

The ampacity of submarine cables is highly imposed by the thermal properties of cable insulation layers and surrounding sediments of the seabed in which they are buried. The ampacity is also severely subject to the losses in the cables, mainly the Joule losses and the magnetic hysteresis losses in the central conductors, the metal sheaths and the armor. The thermal properties are difficult to change for constructed cables, and the loss in the central conductors is inevitable for the load current carrying the required power. A feasible approach is to decrease the losses in the metal sheaths and armors, which can be achieved by suppressing the circulating currents.

High voltage and ultra-high voltage submarine cables usually have single core structure. The mostly used grounding modes of the single-core submarine cable include: (1) Metal sheaths and armors are bonded together to ground at both ends of the TL, without any short-circuit bonding in the middle, namely the two-ends grounding mode. (2) In addition to the grounding at the ends, there are short-circuit connections at some intermediate location of the TL, implemented by connecting the metal sheath and armor together to the ground using some fine metal wires, namely multi-spot grounding mode. (3) In addition to the grounding at the ends, there is semi-conductive over-sheath between the metal sheath and the armor, resembling the whole-line grounding. However, the aforementioned grounding modes will result in considerable circulating currents and losses in the metal sheath and armor, and it is revealed that the three grounding modes have no noticeable differences on increasing the cable ampacity [3]. Some other researchers have slightly improved the typical grounding modes of submarine cables [4, 5], but these methods are only for some specific engineering problems, not applicable for a general case. Although the cross-bonded grounding mode can effectively suppress the circulating currents of land cables, it is infeasible to be applied in submarine cables, due to the seawater environment.

Another common solution for decreasing cable losses is decreasing the cable capacitive charging currents, mainly including two operation schemes: varying the transmission voltage [6] and lowering the operation frequency [7, 8]. In [6], the validity of reducing losses by continuously adjusting the cable operating voltage through transformer online tap changers is demonstrated. While in [7, 8], the fractional frequency transmission system (FFTS) whose operating frequency is lower than that of a conventional AC transmission system is investigated. The performance studies show the dramatic reduction of charging currents in the cable in FFTS. More-over, in [7] it is proposed to combine the voltage regulation with FFTS to minimize losses. Solutions in references [6–8] need additional equipment such as tap changer transformers and AC/AC converters, which are not ideal technically and economically.

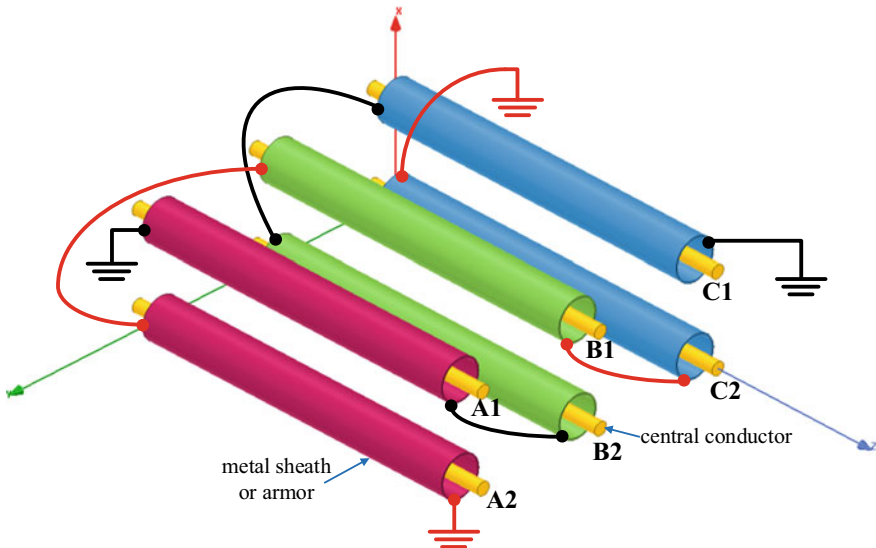
To address the aforementioned issues, this paper proposes a new grounding mode for submarine cable TLs, motivated by the cross-bonded grounding mode of land cables. In the proposed approach, by bonding the metal sheaths and armors in a specific form at the terminals, the circulating currents can be significantly suppressed, thereby to upgrade the ampacity of submarine cables. This new grounding method can be applied without introducing new devices or technologies, which is easy to realize.

## 2 The Proposed New Grounding Mode

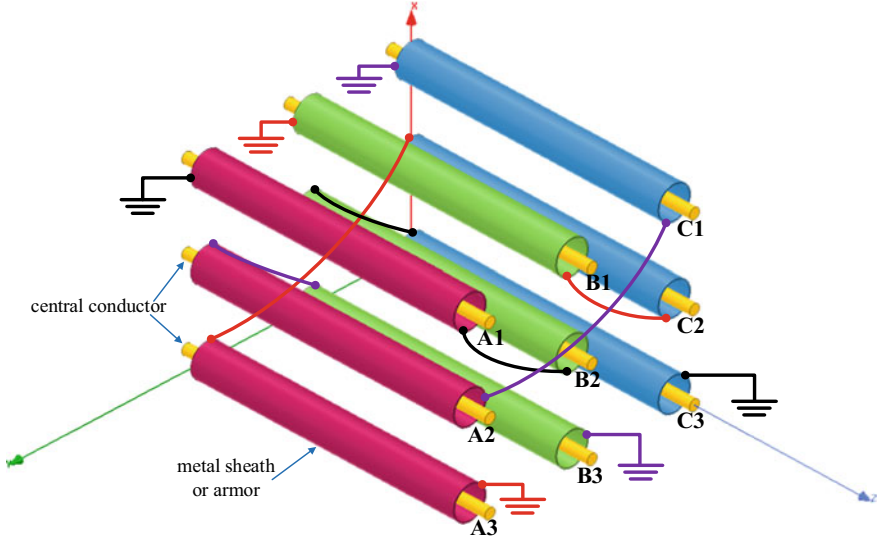
The new grounding mode of one-circuit TL is different from that of the multi-circuit TLs (more than one circuit), but the essences are the same, that is, they both bond the metal sheaths and armors in a cross-linked way.

### A. Multi-circuit transmission lines

For multi-circuit TLs, the grounding mode proposed in this paper requires to apply different phases of current to the central conductors, and the metal sheaths or armors are bonded only at terminal ports for engineering flexibility and feasibility. For cases of double-circuit and triple-circuit submarine cable TLs, the new grounding modes of metal sheaths and armors are shown in Figs. 1 and 2, respectively.



**Fig. 1** Schematic diagram of the new grounding mode for double-circuit submarine TLs. The black lines constitute Loop 1. The red lines constitute Loop 2. Circuit 1 consists of cable A1, B1 and C1. Circuit 2 consists of cable A2, B2 and C2



**Fig. 2** Schematic diagram of the new grounding mode for triple-circuit submarine TLs. The black lines constitute Loop 1. The red lines constitute Loop 2. The purple lines constitute Loop 3. Circuit 1 consists of cable A1, B1 and C1. Circuit 2 consists of cable A2, B2 and C2. Circuit 3 consists of cable A3, B3 and C3

The reference direction of the phase current is along the positive direction of  $z$  axis. For double-circuit TLs, the new grounding mode requires the current phases being  $0^\circ$ ,  $-120^\circ$  and  $120^\circ$  in phase A1, B1 and C1, respectively. Meanwhile the current phases in A2, B2 and C2 are required to be  $180^\circ$ ,  $60^\circ$  and  $-60^\circ$ , respectively. For triple-circuit TLs, the current phases of circuit 1 and circuit 2 are identical with that of the double-circuit TLs, and the current phases of circuit 3 are identical with that of circuit 1. The phase currents of circuit 2 can be derived through shifting the phases of currents in circuit 1 using the phase shifting transformer or power electronic converter. However, since the maximum phase-shifting angle of the phase shifting transformer is  $90^\circ$ , a specific phase-shifting rule is proposed as: A1 shifting  $60^\circ$  to obtain B2, B1 shifting  $60^\circ$  to obtain C2, C1 shifting  $60^\circ$  to obtain A2.

It is assumed that the induced electromotive force (EMF) in the metal sheaths and armors is only determined by their own central conductor current. Obviously, this assumption is reasonable. The larger the cable spacing is, the more accurate this assumption is. Therefore the total induced EMFs of circuit loops in double-circuit TLs and triple-circuit TLs can be described by (1) and (2), respectively.

$$\begin{cases} \xi_{1d} = (-j\omega A_{A1} + j\omega A_{B2} - j\omega A_{C1})L \\ \xi_{2d} = (j\omega A_{A2} - j\omega A_{B1} + j\omega A_{C2})L \end{cases} \quad (1)$$



$$\begin{cases} \xi_{1t} = (-j\omega A_{A1} + j\omega A_{B2} - j\omega A_{C3})L \\ \xi_{2t} = (-j\omega A_{B1} + j\omega A_{C2} - j\omega A_{A3})L \\ \xi_{3t} = (-j\omega A_{C1} + j\omega A_{A2} - j\omega A_{B3})L \end{cases} \quad (2)$$

where,  $\xi_{1d}$  and  $\xi_{2d}$  refer to the EMF in Loop 1 and Loop 2 in double-circuit TLs, respectively;  $\xi_{1t}$ ,  $\xi_{2t}$  and  $\xi_{3t}$  refer to the EMF in Loop 1, Loop 2 and Loop 3 in triple-circuit TLs, respectively;  $A$  is the vector magnetic potential in metal sheaths or armors produced only by its own central conductor current;  $\omega$  represents the electric angular frequency;  $L$  is the total length of the cable lines. Under the condition of equal loads in all cables, each  $\xi$  is obviously equal to zero, which means that there will be no circulating current in every circuit loop.

The submarine TL system consisting of more than three circuits can be decomposed into the aforementioned two modules. That is, a four-circuit TL system can be decomposed into two double-circuit TL systems, a five-circuit TL system can be decomposed into a double-circuit TL system with a triple-circuit TL system, a six-circuit TL system can be decomposed into three double-circuit TL systems or two triple-circuit TL systems. From the previous analysis, with the proposed new grounding mode, no circulating current will be induced in metal sheaths or armors.

#### B. *One-circuit transmission line*

For one-circuit TL, one can not bond the metal sheaths and armors in the previous way as shown in Figs. 1 and 2, due to no additional cables to apply different phases of currents. But the proposed new grounding mode can still be used thanks to the armor of the submarine cable. The specific bonding method is the cross connection between the metal sheaths and the armors, as shown in Fig. 3.

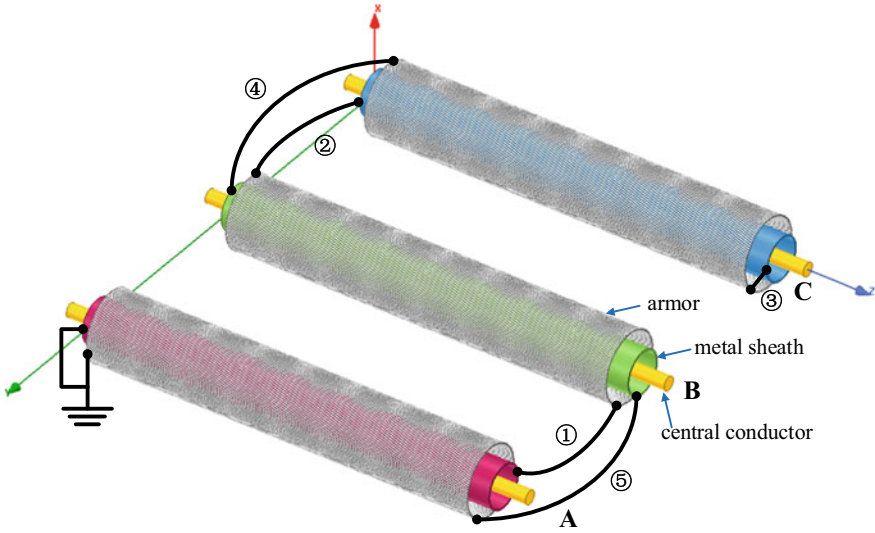
The total induced EMFs of the cross-linked circuit loop in Fig. 3 can be given by:

$$\xi = (-j\omega A_{As} + j\omega A_{Ba} - j\omega A_{Cs} + j\omega A_{Ca} - j\omega A_{Bs} + j\omega A_{Aa})L \quad (3)$$

where,  $\xi$  is the total EMF of the cross-linked loop;  $A$  with subscript “s” refers to the vector magnetic potential in the metal sheath;  $A$  with subscript “a” refers to the vector magnetic potential in the armor.

One now assumes that the induced EMFs in the metal sheaths and armors are only determined by their own central conductor current. Under this assumption and the equal load condition,  $\xi$  is obviously equal to zero, meaning that the circulating current is suppressed effectively.

From the previous qualitative analysis, one can conclude that the proposed new grounding mode has a certain effect on improving the ampacity of submarine cables.



**Fig. 3** Schematic diagram of the new grounding mode for one-circuit submarine TL. The black lines constitute the cross-linked circuit loop of metal sheaths and armors

### 3 Numerical Validations

A two-dimensional finite element model is constructed to validate the proposed grounding mode. The numerical calculation results under two-ends grounding mode and the proposed new grounding mode are compared.

#### A. Finite element modeling

A 1600 mm<sup>2</sup> HYJQ71-F127/220 kV submarine cable is taken as the case study. This cable is explicitly represented as a series of circles, as shown in Fig. 4. The finite element model of double-circuit TLs is provided in Fig. 5. The cables are modeled parallel, which are buried 2 m depth on the saturated sea bed. The phase to phase distance in one circuit is noted by *space*. The vertical distance between two circuits is noted by *height*. The numerical model of the one-circuit TL or the triple-circuit TLs is identical with that of the double-circuit TLs, except a different circuit number. Consequently, the numerical models of the rest TLs are not displayed here to avoid repetition. The simulation model uses the coupled temperature and eddy-current field, where the currents are all in the *z* axis. The constant temperature boundary conditions are applied to all the exterior boundaries of the entire solution domain.

#### B. Comparison of currents under the two grounding modes

In the case study, one calculates the ampacity and circulating currents of the submarine cables at different *space* with the two-ends grounding mode and the new grounding mode. Ampacity of the submarine cable is calculated by using the subtense

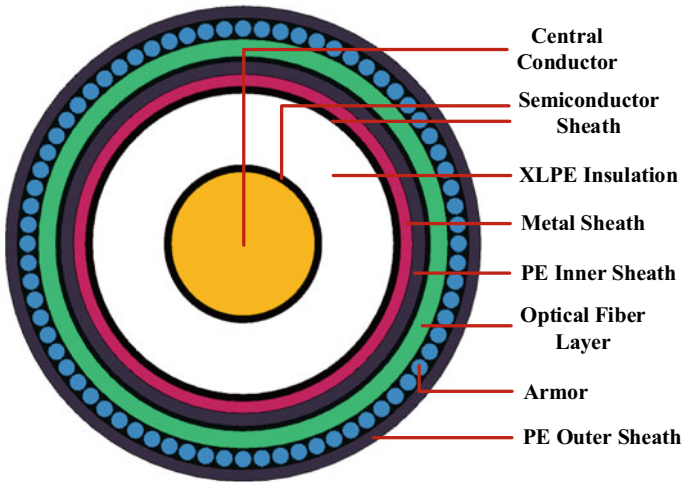


Fig. 4 Configuration of HYJQ71-F127/220 kV submarine cable

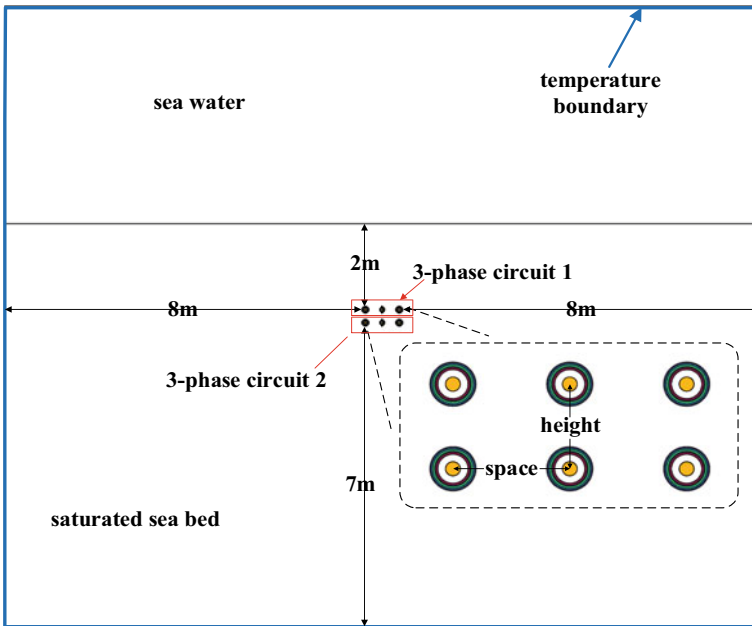
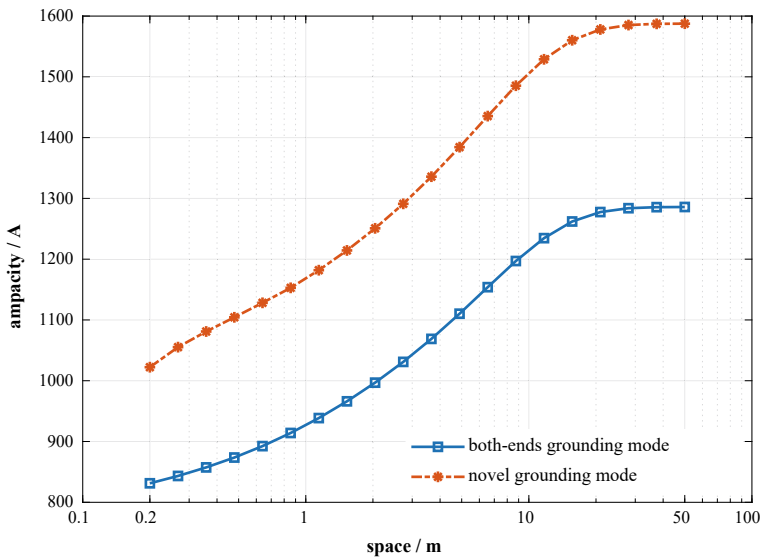
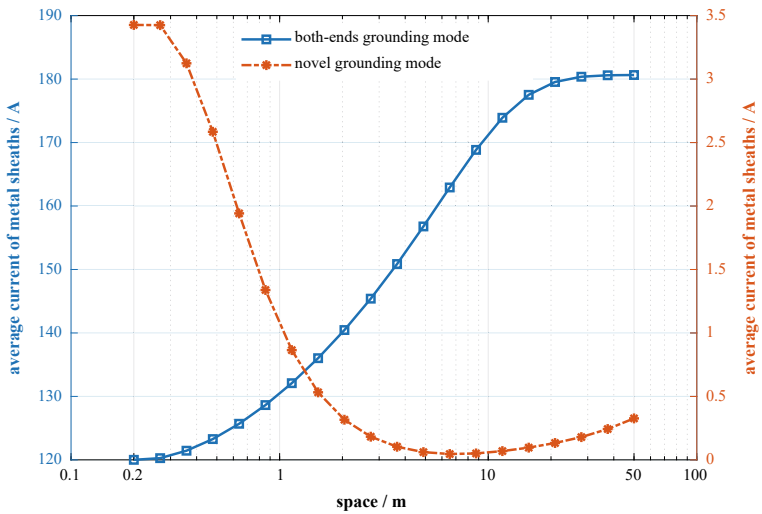


Fig. 5 Schematic diagram of the two-dimensional finite element model

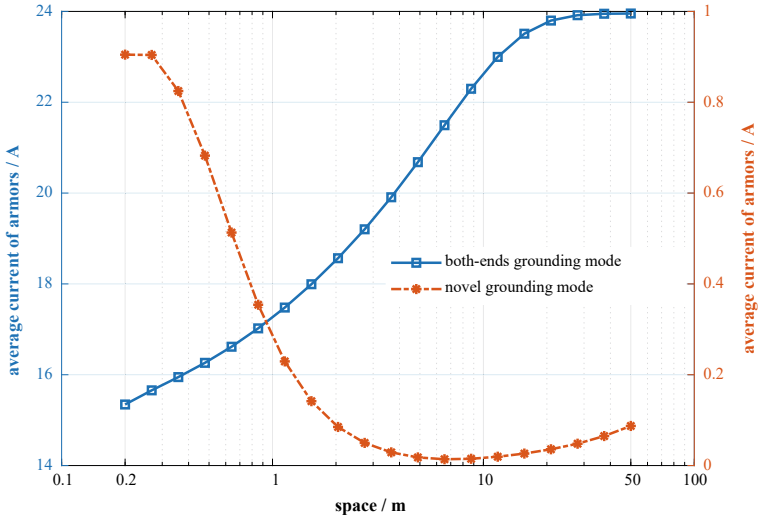
truncation approach [9]. The numerical results of the double-circuit TLs and the triple-circuit TLs are shown in Figs. 6, 7, 8, 9, 10 and 11, with *height* set to 0.5 m.



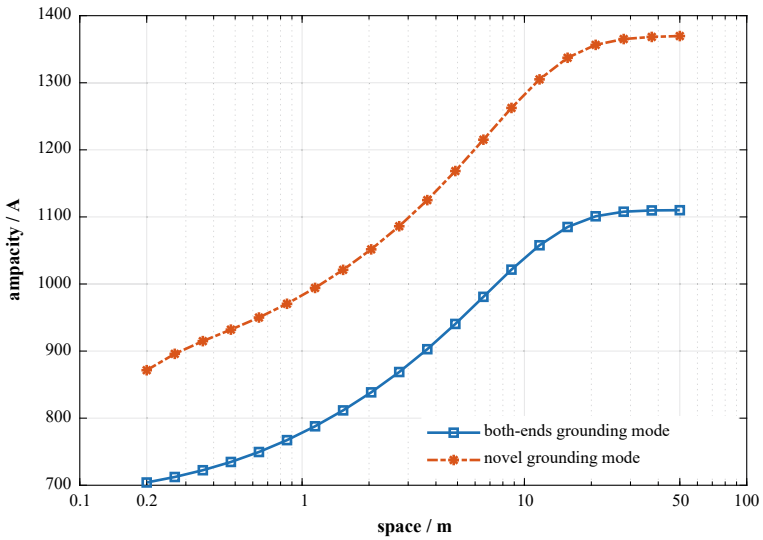
**Fig. 6** Ampacity of double-circuit TLs versus *space* under the two-ends grounding mode and the proposed novel grounding mode



**Fig. 7** Circuiting current in metal sheaths of the double-circuit TLs versus *space* under the two-ends grounding mode and the new grounding mode



**Fig. 8** Circuited current in one armor wire of double-circuit TLs versus *space* under the two-ends grounding mode and the novel grounding mode



**Fig. 9** Ampacity of triple-circuit TLs versus *space* under the two-ends grounding mode and the novel grounding mode

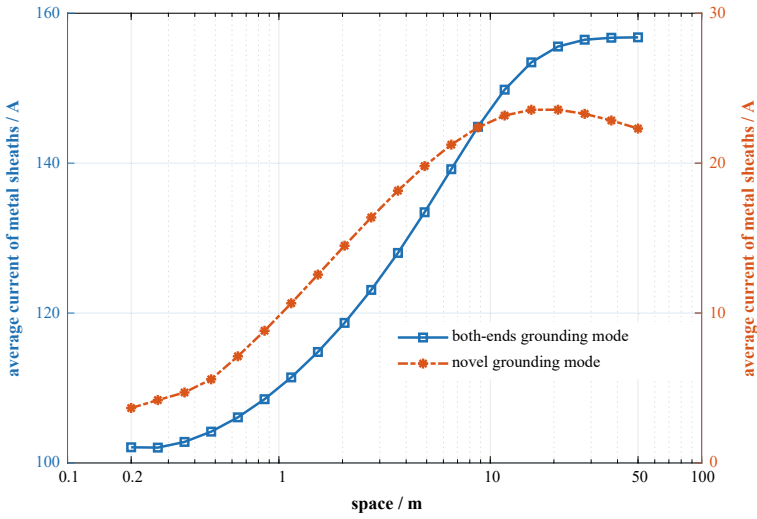


Fig. 10 Circuiting current in metal sheaths of triple-circuit TLs versus *space* under the two-ends grounding mode and the novel grounding mode

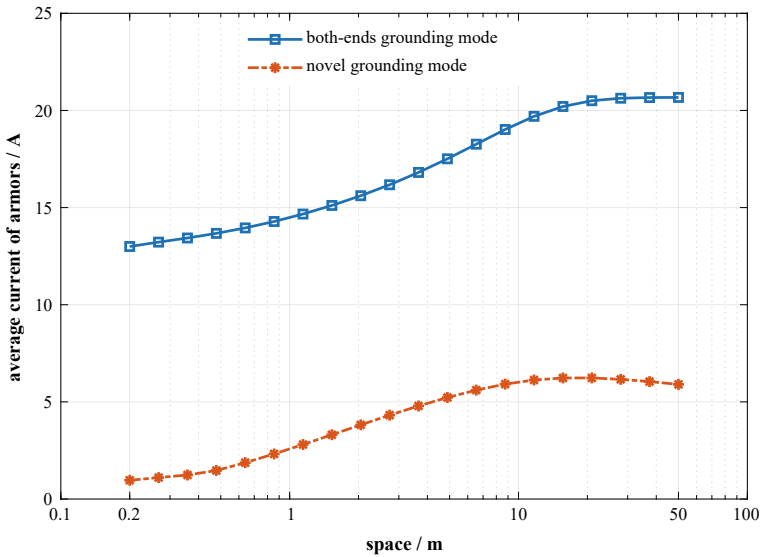


Fig. 11 Circuiting current in one armor wire of triple-circuit TLs versus *space* under the two-ends grounding mode and the novel grounding mode

It is obvious from Figs. 6 and 9 that the ampacity of submarine cables has improved remarkably. In double-circuit TLs (Fig. 6), the ampacity has increased by 262 A on average by using the proposed grounding mode, compared to two-ends grounding mode. While in triple-circuit TLs (Fig. 9), it is increased by 222 A on average. For engineering applications, the distance between adjacent cables in one circuit is usually 50 m. At this distance, the ampacity of double-circuit TLs has increased by 302 A, an increase of 23.5%. While in triple-circuit TLs, it is 260 A increased by 23.4%.

Figures 8 and 11 show the induced currents in armors versus *space*. The armor is twisted, with a different pitch of the central conductors. As a result, every armor wire will sense every side of the cable at some point along its length (cyclic even), which means that all armor wires are indistinguishable. Therefore, all wires will have to carry the same total longitudinal current. In Figs. 8 and 11, the induced current in only one wire of each armor is given, which is enough to represent the total current level in the armor. As seen from Figs. 7, 8, 10 and 11, the circulating currents in the metal sheaths and the armors all are reduced significantly under the proposed grounding mode, either in double-circuit TLs or in triple-circuit TLs. As the induced currents in the sheaths and the armors decrease sharply, the Joule losses decrease sharply too. This is the essential reason why the ampacity can increase markedly.

Numerical results of the double-circuit TLs in Figs. 7 and 8 validate the rationality of the aforementioned assumption in Sect. 2. Under the new grounding mode, the circulating currents in the metal sheaths and armors decrease with the increase of *space*. That is because, when *space* increases, the electromagnetic induction from other cables weakens, resulting it more possible that the induced EMF is produced only by its own central conductor current. According to (1), the EMF is closer to zero, leading to the reduction of the induced currents. Under the two-ends grounding mode, the circulating currents increase with the increment of *space* because the induced EMF tends to be more unbalanced. However, the numerical results of the triple-circuit TLs in Figs. 10 and 11 seem that it does not support this assumption. The induced circulating currents increase with the increment of *space* under the new grounding mode. That is because, there are three circuits interacting each other, more complex as compared to the two circuits. Under this condition, one only increase *space*, without *height*, leading to the rise of unbalanced electromagnetic induction with the increment of *space*. Nevertheless, the new grounding mode is still effective for the three circuits.

The current calculation results of the single-circuit TL are listed in Table 1, with *height* set to 0.5 m and *space* set to 50 m (the normal distance between adjacent submarine cables in the same circuit).

As Table 1 presented, the induced currents in the metal sheaths and the armors decrease dramatically, which are almost eliminated completely, and the ampacity has increased by 260 A, an increment of 19%. The calculation results verify the benefits of the proposed new grounding method.

The circulating currents in different cables are roughly similar to each other, under the same grounding mode. As a result, one calculates the average value of the circulating currents of all cables, for the convenience of comparison. Specifically,

**Table 1** Comparison of currents in single-circuit TL

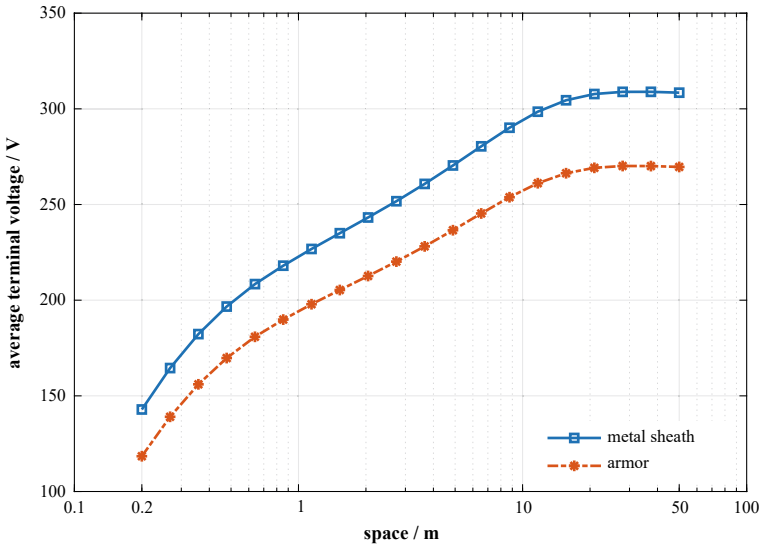
Grounding mode	Ampacity/A	Circulating current in metal sheaths/A	Circulating current in armors/A
New	1627.51	0.0104	0.0104
Two-ends	1367.42	132.65 (average)	1295.80 (average)

for the double-circuit TLs, one calculates the average induced currents of the six cables, for the triple-circuit TLs, one calculates the average induced currents of the nine cables, and for the single-circuit TL under the two-ends grounding mode, one calculates the average induced currents of three cables.

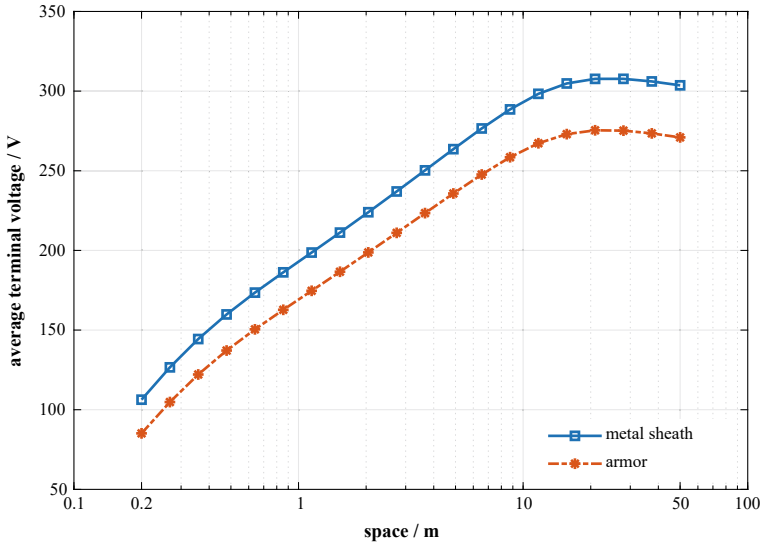
### C. Terminal voltages under the new grounding mode

In the case study, the voltages at the ends of the metal sheaths and the armors under the proposed new grounding mode are calculated, for further investigation of the performance of the proposed method. Nevertheless, in the two-ends grounding mode, the terminal voltages of the sheaths and the armors are always equal to zero. The numerical results of the terminal voltages under the new grounding mode are shown in Figs. 12, 13 and Table 2, with the cable axial length set to 1 km and *height* set to 0.5 m.

The average terminal voltage in Figs. 12 and 13 represents the average voltages on the linking wires at the TL ends, except for the wires linking to ground. As seen from Fig. 12, for a one kilometer long submarine TL system, the terminal voltage can be as high as 308.45 V in the metal sheaths and 269.65 V in the armors under

**Fig. 12** Terminal voltage in double-circuit TLs versus *space* in the new grounding mode





**Fig. 13** Terminal voltage in triple-circuit TLs versus *space* in the new grounding mode

**Table 2** Terminal voltages in single-circuit TL under the new grounding mode

Terminal ID	Terminal voltage/V
①	656.2
②	1104.5
③	1263.1
④	1104.0
⑤	628.1

The *space* is set to 50 m. The terminal ID ① to ⑤ represent the corresponding location shown in Fig. 3

the new grounding mode. While in Fig. 13, these values are 303.63 V in the metal sheaths and 270.95 V in the armors, respectively. However, for the single-circuit TL system, the new grounding mode can lead to a higher voltage level, extremely on the terminal “③”. Therefore, the proposed new grounding mode can be used only with a high insulation level, and the cable length can not be too long in case of the induced high voltages.

Although the new grounding mode will lead to a high induced voltage at the terminals under the inappropriate application, it is only for the power frequency. For operational errors and lightning strikes, high voltage will not be produced, because there are good conductive paths to the ground, not like the single-end grounding.

## 4 Conclusions

The paper proposes a novel grounding mode for submarine cables to enhance the ampacity. The specific bonding methods are discussed in details. Both the qualitative and quantitative analysis show the effectiveness of the proposed method. Moreover, the following conclusions are obtained:

- (1) The essence of the proposed new grounding mode is the cross connection of the metal sheaths and/or armors at the terminals of the transmission lines. This method can be applied either in a one-circuit submarine cable system or in a multi-circuit submarine cable system. Nevertheless, for a multi-circuit cable system, some circuits need to be phase shifted. Considering the power electronic devices have been matured in engineering applications, shifting the current phases is easy to achieve.
- (2) The proposed grounding mode can significantly suppress the circulating currents, thus obviously enhancing the ampacity of cables. The effectiveness of this method is validated by numerical results.
- (3) The proposed grounding mode will inevitably result in the rise of the terminal voltages. Consequently, this method can only be applied within the limitations of insulation grades and laying length. The proposed new grounding mode provides new ideas for upgrading the ampacity of a submarine cable.

## References

1. Duraisamy N, Gooi HB, Ukil A (2018) Ampacity estimation for HV submarine power cables installed in saturated seabed. In: Proceedings of 2018 IEEE international conference on power electronics, drives and energy systems (PEDES), 2018, pp 1–5
2. Bates C, Malmedal K, Cain D (2016) Cable ampacity calculations: a comparison of methods. *IEEE Trans Ind App* 52(1):112–118
3. Liu Y, Xiao Y, Su Y et al (2018) Loss calculation and influence on ampacity of single-core AC submarine cable under different grounding modes. *High Volt Apparatus* 54(10):0056–0062 (in Chinese)
4. Qiu H, Zheng Z, Wang J (2014) Research on sheath grounding method of AC single core submarine cable. *Southern Power Syst Tech* 8(6):62–67 (in Chinese)
5. Zhang C, Liu L, Chen J (2017) Influence of grounding mode of 110 kV submarine cable on carrying capacity and circulation. *Guangdong Elect Power* 30(8):122–127 (in Chinese)
6. Gustavsen B, Mo O (2017) Variable transmission voltage for loss minimization in long offshore wind farm AC export cables. *IEEE Trans Power Del* 32(3):1422–1431
7. Liu S, Wang X, Ning L et al (2017) Integrating offshore wind power via fractional frequency transmission system. *IEEE Trans Power Del* 32(3):1253–1261
8. Kossyvakis DN, Chrysochos AI, Pavlou K (2018) Calculation of losses in three-core submarine cables for fractional frequency transmission operation. In: Proceedings of 2018 IEEE international conference on high voltage engineering and application (ICHVE), pp 1–4
9. Liang Y, Li Y, Chai J et al (2007) A new method to calculate the steady-state temperature field and ampacity of underground cable system. *Trans China Electrotechnical Soc* 22(8):185–190 (in Chinese)

# Preparation and Anti-icing Properties of Chemically Etched Superhydrophobic Aluminum Surface



Dayou Liu , Jiaxuan Han, and Haiyun Jin

**Abstract** Ice coating on overhead transmission lines will cause line disconnection, towers falling or other accidents, which will seriously threaten the safe and steady operation of the power grid. The present anti-icing measures have disadvantages such as passive response, poor effect, and huge energy consumption. In this paper, a superhydrophobic aluminum surface was prepared by chemical etching. The surface contact angle reached  $152^\circ$ , and the rolling angle was  $3^\circ$ . There are mountain-valley rough structures on the surface, which is in Cassie contact state and makes the surface achieve superhydrophobicity status. The effects of solution concentration and etching time on the micro-morphology and hydrophobicity of aluminum surface were investigated, and the anti-icing performance of superhydrophobic aluminum surface was studied. The results show that the contact angle first increases and then decreases with the increase of solution concentration when the etching time is the same. With the increase of etching time, the contact angle first increases and then decreases, and the rolling angle first decreases and then increases. With the etching time of 1 min, the surface reached the superhydrophobic state. Under the same cold surface temperature, with the increase of surface contact angle, the solidification time of water droplets increases, and the superhydrophobic aluminum surface is in Cassie contact state, which has good anti-icing performance.

**Keywords** Transmission line · Anti-icing · Super hydrophobic · Icing characteristics

---

D. Liu · J. Han · H. Jin (✉)  
State Key Laboratory of Electrical Insulation and Power Equipment, Xi'an Jiaotong University,  
Xi'an 710049, China  
e-mail: [hyjin@xjtu.edu.cn](mailto:hyjin@xjtu.edu.cn)

D. Liu  
e-mail: [archiment@xjtu.edu.cn](mailto:archiment@xjtu.edu.cn)

J. Han  
e-mail: [hanjiaxuan@xjtu.edu.cn](mailto:hanjiaxuan@xjtu.edu.cn)

# 1 Introduction

The icing of transmission lines poses a serious threat to the safe and stable operation of the power system, but so far, the problem of icing of transmission lines is still an unsolved scientific and technological problem. In recent years, frequent meteorological activities have caused frequent extreme weather accidents such as low temperature, rain and snow, and the problem of icing in power systems has become more and more prominent [1, 2]. In the process of large-scale power grid construction, more and more “main arteries” of transmission lines will pass through areas where power grids often freeze, such as river valleys, rivers and alpine regions. The scope and influence of icing accidents on transmission lines are also gradually expanding. How the power system responds to the hazards caused by icing, reduces or even completely avoids the occurrence of icing accidents on transmission lines, and ensures safe and reliable operation under extreme weather conditions such as ice, snow, freezing rain, etc., has become an important issue to be solved urgently.

In order to reduce the damage produced by icing of overhead conductors to the power system, researchers have developed a good deal of anti-icing and deicing methods [3]. These anti-icing and deicing methods are mainly divided into four categories: thermal ice melting method, mechanical deicing method, natural passive method and other methods. However, the above method are all passive countermeasures after the transmission line has been icing, and cannot fundamentally prevent the happening of icing accidents. By structuring the surface of overhead lines can restrain the formation and growth of ice coating on transmission lines. It can fundamentally reduce or even completely avoid the occurrence of icing accidents on transmission lines, which has important application prospects [4].

In recent years, researchers from different scientific research institutions have conducted studies on super-hydrophobic surfaces to prevent surface frosting, and found that superhydrophobic surfaces can delay the frosting process on the surface and the superhydrophobic surface frost layer is relatively loose. He [5] et al. studied the frosting process of hydrophobic and superhydrophobic surfaces and found that the frosting process of superhydrophobic surfaces was delayed by 6 min than that of hydrophobic surfaces, and the frost of superhydrophobic surfaces was granular and did not form a dense frost layer. Liao [6] et al. applied a continuous chemical etching method to fabricate micro/nanostructured aluminum surface. This work showed that the as prepared aluminum surface will reduce freezing in glaze ice. After 50 min, only a few separate freezing points were created on the surface in glaze ice. However, most of the superhydrophobic surfaces that have been developed now have disadvantages such as complex technology, special equipment, and high cost. Therefore, the development of a low-cost, easy-to-prepare superhydrophobic coating is of great significance to the anti-icing of transmission lines [7, 8].

In this paper, we prepared a superhydrophobic aluminum surface by chemical etching [9, 10], and the influence of solution concentration, etching time and other factors on the microscopic morphology and hydrophobicity of the aluminum surface

was investigated. Finally, the anti-icing property of superhydrophobic aluminum surface is studied.

## **2 Experimental Section**

### **2.1 Materials**

Electrical pure aluminum wire (aluminum content above 99.6%, Far East Cable Co., Ltd., Wuxi, Jiangsu) is used as the sample in this article; hydrochloric acid (Beijing Chemical Plant); stearic acid (Tianjin Tianli Chemical Reagent Co., Ltd.); other experimental supplies are for analytical purity.

### **2.2 Sample Preparation**

The preparation process is a two-step method: the first step is constructing a suitable microscopic rough structure on the aluminum surface; the second step is to modify the low surface energy.

Firstly, the surface of aluminum sample is pretreated. The surface of electrically pure aluminum is polished by sandpaper to remove the dense oxide layer, and then ultrasonically clean it with water and absolute ethanol for 10 min to remove dirt and other impurities on the surface. Then, the pretreated aluminum surface sample is immersed in hydrochloric acid solution of different concentration and etched for a certain period of time. Finally, low surface energy modification is carried out. Measure a certain volume of ethanol solution in a beaker at 25 °C, add an appropriate amount of stearic acid to the ethanol solution, stir and prepare a 1 wt% stearic acid ethanol solution. The dried sample was immersed in a 1 wt% ethanol solution of stearic acid for 15 min, and finally dried in an oven at 90 °C.

In order to facilitate the comparative study in subsequent experiments, hydrophobic aluminum surface samples were only pretreated and modified with low surface energy, while ordinary hydrophilic aluminum surface samples were only pretreated.

### **2.3 Experiment Method**

The contact angle and rolling angle measurement system used in this paper is JC2000C4, Shanghai ZhongChen Digital Technology Equipment Co., Ltd., China. SEM (VE-9800, Keyence Co. Ltd., Japan) is used to observe the surface morphology of aluminum surface samples. In this paper, the 3D morphology of the aluminum

surface sample is investigated by 3D laser scanning microscope (VK-9700, Keyence Co. Ltd., Japan), Analysis results include surface three-dimensional color image, surface roughness, etc.

The test process of the ice coating characteristics is carried out in a room temperature environment. The specific test steps are:

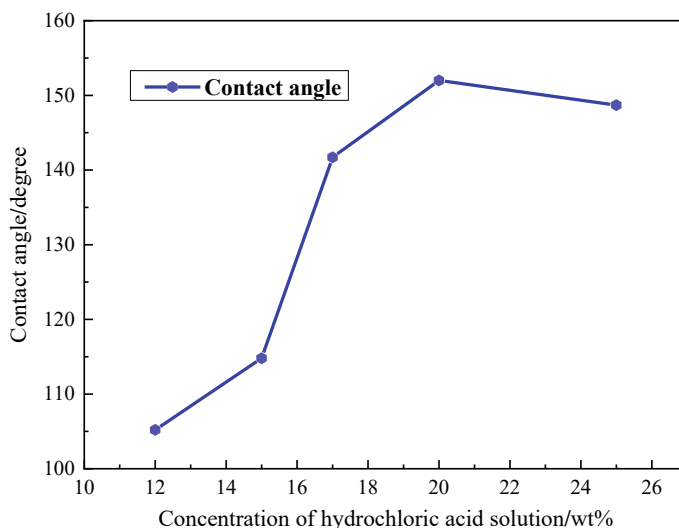
- (1) Set the environment as a dark room. Place the entire Peltier semiconductor refrigeration system in a simple studio, by adjusting the parameters of the PID control system, the chip temperature is constant ( $-5\text{ }^{\circ}\text{C} \pm 0.5\text{ }^{\circ}\text{C}$ ,  $-3\text{ }^{\circ}\text{C} \pm 0.5\text{ }^{\circ}\text{C}$  –  $1\text{ }^{\circ}\text{C} \pm 0.5\text{ }^{\circ}\text{C}$ );
- (2) Place the sample on the chip, use a micro syringe to place a certain volume of pure water on the surface of the sample;
- (3) Place the samples with different hydrophobicity on the surface of the Peltier semiconductor, and quickly place  $15\text{ }\mu\text{L}$  of water droplets on the sample surface using a micro syringe, records the microscopic water droplets' freezing process;
- (4) Import the images taken by the digital camera into the computer for analysis. At each temperature, the icing process was repeated 3 times, take the average value as the value of the water droplet solidification time of the sample.

### 3 Results and Discussion

#### 3.1 *Effect of Solution Concentration on Surface Wettability of Aluminum Surface Samples*

In order to investigate the effect of the concentration of the hydrochloric acid solution on the surface micromorphology and wettability of the aluminum surface samples, the aluminum surface samples were placed in 12, 15, 17, 20 and 25 wt% hydrochloric acid solutions etching for 1 min. The contact angle of water droplets on the surface of the sample is measured.

Figure 1 shows the relationship between the contact angle of aluminum surface and the concentration of the hydrochloric acid solution when the etching time is 1 min. From Fig. 1 can see that after etching in 12, 15, 17, and 20 wt% hydrochloric acid solution for 1 min, the contact angles of water droplets on the aluminum surface were  $105.2^{\circ}$ ,  $114.8^{\circ}$ , and  $141.7^{\circ}$  and  $152^{\circ}$ , respectively, indicating that as the solution concentration increases, the contact angle of the water droplets on the surface also increases. With 20 wt% concentration of the hydrochloric acid solution, it appears the largest contact angle of  $152^{\circ}$ , and it has reached the superhydrophobic state at this time. When the concentration of acid solution is 25 wt%, the contact angle of the sample surface drops to  $148.7^{\circ}$ . This is because as the concentration of the hydrochloric acid solution increases, the etching reaction on the surface of the aluminum surface sample is easier to proceed, so that at the same etching time, when the solution concentration is large, the surface has a rougher microscopic morphology. Therefore, the contact angle of the surface also increases. When the

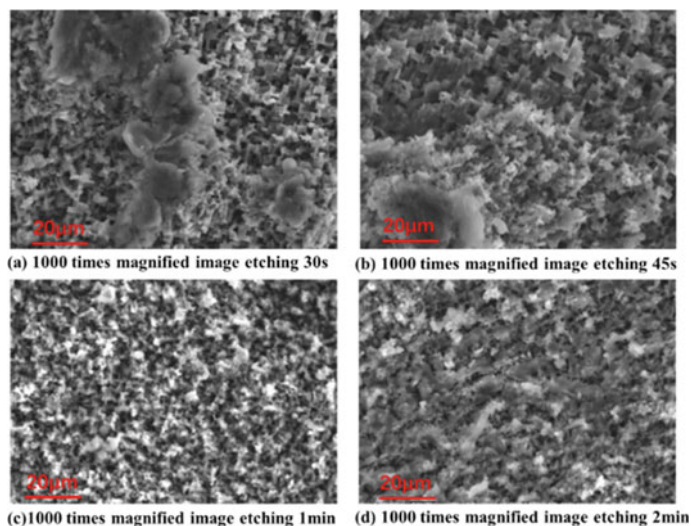


**Fig. 1** The relationship between the contact angle and the concentration of the hydrochloric acid solution

solution concentration increases to 20 wt%, the contact angle reaches the maximum. As the concentration of the hydrochloric acid solution further increases, the size of the micron rough structure on the surface increases, and the contact angle of the sample surface decreases. Therefore, the concentration of the hydrochloric acid solution used for sample preparation in this paper is 20 wt%.

### ***3.2 The Effect of Etching Time on the Surface Wettability of Aluminum Surface Samples***

Figure 2 shows the SEM pictures of the aluminum surface sample etched in 20 wt% hydrochloric acid solution for different time. When the etching time is 30 s, there are a lot of massive protrusions resembling “islands” with sizes between 100  $\mu\text{m}$  and 200  $\mu\text{m}$  on the surface. Except for these massive protrusions, there are evenly distributed block-shaped protrusions and pits on the surface. (Fig. 2a). When the etching time is extended to 45 s, the island-like protrusion structure on the surface is reduced. The block-shaped structure is increased and the size is reduced (Fig. 2b). When the etching time is extended to 1 min, the surface is evenly distributed with block-shaped protrusions and pits with a size of about 3  $\mu\text{m}$ . Due to the reduction in roughness, these building block-type structures are not so obvious. However, there are no larger island-like protrusions that appeared on the surface during 30 and 45 s etching, and there are no larger island-like protrusions (Fig. 2c), and the surface has also formed a micro-nano double composite rough structure similar to the surface of



**Fig. 2** SEM pictures of aluminum surface samples etched in 20 wt% hydrochloric acid solution for different time

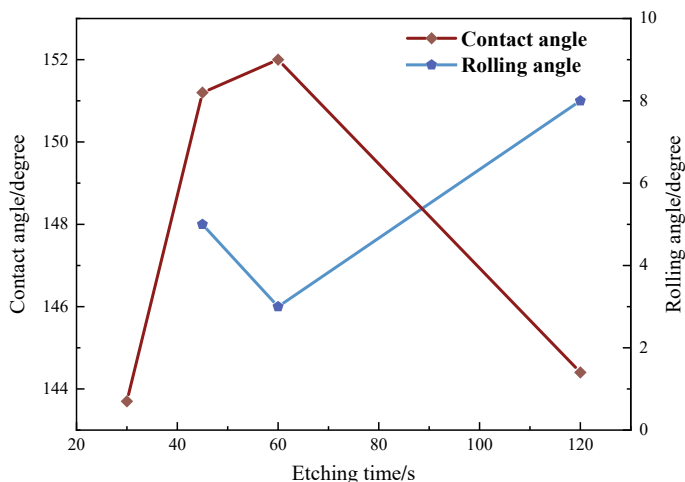
a lotus leaf. When the etching time is extended to 2 min, the surface microstructure changes a lot compared with the previous ones, and there are thin scale-like structures and sponge-like rough structures. The size of these rough structures increases to 15  $\mu\text{m}$  (Fig. 2d).

As shown in Fig. 3. The aluminum surface sample reacts violently in 20 wt% hydrochloric acid solution. The contact angle of sample surface reaches  $143.7^\circ$  after only 30 s of etching, and the contact angle exceeds  $150^\circ$  when the etching time is 45 s and 1 min. The maximum contact angle is  $152^\circ$  at 1 min. However, the contact angle decreases to  $144.4^\circ$  after the etching time is increased to 2 min.

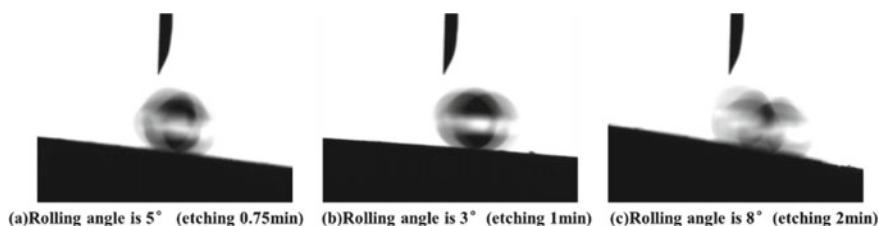
In this paper, the rolling angle of the surface is also measured. As shown in Fig. 4, when the etching time is 45 s, the rolling angle is  $5^\circ$  (Fig. 4a). The rolling angle reaches the minimum value of  $3^\circ$ . When the etching time is 1 min, the water droplets will easily roll off. (Fig. 4b). With 2 min etching time, the rolling angle is  $8^\circ$  (Fig. 4c).

Observing the relationship between the surface wettability of the aluminum surface sample in 20 wt% hydrochloric acid and the etching time, it can be found that the static contact angle of the surface first increases and then decreases with the increase of etching time. The changing law of the rolling angle of the surface is the opposite. First, it decreases with the enlargement of the etching time. After decreasing to the minimum value, the rolling angle increases with the enlargement of the etching time. The maximum value of the contact angle coincides with the minimum value of the rolling angle, which means the surface has the maximum contact angle is  $152^\circ$  when the etching time is 1 min, and the minimum rolling angle is  $3^\circ$  at the same time. The contact angle of the surface is closely related to the micro-topography of the surface, while the rolling angle of the surface is determined by the degree of





**Fig. 3** The relationship between surface wettability of aluminum surface in 20 wt% hydrochloric acid and etching time



**Fig. 4** Rolling angle of water droplets in 20 wt% hydrochloric acid solution etched on aluminum surface for different time

continuity of the gas–liquid–solid three-phase contact line on the surface. The more discontinuous the gas–liquid–solid three-phase contact line is, the smaller the rolling angle of the surface will be.

This change rule is identical with the observation results of the microscopic morphology of the sample surface. After 30 s of etching, a relatively rough structure is formed on the surface, with a large number of block-shaped structures of a few microns in size. Although the surface has a large contact angle, because the gas–liquid–solid three-phase contact line is relatively continuous, the surface has a relatively large rolling angle. When the etching time is increased to 45 s, there are only localized “islands” block protrusions on the sample surface, and the size of the “islands” block protrusions is reduced to 10  $\mu\text{m}$ . As a result, the contact angle of the surface increases, and because the three-phase contact line is discontinuous, the rolling angle drops a lot. When the etching time is 1 min, the surface has formed a composite rough structure, the water droplets appear in the Cassie contact state [11], the contact angle of the surface reaches the maximum, and the discontinuity of

the gas–solid–liquid three-phase contact line is the smallest, so the rolling angle also reached the minimum. When the etching time is 2 min, the fish scale-like structure is shaped on the surface, the contact angle will decrease with the decrease of the solid–gas area fraction, and the rolling angle will increase due to the discontinuity's increasing of its gas–liquid–solid three-phase contact line at this time.

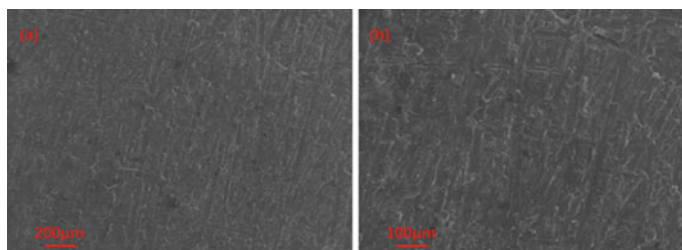
### 3.3 Microscopic Morphology and Wettability of Superhydrophobic Aluminum Surface

#### 3.3.1 Microscopic Morphology of Superhydrophobic Aluminum Surface

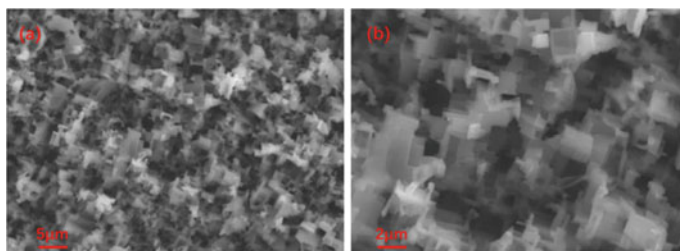
Figure 5 shows the SEM image of the ordinary aluminum surface sample after polishing. The surface of the aluminum surface sample is relatively smooth and flat, and there are many shallow parallel lines. From the pretreatment procedure, it can be judged that these lines are scratches left by polishing with sandpaper.

Figure 6 shows the SEM photo of the microstructure of the aluminum surface sample etched in 20 wt% hydrochloric acid solution for 1 min. It can be seen from the 2000 times magnification image in Fig. 6a that after etching, quite regular pits and protrusions are homogeneously allocated on the surface of the aluminum surface. The size of these regular protrusions and pits are about 3  $\mu\text{m}$ . From Fig. 6b 5000 times magnification image, we can see the stacked rough structure on the surface, and there are still sub-micron rough structures on the surface of the regular protrusions.

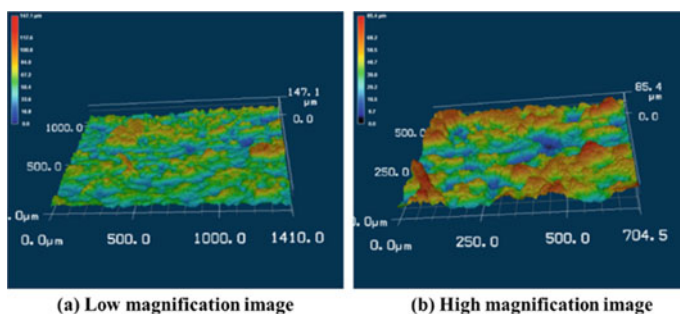
Figure 7 shows the 3D laser scanning image of the aluminum surface sample etched for 1 min in the 20 wt% hydrochloric acid solution. From the low-magnification 3D scanning photo of the aluminum surface sample in Fig. 7a, we can see that there are a large number of mountain-valley rough structures on the surface, and the height of the mountain rough structure in the measured area reaches 147  $\mu\text{m}$ . Figure 7b is a high-magnification 3D scan photo of the aluminum surface sample. The top surface of the protrusions in the picture is grainy, indicating that these protrusions are also composed of secondary rough structures.



**Fig. 5** SEM image of ordinary aluminum surface sample



**Fig. 6** SEM image of aluminum surface sample (20 wt% hydrochloric acid solution, 1 min)



**Fig. 7** 3D laser scanning image of aluminum surface sample (20 wt% hydrochloric acid solution, 1 min)

### 3.3.2 The Wettability of Superhydrophobic Aluminum Surface

The above observation shows that after etching the aluminum surface sample, a double composite rough structure similar to the surface of a lotus leaf is formed on the surface. The contact angles of ordinary and super-hydrophobic aluminum surface samples were measured. Figure 8 shows the contact angles of ordinary and super-hydrophobic aluminum samples. Aluminum material is a typical hydrophilic material. Once the water droplets touch the surface, it spreads out immediately. The static contact angle (CA) is  $82^\circ$  (Fig. 8a). The water droplets on the surface of the super-hydrophobic sample are approximately spherical and show excellent hydrophobicity. The measured CA is as high as  $152^\circ$  (Fig. 8b). The water droplets are in Cassie contact state on the super-hydrophobic surface. It can be calculated that the liquid–gas contact part of the contact interface between the water droplet and the super hydrophobic aluminum wire sample accounts for 89.7% of the entire contact area, and only 10.3% is the liquid–solid contact area, indicating that most of the contact interface of the super-hydrophobic aluminum wire sample is the liquid–gas contact part.

In addition to the contact angle, another important parameter of surface wettability is the rolling angle. For superhydrophobic surface applications in anti-icing field, in addition to having a large CA (generally required  $> 150^\circ$ ), water droplets are easily

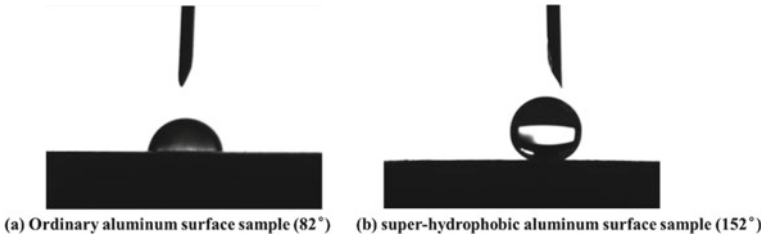


Fig. 8 Contact angle of normal and superhydrophobic aluminum surface sample

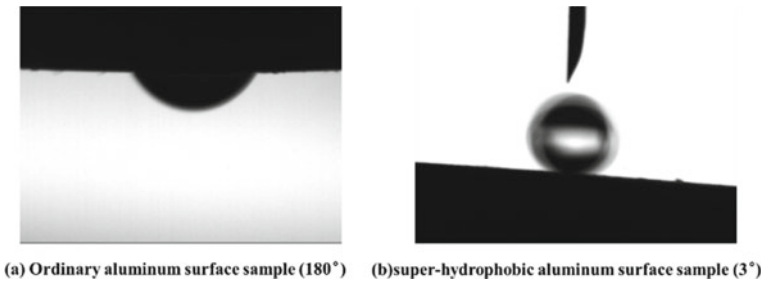


Fig. 9 Rolling angle of normal and superhydrophobic aluminum surface samples

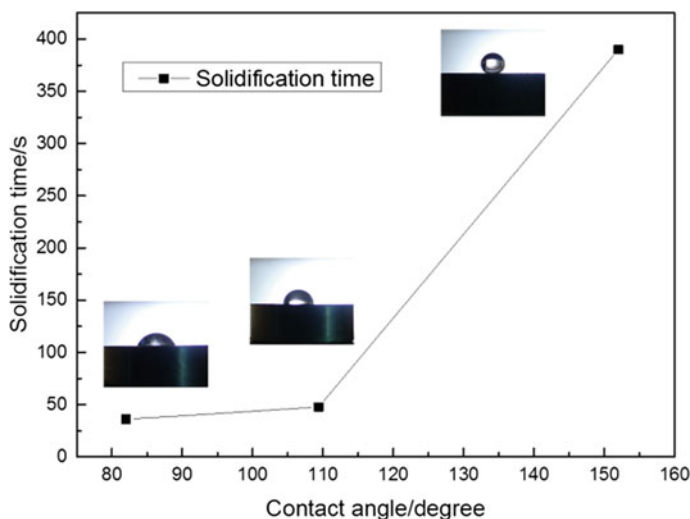
rolled on the surface without adhesion Fig. 9 shows the rolling angles of the ordinary and superhydrophobic aluminum surface samples. Although the ordinary aluminum samples are turned 180°, the water droplets are firmly attached to the surface without rolling off (Fig. 9a). When the superhydrophobic sample is tilted at a very small angle (3°), the water droplets roll off the surface (Fig. 9b).

### 3.4 Ice Coating Characteristics of Superhydrophobic Aluminum Surface

When the water droplets are placed on the cold surface with a constant temperature, the water droplets will transfer heat and freeze. This paper records the solidification time of water droplets on three typical aluminum surface samples (hydrophilic, hydrophobic, and super-hydrophobic) [12].

The water droplet is initially liquid. As shown in Fig. 10, the droplet on the surface of the hydrophilic sample is in the shape of an inverted pot. The spreading area is the largest; the water droplets on the surface of the hydrophobic sample are semicircular and the spreading area is larger; on the surface of the superhydrophobic sample, the water droplets are approximately spherical and the spreading area is the smallest.

As shown in Fig. 10, the relationship between the average of solidification time and the contact angle in the repeated 3 sets of experiments (the temperature of the



**Fig. 10** The relationship between solidification time and contact angle (cold surface temperature is  $-3\text{ }^{\circ}\text{C}$ )

cold surface is  $-3\text{ }^{\circ}\text{C}$ ), it can be seen that the solidification time of the hydrophilic aluminum sample surface and the hydrophobic aluminum sample surface are 36 s and 47.7 s respectively. While the solidification time of the superhydrophobic aluminum sample surface is 6min30s, which is 10.8 times and 8.2 times that of the hydrophilic aluminum sample and the hydrophobic aluminum sample, respectively. The superhydrophobic surface greatly delays the freezing process of water droplets on its surface and shows excellent anti-icing performance.

The above results indicate that the contact angle directly affects the freezing process of water droplets. For hydrophilic and hydrophobic surfaces, both the water droplet and the surface are in Wenzel contact state. However, as the large contact angle of the hydrophobic surface, the contact area between the water droplet and cold surface is reduced. Since the heat transfer rate is proportional to the contact area between the droplet and the cold surface, the solidification time of the hydrophobic surface is slightly delayed than that of the hydrophilic surface. For superhydrophobic surfaces, the water droplets are approximately spherical on the surface, and the contact part between the droplets and the cold surface is much smaller than the other two surfaces. In addition, the vertical height of water droplets on the superhydrophobic surface is greater than that of the other two surfaces, which means that the solidification process has a longer distance to reach the top. Meanwhile, the surface of the water droplet and the superhydrophobic sample is in a Cassie contact state, and there is a large amount of air film at the contact interface. This air film acts as an energy barrier, greatly delaying the heat exchange process between water droplets and the surface, so the solidification time of droplets on superhydrophobic surfaces is much longer than that on hydrophilic and hydrophobic surfaces.

## 4 Conclusion

- (1) In this paper, a superhydrophobic aluminum surface was prepared by chemical etching. The contact angle of the surface is  $152^\circ$ , the rolling angle is  $3^\circ$ , and the surface is distributed with a large number of mountain-valley rough structures, showing a Cassie contact state, reaching a superhydrophobic state.
- (2) Under the same etching time, the contact angle of the aluminum surface increases with the solution concentration, and the contact angle first increases and then decreases. When the concentration of the hydrochloric acid solution is 20 wt%, the surface contact angle reaches the maximum value of  $152^\circ$ . The contact angle of aluminum surface first increases and then decreases with the extension of etching time. The rolling angle first decreases and then increases. The maximum value of the contact angle and the minimum value of the rolling angle coincide, and the aluminum surface reaches a superhydrophobic state at this time.
- (3) Under the same temperature conditions, the solidification time of the water droplets on the cold surface increases with the increase of the contact angle. When the temperature of the cold surface is  $-3^\circ\text{C}$ , Because the surface of superhydrophobic aluminum is in Cassie contact state, the contact part between the water droplet and the surface is small, the distance traveled by the solidification process to the top is longer, and the air film between the water droplet and the surface greatly delays the heat exchange between the water droplet and the surface. Therefore, the solidification time of the water droplets on the superhydrophobic surface is much longer than that of the hydrophilic and hydrophobic surfaces. The solidification time of the superhydrophobic surface is 10.8 times and 8.2 times that of the hydrophilic surface and the hydrophobic surface, respectively, showing good anti-icing properties.

**Acknowledgements** This research is supported by the National Natural Science Foundation of China [grant number 52272073].

## References

1. Li B, Bai J, He JH, Ding C, Dai X, Ci WJ, Zhu T, Liao RJ, Yuan Y (2013) A review on superhydrophobic surface with anti-icing properties in overhead transmission lines. *Coatings* 13(2)
2. Dong BB, Jiang XL, Yin FH (2022) Development and prospect of monitoring and prevention methods of icing disaster in China power grid. *IET Gener Transm Distrib* 16(22):4480–4493
3. Fan B, Zhou LX, Tian Z (2013) The study on factors influencing the ice-melting performance of transmission line. In: *Book the study on factors influencing the ice-melting performance of transmission line 2013*, edn. pp 710–713
4. Li W, Zhan YL, Yu SR (2021) Applications of superhydrophobic coatings in anti-icing: theory, mechanisms, impact factors, challenges and perspectives. *Prog Org Coat* 152

5. He M, Wang JX, Li HL, Jin XL, Wang JJ, Liu BQ, Song YL (2010) Super-hydrophobic film retards frost formation. *Soft Matter* 6(11):2396–2399
6. Liao RJ, Zuo ZP, Guo C, Yuan Y, Zhuang AY (2014) Fabrication of superhydrophobic surface on aluminum by continuous chemical etching and its anti-icing property. *Appl Surf Sci* 317:701–709
7. Wang N, Wang Q, Xu SS (2022) A review on applications of superhydrophobic materials in civil engineering. *Adv Eng Mater* 24(6)
8. Liu WL, Wang SR, Wang GQ, Zhang JP, Zhou C (2022) Investigation on the differences of surface cleaning properties of series of superhydrophobic aluminum alloys. *Colloids Surf A* 651
9. Esmaeilirad A, Rukosuyev MV, Jun MBG, van Veggel F (2016) A cost-effective method to create physically and thermally stable and storable super-hydrophobic aluminum alloy surfaces. *Surf Coat Technol* 285:227–234
10. Li YF, Jin HY, Nie SC, Zhang P, Gao NK (2017) Dynamic behavior of water droplets and flashover characteristics on a superhydrophobic silicone rubber surface. *Appl Phys Lett* 110(20)
11. Liu HD, Liu DY, Li PH, Zeng YJ, Jin HY (2023) Direct observation of the wetting state of Cassie and Wenzel. *Mater Lett* 340
12. Mishchenko L, Hatton B, Bahadur V, Taylor JA, Krupenkin T, Aizenberg J (2010) Design of Ice-free nanostructured surfaces based on repulsion of impacting water droplets. *ACS Nano* 4(12):7699–7707

# Research on High Voltage Pulse Ice-Breaking Technology



Yue Yu, Jiaxuan Zheng, Mingxin Zhang, and Zhiye Du

**Abstract** Ice covering of transmission lines may cause mechanical damage to equipment, including fixtures, conductors, poles and towers, and even lead to serious accidents such as tripping of lines, power failure, burning of wires, and collapse of poles and towers. This paper presents a high voltage pulse ice-breaking technique. The high voltage pulse acts on the ice accumulation covering on transmission lines, breaking down the ice from the inside, forming a high pressure, high temperature plasma channel, and finally breaking the whole ice. In this paper, a high voltage pulse ice-breaking model is constructed based on the structural characteristics of typical transmission line glaze ice and the three-dimensional transient electric field simulation is carried out. The results show that under certain pulse excitation conditions, the bubbles in the ice will be broken down, and the closer the bubbles are to the ice surface, the easier the bubbles will be broken down. The electric field inside the bubbles has the same trend with time, and the electric field intensity increases uniformly with the increase of excitation intensity. This study can provide a reference for the research of power line energy saving and ice breaking.

**Keywords** High voltage pulse · Plasma · Ice covering · The rime · Bubble · Breakdown field strength

## 1 Introduction

For transmission line de-icing, traditional deicing methods mainly include mechanical method and thermal method, while new deicing methods mainly include laser deicing and electric pulse deicing (EIDI). Among them, the energy efficiency of mechanical deicing is only 3–4%, and it costs manpower and material resources. Thermal deicing involves a large-scale power outages and line transformation, which is not conducive to the stable operation of the power grid. Laser ice breaking is limited

---

Y. Yu (✉) · J. Zheng · M. Zhang · Z. Du

School of Electrical Engineering and Automation, Wuhan University, Wuhan, China

e-mail: [2021302191414@whu.edu.cn](mailto:2021302191414@whu.edu.cn)

© Beijing Paiké Culture Commu. Co., Ltd. 2024

X. Dong and L. Cai (eds.), *The Proceedings of 2023 4th International Symposium on Insulation and Discharge Computation for Power Equipment (IDCOMPU2023)*, Lecture Notes in Electrical Engineering 1103, [https://doi.org/10.1007/978-981-99-7413-9\\_3](https://doi.org/10.1007/978-981-99-7413-9_3)

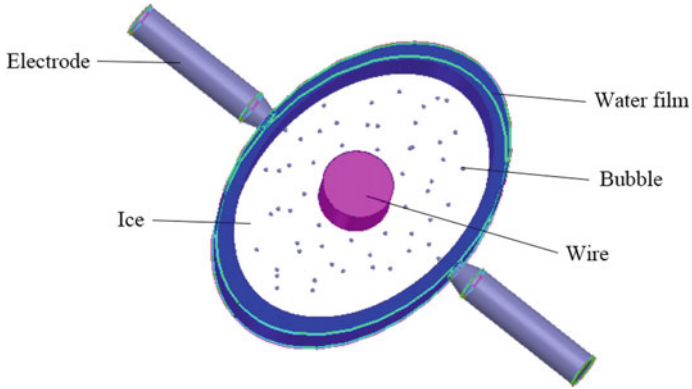


by laser development level and high cost. In addition, EIDI deicing method uses electromagnetic force to shock deicing, which is easy to cause wire shock. In conclusion, the existing deicing methods have certain effects, but there are obvious shortcomings. Therefore, it is necessary to find a more efficient, energy-saving, safe and reliable deicing method [1].

Inspired by the high voltage pulse lithotripsy technology, this paper chooses to study the high-pressure pulse ice-breaking technology. High voltage pulse ice-breaking technology is the high voltage pulse generated by the strong electric field on the surface of the ice, when the electric field intensity reaches a certain value, there will be a discharge phenomenon, so that the ice internally breakdown. A large amount of energy will be released in a short time, so as to form a high pressure, high temperature plasma channel, resulting in ionization of ions in the air, free electrons, water molecules. This process produces a lot of gas and energy, and the bubble expands rapidly, causing the ice from the inside out under enormous stress and split instantly. At the same time, chemical reactions and other changes in the substance will be promoted by the high pressure and high temperature generated in the process of electric breakdown. These combined effects generate electrical and thermal stress in the plasma channel, which causes the ice to break off [2–11].

## 2 Simulation Model Construction

This paper conducts simulation experiments on ice-breaking model based on the three-dimensional transient electric field to explore the conditions of ice-breaking under the action of high voltage pulse. The common form of ice accumulation will transition from crescent shape and fan shape to the oval shape with the increase of freezing rain time. Therefore, the ice accumulation model with oval section is built to represent the general state of ice accumulation. The average thickness of ice sheet is 17.8 mm and the average thickness of surface water film is 2 mm. The actual volume of bubbles in the ice accumulation is small, which is not easy to calculate and observe. Therefore, a spherical bubble is established during modeling and the diameter of the bubble is increased to 0.6 mm, which is equivalent to merging some relatively close tiny bubbles. Due to uneven ice cover in practice, the center of the wire is set slightly away from the center of ice accumulation. A pair of high-voltage electrodes are sandwiched on the thinner sides of the ice sheet, and the heads of the electrodes are inserted into a film of water. The region boundary is drawn outside the model, and the electric field even symmetric boundary is used to simulate the infinite length wire. The overall model and the electrode amplification model are shown in Figs. 1 and 2, and the model size and material properties are shown in Tables 1 and 2, respectively [12–15].



**Fig. 1** Three-dimensional rime icing model

**Fig. 2** Electrode model



**Table 1** Structural dimensions of each part of the model

Structure name	Geometry size
Wire	Diameter: 10 mm
Ice	Short axis radius: 15 mm; Centrifugal rate: 1.5
Water film	Short axis radius: 17 mm; Centrifugal rate: 1.5
Bubble	Radius: 0.3 mm
Electrode head round	Base diameter: 2 mm; Height: 5 mm
Electrode tail cylindrical	Bottom diameter: 4.8 mm; Height: 20 mm

**Table 2** Structural material properties of each part of the model

Structure name	Material	Relative permittivity	Electrical conductivity(Se/m)
Wire	Copper	1	58,000,000
Electrode	Copper	1	58,000,000
Water film	Water fresh	81	0.01
Ice	Ice	4	0.001
Bubble	Air	1.0006	0

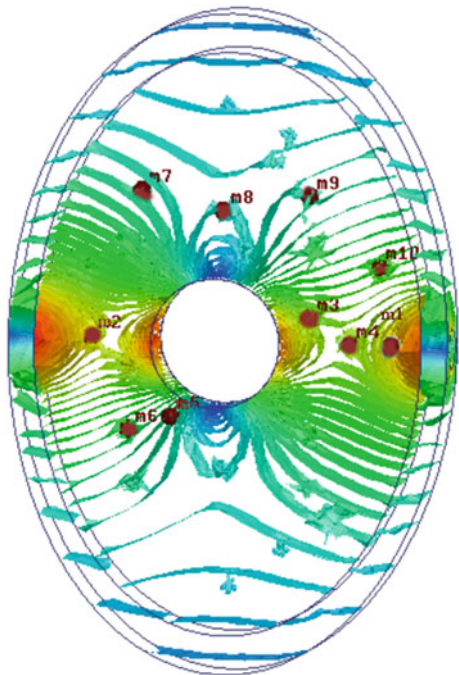
### 3 Simulation Results and Analysis

By observing whether the bubble field strength inside the ice accumulation is greater than the air breakdown field  $E_0$  (select  $E_0 = 3 \times 10^6$  V/m), we can determine whether the ice breakdown occurs. The center of the bubble sphere was selected as the observation point, and the influence of excitation intensity, bubble position, pulse rising edge, electrode position and ice accumulation shape on the electric field intensity of the observation point was investigated by the control variable method.

#### 3.1 Selection of Observation Points

Electrodes are placed on both sides of the short axis of ice accumulation with elliptical section. The Angle between the electrodes is  $\theta = 180^\circ$ , and  $t_r = 250$  ns is the rising edge of pulse excitation. Change the pulse peak voltage  $U$ ,  $U = 30, 50, 70, 90, 110, 130, 150$  kV, and make seven groups of experiment. The simulation results show that the electric field distribution in the ice is roughly the same under the 30–150 kV high voltage pulse excitation, only the values are different. Therefore, the electric field nephogram under 150 kV was selected for overall analysis, as shown in Fig. 3.

**Fig. 3** Electric field nephogram and observation point distribution under 150 kV pulse excitation



As can be seen from Fig. 3, the electric field intensity near the electrode line is the largest, and decreases rapidly to both sides. The intensity of the electric field far away from the electrode line is smaller than that far away, and the attenuation rate is slower. In addition, both the bubbles inside the ice accumulation and the central wire will affect the electric field distribution, and the electric field around the bubbles will be distorted, and the electric field intensity is relatively large. As the electric field intensity near the electrode line is large, it is easy to reach the bubble breakdown field strength. Therefore, a total of 10 bubble sphere centers from  $m_1$ - $m_{10}$  are selected in this area as electric field observation points. If all observation points are broken down, the internal pressure field after the breakdown of bubbles can promote the formation of plasma channels in the ice accumulation, that is, the main discharge channel through the ice can be formed near the electrode.

### ***3.2 Influence of Excitation Intensity on Electric Field Intensity of Observation Points***

The maximum  $E_{\max}$  of field intensity at each observation point in the above seven groups of experiments was recorded during each excitation application process. It was found that only under pulse excitation of  $U = 150$  kV, the  $E_{\max}$  of observation point exceeded the air breakdown field intensity  $E_0$ , so the critical voltage of breakdown could be judged to be around 150 kV. The  $U = 145$  kV experiment is further conducted, and it is found that there are observation points  $E_{\max} < E_0$ . It can be considered that the critical breakdown voltage of ice block under this experimental condition is 150 kV. Further analysis shows that the critical breakdown voltage of each observation point is different, and the observation point near the electrode is more likely to be broken down. According to the breakdown difficulty of different bubbles, the extension process of the main discharge channel of plasma can be roughly simulated, as shown in Fig. 4.

### ***3.3 Effect of Pulse Rising Edge on Electric Field Intensity at Observation Points***

The experimental conditions were set as the reference group  $S_0$ , where the electrodes were placed on both sides of the short axis of the ice accumulation with oval section, the Angle between the electrodes  $\theta = 180^\circ$ , the pulse excitation rising edge  $t_r = 250$  ns, and the peak voltage  $U_0 = 150$  kV. The time variation curve of electric field intensity  $E$  at the observation point under the condition of  $S_0$  is made, as shown in Fig. 5. It can be seen that the electric field intensity increases almost uniformly during the pulse rise, and the electric field increases at different positions.

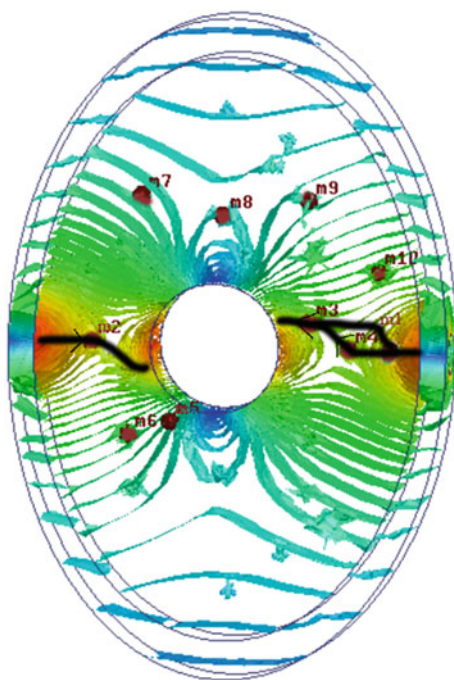


Fig. 4 Oval-section ice-covered plasma main discharge channel

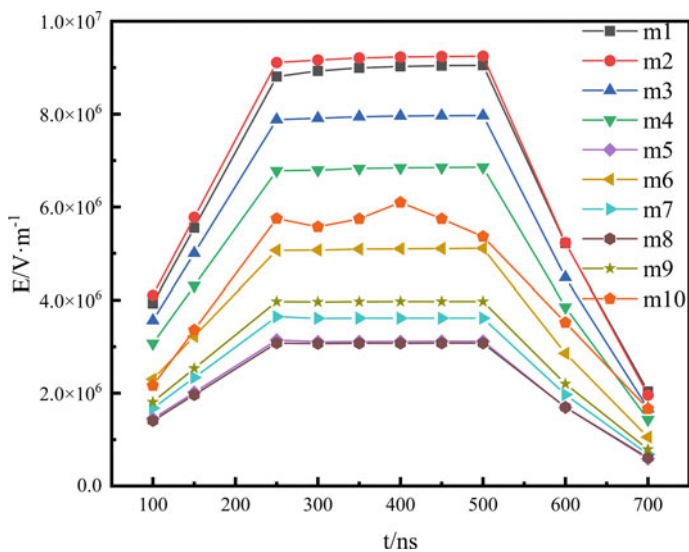
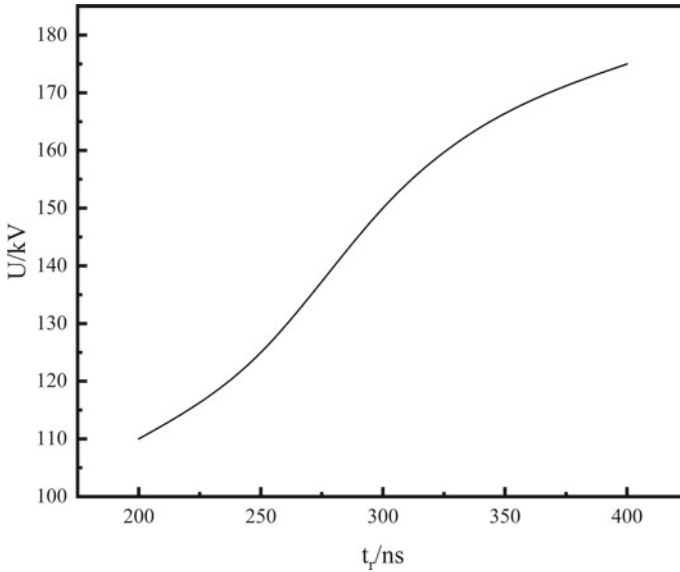


Fig. 5 Time variation curve of electric field intensity at observation point under  $S_0$  condition

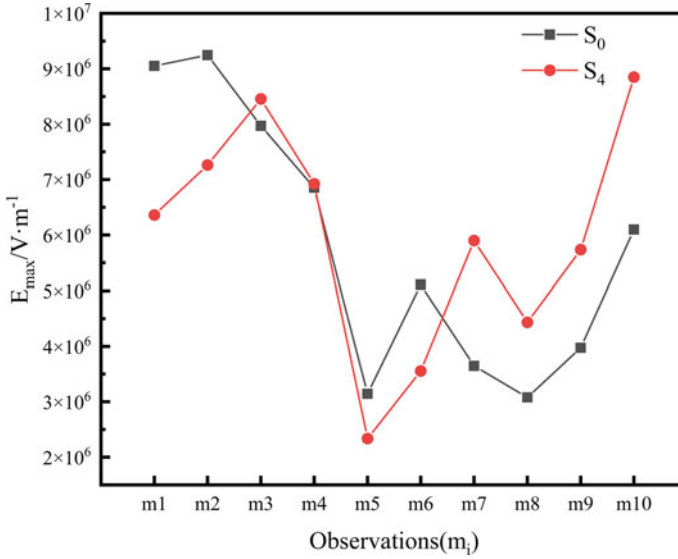


**Fig. 6** Curve of critical breakdown voltage with rising edge of pulse

Next, the influence of different pulse rising edges on the critical breakdown voltage of ice accumulation is explored. Set  $t_r = 200, 300, 400$  ns in the reference group, set the experimental group  $S_1-S_3$ , and make  $U_{min}-t_r$  curve of critical breakdown voltage  $U_{min}$  with  $t_r$  of pulse rising time, as shown in Fig. 6. As can be seen from Fig. 6, as the rising edge of pulse slows down, the critical breakdown voltage of ice accumulation increases, that is, the ice is more difficult to break down. This is because the shorter the pulse rising edge, the greater the induced voltage change rate, resulting in a stronger electric field, easy to lead to bubble breakdown.

### 3.4 Influence of Electrode Position on Electric Field Intensity of Observation Points

The electrode position will affect the position of the main discharge channel and the critical breakdown voltage. In order to find the most efficient and energy-saving icebreaking method, the electrode position is changed for experiments. The ice accumulation at the lower end of the oval section ice cover is thin, but the ice cannot fall off after breakdown, so the electrode clamping at the upper and lower ends is of little significance. The base group clipped the electrode on the middle axis of the ice accumulation, where the thickness was the largest but closest to the wire, and the ice accumulation could fall off after breakdown. If the electrode is adjusted in a position slightly inclined relative to the ice accumulation axis, and the Angle between the



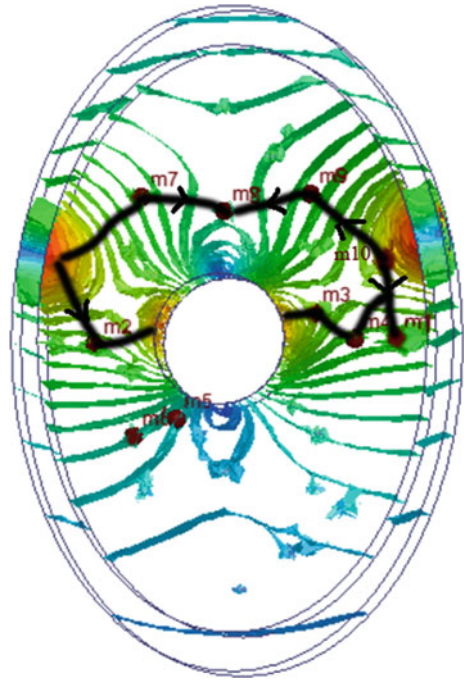
**Fig. 7**  $S_0$  and  $S_4$  under the conditions of the maximum electric field intensity image

electrodes is  $\theta < 180^\circ$ . The thickness here is thin, but it is also slightly far from the wire. It is necessary to judge the difficulty of breakdown.

According to the above analysis, the electrode position of the reference group  $S_0$  was set to change, and the experimental group  $S_4$  was set. The simulation calculation found that under this condition, all the bubbles at the observation point could still be broken down, and the observation points could not be broken down when the voltage was reduced to 145 kV. Therefore, the critical breakdown voltage of  $S_4$  was still about 150 kV. In order to further find the law,  $E_{\max}$ - $m_i$  image curve of maximum electric field intensity of each observation point in groups  $S_0$  and  $S_4$  was made for comparison, as shown in Fig. 7.

As can be seen from Fig. 7, the field intensity of  $m_7$ - $m_{10}$  group  $S_4$  is greater than that of group  $S_0$ , because the four observation points are roughly distributed on the electrode head line of group  $S_4$ , and the electric field intensity of the two groups of  $m_4$  almost coincides, because the electrode distance between  $m_4$  and the two groups is almost equal. Thus, the main discharge channel under  $S_4$  conditions can be simulated, as shown in Fig. 8. It is found that the distance between the discharge channel and the surface of the wire is much farther than that of group  $S_0$ , so the ice is not easy to fall off. In conclusion, the electrode position of the reference group  $S_0$  is more appropriate.

**Fig. 8** S<sub>4</sub> Simulated plasma main discharge channel

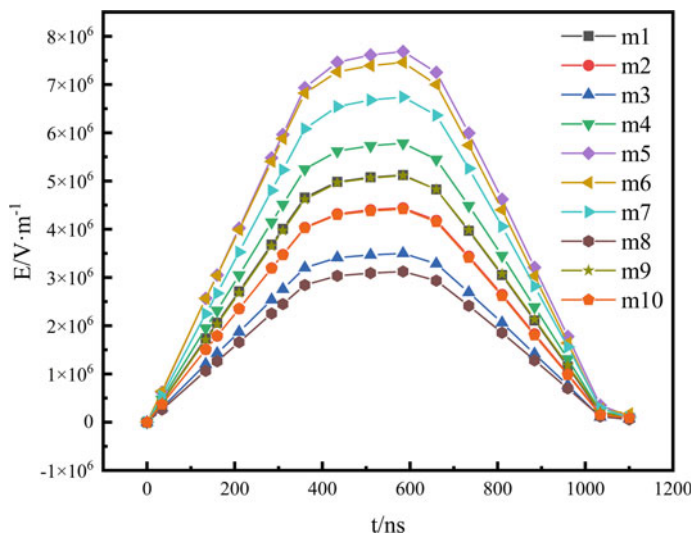


### 3.5 Research on Breakdown Conditions of Crescent-Shaped Ice Accumulation Observation Points

As ice accumulation with crescent section often occurs in nature, the breakdown conditions of ice accumulation with crescent section will be explored next. A crescent-shaped model was constructed, and the conclusions obtained from ice accumulation in oval section were applied. Experimental group S<sub>5</sub> was set: electrode position was close to the wire, and pulse rising time  $t_r = 400$  ns. Crescent-shaped ice deposits usually occur at the beginning of freezing rain and are therefore smaller in size. Ten observation points from  $m_1$  to  $m_{10}$  were set, and the critical breakdown voltage was 40 kV by changing the peak pulse voltage  $U$ .

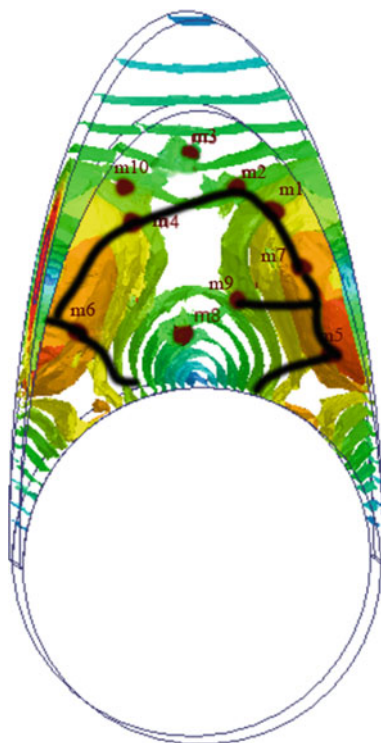
Curve E-t of electric field intensity at each observation point changing with time under the condition of  $U = 40$  kV is made, as shown in Fig. 9. Compared with Fig. 5, it can be seen that the electric field intensity of the observation points with crescent-shaped section and elliptic section is consistent with the pulse waveform, while the curve shape is slightly different. In addition, the electric field intensity of different observation points in the crescent section can be compared, so as to predict the breakdown difficulty and sequence of each bubble, and simulate the main discharge channel, as shown in Fig. 10.





**Fig. 9** S<sub>5</sub> Electric field intensity curve with time

**Fig. 10** Crescent model simulates the main discharge channel of plasma



## 4 Conclusion

The following conclusions can be drawn through the simulation experiment of the high voltage pulse ice-breaking process:

- (1) The electric field intensity in the bubble near the electrode line is the largest, and the field intensity decreases rapidly away from the electrode. The electric field distribution will be affected by the bubbles inside the ice accumulation and the central wire, and the electric field around the bubbles will be distorted, and the electric field intensity is large. It is inferred that the main plasma discharge channel in the ice accumulation should extend from the bubble near the electrode.
- (2) The rising edge of pulse voltage has great influence on the critical breakdown field strength of ice accumulation. When keeping the voltage peak constant by changing the rising edge time appropriately ( $0 < t_r < 500$  ns), it is found that the shorter the rising edge time is, the greater the change rate of induced voltage, the greater the strength of the electric field in the bubble, and the easier to achieve breakdown.
- (3) Electrode position will affect the breakdown degree of ice accumulation. The electrode is relatively clamped in the middle of the oval section of the ice accumulation, and the position closest to the inner wrapped wire is the easiest to achieve the ice shedding.
- (4) After the pulse voltage excitation with the same waveform is applied to the crescent-section ice accumulation and oval section ice accumulation, the variation trend of the internal bubble electric field intensity is roughly the same, and the critical breakdown voltage is different due to the difference of ice thickness.

## References

1. Wang D, Zhou C, Ma Y et al (2022) Study on ice cover of overhead power lines. *Electr Technol* 2022(7):76–80, 84 (in Chinese)
2. Zhang Z, Pei Y, Liu Z et al (2012) Experimental study on rock breakdown characteristics under high pressure short pulse. *High Voltage Eng* 38(7):1719–1725 (in Chinese)
3. Zhang D, Zhu J, Liu W et al (2016) Lithotripsy mode of solid-liquid interface discharge of coaxial electrode. *High Voltage Engineering* 42(12):3753–3757 (in Chinese)
4. Zheng J, Wei Y (2021) Multi-dimensional evaluation of icing state of transmission lines and insulators in natural environment. *Comput Simul* 38(1):88–91 + 186 (in Chinese)
5. Liu C, Liu J (2011) Icing mechanism of transmission line conductor and icing model of rain frost. *High Voltage Eng* 37(1):241–248 (in Chinese)
6. Huang G (2013) Study on high voltage pulse discharge crushed rock. Huazhong University of Science and Technology, Hubei. <https://doi.org/10.7666/d.D410748> (in Chinese)
7. Che L Gu X, Li H (2021) Numerical simulation of high-voltage pulse discharge based on crushed hard rock. *J Nanjing Univ Sci Technol* 45(5):521–528 (in Chinese)
8. Lisitsyn IV, Inoue H, Katsuki S, Akiyama H (1999) Use of inductive energy storage for electric pulse destruction of solid materials. *IEEE Trans Dielectr Electr Insul* 6(1):105–108

9. Satoshi Ihara, Yuichi Kominato, Kazuyuki Fukuda et al (2014) Dependence of generator parameters on pulsed power ice breaking. *Electr Eng Japan* 186(2):1–9
10. Ihara S, Yamabe C (2003) Breaking of ice sheets using shock waves produced by pulsed power. *Japan J Appl Phys* 42(Part 2, No. 5A):L489–L490
11. Vazhov VF, Gafarov RR, Datskevich SY et al (2010) Electric-pulse breakdown and the breakage of granite. *Tech Phys* 55(6):833–838
12. Sun J (2009) Simulation study on icing disaster of high-voltage transmission line—dancing finite element analysis based on ANSYS. *China University of Geosciences (Wuhan), Hubei* (in Chinese)
13. Zhou C, Huang D, Sun Z (2022) Research progress on icing process and typical dancing characteristics of high-voltage transmission line[J]. *Southern Power Grid Technol* 16(05):134–144
14. Zhou C, Chao M (2023) Calculation of three-dimensional time-varying ice accumulation of overhead transmission wires. *J Harbin Inst Technol* 55(01):116–124 (in Chinese)
15. Lou W, Bai H (2022) Study on wind load increase coefficient of conductor with various iced shapes. *High Voltage Apparatus* 58(10):8–15 (in Chinese)

# Design and Implementation of Electric Field-Induction Based Energy Harvesting System for High Voltage Power Transmission Lines



Yan Jiang, Zheng Zhou, Zhifeng Sun, Wentao Liu, Lei Tao, Xuanan Song, and Xingran Gao

**Abstract** High-voltage transmission line online monitoring device can effectively promote the safety and stability of the power system, thus acting as an important part of the smart grid. However, for practical applications, the power supply problem is always the key limitation that restricts the development of online monitoring device. To provide stable and reliable power supply to the online monitoring devices, a space energy harvesting system based on the electric field induction is proposed to pick up power from the high voltage (HV) electric field around the transmission lines. Firstly, the system structure is demonstrated, with the analysis of the system's working principles. Then, the coupling plates for space energy harvesting is optimized, with the use of frame-shaped plates to seek a balance between the power level and the system sizes. Furthermore, based on the system's quasi-current source characteristics, a DC/DC converter is designed to notably improve the output power level. Finally, with respect to the discontinuous power demand of the on-line monitoring device, a hysteresis discharge mechanism is designed. Both the theoretical and the experimental results show that the system is able to output more than 25mW

---

Y. Jiang · Z. Zhou · Z. Sun · L. Tao · X. Song  
Information and Communication Company, Hubei Electric Power Co., Ltd., State Grid,  
Wuhan, Hubei, China  
e-mail: [15827718@qq.com](mailto:15827718@qq.com)

Z. Sun  
e-mail: [szf618@163.com](mailto:szf618@163.com)

X. Song  
e-mail: [2702877914@qq.com](mailto:2702877914@qq.com)

W. Liu  
Xiangyang Power Supply Company, State Grid, Xiangyang, Hubei, China  
e-mail: [405626460@qq.com](mailto:405626460@qq.com)

X. Gao (✉)  
School of Electrical Engineering and Automation, Wuhan University, Wuhan, Hubei, China  
e-mail: [gaoxran@foxmail.com](mailto:gaoxran@foxmail.com)

power stably. With the use of energy storage module, the on-line monitoring device is able to upload the picture information every two hours.

**Keywords** HV transmission line · Energy harvesting · Electric field induction · DC-DC converter

## 1 Introduction

In recent years, both the State Grid and the China Southern Power Grid have put forward the concept of smart grids to improve the reliability, flexibility and sustainability of the power system. With the development of Internet of Things technology, a large number of online monitoring devices have been widely applied, which can provide high accuracy and high-density monitoring information for early warning, active self-healing and disaster prevention of the power system, especially of the high-voltage transmission lines [1–3]. These monitoring devices contain a large number of intelligent sensors, which are installed on the pylons of the transmission lines to monitor the running status of the lines in real time, including electrical information (such as voltage, current, etc.) [4], mechanical information (such as snow covered with ice, cable waving, etc.) [5], climatic information (such as wind speed, flashover, pollution, etc.) [6] and other information. However, these on-line monitoring devices usually require a stable and reliable power supply to support their long outdoor work.

At present, researchers have proposed a variety of schemes for on-line monitoring device functions. Among them, literature [7] uses wind energy, solar energy and energy storage devices to obtain electric energy. However, this scheme is greatly affected by the weather, which is prone to failure under continuous rain and snow in southern China. Literature [8] proposes a method of wireless power transfer using laser. But it has the problems that the system is expensive and the laser source needs to be carried manually. Literature [9] proposes that capacitive voltage divider can be used to take capacitive power. But there are also problems of bulky device and the risk of insulation breakdown. Literature [10, 11] proposed the scheme of using current transformer to take electricity from the power frequency magnetic field around the high voltage (HV) lines. However, current transformer is installed on the high voltage line. Due to the need of insulation, the online monitoring device at the grounded tower side is difficult to use the harvested power. In further, literatures [12–15] put forward a functional method based on wireless power transfer technology. The basic method is to first use CT device to pick up electric energy from the power frequency magnetic field around the transmission line in the way of magnetic field induction coupling, and then transmit the power to the grounded tower wirelessly. Thus, it can supply power to on-line monitoring device without destroying the insulation. However, on the one hand, the system is complex and the reliability is low. On the other hand, it is also limited by the load current through the line. As a result, it cannot reliably output electric energy when the load current is low. The comparison of various existing energy supply methods is listed in Table 1.

**Table 1** Comparison of the current power supplies

Serial number	Mode of energy supply	Disadvantage
1	Renewable energy (wind and solar)	Affected by weather Reliability problems
2	Laser	High cost Manual handling of laser source
3	Capacitive voltage divider	Bulky device Insulation damage risk
4	Induction fetching/wireless power transfer	Complex system Limited by load current

In order to improve the energy supply stability, an electric field-induction based space energy harvesting method of HV transmission lines is proposed in this paper. The basic idea is that the energy harvesting plates are deployed at the grounded tower side to form capacitive coupling with the HV line, so as to realize the collection of space electric field energy. In this paper, the feasibility and effectiveness of the proposed method are verified by theoretical analysis, system simulation and experimental tests. The original contributions of this paper are concluded as follow.

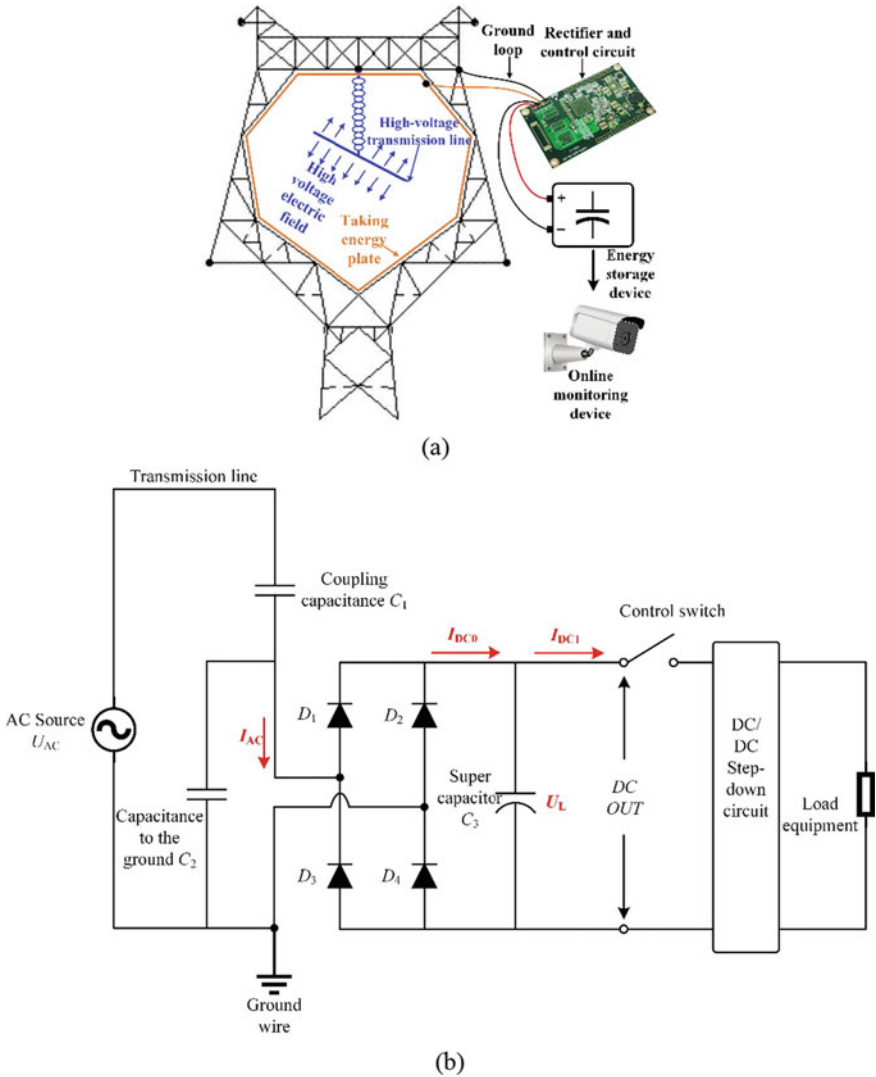
1. The system architecture of unipolar plate electric field induction space energy harvesting is designed. Essentially, only one coupling plate is needed to realize the space electric field energy harvesting.
2. Using the edge effect of charge distribution, a frame-shaped coupling plate is designed to reduce the plate size while simultaneously maintaining the output power.
3. By considering the system as a quasi-current source, a DC/DC converter is designed to greatly improve the output power of the system.
4. With respect to the discontinuous power requirement of the online monitoring device, a hysteresic control mode of the system's output power is designed, which can realize the photo-feedback every 2 h.

## 2 Overall System Structure

The overall structure of the electric field induction-based energy harvesting system is shown in Fig. 1a. Metallic plates are deployed inside the tower, surrounding the HV line. Consequently, the plates form capacitive coupling with the HV line. Particularly, the plates are isolated from the tower with small insulators. As a result, a complete circuit loop is formed with the HV line, the remote transformer, the earth ground, and the energy harvesting plates. Among them, the coupling capacitance formed by the plates and the HV line will generate power-frequency induced current when the line voltage changes. Followingly, this induced current will be converted into direct current with a rectifier and control circuit, and then supplied to the energy storage

device. When the voltage of the energy storage device reaches the threshold value, the energy will be released to the load, such as the online monitoring device.

Figure 1b shows the circuit scheme of the proposed system. Here, the high-voltage transmission line, the remote transformer and the grounded tower are collectively considered as an AC voltage source,  $U_{AC}$ , whose voltage is determined by the voltage level of the line. The coupling capacitance between the energy harvesting plates and the transmission line is denoted as  $C_1$ , and the coupling capacitance between the



**Fig. 1** The structure of the electric field induction-based space energy harvesting system for high-voltage power transmission lines. **a** The overall system structure. **b** The circuit scheme

energy harvesting plates and the tower is labeled as  $C_2$ . The energy harvesting plates and the grounded tower are used as a pair of AC inputs of the rectifier bridge to charge the supercapacitor module  $C_3$ . When the voltage of  $C_3$  module reaches the threshold, the control switch will be closed and electrical power is output to the DC/DC converter at the rear stage. Then, the DC power is converted into the standard 12 V power supply to feed the load.

For practical implementation, the proposed system should meet the following three conditions:

1. The system has a large output power, so that enough power can be collected in a short time (such as 2–3 h) for online monitoring equipment to complete the photo taking and data feedback.
2. The size/weight of the energy plate is appropriate, easy to install, and has the ability to adapt to outdoor wind and snow.
3. An appropriate workflow should be designed to enable the energy storage device to release and store electric energy according to the state of energy storage.

### 3 System Analysis and Optimal Design

#### 3.1 System Analysis and Output Power Promotion

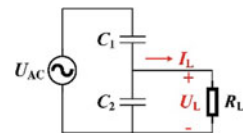
For the circuit scheme shown in Fig. 1b, the rectifier bridge and the post-stage circuit are regarded as load  $R_L$  in a whole. Then, the simplified equivalent circuit of the system can be obtained, as shown in Fig. 2.

According to the equivalent circuit shown in Fig. 2, the charging current of the load can be calculated as shown in Eq. (1):

$$I_L = \frac{U_{AC} \cdot \left( \frac{1}{j\omega C_2} \parallel R_L \right)}{\left( \frac{1}{j\omega C_1} + \frac{1}{j\omega C_2} \parallel R_L \right) \cdot R_L} \quad (1)$$

In Eq. (1),  $\omega$  represents the angular frequency of the power system. In Eq. (1), the voltage of  $U_{AC}$  is determined by the line voltage. As a result, the larger the coupling capacitance  $C_1$  is, the smaller the loop impedance is, and the larger the charging current  $I_L$  will be. The larger the coupling capacitance  $C_2$  is, the smaller the shunt impedance will be. Consequently, the voltage over the load will also be smaller, resulting in a smaller charging current  $I_L$ . Therefore, in order to obtain a

**Fig. 2** Equivalent circuit of the energy harvesting system





larger charging current  $I_L$ , it is necessary to obtain a larger  $C_1$  value and a smaller  $C_2$  value through reasonable design. On the other hand, for a real system, the impedance of  $C_1$  is usually much greater than that of  $C_2$ , and the impedance of  $C_1$  and  $C_2$  are both much greater than  $R_L$ . As a result, the charging current  $I_L$  can be approximately determined by  $U_{AC}$  and  $C_1$  and can be considered as a quasi-current source, as shown in Eq. (2):

$$I_L \approx U_{AC} \cdot j\omega C_1 \quad (2)$$

Table 2 shows the practical parameters of an electric field induction-based energy harvesting system installed on a 110 kV tower (single-phase voltage to ground is  $1/\sqrt{3}$  of line voltage). In Table 2  $C_1$  has a value of about 40 pF, and  $C_1$  has an impedance of about 79.6 M $\Omega$  at power frequency, much higher than  $C_2$ 's 2.1 M $\Omega$ . At the same time, the impedance of  $C_1$  and  $C_2$  is much larger than the impedance range of  $R_L$  in the tens of k $\Omega$ . Therefore, the charging current can be approximately calculated by Eq. (2).

Further, the harvested power of the system can be obtained from Eq. (2):

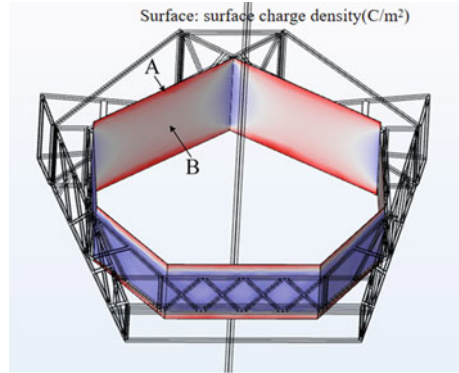
$$P_L = I_L \cdot U_L \quad (3)$$

It can be seen that under the condition that the charging current  $I_L$  is approximately constant, the higher the charging voltage of the energy storage module  $C_3$  is, the higher the harvested power will be. However, electrical devices such as in-line monitoring devices are usually operated with 12 V. If a 12 V energy storage module is used for energy storage, the overall harvested power is small, less than 10 mW. Therefore, as shown in Fig. 1b, a DC/DC converter is added to the last stage of energy storage module  $C_3$ . The system charges and stores energy at a high voltage. When releasing electric energy, it is converted to 12 V by the DC/DC and then supplied to electrical load. In particular, when the charging voltage of  $C_3$  is larger than 40 V, the harvested power will exceed 25 mW, thus effectively improving the system's output power.

**Table 2** Practical circuit parameters of the energy harvesting system for 110 kV level lines

Parameter name	Parameter value	Parameter name	Parameter value
$U_{AC}$	63.5 kV	Charging voltage $U_L$	0–60 V
$C_1$	39.9 pF	Charging current $I_L$	0.68 mA
$C_2$	1522 pF	Equivalent load $R_L$	0–100 k $\Omega$

**Fig. 3** Charge distribution of full-area coupling plate



### 3.2 Optimal Design of Energy Harvesting Plates

Considering that the energy harvesting plates are used in outdoor conditions, the system needs to deal with windproof, snow and water problems. As a result, the full-area plates are optimized to hollow frame-shaped ones. Consequently, this optimization work can significantly reduce the weight and size of the energy harvesting plates, making the system easier to install and implement.

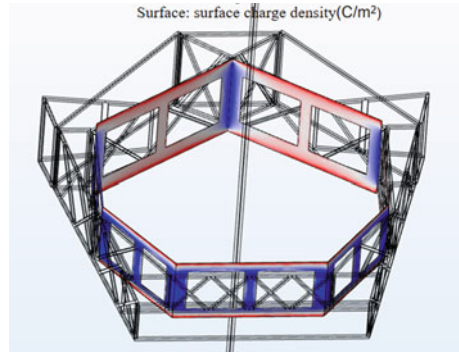
The optimization of energy harvesting plates is based on the edge effect of charge distribution [16, 17]. As shown in Fig. 3, when the coupling distance is large, the charge on the coupling plate is mainly distributed in the edge region. Thus, it is the edge region of the plate that plays a major role in the coupling capacitance. In Fig. 3, the charge density of the edge point A is  $3.629\text{E-}9$  nC, and that of the center point B is  $0.463\text{E-}9$  nC. It can be seen that the charge density of the edge region is more than 7.8 times that of the central region. Therefore, the coupling capacitance between the high-voltage transmission wire is mainly determined by the edge region of the energy harvesting plate. The center region of the energy harvesting plate can be removed without significantly affecting the coupling capacitance  $C_1$ .

Figure 4 shows the simulation diagram of the energy harvesting plate after the removal of the center area, and the comparison between the full-area plate and the frame-shaped plate is shown in Table 3. It can be seen that 80% of coupling capacitance  $C_1$  remains after 70% of the plate area is removed. According to the above results, this paper decides to use the frame-shaped plate for space energy harvesting, so as to obtain better adaptability to outdoor working conditions, and also to reduce the difficulty of construction and installation.

### 3.3 Charge and Discharge Process Design

Generally speaking, the power consumption of online monitoring devices is between several hundred mW and several W, which is much larger than the system output

**Fig. 4** Charge distribution of frame-shaped coupling plate



**Table 3** Comparison between the full-area coupling plate and the frame-shaped coupling plate

Object	Area ratio (%)	Capacitor to the wire $C_1$ (pF)	Capacitor to ground $C_2$ (nF)
Full-area coupling plate	100	49.1	2.02
Frame-shaped coupling plate	30	39.9	1.52

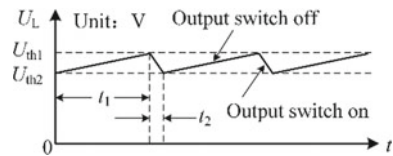
power of tens of mW. However, practically, the photo taking and data uploading of line snow, ice and fouling conditions do not require continuous operation. Therefore, the energy harvesting system proposed in this paper is designed with a hysteresis mode of operation. When the voltage  $U_L$  of energy storage module  $C_3$  reaches a certain voltage threshold  $U_{th1}$ , the output control switch is closed, allowing the online monitoring device to complete a state monitoring and data upload with higher power; when  $U_L$  is lower than a certain voltage threshold  $U_{th2}$ , the output switch is disconnected and energy storage continues to charge itself.

The workflow of the system is shown in Fig. 5. When the output switch is disconnected, the super capacitor  $C_3$  starts to charge, and the voltage rises slowly; after lasting for  $t_1$ , the voltage of  $C_3$  reaches  $U_{th1}$ , the output switch is closed and the super capacitor  $C_3$  starts to discharge, and the voltage drops rapidly; after lasting for  $t_2$ , the voltage decreases to  $U_{th2}$ , the output switch is disconnected and  $C_3$  continues to store power; and so on.

After the output switch is closed, the total output energy can be calculated as:

$$W_L = 0.5 \cdot C_3 (U_{th1}^2 - U_{th2}^2) \tag{4}$$

**Fig. 5** Charge/discharge process of the system



Shown as Eq. (4), the larger the capacitance value of the supercapacitor module  $C_3$  is, the more electrical energy is released in a single release, and the longer the online monitoring device can be supported to work. On the other hand, the larger the difference between  $U_{th1}$  and  $U_{th2}$ , the more electrical energy is released in a single release. However, when selecting the  $U_{th1}$  and  $U_{th2}$  in the actual design, not only the withstand voltage value of the power device should be considered, but also a high enough voltage value should be maintained to increase the harvested electrical power.

## 4 System Simulation Verification

### 4.1 Simulation of Power Output Characteristics

According to the circuit topology shown in Fig. 1, the simulation system is built in Simulink software, and the simulation parameters were set as Table 2. Among them, the equivalent load  $R_L$  is set as 60 k $\Omega$ , and the supercapacitor module  $C_3$  is set as 100  $\mu$ F to shorten the simulation time, thus the output voltage can reach a stable value as soon as possible without affecting the overall trend.

The simulation results are shown in Fig. 6, where  $I_{AC}$  is the charging current on the AC side,  $I_{DC0}$  is the charging current after the rectifier bridge and before capacitor  $C_3$ ,  $I_{DC1}$  is the DC current supplied to the load by capacitor  $C_3$ , and  $U_L$  is the output voltage of  $C_3$ . It can be concluded from the simulation results as follow.

1. The charging current  $I_{AC}$  on the AC side is constant with an amplitude of 1.2 mA and a frequency of 50 Hz.

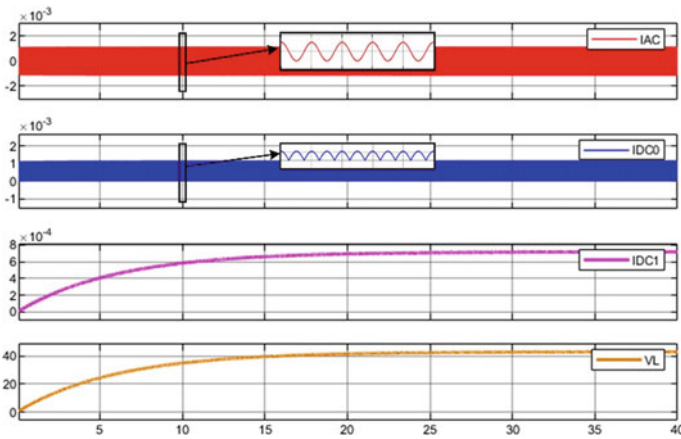


Fig. 6 Simulation results of the energy-harvesting system

2. The charging current  $I_{DC0}$  is also constant after rectification and has an amplitude of 1.2 mA, which is a 100 Hz half-wave. Part of  $I_{DC0}$  is used to charge capacitor  $C_3$ , which makes the output voltage  $U_L$  rise continuously, and part of  $I_{DC1}$  is used to supply the load, i.e.  $I_{DC1}$ . When  $C_3$  is charged, the value of  $I_{DC1}$  is 0.68 mA in the balanced state.
3. The equivalent load value gradually increases to 65 k $\Omega$  as the load voltage  $U_L$  rises from zero to a stable voltage of 44 V. During this process, the  $I_{AC}$  always maintains a magnitude of 1.2 mA. It can be seen that the charging current is almost independent of the load impedance, and the system can be approximated as a current source.

In addition, adjusting the capacitance value between the energy harvesting plates and the ground tower  $C_2$  from 0 pF to the simulated value of 1.52 nF,  $I_{DC0}$  and  $I_{DC1}$  in the equilibrium state remain almost unchanged, which shows that the effect of  $C_2$  on the output current is also negligible.

## 4.2 Simulation of System Safety

The potential distribution of the system is analyzed using COMSOL simulation software. As shown in Fig. 7, a power frequency voltage of 63.5 kV (rms) is applied to the high-voltage transmission conductor and the potential values are derived from point A to C in Fig. 7. The derived results are shown in Fig. 8. As seen from Fig. 8, the potential distribution in the case with the plates is only about 5% deviation around the wire at the center point B compared to the case without the plates, and the potential distribution in other places remains the same as that of the case without the plates. It can be concluded that the high-voltage transmission line is still within its safe margin after adding the energy harvesting plates.

## 5 System Experiment Verification

### 5.1 Experimental Setup

In order to verify the feasibility and effectiveness of the proposed energy harvesting system, a high-voltage test setup was built and verified by practical tests. The experimental setup is shown in Fig. 9a. The test system consists of five parts: 110 kV level insulator string, simulated power transmission line, coupling plates, energy storage device and ground cables. Among them, the simulated power transmission line is connected to the output of a high-voltage generator to provide 63.5 kV ( $110 \text{ kV}/\sqrt{3}$ ).

A dimensional drawing of the coupling plates is shown as Fig. 9b, simulating a 110 kV level M1-type tower with an 1:1 ratio. Here, the maximum width in the

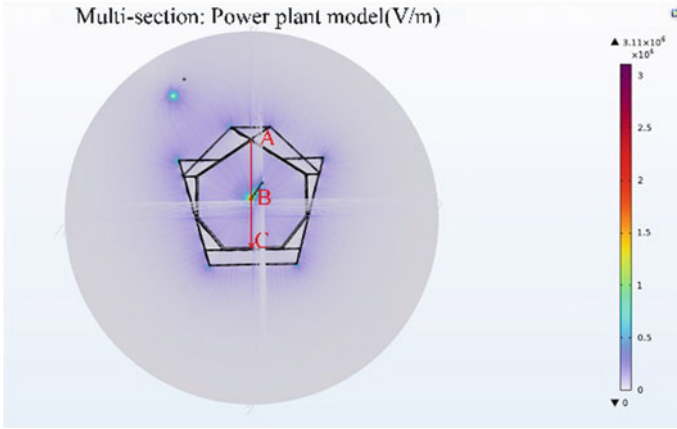


Fig. 7 Simulation model of the space electric field strength

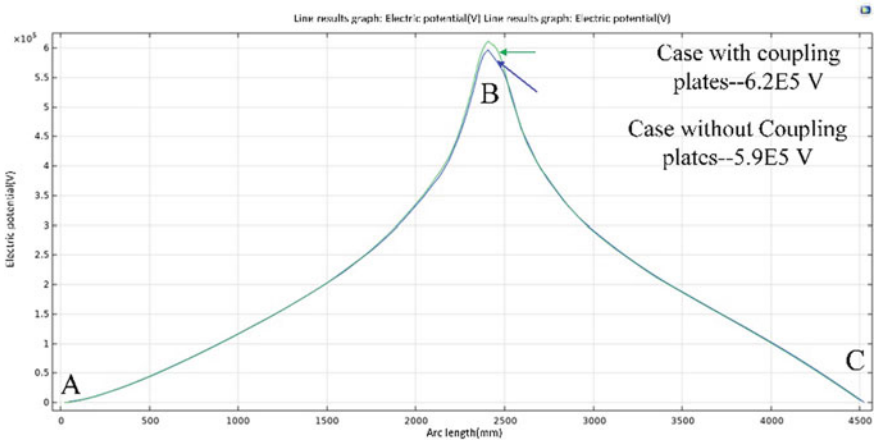
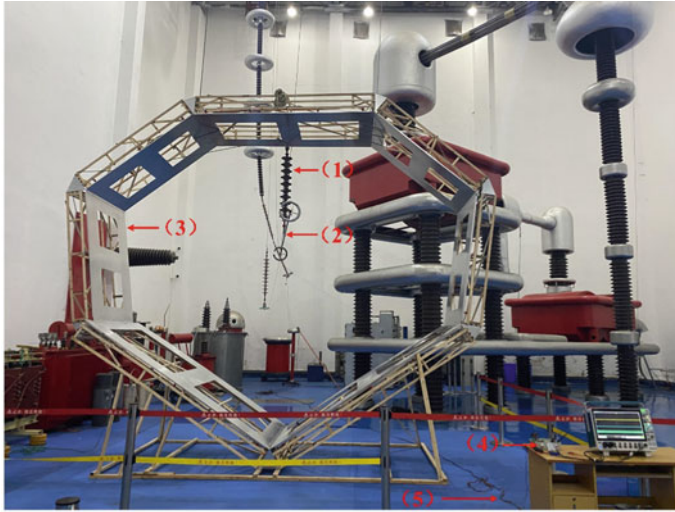


Fig. 8 Comparison of the voltage difference between cases with and without the coupling plates

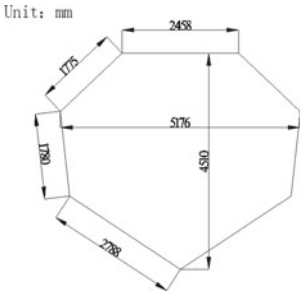
transverse direction is 5176 mm, and the maximum height in the longitudinal direction is 4510 mm. Meanwhile, the coupling plates is supported by a wooden frame to maintain insulation from the ground.

Figure 9c gives the circuit device, containing the rectifier bridge, the supercapacitor energy storage module, and the DC/DC converter module. In particular, for the AC input of the rectifier bridge, it is connected to the ground terminal of the high-voltage generator and the energy harvesting plates. Thus, the system forms a complete closed loop through the high-voltage output terminal of the high-voltage generator, the ground terminal of the high-voltage generator, the simulated power transmission line, the coupling plates, the rectifier bridge, and the ground terminal of the high-voltage generator.

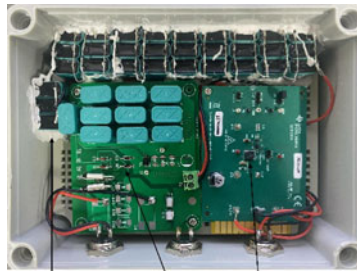


(1) 110kV insulator string; (2) Analog wires; (3) Coupling pole plate; (4) Energy storage device; (5) Ground circuit

(a)



(b)



(c)

**Fig. 9** Experimental setup of energy harvesting system. **a** Overall setup; **b** Dimensions of the energy harvesting plates; **c** Energy harvesting circuits

On the other hand, considering the small output current ( $<1$  mA) of the energy harvesting system, each component of the circuit needs to ensure a very low leakage current. The key components and their leakage current parameters are listed in Table 4, which shows that the overall leakage current of the circuit is below  $50 \mu\text{A}$ , less than one-tenth of the system's charging current. Among them, the DC/DC converter is realized with TI's LMR36506-Q1 to take advantage of its ultra-low quiescent current. At the same time, by adjusting the level of its enable pin, it can be controlled to work in normal output mode or standby mode. Considering that the maximum operating voltage of this type of IC is 65 V, the actual design threshold

**Table 4** The key components and their leakage current

Circuit components	Model/Supplier	Leakage current parameters
Rectifier diodes $D_1-D_4$	1N4148/Onsemi	$5 \mu\text{A}@75 \text{V}$
Supercapacitor module $C_3$	CHM-6R0L105R/Zhi Fengwei	$3 * 6 \mu\text{A}$ (three groups in parallel)
DC/DC control chip	LMR36506-Q1/TI	$18 \mu\text{A}$

voltage of normal output  $U_{th1}$  is 55.8 V and the threshold voltage of standby mode  $U_{th2}$  is 42.3 V.

## 5.2 Experimental Results

Considering that the high voltage generator can only work continuously for 5 min during the test, if a supercapacitor is used as a load, the charging time will reach several hours and the whole experiment cannot be completed. Therefore, in order to shorten the test time, the energy storage device used for the actual test was a 100 V/220  $\mu\text{F}$  electrolytic capacitor. In addition, the load was a 12 V/2.5 W LED strip. This is because the actual online monitoring device used has a maximum power of 2.5 W at full power operation. It should be noted that for the online monitoring device, the maximum power only occurs during the process of taking photos and data uploading, which lasts no more than 30 s. During the idle period, its standby power consumption is only 0.15 W.

According to the device shown in Fig. 9, 63.5 kV ( $110 \text{kV}/\sqrt{3}$ ) is applied to the simulated power transmission line and the waveforms of charging and discharging process are captured. Particularly, the charging current, measured by a milliammeter, is 0.64 mA. Considering the effect of stray capacitance between the coupling plates and the grounded tower and the effect of leakage current of the circuit components, the charging current of 0.64 mA is in line with the theoretical expectation.

The voltage waveforms of the energy storage capacitor during the charging and discharging process is shown in Fig. 10. It can be seen that the energy storage module starts to release power when the voltage reaches 55.8 V, and the DC/DC converter outputs 12 V. When the voltage of the energy storage module drops to 42.3 V, it stops releasing and the DC/DC converter outputs zero and enters standby mode. The actual energy storage module is a 0.3 F/60 V supercapacitor module, which can release 198.6 J of electrical energy at one time according to the above thresholds, and can support the online monitoring device to work at full power for 80 s and in standby mode for 1324 s. In addition, according to the testing result of 0.64 mA charging current, it takes 5.51 h to charge to the release threshold for the first time. After that, the power is released every 2 h.

Finally, the system proposed in this paper was implemented on a 110 kV catenary tower of the Yujie Line of Xiangyang Power Supply Company, as shown in Fig. 11.



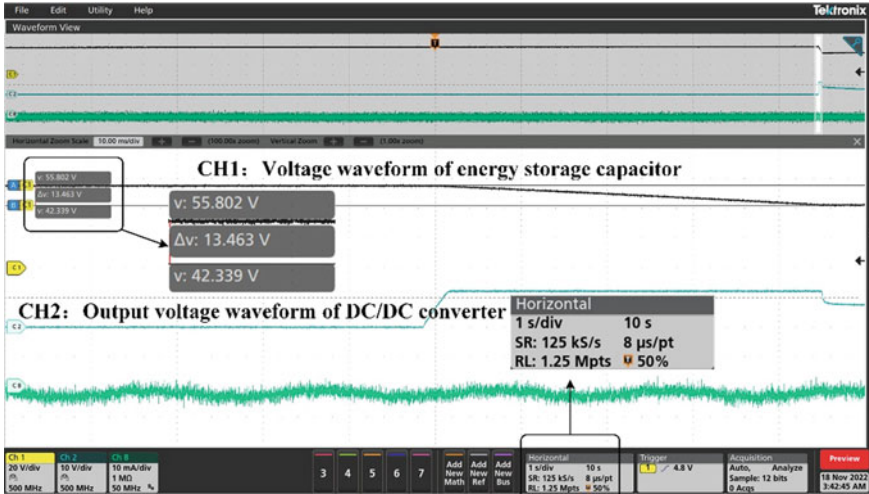


Fig. 10 Charge and discharge threshold waveform of energy storage capacitor



Fig. 11 Practical system in outdoor environment and the captured picture

The system can upload field pictures periodically. The above results have verified the feasibility and effectiveness of the proposed system.

## 6 Conclusion

In this paper, we propose a space energy harvesting scheme based on high-voltage electric field induction of transmission lines with low-cost and high-reliability for online monitoring devices. Through the optimized design of circuit topology,

coupling plates, charging and discharging modes, the proposed space electric field energy harvesting system is able to output 25 mW power stably. By using a super-capacitor module, it can support the online monitoring device to upload field pictures every 2 h. At the same time, the system is simple and reliable in structure, easy to install, and suitable for harsh outdoor conditions. In addition, this paper also verifies the safety performance of the system through finite element simulation.

**Acknowledgements** The work was supported by a technology project (Project No. 521533200083) from Hubei Electric Power Co., Ltd., State Grid, China.

## References

1. Ou QH, Wang Z, Zhen Y et al (2013) Status monitoring and early warning system for power distribution network based on IoT technology. In: Proceedings of 3rd international conference on computer science & network technology, Dalian, China, pp 641–645
2. Peng L, Xin-bo H, Long Z et al (2013) Research and design of transmission line condition monitoring agent. Proc CSEE 33(16):153–161 (in Chinese)
3. Long Y, Wei-xun L, Yi-peng L et al (2020) Research on cloud-based monitoring system for smart grid. Electrical Measurement & Instrumentation 57(23):87–91 (in Chinese)
4. Sun X, Huang Q, Jiang LJ et al (2014) Overhead high-voltage transmission-line current monitoring by magneto resistive sensors and current source reconstruction at transmission tower. IEEE Trans Magnet 50(1):4000405
5. Yin T, Chen XS, Du Y, He YJ (2008) Research on power supply employed in ices real-time monitoring system of high-voltage transmission lines. In: Proceedings of International Conference High Voltage Engineering and Application, Chongqing, China, pp 626–628
6. Guo W, Zhou S-L, Wang L et al (2019) Design and application of online monitoring system for electrical cable states. High Voltage Eng 45(11):3459–3466 (in Chinese)
7. Ye F, Qian Y, Hu RQ (2015) Energy efficient self-sustaining wireless neighborhood area network design for smart grid. IEEE Trans Smart Grid 6(1):220–229
8. Wang Z, Zong F, Wang W et al (2010) Development of power supply in high voltage side of transmission lines. Power Syst Clean Energy 26(6):24–27
9. Moser MJ, Bretterklierer T, Zangl H, Brasseur G (2011) Strong and weak electric field interfering: Capacitive icing detection and capacitive energy harvesting on a 220-kV high-voltage overhead power line. IEEE Trans Industr Electron 58(7):2597–2604
10. Jie L, Changtao C (2018) Optimization analysis and experiment verification of current transformer power supply based on starting current. High Voltage Eng 44(6):1774–1781 (in Chinese)
11. Zhang Q, Li H, Cheng H et al (2016) Research on on-line monitoring technology of active electronic current transformer. High Voltage Technol 42(1):208–213 (in Chinese)
12. Chen JF, Hua ZY, Wang SM, Cheng YZ, Liu MH (2016) Investigation of wireless power transfer for smart grid on-line monitoring devices under HV condition. In: Proceedings of 2nd International Workshop Wireless Technology Innovation in Smart Grid, Madrid, Spain, pp 1307–1312
13. Zhou H, Gao XR, Lai JG et al (2018) Natural frequency optimization of wireless power systems on power transmission lines. IEEE Access 6:14038–14047
14. Xing-kui M, Qi-sheng H, Shi-fa L et al (2017) Contactless powering via magnetic resonance for on-line monitoring wireless sensor of high-voltage electrical equipment. High Voltage Eng 43(11):3718–3725 (in Chinese)

15. Gao XR, Liu CH, Zhou H et al (2021) Design and analysis of a new hybrid wireless power transfer system with a space-saving coupler structure. *IEEE Trans Power Electron* 36(5):5069–5081
16. Minter TM (2014) The many capacitance terms of two parallel discs in free space. *Europe J Phys* 35(3):1–15
17. Nishiyama H, Nakamuraakamura M (1993) Capacitance of disk capacitors. *IEEE Trans Components Hybrids Manuf Technol* 16(3):360–366

# Defect Identification Method Based on Casing Internal Temperature Variation



Jingling Sun, Xiaowen Wu, Wei Xiao, and Ping Peng

**Abstract** Bushing is an important component of transformers, mainly serving as insulation and mechanical support. Its operating status is of great significance for the normal operation of transformers. This paper judges whether the defect identification method based on the temperature change inside the bushing is feasible by analyzing the temperature change inside the transformer oil paper bushing, the temperature field distribution of the bushing, the influence of the temperature distribution of the bushing conductive rod, and the temperature field distribution of the insulating oil under different defects. The analysis result has reference significance for the safe operation of the oil-paper capacitor bushing.

**Keywords** Oil-paper capacitive bushing · Temperature variation · Failure recognition

## 1 Introduction

Casing failure is the main cause of catastrophic failure of power transformer [1]. Casing failure harms not only its own unplanned outage, but also the surrounding important equipment. According to the accident statistics of China Electric Power Research Institute, the insulation and discharge failure of oil-immersed bushing leads to the fire accident rate of power transformer as high as 83% [2]. The National Power Reliability Analysis Center points out that casing failure is the primary cause of unplanned outage of 220 and 500 kV transformers [3]. In the process of design, manufacturing, installation, operation and maintenance, casing insulation defects

---

J. Sun (✉) · X. Wu · W. Xiao

School of Information and Electrical Engineering, Hunan University of Science and Technology, Xiangtan 411201, China

e-mail: [sunjingling@mail.hnust.edu.cn](mailto:sunjingling@mail.hnust.edu.cn)

P. Peng

State Grid Hunan Electrical Power Company Limited Research Institute, Changsha 410006, China

© Beijing Paiké Culture Commu. Co., Ltd. 2024

X. Dong and L. Cai (eds.), *The Proceedings of 2023 4th International Symposium on Insulation and Discharge Computation for Power Equipment (IDCOMPU2023)*, Lecture Notes in Electrical Engineering 1103, [https://doi.org/10.1007/978-981-99-7413-9\\_5](https://doi.org/10.1007/978-981-99-7413-9_5)

have latent potential. If not detected and eliminated in time, deterioration will gradually develop and cause discharge problems after operation [4]. Lead to casing insulation breakdown explosion and other serious consequences. This is enough to show that casing defect identification, early intervention, is the key to reduce the occurrence of accidents.

A lot of research work has been carried out on the internal temperature of high pressure oil paper capacitor bushing. A method for detecting insulation defects in power system transformer bushings based on infrared detection technology is proposed, using power transformer bushings as the research object. Simulation results showed that using this method for detecting insulation defects in power system transformer bushings has high output stability, good positioning accuracy, and improved the accurate identification ability of defect faults [5]. In the aspect of casing heating defect fault diagnosis, the relative area of the fault area and the relative longitudinal axis position are extracted as the characteristic parameters, and the K-means clustering algorithm is used to realize the classification of casing fault types [6]. Zhou Kehui et al. extracted the average temperature of different grid regions of the casing for voltage heating type defect detection, but the vertex should be selected first for box selection of the target region [7, 8]. Authors in [9] argues that transformer failures in power systems are caused by bushings, which are susceptible to high dielectric and thermal stresses. Lu Geifeng et al. studied a portable device for detecting electrically-charged discharge of casing end panel based on real-time non-contact discharge signal detection. By observing signal waveform, discharge magnitude and frequency spectrum changes, the fault situation can be determined, and the fault location can be found timely and accurately [10]. Xu Yang et al. measured partial discharge data of several typical defects on a 110 kV transformer casing model by using the end screen sensing method, and compared the measurement results with the pulse current method, high frequency current mutual inductance method and ultrahigh frequency method, and analyzed the advantages and disadvantages of the end screen sensing method and its reliability [11]. In the traditional method, insulation defect distribution model of transformer bushing in power system is constructed, infrared characteristics are analyzed, and insulation defect location of transformer bushing in power system is carried out. However, the accuracy of insulation defect detection of transformer bushing in power system by traditional method is not high, and the positioning accuracy is not good [12]. P.P. Hebert proposed a thermal path model using finite element difference method to determine the maximum hot spot of casing under load [13].

However, at present, there are few studies to judge the defects according to the temperature changes caused by moisture inside the oil paper casing. Considering the conductor Joule heat loss, eddy current loss and medium loss inside the oil paper casing, the magnetic thermal coupling finite element analysis model is established to analyze the temperature distribution and hot spot change inside the casing under different moisture conditions.

## 2 Thermal Analysis of Oil Paper Capacitor Bushing

During the operation of oil-paper capacitor casing, metal components and capacitor cores will generate losses during the conversion of electromagnetic energy, which are all converted into heat. The heat source of the casing mainly includes resistance loss of current-carrying components, eddy current loss of the flange and dielectric loss of the capacitor core.

### 1. Joule heat loss of conductor

Joule heat loss of metal part of casing under steady current load can be calculated by finite element method.

$$P_1 = kI^2R \quad (1)$$

where  $I$  is the carrying capacity of the guide rod in the center of the casing,  $R$  is the resistance value of the central conductor rod per unit length,  $k$  is skin effect coefficient.

### 2. Eddy current loss

The dielectric loss distribution of insulation material in casing under steady-state voltage load can be calculated by finite element method.

Under AC excitation condition, the working frequency of the casing is  $f$ . For the medium with electric field intensity  $E$ , dielectric loss factor  $\tan\delta$  and relative dielectric constant  $\varepsilon_r$ , the unit volume loss power  $q$  is

$$q = 2\pi f \varepsilon_0 \varepsilon_r E^2 \tan \delta \quad (2)$$

The heat value of dielectric loss in casing medium is calculated by finite element method:

$$P_2 = \sum_{i=1}^M 2\pi f \varepsilon_0 \varepsilon_r E^2 \tan \delta \cdot V_i \quad (3)$$

where  $V_i$  is the unit volume.

### 3. Dielectric loss

The formula for calculating eddy current loss on Flange is

$$J = -j\omega\sigma A \quad (4)$$

$$P_3 = \frac{1}{\sigma} \int J^2 dV \quad (5)$$

where  $J$  is the current density on the flange,  $\sigma$  is the conductivity of the flange,  $A$  is the vector magnetic potential of the flange.

Because the resistivity of the casing conductor is related to its operating temperature. Therefore, the power loss of casing components needs to be calculated by multi-physical field iteration method, as shown in Fig. 1.

Before calculating the power loss, the initial temperature of the conducting rod of the oil-paper capacitor bushing was assumed first, and the initial temperature was used for the 3D eddy current field analysis, and the calculated power loss was used as the temperature field analysis model of the volume heat source input to the casing. Through the temperature field analysis, the new temperature of the conductor rod of the casing is obtained and compared with the initial temperature. If the error is less than 3%, the iterative calculation is stopped and the final power loss of the casing is obtained according to the eddy current analysis results. Otherwise, the initial temperature is improved and the above calculation process is repeated until convergence.

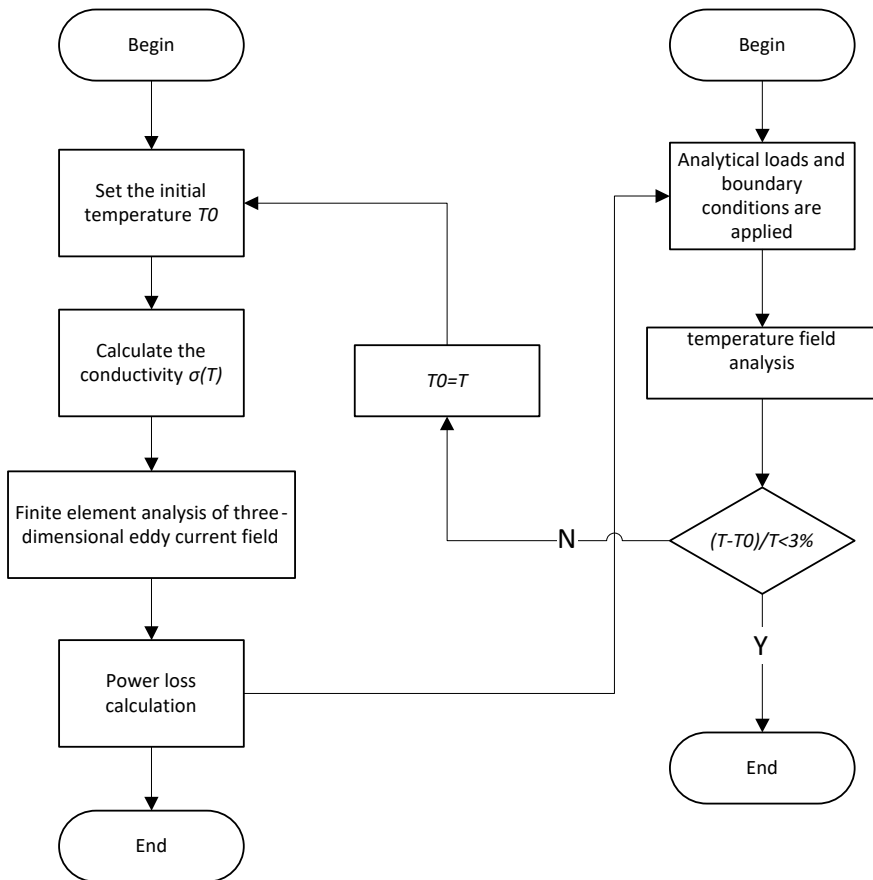


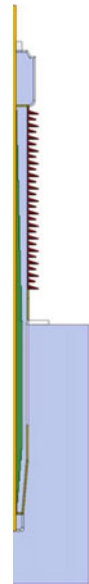
Fig. 1 The iterative solving process of casing eddy current and temperature field

It can be seen from the internal and external structure that the oil-paper capacitor bushing is axisymmetric. In the process of temperature field analysis, in order to reduce calculation amount and improve calculation efficiency, it can be equivalent to a two-dimensional axisymmetric model for analysis, as shown in Fig. 2. The porcelain bushing under the casing is completely immersed in transformer oil. In order to simulate the actual working state of the casing, a transformer oil area is added around the porcelain casing under the casing, the thickness of which is 3 times the diameter of the casing.

Only steady-state thermal analysis is considered here, so the physical property parameters of materials in the temperature field calculation model are only thermal conductivity parameters. Table 1 shows the thermal and physical property parameters of each part of the oil-paper insulated bushing during the specific calculation.

PLANE77 and SURF151 units were used to analyze the temperature field of oil paper casing. SURF151 unit is overlaid on the surface of PLANE77 unit to simulate convective heat transfer and heat radiation effects on the casing surface.

**Fig. 2** Casing two-dimensional temperature field solution area

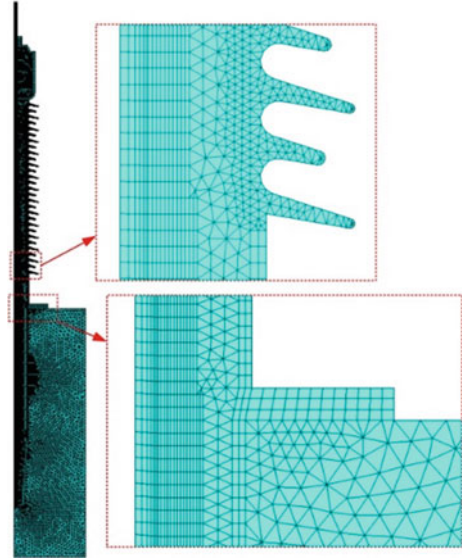


**Table 1** Thermal property parameters of casing material

Materials	Thermal conductivity/(W (m K) <sup>-1</sup> )
Cuprum	377
Aluminium alloy	199
Electric insulating oil	0.128
Oil paper	0.202
Porcelain bushing	0.27



**Fig. 3** Meshing of casing two-dimensional temperature field



Because there is less insulating oil inside the casing, only the heat conduction and heat dissipation mode of insulating oil is considered here. In the specific analysis, quadrilateral mapping grid is used to divide the conductive rod, oil paper, oil pillow, flange, pressure equalizing ball and other parts with relatively regular shape, and triangular free grid is used to divide the porcelain bushing, insulation oil and other parts. The number of temperature field analysis grids of the entire oil-paper capacitor bushing is 15207 units, and the specific grid division results are shown in Fig. 3.

Assuming that the insulating oil area around the porcelain bushing is far enough away from the casing, the temperature of its outermost boundary  $\Gamma_1$  is not affected by the casing temperature, which conforms to the first type of boundary conditions:

$$T|_{\Gamma_1} = T_0 \quad (6)$$

The radiation and convective heat transfer coexist on the outer surface  $\Gamma_2$  of the porcelain bushing on the casing, which is a nonlinear boundary condition. The boundary condition can be expressed as:

$$-\lambda \frac{\partial T}{\partial n} \Big|_{\Gamma_2} = \varepsilon \sigma (T_w^4 - T_0^4) + h(T_w - T_0) \quad (7)$$

where  $T_0$  is the ambient temperature,  $n$  is the direction of the normal outside the boundary plane.

### 3 The Effect of Internal Moisture on the Temperature Rise of Oil-Paper Casing

Operating experience has shown that dampness in the casing core is one of the common causes of casing operation accidents. The oil immersed casing can withstand long-term erosion such as sunlight, wind and sand, dirt, rain, snow, and ice. Under long-term action, water easily invades from the weak link of the casing to the inside of the casing. Moisturized casing not only accelerates insulation aging, but also leads to increased dielectric loss of the insulation material. If severely affected by moisture, it can affect heat dissipation. Damaged sealing rings at positions such as the conservator and flange, as well as improper on-site oil extraction operations that result in inadequate tightening of the conservator sealing bolts, may cause external air carrying moisture to be sucked into the casing. Due to the strong hydrophilicity of the insulation paper, when the bushing absorbs moisture, the degree of moisture on the oil-immersed insulation paper of the capacitor core will gradually increase during long-term operation. Damping of oil-paper insulation can cause dielectric loss  $\tan \delta$ . As it increases, its insulation strength will significantly decrease. When the capacitor core is operated in this damp state for a long time, it is easy to cause insulation breakdown accidents. If the moisture condition is very severe, arc discharge or flashover discharge will occur inside the casing. High energy discharge can generate gas and cause the casing to explode.

#### 3.1 The Insulation Oil is Evenly Damped

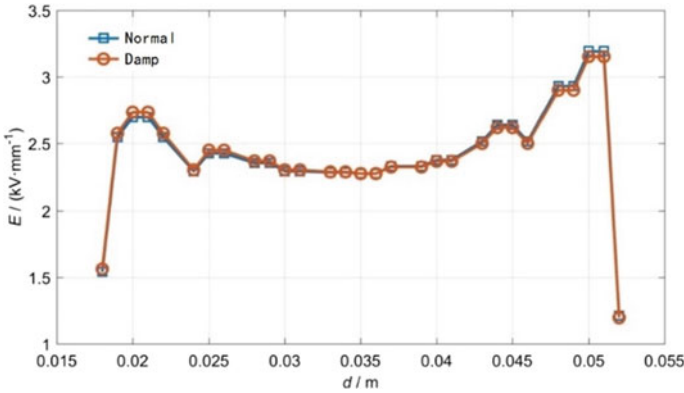
Dielectric loss is an important characteristic quantity that characterizes the degree of moisture damage to the casing. The relative dielectric constant and dielectric loss factor of insulating oil and oil paper under damp conditions are shown in Table 2.

When moisture enters the interior of the casing, the dielectric constant and dielectric loss factor of the insulation oil and oil paper of the casing increase to a certain extent.

In order to observe the electric field distribution of the casing oil paper and insulation oil, Fig. 4 shows the radial electric field distribution of the casing core. From the figure, it can be seen that the electric field strength of the capacitor core slightly increases near the zero screen after being evenly damped, and slightly decreases near

**Table 2** Electrical properties parameters of casing materials under damp conditions

Parameter	Electric insulating oil		Impregnated insulation paper	
	Dry (10 ppm)	Damp (50 ppm)	Dry (0.5%)	Damp (5%)
Relative dielectric constant	2.13	4.58	4.3	5.17
Dielectric loss factor	0.00286	1.04	0.0038	0.004



**Fig. 4** Radial electric field distribution of damp bushing capacitor core

the end screen. However, the overall distribution characteristics have not changed significantly, showing a high electric field strength between the zero screen and the end screen, and a low electric field strength in the middle screen.

After being damp, the comparison of dielectric losses in various parts of the casing is shown in Table 3. The dielectric loss of each part of the casing increases to a certain extent. In contrast, the dielectric loss of porcelain bushing can still be ignored. It can be expected that the dielectric loss of casing components will increase further with the increasing degree of dampness.

Regardless of Joule heat loss of conductors such as conductor rod, flange, pressure equalizing ball and oil pillow, the temperature field distribution of casing due to dielectric loss under normal and damp conditions is shown in Fig. 5. After damp, the temperature rise caused by dielectric loss is 5.2K, indicating that the casing temperature is directly related to the condition of damp, and damp insulation can cause the operating temperature of casing to rise.

In order to further study the temperature rise changes of the casing under the combined effect of Joule heat loss and dielectric loss, the two were used as heat sources for casing temperature rise calculation. The calculation results are shown in Figs. 6 and 7. From Fig. 6, it can be seen that after considering the losses of the damped medium and the Joule heat loss of the conductor, the overall temperature rise of the casing after being damped increased by 6.7 K, and the temperature field

**Table 3** Comparison of total dielectric loss of each part of the casing before and after damping

Materials	Normal dielectric loss/W	Loss of damp medium/W
Insulating oil	0.02	9.13
Oil paper	1.54	1.96
Porcelain bushing	7.31e-4	1.20e-3

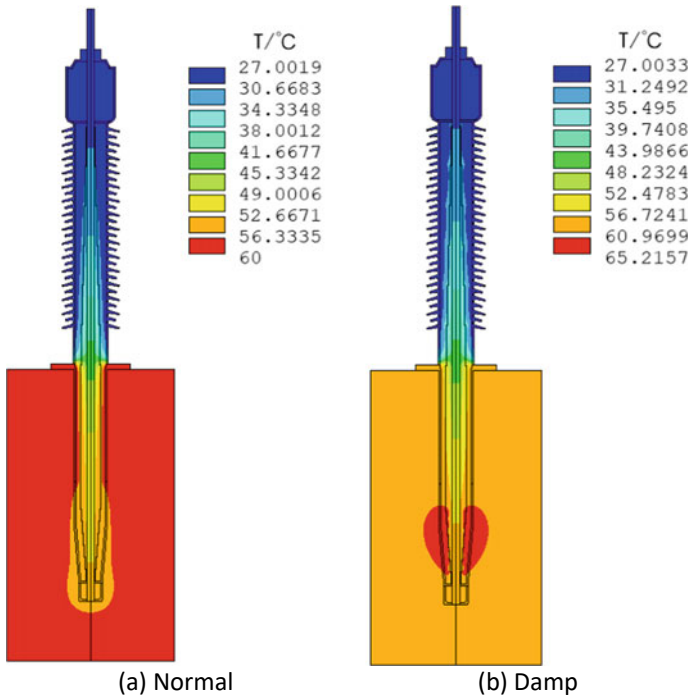


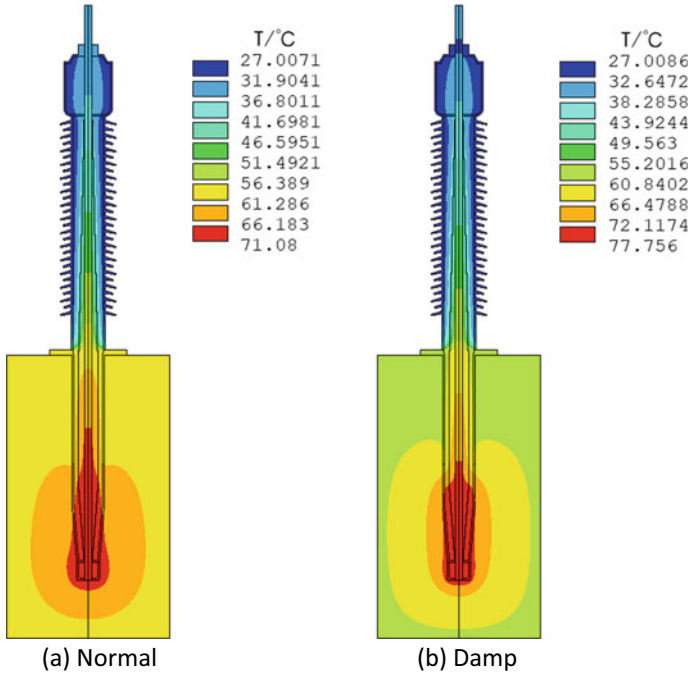
Fig. 5 Distribution of dielectric loss temperature of insulated moisturized bushing

distribution changed to some extent. The calculation results once again indicate that the dampness of the casing has a significant impact on its operating temperature.

### 3.2 Moisture on the Final Screen

Typical cases of casing moisture failure include loose oil gauge on the oil conservator at the head of the casing, hidden cracks in the ceramic bushing on the capacitor casing, and water ingress due to the flange disc oil plug not being tightened. The hydrophilicity of insulation paper is much better than that of insulation oil, so after water enters the casing, most of it diffuses into the oil paper after passing through the insulation oil. Assuming that the insulation oil is normal and the end screen is damp, the parameters of the oil paper bushing are shown in Table 4.

In order to more clearly analyze the change of electric field intensity of the capacitor core before and after the end screen is wetted, Fig. 8 shows the change of radial electric field intensity distribution of the capacitor core before and after the end screen is wetted. It can be seen that after the end screen is damp (with a moisture content of 5%), the electric field strength of other screens in the core increases, with the middle



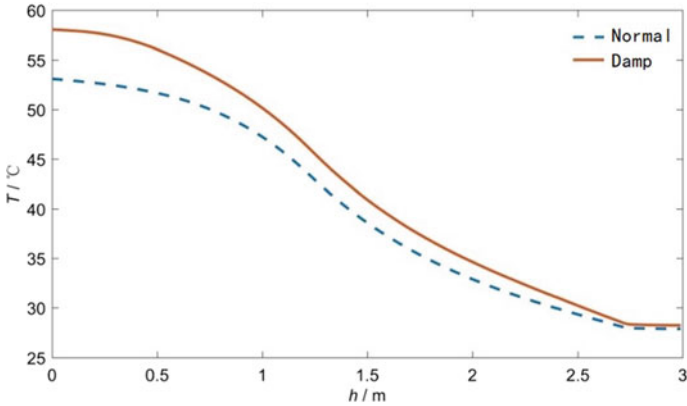
**Fig. 6** Temperature distribution of insulated moisturized bushing

layer core having the lowest increase in electric field strength and the innermost layer and the second to last screen core having the highest increase, reaching 0.068 kV/mm and 0.088 kV/mm, respectively. It is worth noting that at this point, the electric field intensity of the end screen significantly decreases, with a maximum decrease of 0.44 kV/mm.

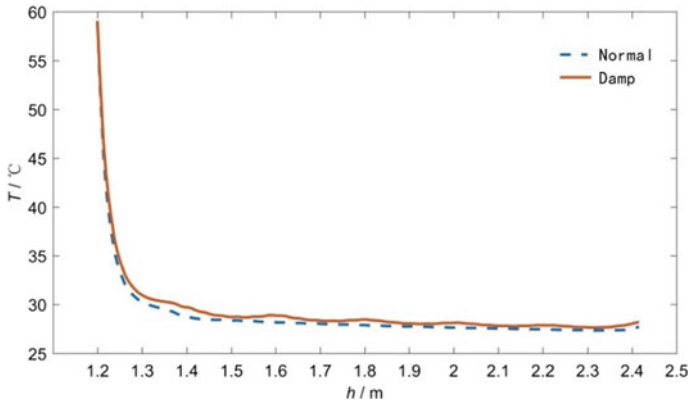
As shown in Fig. 9, after the end screen is slightly damp, the overall temperature field distribution of the casing remains unchanged, and the maximum temperature rise only increases by 0.04 K. From this, it can be seen that the dampness of the end screen did not have a significant impact on the temperature rise of the casing. It is difficult to detect slight dampness defects in the end screen through the temperature rise of the casing.

### 3.3 Zero Screen Moisture

After the zero screen is damp, the potential distribution of the casing is similar to that of a uniform damp, and there is no significant change. However, the electric field strength changes to a certain extent, and the maximum electric field strength is higher than normal operating conditions.



(a) Conducting rod



(b) Upper porcelain bushing

**Fig. 7** Dielectric loss temperature distribution in the height direction between the conductive rod and the upper porcelain bushing of insulated moisturized bushing

**Table 4** Electrical property parameters under damping conditions at the end screen

Parameter	Electric insulating oil	Impregnated insulation paper	
	Dry (10 ppm)	Dry (0.5%)	Damp (5%)
Relative dielectric constant	2.13	4.3	5.17
Dielectric loss factor	0.00286	0.0038	0.004

Figure 10 shows the change of radial electric field intensity distribution of the capacitor core before and after the zero screen is wetted. It can be seen that after the zero screen is damp (with a moisture content of 5%), the electric field strength of other screens in the core increases, with the middle layer core having the lowest increase in electric field strength and the end screen core having the highest increase,

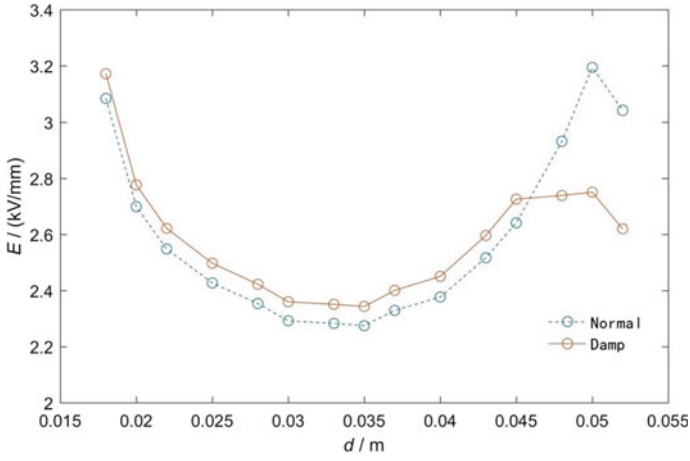


Fig. 8 Radial electric field distribution of the capacitor core before and after the last screen is damp

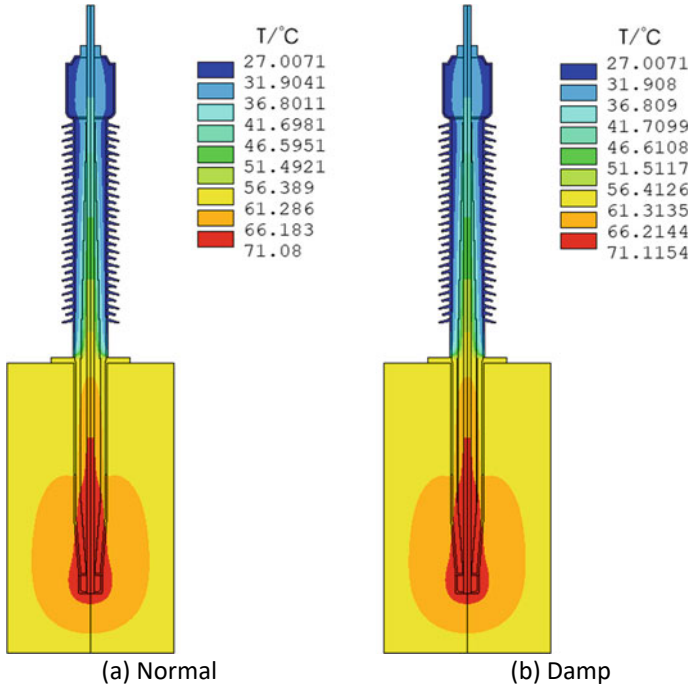
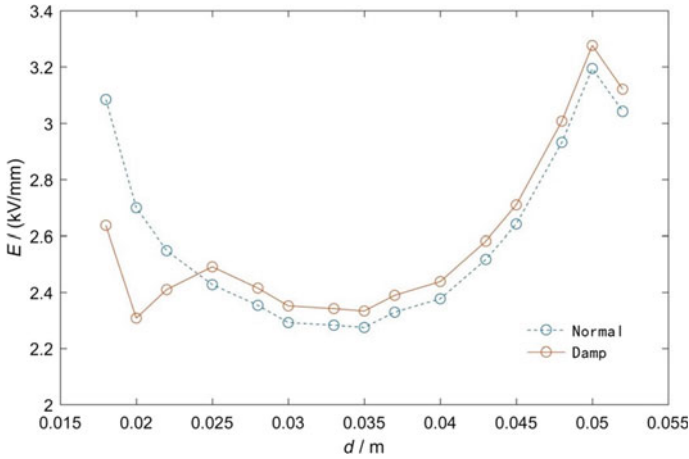


Fig. 9 Temperature distribution of end screen wetted casing



**Fig. 10** Radial electric field distribution of capacitor core before and after zero screen damping

**Table 5** Comparison of dielectric loss of each part of zero screen before and after damp exposure

Materials	Normal dielectric loss	Loss of damp medium
Electric insulating oil	0.02	0.02
Oil paper	1.54	1.59
Porcelain bushing	7.31e-4	7.12e-4

reaching 0.059 and 0.082 kV/mm, respectively. It is worth noting that at this point, the zero screen electric field intensity significantly decreases, with a maximum decrease of 0.45 kV/mm.

Before and after the zero screen is damp, the dielectric loss of each part of the casing is shown in Table 5. After slight moisture exposure, the oil paper dielectric loss in the casing increases slightly from 1.54 to 1.59 W. Similar to the end plate damp, but this part of the loss is much lower than the casing loss. Therefore, slight moisture exposure (5% moisture mass fraction) in the zero screen leads to a small change in casing temperature rise.

## 4 Conclusion

The temperature of the casing after being damp is related to the dielectric loss, but the temperature rise of the porcelain bushing caused by slight moisture is less significant, with an average change of 5 °C in conductor temperature and 1 °C in porcelain bushing temperature. In the actual inspection process, attention should be paid to the differential temperature rise of the casing through horizontal comparison. For cases where the overall temperature of the casing is relatively uniform, but the







temperature rise amplitude is relatively high compared to other phases of the casing, special attention should be paid.

## References

1. Dong W (2020) Transformer bushing fault diagnosis and state evaluation technology based on multi-source detection data. North China Electric Power University. <https://doi.org/10.27139/d.cnki.ghbdu.2020.000340> (in Chinese)
2. Zhao Z, Xu Z, Wang J, Jianxin G, Yu X, Li G (2015) Research on fire safety of large power transformers. High Voltage Technol 41(10):3378–3384. <https://doi.org/10.13336/j.1003-6520.hve.2015.10.026> (in Chinese)
3. Chen L, Hu X (2009) Reliability analysis of national power transmission and transformation facilities in 2008. Electric Power China 42(05):1–6 (in Chinese)
4. Dai Q (2019) Oil impregnated paper bushing be affected with damp be affected with damp degradation process and defect diagnosis research. North China Electric Power University, Beijing. <https://doi.org/10.27140/d.cnki.ghbbu.2019.000026> (in Chinese)
5. Yang D, Chen R, Tong H, Tan X (2021) Fault detection of transformer casing insulation defects based on infrared detection technology. Autom Instrum 36(5):57–61. <https://doi.org/10.19557/j.cnki.1001-9944.2021.05.012> (in Chinese)
6. Jiang J, Bie Y, Li J, Yang X, Ma G, Lu Y, Zhang C (2021) Fault diagnosis of the bushing infrared images based on mask R-CNN and improved PCNN joint algorithm. High Voltage 6(1):116–124
7. Zhou K, Liao Z, Chen L, Huang J (2019) Infrared image state analysis of voltage heating device based on double background separation and adaptive mesh. Power Syst Protect Control 47(24):123–130. <https://doi.org/10.19783/j.cnki.pspc.190202> (in Chinese)
8. Zhou K (2020) Intelligent infrared image analysis of key transformer equipment based on improved AlexNet model. South China University of Technology. <https://doi.org/10.27151/d.cnki.ghnlu.2020.001096> (in Chinese)
9. Analysis of replies to the 1997 technical questionnaire on power transformer failures and troubles. In: Proceedings of the sixty-fourth annual international conference of double clients, 1997. pp 8–2.1
10. Lu G, Hou P, Fan Q et al (2018) A kind of ultrasonic test device for transformer casing end plate discharge. Electr Measure Instrum 55(17):120–124 (in Chinese)
11. Xu Y, Liu W, Gao W (2020) Research on sensitivity of casing end plate sensing method for transformer partial discharge detection. Transformer 2020(06):49–54. <https://doi.org/10.19487/j.cnki.1001-8425.2020.06.010> (in Chinese)
12. Zhang L, Yuan X, Wu X et al (2018) Performance evaluation of high-power SiC MOSFET modules in comparison to Si IGBT modules. IEEE Trans Power Electron 34(2):1181–1196
13. Hebert PP, Steed RC (1978) A high voltage bushing thermal performance computer model. IEEE Trans Power Appar Syst 6:2219–2224

# Influence of Main Shield Voltage Distribution Configuration on the Post-arc Sheath Development of Vacuum Interrupters



Hui Chen , Xian Cheng , Guowei Ge , and Shuai Du 

**Abstract** In this paper, the plasma ion and electron density in the post-arc stage of vacuum circuit breakers and the influence of the main shield voltage distribution configuration on this article are simulated by a 2-D particle-in-cell model and probe diagnosis experiments. In the simulation of the distribution of charged particles and the rate of development of the sheath, there is no applied magnetic field. The main shielding voltage distribution in the post-arc stage is the main cause of the asymmetric distribution of charged particles, which also slows down the attenuation process of the plasma. The main shield voltage distribution configuration in the post-arc phase not only accelerates the media recovery of the post-arc phase of the vacuum circuit breaker, but also reduces the risk of the vacuum circuit breaker breaking down when the large fault current is disconnected in the post-arc phase. In addition, the main shield voltage distribution configuration can accelerate the ions and electrons decay and the development of the post-arc sheath layer, as well as make the post-arc potential distribution more uniform and enhance the internal insulation of the vacuum interrupter. The probe diagnosis results show that the attenuation of residual plasma is the fastest when the main shield voltage distribution configuration is 50%TRV, and the distribution of cathode spots is more uniform in arc extinguishing, which is more favorable to the diffusion of the remaining plasma.

**Keywords** Vacuum circuit breaker · Self-voltage sharing vacuum interrupters · PIC simulation · Probe diagnosis · Vacuum arc

---

H. Chen · X. Cheng · G. Ge (✉) · S. Du  
School of Electrical and Information Engineering, Zhengzhou University, Zhengzhou 450001, China  
e-mail: [ggw@zzu.edu.cn](mailto:ggw@zzu.edu.cn)

He'nan Engineering Research Center of Power Transmission and Distribution Equipment and Electrical Insulation, Zhengzhou 450001, China

© Beijing Paiké Culture Commu. Co., Ltd. 2024  
X. Dong and L. Cai (eds.), *The Proceedings of 2023 4th International Symposium on Insulation and Discharge Computation for Power Equipment (IDCOMPU2023)*, Lecture Notes in Electrical Engineering 1103, [https://doi.org/10.1007/978-981-99-7413-9\\_6](https://doi.org/10.1007/978-981-99-7413-9_6)

## 1 Introduction

Vacuum circuit breakers are widely used in low and medium voltage applications because of their environmental friendliness, long life and good maintenance [1, 2]. With the increasing voltage level of its application, the main shield of vacuum circuit breaker interrupter is more and more prominent, and there is a lack of research on the main shield of vacuum interrupter at home and abroad. Yusuke Nakano investigates the feasibility of using the electrical potential control effect of steam shields to increase the withstand pressure of the vacuum interrupter inside [3]. Yuan Zhao studied the dynamic properties of the vacuum arc cathode spots dissipation process [4, 5]. Asaad Shemshadi proposes a new finite-element modeling of the plasma diffusion process between electrodes inside a vacuum interrupter. To better understand the diffusion process of vacuum plasma in the vacuum interrupter, a new set of coupled equations is employed, including the Stefan-Maxwell diffusion equation, considerations for collisions and interactions between particles, and calculations of coulombic integral plasma conductivity [6]. Liu Zhiyuan studied the characteristics of vacuum arc and the short-circuit current breaking ability under the minimum number of arc burns [7, 8]. Liu Liming conducted an experimental study on the cathode spot velocity in the vacuum arc with high  $di/dt$  [9–11]. Vahid vahedi et al. have established Two-Dimensional Bounded Plasma Simulation Codes [12]. Wang Lijun used the two-dimensional particle simulation method to study the influence of transverse magnetic field on plasma attenuation in the post-arc stage of vacuum circuit breaker [13, 14]. Geng yingsan studied the pre-breakdown properties spiral-shaped TMF contacts [15]. Mo Yongpeng studied the influence of the transient breaking voltage of the mechanical HVDC circuit breaker on the post-arc medium recovery process [16, 17]. Huang Xiaolong designed a new DC vacuum interrupter, which has the key characteristics of high peak and low remanence [18].

Vacuum circuit breaker gradually developed from column to canister type, canister type vacuum circuit breaker whose structure main shield to ground stray capacitance is significantly increased relative to column type, thus causing the interrupter chamber main shield voltage division uneven problem. Conventional equalization methods are mainly external equalization capacitors, which not only equalize the main shield, but also well solve the equalization between series breakers. However, for the requirements of the compact design structure of the canister circuit breaker, the traditional equalization method of external capacitor gradually fails to meet the requirements, therefore, this paper carries out a study of the post-arc microscopic characteristics for the proposed integrated self-averaging vacuum interrupter [19]. The two-dimensional post-arc electron and ion density distributions, post-arc sheath potential distributions, and the changes of adsorbed electron and ion currents in contacts and shields under different equalization configurations are obtained by numerical simulations for different equalization configurations; the decay process of post-arc residual plasma under different equalization configurations is diagnosed by probes, and the development process of vacuum arc and the dynamic changes of cathode spots during the arc extinguishing stage are observed by high-speed cameras.

## 2 Particle Simulation and Results

### 2.1 Particle Simulation Model

The simulation model is shown in Fig. 1. To meet the plasma frequency requirement, the simulation time step is  $5 \times 10^{-12}$  s, and the simulation duration is 8  $\mu$ s. The simulation area is 120 mm long and 70 mm wide, and in order to meet the requirements of the Debye length, the number of grid sections are 240 long and 140 wide, respectively, with a contact diameter of 50 mm and a gap of 10 mm. In order to correspond to the experiments below, the TRV drop rate is set to  $-0.05$  kV/ $\mu$ s, and the initial plasma density is  $10^{17}$  m $^{-3}$ . The post-arc cathode was set to TRV, the post-arc anode was ground potential, and the main shield was post-arc anode polarity, 0.25 TRV, 0.50 TRV, 0.75 TRV respectively.

In this part, we investigate the attenuation characteristics of ions and electrons in the plasma under different shielding potentials. Figure 2 shows the density distribution of the post-arc stage of charged particles. Distributions of electric potential in the case of the shield on post-arc anode polarity, 0.25 TRV, 0.50 TRV, 0.75 TRV are shown in Fig. 3.

Under the effect of different potential, electrons escape rapidly from the gap between electrodes, which is shown in Fig. 2. Ions cannot respond to the TRV as rapidly as electrons. Consequently, an ion sheath is formed close to the post-arc cathode as shown in Fig. 3. We can see that the electrons in the plasma gradually reach the post-arc anode and are then absorbed. Simultaneously, electrons at the edge of the plasma move towards the shield. The radial diffusion of electrons decreases with increasing shield potential, and the increasing shield potential limits the radial motion of electrons. The development rate of the sheath increases with the increase of

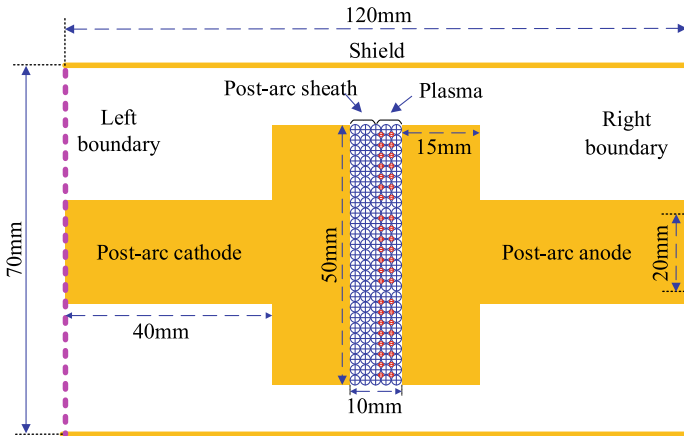
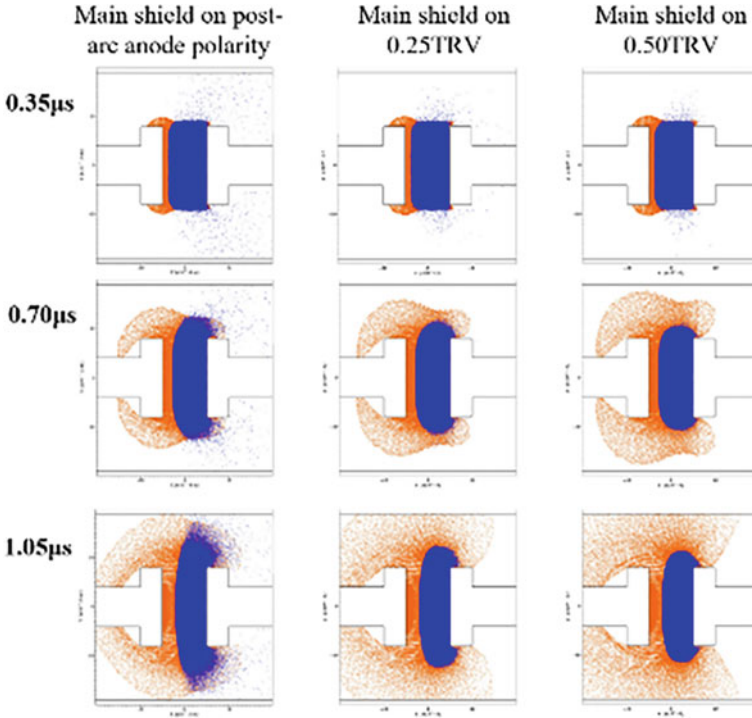


Fig. 1 Diagram of the simulation model



**Fig. 2** Electron density and ion density distribution plot at different times after current-zero; the post arc cathode is on the left

the shield potential. Compared with the shield potential which is the post-arc anode polarity, the other cases have a more uniform post-arc potential distribution.

## 2.2 Simulation Results

The post-arc anode, post-arc cathode, and shield post-arc current changes are shown in Fig. 4. As can be seen from the figure, with the increase of shield potential, the after-arc cathode after-arc current changes little, after-arc anode and shield current changes are relatively obvious, so the after-arc current is mainly generated by the after-arc anode and shield adsorption electrons and ions. When the shield potential is 0.00 TRV, the trend of the post-arc current generated on the shield is different from other cases, as shown in Fig. 4c, which shows a trend of first decreasing, then increasing and then decreasing, and finally tends to be smooth.

Figure 5a shows how the total post-arc current changes, then by integrating the post-arc current, the post-arc charge variation is acquired, which is shown in Fig. 5b. As shown in the figure, with the increase of shield potential, the value of post-arc

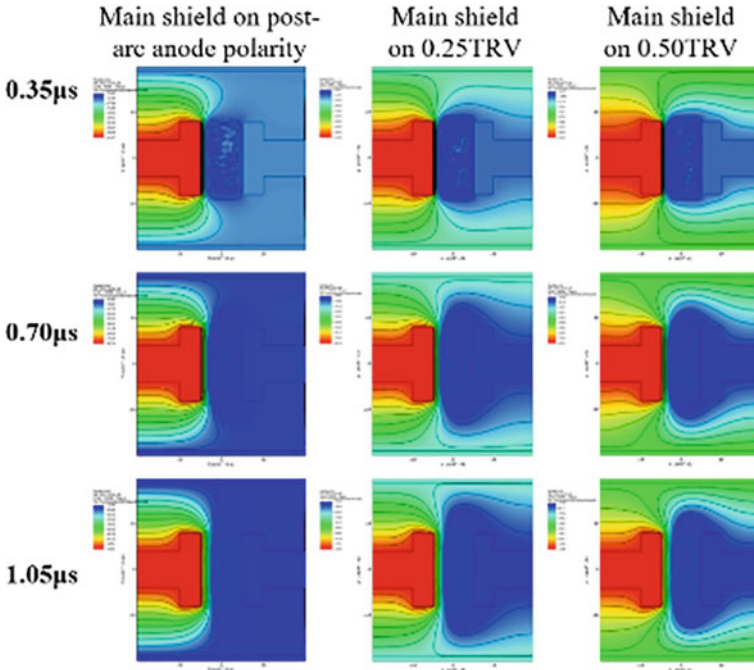


Fig. 3 Electric potential distribution plot at different times; the post-arc cathode is on the left

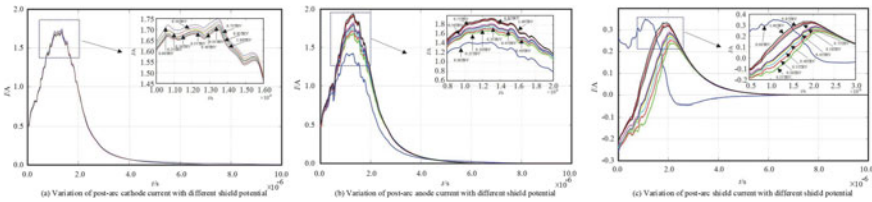


Fig. 4 Post-arc current change of post-arc cathode, post-arc anode and shield

charge gradually increases. When the shield potential is set to 0.00 TRV, the post-arc charge is the smallest and the medium recovery and opening capacity is the strongest, which is because when the shield potential is the ground potential, the shield is equivalent to the post-arc anode, which is equal to increasing the area of the post-arc anode and is more conducive to the diffusion of the post-arc residual plasma.

The diffusion of post-arc residual plasma is a very important process of vacuum circuit breaker, and the electron density of post-arc residual plasma is also an important parameter of vacuum circuit breaker, which directly determines the medium recovery process post-arc and affects the successful opening of vacuum circuit breaker. Therefore, this paper carries out a probe diagnostic study of post-arc residual

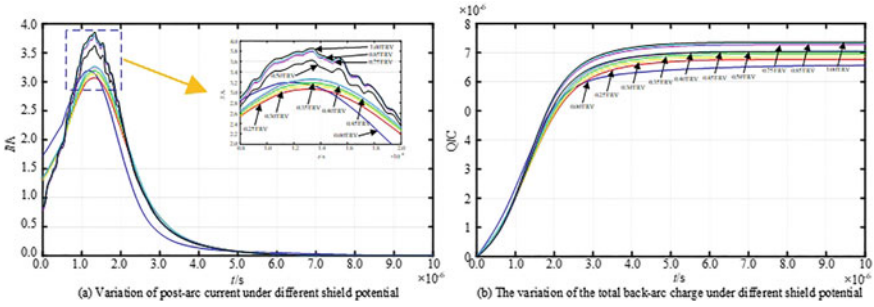


Fig. 5 Post-arc current and post-arc charge change

plasma by attaching different sizes of equalizing capacitors to the two ends of the shield to produce different sizes of shield potentials.

### 3 Probe Diagnosis Experimental and Results

#### 3.1 Experimental Setup

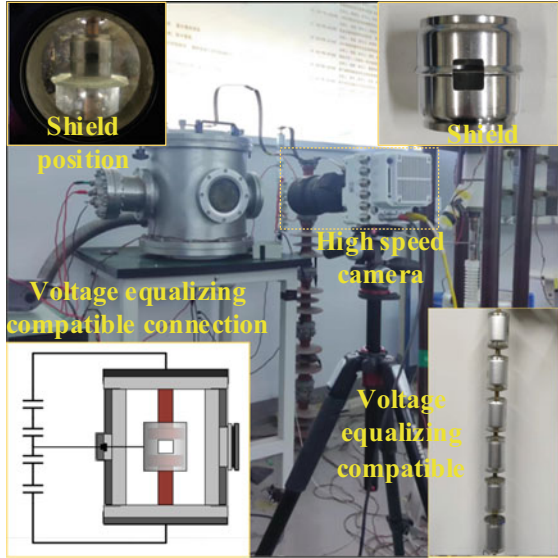
The probe diagnostic experimental system is shown in Fig. 6. It mainly includes the equalizing capacitor, shield, high-speed camera, etc. Using the synthetic test circuit and the detachable vacuum chamber, the development process of the vacuum arc and the quenching position of the cathode spot are observed by the high-speed camera. The arrangement of the equalizing capacitor and the corresponding shield potential are shown in Table 1.

#### 3.2 Experimental Results

The transient recovery voltage and shield waveforms are shown in Fig. 7. The residual plasma electron density changes after the arc at different shield potentials are shown in Fig. 8. As can be seen from the figure, the initial value and decay time of residual plasma electron density after the arc are different for different shield potentials, and when the shield potential is 0.50 TRV, the initial value of electron density after the arc is  $3.47 \times 10^{10} \text{ cm}^{-3}$ , at which time the electron density decays fastest and the decay time is about 18  $\mu\text{s}$ .

The vacuum arc cathode spot extinguishing process at different shield potentials is shown in Fig. 9. As can be seen from the figure, the distribution of cathode spots in the arc extinguishing stage will be different at different shield potentials, and the distribution of cathode spots in the arc extinguishing stage will be relatively uniform

**Fig. 6** Diagnostic experiment system



**Table 1** Arrangement of equalization capacitors and corresponding shield potential

Shield potential	Arrangement of equalization capacitors
Suspension potential	
0.00 TRV	
0.25 TRV	250 pF (High voltage side), 750 pF (Low voltage side)
0.30 TRV	300 pF (High voltage side), 700 pF (Low voltage side)
0.50 TRV	500 pF (High voltage side), 500 pF (Low voltage side)
0.75 TRV	750 pF (High voltage side), 50 pF (Low voltage side)
1.00 TRV	

compared with the case of no uniform pressure. The cathode spot distribution and extinguishing position will have an impact on the shield potential after the arc, and will also affect the diffusion of residual plasma after the arc.



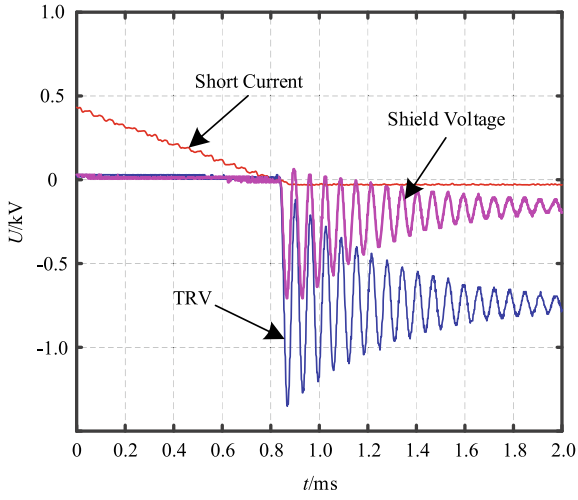


Fig. 7 The waveform of transient recovery voltage

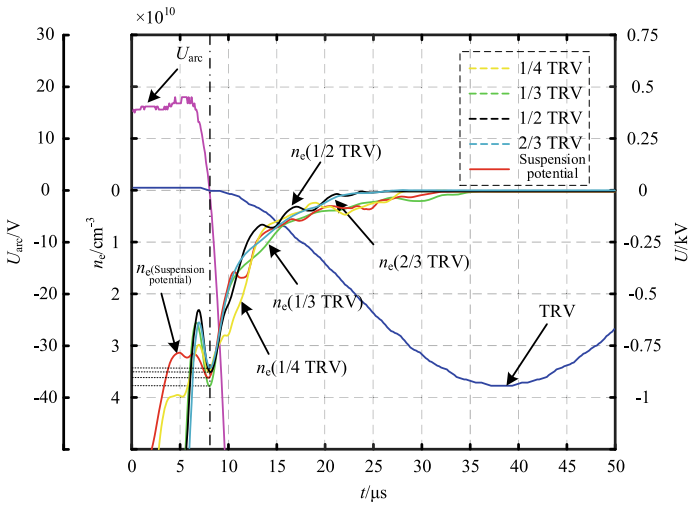


Fig. 8 The waveform of post-arc electron density decay

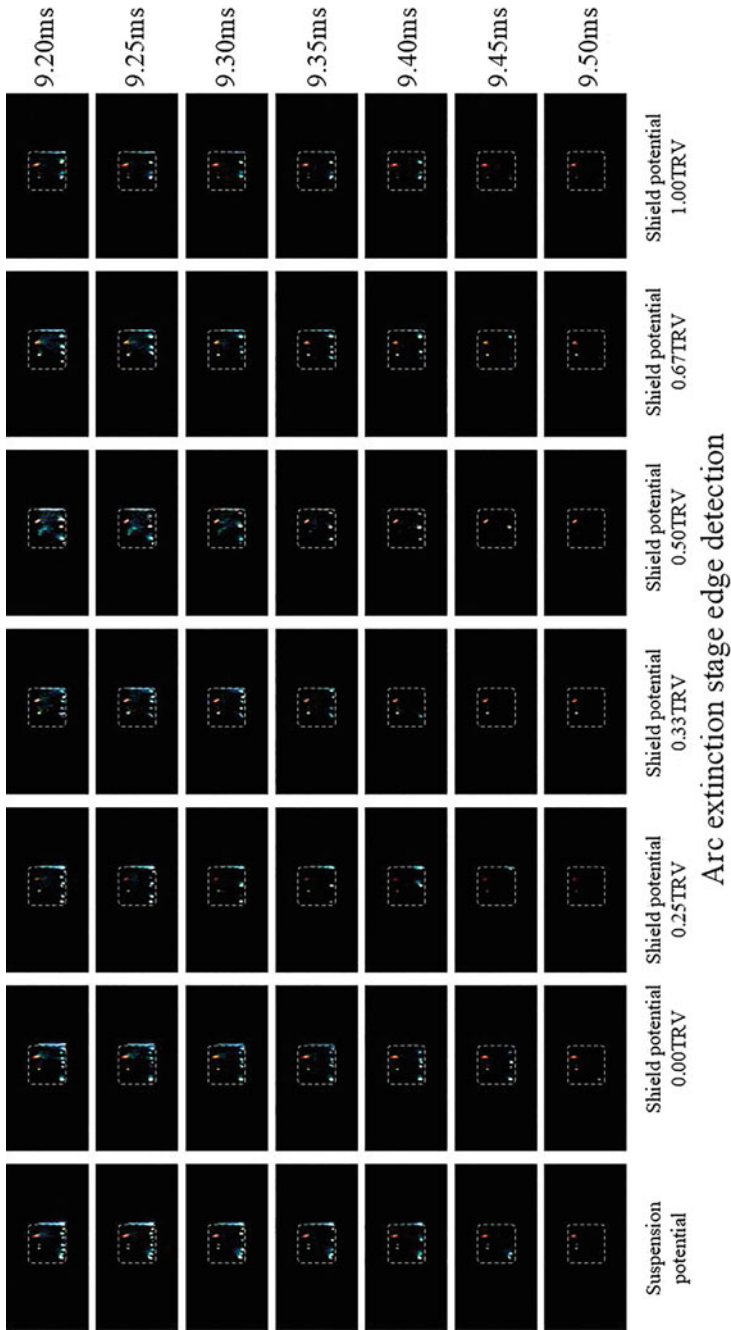


Fig. 9 Vacuum arc cathode spot extinguishing process

## 4 Conclusions

In this paper, the influences of Main Shield Voltage Distribution Configuration on the Post-arc Sheath Development of Vacuum Interrupters were simulated. The main conclusions are as follows:

1. Particle simulation shows that the smaller the potential of the main shield, the smaller the post-arc charge, and the stronger the breaking ability of the vacuum interrupter. It works best at 50%TRV of main shield potential.
2. The probe diagnostic showed that when the main shield potential was 50%TRV, the initial value of post-arc electron density was the minimum, about  $3.47 \times 10^{10} \text{ cm}^{-3}$ , electron density decays the fastest, about 18  $\mu\text{s}$ .
3. Different voltage configurations of the main shield will affect the development of vacuum arc. In the quenching stage of the arc, the distribution of cathode spots is more uniform than that of nonpartial voltage measures, which will affect the two-dimensional distribution of post-arc electron density and is more conducive to the diffusion of residual plasma in the post arc.

## References

1. Taylor ED (2022) Electrical life of vacuum interrupters for load current switching. *IEEE Trans Plasma Sci* 50(9):2642–2651
2. Nakano Y (2018) Increasing the internal field strength of vacuum interrupters with vapor shield potential control. *IEEE Trans Power Deliv* 33(6):3155–3161
3. Kuhn B (2020) Recent developments of field grading for high voltage vacuum circuit breakers, Budapest, Hungary, pp 1265–1275
4. Liu L (2022) Dynamic characteristics of cathode spots during expansion process in a vacuum arc. *J Phys D: Appl Phys* 55(47)
5. Sarrailh P (2008) Two-dimensional simulation of the post-arc phase of a vacuum circuit breaker. *IEEE Trans Plasma Sc* 36(4):1046–1047
6. Shemshadi A (2019) Modeling of plasma dispersion process in vacuum interrupters during postarc interval based on fem. *IEEE Trans Plasma Sci* 47(1):647–653
7. Guan C (2022) A relationship between vacuum arc characteristics and short-circuit current interrupting capability at minimum arcing times. *IEEE Trans Plasma Sci* 50(9):2670–2680
8. Wei L (2022) Investigation on the arc appearance during the arc slot crossing process between the spiral type contacts. *IEEE Trans Plasma Sci* 50(6):1739–1748
9. Liu L (2022) Experimental investigation on the velocity of cathode spots in a vacuum arc with high di/dt. *J Phys D: Appl Phys* 55(19)
10. Sarrailh P (2008) Plasma decay modeling during the post-arc phase of a vacuum circuit breaker. In: 2008 23rd International symposium on discharges and electrical insulation in vacuum, pp 406–409.
11. Rowe S (2010) Post-arc period of vacuum circuit breakers: new 2d simulation and experimental results. In: 24th ISDEIV 2010, pp 423–426
12. Vahid V (1997) Simultaneous potential and circuit solution for two-dimensional bounded plasma simulation codes. *J Comput Phys* 131(1)
13. Wang D (2020) 2-d particle simulation on the influence of transverse magnetic field on the plasma decay in postarc stage of vacuum circuit breakers. *IEEE Trans Plasma Sci* 48(11)

14. Wang D (2020) Two-dimensional kinetic simulation of plasma dynamics in the post-arc stage of vacuum circuit breakers. *Phys Plasmas* 27(1)
15. Geng Y (2022) Prestrike characteristics of single-break vacuum circuit breakers with cup-type AMF contacts and spiral-type TMF contacts under inrush current conditions. *IEEE Trans Plasma Sci* 50(9):2660–2669
16. Mo Y (2022) Research on the transient interrupting voltage of mechanical HVDC circuit breaker and its influences on the postarc dielectric recovery process. *IEEE Trans Plasma Sci* 50(12):4944–4950
17. Yongpeng MO (2022) Study of post-arc residual plasma dissipation process of vacuum circuit breakers based on a 2d particle-in-cell model. *Plasma Sci Technol* 24(04):127–135
18. Xie Y (2023) Design and study of the key characteristics of a new dc vacuum interrupter with a high peak and low residual magnetic field. *IEEE Trans Plasma Sci* 51(3):687–699
19. Guowei GE et al (2021) Special self-voltage sharing vacuum interrupter for series-connection. *Power Syst Technol* 45(04):1618–1625

# Simulation Study on Spatial Distribution Characteristics of Partial Discharge UHF Signal in Transformer Outlet Device



Yuntian Guo, Hao Liu, Guoming Ma, Zhenxing Fan, Dan Zhou,  
and Shicong Zhai

**Abstract** The power transformer plays a critical role in power grid. In the case of extra-high and ultra-high voltage transformers, an indirect central outlet device is commonly employed. This device, however, poses a vulnerability to transformer insulation due to concentrated field strength. Consequently, it becomes imperative to investigate the detection of partial discharges (PD) in the outlet device. The ultra-high frequency (UHF) method is widely utilized for monitoring PD in electrical equipment due to its high sensitivity. This study focuses on accurately modeling the indirect outlet device and employs the time-domain finite difference simulation method to study signals characteristics associated with PD in the outlet device. The simulation results provide evidence that when PD takes place in the outlet device, the UHF signal effectively propagates into the external space through the oil channel between the casing and bushing. The location and magnitude of the PD have a significant influence on the time-domain waveform of the UHF signal.

**Keywords** On-line monitoring · Power transformer · Electromagnetic wave signal

---

Y. Guo (✉) · H. Liu · G. Ma · Z. Fan · S. Zhai

State Key Laboratory of Alternate Electrical Power System with Renewable Energy Sources,  
North China Electric Power University, Beijing 102206, China

e-mail: [yuntian.guo@ncepu.edu.cn](mailto:yuntian.guo@ncepu.edu.cn)

H. Liu

e-mail: [liu\\_hao@ncepu.edu.cn](mailto:liu_hao@ncepu.edu.cn)

G. Ma

e-mail: [ncepumgm@ncepu.edu.cn](mailto:ncepumgm@ncepu.edu.cn)

Z. Fan

e-mail: [120222201739@ncepu.edu.cn](mailto:120222201739@ncepu.edu.cn)

S. Zhai

e-mail: [120212201359@ncepu.edu.cn](mailto:120212201359@ncepu.edu.cn)

D. Zhou

Electric Power Research Institute of Guangdong Power Grid Co., Ltd., Guangzhou 510080, China

e-mail: [dan\\_zhou@189.cn](mailto:dan_zhou@189.cn)

© Beijing Paiké Culture Commu. Co., Ltd. 2024

X. Dong and L. Cai (eds.), *The Proceedings of 2023 4th International Symposium on Insulation and Discharge Computation for Power Equipment (IDCOMPU2023)*, Lecture Notes in Electrical Engineering 1103, [https://doi.org/10.1007/978-981-99-7413-9\\_7](https://doi.org/10.1007/978-981-99-7413-9_7)

# 1 Introduction

As an important component of the high-voltage power grid, transformers play a crucial role in ensuring the safety and economic benefits of the power grid. Currently, China has constructed and put into operation multiple  $\pm 1100$  kV ultra-high voltage direct current transmission lines, and converter transformers are one of the most critical equipment in DC transmission projects [1–3]. The outlet device is important components of large power transformer and also a weak part of transformer insulation. The central indirect high-voltage device is the most popular method for its high economic efficiency.

The outlet device of the transformer refers to the insulation structure connecting the winding and the outlet bushing of the transformer. This part usually uses oil-paper composite insulation structure, mainly composed of equipotential balls, equipotential tubes, insulating paper tubes, support bars, and steel shells. Multiple layers of insulating paper tubes are placed near the equipotential tubes to divide the oil gap, achieve a uniform electric field and improve the insulation strength. An insulating bushing is installed above the outlet device, which is connected to the outlet device through bolts. During long-term operation, the outlet device often experiences PD due to construction techniques and insulation degradation, which can develop into more severe accidents [4, 5].

PD can be detected through methods such as ultrasonic detection, electrical detection, UHF detection, optical detection, or capacitive detection, which analyze different aspects of the signals generated by partial discharge events. [6]. The UHF method is based on the radiation characteristics of PD under high frequencies. It uses an antenna to receive signals and detects the presence of PD. The advantage of UHF for PD is its ability to capture and analyze electromagnetic waves over longer distances, enabling remote monitoring of PD events and facilitating detection in hard-to-reach areas [7]. Therefore, the UHF method can be applied to the detection of PD in outlet devices.

On the one hand, there is no UHF sensor inside the outlet device in the engineering field, and the UHF sensor is often installed on the transformer body and the oil drain valve. On the other hand, the existence of various media and metal structures causes the electromagnetic waves generated by PD to undergo multiple refractions and reflections, making the propagation characteristics of electromagnetic waves very complicated [8]. Therefore, in order to achieve highly sensitive detection of PD in the outlet device, it is important to obtain its propagation characteristics.

This article studies the PD fault of the outlet device [9], analyze its propagation characteristics, and the impact of the PD capacity on signal features.

## 2 The Establishment of Simulation Model

This study presents a model of a transformer based on its actual on-site operation. Taking into account the intricate structure of the outlet device and its impact on electromagnetic wave propagation characteristics, an accurate representation of the outlet device and the upper installed bushing is developed. The outlet device consists of various components such as an equipotential ball, equipotential tube, and insulation paper cylinder. On the other hand, the oil-immersed bushing comprises a porcelain bushing, conductor rod, and multi-layered capacitance screen. To focus specifically on the signal characteristics of PD in the outlet device, simplifications are made to the transformer's main body. The electromagnetic and physical parameters of the materials used in the simulation are obtained from product manuals or relevant literature. The following diagram illustrates the simulation model utilized in this study (Fig. 1).

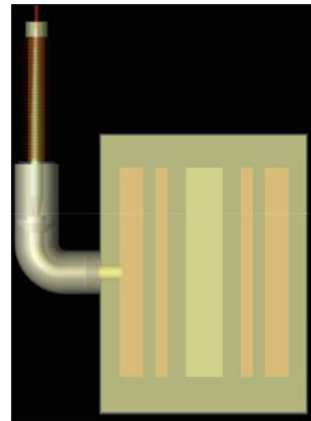
Gaussian pulse current is frequently employed in simulation studies to replicate the ultrahigh frequency signals produced by PD [10]. The formula representing Gaussian pulse current is provided below:

$$I(t) = I_0 \exp\left(-\frac{4\pi(t - t_0)^2}{t_0^2}\right) \quad (1)$$

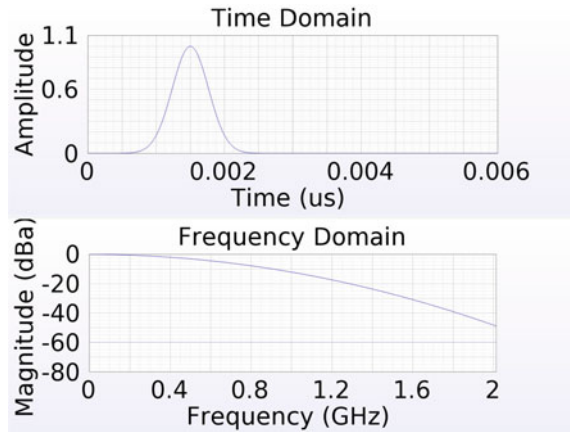
The pulse width, denoted as  $t_0$ , and the current amplitude, denoted as  $I_0$ , are important parameters in this context. By adjusting these values, various types of PD can be simulated in computer simulations. The simulation produces both time-domain and frequency-domain waveforms for the Gaussian pulse excitation. The visual representations of these waveforms are presented below (Fig. 2).

Based on the common faults that occur during actual operation, three PD sources were set up in this simulation, labeled as P1, P2, and P3. Among them, P1 and P2 were used to simulate the suspended discharge caused by the looseness of bolts due

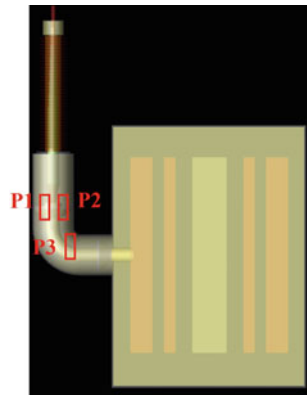
**Fig. 1** The simulation model



**Fig. 2** Gaussian pulse waveform used as an excitation for PD



**Fig. 3** Schematic diagram of the region of PD in the simulation

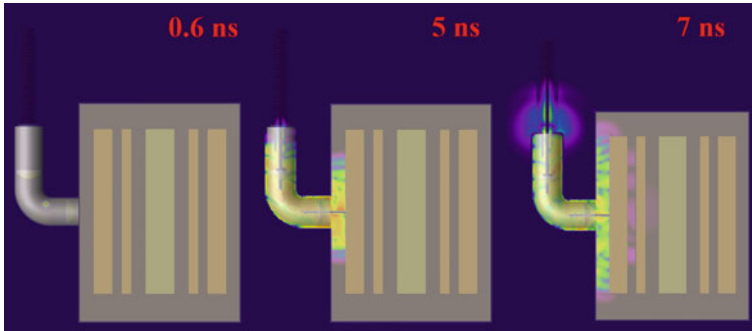


to long-term operation, resulting in the detachment of the outlet device from the bushing. P3 was used to simulate the PD caused by the distortion of the electric field due to the settling of suspended metal particles on the insulating paper tube of the lead device in the transformer oil (Fig. 3).

### 3 Evaluation of UHF Signal Propagation Characteristics

In this analysis, the propagation characteristics of UHF signals of PD were examined, using the PD P3 at the insulating paper tube as an example. Figure 4 illustrates the findings, indicating that when PD takes place, the electromagnetic wave exhibits a spherical wave propagation pattern. As the wave diffuses towards the upper part of the outlet device and the interior of the transformer, it undergoes multiple reflections





**Fig. 4** Schematic diagram of UHF signal propagation during PD at insulating paper tube

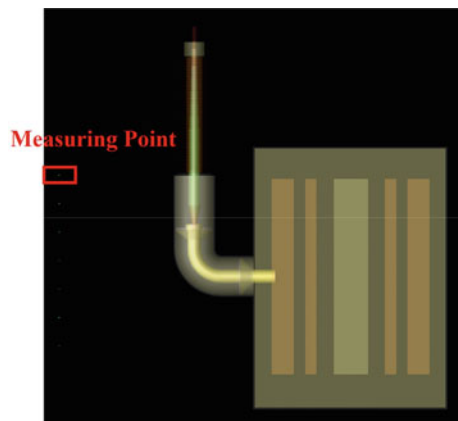
and refractions due to the structural influences. However, the UHF signal is unable to directly penetrate the metal shell due to its limited penetration depth.

After a time delay of 5 ns, a portion of the UHF signal propagates through the oil channel of the outlet device, extending to the external space. Simultaneously, another portion travels upwards along the coaxial waveguide structure created by the multi-layer capacitance screen of the bushing, reaching the upper part of the bushing.

In order to compare the variations in UHF signals during PD at different locations, Gaussian current signals of equal magnitude were applied to P1, P2, and P3 respectively. To capture the waveform of the UHF signal during PD, measurement points were strategically positioned 1 m to the left of the outlet device. The specific location of the measuring point can be observed in Fig. 5.

In Fig. 6, the UHF signals within the first 40 ns are shown when PD equivalent to 800 pC occurs at P1, P2, and P3 positions by setting  $I_0$ . Comparing the waveforms of P1 and P2, no significant differences in waveform shape, amplitude, and arrival time of signals are observed when PD occurs at different positions of the equipotential ball.

**Fig. 5** Measuring point position of UHF signal



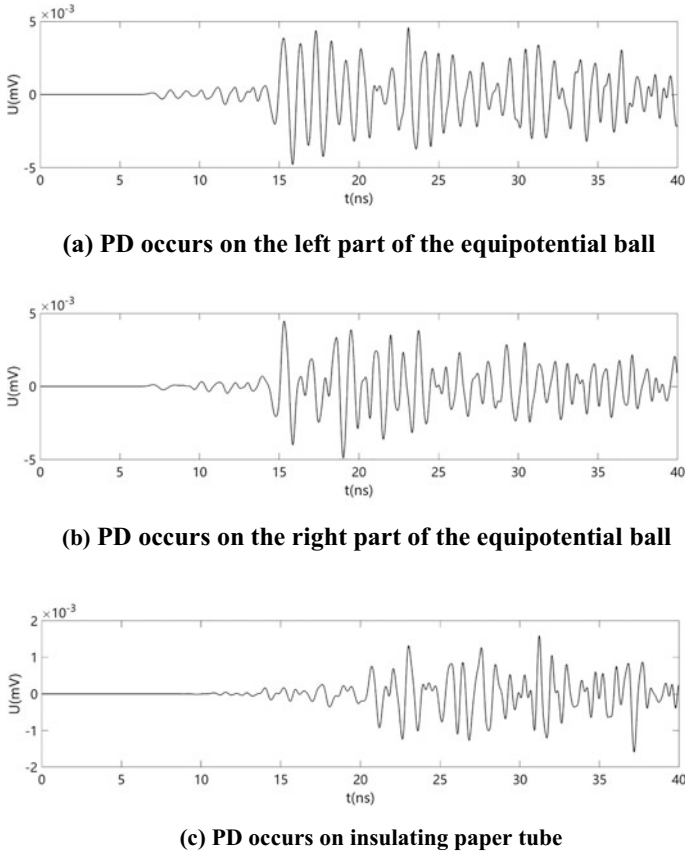


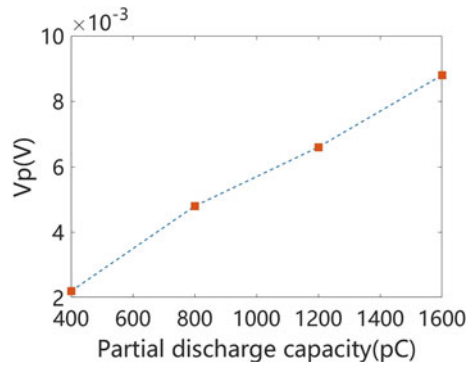
Fig. 6 UHF signals of PD at different region

Comparing P1 and P3 waveforms, it can be seen that when PD occurs at the insulating paper tube, the longer propagation distance causes a significant delay and attenuation of the UHF signal amplitude. Based on the above analysis, selecting a suitable UHF sensor installation location can achieve initial fault location and fault type diagnosis on the basis of PD detection.

#### 4 Examination of the Impact of Partial Discharge on Waveform Analysis

In the preceding section, we examined the propagation characteristics of UHF signals generated by PD. The findings indicated that only a small portion of the electromagnetic waves produced by PD can effectively propagate through the oil channel

**Fig. 7** Amplitude of UHF signal under different PD capacity



between the bushing and the outlet device, reaching the free space. Consequently, to aid in sensor design and enhance detection sensitivity, it becomes imperative to analyze the UHF signal waveforms under various levels of PD.

For this purpose, we selected the P1 point, located on the left side of the equipotential ball, as the source of PD. Simulations were conducted to replicate PD with power levels of 400, 800, 1200, and 1600 pC, achieved by adjusting the value of  $I_0$ . The simulation results are depicted in Fig. 7, presenting an overview of the findings.

From Fig. 7, it can be seen that when PD occurs at the equipotential ball, the amplitude of the UHF signal increases almost linearly with the increase of the discharge quantity.

## 5 Summary

Based on the aforementioned analysis, the following conclusions can be derived.

The occurrence of PD at the outlet device has an impact on the propagation behavior of the UHF signal. This propagation is influenced by the structural characteristics of the outlet device, resulting in the UHF signal spreading to the external space through a series of reflections and gaps between the casing and the outlet device, facilitated by the sleeve.

By carefully selecting an appropriate position for the UHF sensor, it becomes feasible to make a straightforward assessment of the type and magnitude of PD faults transpiring in the outlet device.

These findings highlight the significance of understanding the propagation characteristics of UHF signals during PD events and emphasize the potential for effective fault diagnosis based on UHF signal analysis.

**Acknowledgements** This work has received support from the Scientific Project (No. GDKJXM20201973) provided by Guangdong Power Grid Co., Ltd.

## References

1. Cavallini A, Montanari GC, Tozzi M, Chen X (2011) Diagnostic of HVDC systems using partial discharges. *IEEE Trans Dielectr Electr Insul* 18:275–284. <https://doi.org/10.1109/TDEI.2011.5704519>
2. Jacob ND, Mcdermid WM, Kordi B (2012) On-line monitoring of partial discharges in a HVDC station environment. *IEEE Trans Dielectr Electr Insul* 19:925–935. <https://doi.org/10.1109/TDEI.2012.6215096>
3. Alassi A, Bañales S, Ellabban O, Adam G, MacIver C (2019) HVDC Trans: Technolo Rev Market Trends Future Outlook. *Renew Sustain Energy Rev* 112:530–554. <https://doi.org/10.1016/j.rser.2019.04.062>
4. Jiang J, Chen J, Li J, Yang X, Bie Y, Ranjan P, Zhang C, Schwarz H (2021) Partial discharge detection and diagnosis of transformer bushing based on UHF Method. *IEEE Sens J* 21:16798–16806. <https://doi.org/10.1109/JSEN.2021.3066809>
5. Ren M, Zhou J, Miao J (2021) Adopting spectral analysis in partial discharge fault diagnosis of GIS with a micro built-in optical sensor. *IEEE Trans Power Delivery* 36:1237–1240. <https://doi.org/10.1109/TPWRD.2020.3028511>
6. Wu M, Cao H, Cao J, Nguyen H-L, Gomes JB, Krishnaswamy SP (2015) An overview of state-of-the-art partial discharge analysis techniques for condition monitoring. *IEEE Electr Insul Mag* 31:22–35. <https://doi.org/10.1109/MEL.2015.7303259>
7. Tang Z, Li C, Cheng X, Wang W, Li J, Li J (2006) Partial discharge location in power transformers using wideband RF detection. *IEEE Trans Dielectr Electr Insul* 13:1193–1199. <https://doi.org/10.1109/TDEI.2006.258190>
8. Cheng J, Xu Y, Ding D, Liu W (2021) Investigation of the UHF partial discharge detection characteristics of a novel bushing tap sensor for transformers. *IEEE Trans Power Delivery* 36:2748–2757. <https://doi.org/10.1109/TPWRD.2020.3026102>
9. Zheng S, Li C, Tang Z, Chang W, He M (2014) Location of PDs inside transformer windings using UHF methods. *IEEE Trans Dielectr Electr Insul* 21:386–393. <https://doi.org/10.1109/TDEI.2013.003863>
10. Hoshino T, Maruyama S, Sakakibara T (2009) Simulation of propagating electromagnetic wave due to partial discharge in GIS using FDTD. *IEEE Trans Power Delivery* 24:153–159. <https://doi.org/10.1109/TPWRD.2008.2008474>

# Temperature Field Simulations of Three-Layer Extrusion in 110 kV Grafted Polypropylene Power Cables



Ji Wu, Shangshi Huang , Xin Yu, Haihan Cheng , Shihu Yu, Shixun Hu , Qi Li , and Jinliang He 

**Abstract** The three-layers extrusion was used in grafted polypropylene (PP) cables producing, and there occurred a color difference in insulating layer due to the temperature characteristics of materials and big section. In this paper, the temperature field simulation of three-layer extrusion was studied in 110 kV grafted PP power cables. Firstly, the thermal conductivity of insulating and shielding materials were tested. Then, the COMSOL Multiphysics was used to calculated the temperature field distribution by importing the measured data. Finally, the simulation results were obtained and analyzed. The conclusion is that the conductor temperature has a great influence on the temperature field distribution, while the atmosphere temperature on the temperature field distribution. It will guide the production and manufacturing of grafted PP insulated power cables in 110 kV and higher voltage levels in the future.

**Keywords** Grafted polypropylene · Power cables · Three-layer extrusion · Temperature field · Simulation calculations

## 1 Introduction

Power cables will gradually replace the mainstream power transmission and distribution systems in urban power, long-distance trans-sea power, far offshore wind power and onshore new energy power. Currently, the cross-linked polyethylene(XLPE) is widely used as the power cable insulating material, but it is unrecyclable after the end of the cable service, and increases energy consumption and carbon emissions in the manufacturing processes due to cross-linked and degassed. Hence, it is urgent to develop the cable insulation materials with recyclable, low-carbon emissions, high

---

J. Wu · X. Yu · S. Yu

Guangdong Power Grid Company Limited Electricity Research Institute, Guangzhou 510062, China

S. Huang (✉) · H. Cheng · S. Hu · Q. Li · J. He

Tsinghua University, Beijing 100084, China

e-mail: [huangshangshi93@163.com](mailto:huangshangshi93@163.com)

© Beijing Paiké Culture Commu. Co., Ltd. 2024

X. Dong and L. Cai (eds.), *The Proceedings of 2023 4th International Symposium on Insulation and Discharge Computation for Power Equipment (IDCOMPU2023)*, Lecture Notes in Electrical Engineering 1103, [https://doi.org/10.1007/978-981-99-7413-9\\_8](https://doi.org/10.1007/978-981-99-7413-9_8)

efficiency, and stability [1–3]. The polypropylene (PP) is expected to become the new generation of cable insulating material, because of excellent high-temperature electrical insulating properties, low-carbon emission in the life cycle, and recycling after the end of cable service. The PP insulating materials have been paid great attention by the academia and industry in power cables [4–7].

In preliminary studies, the grafted PP insulating materials have been prepared and characterized. The styrene groups have been grafted in original PP materials by aqueous phase grafting technology [8, 9]. The benzoyl peroxide (BPO), as the initiator, is employed for generating the free radical in reaction process. After the free radical taking the hydrogen atom from PP side chains, it occurs the grafting reaction of PP with styrene monomers [10]. The grafted PP is modified by chain control technology to form the final PP cable insulating materials from jointly development of Tsinghua University and Sinopec (Beijing) Chemical Industry Research Institute. So far, the PP cable insulating materials have been adopted to produce the distribution power cables in 10 and 35 kV, which have been operated in Hangzhou (Zhejiang province, China), Dongguan (Guangdong province, China), Shaoguan (Guangdong province, China) and Qinzhou (Guangxi province, China). At present, the grafted PP power cables in 110 kV is trial-produced. The three-layers extrusion is used in producing process, and there occurs a color difference in insulating layer due to the temperature characteristics of materials and big section of cables.

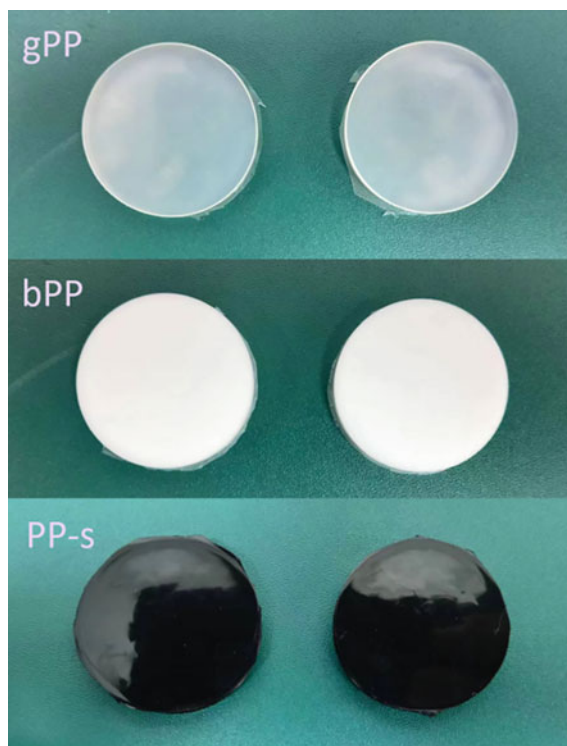
This paper has studied the temperature field simulations of three-layers extrusion for 110 kV grafted polypropylene power cables. The purpose is to make clear the producing and processing technology in 110 kV grafted PP power cables, avoid the color difference, enhance the whole properties of the PP power cables. At first, the thermal parameters of insulating and shielding materials have been tested in different temperatures by thermal constant analyzer. Then, the COMSOL Multiphysics simulation software has been used to calculated by importing the measured thermal parameters after setting the geometric and boundary parameters. Ultimately, the simulation results have been analyzed and the producing and processing guidance schemes have been provided.

## 2 Samples Preparation and Test

### 2.1 Samples Preparation

The grafted PP cable insulating material is provided by jointly development of Tsinghua University and Sinopec (Beijing) Chemical Industry Research Institute, marked as gPP. For comparison, it is selected a commercial PP cable insulating material in the same voltage level, which adopts blending process, marked as bPP. The shielding material is selected a suitable one, marked as PP-s. The three materials were pressed by heat into columnar block with bottom diameter of 30 mm and thickness of 4 mm, as shown in Fig. 1. The materials were first preheated at 200 °C

**Fig. 1** The photos of samples

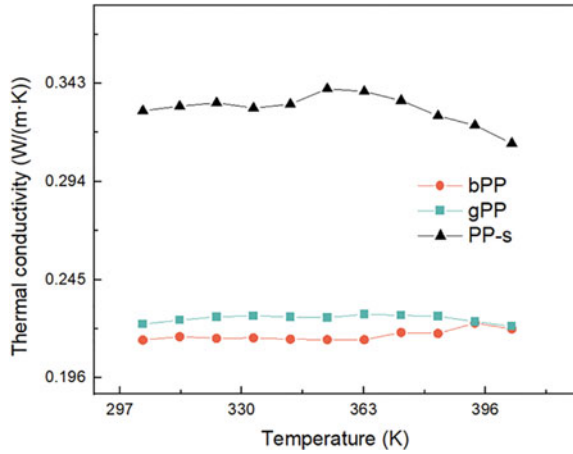


(473.15 K) for 10 min, then pressurized at 200 °C and 10 MPa for 5 min, and then pressurized at 200 °C and 15 MPa for 5 min, finally cooled to ambient temperature through circulating water. The samples were left in vacuum oven at 80 °C (353.15 K) for 24 h.

## 2.2 *Samples Test*

This paper mainly considered the temperature field simulation by importing thermal conductivity, hence the Hot Disk thermal constant analyzer was used to test the thermal conductivity, with test temperatures from 30 °C (303.15 K) to 130 °C (403.15 K) and interval of 10 °C (283.15 K). The thermal conductivity was tested 5 times at the same temperature, and testing interval of 5 min. The probe was sandwiched by two identical samples. The stainless steel block close outside the sample was used as the thermal background. The probe itself could heat and detect, and then transmitted the information to the host machine. The samples, probe and stainless steel were put into the oven, it could achieve the thermal conductivity test at different temperatures.

**Fig. 2** Thermal conductivity with temperatures



### 2.3 Test Results

The test results of thermal conductivity changes with temperatures are shown in Fig. 2. The thermal conductivity of two materials indicate a bit of change with temperature. The thermal conductivity of gPP is stable at different temperatures, which of values are from 0.2218 W/(m K) to 0.2268 W/(m K). And the thermal conductivity values of bPP are from 0.2149 W/(m K) to 0.2234 W/(m K). The thermal conductivity of gPP is a little higher than that of bPP, due to the grafted groups generating the physical entanglement to enhance the interfacial interaction in gPP material. The thermal conductivity of PP-s is stable at different temperatures as shown in Fig. 2, its value of 0.33 W/(m K) approximately.

## 3 Thermal Field Simulation and Analysis

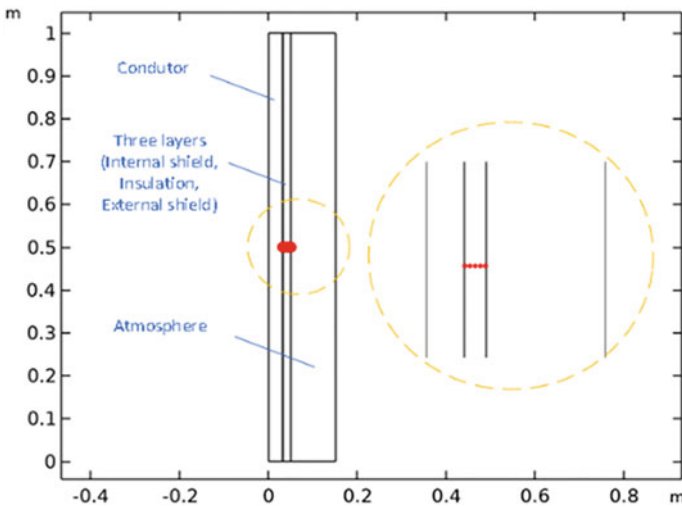
### 3.1 Simulation Model and Parameters

The two-dimensional axisymmetry was used in the simulation model, as shown in Fig. 3. The three-layer extrusion structure was suitable for the cable modeling, including conductor, three layers (internal shield, insulation, and external shield), and atmosphere. The material of conductor was copper with build-in thermal conductivity of 400 W/(m K). The internal and external shield materials were the same and with the same thermal conductivity which roots in testing results. The thermal conductivity of insulating material originated from testing results. All the testing results were fitted by using segmented cubic interpolation before importing, and extrapolated by constant. The nitrogen was used to fill the atmosphere with pressure of 1 MPa, and flow rate of 1 m/s in the axial direction. The geometric and material parameters were



shown in Table 1. The COMSOL Multiphysics finite element software was used to simulated, due to its strong multi-physical field-coupled computing ability.

Both the solid state and the fluid heat transfer modules were used in the simulation, and transient study was employed with time from 0 to 600 s and interval of 1 s. By the auxiliary method, the thermal field at different temperatures of conductor and atmosphere was studied for simulating the conditions of no-heated conductor and no-heated atmosphere, heated conductor and no-heated atmosphere, and no-heated conductor and heated atmosphere. For analyzing the temperature changes at different insulating layer positions, five two-dimensional interception points were selected with the same intervals as shown in Fig. 3.



**Fig. 3** Geometric modelling

**Table 1** Geometric and material parameters

Parts	Thickness (mm)	Material	Thermal conductivity (W/m K)
Conductor	31.25 (radius)	Build-in copper	400
Internal shield	1.00	Sample material	Imported data
Insulation	17.50	Sample material	Imported data
External shield	1.00	Sample material	Imported data
Atmosphere	100.00	Build-in nitrogen	k(T)

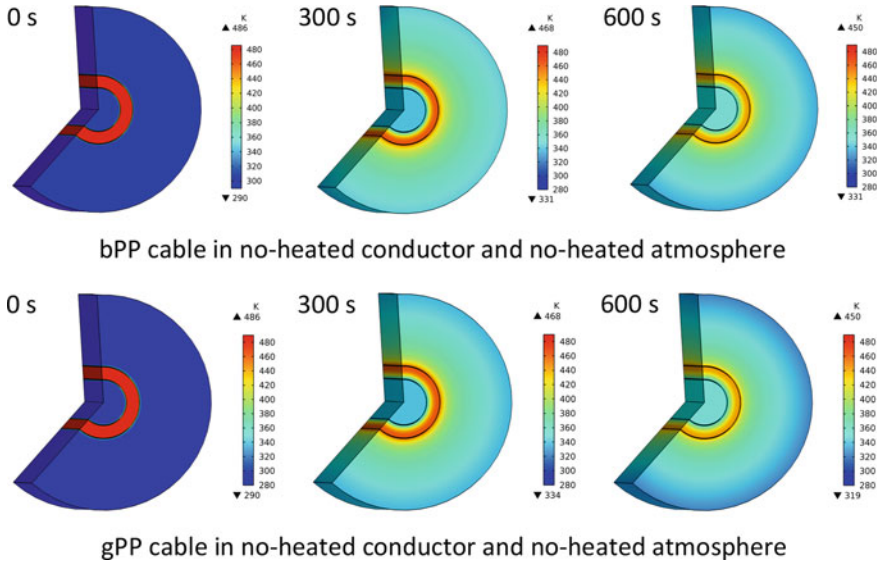
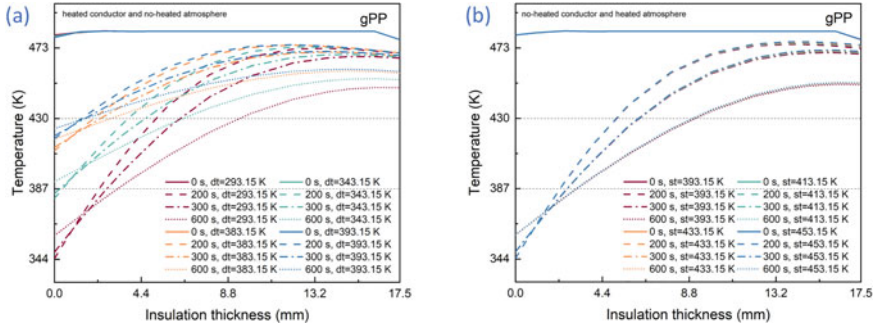


Fig. 4 Temperature changes of bPP cable and gPP cable extrusion with time

### 3.2 Simulation Results and Discussion

In the condition of no-heated conductor and no-heated atmosphere, the temperature distribution of bPP cable and gPP cable are similar, due to their similar thermal conductivity, as shown in Fig. 4. Hence, the subsequent analysis results mainly focus on the temperature field changes of the insulating layer during the extrusion of the gPP cable.

The temperature changes of gPP cable extrusion insulation thickness at different time in the different conditions are shown in Fig. 5. The conductor heated temperatures are 20 °C (293.15 K), 70 °C (343.15 K), 110 °C (383.15 K) and 120 °C (393.15 K), respectively. It is found that different conductor heated temperatures have a great impact on the insulating layer temperature field during cable extrusion. The temperature field changes decrease with the increasing of conductor temperature. At the same heated temperature of conductor, the temperature field distribution of the insulating layer gradually increases from 0 to 300 s, that is, the internal and external temperature difference increases. The temperature field change amplitude gradually decreases after 300 s and stabilizes after 400 s. The 387 and 430 K temperature reference lines are also set to indicate the crystallization peak temperature and the melting peak temperature of the gPP material, respectively. The conductor temperature is 293.15 K, that is, when the conductor is not heated, the temperature of insulating layer near the conductor is lower than the gPP material crystallization temperature. However, the insulating layer temperature distribution is hardly lower than the gPP material crystallization temperature, when the conductor temperature



**Fig. 5** Temperature changes of gPP cable extrusion insulation thickness at different time. **a** Heated conductor of 293.15 K, 343.15 K, 383.15 K, and 393.15 K respectively, and no-heated atmosphere. **b** No-heated conductor and heated atmosphere of 393.15 K, 413.15 K, 433.15 K, and 453.15 K respectively

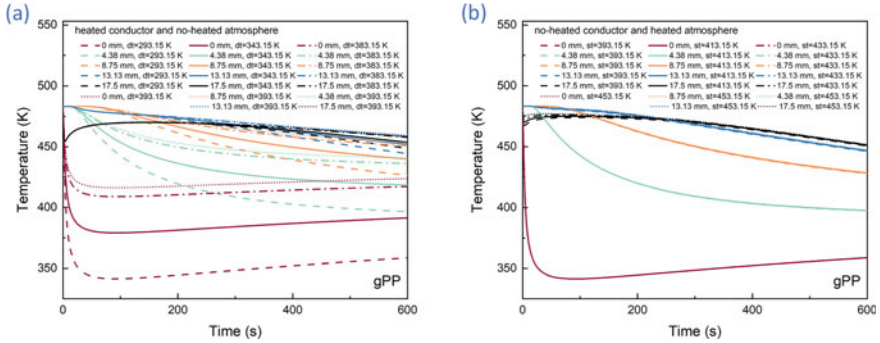
is 343.15 K. Furthermore, the temperature distribution of the insulating layer is all higher than the crystallization temperature of the gPP material, when the conductor temperature is 383.15 and 393.15 K. It shows that in the three-layers extrusion of polypropylene cable, the production process of conductor heating should be adopted, and the heated conductor temperature should be higher than 343.15 K, that is 70 °C, to ensure the spherocrystal development of the PP insulating material.

The temperature changes of gPP cable extrusion insulation thickness at different insulating thickness points in the different conditions are shown in Fig. 6. The atmosphere temperatures are 120 °C (393.15 K), 140 °C (413.15 K), 160 °C (433.15 K) and 180 °C (453.15 K), respectively. It is found that the heated temperature of different atmospheres has less influence on the temperature field of the insulating layer during the cable extrusion process. With the increasing of the atmosphere temperature, the temperature field distribution of the insulating layer is basically unchanged with time. Therefore, in the three-layers extrusion of polypropylene cable, the conductor temperature has a great influence on the temperature field distribution, while the atmosphere temperature on the temperature field distribution.

## 4 Conclusions

This paper has studied the temperature field simulations of three-layers extrusion for 110 kV grafted polypropylene power cables, and the obtained conclusions are shown as follow.

1. From the results of thermal conductivity, the blending PP and grafting PP have the similar thermal conductivity of 0.22 W/(m K) approximately, and less variable with temperature. The thermal conductivity of PP shielding material is 0.33 W/(m K) approximately.



**Fig. 6** Temperature changes of gPP cable extrusion with time at different insulation thickness points. **a** Heated conductor of 293.15 K, 343.15 K, 383.15 K, and 393.15 K respectively, and no-heated atmosphere. **b** No-heated conductor and heated atmosphere of 393.15 K, 413.15 K, 433.15 K, and 453.15 K respectively

2. By the simulation of cable extrusion, it is found that the conductor temperature has a great influence on the temperature field distribution, while the atmosphere temperature on the temperature field distribution. Hence, the conductor heating temperature should be studied further to optimize the processing of polypropylene cables.

**Acknowledgements** This research was funded by Science and Technology project of China Southern Power Grid Company, grant number GDKJXM20220366 (036100KK52220039) .

## References

1. Hu S, Zhang W, Wang W, Li J, Shao Q, Zhang Y, Zhang Q, Huang S, Hu J, Li Q, He J (2022) Comprehensive comparisons of grafting-modified different polypropylene as HVDC cable insulation material. *IEEE Trans Dielectr Electr Insul* 29:1865–1872
2. Zhou Y, Peng S, Hu J, He J (2017) Polymeric insulation materials for HVDC cables: development, challenges and future perspective. *IEEE Trans Dielectr Electr Insul* 24:1308–1318
3. Huang X, Zhang J, Jiang P, Tanaka T (2020) Material progress toward recyclable insulation of power cables part 2: polypropylene-based thermoplastic materials. *IEEE Electr Insul Mag* 36:8–18
4. Zhang L, Wang Z, Tian J, Meng S, Zhou Y (2022) Thermal aging properties of 500 kV AC and DC XLPE cable insulation materials. *Polymers* 14:5400
5. Kim D, Lee SH, Kwon TH, Kwon I, Han DH, Park H, Han SW, Lee DH, Yu S (2023) Study on high-temperature and high-voltage insulation characteristics of polypropylene blend with highly packed elastomeric domains for power cable applications. *Polym Test* 120:107942
6. Du B, Zhang J, Xiao M, Liu H, Ran Z (2023) Dielectric breakdown performance of deashed polypropylene for HVDC film capacitors. *IEEE Trans Dielectr Electr Insul* 29:2209–2217
7. Lee SH, Kim D, Kwon I, Kwon TH, Park H, Han DH, Han SW, Lee JH, Lee DH, Yu S (2023) Polystyrene: a self-dispersing, ultralow loading additive for improving the breakdown strength of polypropylene for high voltage power cable applications. *ACS Appl Polym Mater* 5:165–171

8. Hu S, Dong X, Wang W, Huang S, Hu J, Li Q, He J, Shao Q, Yuan H, Shi H, Song W (2022) Dielectric properties improvement of grafting-modified polypropylene by silane for HVDC cable insulation. *IEEE Trans Dielectr Electr Insul* 28:2004–2010
9. Yuan H, Zhou Y, Zhu Y, Hu S, Yuan C, Song W, Shao Q, Zhang Q, Hu J, Li Q, He J (2020) Origins and effects of deep traps in functional group grafted polymeric dielectric materials. *J Phys D* 53:475301
10. Chmela S, Fiedlerova A, Janigova I, Novak I, Borsig E (2011) Grafting of iPP powder with methacrylate monomers in water medium. *J Appl Polym Sci* 119:2750–2758

# The Electrical-Thermal Coupling Simulation of Grafted Polypropylene Used in High-Voltage Direct Current Cables



Yazhou Fan, Wenjia Zhang, Xiangyang Peng, Shangshi Huang, Ying Li, Shixun Hu, Qi Li, and Jinliang He

**Abstract** Under direct current (DC) operation conditions, local electric field in insulation layer will be distorted, leading to insulation failure. Since the conductivity of insulating materials generally corresponds positively with temperature, a temperature gradient will form inside the insulating material during cable operation, making the conductivity distribution uneven and causing the “electric field reversal” phenomenon in the cable insulation layer. The distribution of the electric field and temperature field of the polypropylene grafted as the cable insulation under the electric heating-coupling field is yet to be studied. Studies have proved that by grafting modification the insulating properties of materials can be improved. This paper studied the and conductivity characteristics of grafted polypropylene materials, and selected one type for more experiments to obtain the material’s conductivity-temperature-electric field strength characteristic equation through data fitting. A model of a 100 kV DC cable was established in COMSOL, and simulation of the cable section’s electric heating-coupling field was performed, revealing the temperature and electric field distribution inside the insulation layer when the cable is rated, overloaded, or short-circuited. This paper can provide some reference for operational analysis of polypropylene-insulated HVDC cables.

**Keywords** Grafted polypropylene · High-voltage direct cable · Electrical-thermal coupling simulation

---

Y. Fan · X. Peng · Y. Li

Guangdong Power Grid Company Limited Electricity Research Institute, Guangzhou 510062, China

W. Zhang (✉) · S. Huang · S. Hu · Q. Li · J. He

Department of Electrical Engineering, The State Key Laboratory of Control and Simulation of Power System and Generation Equipment, Tsinghua University, Beijing 100084, China  
e-mail: [zhangwenjiacn@163.com](mailto:zhangwenjiacn@163.com)

© Beijing Paiké Culture Commu. Co., Ltd. 2024

X. Dong and L. Cai (eds.), *The Proceedings of 2023 4th International Symposium on Insulation and Discharge Computation for Power Equipment (IDCOMPU2023)*, Lecture Notes in Electrical Engineering 1103, [https://doi.org/10.1007/978-981-99-7413-9\\_9](https://doi.org/10.1007/978-981-99-7413-9_9)

## 1 Introduction

In the alternating current (AC) transmission system, with the improvement of the voltage level, the transmission loss will be greatly increased, and the transmission efficiency will be significantly reduced. In contrast, in the field of direct current (DC) transmission, High-voltage direct current (HVDC) cable transmission system shows great superiority [1, 2]. Cross-linked polyethylene (XLPE) is one of the most widely used polymeric insulating materials for HVDC cable insulation. After the crosslinking, XLPE changes to thermosetting plastic, which cannot be recycled. In addition, the cross-linking process is complex, the output rate is low, and the by-products have a great impact on the insulation properties of materials [1, 2]. So, it is necessary to look for renewable DC cable insulation materials with excellent performance and simple manufacture.

Polypropylene (PP), as another potential environment-friendly insulating material, has received extensive attention in recent years [1, 2]. PP material itself has high mechanical strength and excellent heat resistance, which allows the working temperature to maintain at 90 °C for a long time. It does not need cross-linking treatment, and it is a typical thermoplastic material, which can be recycled and is an environment-friendly material [1, 2]. However, due to the accumulation of space charge in DC electric field, methods like blending modification, nano modification, grafting modification and so on are applied to PP to improve the insulation performance [1–4]. Grafting can improve the performance of PP while avoiding the problem of uneven dispersion [4].

In this paper, the feasibility of grafted polypropylene used in high voltage DC cable was studied, and the electrical properties of polypropylene grafted with different grafted monomers were obtained through experiments. The conductance-temperature dependence of one of the materials is fitted by the experimental results, and then the distribution of electric field and temperature field in the rated and short-circuit operation of the cable is calculated by COMSOL simulation of the electrothermal coupling field.

## 2 Methods

### 2.1 Materials and Sample Preparation

The names, item numbers and manufacturers of the raw materials used in this paper are shown in Table 1.

The grafted materials of PP grafted with St, MMA and VTES monomers are named PP-g-St, PP-g-MMA and PP-g-VTES, respectively. The reaction container is filled with nitrogen. T30s powder is weighed, added to the reaction container. Then the grafting monomer is weighed, and an appropriate amount of initiator BPO is added into the solution. Then the solution is added to the reaction container and

**Table 1** Names, item numbers and manufacturers of the raw materials used

Material	Item No.	Manufacturer
PP	T30s	Sinopec Maomign Petrochemical Co., Ltd.
Vinyltriethoxysilane (VTES)	–	J&K Scientific Ltd.
Methyl methacrylate (MMA)	–	J&K Scientific Ltd.
Styrene (St)	–	J&K Scientific Ltd.
Dibenzoyl peroxide (BPO)	–	Xilong Scientific Co., Ltd.

mixed with the T30s powder, and the mixed material is stirred for 30 min. Then the reaction container was heated to 90 °C for 4 h. Finally, the heating was stopped and purged with nitrogen.

In order to test the electrical properties of the sample, the 200  $\mu\text{m}$  flake sample is prepared to test the space charge characteristics, and the 100  $\mu\text{m}$  flake sample is made to test the FT-IR and volume conductivity. The polypropylene particles are preheated at 200 °C for 5 min, then continue to press to the 15 MPa for 10 min, and finally move to the cooling place of the pressing machine to cool for 5 min to prepare the flake sample.

## 2.2 Experiment

### FT-IR Characteristics

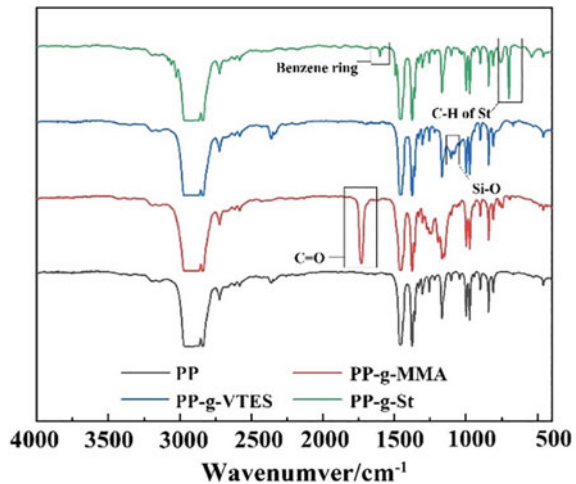
In order to characterize the successful grafting of the group in the PP matrix, the infrared experiments (Nicolet iS10, Thermo Fisher Scientific) are carried out on the flake samples prepared in 2.1. The scanning wavelength range is 4000–400  $\text{cm}^{-1}$ , the scanning times is 32 times, and the resolution is 4  $\text{cm}^{-1}$ .

### Volume Conductivity

The volumetric conductivity was measured by three-electrode method. The initial field strength of the test is 10 kV/mm, and the step-up of 10 kV/mm is carried out every 10 min step by step to 80 kV/mm. When measuring the volume conductivity, the temperature is controlled at 30 and 90 °C, at first. After the better material is selected, the volume conductivity properties of the materials at 50 and 70 °C are tested in order to better fit the characteristics of volume conductivity-temperature-electric field strength.



**Fig. 1** FT-IR spectra of the four samples



### 3 Results

#### 3.1 FT-IR Characteristics

The FT-IR spectra of the four samples are shown in Fig. 1. Compared with the pure PP, the material grafted with MMA has an absorption peak near  $1650\text{ cm}^{-1}$ , which is the stretching vibration of carbon–oxygen double bond, indicating that the MMA monomer is grafted. The spectrum of PP grafted with VTES shows an absorption peak near the wavenumber of  $1080\text{ cm}^{-1}$ , which refers to the silicon-oxygen bond, indicating that the VTES monomers has been successfully grafted. The PP material grafted with St has an absorption peak near the  $1600\text{ cm}^{-1}$ , which represents the benzene ring skeleton. And the absorption peak appears near the  $698\text{ cm}^{-1}$ , which indicates that the C-H bond vibration of the monosubstituted benzene ring in the grafted styrene, proving that the styrene monomers are successfully grafted to PP.

#### 3.2 Volume Conductivity

The volume conductivity properties of the four samples measured at 30 and 90 °C are shown in Fig. 2. It can be seen that whether at room temperature or high temperature, PP-g-VTES samples maintain a low level of electrical conductivity at low field strength 20 kV/mm and below. With the increase of electric field strength, the volume conductivity increases rapidly, which is much higher than that of PP-g-St and PP-g-MMA, and even higher than that of pure PP. Higher volume conductivity means more serious loss under DC conditions. Although the volume conductivity of PP-g-St and PP-g-MMA increases with the increase of field strength, the increase of

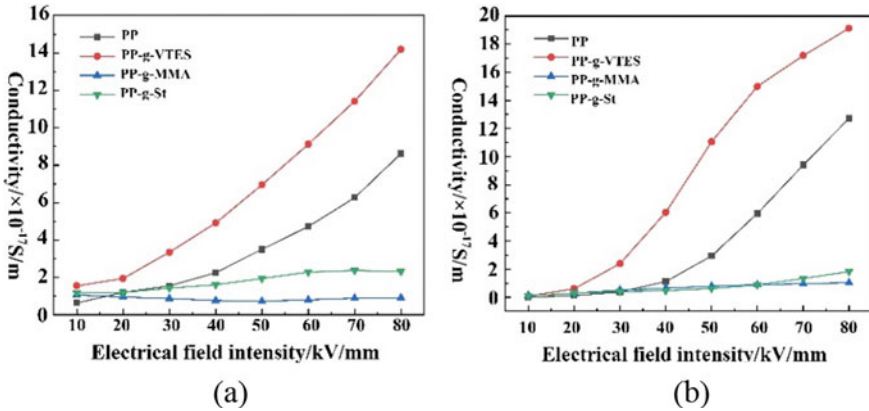


Fig. 2 Volume conductivity of the four samples: **a** at 30 °C; **b** at 90 °C

conductivity is not obvious. And their volume conductivity is much lower than that of PP indicating that St and MMA monomers can significantly reduce the volume conductivity of PP. However, there is no significant difference in volume conductivity between PP-g-MMA and PP-g-St.

## 4 Simulation

### 4.1 Conductivity-Temperature-Electric Field Dependence

According to the experimental results of Sect. 3.2, it is found that PP-g-St material has excellent conductivity characteristics as HVDC cable insulation materials. So, the conductivity properties of PP-g-St materials at 50 and 70 °C are tested. The results are shown in Fig. 3.

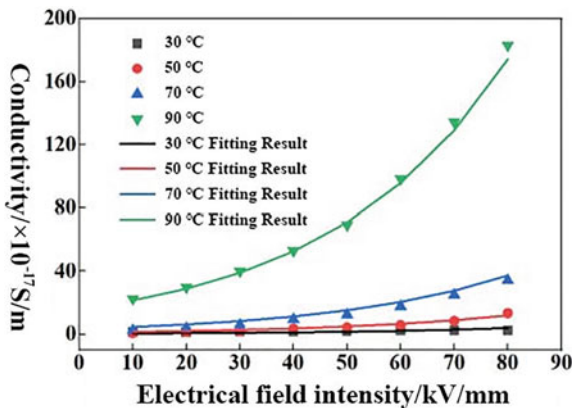
The relationship between volume conductivity of polymer and temperature and electric field strength is already studied and is shown as Eq. (1) [5]:

$$\sigma(T, E) = 1/A \times \exp(a \times T) \times \exp(b \times E) \tag{1}$$

where  $\sigma(T, E)$  represents the volume conductivity at temperature  $T$  and electric field  $E$ . Parameter  $A$  represents the volume conductivity at temperature ( $T = 0$ ) and electric field ( $E = 0$ ). Parameter  $a$  and  $b$  is the temperature coefficient of resistivity and the conductivity field strength coefficient, respectively.

According to the conductivity results, the parameters  $A, a, b$ , in Eq. (1) are obtained by using the fitting toolbox of MATLAB. The fitting results are shown in Fig. 3 and Table 2.

**Fig. 3** Volume conductivity PP-g-St at different temperatures and the fitting result



**Table 2** Fitting results of volume conductivity of PP-g-St

Conductivity/S/m	SSE	R-square	Adjusted R-square	RMSE
$1.1908e-25 * \exp(0.05675 * T) * \exp(2.997e-08 * E)$	5.121	0.9286	0.9237	0.4202

### 4.2 Model and Parameter Setting

In this paper, Comsol is used to study the temperature field and electric field distribution of HVDC cable. The current of AC/DC module and the solid heat transfer part of heat transfer module need to be used in the simulation of electrothermal coupling field.

Th geometric model of the cable is shown in Fig. 4.

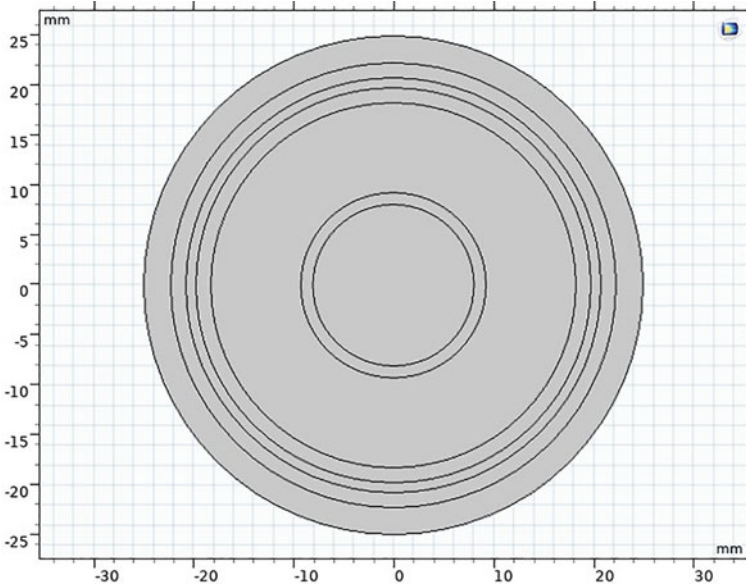
The specific geometric parameters of each part of the DC cable are shown in Table 3.

The performance parameters of cable materials are shown in Table 4.

### Rated Operation

When the cable is rated, the temperature of cable conductor is 70 °C [6], which requires the calorific value to be set as 313,200 W/m<sup>3</sup>.

Figure 5a shows the radial temperature distribution of the DC cable after rated operation. The temperature of each part of the cable decreases gradually along the radial direction of the cable. The highest temperature of the cable insulation layer is 64.75 °C near the conductor, the lowest temperature is 33.52 °C. Figure 5b shows the radial potential distribution. The potential of the cable during rated operation is almost uniformly distributed inside the cable insulation. Figure 5c shows the radial electric field strength distribution inside the insulation. It can be found that the electric field strength of the insulating layer near the conductor is low, while the electric field strength of the insulating layer far away from the conductor is high, and the electric



**Fig. 4** Geometric model of the cable

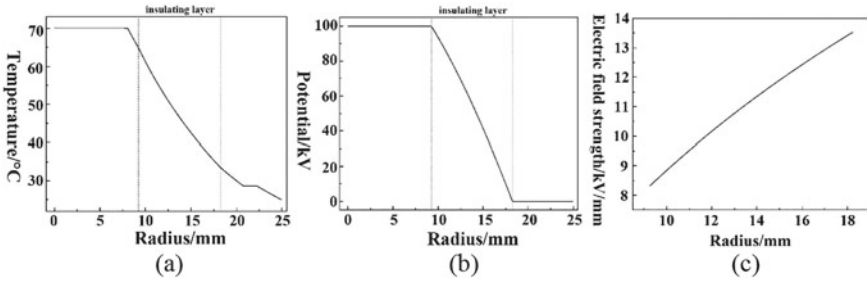
**Table 3** Geometric parameters of each part of DC cable

Name	Thickness/mm	Outer radius/mm
Conductor	–	8.05
Inner shield	1.2	9.25
Insulation	9	18.25
Inner shield	1.5	19.75
Water barrier	1	20.75
Lead sheath	1.5	22.25
Outer sheath	2.7	24.95

field reversal has occurred. This is because the electrical conductivity of the insulating material has a positive correlation with temperature. The temperature of the cable insulation near the conductor is higher than that of the outer layer. Therefore, the electrical conductivity distribution decreases gradually from the inside to the outside along the radial direction, while the conductivity increases gradually from the inside to the outside, so the electric field strength of the outer layer of the cable insulation is high and the field strength of the inner layer is low. The lowest electric field strength is 8.32 kV/mm, and the highest electric field strength of the insulation part can reach 13.53 kV/mm.

**Table 4** Parameters of the materials used in DC cable

Material	Heat Capacity/J/(kg * K)	Thermal conductivity/W/(m * K)	Conductivity/S/m	Density/kg/m <sup>3</sup>	Relative permittivity
Aluminium	900	160	6.292e7	2700	1
Semiconductor	2300	0.27	0.1	941	1
PP-g-St	22,500	0.22	$1.1908e-25 * \exp(0.05675 * T) * \exp(2.997e-08 * E)$	922	2.5
Pb	130	34.8	1e7	11,300	1
LDPE	2250	0.32	1e-16	922	2.1



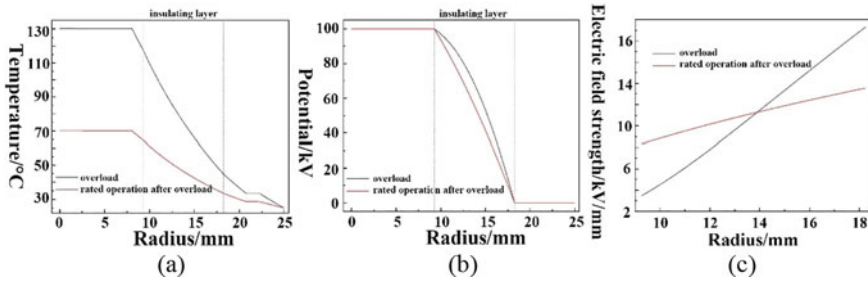
**Fig. 5** Insulation part in rated operating cable: **a** Radial temperature distribution; **b** Radial potential distribution; **c** Radial electric field distribution

**Overload**

The maximum allowable working temperature of cable overload is 130 °C [7] during when the heat generation of cable conductor is 7,32,200 W/m<sup>3</sup>. Figure 6a shows the radial temperature distribution. The results show that the core of 100 kV DC cable is stable at 130 °C during overload operation, and the temperature of each part of the cable decreases gradually along the radial direction of the cable. The highest temperature of the cable insulation layer near the conductor is 117.92 °C. The lowest temperature far away from the conductor is 44.79 °C. After the removal of overloaded operation, the temperature of each part of the cable has reached the rated operating level. Figure 6b shows the radial potential distribution. From the potential-radius curve, compared with the rated operation, the potential of the cable during overload operation is no longer so evenly distributed in the cable insulation, while the potential distribution becomes uniform at rated operation after overload. Figure 6c shows the radial electric field strength distribution inside the insulation. It can be found that the electric field strength near the conductor inside the insulation layer is low, and the non-uniform degree of the field strength distribution increases after overload operation, and the lowest value of the field strength decreases to 3.47 kV/mm. The highest field strength of the insulation part can reach 19.30 kV/mm, which is higher than the maximum field strength of rated operation by 5.77 kV/mm. The electric field intensity distribution returned to the rated operation level after the removal of overload and return to the rated condition.

**Short Circuit**

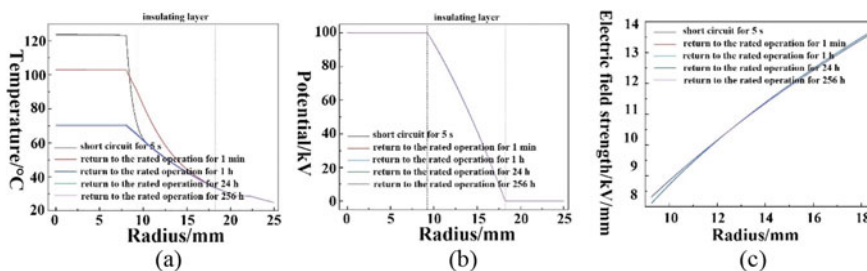
For the short-circuit current of different voltage levels, transmission capacity and different locations, it is found that the short-circuit current coefficient coincides in the range of 7.608–11.316 [8–10], so the short-circuit current coefficient is 10 in this section. According to the current thermal effect formula, the calorific value of the short-circuit fault is 100 times that of the rated operation. So, the calorific value is 31,320,000 W/m<sup>3</sup>. GB/T 12706.3-2020 [11] stipulates that cables should withstand temperature for 5 s, so the short-circuit fault lasts for 5 s. It is found that the temperature distribution of the cable can be stable in about 1 h, so the research results within 1 h should be inserted in the simulation study. However, the thermal



**Fig. 6** Insulation part in overloaded cable. **a** Radial temperature distribution; **b** Radial potential distribution; **c** Radial electric field distribution

conductivity of the cable insulation is slow, and the change of the cable field strength distribution lags behind the temperature distribution, so it does not need to be studied to the order of seconds. After comprehensive consideration, the study was carried out at 1 min, 1, 24 and 256 h after the short circuit occurred for 5 s and the fault was removed and put back into rated operation.

Figure 7a shows the radial temperature distribution of cable after 5 s of short circuit fault and recovery of rated operation 1 min, 1, 24 and 256 h after removal of the fault. The result shows that after 5 s of short circuit, the core temperature reaches 123.81 °C, and the temperature of each part of the cable along the radial direction decreases gradually. Due to the slow heat conduction of semi-conductive materials and cable insulation materials, the temperature of cable insulation is almost unchanged. Only part of it increases near the conductor, the highest temperature is 71.95 °C, and the maximum temperature is only 7.20 °C higher than that of the previous rated operation. After the removal of the short circuit fault, the heating of the core during rated operation is not enough to keep the core temperature rising, while the temperature of the insulation part of the cable increases gradually and then decreases. After 1 min, the highest temperature of the insulation part of the cable increases to 90.70 °C, which is 25.95 °C higher than that of the rated operation, the temperature of the outer layer of the insulation of the cable is almost unchanged. After 1 h, the temperature of each part of the cable reaches a stable level and almost no longer changes. Figure 7b shows the radial potential distribution of the cable. It can be seen that the five potential distribution curves at different times almost coincide, and the potential distribution inside the cable is relatively uniform. Figure 7c shows the radial field strength distribution. It can be found that the electric field reversal phenomenon still exists. The lowest field strength decreases to 8.10 kV/mm, and the highest field strength of the insulation reaches 13.61 kV/mm.



**Fig. 7** Insulation part in short-circuit cable. **a** Radial temperature distribution; **b** Radial potential distribution; **c** Radial electric field distribution

## 5 Conclusion

In this paper, the conductivity and space charge characteristics of PP, VTES-g-PP, MMA-g-PP and St-g-PP are compared. It is found that the conductivity of grafted MMA and St is significantly lower than that of pure PP, and the accumulation of space charge is also inhibited.

After selecting St-g-PP, the experimental data of conductivity of St-g-PP at 30, 50, 70 and 90 °C are obtained. According to these data, the relationship between conductivity, temperature and field strength is fitted. Using Comsol Multiphysics, the conductivity-temperature-electric field function is used to simulate the cable at rated, overloaded and short-circuit conditions. Through the coupling calculation of electric field and temperature field, the radial distribution of temperature field, potential and electric field intensity in the cable under these three conditions is obtained, and the phenomenon of “electric field reversal” appears in all three conditions. During the overloaded operation, the highest temperature of the cable insulation is 117.92 °C, and under the overload condition, the mid-field strength of the insulation can reach 19.3 kV/mm. After the occurrence of the short circuit fault, the highest temperature of the insulating layer can reach 90.70 °C, and the highest field strength of the insulating layer is 13.61 kV/mm.

**Acknowledgements** This research is supported by science and technology project of China Southern Power Grid Corporation (Grant No. GDKJXM20220366 (036100KK52220039)).

## References

1. Muhanmad A, Zulkurnain A, Kwan L, Muhanmad T (2021) Polypropylene-based nanocomposites for HVDC cable insulation. *IET Nanodielectr* 4(3):84–97
2. Yingwei O, Amir P, Anja L, Xiangdong X, Thomas G, Per-Ola H, Christian M (2021) High-temperature creep resistant ternary blends based on polyethylene and polypropylene for thermoplastic powercable insulation. *J Polym Sci* 59(11):1084–1094



3. Shixun H, Hao Y, Qi Z, Jun L, Mingti W, Shangshi H, Jun H, Qi L, Jinliang H (2022) Deep trap origins, characteristics, and related mechanisms in chemically grafted polypropylene with enhanced direct current volume resistivity. *J Phys Chem C* 126(38):16280–16288
4. Linzhen F, Qi L, Hao Y, Shangshi H, Jinliang H (2022) Influence and mechanism of grafting on thermal oxidative aging of polypropylene. In: *Proceedings of the CSEE*, vol 42, no 11 pp 4227–4238 (in Chinese)
5. Fabiani D, Montanari C, Laurent C, Teysseire G, Morshuis F, Bodega R, Dissado L (2008) HVDC cable design and space charge accumulation. Part 3: effect of temperature gradient. *IEEE electrical insulation magazine*, vol 24, no 2, pp 5–14
6. Haitian W, Xianzhang L, Yuming Z, Yuzhen Z, Miao H, George C (2009) Research on electrical performances of HVDC crosslinked polyethylene cable using Chinese base material. In: *Proceedings of the CSEE*, vol 39, no 13, pp 3980–3989 (in Chinese)
7. Xiaoxiao C, Jianwei M, Yike Y, Zhiyuan G, Wenfei L, Zhousheng Z (2017) Research on short-time overload current limit for high voltage XLPE power cables. *High Voltage Apparatus* 53(4):150–155 (in Chinese)
8. Liang Z, Bei L, Guangquan B, Zhigang C, Jiefeng Z (2006) Study on dynamic equivalence of  $\pm 800$  kV DC transmission system from Yunnan to Guangdong. *Power Syst Technol* 30(16):6–10 (in Chinese)
9. Maosheng D, Feng G, Hongqiang L (2015) Influence of UHV DC power transmission from Shanghai Temple to Shandong accessing on Ningxia power grid. *Ningxia Electric Power* 2015(3):1–6, 18 (in Chinese)
10. Zhanxun Y, Qianru Z, Chengyong Z, Rulian Z, Pengjie W (2011) Study on influence of HVDC commutation failure on AC line protection. Part one: modeling and simulation of Shandong Grid with DC feed-in system based on EMTDC. *Power Syst Protect Control* 39(24):58–64 (in Chinese)
11. China Electrical Equipment Industry Association (2020) Power cables with extruded insulation and their accessories for rated voltages from 1 kV ( $U_m = 1.2$  kV) up to 35 kV ( $U_m = 40.5$  kV)—Part 3: cables for rated voltages of 35 kV ( $U_m = 40.5$  kV): GB/T 12706.3-2020. Standards Press of China (in Chinese)

# Optimization Technology of Finite Element Stepper Motor Based on Parametric Modeling



Jiaxin Chen, Houlong Chen, Xiaoming Zhou, and Ji Zheng

**Abstract** Since the electromagnetic torque of hybrid stepper motor (HSM) is generated by the cogging effect, the change of tooth geometric parameters has a great influence on its performance. When the finite element software is used for optimization, the modeling workload is large. In this paper, the HSM parametric simulation model is established based on ANSYS software, and the geometric parameters of the tooth can be adjusted to improve the efficiency of the optimization design. Based on the parametric simulation model, the influence of the tooth width angle pitch angle ratio of the rotor and stator and the change of the stator pitch angle on the cogging torque and the holding torque is analyzed, and the tooth geometry parameters that take into account the waveform and amplitude of the holding torque are obtained.

**Keywords** Hybrid stepper motor · Parametric modeling · Cogging torque · Holding torque

## 1 Introduction

HSM is widely used in machine tools, robots, aviation, aerospace and other fields because of its simple structure, easy control, fast response and high reliability [1–3]. Due to the high saturation of the HSM teeth and the high nonlinearity of the magnetic circuit, the calculation results obtained by the traditional analytical formula method are difficult to meet the actual accuracy requirements [4, 5]. Therefore, it is necessary

---

J. Chen (✉) · H. Chen · X. Zhou  
College of Mechanical Engineering, Donghua University, Shanghai 201620, China  
e-mail: [chjiaxin@dhu.edu.cn](mailto:chjiaxin@dhu.edu.cn)

H. Chen  
e-mail: [chenhl@mail.dhu.edu.cn](mailto:chenhl@mail.dhu.edu.cn)

J. Zheng  
Shanghai Institute of Aerospace Mechanical and Electrical Engineering, Shanghai 201109, China  
e-mail: [13671886678@139.com](mailto:13671886678@139.com)

to use the finite element method with higher accuracy to calculate the electromagnetic performance of HSM. Cogging torque and holding torque are two important performance indexes of HSM [6, 7], and the above two indexes are particularly sensitive to the change of tooth geometric parameters. When analyzing its performance index in finite element software, it is necessary to analyze the combined influence of different tooth geometry parameters. There are only traditional motor structures in the commonly used finite element analysis software ANSYS model library, so it is particularly important to establish a parametric model in ANSYS for motor optimization design. Reference [8] introduces a parametric modeling method of doubly salient permanent magnet motor. According to the topology of the motor, the basic unit of the motor is determined. On the basis of the basic unit, the parametric model of the whole motor can be drawn quickly by mirroring, rotating and copying. In Ref. [9], a detailed account of the results of two-dimensional and three-dimensional finite-element analyses, conducted with different tooth/width pitch ratios and also with various tooth/slot shapes such as rectangular, trapezoidal, triangular, and circular, is presented. In Ref. [10], the influence of tooth height pitch ratio, tooth width pitch ratio and different pitch of stator and rotor on HSM performance was analyzed by using two-dimensional HSM equivalent model. Based on the equivalent two-dimensional finite element model, Reference [11] analyzed the influence of different step angles and different air gaps on the cogging torque.

## 2 Parametric Modeling of HSM Based on ANSYS

### 2.1 Model Parameter Formulation

HSM is mainly composed of stator, rotor, winding coil, bearing, end cover and shaft. When analyzing the electromagnetic characteristics, only the rotor, stator and coil are considered. In the early stage of parametric modeling, it is necessary to formulate the parameters of the parametric model. Taking the two-phase 42 HSM as an example, the rotor has 50 teeth, the rotor pitch angle is  $7.2^\circ$ , the stator has eight large poles, and each pole has six teeth. The geometric parameters of each component are shown in Table 1, Fig. 1.

The parameters in Table 1, the length unit is mm, the angle unit is degree, and the current unit is A.

### 2.2 Rotor Parametric Modeling

In Fig. 1,  $l$  is the line connecting the center of the tooth bottom circle and the center of the rotor,  $\alpha$  is the angle between  $l$  and the tooth side, and the tooth bottom circle is tangent to the tooth side.

**Table 1** HSM model parameters

Parameter	Describe	Value
RR	Rotor outer radius	12.89
b	Rotor tooth width angle pitch angle ratio	0.5
bh	Rotor tooth height pitch ratio	0.45
G	Air gap	0.04
RZ	Rotor stack thickness	5.5
O	Shaft radius	2.5
RS	Inner radius of stator	12.93
a	Stator pitch angle	7.2
c	Stator tooth width angle pitch angle ratio	0.5
ch	Stator tooth height pitch ratio	0.45
D	Total thickness of stator teeth	1.8
N	Stator pole width	3.5
M	Stator yoke thickness	2.4
RM	Outer radius of magnet steel	12
RM1	Inner radius of magnet steel	3.5
MZ	Magnet thickness	1
T	Frame width	42
E	Base chamfer radius	25
FA	Assembly hole spacing	31
F	Assembly hole diameter	3.5
Num	Number of coils	24
I	Rating current	1

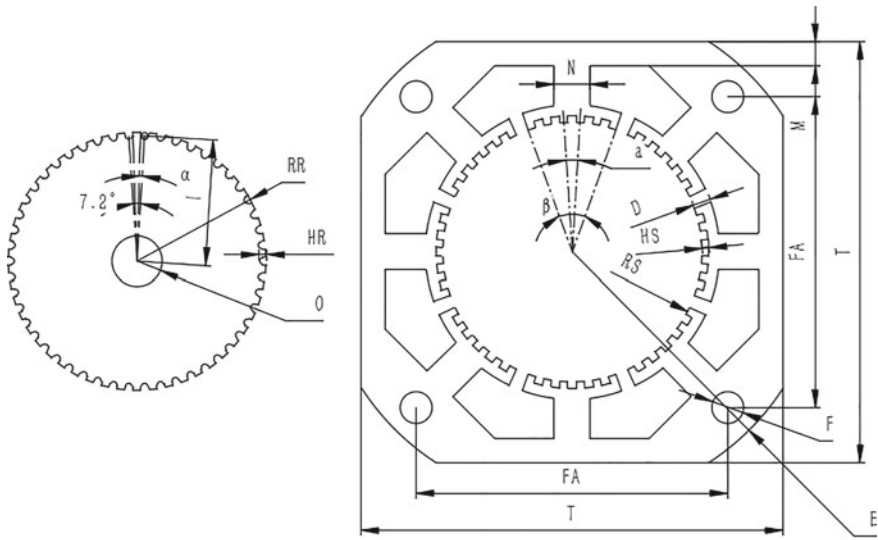
$$\alpha = \frac{7.2(1-b)}{2} \tag{1}$$

The triangle in which  $\alpha$  is located satisfies:

$$l - l\sin\alpha = RR - HR \tag{2}$$

$$l = \frac{RR-HR}{1-\sin\alpha} \tag{3}$$

The rotor lamination is decomposed into three parts: tooth, rotor yoke and tooth bottom circle. The tooth and the rotor yoke are summed by Boolean operation, and then subtracted from the tooth bottom circle to the rotor lamination. The parametric modeling method is introduced below. Firstly, the rotor yoke is drawn. According to the geometric relationship in Fig. 1, the circle is drawn with the distance ( $l\cos\alpha$ ) between the tooth bottom circle and the tooth side tangent point to the center of the rotor circle as the radius, and the shaft hole is subtracted. Secondly, draw a tooth array of 50. Finally, the bottom circle of the tooth is drawn, and its radius is  $l\sin\alpha$ .



**Fig. 1** Geometric model parameters of rotor and stator

The angle between the line connecting the center of the circle and the center of the rotor and the symmetrical axis of the tooth is  $3.6^\circ$ . The modeling method of a tooth of the rotor is as follows:

As shown in Fig. 2, the tooth is a quadrilateral composed of two arcs and two straight lines at the origin of the center of the two circles. L1 is the addendum arc with a radius of RR, L2 is the dedendum arc with a radius of RR-HR, and the center angle of the two arcs is  $7.2^\circ \cdot b$ . The Draw center point arc command in ANSYS is used to draw the L1 parameter setting as shown in Fig. 3, and only the arc radius is changed when drawing L2. According to the geometric relationship, the tooth side line segment L3 is drawn, and L4 can be drawn by mirror L3. A tooth surface is obtained by forming a surface of four lines.

**Fig. 2** Rotor tooth model

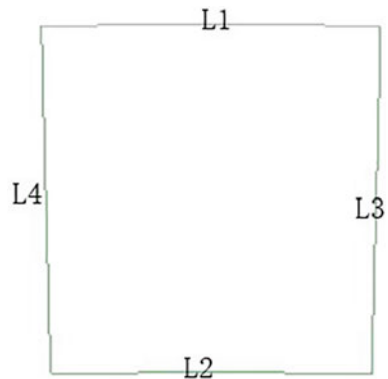


Fig. 3 L1 parameter setting

Name	Value
Segment Ty...	Center Point Arc
Start Point	$RR \cdot \cos(3.6 \cdot b / 180 \cdot \pi)$ , $RR \cdot \sin(3.6 \cdot b / 180 \cdot \pi)$ , 0mm
Center Point	0, 0, 0
Angle	-7.2deg*b
Plane	XY
Number of ...	0

The drawn rotor lamination is transformed into a volume using the sweep along vector command. The vector Z-axis parameter is RZ. Another rotor lamination can be quickly obtained by using a linear array and rotating movement. The Z-axis parameter of the linear array is RZ + MZ, and the rotation angle is 3.6°. The magnetic steel model can be obtained by drawing two cylinders through Boolean operation. It should be noted that the center coordinate of the cylinder is (0, 0 mm, RZ), the height is MZ, and the parametric model of the rotor is established.

### 2.3 Stator Parametric Modeling

Firstly, the stator casing is created. The modeling idea is that the casing can be obtained by intersecting the chamfer circle (radius is E) of the frame with the square (side length is T), and then subtracting the regular octagon and the assembly hole. Secondly, a stator pole is created, and eight of its circular arrays are summed with the stator casing by Boolean operation. The stator pole is decomposed into three parts: stator tooth, stator tooth yoke and pole body. Using the method of creating rotor teeth, a stator tooth is created on the X axis, and then it is rotated along the Z axis to move half of the pitch angle ( $0.5 \cdot a$ ), and then six teeth are obtained through the array. The radius of the tooth top arc is RS, the radius of the tooth root arc is RS + HS, and the center angle is  $ac$ . The same method is used to create the stator yoke. The top circle is RS + D, the bottom circle is RS + D - HS, and the central angle is  $a \cdot (5 + c)$  according to the geometric relationship. The polar body is a rectangle with a width of N, and the upper edge is flush with the inner wall of the casing. In order to prevent the parameter change from affecting the model, the lower edge of the rectangle is tangent to the top circle of the stator tooth yoke, and its height expression is  $0.5 \cdot T - M - RS - HS$ . Then use the sweep along vector command to transform the created surface into a body.

Because the geometric size of the coil has little effect on the performance of HSM, the parametric modeling method can refer to the above, so it is no longer described here. The fully parameterized HSM simulation model established by the above method is suitable for HSM simulation of all models with the same structure.

### 3 HSM Optimization Based on Parametric Model

The cogging torque and holding torque of HSM are analyzed by using the established parametric model. This paper focuses on the analysis of the influence of tooth parameters on the performance of HSM. Bo et al. [10] analyzed the influence of tooth height on the performance of HSM, and proposed that tooth height has little effect on the performance of HSM. This paper no longer analyzes the influence of tooth height. The main analysis is the influence of tooth width angle pitch angle ratio of rotor and stator and stator pitch angle on motor performance. The simulation process is as follows:

Firstly, the ratio of rotor and stator tooth width angle to pitch angle is equal (the value of  $c$  is changed to  $b$  in the ANSYS parametric list), and the value of  $b$  is selected according to the simulation results. Secondly, the stator pitch angle is roughly scanned in the case of primary  $b$  value, and the stator pitch angle is determined according to the simulation results. Finally, the influence of different  $b$  and  $c$  values on the performance of the motor is further analyzed by reducing the parameter change step.

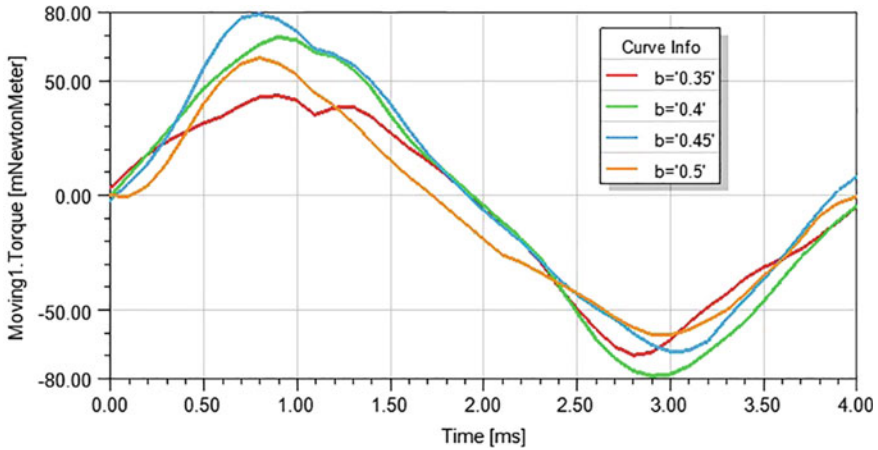
#### 3.1 The Influence of Tooth Width Angle Pitch Angle Ratio on HSM Performance

Make the rotor and stator tooth width angle pitch angle ratio equal, namely  $b = c$ . Parametric scanning was performed on the ratio of tooth width angle to tooth pitch angle, ranging from 0.35 to 0.5, with a change step of 0.05. The simulation results are shown in Table 2, and the torque waveform is shown in Fig. 4.

Table 2 shows that when  $b = c$ , with the decrease of  $b/c$ , the cogging torque and holding torque increase first and then decrease. Properly reducing  $b/c$  can increase the amplitude of holding torque and increase the HSM torque density, but the cogging torque also increases, which is not conducive to the holding torque waveform, as can be seen from Fig. 4. If the maximum holding torque is the design goal, the tooth width pitch ratio can be selected as 0.45. If the holding torque amplitude and waveform are taken into account, the ratio of tooth width angle to pitch angle can be preliminarily selected as 0.4.

**Table 2** T The effect of different  $b/c$  on HSM performance

$b (c = b)$	0.35	0.4	0.45	0.5
Cogging torque/mNm	13.9	16.5	18.8	17.0
Holding torque/mNm	56.4	73.7	73.4	60.3



**Fig. 4** Different b/c holding torque waveforms

**Table 3** The effect of a on HSM performance

Stator pitch angle	6.8°	7°	7.2°	7.4°
Cogging torque/mNm	10.4	12.2	16.5	7.4
Holding torque/mNm	58.1	63.5	73.7	55.0

### 3.2 The Influence of Stator Pitch Angle on Cogging Torque and Holding Torque

When  $b = c = 0.4$ , the stator pitch angle is parametrically scanned, ranging from  $6.8^\circ$  to  $7.4^\circ$ , and the change step is  $2^\circ$ . The simulation results are shown in Table 3, and the torque waveform is shown in Fig. 5.

It can be seen from Table 3 and Fig. 5 that the cogging torque and holding torque will be reduced by adjusting the stator pitch angle, and the holding torque waveform can be significantly improved. When the stator pitch angle increases, the torque decreases greatly, which is not conducive to HSM power output. In order to balance the amplitude and waveform of the holding torque, the stator pitch can be selected as  $7^\circ$ .

### 3.3 Rotor, Stator Different Tooth Width Pitch Angle Ratio

When  $a = 7^\circ$ , the influence of different rotor and stator tooth width angle pitch angle ratio near 0.4 on the performance of the motor is analyzed.

As shown in Fig. 6, when the stator tooth width angle pitch angle ratio  $c$  is between 0.38 and 0.42, and the rotor tooth width angle pitch angle ratio  $b = 0.42$ , the cogging



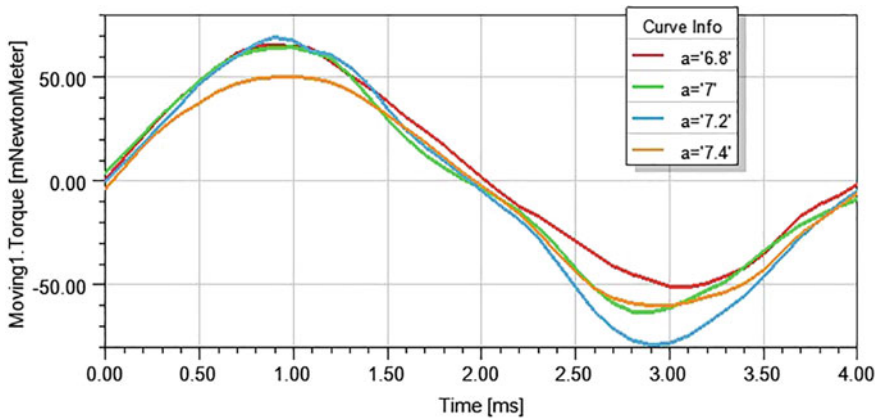


Fig. 5 Different a hold torque waveform

torque and holding torque amplitude reach the maximum. At the same time, when the stator tooth width angle pitch angle ratio  $c = 0.42$ , the holding torque is larger. Therefore, when  $b = c = 0.42$ , a larger holding torque amplitude can be obtained. If both the torque waveform and amplitude are taken into account, the cogging torque is as small as possible and the holding torque is as large as possible when the parameters are selected. When  $(b, c) = (0.4, 0.42)$ , the torque waveform is better. On the contrary, when  $(b, c) = (0.44, 0.4)$ , it is not friendly to maintain the torque waveform, and it is avoided as much as possible when selecting the parameters (Fig. 7).

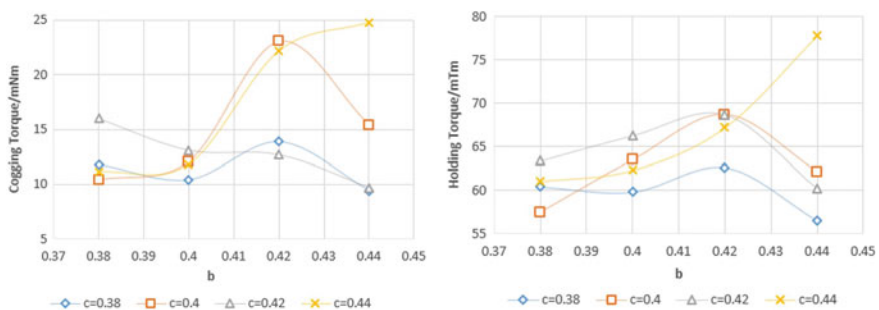


Fig. 6 Cogging torque and holding torque amplitude curves of different b and c combinations

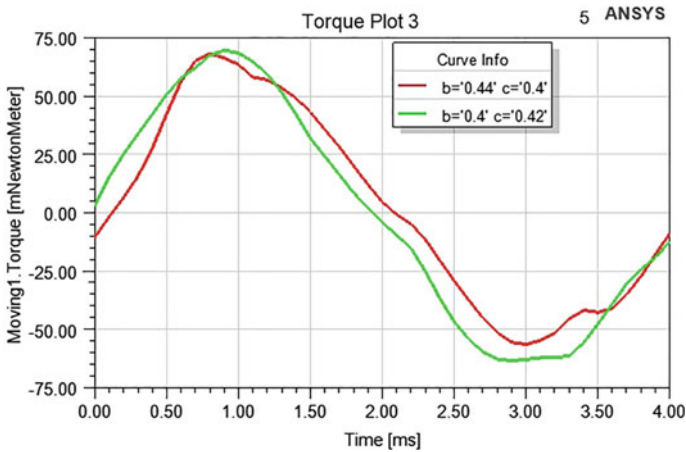


Fig. 7 Comparison of different parameters to maintain torque

### 4 Conclusion

From the optimization process, the performance of HSM is extremely sensitive to the change of tooth parameters, and the establishment of parametric simulation model in ANSYS provides great convenience. Establishing parametric model in ANSYS is of great significance to the analysis of power equipment. By analyzing the influence of tooth geometric parameters on HSM performance, the following conclusions are obtained: (1) Reducing the ratio of tooth width angle to pitch angle to 0.4–0.45 can increase the torque density of HSM; (2) Adjusting the stator pitch angle can effectively improve the holding torque waveform; (3) Taking into account the waveform and amplitude of the holding torque, the tooth geometric parameters of  $b = 0.4$  and  $c = 0.42$  can be selected.

**Acknowledgements** This work is supported by Textile Vision Basic Research Fund of China National Textile & Apparel Council (Grant No. 201506).

### References

1. Kosaka T, Pollock C, Matsui N (2004) 3 dimensional finite element analysis of hybrid stepping motors taking inter-lamination gap into account. In: Second international conference on power electronics, machines and drives (PEMD), pp 534–539. IET, Edinburgh
2. Praveen RP, Ravichandran MH, Achari VTS et al (2009) Design and finite element analysis of hybrid stepper motor for spacecraft applications. In: International Electric Machines and Drives Conference. IEEE, Miami, pp 1051–1057

3. Mathew R, Hiremath SS (2021) Control of stepper motor driven differential drive robot for tracking waypoint trajectories: modeling, simulation, optimization and experimental investigations. *Int J Model Simul* 41(3):1–19
4. Shengwei HUO, Shuhong WANG, Chong HE et al (2012) Research on static performance of two-phase hybrid stepping motor based on maxwell 3D. *Micromotors* 45(9):53–56 (in Chinese)
5. He L, Chen M, Chen Q (2020) Optimization and design of super hybrid stepping motor based on the 3D finite element analysis. In: 23rd International Conference on Electrical Machines and Systems (ICEMS). IEEE, Hamamatsu, pp 1432–1437
6. Ionică I, Modreanu M, Morega A et al (2019) Numerical analysis of a hybrid stepper motor for the electromagnetic torque calculation. In: 11th International symposium on advanced topics in electrical engineering (ATEE). IEEE, Bucharest, pp 1–6
7. Tong Y, Yuehua X, Bo J et al (2015) Method for minimizing cogging torque in two-phase hybrid stepper motor. *Navigation Control* 14(04):8–14 (in Chinese)
8. Ruiwu C, Kai W, Wenxin H (2020) Teaching practice of parametric modeling of special motors based on the ANSYS. *J Electr Electron Teach* 42(6):21–24 (in Chinese)
9. Rajagopal KR, Singh B, Singh BP (2003) Optimal tooth-geometry for specific performance requirements of a hybrid stepper motor. *IEEE Trans Magn* 39(5):3010–3012
10. Bo J, Yajun D, Tong Y (2016) Design of hybrid stepper motor used for solar panel driven system. *Navigation Control* 15(3):87–82 (in Chinese)
11. Weiwei C, Mojia G, Hongyan Z (2022) Design and study based on 2D FEM for cogging torque of a hybrid stepper motor. *Small Spec Electr Mach* 50(8):23–26 (in Chinese)

# Research on Several Key Technologies for the Development of Power Analyzer



Jiaxin Chen, Xiaoming Zhou, and Hua Hua

**Abstract** This paper presents several technologies for the development of a power analyzer based on FPGA high-speed synchronous acquisition and real-time transmission strategy in order to meet the requirements for the power analyzer's accuracy, sampling rate, real-time, and synchronization in measuring high-frequency harmonic signals. The method of synchronous sampling of two ad9226 processors can simultaneously sample four analog signals at a sampling rate of 10MSPS per channel, followed by a ping-pong operation for alternate caching. The system uses Xilinx's Tri-Mode Ethernet IP core based on the AXI bus for UDP communication between the FPGA and PC. The PC calculates and analyses the user's signal. In the meantime, the optical transceiver module is added to replace the cable with an optical cable in order to accomplish electrical isolation via photoelectric conversion, thereby preventing potential ground faults during the measurement process and ensuring reliable data transmission. After experimental analysis, the synchronous sampling rate and real-time performance meet expectations, the data transmission rate reaches 640 Mbit/s, and the accuracy of signal measurement reaches 0.095%.

**Keywords** Power analyzer · FPGA · Ping-pong operation · AXI · Synchronous sampling · Optical fiber communication · Electrical isolation

## 1 Introduction

As an instrument with waveform display and high-precision power operation functions, the power analyzer serves a crucial role in the monitoring of complex power systems [1]. It can measure voltage and current signals in real-time for power calculation, and analyze the waveform of the signal in time-domain or frequency-domain

---

J. Chen (✉) · X. Zhou  
College of Mechanical Engineering, Donghua University, Shanghai 201620, China  
e-mail: [chjiaxin@dhu.edu.cn](mailto:chjiaxin@dhu.edu.cn)

H. Hua  
Xuancheng Meteorological Bureau, Anhui 24200, China

© Beijing Paiké Culture Commu. Co., Ltd. 2024  
X. Dong and L. Cai (eds.), *The Proceedings of 2023 4th International Symposium on Insulation and Discharge Computation for Power Equipment (IDCOMPU2023)*, Lecture Notes in Electrical Engineering 1103, [https://doi.org/10.1007/978-981-99-7413-9\\_11](https://doi.org/10.1007/978-981-99-7413-9_11)

[2]. For high-frequency signals with numerous harmonics, the number of channels, sampling rate, real-time, synchronization, and precision of the power analyzer must be increased. Domestic instruments of multi-channel continuous sampling analysis and calculation capability are inadequate, and it is difficult to enhance analysis accuracy and the depth of harmonic analysis for high-frequency fundamental waves. for a scene that requires high-speed data acquisition, the amount of data is enormous [3] for a scene that necessitates high-speed data acquisition, and the record duration is constrained by the board's resources. When measuring a high-frequency current signal, the accuracy is also affected by the sensor bandwidth [4], making it challenging to accurately figure out the product's power parameters. Besides, measurement fails to ensure electrical isolation through the shunt.

Aiming at several aforementioned issues, this paper proposes a technique for real-time transmission of multi-channel sampling based on FPGA to the host computer for power analysis, which assures reliable transmission under multi-channel conditions and a high sampling rate. In the meantime, traditional Gigabit Ethernet-based ground test equipment is typically connected via cable, but transmission via cable presents issues such as high transmission loss and signal non-isolation [5]. The measurement of voltage and current signals with frequencies higher than the bandwidth of the sensor needs sampling resistance, but it can't achieve circuit isolation. Therefore, an optoelectronic conversion module is required to ensure signal quality through the optical port transmission [6], so the FPGA is electrically isolated from the host computer to prevent the combination of the signal acquisition end and the ground source of the host computer together, which could result in ground loops that lead to inaccurate measurements or even chip breakdown.

## 2 System Solution Design

Figure 1 depicts the system block diagram, which consists of a signal conditioning circuit, two AD9226 data acquisition modules, a Xilinx XC7A100T chip, the internal BRAM, a Tri-Mode Ethernet module, an optical port module, a PC, etc.

After the conditioning circuit, the four analog signals are input to two ad9226 for analog-to-digital conversion, with the FPGA processor providing the sampling clock. FPGA alternately caches the 64-bit synchronous data of the four channels into the block RAM via the input selection controller, while simultaneously enabling the UDP module to output the GMII mode data from BRAM to the axi control engine, and then axi control engine converts GMII mode data into AXI4-Stream mode data. The Tri-Mode Ethernet top layer module converts the AXI4-Stream mode data into GMII mode data and sends it to Ethernet 1000BASE-X PCS/PMA or SGMII LogiCORE IP, and finally, the LogiCORE IP outputs it to the PC in the form of network data stream through the optical port.

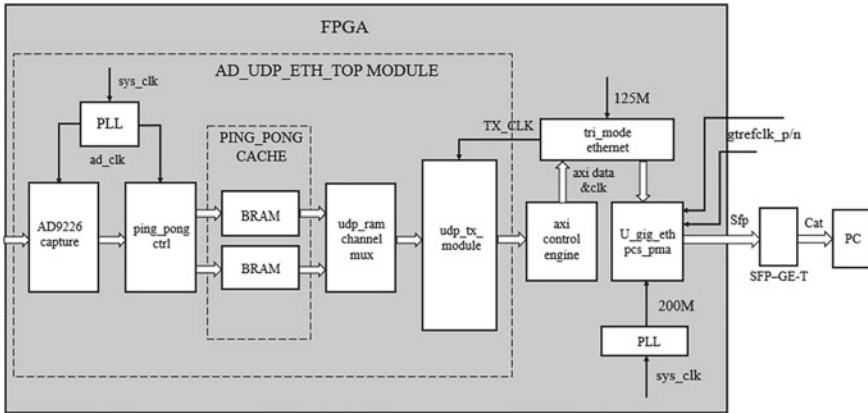


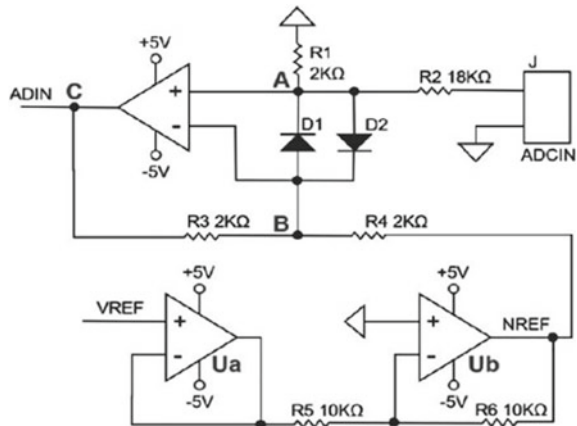
Fig. 1 Power analyzer system diagram

### 3 Part of the Hardware Circuit Design

#### 3.1 Attenuation Circuit

The AD9226 has a range of input requirements. The reference voltage VREF used in this design is 2 V, and the chip can directly acquire continuous signals from 1 to 3 V. In order to successfully acquire data in a larger voltage range, it is necessary to add a potential shift and attenuation circuit before the A/D conversion, as shown in Fig. 2.

Fig. 2 Attenuation circuit



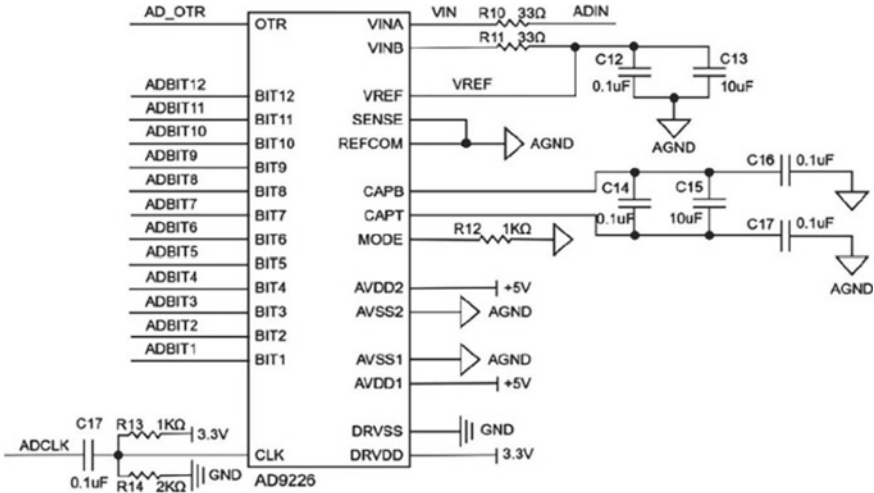


Fig. 3 AD9226 peripheral circuit

### 3.2 ADC Data Acquisition Module

The AD9226 chip is selected for analog-to-digital conversion. It is a single-chip, 12-bit, 65 MSPS ADC with a single power supply and an on-chip high-performance sample-and-hold amplifier and reference voltage source. It uses a multi-stage differential pipeline architecture with a data rate of up to 65 MSPS, and has low power consumption and high-cost performance. The chip peripheral circuit is shown in Fig. 3.

## 4 FPGA Functional Module Design

### 4.1 Data Cache Module

In order to ensure continuity and real-time sampling of 4-channel data, data acquisition, caching, and transmission are performed simultaneously. However, since the rate of each component processing data can be very different, the problem of rate mismatch can result in data loss. Therefore, in order to satisfy the system requirement of real-time storage and transmission, a ping-pong transmission method [7] is used for data caching in this system.

On Vivado software, the four 32-bit block RAMs are required to take turns reading and writing in order to implement the real-time caching function. As shown in Fig. 4, after receiving the acquisition command from the PC, the FPGA sends a synchronous clock to the ADC, the acquisition module then receives the ADC data and converts

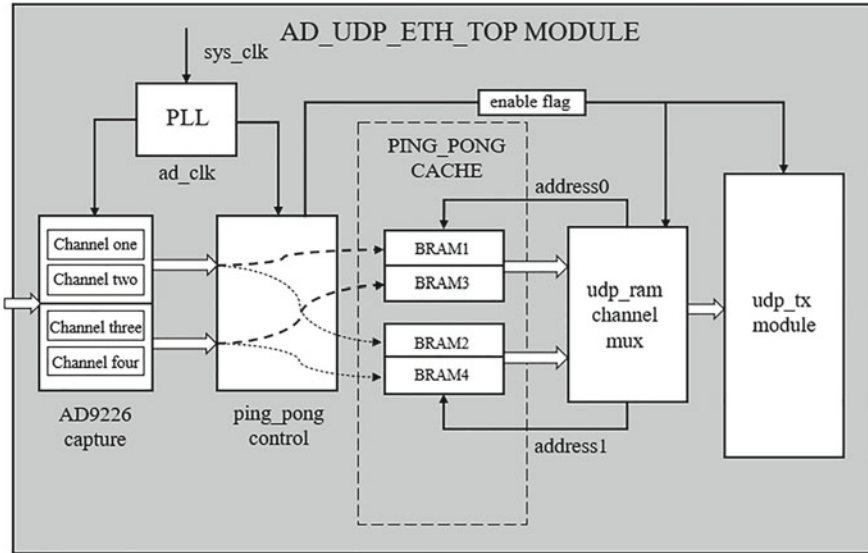


Fig. 4 Data cache module

four channels of 12-bit data into two channels of 32-bit data. The Ping-Pong controller starts to write data in RAM1 and RAM3 sequentially. When RAM1 and RAM3 are full, the Ping-Pong controller starts to write data in RAM2 and RAM4, and enables the flag signal to read data from RAM1 and RAM3 to the upper module over UDP. After all the data in RAM1 and RAM3 is finished and RAM2 and RAM4 have reached capacity, the acquired data is repeated to be written in RAM1 and RAM3. Repeat this sequence, the system can realize the real-time storage and transmission function.

### 4.2 UDP Module

UDP packets are generated by the UDP module using a finite-state machine. When the transmit enable signal is received, the transmitter module begins to send the Preamble, Start frame delimiter, Ethernet frame header, IP header, UDP header, UDP data, and CRC checksum in sequence. The UDP data is derived from the data in the two RAM blocks to be sent each time. The valid data segment input is 64-bit, and the GMII interface is an 8-bit interface. After reading the data from RAM once, the UDP module will cycle through eight times and then add 1 to the memory address in RAM, to store the 64-bit data of the next address, waiting for the next transmission, thus achieving the function of 64-bit data to 8-bit data.



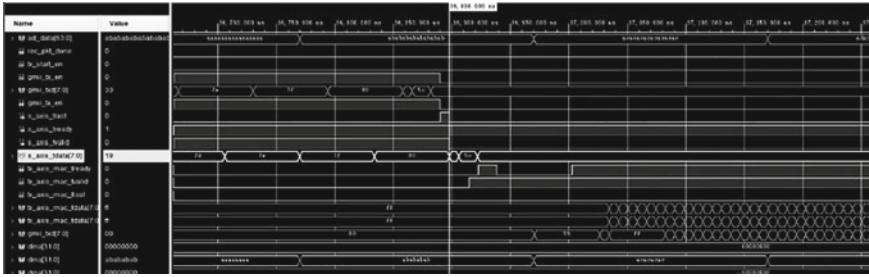


Fig. 5 Data waveform of axi-fifo and Tri-Mode Ethernet

### 4.3 AXI-Based Tri-Mode Ethernet Module

AXI protocol is a high-performance, high-bandwidth, low-latency on-chip bus that features separate address/control and data phases. AXI protocol facilitates three distinct interface types: AXI4 is designed for memory-mapped interfaces and supports bursts of up to 256 data transfer cycles with a single address phase, making it an efficient and high-performance protocol; AXI4-Lite is a subset of the AXI4 protocol, providing a register-like structure with reduced features and complexity [8]; AXI4-Stream is a protocol designed for transporting arbitrary unidirectional data [9, 10]. It is for high-speed streaming data transfer, allowing unlimited data burst transfer.

This system involves high-speed AD acquisition transmission, using AXI4-Stream protocol. Compared to AXI-FULL, AXI4-Stream cancels AW/AR (Address Write/Read) channels. VALID indicates that the master is driving a valid transfer and READY indicates the slave is ready to accept it. Only when VALID and READY are both high, data can be sent properly.

The Tri-Mode Ethernet IP core provided by Xilinx is called to realize the inter-conversion of GMII mode data and AXI4-Stream mode data, and the AXI interface control module is designed to interconvert the AXI4-Stream mode data and GMII mode data to communicate with the UDP module, thus connecting the data stream between the UDP module and the Tri-Mode Ethernet top-level module (Fig. 5).

### 4.4 Optical Conversion Codule

Optical modules are capable of conversion between optoelectronic signals, with receiving and transmitting functions, usually consisting of optoelectronic devices, functional circuits, optical interfaces, etc. The optical module used in this system is SFP. The design uses the idea of “GMII + optical interface” with Gigabit Ethernet protocol, so the transmission system rate is 1 Gbps. The interface level is compatible with PECL or LVPECL level standards by changing the supply voltage [11].

GTP is Xilinx’s own serial high-speed transceiver channel with transceiver rates ranging from 500 Mb/s to 6.6 Gb/s per channel. GTP transceiver is the essential component required by FPGA to realize high-speed optical port communication.

The Xilinx 1G/2.5G Ethernet PCS/PMA or SGMII IP core offers a Physical Coding Sublayer (PCS) and a Physical Media Attachment (PMA) sublayer for 1/2.5 Gigabit Ethernet employing GTP high-speed transceivers. It functions in accordance with the 1000BASE-X or 2500BASE-X standard. In this system, the PCS implements 8b/10b encoding of GMII type data input in parallel from Tri-Mode Ethernet, and the PMA implements parallel-serial conversion to connect to an external off-the-shelf SFP (Small Form-Factor Pluggable) optical module, then the optical module sends the data to the host computer through SFP to complete the communication with the host computer.

### 5 Simulation and Experiment

In this system, the FPGA communicates with the PC through the optical port using UDP. The simulation and experiment mainly verify the real-time reliability of the data acquisition and transmission, and whether there is error and package loss in the data stream actually received by the PC.

Firstly, the experiment is simulated by SIMULATION which comes with Vivado software. At a sampling rate of 10 MSPS, 8 bytes of data from four channels are collected synchronously, and each byte is incremented by 1 under each sampling clock. As shown in Fig. 6, the data stream is alternately cached between RAM1, RAM3, and RAM2, RAM4 via the ping-pong operation, and then output to the UDP sending module. After each cache swap, the data stored in the previous stage is read by the subsequent module. The data segments in the UDP packet output to the optical port are also transmitted from 01, 02...FF cyclically, and the experimental results indicate that the data are transmitted continuously without interruption.

Secondly, during the actual test, the signal generator outputs a high-frequency sinusoidal AC voltage at 20 kHz, the PC sends the acquisition command through the serial port, and the FPGA starts a four-way synchronous acquisition and transmits the data to the PC through the optical port. The PC analyzes packets captured by



Fig. 6 Transmission of sampled data to the optical module

1	0.000000	192.168.0.2	192.168.0.3	UDP	1066 8080 → 8080 Len=1024
2	0.000000	192.168.0.2	192.168.0.3	UDP	1066 8080 → 8080 Len=1024
3	0.000000	192.168.0.2	192.168.0.3	UDP	1066 8080 → 8080 Len=1024
4	0.000000	192.168.0.2	192.168.0.3	UDP	1066 8080 → 8080 Len=1024
5	0.000000	192.168.0.2	192.168.0.3	UDP	1066 8080 → 8080 Len=1024

```

> Frame 1: 1066 bytes on wire (8528 bits), 1066 bytes captured (8528 bits) on interface
> Ethernet II, Src: Xilinx_01:fe:c0 (00:0a:35:01:fe:c0), Dst: Broadcast (ff:ff:ff:ff:ff:ff)
> Internet Protocol Version 4, Src: 192.168.0.2, Dst: 192.168.0.3
> User Datagram Protocol, Src Port: 8080, Dst Port: 8080
▼ Data (1024 bytes)
  Data: 0ffc0878004108980ff90873004008930ffa0871003e08940ffa0873004108960ffa0872...
  [Length: 1024]

```

**Fig. 7** Effective data from UDP package captured by Wireshark

Wireshark. The transmission rate of the Ethernet packet is 78125PPS, and each packet contains 1024 bytes of valid data (Fig. 7).

Finally, MATLAB was utilized to manually displacement the UDP data packet contents. The four synchronous acquisition data were converted into voltage values every 12 bits, according to the order of UDP data packets. The most significant bit is the sign bit with 0 for positive and 1 for negative. The remaining eleven bits hold the magnitude of the number. The formula for calculation is as follows:

$$D = \frac{1}{5} V_{in} \times 2048 \quad (1)$$

Ten consecutive cycles are sampled for time domain and frequency domain analysis. The accuracy of this system is compared with an existing 32-bit data acquisition system as calibration. Figure 8 shows the four-channel synchronous acquisition time-domain diagram and the amplitude-frequency curves of the data of the selected acquisition channels. It can be seen that the fundamental wave amplitude is 4.201 V and the fundamental frequency is 20 k, which is consistent with the actually acquired signal. Figure 9 shows the same set of signal data collected in real-time by 32-bit ADC, with a fundamental amplitude of 4.196 V. The accuracy of signal acquisition of this power analyzer reaches 0.095%.

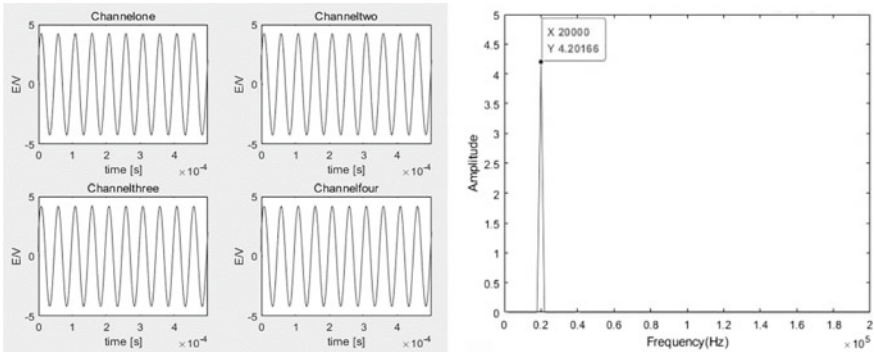


Fig. 8 Time-domain and frequency-domain of the signal collected by the system

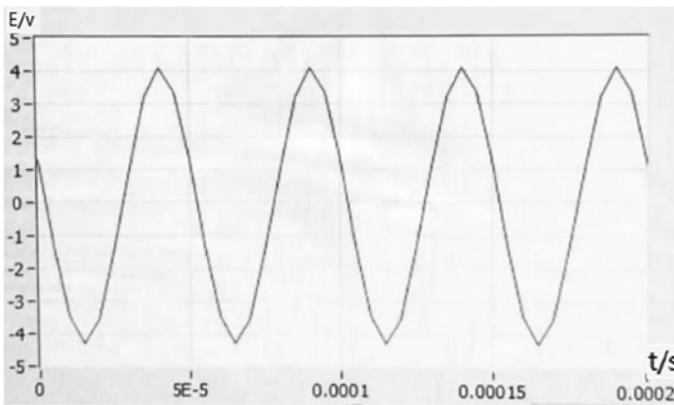


Fig. 9 Time-domain of the signal collected by the calibration system

## 6 Conclusion

Based on the power analyzer designed by FPGA, this paper proposes ping-pong cache strategy and uses Xilinx's Tri-Mode Ethernet IP for udp communication with the host computer through optical network. It overcomes the limitations of power analyzer multi-channel data acquisition in real time, such as low accuracy in high-frequency signal acquisition and inability to achieve electrical isolation. The preliminary test results of data acquired by the host computer indicates that the system can effectively and accurately measure the signal. The sampling rate per channel reaches 10 MSPS, the real-time data transmission rate is up to 640Mbps, the accuracy is 0.095%, and it can achieve electrical isolation during the acquisition process for safe and productive measurements in the electronic measurement field.

**Acknowledgements** This research is supported by the Textile Vision Basic Research Foundation of China National Textile & Apparel Council (Grant No. 201506).

## References

1. Ziling C (2022) Design and implementation of synchronous sampling and data transmission module in oscillator power analyzer. University of Electronic Science and Technology, pp 25–37 (in Chinese)
2. He Y, Zhang M, Yuan H, Wen X, Zhao Y (2023) Analysis of the method and principle of measuring the average power of equipment based on DC power analyzer. *J Phys Conf Ser* 2450
3. Amaya L, Inga E (2022) Compressed sensing technique for the localization of harmonic distortions in electrical power systems. *Sensors* 22(17):15–17
4. Passow D, Beltle M, Tenbohlen S, Hohloch J (2020) Bandwidth and detection sensitivity analysis of integrated capacitive PD sensors for pre-molded cable joints. *IEEE Trans Dielectr Electr Insul* 27(6):57–58
5. Xin Y, Wen F, Zhang K (2021) Long-distance high-speed data transmission based on Serial RapidIO. *Electron Meas Technol* 44(21):125–132 (in Chinese)
6. Zhang XD, Xia YW, Wang CY (2007) FPGA-based low-speed optical port transmission module design. *Comput Knowl Technol (Academic Exchange)*:1669–1670 (in Chinese)
7. Zhang SP, Li ZQ, Zhang JF (2016) A high-speed real-time data acquisition and processing system design. *Firepower Command Control* 41(7):125–129 (in Chinese)
8. Sangani H, Mehta US (2022) UVM-based verification of read and write transactions in AXI4-Lite Protocol. In: 2022 IEEE region 10 symposium (TENSYP), pp 1–5
9. How-AXI4-Stream-Works. <http://docs.xilinx.com/r/en-US/ug1399-vitis-hls/How-AXI4-Stream-Works>. Accessed 23 Apr 2023
10. Xiong X, Du X, Zheng B, He S, Li Y, Yang W, Feng S (2022) Analysis of the impact on soft error in AXI CDMA based on Xilinx Zynq-7000 FPGA. *Nucl Inst Methods Phys Res A* 1037
11. Yan KR, Yan GC, Zhang KH (2022) Design of ZYNQ Gigabit Ethernet optical transceiver module for long-distance transmission. *Microcontroller Embedded Syst Appl* 22(12):88–91 (in Chinese)

# Experimental and Simulation Verification of the Effects of Different Metal Particle Impurities on the Electrical Properties of Alumina/Epoxy Composites for GIL Insulators



Hang Yuan , Sijia Zhu, Shuang Yan, Dingxin Wei, Zishi Yang , Yutong Zhang, Peng Liu, and Zongren Peng

**Abstract** This paper studies how metal impurities in alumina fillers affect the electrical properties of epoxy/alumina composites, which are used for gas-insulated transmission line insulators. The paper prepares samples with aluminum, copper and iron particles, and measures their glass transition temperature, dielectric spectrum and temperature spectrum, power frequency breakdown strength and volume resistivity. It also uses COMSOL Multiphysics software and Latin hypercube sampling technique to model and simulate the dielectric constant and electric field distribution of the samples. The results show that metal impurities lower the volume resistivity and breakdown strength, increase the dielectric constant and loss, and distort the electric field of the composites. The simulation results match well with the experimental data. The paper offers theoretical and experimental guidance for improving the electrical properties of epoxy/alumina composites.

**Keywords** Metal impurity particles · Alumina/epoxy composites · Electrical properties · Latin hypercube sampling · Finite element simulation

## 1 Introduction

The 1000 kV Sutong GIL corridor in China shows the feasibility and stability of the UHV GIL technology [1]. Epoxy/alumina composites have high mechanical strength, thermal conductivity, and insulation performance. They are used for making GIL insulators and other insulation parts [2–4]. However, metal impurities in the alumina

---

H. Yuan · S. Zhu · S. Yan · D. Wei · Z. Yang (✉) · Y. Zhang · P. Liu · Z. Peng  
State Key Laboratory of Electrical Insulation and Power Equipment, Xi'an Jiaotong University,  
Xi'an 7100049, China  
e-mail: [675172784@qq.com](mailto:675172784@qq.com)

filler may worsen the electrical properties of the epoxy composites, such as dielectric constant, dielectric loss, space charge density, breakdown strength and volume resistivity [5]. Thus, it is important to study how different metal impurities affect the electrical properties of alumina/epoxy composites for improving the composite design and insulation reliability.

The literature on how different metal impurities affect the electrical properties of alumina/epoxy composites is limited. Wang et al. [5] studied the effect of  $\text{Na}^+$  in alumina filler on the epoxy composite insulation for basin-type insulators. They found that  $\text{Na}^+$  lowered the resistivity and breakdown strength of alumina epoxy, and worsened the flashover performance and damage extent of the materials under electric field stress. Liu and Wu et al. [6] simulated the impact of metal particles on the electric field of GIL insulators. They found that the electric field distortion depended on the size and position of metal particles. Lü et al. [7] examined the effects of  $\text{Fe}^{2+}$ ,  $\text{Pb}^{2+}$  and  $\text{Cu}^{2+}$  on the structure and corrosion resistance of zincate zinc plating layer. They found that metal ions decreased its corrosion resistance. However, these studies did not systematically analyze and compare the parameters such as glass transition temperature, volume resistivity and electric field distribution of epoxy composites with different metal impurities.

This paper aims to study how different metal impurities (aluminum, copper and iron) affect the electrical properties of alumina/epoxy composites by using experimental and simulation methods. First, it makes samples with aluminum, copper and iron particles with the same mass fraction (0.1% of the alumina filler mass), and measures their parameters such as glass transition temperature, dielectric constant, dielectric loss tangent, power frequency breakdown strength and volume resistivity. Second, it builds a three-dimensional sample model using COMSOL Multiphysics software, and generates metal particles with random distribution using Latin hypercube sampling technique. It simulates and compares the dielectric constant and electric field distribution of the sample with the experimental data and formula prediction results. This paper provides some theoretical and experimental guidance for improving the electrical properties of alumina/epoxy composites.

## 2 Experiment

The materials used in this study were: bisphenol A epoxy resin (5531), carboxylic acid anhydride curing agent HT903C1, alumina powder (10  $\mu\text{m}$ ), aluminum powder (13  $\mu\text{m}$ , 1000 mesh), copper powder (13  $\mu\text{m}$ , 1000 mesh), and iron powder (13  $\mu\text{m}$ , 1000 mesh).

The samples were made with the weight ratios of alumina, epoxy resin, curing agent and impurity being 100:100:38:0.1. The epoxy resin was heated to 110 °C and mixed with the dried alumina powder and impurity powder. The mixture was stirred for 4 h in a 120 °C oil bath pot, and vacuum degassed for 4 h. Then, the curing agent was added and stirred for 15 min. The mixture was cast into a preheated mold. The

sample was obtained after curing with the program of 100 °C/1 h + 120 °C/2 h + 130 °C/2 h + 140 °C/18 h.

The dielectric constant and dielectric loss tangent of the sample were measured using the Concept80 spectrometer. The frequency range was 0.1 Hz–1 MHz, and the temperature was from 25 to 150 °C with a step of 25 °C. The sample was a circular slice with a diameter of 45 mm and a thickness of 1 mm. The power frequency breakdown strength of the sample was measured using a breakdown voltage tester with a spherical electrode-plate configuration. A disk-shaped sample with a diameter of 100 mm and a thickness of 1 mm was used, and the voltage was increased at 0.5 kV/s. The electrode system was in transformer oil to prevent surface flashover. According to the standard GBT/1411-2002, the electrode tip and the sample surface were at an angle of 30°, and the gap between them was  $6.35 \pm 0.1$  mm. The electrode was  $35 \pm 0.1$  mm away from the sample surface. The sample was exposed to a voltage of 12.5 kV, and the current was changed in seven stages, from 10 to 40 mA. The duration of each stage was different. The current level and time were adjusted for different stages. An arc was formed on the sample and eroded the epoxy resin surface. Following the standard GBT/1410-2006, a 6517B high resistance meter with a temperature-controlled three-electrode system was used to measure the DC resistance of epoxy composites. The temperature range was 25–150 °C and the volume resistivity was calculated. The filter net with black impurities from the casting of GIL insulators was analyzed by an EDX8000 X-ray fluorescence spectrometer. The microstructures of alumina filler particles, copper powder particles and aluminum powder particles were observed by a ZEISS EVO10 scanning electron microscope at 15 kV. A Carl Zeiss GeminiSEM 500 scanning electron microscope was used to observe the microstructure of iron powder particles.

### 3 Results and Discussion

#### 3.1 Element Analysis and Micro-morphology Analysis

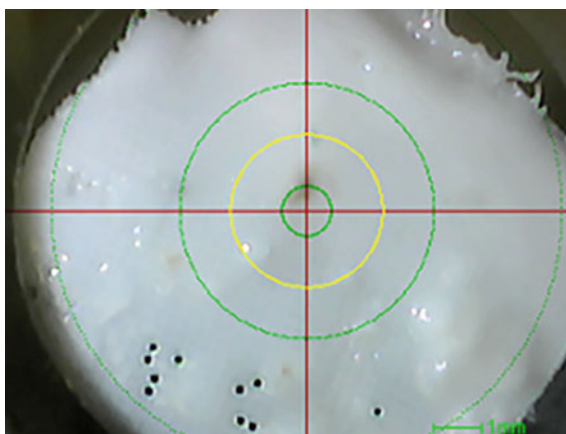
A filter net with black impurities from the epoxy casting site for GIL insulators of a plant was sampled and analyzed. The elements of the epoxy composite material and the impurities on the filter net surface were tested by X-ray fluorescence spectroscopy, with the lowest detectable element being Al. Table 1 shows the elemental analysis results. Based on the data and literature [8], this study selected aluminum powder, copper powder and iron powder as different metal impurities to study their effects on the electrical properties of alumina epoxy composites. Figure 2 shows the scanning electron microscopy images of the alumina filler and metal impurity particles. The alumina filler was blocky and irregular, while the metal particles were mostly spherical or near-spherical.



**Table 1** Element analysis results of filter screen containing black impurities

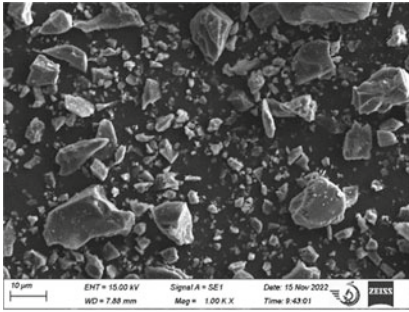
Element	Atomic content /%
Al	97.830
Cl	0.956
Fe	0.294
S	0.227
Cu	0.168
Ca	0.151
K	0.103
Ti	0.103
Cr	0.074
Zn	0.049
Ga	0.046

**Fig. 1** Epoxy cast filter screen containing black impurities

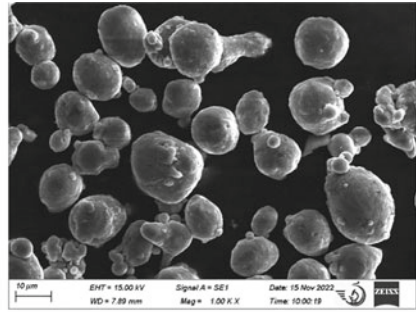


### 3.2 Glass Transition Temperature

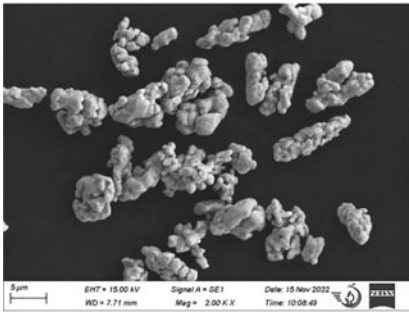
Figure 3 displays the DSC curves of the alumina epoxy composites with or without various metal particles. The glass transition temperature ( $T_g$ ) of the composites was determined by the DSC analysis. As can be seen, the incorporation of metal impurities had negligible influence on the  $T_g$  of the composites. The  $T_g$  of the alumina epoxy composites fabricated in this study ranged from 114 to 117 °C (Table 2).



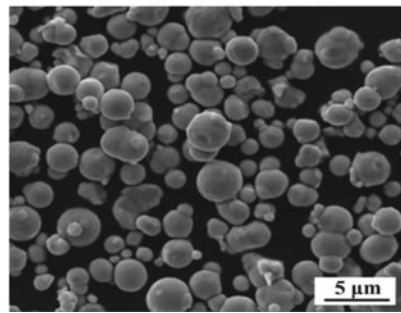
(a) alumina particles at 1000x



(b) aluminum particles at 1000x



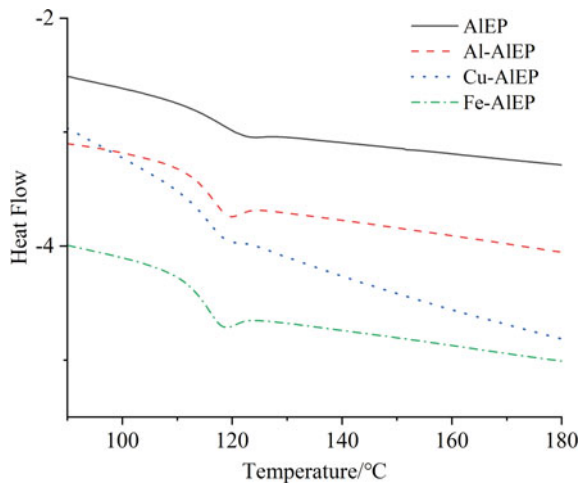
(c) copper particles at 2000x



(d) iron particles at 2000x

Fig. 2 SEM images of alumina fillers and metal impurity particles

Fig. 3 DSC test curve of the samples



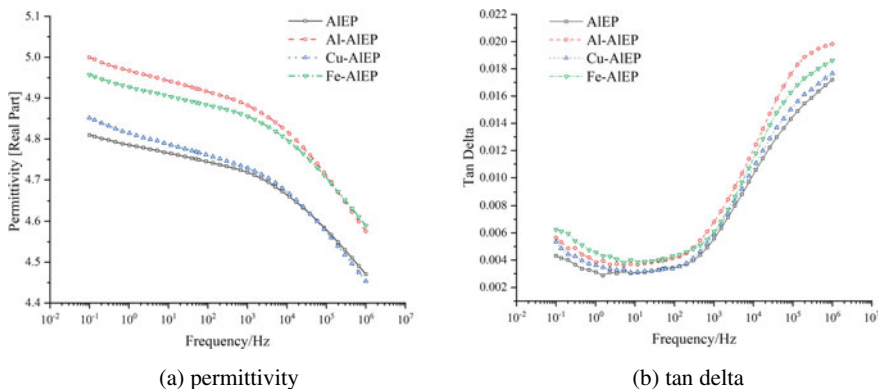
**Table 2** Glass transition temperature of the sample

Specimen	Glass transition temperature/°C
AIEP	116.02
Al-AIEP	115.61
Cu-AIEP	115.66
Fe-AIEP	114.48

### 3.3 Permittivity and Tan Delta

Figure 4a illustrates the variation of the dielectric constant of the alumina epoxy composites with or without various metal particles as a function of frequency at 25 °C, where the frequency spanned from 0.1 Hz to 1 MHz. As can be seen, at 25 °C, the real part of the dielectric constant of all specimens declined with the rising frequency, which was attributed to the fact that the relaxation polarization within the composites was gradually unable to fully develop as the frequency increased, leading to a decreasing tendency of the overall dielectric constant. At a fixed frequency, the real part of the dielectric constant of the alumina epoxy specimens with aluminum powder and iron powder was marginally higher than that of the alumina epoxy specimens with copper powder and without metal particles.

Figure 4b shows the dielectric loss tangent of the alumina epoxy composites with or without different metal particles as a function of frequency at 25 °C, where the frequency ranged from 0.1 Hz to 1 MHz. It can be seen that at 25 °C, the dielectric loss of all samples first decreased and then increased with the increasing frequency, and the increase was more obvious in the frequency domain of 10<sup>2</sup> Hz–1 MHz. This was because the relaxation polarization in the composites could not follow the electric field change rate as the frequency increased, leading to a significant increase



**Fig. 4** The variation curves of the real part of the permittivity and tan delta of the samples with frequency

of the loss. At a fixed frequency, the dielectric loss of the alumina epoxy samples with Al powder and Fe powder slightly increased.

Figure 5 shows the dielectric constant and the dielectric loss tangent of the alumina epoxy composites with or without different metal particles as a function of temperature at 50 Hz, where the temperature ranged from 25 to 150 °C. In the temperature domain of 25–100 °C, the real part of the dielectric constant and the dielectric loss tangent of the composites both increased gradually with the temperature. At power frequency, the order of the dielectric constant of different samples at a fixed temperature was: Al-AIEP > Fe-AIEP > Cu-AIEP > AIEP. When the temperature exceeded 100 °C, near the glass transition temperature, the real part of the dielectric constant of all samples showed a sharp upward trend. This was because the epoxy resin changed from glassy state to rubbery state, causing more active movement of the epoxy chain segments. This movement enhanced the rotational polarization of epoxy materials quickly at this time, making the real part of the dielectric constant of composites increase rapidly.

At power frequency, under the same temperature, the incorporation of metal impurities elevated the dielectric loss of the composites. At low frequency, the dielectric loss of the materials resulted from the dielectric conductivity. The introduction of metal particles enhanced the conductivity of the materials, and the dielectric loss also rose correspondingly. With the rising temperature, the dielectric loss tangent was basically stable. When the temperature neared the glass transition temperature, it started to increase swiftly, and a “glass transition peak” emerged around the glass transition temperature. At 150 °C, the conductivity of metal impurities made the dielectric loss of composites markedly higher than that of composites without metal impurities.

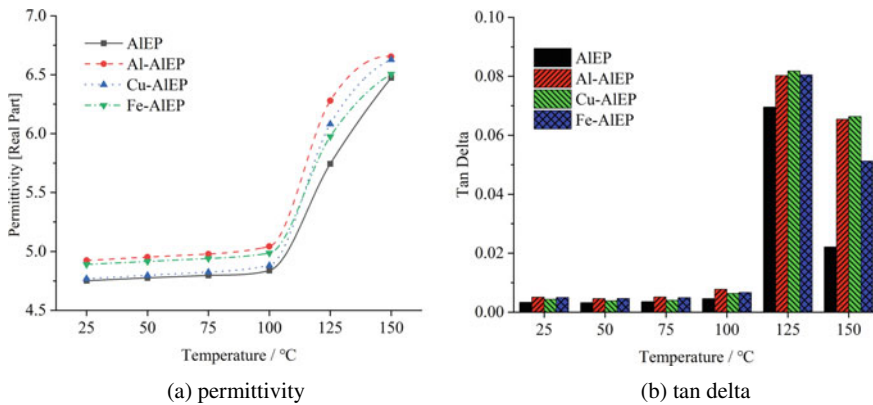


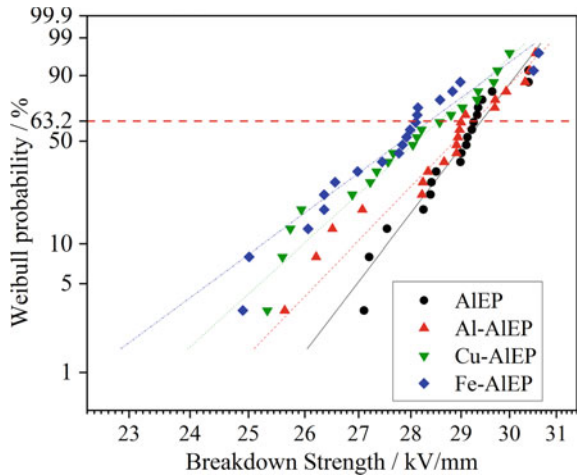
Fig. 5 The variation curves of the real part of the permittivity and tan delta of the samples with temperature

### 3.4 Power Frequency Breakdown Strength and Volume Resistivity

Figure 6 shows the Weibull distribution of the breakdown strength of the alumina epoxy composites with different metal particles. Table 3 lists the scale and shape parameters of the specimens. Figure 8 reveals that the breakdown strength of the alumina epoxy with metal impurities was slightly lower than that without metal impurities, and the order of the breakdown strength was: AIEP > Al-AIEP > Cu-AIEP > Fe-AIEP. Moreover, adding metal impurities reduced the shape parameters, indicating the dispersion degradation of the specimens.

Figure 7 shows the volume resistivity of the alumina epoxy composites with different metal particles. It can be seen that the volume resistivity of all specimens decreased with the increasing temperature, and a sharp drop occurred in the range of 100–125 °C. This was because the higher temperature increased the thermal motion of epoxy resin molecules, enhanced the electron migration rate, and lowered the resistivity. When the temperature reached the glass transition temperature, the epoxy resin changed from glassy state to rubbery state, and the molecular chains became more flexible, causing a significant decrease of resistivity. At the same temperature, the volume resistivity of alumina epoxy specimens with metal doping was lower than

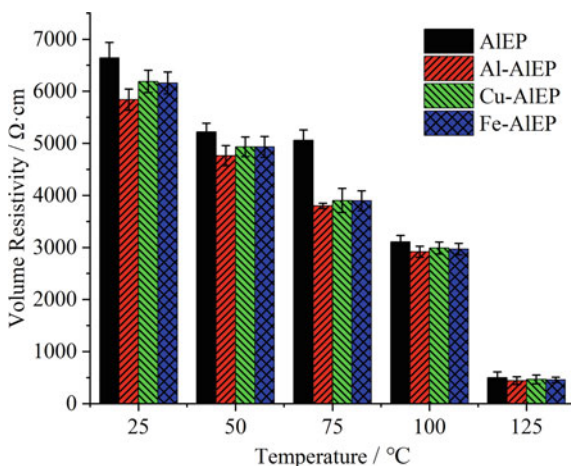
**Fig. 6** Weibull distribution of power frequency breakdown strength of samples



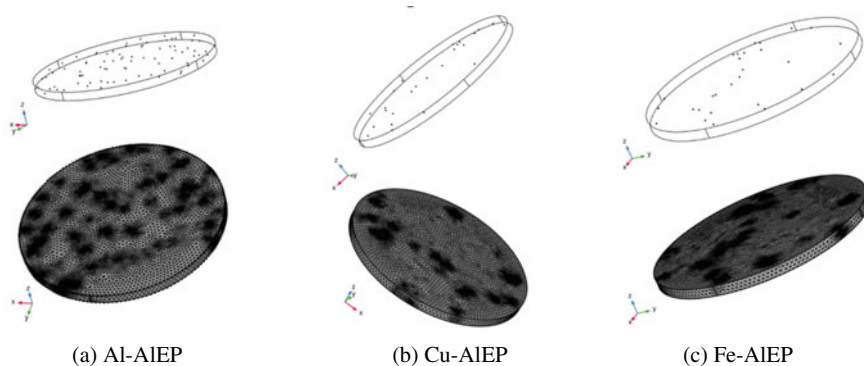
**Table 3** Scale and shape parameters of power frequency breakdown tests on samples

Specimen	$\alpha$ /kV/mm	$\beta$
AIEP	29.41077	34.27083
Al-AIEP	29.26992	27.06348
Cu-AIEP	28.56104	23.71114
Fe-AIEP	28.36347	19.32438

that without metal impurities. This was mainly because metal particles increased the material dielectric loss and conductivity, leading to a reduction of the overall volume resistivity.



**Fig. 7** Volume resistivity of the samples



**Fig. 8** Model of alumina epoxy containing metal impurity particles after Latin supercube sample preparation

**Table 4** Table of simulation parameters

Materials	Permittivity ( $f = 50\text{Hz}$ )	Conductivity/ $\text{S m}^{-1}$
Alumina epoxy resin	4.75	$9.024 \times 10^{-15}$
Aluminum powder particles	10,000	$3.77 \times 10^7$
Copper powder particles	10,000	$5.998 \times 10^7$
Iron powder particles	10,000	$3.774 \times 10^7$

## 4 Simulation

### 4.1 Model Setup

This paper used COMSOL Multiphysics finite element simulation software to establish a three-dimensional model of alumina epoxy composites with different metal impurity particles uniformly and randomly dispersed. The objects to be simulated were all curved surfaces, so free meshing (very fine) was used. The object to be simulated was a cylinder with dimensions of  $\Phi 1100\mu\text{m} \times 100 \mu\text{m}$ , based on the actual dimensions of the alumina epoxy composite specimen measured by dielectric spectroscopy, which was  $\Phi 11\text{mm} \times 1 \text{mm}$ . Table 4 shows the parameters of the alumina epoxy composites with different metal impurities, based on the experimental results, the COMSOL software material library and the relevant literature [9].

Assuming ideal conditions, the matrix is an alumina-epoxy composite with uniformly distributed alumina filler in the epoxy matrix; both the alumina-epoxy composite and the metal impurity particles are isotropic and continuous media; the metal impurity particles are spherical in shape; the properties of the alumina-epoxy composite and the metal impurity particles are temperature-independent.

### 4.2 Theoretical Numerical Prediction Formula

Effective medium theory is a theoretical model that describes the macroscopic properties of composite materials, and involves the analysis or theoretical modelling of their macroscopic properties. Based on this theory, many formulas and models have been proposed by scholars to calculate and predict the dielectric properties of two-phase composite materials such as Maxwell–Garnett (MG) formula, Bruggeman (BM) formula and Lichtenecker (Li) formula. Different formulas are suitable for different scenarios, MG formula is mainly for spherical particle filling with low volume fraction, BM formula is for two-phase composite materials with high filler content, Li formula is for isotropic and asymmetric composite materials [10]. In this study, the metal impurity particles have a low volume fraction, large inter-particle distance, and weak inter-particle interaction. The classical MG formula is used for numerical prediction, which is as follows:

$$\frac{\varepsilon_{eff} - \varepsilon}{\varepsilon_{eff} + 2\varepsilon} = f_s \frac{\varepsilon_s - \varepsilon}{\varepsilon_s + 2\varepsilon} \quad (1)$$

where,  $\varepsilon_{eff}$  is the effective dielectric constant of the composite material,  $\varepsilon_s$  is the dielectric constant of the filler phase of the composite material,  $\varepsilon$  is the dielectric constant of the matrix phase of the composite material, and  $f_s$  is the volume fraction of the filler phase.

### ***4.3 Random Distribution of Metal Impurity Particles by Monte Carlo Method Based on Latin Hypercube Sampling***

Monte Carlo method is a common and practical random simulation method, which uses probability and statistical theory, and random sampling for simulation and calculation. However, when using this method for random experiments, a large number of experimental samples are usually needed to achieve the desired accuracy [11]. To meet the requirements of higher simulation accuracy and efficiency, Latin hypercube sampling (LHS) divides the dimensions of each variable in the high-dimensional sampling problem into  $n$  equal-probability parts, and extracts the same number of samples from each part. In this study, this method ensures that all parts of the alumina epoxy three-dimensional model have metal particles, and avoids duplicate sampling and improves sampling efficiency [12]. The number of metal particles in Al-AIEP, Cu-AIEP and Fe-AIEP, i.e. the sampling size, are set to  $N = 82, 25, 28$  respectively according to their corresponding average particle size, density and weight ratio. The average value of the dielectric constant values calculated by 50 times of sampling and simulation is the final simulation result. Figure 8 shows the three-dimensional models of Al-AIEP, Cu-AIEP and Fe-AIEP samples after one sampling.

### ***4.4 Boundary Conditions and Equivalence Principle***

The three-dimensional model is equivalent to an alumina epoxy composite dielectric, and a parallel plate capacitor is applied to its upper and lower surfaces. A voltage  $\varphi$  is applied to the upper plate, and the lower plate is grounded (potential is 0). The side surface uses continuous periodic conditions, and its boundary conditions satisfy Eqs. (2), (3) and (4). In Eq. (2),  $\tilde{\varepsilon}$  is the complex dielectric constant,  $\varepsilon'$  and  $\varepsilon''$  are the real and imaginary dielectric constants, respectively;  $\varepsilon_0$  is the dielectric constant measured when the space between the plates is vacuum. The ratio of the effective dielectric constant  $\varepsilon_{eff}$  of the composite material to  $\varepsilon_0$  is equal to the ratio of the charge on the plates when the composite material is between the plates to the charge on the plates when the space between the plates is vacuum. The dielectric constant



of the composite material is determined by simulating and calculating the surface charge on the plates.

$$\nabla \cdot (\epsilon_0 \tilde{\epsilon}(x, y, z) \nabla \tilde{\varphi}) = 0 \tag{2}$$

$$\tilde{\epsilon}(x, y, z) = \epsilon'(x, y, z) - i \epsilon''(x, y, z) \tag{3}$$

$$\tilde{\varphi} = \varphi_0 e^{i\omega t} \tag{4}$$

### 4.5 Simulation Results

Figure 9 shows the electric field distribution for Al-AIEP, Cu-AIEP and Fe-AIEP. It is clear that some metal particles do not cause significant electric field changes in their vicinity. However, the existence of metal particles results in distorted electric fields, which are mainly due to the charge accumulation and polarization effects of metal particles. For example, in region 1 of Fig. 9a, the electric field inside the aluminum powder particles is much lower than that in the alumina epoxy matrix, and the electric field at the upper and lower ends of the particles is higher than that in the surrounding matrix, while the electric field at the left and right ends of the particles is lower than that in the surrounding. In region 1 of Fig. 9b, a two-dimensional distorted electric field appears on the bottom tangent plane of the copper powder particles, forming a circular low electric field area with the tangent point as the center and a high electric field ring around it. In region 2 of Fig. 9c, a circular distorted electric field with a higher internal electric field also occurs in the alumina epoxy matrix without nearby metal particles. The distorted electric fields will reduce the breakdown resistance and dispersion of composite materials.

Figure 10 shows the experimental values, MG formula theoretical predicted values and finite element simulation results of the real part of the dielectric constant of

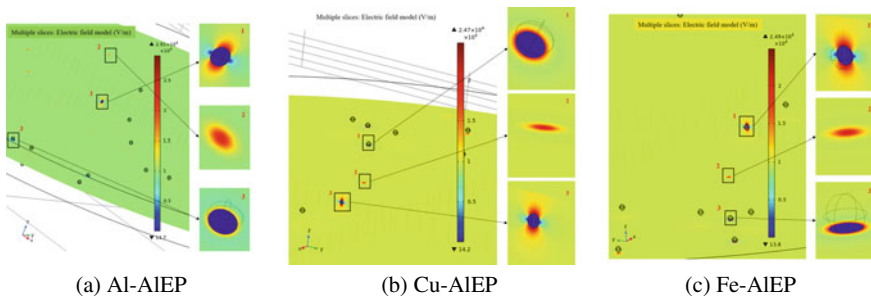
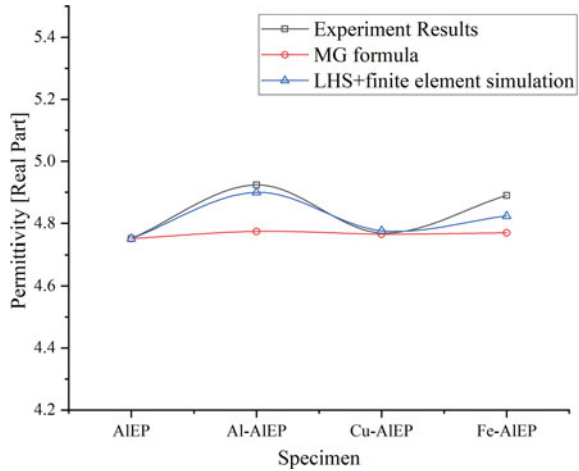


Fig. 9 Electric field distribution of alumina epoxy containing different metal particles

**Fig. 10** Experimental values, theoretical formula calculations, and simulation values of the real part of the dielectric constant



alumina epoxy. It is seen that the MG formula calculation results differ greatly from the experimental values, and the predicted values of different types of metal particles are similar. Moreover, due to the low filler volume fraction, the MG formula predicts that the dielectric constant of alumina epoxy with metal impurities is close to that of pure alumina epoxy. The simulation results match well with the experimental values, which indicates that it is feasible to use the Latin hypercube sampling technique based Monte Carlo random method to distribute metal particles, and then combine finite element simulation to simulate the real part of the dielectric constant.

## 5 Conclusions

This paper studies the effects of different metal impurity particles on the electrical properties of alumina/epoxy composites, prepares alumina epoxy samples doped with aluminum, copper and iron particles of the same mass fraction, and measures their glass transition temperature, breakdown strength and volume resistivity. This paper also uses COMSOL Multiphysics software to build a three-dimensional alumina epoxy sample model, uses Latin hypercube sampling technique to generate randomly distributed metal particles, and simulates the dielectric constant and electric field distribution of composites. The main conclusions of this paper are as follows:

Metal impurities slightly reduce the volume resistivity and breakdown strength of composites, increase the dielectric constant and dielectric loss. Metal impurity particles cause the electric field distortion.

The type of metal impurity affects the electrical properties of composites, among which aluminum powder and iron powder affect the dielectric constant of composites more, and iron powder affects the power frequency breakdown strength of composites more.

The simulation results agree with the experimental results, indicating that finite element simulation and Latin hypercube sampling technique combined can effectively simulate the dielectric constant and electric field distribution of composites, providing a powerful tool for further optimizing the design of composites.

**Acknowledgements** This work was supported by the Science and Technology Project of State Grid Corporation SGHBDK00SBJS2000363.

## References

1. Liu Z, Wang C, Lu S et al (2020) Key technical parameters of UHV GIL in Sutong utility tunnel project. *Power Syst Technol* 44(6):2377–2385
2. Wu Z, Gong A, Wang H et al (2021) Experimental and simulation study on cure-induced distortion of epoxy composite used in GIL insulators. *High Voltage Eng* 47(10):3590–3599
3. Zhu, S, Liu M, Yuan H et al (2022) Molecular simulation on dielectric and mechanical properties of epoxy-polyether amine resin. In: *Proceedings of the IEEE conference on electrical insulation and dielectric phenomena (CEIDP)*. IEEE, Denver, pp 87–90
4. Liu P, Xie Z, Pang X et al (2022) Space charge behavior in epoxy-based dielectrics: progress and perspective. *Adv Electron Mater* 8(10):1–28
5. Wang X, Zhao Y, Yang K et al (2020) Effect of Na<sup>+</sup> on the electrical properties of alumina/epoxy composite insulation materials. *High Voltage Eng* 46(12):4146–4154
6. Liu P, Wu Z, Zhu S et al (2022) Simulation on electric field distribution of 1 100kV AC tri-post insulator influenced by defects. *Trans China Electrotechnical Soc* 37(2):469–478
7. Lü L, Wang L, Liao G et al (2021) Influence of different metal impurities on structure and corrosion resistance of zinc coating formed in alkaline zincate system. *Plat Finish* 43(12):17–22 (in Chinese)
8. Wijayaratne H, Hyland M, McIntosh G et al (2018) Balancing sodium impurities in alumina for improved properties. *Metall Mater Trans B* 49(5):2809–2820
9. Liu H, Jia Z (1983) The dielectric constant of metals. *College Phys 2* (in Chinese)
10. Li G, Zhang L, Du N et al (2017) Composite material theoretical models for dielectric behavior of biological systems. *Mater Rev* 31(15):36–41
11. Zhong R, Zheng Q, Xiang T et al (2018) A modified general effective medium formula for calculating the effective dielectric properties of particle-filled binary composite materials. *Mater Rev* 32(24):4258–4263
12. Fu W, Wang Y, Shen H et al (2022) Residential customer baseline load estimation based on latin hypercube sampling and scenario subtraction. *Power Syst Technol* 46(6):2298–2307

# Research on 10 kV Nonlinear Materials Terminal Accessories for Polypropylene-Insulated Cables



Zhiwen Huang, Qinghao Yang, Yifan Zhou, and Jun Hu

**Abstract** Power cables are important power equipment in high-voltage power transmission systems. Compared with cross-linked polyethylene (XLPE), polypropylene (PP) is environmentally friendly and has better insulation properties. As a result, PP-insulated cables are gaining traction rapidly. In this paper, the simulation research of 10 kV PP-insulated cable terminal accessories is carried out. The effects of different materials, including conventional semi-conductive materials and various nonlinear materials, on voltage equalization are examined using accessories with a stress cone structure. The results show that appropriate nonlinear materials outperform semi-conductive materials. A novel structure of the accessories with a field grading layer based on nonlinear materials is proposed and the uniformed electric field distribution is obtained. The novel scheme, as compared to the conventional semi-conductive stress cone, considerably simplifies the geometric structure of the accessories while successfully controlling the concentration of internal electrical stress.

**Keywords** Nonlinear materials · Terminal accessories · Polypropylene insulated cables

## 1 Introduction

With the continuous improvement of the voltage level of the current power system and the increased transmission capacity, the operational stability of power cables is facing significant challenges [1]. Currently, the main insulation material used in cables is cross-linked polyethylene (XLPE), and existing products cover a wide range of voltage levels. However, there is a limitation with XLPE in that the maximum operating temperature of its products is only 70 °C, increasingly impeding the requirements for large-capacity electric energy transmission within the power grid. On the

---

Z. Huang · Q. Yang · Y. Zhou · J. Hu (✉)

State Key Laboratory of Power Systems, Department of Electrical Engineering, Tsinghua University, Beijing, China

e-mail: [hjun@tsinghua.edu.cn](mailto:hjun@tsinghua.edu.cn)

© Beijing Paiké Culture Commu. Co., Ltd. 2024

X. Dong and L. Cai (eds.), *The Proceedings of 2023 4th International Symposium on Insulation and Discharge Computation for Power Equipment (IDCOMPU2023)*, Lecture Notes in Electrical Engineering 1103, [https://doi.org/10.1007/978-981-99-7413-9\\_13](https://doi.org/10.1007/978-981-99-7413-9_13)

147

other hand, XLPE, due to its thermosetting nature, poses a significant challenge for recycling, which unfortunately results in environmental pollution and energy consumption during production and usage. Polypropylene (PP), with its exceptional thermal, electrical, and high-temperature mechanical properties, is an environmentally friendly insulation material that researchers have recently taken into careful consideration for its use in HVDC cable insulation. As a result, it has garnered more attention from industry and academia alike [2, 3]. Compared with XLPE, PP is a thermoplastic material that can easily be recycled, making it more eco-friendly. It also boasts a high operating temperature and can remain stable at temperatures above 90 °C for extended periods of time, providing better insulation performance than XLPE. As a result, PP is becoming an attractive choice for cable insulation, showcasing great potential for future applications. However, with the development of new cables and advancements in insulation technology, it is crucial to design suitable cable terminal accessories for this new insulation material to improve the performance and efficiency of future power cable systems.

The cable terminal accessory is located at the terminal position of the line. To ensure the creepage distance between the high voltage and the ground, the outer shielding layer of the cable needs to be peeled off for a certain length at the terminal, forming a rod-plate structure between the grounding shielding layer and the high voltage conductor, causing the field strength concentration at the end of the shielding layer. This location is often the location of the maximum field strength inside the whole main insulation. High field strength is easy to damage the main insulation and causes partial discharge, thereby endangering the stable operation of the power system. Therefore, it is of great significance to improve the field strength distribution inside the cable accessories reasonably, so that the field strength distribution at the key positions, especially at the end of the shield layer, is more uniform, which is of great significance to ensure the long-term safe and stable operation of the cable. The conventional method achieves a uniform electric field by setting a unique semiconductor stress cone extension structure inside the cable termination. This eliminates the tip structure at the end of the shield, so that the field strength is no longer concentrated near the end of the shield, but is more evenly distributed on the surface of the stress cone. However, this method is difficult in the process of production and installation, resulting in frequent engineering errors; The difficulty of its production and design also increases with the increase of voltage level. In the high voltage level, if the actual shape of the stress cone and the design are slightly different, the product is difficult to pass various tests [4]. On the other hand, its voltage equalization effect is still not ideal when the voltage level is high, and it is prone to partial discharge phenomenon.

Nonlinear materials exhibit a nonlinear trend with changes in the electric field due to their nonlinear conductivity, which making them useful to be applied in power equipment to deal with the issues of electrical overstress. This method, also known as materials field grading, uses the electrical field-dependent effect of the material itself to create a negative feedback mechanism that regulates the distribution of the electric field in power equipment after applying a voltage. Compared with traditional methods, material field grading has better electric field regulation ability and has

found widely application in motor coils, bushings, and power electronic devices [5, 6].

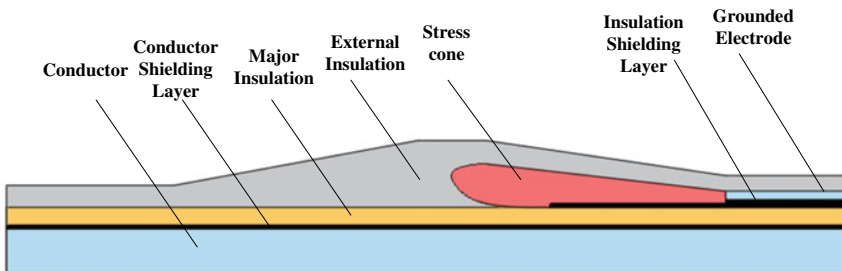
In this paper, a simulation model of the 10 kV AC cable terminal accessory was established. By replacing the stress cone with different nonlinear materials, the electric field distribution under typical operating scenarios is obtained and analyzed. Then, a novel simplified structure of the cable terminal accessory based on the field grading layer was proposed. The excellent electric field grading effect of the nonlinear materials was verified by the simulation and the optimal scheme was selected.

## 2 Simulation Model

The most commonly used prefabricated cable termination accessories are stress cone structures, as shown in Fig. 1. It is to add a stress cone conductor to the shielding layer to achieve the purpose of extending the electrode and transferring the position of the electric field concentration from the end of the main insulation shield to the stress cone surface, so as to get the role of geometric field grading. To optimize it, this traditional scheme can be compared with an electric field nonlinear material that compares the electric field distribution inside the attachment when using a variety of different materials.

The cable termination was modeled using COMSOL Multiphysics. Since the accessory structure was axisymmetric of rotation, a two-dimensional axisymmetric geometry was created for simplifying the calculation. Referring to the terminal size of a 10 kV XLPE cable, the inner diameter of the conductor is 11.28 mm, the outer diameter is 22.56 mm, the thickness of the conductor shielding layer is 1 mm, the thickness of the main insulation is 4.5 mm, and the maximum thickness of the outer insulation is 17 mm.

The material parameters of each part of the cable terminal accessory are shown in Table 1, wherein the high-voltage conductor and grounded electrode were set as copper, the conductor shielding layer and the main insulation shielding layer were



**Fig. 1** The cable termination accessory structure with conventional stress cone

**Table 1** Electrical parameters of materials in simulation

Material	Conductivity (S/m)	Relative permittivity
Copper	$5.8e^7$	$1e^5$
Semiconductor material (Sample 0)	$1e^{-3}$	50
PP	$1.06e^{-16}$	2.1
SiR	$1.29e^{-14}$	3.3
Nonlinear materials	$\sigma = f(E, T)$	20
Air	$5e^{-15}$	1

set as a kind of semi-conductive materials (Sample 0), the main insulation was set as PP, and the external insulation was set as silicone rubber (SiR).

In general, the unique electrical behaviour of nonlinear materials derives from the double Schottky barrier formed by unique functional fillers (e.g., zinc oxide, silicon carbide) in the polymer matrix. In early research, researchers replaced various insulation materials (such as silicone rubber and epoxy resin) as the matrix and obtained composite materials with excellent nonlinear conductivity properties, which provided a theoretical basis for the application in various use scenarios [10]. For better compatibility, the nonlinear composite material used the same insulation matrix as the external insulation, and the nonlinear conductivity is always described by Eq. 1.

$$\sigma = \sigma_0 \cdot e^{A \cdot E} \quad (1)$$

where  $\sigma_0$  (initial conductivity) is the conductivity under 0 V/m electric field,  $E$  is the applied electric field, and  $A$  is the nonlinear coefficient.

For different adaptive materials, the initial conductivity  $\sigma_0$  and the nonlinear coefficient  $A$  (which is mainly determined by the matrix and filler concentration) are generally different. In order to select the optimal scheme, five nonlinear materials with different nonlinear coefficients and initial conductivity were selected, and their current density  $J$ —electric field  $E$  characteristics of them were shown in Fig. 2.

The threshold electric field is usually used to compare the sensitivity of different nonlinear materials to the applied electric field, which is defined as the applied electric field as the material passes through  $3 \mu\text{A}/\text{cm}^2$  current. After fitting the curves based on Eq. 1, the relevant parameters of the above samples are shown in Table 2.

### 3 Results and Analysis

First, the nonlinear material is laid in the stress cone and the original semi-conductive material is replaced to verify the field grading effect of the nonlinear material. Apply a 10 kV AC voltage to the guide rod and calculate the distribution of the electric

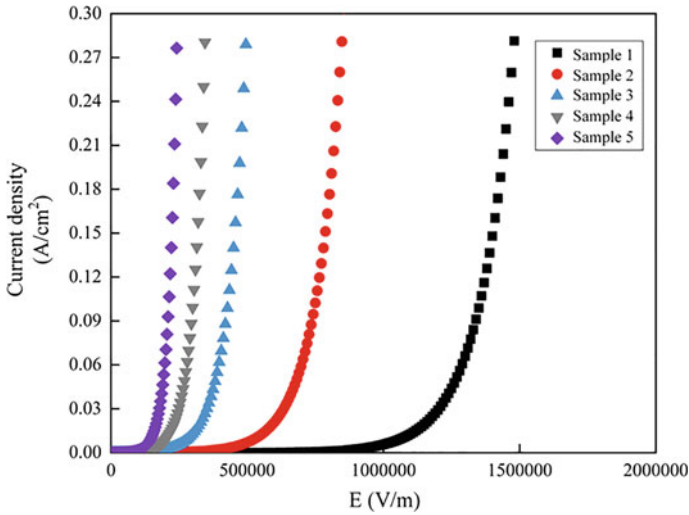


Fig. 2 J-E characteristics of different nonlinear materials

Table 2 Parameters of nonlinear materials

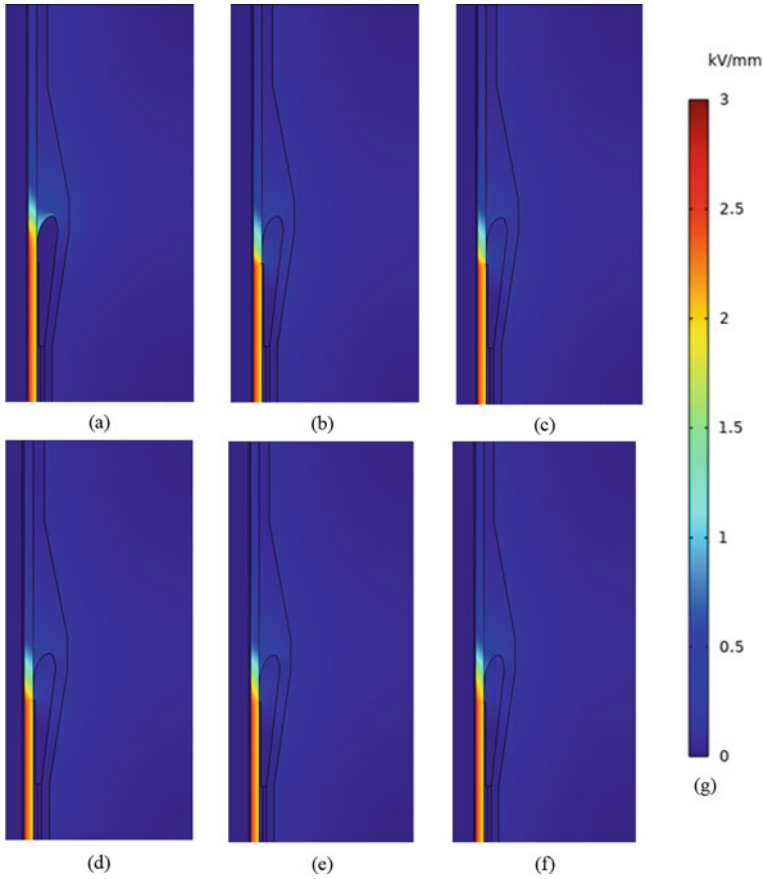
Material	$\sigma_0$ (S/m)	A (m/V)	Electric field threshold (V/mm)
Sample1	3.64e - 12	7.34e - 6	1200
Sample2	1.47e - 10	9.11e - 6	650
Sample3	8.19e - 10	1.32e - 5	350
Sample 4	8.19e - 10	2.0e - 5	250
Sample 5	8.19e - 10	3.0e - 5	180

field in the cable accessories each time during a cycle. The calculation results of the electric field are shown in Fig. 3.

It can be seen from Fig. 3 that when the conventional semi-conductive material is used, the field strength on the stress cone is more concentrated, and when it is replaced with the nonlinear material, the electric field has a certain degree of reduction. However, at the end of the insulation shielding layer, because the conductivity of the nonlinear material is lower than that of the semi-conductive material, the field strength at the point in the major insulation is higher. The electric field distribution was extracted along the stress cone surface, as shown in Fig. 4.

In Fig. 4, it can be observed that the use of nonlinear material has a marked reduction effect on the electric field overstress along the stress cone. This can be attributed to the fact that the nonlinear material exhibits high conductivity at the concentration point of the electric field and low conductivity at the insulation junction, thus achieving a smooth transition of the electrical properties from the grounded material to the insulation material. This property of nonlinear materials can effectively



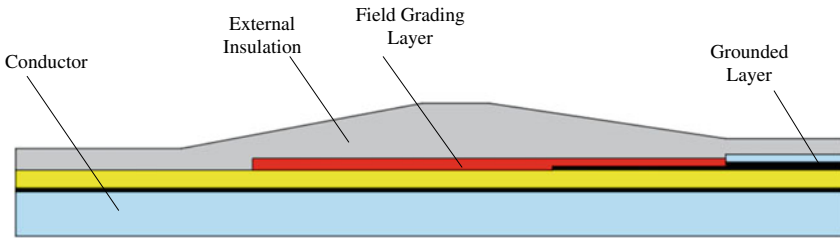
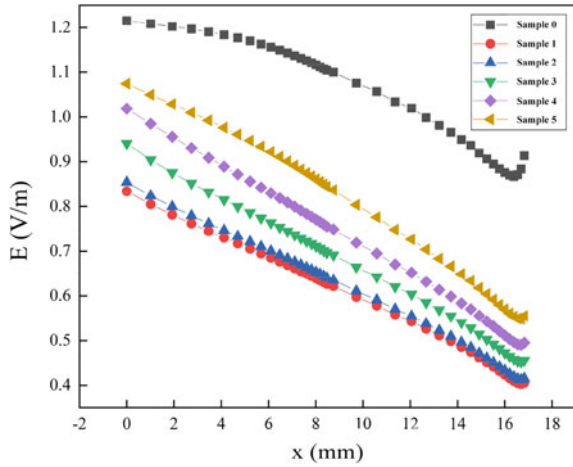


**Fig. 3** The distribution of electric field with different materials of the stress cone: **a** is the control group with stress cone based on conventional semi-conductive, **b–f** are the groups with stress cones based on nonlinear materials Sample 1–5, **g** is the legend

regulate the distribution of the electric field, as well as reduce the likelihood of electrical breakdown, thus ensuring the safe and stable operation of power equipment. At the same time, the lower the threshold field of the adaptive material, the greater its initial conductivity, so the electric field concentration is more likely to occur at the junction between the stress cone and the external insulation. Compared with the semi-conductive group, when using nonlinear materials Sample 1–5, the weakening degree of electric field strength at the root of the stress cone was 32.0%, 30.3%, 22.9%, 16.4%, and 12.3%, respectively, and the weakening degree of the head of the stress cone was 53.8%, 52.7%, 48.4%, 44.0%, and 37.4%, respectively.

As the voltage level of the cable increases, the difficulty of designing and fabricating stress cones with unique geometries increases dramatically. In fact, we can completely rely on the field grading of nonlinear material pressure to control the stress

**Fig. 4** Distribution of electric field along the surface of stress cone surfaces with different materials

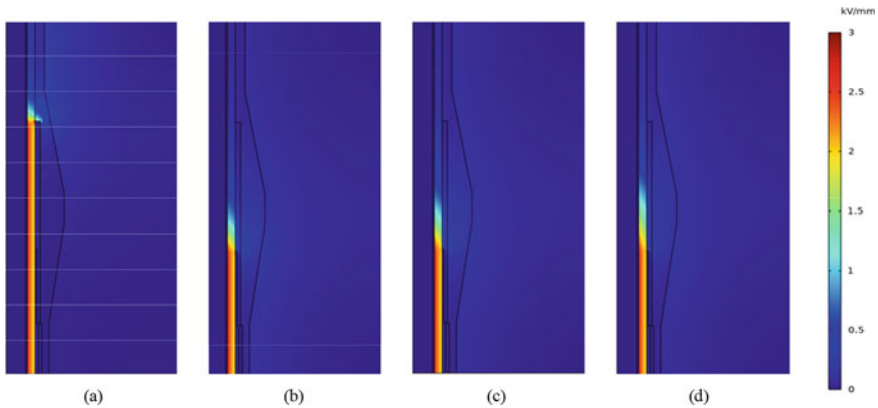


**Fig. 5** A novel cable termination accessory structure with field grading layer

concentration problem of cable terminations. To solve this problem, we designed a new cable accessory with a field grading layer, as shown in Fig. 5.

In this structure, samples 3, 4, and 5 with good field grading effects selected in the previous section were laid at the end of the grounding screen to achieve uniform electric field distribution, and traditional semi-conductive material was used as a reference. The simulated electric field distribution is shown in Fig. 6.

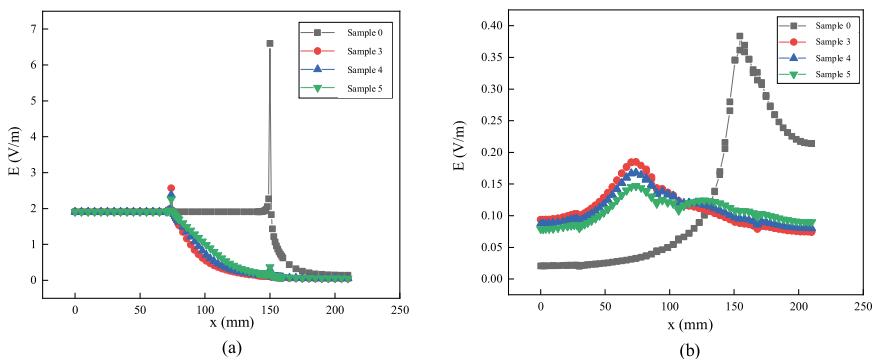
It can be seen from the Fig. 6 that when semi-conductive material was used, there is an electrical field concentration phenomenon at the end of the field grading layer, and the field strength at this location was much higher than the field strength of the surrounding area, which was several times to the surrounding field strength. Because the conductivity of semi-conductive materials is much higher than that of PP and silicone rubber, a structure similar to that of the end of the main insulation shield would form at the end of the field grading layer which causes uneven distribution of electric fields. When using nonlinear materials, the electric field strength at this point was significantly reduced, and the internal field strength distribution of the attachment was relatively uniform. Taking the interface of the main insulation and the external insulation as the reference, two axial line segments with a 0.01 mm



**Fig. 6** The distribution of electric field in the accessories with the field grading layer based on different materials. **a** The reference scheme is based on semi-conductive materials. **b–d** The schemes are based on nonlinear materials 3, 4, and 5

vertical distance from the inside and outside were taken as the samples to analyze the electrical field distribution on these two lines, as shown in Fig. 7a, b.

It can be seen that the use of nonlinear materials can greatly weaken the field strength in the main insulation near the end of the field grading layer. While using semiconductive materials, the electric field intensity in this area measures approximately 6.59 kV/mm, it drops below 0.4 kV/mm when nonlinear materials are employed. The field strength of the point increases slightly as the threshold field strength of the material decreases, because the threshold field strength makes the material easier to conduct, the conductivity of the material increases, and the gap between the conductivity of the main insulation and silicone rubber increases, resulting in an increase in the field strength at this location. As the threshold field strength of the material decreases, the field strength at the triple point of nonlinear materials, main insulation and external insulation also slightly increases, because



**Fig. 7** The axial electric field distribution in the **a** main insulation and **b** the outer insulation

the decrease in threshold makes the material easier to conduct, the conductivity of the material also increases, and the difference with the conductivity of the insulation also increases, resulting in an increase in the field strength at this location. However, none of the three chosen materials caused this field strength to surpass the maximum field strength of other sites inside the insulation.

Figure 7b shows the axial electric field distribution of the electric field in the outer insulation section, and when semi-conductive is used, the maximum field strength inside the accessory still appears at the end of the field grading layer at 3.71 kV/mm. When using Samples 3 and 4, the maximum field strength in the attachment appears at the end of the shielding layer, at this time the nonlinear materials are in the conduction state, and the field strength is near the threshold field strength of the material, so as the threshold field strength of the material decreases, the field strength of this point also decreases. When using Sample 5, this point electric field is smaller than the electric field at the end of the equalizing tube, so the best voltage equalization effect is achieved.

## 4 Conclusion

In this paper, the simulation research of 10 kV PP-insulated cable terminal accessories is carried out. Based on the accessories with conventional stress cones, the voltage equalization effect of traditional semiconductive materials and various adaptive materials is evaluated. Compared with the semi-conductive material, when using nonlinear materials Sample 1–5, the weakening degree of electric field strength at the root of the stress cone was 32.0%, 30.3%, 22.9%, 16.4%, and 12.3%, respectively, and the weakening degree of the head of the stress cone was 53.8%, 52.7%, 48.4%, 44.0%, and 37.4%, respectively.

As the voltage level of the cable increases, the difficulty of designing and fabricating stress cones with unique geometries increases dramatically. To deal with this issue, a novel structure of the accessories with a field grading layer based on nonlinear materials is proposed. According to the calculation results, the novel scheme, as compared to the conventional semi-conductive stress cone, considerably simplifies the geometric structure of the accessories while successfully controlling the concentration of internal electrical stress.

**Acknowledgements** This work is supported in part by the National Key R&D Program of China (2018YFE0200100), and the Natural Science Foundation of China (51921005, 52125703, 52207029, and 52107016).

## References

1. Montanari GC, Morshuis PHF, Zhou M et al (2017) Criteria influencing the selection and design of HV and UHV DC cables in new network applications. *High Voltage* 3(2):90–95
2. Zhou Y, Hu S, Yuan C, Hu J, Li Q, He J (2015) Recyclable polypropylene-based insulation materials for HVDC cables: progress and perspective. *CSEE J Power Energy Syst* 1–10
3. Hu S, Wang W, Dang B, Zhou Y, Yuan C, Hu J, Li Q, He J (2020) Thermal properties and space charge behavior of thermally aged polypropylene/elastomer blends nanocomposite. *IEEE Trans Dielectr Electr Insul* 27(2):521–527
4. Reed CW (2017) An assessment of material selection for high voltage DC extruded polymer cables. *IEEE Electr Insul Mag* 33(4):22–26
5. Zhao X, Yang X, Gao L et al (2017) Tuning the potential distribution of AC cable terminals by stress cone of nonlinear conductivity material. *IEEE Trans Dielectr Electr Insul* 24(5):2686–2693
6. Huang Z, Yang X, Yuan Z, Sun Y, Liu X, Sun G, Hu J, He J (2022) Time-domain response model of nonlinear dielectric properties for electrical field grading composites. *Compos Sci Technol* 232(8):109777

# Mechanism of Surface Charge Regulation with Nonlinear Conductivity Coating in C<sub>4</sub>F<sub>7</sub>N/CO<sub>2</sub> Mixture



Peng Sun, Jinshu Li, Junhong Chen, Wei Yin, Junbo Deng, Jianben Liu, and Yan Liu

**Abstract** The study of charge regulation mechanism in C<sub>4</sub>F<sub>7</sub>N/CO<sub>2</sub> is of significant importance for advancing the applications of C<sub>4</sub>F<sub>7</sub>N/CO<sub>2</sub>. In this study, coating samples with varying SiC content were fabricated using conventional brush coating method, and the surface charge distribution of these samples under negative voltage was measured using a surface potential measurement system. The results revealed that in the absence of coating, the surface charge in C<sub>4</sub>F<sub>7</sub>N/CO<sub>2</sub> exhibited bipolar distribution, with a large number of negative charges concentrated near the high voltage electrode and a small number of positive charges concentrated near the ground electrode. When coatings existed, the pattern of surface charge distribution changed. Under the same voltage, with the increase of SiC content, the maximum potential along the electrode centerline first increased and then decreased, reaching a decrease of 70.7% at 30% wt of SiC content, and charges on both sides of the electrode continuously increased. Through the measurement of coating material's conductivity and trap distribution characteristics, it was found that the coating material reduced the

---

P. Sun · J. Li · J. Chen · W. Yin · J. Deng (✉)

State Key Laboratory of Electrical Insulation and Power Equipment, Xi'an Jiaotong University, Xi'an, China

e-mail: [dengjb@mail.xjtu.edu.cn](mailto:dengjb@mail.xjtu.edu.cn)

P. Sun

e-mail: [Sunpeng1069@stu.xjtu.edu.cn](mailto:Sunpeng1069@stu.xjtu.edu.cn)

J. Li

e-mail: [tyscsq@stu.xjtu.edu.cn](mailto:tyscsq@stu.xjtu.edu.cn)

J. Chen

e-mail: [cjunhong@stu.xjtu.edu.cn](mailto:cjunhong@stu.xjtu.edu.cn)

J. Liu · Y. Liu

State Key Laboratory of Power Grid Environmental Protection, China Electric Power Research Institute, Wuhan, China

e-mail: [liujianben@epri.sgcc.com.cn](mailto:liujianben@epri.sgcc.com.cn)

Y. Liu

e-mail: [liuyan5@epri.sgcc.com.cn](mailto:liuyan5@epri.sgcc.com.cn)

© Beijing Paiké Culture Commu. Co., Ltd. 2024

X. Dong and L. Cai (eds.), *The Proceedings of 2023 4th International Symposium on Insulation and Discharge Computation for Power Equipment (IDCOMPU2023)*, Lecture Notes in Electrical Engineering 1103, [https://doi.org/10.1007/978-981-99-7413-9\\_14](https://doi.org/10.1007/978-981-99-7413-9_14)

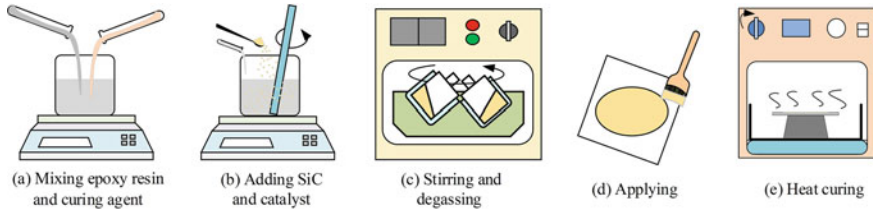
surface trap energy level, increased the trap density, and exhibited nonlinear conductivity characteristics. It is suggested that nonlinear conductivity played a role in equalizing the electric field, reducing the gas ionization in  $C_4F_7N/CO_2$ . Lower trap energy level and higher conductivity will promote charge gas neutralization and accelerate surface conduction. The combined effect of both factors effectively suppresses the charge accumulation at the electrode front origin. However, the increased conductivity and trap density also promotes charge injection and charge-captured possibility, as a result of the lack of dissipation channels, the charges at both sides of the electrode increase with the increase of SiC content.

**Keywords**  $C_4F_7N/CO_2$  · Surface charge · Charge regulation

## 1 Introduction

The  $SF_6$ , which is widely used in power equipment, has a very high global warming potential and does not comply with China's development goals of 'carbon peak and carbon neutrality'.  $C_4F_7N/CO_2$  mixture has a lower warming potential and higher insulation strength and is expected to replace  $SF_6$  in power equipment [1]. In recent years, there have been some practical applications of  $C_4F_7N/CO_2$  mixture [2]. However, the utilization of  $C_4F_7N/CO_2$  mixture has not fully addressed the inherent issues at the gas–solid interface. In practical operation, the accumulation of surface charges on the dielectric surface can serve as seed charges for the initiation of surface discharge, facilitating the formation of initial electron avalanches. Moreover, these charges can also participate in the discharge development process, promoting the formation of streamers and subsequently reducing the flashover voltage [3, 4]. Therefore, it is imperative to explore the charge regulation methods applicable to  $C_4F_7N/CO_2$  mixture.

Currently, extensive researches have been conducted on the surface charge regulation technology. Surface coating technology, which can change the material properties by constructing functional coatings on dielectric surfaces without altering the properties of the substrate, has shown promising application prospects. Deng Junbo et al. have prepared nonlinear coatings (SiC/epoxy resin) in  $SF_6/N_2$  and air, and the results showed that the accumulation of surface charges increases first and then decreases with the increase of SiC content. This is due to the fact that the SiC fillers increase the probability of trapping due to the increase of surface trap density, while also increasing the surface conductivity, which accelerates the charge dissipation rate. The result is a competition between these two effects [5]. To mitigate the problem of surface insulation failure caused by the nonlinear conductive coating under over-voltage, they proposed a solution using local coating and gradient coating [6]. Zhao Huicun et al. used a segmented coating method to apply high-conductivity, low-conductivity, and non-linear coatings on high-voltage electrode, ground electrode, and plane area, respectively, to reduce the overall surface charge on insulators [7].



**Fig. 1** Coating manufacturing process

In summary, some researches have been made in coating technology to suppress surface charges. However, those studies were mainly based on  $\text{SF}_6$ ,  $\text{SF}_6/\text{N}_2$  mixture, which did not consider the compatibility and the effectiveness with  $\text{C}_4\text{F}_7\text{N}/\text{CO}_2$  mixture. Therefore, in-depth researches on surface charge regulation methods for  $\text{C}_4\text{F}_7\text{N}/\text{CO}_2$  mixture is needed to promote the application of  $\text{C}_4\text{F}_7\text{N}/\text{CO}_2$  mixture.

## 2 Experimental Setup

### 2.1 Coating Manufacturing Processes

The epoxy resin/ $\text{Al}_2\text{O}_3$  composite flat samples were purchased from Shandong Taikai Co., Ltd. The mass ratio of curing agent, epoxy resin, and micro-alumina filler is 4:11:35. The dimensions of the samples are  $70 \text{ mm} \times 70 \text{ mm} \times 2 \text{ mm}$ . The SiC coating is manufactured using the method shown in Fig. 1.

The mass ratio between E51 epoxy resin and MeHHPA is 100:80, and the mass ratio between E51 and catalyst DMP30 is 25:0.1. In this study, samples with SiC content of 10% wt, 20% wt, and 30% wt in the coating were prepared, respectively. In addition, the original samples were also measured for comparison.

### 2.2 Experimental System and Test Processes

The surface potential measurement system was used in this study to measure the surface charge accumulation characteristics of two-dimensional planar materials under high-pressure atmospheric conditions. As shown in Fig. 2, the measurement system consists of a high-voltage generation circuit, a high-pressure chamber, vacuum pumping and gas filling circuit, displacement control and data acquisition system and other components.

The experimental transformer can generate DC voltage of  $\pm 140 \text{ kV}$  through built-in silicon stack rectification. The electrostatic probe is connected to the electrostatic voltmeter (Trek Model 341B) via an adapter flange after being led out from the



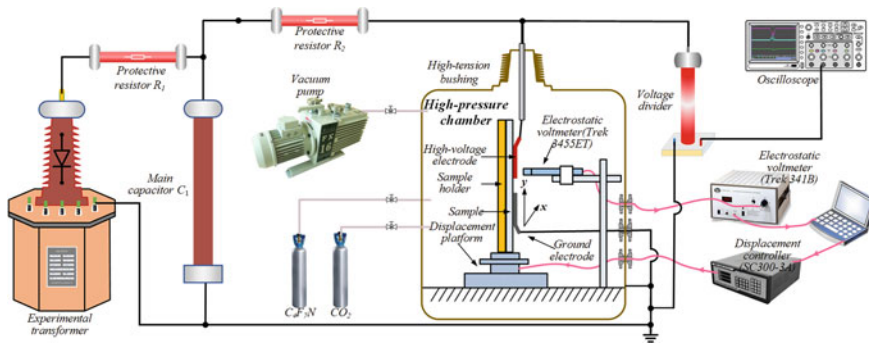


Fig. 2 Surface potential measurement system

inside of the chamber. The electrostatic voltmeter has a measuring range of  $-20$  kV to  $20$  kV and a response time of  $1$  kV/ $200$   $\mu$ s. The circuit functions as a measurement circuit and, in coordination with the displacement platform, allows for scanning of the surface potential of the dielectric after applying voltage.

In this paper, a planar electrode structure is used to construct a highly non-uniform electric field, as shown in Fig. 3a. The stainless steel electrodes have a thickness of  $0.7$  mm and are well-polished with a surface roughness of less than  $0.1$   $\mu$ m. The front end of the electrodes is semi-circular with a diameter of  $20$  mm, and the electrode spacing is set at  $10$  mm.

Before applying voltage, first eliminate residual charges on the surface of the sample. Then place the electrode structure and the sample into the chamber, set the experimental gas, and apply voltage. After applying voltage, perform scanning according to the method shown in Fig. 3b. The scanning distance along the Y direction is  $30$  mm, and the scanning distance along the X direction is  $40$  mm.

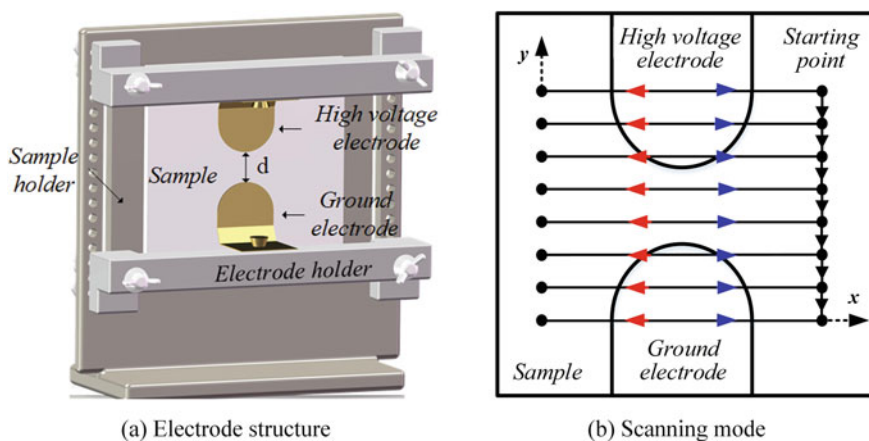


Fig. 3 Planar electrode structure and scanning mode

### 3 Results and Discussion

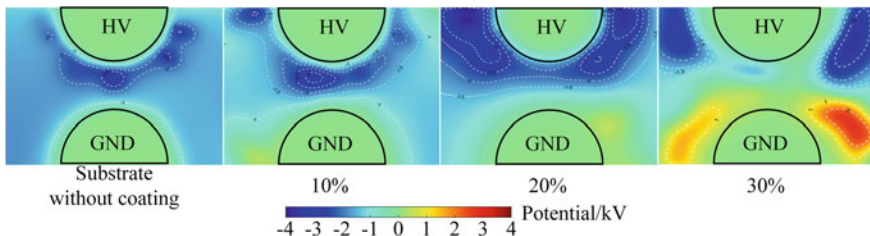
#### 3.1 The Results of Surface Potential Measurements

To investigate the effect of SiC coating on charge accumulation regulation, different SiC content coated samples were applied  $-25$  kV DC voltage for 10 min, the gas atmosphere is  $20\%$   $C_4F_7N/CO_2$  at  $0.1$  MPa, the results are shown in Fig. 4.

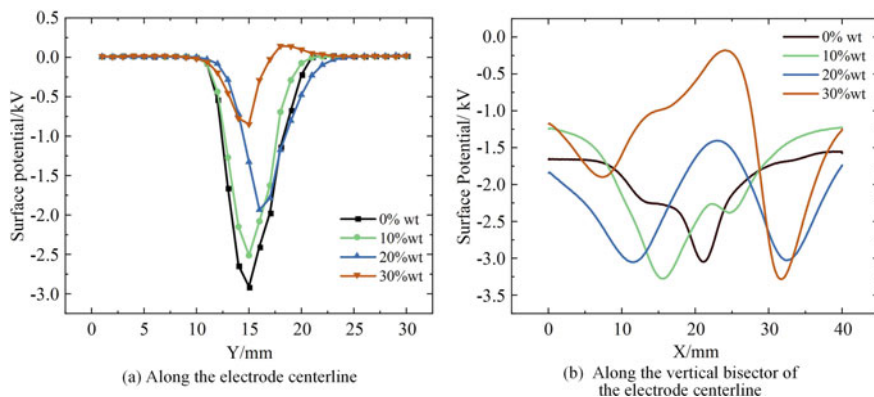
Under negative polarity voltage, when there was no coating on the surface of the sample, the basic distribution of surface charges in  $C_4F_7N/CO_2$  was as follows: a large number of home-charges accumulated near the high voltage electrode, with pronounced charge accumulation in the strong field region near the centerline of the two electrodes, and a small number of hetero-charges accumulated near the ground electrode.

With the presence of SiC coatings, the distribution of surface charges changed in  $C_4F_7N/CO_2$  as the SiC content increased under the same applied voltage. When the SiC content was  $10\%$  wt, the distribution of surface charges was similar to that without coatings. When the SiC content was  $20\%$  wt, the negative charges still concentrated near the high-voltage electrode, but the distribution pattern changed significantly. The potential on both sides of the high voltage electrode was higher than that at the front end of the electrode, and the potential at the front end of the electrode decreased significantly compared to the case with  $10\%$  wt SiC, while the positive potential region near the ground electrode expanded significantly. When the SiC content reached  $30\%$  wt, a large number of negative charges were concentrated on both sides of the high voltage electrode, and only a small number of negative charges remained at the front end of the high-voltage electrode, with almost no charge accumulation. The positive potential region near the ground electrode became more pronounced, existing on both sides of the electrode, and no charge accumulation was observed at the front end of the ground electrode.

To analyze the changes in surface potential in different regions, this study statistically analyzed the distribution of surface potential along the electrode centerline and vertical bisectorto the electrode centerline in different samples, as shown in Fig. 5.



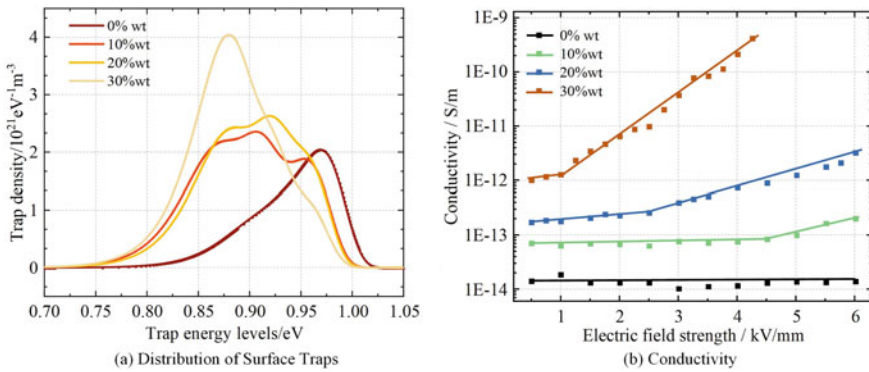
**Fig. 4** The distribution of surface potential in samples with different SiC content coatings under DC voltage



**Fig. 5** Surface potential at different locations

As seen from the Fig. 5a, with the increase of SiC content, the maximum surface potential along the electrode centerline decreases continuously. When the SiC content is 10% wt, 20% wt, and 30% wt, the maximum surface potential along the electrode centerline decreases from the original value of  $-2.91$  kV to  $-2.51$  kV,  $-1.93$  kV, and  $-0.85$  kV, respectively. However, by observing the equipotential lines on the surface, it can be noticed that when the SiC content in the coating is 10% wt, the surface potential at the front end of the electrode is higher than the surface potential in the same region of the original sample. However, due to uneven surface charge distribution, the region with the highest surface potential at the front end of the electrode is located on both sides of the electrode centerline, resulting in the potential along the electrode centerline not passing through the region with the highest surface potential at the front end of the electrode. The maximum potential along the electrode centerline decreased by 70.7% when the SiC content was 30% wt.

Under negative polarity voltage, the surface potential along the vertical bisector of the original sample and the sample with 10% wt SiC content coating only shows a single peak, and the peak for the sample with 10% wt SiC content is higher than that of the original sample, once again confirming that the 10% wt SiC coating increases surface charge accumulation. When the SiC content is 20% wt and 30% wt, a double peak appears in the surface potential along the vertical bisector, located in the regions on both sides of the electrode, and the maximum potential even exceeds the maximum potential along the vertical bisector of the original sample. At the same time, at the position 20 cm along the vertical bisector, the potential decreases significantly, which is consistent with the surface potential along the centerline shown in Fig. 5(a). When the SiC content is 20% wt and 30% wt, the potential at the front end of the electrode decreases, suppressing charge accumulation, but the charge accumulation in the regions on both sides of the electrode significantly increases.



**Fig. 6** Electrical characteristics of the coating

### 3.2 Mechanism of Charge Regulation

To explain the aforementioned experimental phenomena, this study conducted measurements and calculations of the conductivity of the coating material and the distribution of surface electron traps using a three-electrode system and isothermal surface potential decay method [8], as shown in Fig. 6. With the increase of SiC content, the surface trap density of the samples increases, and the energy levels decrease. The changes in trap characteristics promote carrier migration, resulting in non-linear conductivity characteristics of the coating.

When there is no coating present, the surface charge on the samples exhibits a bipolar distribution, which is the result of the combined effect of gas ionization and charge injection from the electrodes [9, 10]. The changes in surface charge distribution with the presence of the coating can be explained by the following mechanisms:

When the SiC content is 10% wt, the coating conductivity is still relatively low despite the increase due to the presence of SiC. The nonlinearity of the conductivity is not significant, and the trap energy levels are relatively high. As a result, the migration rate of charge carriers under the influence of electric field is slow. Meanwhile, the increased conductivity leads to more pronounced charge injection from the electrodes, and the trap density also increases, resulting in higher charge capture capability. As a result, a large number of injected charges do not dissipate in a timely manner, leading to increased charge accumulation due to electrode injection. In addition, the low nonlinearity of conductivity in the coating results in less effective homogenization of electric field by the SiC coating, and therefore, the reduction of charge generation from the gas side is not significant. Trap capture probability is increased, and the suppression effect on charge generation from the gas side is not significant. The combined effect of these factors results in enhanced charge accumulation when the SiC content is 10% wt.

When the SiC content increases to 20% wt, the conductivity of the coating further increases, and the trap density also increases, resulting in more injected charges that are prone to be captured by traps. However, the increased conductivity and the further decrease in trap energy levels also result in faster migration rate of charge carriers and higher probability of trap detrapping. Due to the higher conductivity, the region near the electrode front has higher conductivity and faster charge migration, resulting in more pronounced charge dissipation in the formation of high-voltage electrode and ground electrode discharge channels. Under the influence of electric field, charges migrate along the electric field lines and neutralize or eventually merge into the ground electrode with the charges generated by gas ionization. At the same time, the effect of non-linear conductivity coating on homogenizing electric field becomes more pronounced, leading to further reduction of charge generation from the gas side. However, due to the weak electric field at the sides of the electrode, a large number of injected charges do not have a clear channel for dissipation. In addition, the increased surface trap density of the coated layer further enhances the probability of charge trapping.

When the SiC content reaches 30% wt, the conductivity further increased and the trap energy levels become shallower, resulting in faster carrier migration. At this point, the migration and dissipation of charges outweigh the accumulation of charges. As a result, the charges at the high-field region of the electrode dissipate quickly, inhibiting charge accumulation. However, in the regions at the sides of the electrode where the electric field is weak and lacking in dissipation channels, and with higher trap density, charge accumulation outweighs charge migration and dissipation, leading to further enhancement of charge accumulation.

## 4 Conclusion

The main conclusions of this study are as follows:

- (1) Under negative DC voltage, with the increase of SiC content, the charges on the electrode front end origin increased initially and then decreased. When the SiC content reached 30% wt, the maximum potential along the centerline of the electrode decreases by 70.7% compared to the original sample under negative polarity, while the charges at the sides of the electrode continue to increase.
- (2) The nonlinear electrical conductivity characteristics of the coating play a role in homogenizing the electric field, reducing the field strength at the triple junction, and suppressing the ionization of  $C_4F_7N/CO_2$ . Lower trap levels and higher electrical conductivity promote charge gas neutralization, accelerate surface conduction, and ultimately facilitate charge dissipation along the surface. The combined effect of these factors effectively inhibits the accumulation of charges at the front end of the electrode.

- (3) The increase in electrical conductivity and trap density promotes the injection and capture of charges at the electrode due to higher SiC content and voltage. As a result of the lack of dissipation channels, the charges at both sides of the electrode increase with the increase of SiC content.

**Acknowledgements** This work is supported by Open Fund of State Key Laboratory of Power Grid Environmental Protection (No. GYW51202201416).

## References

1. Deng J, Dong J, Chen J et al (2022) Research advances in interface insulation characteristics of SF<sub>6</sub> alternative gases. *High Voltage Eng* 48(02):661–673 (in Chinese)
2. Xiao X, Shi XY, Lin JT et al (2023) Analysis on the control strategy of the strong greenhouse insulating gas SF in high-voltage electrical equipment under the goal of “emission peak and carbon neutrality. *Proceedings of the CSEE* 43(01):339–358 (in Chinese)
3. Qi B, Gao CJ, Zhao LJ et al, Influence of surface charge on flashover voltage of gas insulated substation basin insulator under AC and DC voltage. *High Voltage Eng* 43(3):915–922 (in Chinese)
4. Li CY, Zhu Y, Hu J et al (2020) Charge cluster triggers unpredictable insulation surface flashover in pressurized SF<sub>6</sub>. *J Phys D Appl Phys* 54(1):015308
5. Xue JY, Chen JH, Wang H et al (2019) The regulation mechanism of SiC/epoxy coatings on surface charge behavior and flashover performance of epoxy/alumina spacers. *J Phys D Appl Phys* 52(40):405502
6. Xue JY, Chen JH, Dong JH et al (2020) Enhancing flashover performance of alumina/epoxy spacers by adaptive surface charge regulation using graded conductivity coating. *Nanotechnology* 31(36):364002
7. Wang WQ, Zhao HC, GAO Y et al (2023) Surface charge suppression experimental analysis of disc insulator based on zoning coating. In: *Proceedings of the CSU-EPISA*. <https://doi.org/10.19635/j.cnki.csu-epsa.001105>. Accessed 21 Apr 2023 (in Chinese)
8. Shen WW, Mu HB, Zhang GJ et al (2013) Identification of electron and hole trap based on isothermal surface potential decay model. *J Appl Phys* 113(8):083706
9. Pan ZJ, Pan C, Tang J et al (2022) Influence of SiC/Epoxy coating on surface charging phenomenon at DC voltage—Part I: charge accumulation. *IEEE Trans Dielectr Electr Insul* 29(4):1333–1342
10. Xue J, Wang H, Chen JH et al (2018) Accumulation and decay characteristics of surface charges on epoxy composite insulation in SF<sub>6</sub> under DC voltage. *High Voltage Eng* 44(12):3824–3832 (in Chinese)

# Prediction Model of Strong Electromagnetic Effect Phenomenon Based on Complement Naive Bayes



Zhihao Liu, Xuan Cao, Mengxue Li, and Haipeng Wang

**Abstract** Strong electromagnetic effects imperil the safety of shipboard electronic systems and components. To ensure their safety, it is necessary to predict strong electromagnetic effect phenomena. However, the acquisition and simulation of strong electromagnetic effect data are troublesome, resulting in the problem of small sample sizes and sample imbalance when predicting phenomena involving strong electromagnetic effects. To resolve the aforementioned issues, this paper proposes a prediction model based on the CNB classifier. The model selects the features, concatenates the discrete features prior to data processing, and then uses the term frequency–inverse document frequency (TF-IDF) algorithm to encode the feature word weights. The vectors are finally fed to a CNB classifier calibrated with an isotonic probability for prediction. In experiments with traditional plain Bayes, the Isotonic probabilistic calibrated CNB classifier achieves an accuracy score of 0.94 on the strong EM effect dataset. This result demonstrates the model’s superior performance. The model avoids the problems of small sample size influencing model performance and the tendency of the classifier to favor large categories while ignoring small ones, safeguarding against the prediction of the strong EM effect phenomenon.

**Keywords** Small sample size · Strong electromagnetic effect · Sample imbalance · Phenomenon prediction · Complement naïve bayes

---

Z. Liu · X. Cao · H. Wang (✉)  
School of Information Science and Technology, Fudan University, Shanghai 200433, China  
e-mail: [hpwang@fudan.edu.cn](mailto:hpwang@fudan.edu.cn)

Z. Liu  
e-mail: [22210720184@m.fudan.edu.cn](mailto:22210720184@m.fudan.edu.cn)

X. Cao  
e-mail: [20210720160@fudan.edu.cn](mailto:20210720160@fudan.edu.cn)

M. Li  
China Ship Development and Design Centre, Wuhan 430064, China  
e-mail: [c13161068262@163.com](mailto:c13161068262@163.com)

# 1 Introduction

With the development of electromagnetic technology, our electromagnetic environment has become more and more complex, and we have to start considering the impact of strong electromagnetic effects on us [1]. Ships have a lot of electronic integrated components and electronic systems, which are the guarantee of normal navigation and sea operation of ships. But during the navigation of the ship, it is affected by the complex electromagnetic environment, especially the strong electromagnetic environment. By coupling [2], the strong electromagnetic environment may lead to the damage of integrated devices and the failure of electronic systems. Therefore, we hope to be able to make the prediction of the corresponding effect phenomena when the ship encounters the complex strong electromagnetic environment afterwards by analyzing and mining the historical data, and we are better able to make the appropriate protection plan based on the possible problems.

However, both real data recording and simulation data collection are often not easy and will consume a lot of human resources and time, which will lead to two problems with our historical data, one problem is that the sample size is relatively small, and the other problem is that the sample has an imbalance problem. Traditional data mining algorithms, whether facing the small sample problem or the sample imbalance problem, will be greatly affected, and the prediction results will be greatly deviated.

Considering the limitations of traditional data mining algorithms facing the above two problems, this paper proposes a strong electromagnetic effect phenomenon prediction algorithm based on complementary set Bayesian classification, using historical data mining analysis to avoid the influence of small samples as well as sample imbalance on the model to the maximum extent, which plays a good role in guaranteeing the protection suggestions for ships in the strong electromagnetic environment.

## 2 Methodology

### 2.1 *Complement Naive Bayes*

Plain Bayes [3] is the conditional probability of correctly classifying the text to be classified into category based on the minimum error [4]. In the multinomial naive bayes model, a document is regarded as consisting of a sequence of feature words and it is assumed that any word in the document is independent of its position in the document as well as the context, and it is also assumed that there is no dependency between the feature terms of the document to be classified. The following equation is accessible:



$$p(D_i|C_j) = \prod_{i=1}^n p(x_i|C_j) \tag{1}$$

The complement naive bayes (CNB) algorithm is formed on the basis of the multinomial naive bayes algorithm [5]:

$$p(x_i|\overline{C_j}) = \frac{\sum_{k=1,xi \notin C_j}^{|D|} D_{ik} + a}{\sum_{i=1,xi \in C_j}^{|m|} \sum_{k=1}^{|D|} D_{ik} + a|n|} \tag{2}$$

The balancing factor  $a$  takes values in the range  $[0,1]$ ,  $n$  denotes the number of categories of documents,  $D$  denotes the total number of documents, and  $m$  denotes the total number of feature items,  $\sum_{k=1,xi \notin C}^{|D|} D_{ik} + a$  denotes the sum of the number of occurrences of feature item  $x$  in each document of all categories except category  $C_j$ ,  $\sum_{i=1,xi \in C}^{|m|} \sum_{k=1}^{|D|} D_{ik} + a|n|$  denotes the total number of occurrences of feature items of categories other than category  $C_j$  in documents of categories other than category  $C_j$ .

## 2.2 Term Frequency–Inverse Document Frequency

In the data mining process, we need to transform the text to another dimension if we want to operate with it, that is, encode it into a language that the algorithmic model can understand. Our algorithmic model typically receives vectorized data as input, so we must employ some methods to extract features for encoding. Each word in the training set text is a feature, and if we use conventional word frequency statistics (the number of times the feature word appears in the text) to represent the vector, some very common words will be heavily weighted because they appear in every text. But in fact, such words are less important than other words that occur less frequently, so we consider using the Term Frequency–Inverse Document Frequency (TF-IDF) algorithm [6] to encode them, a prevalent weighting method in text mining.

TF-IDF has two meanings: Term Frequency (TF) and Inverse Document Frequency (IDF). TF is also the word frequency we mentioned previously, and the vectorization we performed previously consisted of calculating the frequency statistics of each word in the text and using them as the text feature.

IDF reflects the prevalence of a word in all texts; therefore, if a word appears in many texts, its IDF value should be low. When a word appears in fewer texts, its IDF value should be higher. Here is the IDF formula for the word  $x$ :

$$IDF(x) = \log \frac{N}{N(x)} \tag{3}$$

$N$  is the total number of texts in the corpus, and  $N(x)$  is the total number of texts in the corpus containing word  $x$ . However, a certain rare word is not in the corpus,

so our denominator is 0, and the IDF is meaningless [7]. We must perform some smoothing so that terms not present in the corpus can also be assigned a suitable IDF value. The equation after smoothing is as follows:

$$IDF(x) = \log \frac{N + 1}{N(x) + 1} + 1 \quad (4)$$

Using the following formula, we can then determine a word's TF-IDF value:

$$TF - IDF(x) = TF(x) * IDF(x) \quad (5)$$

$TF(x)$  indicates the frequency of the word  $x$  within the current text.

The high word frequency within a particular document, and the low document frequency of that word in the whole set of documents, can produce a high weight TF-IDF.

The TF-IDF tends to filter out common words and keep important words. The higher the TF-IDF of a word in an article, the higher the importance of the word in the article in general.

### 2.3 Probabilistic Calibration

For the plain Bayesian, we wish to increase the prediction confidence of the model and may calibrate the probabilistic algorithm using isotropic regression. There are two general types of isoproximation regression, a parametric calibration method based on Platt's Sigmoid model [8] and a nonparametric calibration method based on isotonic calibration [9]. In this case, Isotonic is used to perform the calibration, and the procedure is as follows:

**Step 1.** Train a classifier model using sample feature  $X$  and target variable  $Y$ . (Unrestricted classifier type).

**Step 2.** The prediction results are obtained by using the model to predict the samples.

**Step 3.** Use the predicted result as  $x$  and the corresponding label as  $y$ .

**Step 4.** Substitute into the formula:

$$f(x) = \sum_{i=1}^n w_i (y_i - x_i)^2 \quad (6)$$

## 2.4 StratifiedKFold

Typically, we employ cross-validation to assess the performance of the model. Cross-validation means to entails separating the obtained sample data into distinct training and testing sets, then using the training set to train the model and the testing set to evaluate its prediction. The most prevalent KFold cross-validation method randomly divides the sample data into K copies, with K-1 copies serving as the training set and the remaining copy serving as the test set. When the round is completed, K-1 copies are randomly selected again to train the data. After multiple rounds, we can evaluate the model's accuracy based on its average score, thereby adjusting it to reduce the chance introduced by a single random division and improve its generalization ability the actual graph (see Fig.1) and formula of KFold cross-validation are as follows:

$$E = \frac{1}{n} \sum_{i=1}^K E_i \quad (7)$$

However, there is a sample imbalance problem in our EM effect dataset, and using KFold cross-validation will probably lead to a random division of the data into categories, such as all 0 labels in the first fold training set and all 1 labels in the second fold test set. In light of the sample imbalance issue, this paper employs StratifiedKFold cross-validation [10], which follows the same logic and structure as KFold, but employs a hierarchical partitioning method for the data partitioning details, so that each subset contains the same proportion of categories as the original data set.

## 3 Experiment

### 3.1 Data Pre-Processing

Our original data is tabular, and we first visualize it to determine the number of each feature and the heat map (see Figs. 2 and 3). According to the two figures below, the Injection site, Effect curve data, Effect curve image, and Voltage threshold characteristics have more absent values and lower correlation. Then, we perform feature selection [11] to eliminate features with low correlation and an excessive number of missing values.

The algorithm flow reveals that, prior to the encoding operation, the features should be concatenated and textualized in preprocessing, and connect the discrete features into feature text, which is also more convenient for the algorithm user to operate. Then, we conclude our data preprocessing by removing stop words from the concatenated feature text and separating words.

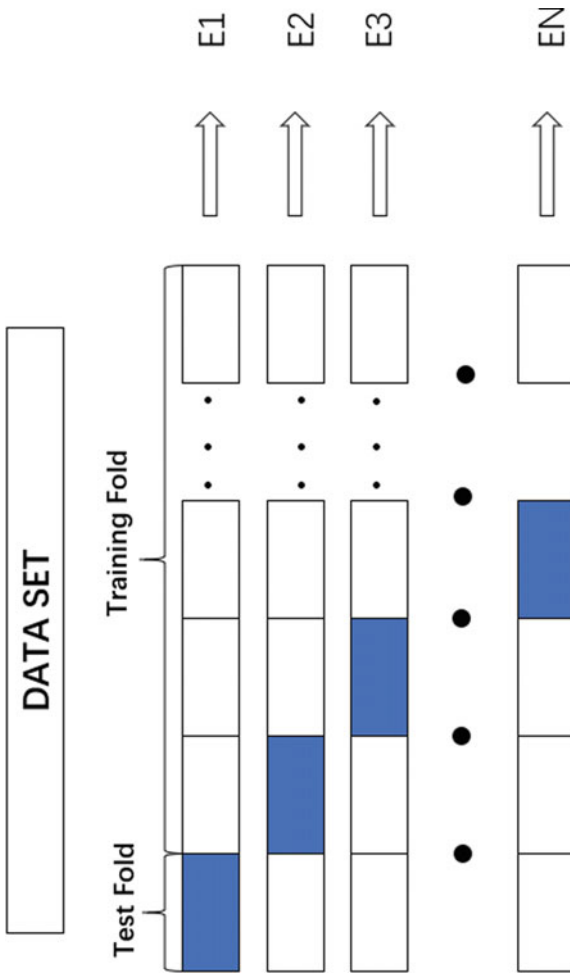


Fig. 1 KFold cross validation structure diagram

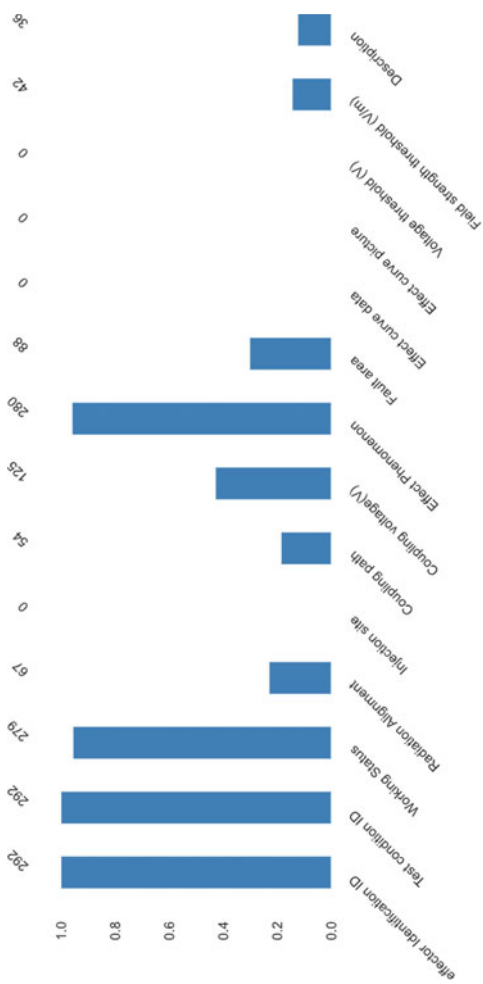


Fig. 2 Characteristic value chart

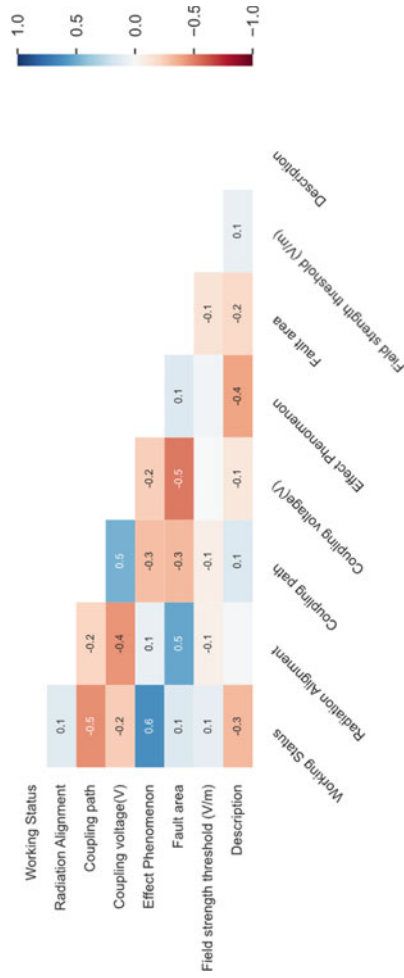


Fig. 3 Feature correlation coefficient matrix heat map

### 3.2 *TFIDF-CNB Model Training*

According to the algorithm's flowchart, there are three more steps after the data preprocessing described above.

**Step 1.** Text vector: The TFIDF algorithm processes the inputted strong EM effect description statements, calculates the TFIDF values of the feature words, and generates a feature-weighted vector space.

**Step 2.** The generated vector space containing feature information is input to our complementary set of ordinary bayesian classifier (CNB), and the model is constructed and trained using this information.

**Step 3.** We employ probabilistic calibration for the complementary set of plain Bayesian classifiers for model construction and training.

For the trained model enter "Effector-1 operating state is charged, the radiation is aligned with the secondary flap, the azimuthal angle is 90, the coupling path is the back door and the coupling voltage is less than 0.1 V, the field strength threshold 3100.0 V/m, the cable is wrapped with copper foil coupling path is the back door and the coupling voltage is less than 0.1 V, the field strength threshold 3100.0 V/m, the cable is wrapped with copper foil paper" will give the corresponding predicted result "Communication abnormalities".

The dataset used for testing is preprocessed, feature extracted, vectorized in the same way, and then output using a trained complement naive ayesian classifier.

### 3.3 *Result*

We trained and evaluated the multinomial naive bayes (MNB), bernoulli naive bayes (BNB), and complement naive bayes (CNB) models, as well as the models after probabilistic calibration of each of these three models. The model performance is then validated using StratifiedKfold; the obtained results are displayed in Table 1 and Fig. 4.

From the preceding table and comparison graphs, it is evident that the CNB model itself is superior to the other models. Following probabilistic calibration, each model's results are enhanced. The CNB model with the Isotonic probability calibration has the best result. Consequently, the CNB-based algorithm proposed in this paper for the prediction of strong electromagnetic effect phenomena obtains better results in comparison to other conventional data mining algorithms.

**Table 1** Model accuracy

Models	Probabilistic calibration	Scores
Multinomial naive bayes		0.796
Multinomial naive bayes	Sigmoid	0.865
Multinomial naive bayes	Isotonic	0.899
Bernoulli naive bayes		0.795
Bernoulli naive bayes	Sigmoid	0.779
Bernoulli naive bayes	Isotonic	0.824
Complement naive bayes		0.872
Complement naive bayes	Sigmoid	0.913
Complement naive bayes (ours)	Isotonic	0.941

## 4 Conclusion

This paper demonstrates the excellent performance of the proposed algorithm by comparing the CNB-based prediction model of effect phenomena using strong electromagnetic effect data set with the traditional plain Bayesian algorithm. The algorithm can avoid the problem of small sample size and unbalanced samples, and provides a solution to the low performance of the model due to the difficulty of data collection of strong electromagnetic effect phenomena, and also plays a good role in the recommendation of ship protection against strong electromagnetic effect.



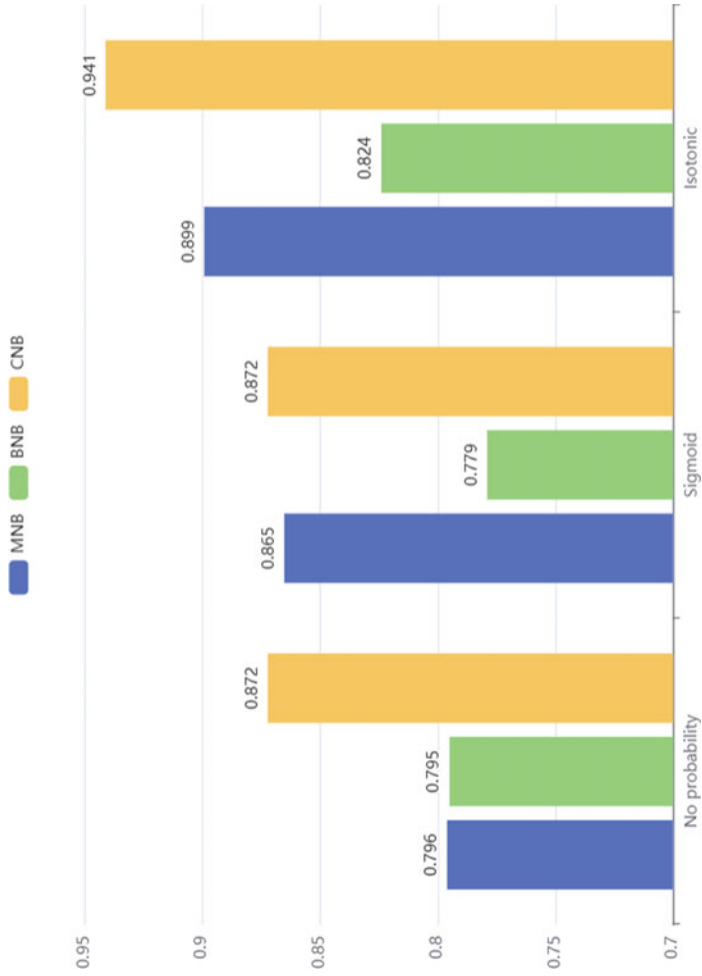


Fig. 4 Score comparison chart

## References

1. Jin WX, Jin HJ, Cheng GX et al (2021) Exploration of user participation in carbon transaction benefits in electricity-carbon linkage. In: 2021 6th international conference on power and renewable energy. IEEE, pp 1428–1432
2. Li IRR, Liu S, Gu Y (2018) A report on the effect of electromagnetic radiation on the growth of silkworm in mobile phone. *Imaging Radiat Res* 1(1)
3. Ko Y (2017) How to use negative class information for Naive Bayes classification. *Inf Process Manage* 53(6):1255–1268
4. Liu P, Yu H, Xu T et al (2017) Research on archives text classification based on Naive Bayes. In: 2017 IEEE 2nd information technology, networking, electronic and automation control conference. IEEE, pp 187–190
5. Chen K, Huang Y, GAO W et al (2018) An improved Naive Bayesian text classification algorithm based on weighted features and its complementary set. *J Harbin Univ Sci Technol* 23(4):69–74 (in Chinese)
6. Yoo JY, Yang D (2015) Classification scheme of unstructured text document using TF-IDF and naive bayes classifier. *Adv Sci Technol Lett* 111(50):263–266
7. Tang Z, Li W, Li Y (2020) An improved term weighting scheme for text classification. *Concurrency Comput Pract Experience* 32(9):e5604
8. Platt J (1999) Probabilistic outputs for support vector machines and comparisons to regularized likelihood methods. *Adva Large Margin Classifiers* 10(3):61–74
9. Allikivi ML, Kull M (2020) Non-parametric Bayesian isotonic calibration: fighting over-confidence in binary classification. In: Machine learning and knowledge discovery in databases: European conference, proceedings, Part II. Springer, Würzburg, Germany, pp 103–120
10. Prusty S, Patnaik S, Dash SK (2022) SKCV: stratified K-fold cross-validation on ML classifiers for predicting cervical cancer. *Front Nanotechnol* 4:972421
11. Khaire UM, Dhanalakshmi R (2022) Stability of feature selection algorithm: a review. *J King Saud Univ Comput Inf Sci* 34(4):1060–1073

# Evaluation and Optimization Schemes of Eddy Current Loss on Structural Components for High Voltage Converter Transformer



Min Shen, Penghong Guo, Yanling Wang, Youliang Sun, and Xiangdong Yu

**Abstract** Compared with the traditional alternating current (AC) transmission system, High-voltage direct current (HVDC) transmission technology plays an essential role in the long distance, large capacity, and regional power grid interconnection, for its characteristics of higher economy, reliability, and stability. As the key power equipment in the HVDC transmission system, the converter transformer cooperates with the converter valve to achieve AC and DC conversion. Due to the large capacity, high impedance, harmonics, DC bias, and other working conditions for the converter transformer, the eddy current loss of the structural components induced by leakage magnetic flux, will be increased significantly and result in the efficiency reduction and local overheating problem, endangering the operational reliability of itself and the power system. In a flexible HVDC transmission system, regarding the converter transformer as the research object, the optimal composite shielding scheme is proposed and determined by the optimization design and finite element analysis (FEA) calculation, which are based on the values and distribution of leakage flux and loss density. Furthermore, the experimental results verify the proposed overall leakage magnetic flux control scheme.

**Keywords** HVDC transmission system · Eddy current loss · Optimization design · Composite shielding scheme · Converter transformer

---

M. Shen (✉) · Y. Wang  
School of Intelligent Manufacturing and Control Engineering, Qilu Institute of Technology,  
Jinan 250200, China  
e-mail: [1287636416@qq.com](mailto:1287636416@qq.com)

Y. Wang  
e-mail: [gphong128@163.com](mailto:gphong128@163.com)

P. Guo · Y. Sun  
Shandong Power Equipment Co., Ltd., Jinan 250022, China  
e-mail: [66313352@qq.com](mailto:66313352@qq.com)

X. Yu  
School of Electrical Engineering and Automation, Hefei University of Technology, Hefei 230009,  
China  
e-mail: [yuxiangdong@mail.hfut.edu.cn](mailto:yuxiangdong@mail.hfut.edu.cn)

# 1 Introduction

During past decades, flexible HVDC technology has been proposed by Boon-TeckOoi in Canada in 1990 and developed by ABB, Siemens, and other enterprises and research institutions in promotion and application [1–3]. It is a new generation of high voltage direct current transmission technology based on voltage source converter, self-shutting device (IGBT), and pulse width modulation (PWM) technology, short for voltage source converter based high voltage direct current transmission (VSC-HVDC). An example is shown in Fig. 1. Compared with traditional HVDC, it has advantages in AC system interconnection, large-scale new energy grid connection, isolated island power supply, urban distribution network capacity improvement, and other aspects [4], and gained significant attention in recent years for its ability to enhance power transmission efficiency and reliability, and will be the leading technology in the field of transmission and distribution in the future.

The HVDC back-to-back station, in which both the rectifier and the inverter are located in the same station and are normally used to create an asynchronous interconnection between two AC networks with the same or different frequencies and other benefits for reducing short circuit current. The structural diagram of modular multilevel converter (MMC) back-to-back flexible DC converter system (BTB VSC-HVDC), is the popular and advanced technology for utilizing submodule cascade instead of IGBT of two and three-level VSC directly in series [5], reducing manufacture difficulty greatly, promoting the development of flexible DC transmission projects [6].

The converter transformer is critical power equipment of the power system. Many researchers have conducted theoretical analysis, FEA simulation, and experimental studies on insulation, losses, temperature-rise, vibration, and unconventional conditions such as harmonic and DC magnetic bias to evaluate the feasibility and validation of different schemes and designs [7–9]. Reducing losses in structural components of converter transformers and avoiding local overheating is one of the key technology of transformer design. Therefore, it is of great practical significance to study and optimize the leakage flux control schemes of the converter transformer. A closed path or loop of the shielding plates is recommended in [10]. And the lobe-type magnetic shielding is adopted to analyze leakage flux and stray losses of autotransformer structural parts [11]. But research results on leakage magnetic control and eddy current loss calculation on structural components of flexible converter transformer lack of comprehensive and in-depth optimization design scheme.

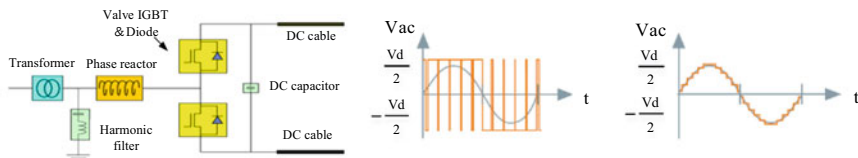


Fig. 1 The VSC-HVDC transmission system

In this paper, in order to control leakage flux and eddy current loss on structural components, the comparison of multiple different shielding schemes including electromagnetic shielding, magnetic shielding, and their combination is calculated and analyzed. Therefore, a new composite shielding scheme of the converter transformer of DFPZ-RZ-575MVA/500-300kV is proposed and verified by experimental test. Moreover, the comprehensive shielding scheme is determined. It can provide instructions for the optimization design of the converter transformer.

## 2 Method Description

### 2.1 Leakage Magnetic Field Analysis and Eddy Current Loss Calculation

The  $A$ - $V$ - $A$  method [12] has the advantage of calculating three-dimensional (3D) nonlinear time-harmonic field in the eddy current region (tie-plate, clamp, oil tank). The governing equation is in (1) and derived to (2), according to the Maxwell equations, where  $A$  is magnetic vector potential and  $V$  is electrical scalar potential.  $\sigma$  (S/m) and  $\mu$  (H/m) represents the conductivity and permeability of the conductor, respectively.

$$\nabla \times \frac{1}{\mu} \nabla \times \mathbf{A} - \left[ \nabla \frac{1}{\mu} \nabla \cdot \mathbf{A} \right] + \sigma \left( \frac{\partial \mathbf{A}}{\partial t} + \nabla \frac{\partial V}{\partial t} \right) = 0 \quad (1)$$

$$\nabla \cdot \sigma \left( -\frac{\partial \mathbf{A}}{\partial t} - \nabla \frac{\partial V}{\partial t} \right) = 0 \quad (2)$$

The equation in non-eddy current area (winding, oil) is listed in (3).

$$\nabla \times \frac{1}{\mu_0} \nabla \times \mathbf{A} - \left[ \nabla \frac{1}{\mu_0} \nabla \cdot \mathbf{A} \right] = 0 \quad (3)$$

where  $\mu_0$  is the Vacuum permeability (H/m),  $A$  and  $V$  on the node are calculated by 3D FEM, and then the magnetic flux density  $\mathbf{B}$  and the electric field  $\mathbf{E}$  on the unit is expressed by Eqs. (4) and (5), and finally the eddy current density  $\mathbf{J}$  and magnetic field strength  $\mathbf{H}$  of the steel plate can be obtained through the constitutive relationship between Maxwell's fundamental equation and its field quantity.

$$\mathbf{B} = \nabla \times \mathbf{A} \quad (4)$$

In nonconductive parts:

$$\mathbf{E} = -\frac{\partial \mathbf{A}}{\partial t} - \nabla V \quad (5)$$

The skin depth of  $\delta$  (mm) is obtained by (6) and the angular frequency is  $\omega$  (rad/s).

$$\delta = \sqrt{\frac{2}{\mu\omega\sigma}} \quad (6)$$

The eddy current loss calculation of the converter transformer is applied to utilize the surface impedance (SI) method, as follows in (7).

$$Z = \frac{\mathbf{E}}{\mathbf{H}} = (1 + j) \frac{1}{\sigma\delta} \quad (7)$$

Based on the above derivation results, when the SI equivalent treatment is applied to the conductive steel, the formula for calculating the eddy current loss  $P_e$  is as follows:

$$P_e = \sqrt{\frac{\omega\mu}{8\sigma}} \iint \mathbf{H}_t \mathbf{H}_t^* ds \quad (8)$$

where  $\mathbf{H}_t$  is the tangential component of the magnetic field intensity on loss surface.  $\mathbf{H}_t^*$  is the conjugate of  $\mathbf{H}_t$ . In the region without using the surface impedance method, the eddy current loss of the structural parts is calculated in (9).

$$P_e = \int_v \frac{\mathbf{J} \cdot \mathbf{J}}{\sigma} dV \quad (9)$$

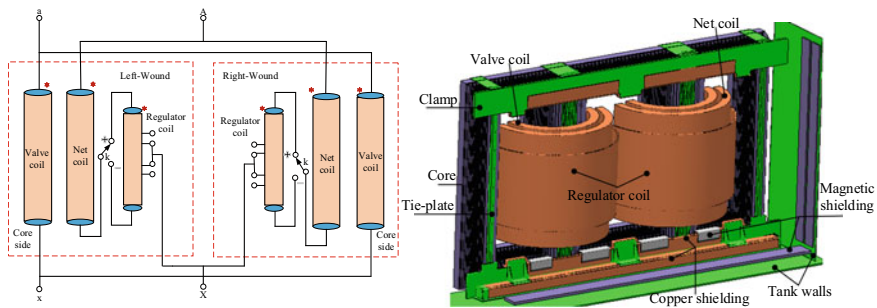
## 2.2 Main Parameters and Simulation Model

The technical parameters of converter transformer are listed in Table 1.

In the converter transformer with two column parallel structure, the windings are arranged from inside to outside as valve coil, net coil, and regulating coil. Based on the actual dimensions, the FEM simulation model with the corresponding structural simplification is established, shown in Fig. 2.

**Table 1** Technical parameters of converter transformer

Main parameters	Describe and value
Type	DFPZ-RZ-575MVA/500-300kV
Structure form of core	Signal-phase four limbs
Rated capacity (MVA)	575
Rated voltage ratio (kV)	$(525/\sqrt{3} \pm 4 \times 1.25\%)/(300/\sqrt{3})$
Cooling mode	Oil orientation air forced (ODAF)
Impedance voltage percentage Uk%	18%
Connection symbol	Ii0
Voltage regulation mode	On-line tap changer (OLTC)



**Fig. 2** The structural arrangement of coil and 3D simulation model

### 3 Estimation and Determination of Shielding Schemes

#### 3.1 Determination of Shielding Scheme on Lower Clamps

The original scheme with the thickness of electromagnetic shielding (copper shielding) only on clamps is 6 mm. Utilizing the FEA, the maximum magnetic density ( $B_m$ ) of lower clamp is about 1.55 T, located at the corner of the lower clamp in Fig. 3a. As shown in Fig. 3b, the maximum loss density is  $2.47 \times 10^7 \text{ W/m}^3$ , exceeding the standard with a risk of local overheating.

The different optimization shielding schemes on clamps are shown in Fig. 4.

Compared with the original scheme, among them, the  $B_m$  on the lower clamp of scheme 4 decreased by 14.19% to 1.33T, and eddy current loss density  $P_v$  is about 34% reduction, respectively, as shown in Fig. 4d.

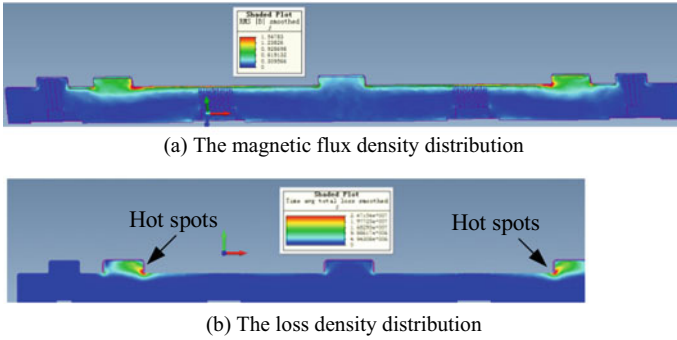


Fig. 3 The impact of copper shielding scheme on lower clamps

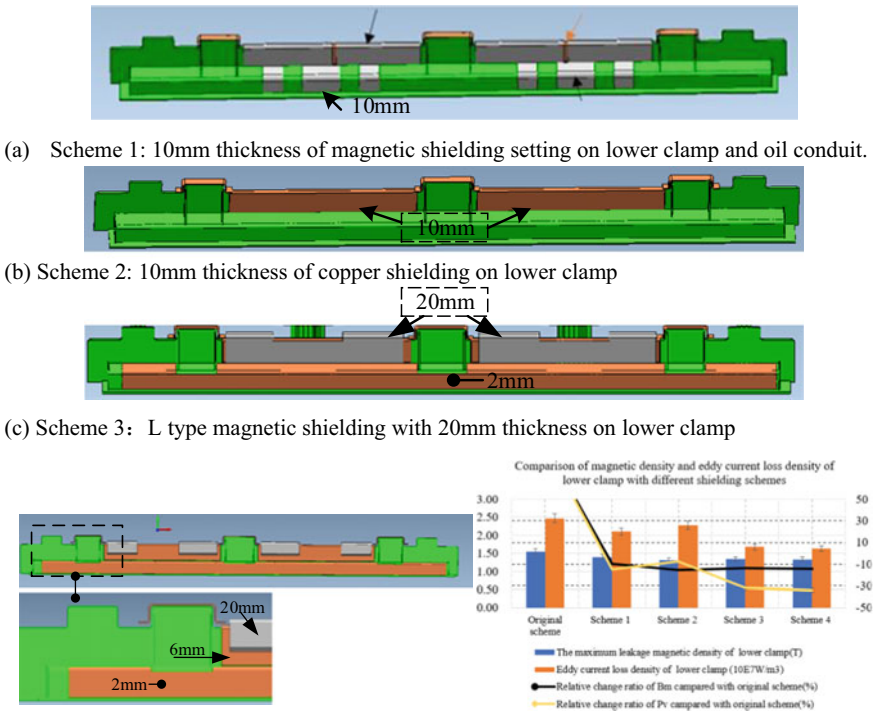
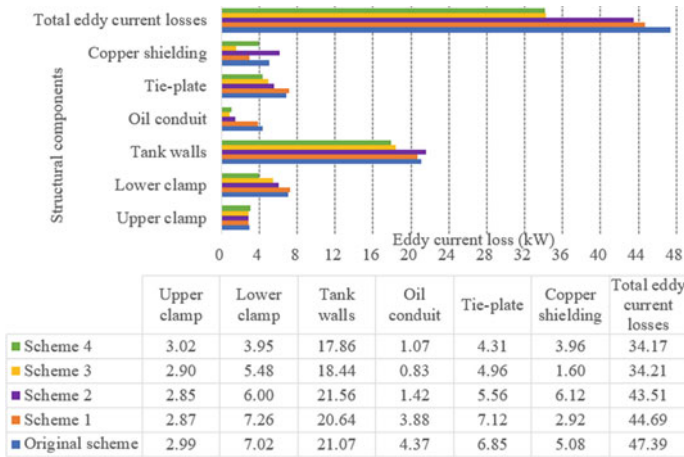


Fig. 4 The composite shielding schemes arrangement on lower clamp and comparison results

### 3.2 Scheme Comparison for Eddy Current Loss of Structural Components

Neglecting the eddy current loss of magnetic shielding, it is obtained from Fig. 5 that scheme 4 is the optimal leakage magnetic control scheme with a minimum total eddy





**Fig. 5** The comparison of different shielding schemes impact on eddy current loss

current loss of 34.17 kW. Considering the cost-effectiveness ratio of eddy current loss reduction and the convenience of technological operability in the shielding scheme, scheme 2 and 4 is recommended.

### 3.3 Shielding Evaluation on Oil Tank

Based on scheme 4, then the comparative evaluation of the shielding scheme of the tank bottom whether the magnetic shielding is moved up 100 mm is analyzed and the results are shown in Fig. 6. Scheme 5 represents a 100 mm lift of the magnetic shield, which is superior to scheme 6 in terms of overall eddy current loss and magnetic density reduction of structural components.

### 3.4 Overall Leakage Flux Control Scheme and Results

Based on the above calculation and analysis, shielding scheme 4 and shielding scheme 5 are selected and determined as the overall optimization leakage magnetic control scheme. The calculation results are shown in Fig. 7. The Bm of the tie-plate, oil tank, and magnetic shielding, all structural components are within a reasonable range and there is no local overheating problem.

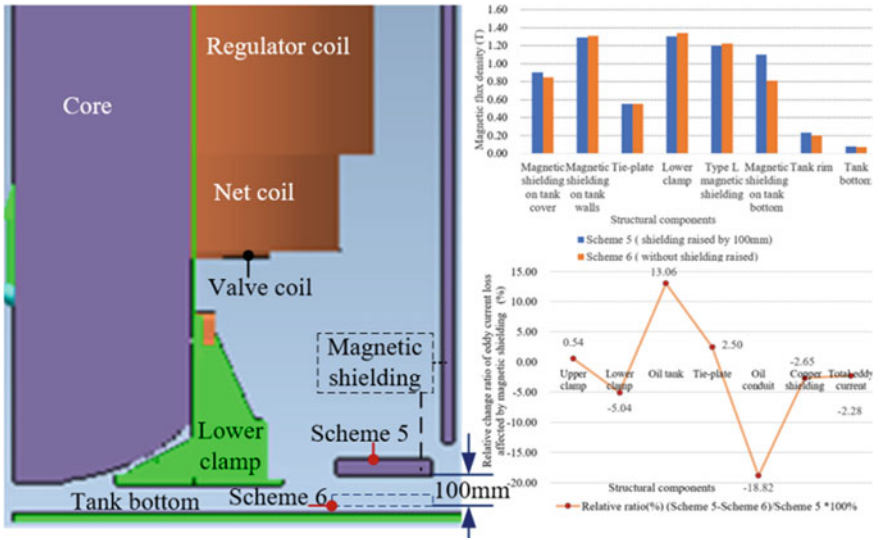


Fig. 6 The comparison of shielding schemes and analysis

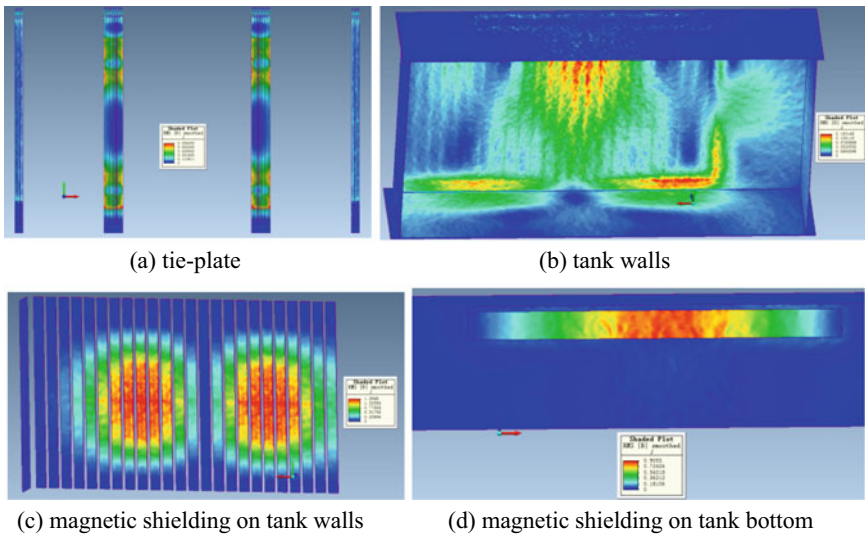


Fig. 7 The  $B_m$  distribution of overall leakage flux control scheme



**Fig. 8** Experimental connection scheme and test process

## 4 Experimental Results and Validation

### 4.1 Experimental Test Process

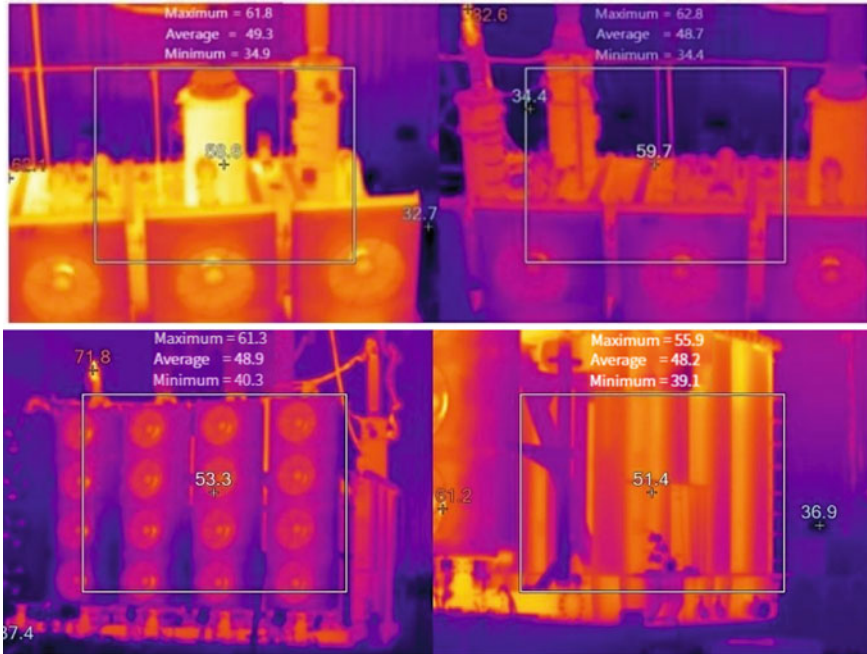
The connection and test process of converter transformer is shown in the Fig. 8.

### 4.2 Experimental Results and Analysis

The load test results show that the additional loss of the converter transformer is reduced by 25.2% compared with the design value. The ambient temperature is 37.1 (°C) and temperature-rise test results are listed in Table 2. The hot spots and temperature distribution on tank walls have been shown in Fig. 9. The maximum

**Table 2** Temperature-rise test results of converter transformer

Structural components	Calculated or design values (K)	Guaranteed or protocol values (K)
Top oil temperature rise	18.83	40
Average temperature rise of oil	16.84	–
Average temperature rise of net windings	34.37	52
Average temperature rise of valve windings	35	52
Hot spot of net windings	40.58	63
Hot spot of valve windings	42.44	63
Metal Structural parts	25	75



**Fig. 9** Temperature rise distribution on tank walls obtained by thermal imaging camera

temperature rise is about 25.7 (K), less than the guaranteed value of 75 (K). Above all, the optimal shielding scheme is further verified by no local overheating and loss reduction.

## 5 Conclusion

In the BTB VSC-HVDC transmission system, a new composite shielding scheme is proposed to solve the key technical problems of leakage magnetic control for converter transformers with large capacities. It has an excellent performance in reducing eddy current loss and eliminating hot spots, which is determined by comparative calculation and analysis of several shielding schemes. Besides, the position of magnetic shielding at the tank bottom has an impact on the leakage flux density value, distribution, and eddy current loss of the structural parts. The overall magnetic leakage control scheme should be considered and calculated to obtain an advanced and efficient shielding scheme and the optimal design with feasibility and validation. Finally, the proposed optimal shielding scheme has passed all experimental tests and validation. At present, it is a flexible converter transformer with the largest capacity, lowest loss, and highest energy efficiency level at home and abroad.

**Acknowledgements** This work was supported by Shandong Power Equipment Co., Ltd, and sponsored by the project of Research on IGBT Failure Prediction of High-power, High-Voltage Inverter Based on Data-Driven (ZR2020KA007).

## References

1. TeckOoi B, Wang X (1990) Voltage angle lock loop control of the boost type PWM converter for HVDC application. *IEEE Trans Power Deliv* 5(2):29–235
2. ABB (2005) It's time to connect—technical description of HVDC light technology. ABB Power Technology AB, Sweden
3. Ghat MB, Patro SK, Shukla A (2021) The hybrid-legs bridge converter: a flexible and compact VSC-HVDC topology. *IEEE Trans Power Electron* 36(3):2808–2822
4. Zhang Z, Zhao X (2023) Coordinated power oscillation damping from a VSC-HVDC grid integrated with offshore wind farms: using capacitors energy. *IEEE Trans Sustain Energy* 14(2):51–762
5. Chen Y, Yin X, Wang X et al (2019) A new kind of hybrid UHVDC system dedicated for long-distance power delivery and regional power grids back-to-back hierarchical interconnection. In: 10th international conference on power electronics and ECCE Asia (ICPE 2019–ECCE Asia), pp 1–7. Busan
6. Wu S, Qi L, He Z et al (2022) A voltage-boosting submodules based modular multilevel converter with temporary energy storage ability for fault ride through of offshore wind VSC-HVDC system. *IEEE Trans Sustain Energy* 13(4):2172–2183
7. Forrest JAC (1991) Harmonic load losses in HVDC converter transformers. *IEEE Trans Power Deliv* 6(1):153–157
8. Wang H, Zhang L, Sun Y et al (2022) Influence of direct current bias on vibration characteristics of converter transformer. In: 4th international conference on smart power & internet energy systems (SPIES), Beijing, pp 372–377
9. Liu Y et al (2016) Study of the stray losses calculation in structural parts for HVDC converter transformers based on the TEAM Problem 21 Family. *IEEE Trans Power Deliv* 31(2):605–612
10. Wang T, Yuan W, Fu D et al (2019) Improvement of magnetic shielding for transformers based on the magnetic flux characteristics at shielding ends. *IEEE Trans Magn* 56(1):1–4
11. Li L, Fu WN, Ho SL et al (2014) Numerical analysis and optimization of lobe-type magnetic shielding in a 334 MVA single-phase auto-transformer. *IEEE Trans Magn* 50(11):1–4
12. Cheng Z, Takahashi N (2009) Electromagnetic and thermal field modeling and application in electrical engineering, 1st edn. Science Press, Beijing

# Simulation Study on Spread Characteristics of Wildfire Near Transmission Lines



Jun Xu, Chaoying Fang, Shiyun Cao, and Shengwen Shu

**Abstract** Wildfires have become an important factor threatening the safe and stable operation of transmission lines, and large-scale wildfires can significantly reduce the air gap insulation level of transmission lines and cause line tripping. Therefore, based on the principle of cellular automata and Wang Zhengfei's model of wildfire spread, this paper analyzes in detail the effects of factors such as slope, wind speed, wind direction, and fuel type on the speed of wildfire spread and the area of the fire site, and predicts the time when the wildfire arrives below the transmission line. The results indicate that the established model can preliminarily reflect the spread law of wildfires, and has a certain guiding role for the safe and stable operation of the power grid.

**Keywords** Wildfire spread · Transmission lines · Cellular automata

## 1 Introduction

Transmission lines in China are widely distributed in the mountains and jungles, often crossing mountainous areas with lush vegetation [1]. In recent years, frequent forest fires have seriously threatened the safe and stable operation of China's power grid. The combustion and spread of wildfires is a very complex process, and there are many factors that affect their spread. In order to more intuitively describe the process of mountain fire combustion, people have adopted some mathematical models to analyze the quantitative relationship between wildfire behavior and various factors. Among them, many scholars at home and abroad have proposed their own contagion models, mainly including the McArthur model in Australia, the Rothermal model

---

J. Xu · C. Fang

Electric Power Research Institute, State Grid Fujian Electric Power Co., Ltd., Fuzhou 350108, China

S. Cao · S. Shu (✉)

College of Electrical Engineering and Automation, Fuzhou University, Fuzhou 350108, China  
e-mail: [shushengwen@fzu.edu.cn](mailto:shushengwen@fzu.edu.cn)

© Beijing Paiké Culture Commu. Co., Ltd. 2024

X. Dong and L. Cai (eds.), *The Proceedings of 2023 4th International Symposium on Insulation and Discharge Computation for Power Equipment (IDCOMPU2023)*, Lecture Notes in Electrical Engineering 1103, [https://doi.org/10.1007/978-981-99-7413-9\\_17](https://doi.org/10.1007/978-981-99-7413-9_17)

in the United States [2], and the Wang Zhengfei model in China. McArthur from Australia conducted wildfire experiments and calculated the relationship between various fire risk indices and factors such as wind speed, humidity, and temperature, which has a guiding role for forest fires in Australia [3]. Yao Yanxia selected the American Rothermal model, optimized the lack of boundary point separation in the fire evolution range through Huygens principle, and completed a more realistic fire evolution visualization [4]. Tang Xiaoyan et al. combined grid data with Wang Zhengfei's model and implemented dynamic simulation of forest fire spread using maze algorithm [5]. Karafyllidis improved the cellular automata model by using parallel computing methods during the simulation process [6, 7]. Liu Hui considered the differences between neighboring cells and secondary cells of cells, and also improved the cellular automaton model [8], and proposed a new method for transmission line trip probability [9]. Based on the models of Wang Zhengfei and Mao Xianmin, Zhang Quanwen combined GIS with cellular automata to achieve three-dimensional visualization of Yunnan 3.29 fire [10].

Based on the above research, this article combines the principle of cellular automata and selects the Wang Zhengfei model that is suitable for China's national conditions. It fully considers the effects of factors such as slope, temperature, wind speed, wind direction, and vegetation on the spread of wildfires, and solves the burning speed of wildfires in eight directions around them. Through Python simulation, the spread law under the influence of step, wind speed, wind direction, vegetation, and slope is simulated, and predicted the time when the wildfire will spread to the transmission line in the actual environment.

## 2 Methods

### 2.1 Wildfire Spread Model

For different countries and regions, the causes of wildfires and the importance of various spreading impact factors are not entirely the same. Therefore, a model suitable for China, Wang Zhengfei, was selected and corrected.

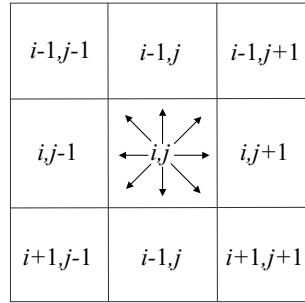
#### (1) Initial spreading speed of wildfire

When a mountain fire occurs on a level and windless ground, the spreading speed of the fire is defined as the initial spreading speed  $R_0$ . The initial spreading speed mainly depends on the temperature and humidity of the environment.

$$R_0 = aT + ch - D \quad (1)$$

In the expression,  $T$  is the real-time temperature of the day,  $h$  is the daily minimum relative humidity (%),  $a$  is 0.03 and  $c$  is 0.05,  $D$  is a constant of 0.3.

**Fig. 1** Eight directional schematic diagram



**Table 1** Combustible coefficient table

Combustible type	Thatch grass	Cedar	Straw	Grassland	Pine needle
Combustible coefficient $K_s$	0.9	0.8	0.6	0.5	0.4

(2) Considering the spread speed of multiple factors

The eight directional propagation speed considering wind speed and direction is shown in Fig. 1. Taking the spreading speed in the northwest direction as an example [11]:

$$R_{i-1,j-1} = R_0 K_s \exp^{0.1783V \cos(315^\circ - \theta)} \exp^{3.533(-1)^G \left| \frac{h_{i-1,j-1} - h_{i,j}}{\sqrt{2}a} \right|^{12}} \tag{2}$$

In the formula,  $K_s$  represents the combustible coefficient, and its values are shown in Table 1.  $\theta$  represents the angle between the wind direction and the due north direction, and  $a$  represents the length of the cell's side.  $G$  represents slope, when the aspect is uphill,  $G = 0$ ; when the aspect is downhill,  $G = 1$ .

## 2.2 Cellular Automata Wildfire Spread Rules

Cells can be represented by grid pixels, and each grid is a cell. The pixel value represents the state of the cell, and the migration of the cell state is manifested as forest fire spread. When writing a program, cells can be located by column and column numbers, and each grid has its own corresponding column and column number.  $S$  represents the state of the cell,  $S = 0$  represents unburned,  $S = 1$  represents initial combustion (which has just completed combustion but has not yet spread to the surrounding area),  $S = 2$  represents complete combustion and the ability to ignite surrounding cells,  $S = 3$  represents gradual extinction,  $S = 4$  represents complete extinction. After inputting fire information,  $S = 2$  cells continuously ignite their neighboring combustible cells over time, forming a behavior of forest fire spreading



continuously. If  $S = 0$  and there is an initial burning cell with a state of  $S = 1$  in the neighborhood, calculate the cell value at the next time using formula (3); If  $S = 1$  at this point, set the state of the cell at the next moment to complete combustion; If  $S = 2$  and neighborhood  $S \geq 2$  or non-combustible, it will gradually extinguish; If  $S = 3$ , the cell will completely extinguish at the next moment.

$$S_{i,j}^{t+1} = S_{i,j}^t + \frac{(R_{i-1,j}^t + R_{i,j-1}^t + R_{i+1,j}^t + R_{i,j+1}^t) \Delta t}{a} + \frac{\left[ (R_{i-1,j}^t)^2 + (R_{i-1,j+1}^t)^2 + (R_{i-1,j-1}^t)^2 + (R_{i+1,j+1}^t)^2 \right] \Delta t^2}{2a^2} \quad (3)$$

In the equation,  $\Delta t$  is the time step, representing the time interval for updating the combustion status of the cell;  $t$  is the current time,  $t + \Delta t$  is the next moment;  $(i, j)$  are the cell row and column numbers, representing the geographical location of the cell.

Therefore, Python is used to traverse the cells that may change the combustion state in the fire field at time  $t$  and calculate the next state at time  $t + \Delta t$ . And then, we have obtained a cellular automaton model for wildfire propagation.

### 3 Simulation of Wildfire Spread

#### 3.1 Selection of Step

The simulation time is selected to be 60 min, and the combustible coefficient  $K_S$  is 1. The simulation site is calm, flat, and the combustible is uniform. The simulation results are shown in Fig. 2:

As shown in the figure, when the step is 0.5 min, the fire area size is consistent and the results are more accurate. However, when the step is greater than or equal to 1 min, the fire area gradually decreases. Therefore, when the data processing is large, the maximum step that can be selected is 1 min, while when the data volume is small, the step is generally selected as 0.5 min. Therefore, the step selected in this article is 0.5 min.

#### 3.2 No Wind, Flat, and Even Combustible Materials

Assuming the combustible coefficient  $K_S$  is 1 and the step is 0.5 min, the spreading speed in all eight directions is 1.3. The center of the fire point is marked in red  $\times$  express. The red part represents the completely burned area, which can spread the

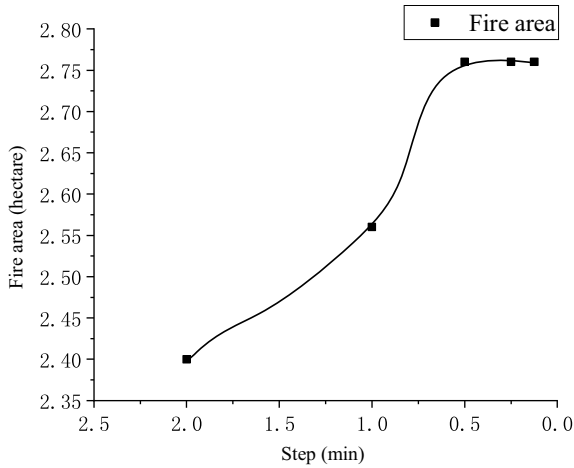


Fig. 2 Relationship between fire area and step

field, the yellow part represents the partially burned area, and the neighboring cells that have already been completely burned are set to black. The spreading results are shown in Figs. 3 and 4.

It can be seen that as the spread time increases, the spread of the fire gradually intensifies, and the growth rate is much faster than the growth of the spread time. At the same time, it can be seen from the fitting curve that there is a square fold relationship between the increase in fire area and the increase in spread time. Therefore, it is very necessary to control the fire as soon as possible, and within one hour is the best.

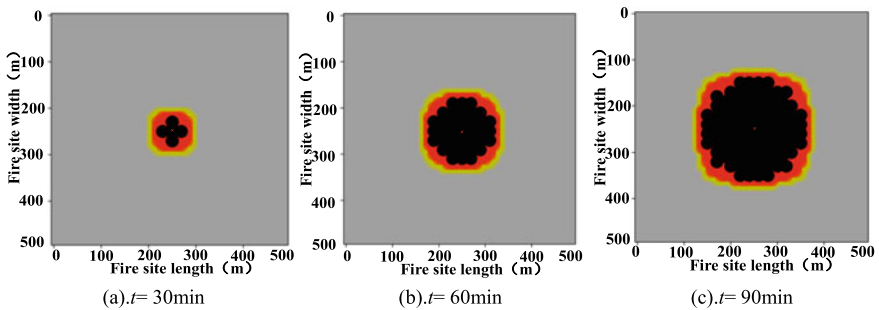
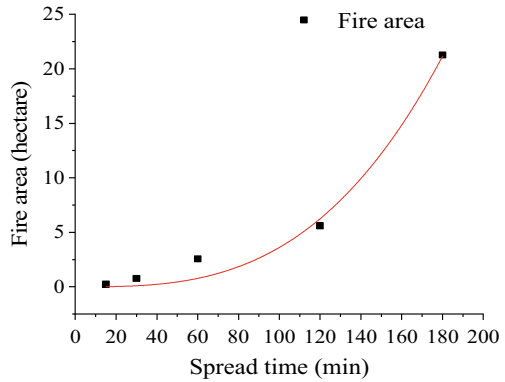


Fig. 3 Spread results at different times

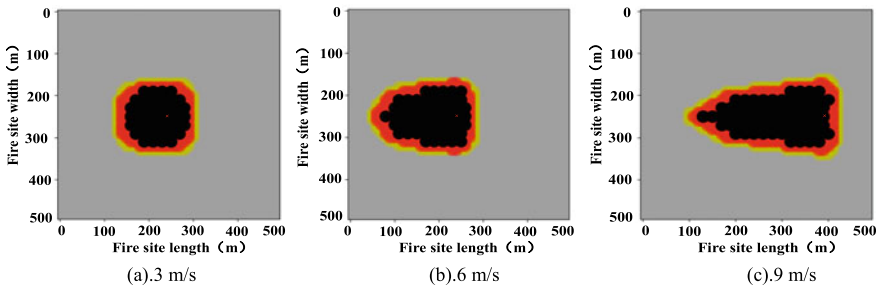
**Fig. 4** Fitting curve of fire area and spread time



### 3.3 Windy, Flat, and Even Combustible Materials

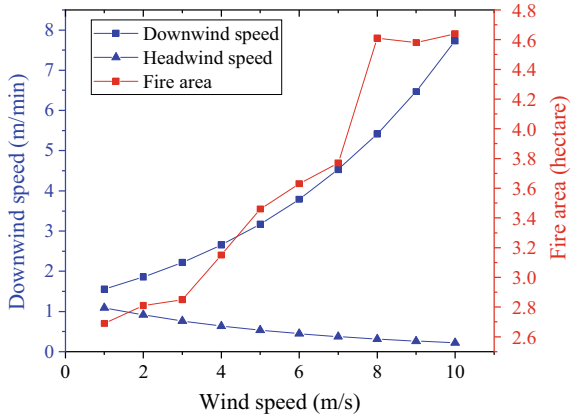
Assuming that the simulation time is all 60 min, the combustible coefficient  $K_S$  is 1, the step is 0.5 min, and the wind direction is due east. For ease of display, I have shifted the ignition point at a wind speed of 9 m/s towards the due east direction. Figures 5 and 6 shows the range of the fire site under different wind speeds, as well as the relationship curves between the fire site area, spreading speed, and wind speed.

From this, it can be concluded that as the wind speed steadily increases, the growth rate of downstream spread speed accelerates, while the reduction rate of upstream spread speed decreases, which has a huge impact on the downstream direction. At the same time, the area of the fire increases with the increase of wind speed, and the shape of the fire gradually changes from circular to flatter. The influence of wind speed on the area of the fire first increases and then slows down. When the wind speed is 3–8 m/s, the change in wind speed has a significant impact on the range of the fire.



**Fig. 5** Spread results of different wind speeds

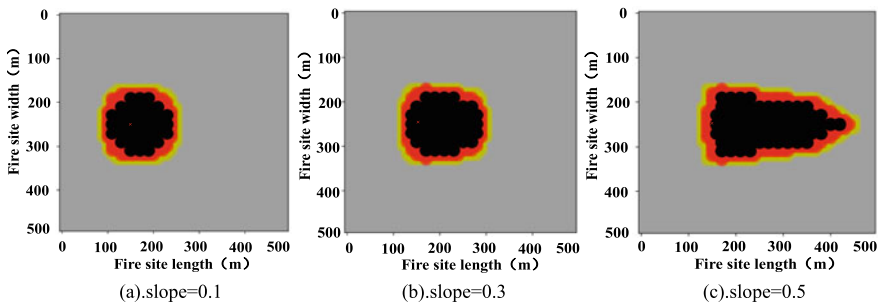
**Fig. 6** Wind speed impact curve



### 3.4 No Wind, Uneven, and Even Combustible Materials

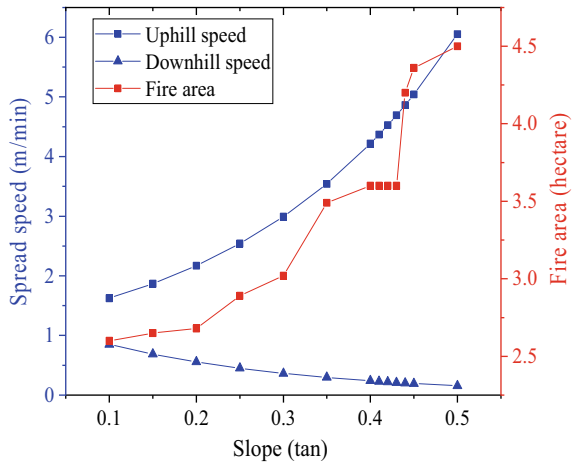
Assuming that the simulation time is all 60 min, the combustible coefficient  $K_S$  is 1, the step is 0.5 min, and slope to the west (high in the west and low in the east). The spread results are shown in Figs. 7 and 8.

As the slope rises, the growth of downstream spread speed accelerates, while the decrease of upstream spread speed slows down, causing a huge impact on the uphill direction. At the same time, the area of the fire site increases with the increase of slope, and the upward trend first becomes faster and then slower. The shape of the fire site gradually changes from circular to flatter. When the slope is within the range of 0.2–0.45, the impact of the slope on the fire area is significant.

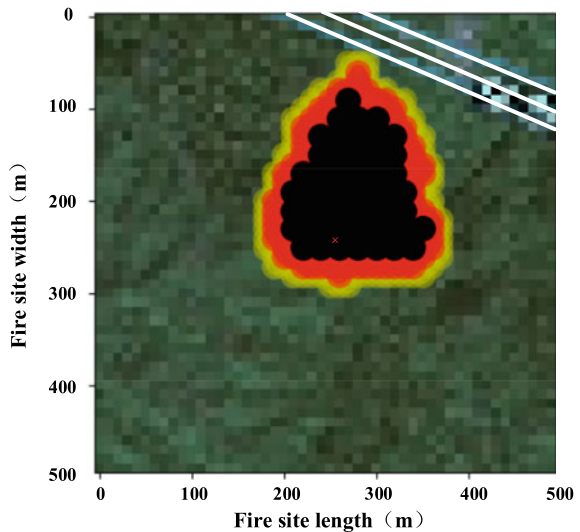


**Fig. 7** Impact of slope on spread results

**Fig. 8** Diagram of the relationship between spreading speed and fire area and slope



**Fig. 9** Results of fire spread below the transmission line



### 4 Example Analysis of a Fire Scene Below a Transmission Line

Select an area with a longitude and latitude range of 119.43735, 26.09186 (bottom left coordinate) to 119.442348, 26.087374 (top right coordinate) in the Gu Mountain, with a size of 500 m \* 500 m, as the experimental area, as shown in Fig. 9. The daily temperature is 30 °C, the daily relative minimum humidity is 30%, the wind speed is 1 m/s, and the wind direction is southerly. Calculate  $R_0 = 0.603$  m/min, and set the step to 0.5 min. The center of the fire is the center of the region, with a transmission

line running through the fire area in the northeast direction. At this time, the distance from the transmission line to the edge of the fire is less than 500 m, reaching a level 1 alarm.

According to the spread results, it can be seen that the fire will spread below the transmission line after 53.5 min, which will affect the safe and stable operation of the transmission line.

## 5 Results

This article selects the Wang Zhengfei model and the cellular automata model to simulate the process of wildfire propagation in detail, and calculates the time it takes for the flame edge to spread below the transmission line in actual wildfires: 53.5 min. The calculation example shows that the appropriate step size should be 0.5 min, and the increase in fire area is basically proportional to the increase in spreading speed. As the wind speed and slope increase, the propagation speed in both the downwind and uphill directions increases sharply. Therefore, early control of the fire is extremely important for the stable operation of transmission lines.

**Acknowledgements** This work was supported by the Science and Technology Projects of State Grid Fujian Electric Power Co., Ltd (No. 521304220007).

## References

1. Yang C, Ning X, Xu H et al (2023) Overview of mountain fire monitoring and early warning for power grid demand, pp 1–13, 23 Apr 2023 (in Chinese)
2. Rothermel RC (1972) A mathematical model for predicting fire spreading wildland fuels. 16 Apr 2020
3. McArthur AG (1967) Fire behavior in eucalypt forests. ACT, Canberra. Forestry and Timber B UREAU, vol 12
4. Yao Y, Miao S, Huang X et al (2022) A forest fire spread simulation method of coupling Rothermel model and particle system, vol 545, no 8, pp 75–80 (in Chinese)
5. Tang X, Meng X, Ge H et al (2003) Research on forest fire spreading simulation based on raster structure and its realization. J Beijing For Univ 01:53–57 (in Chinese)
6. Karafyllidis I, Ioannidis A, Thanailakis A, Tsalides PH (1997) Geometrical shape recognition using a cellular automaton architecture and its VLSI implementation. Real-Time Imagin 3:243–254
7. Karafyllidis I (2004) Design of a dedicated parallel processor for the prediction of forest fire spreading using cellular automata and genetic algorithms. Eng Appl Artif Intell 17:19–36
8. Liu H, Li P, Lin J et al (2019) New algorithm of forest fire spread simulation based on cellular automata and power line fault probability calculation. China Electric Power 52(11):85–93 (in Chinese)
9. Liu H, Yang T, Lin J et al (2022) Calculation of transmission line trip probabilities under forest fire condition. 55(3):125–133 (in Chinese)

10. Zhang Q, Yang Y, Wang T et al (2021) 3D visual simulation of plateau forest fire spread based on cellular automata. *Sci Technol Eng* 21(4):1295–1299 (in Chinese)
11. Zhang F (2011) Research on the model and simulation of the forest fire spread based on geographic cellular automata. Shantou University (in Chinese)

# Modeling and Simulation of the Dynamic Characteristics of Vacuum Arc in DC Interruption Based on Artificial Current Zero When the Current is Close to Zero



Jing Jiang, Lulin Kuang, Guoqing Wang, Zhongxi Liang, Yu Zhang, Le Du, Qianyi Liang, and Jinwei Lu

**Abstract** During the rapid current falling phase of DC breaking, due to the current drops quickly, resulting in a strong eddy current effect, which makes that the variation of the axial magnetic field (AMF) produced by AMF contact obviously lags behind that of current. Therefore, when the current approaches zero, the strength of AMF in the electrode gap is still strong. According to previous research, when the current density of high-current vacuum arc is less than  $500 \text{ A/cm}^2$  or the strength of the AMF is greater than  $10 \text{ mT/kA}$ , the vacuum arc (VA) is a multi-cathode vacuum arc. This article aims to study the dynamic properties of VA in DC breaking process based on artificial current zero when the current approaches zero. The dynamic characteristics of single-cathode spot jet are simulated by 2D transient MHD model. The simulation results indicate that the ion density, axial current density, ion pressure, ion temperature and electron temperature of plasma decrease with the decrease of arc current, and the diffusion degree of arc shape decreases with the decrease of current.

**Keywords** Vacuum arc · DC interruption · Dynamic characteristics · Modeling and simulation · Transient model

## 1 Introduction

The flexible interconnection of large electrified wire netting based on flexible direct current transmission technology is the main construction content of China's power grid planning [1], and a high-voltage DC circuit breaker with the ability to fast isolate short-circuit faults is crucial for ensuring their safe and stable operation. Although a large number of prototypes of mechanical DC circuit breakers have been developed both domestically and internationally, there is still a significant lack of critical basic research in the rapid DC breaking process, especially the dynamic properties of VA

---

J. Jiang (✉) · L. Kuang · G. Wang · Z. Liang · Y. Zhang · L. Du · Q. Liang · J. Lu  
CSG Guangdong Guangzhou Power Supply Bureau, Guangzhou 510000, China  
e-mail: [986821689@qq.com](mailto:986821689@qq.com)

© Beijing Paiké Culture Commu. Co., Ltd. 2024  
X. Dong and L. Cai (eds.), *The Proceedings of 2023 4th International Symposium on Insulation and Discharge Computation for Power Equipment (IDCOMPU2023)*, Lecture Notes in Electrical Engineering 1103, [https://doi.org/10.1007/978-981-99-7413-9\\_18](https://doi.org/10.1007/978-981-99-7413-9_18)



in the DC breaking process, which is also one of the key factors affecting the success of DC breaking.

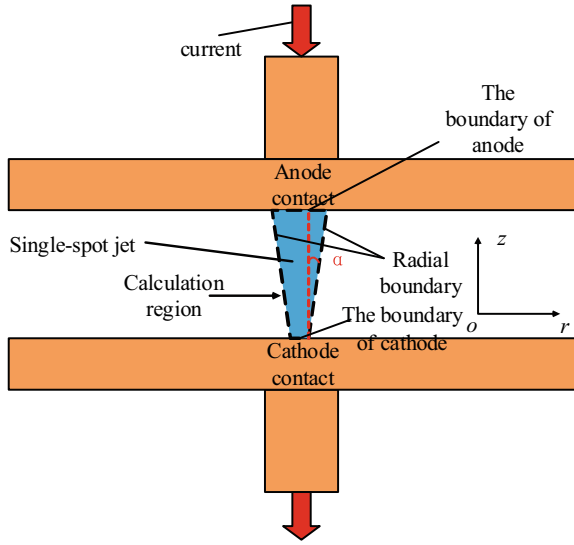
The DC interruption method based on forced zero crossing technique is one of the most common DC breaking technologies nowadays [2], which is very suitable for short-circuit breaking in HVDC power grids due to its characteristics.

Modeling and simulation of the arc characteristics in DC breaking process is very helpful to understand the physical characteristics of arc. Below is a brief introduction to the research process of the simulation of VA characteristics. Boxman et al. first used the theory of fluid mechanics to simulate the properties of VA in the 1970s [3]. In the 1990s, Keidar and Beilis et al. improved the numerical model of VA [4]. They coupled the electromagnetic field equation and fluid mechanics equation to solve it. Later, they considered the impacts of the azimuthal magnetic field generated by the arc and the external AMF in the simulation [5], and also solved the electron energy conservation equation to obtain the distribution of the electron temperature [6]. Schade et al. further improved the numerical model of VA by considering the energy conservation equations of electrons and ions in simulation [7, 8]. Wang et al. took into account the impacts of ion kinetic energy and viscosity in the MHD model of vacuum arc, and simulated the VA characteristics under supersonic and subsonic conditions by establishing a 2D steady-state MHD model [9, 10]. Afterwards, they extended the 2D steady-state MHD model to a 3D steady-state MHD model [11], taking into account the spatial distribution of the AMF generated by the AMF contact [12]. They also simulated and analyzed the characteristics of arc under the action of extraneous transverse magnetic field [13]. Shmelev et al. built a hybrid model, through which the VA properties in the multi-cathode spot jet mixing process were simulated [14].

At present, the research on the simulation of VA dynamic characteristics in DC breaking process is very limited. Greenwood et al. [15] built a one-dimensional model to simulate the properties of DC arc, in which fluid theory was used to simulate the characteristics of plasma. Jaidian et al. [16] established a 2D transient model on the basis of the magnetohydrodynamics theory to simulate the properties of VA during the DC breaking process. Liu et al. [17] used COMSOL software to establish a 2D fluid-chemical mixed model of DCVA on the basis of MHD theory. Hashemi et al. [18] built a 2D transient MHD model, through which the characteristics of DCVA in a rapid transverse magnetic field were simulated. Wang et al. [19] built a 3D transient MHD model to simulate the dynamic properties of VA during the rapid current falling phase in DC interruption, and also conducted simulation calculation for the initial diffusion stage of DCVA [20].

This article aims to study the dynamic properties of VA in direct current interruption on the basis of artificial current zero when the current is close to zero. A 2D transient MHD model is built, based on which the dynamic characteristics of single cathode spot jet are simulated. The dynamic characteristics of ion pressure, ion number density, axial current density, ion temperature and electron temperature of single cathode spot jet when the current is close to zero were obtained.

**Fig. 1** Physical model of single-cathode spot jet



## 2 Physical Model and Assumptions

### 2.1 Physical Model

The simulation uses a 2D transient MHD model [21]. Figure 1 is the physical model diagram of this simulation. The simulation model contains a cathode spot jet with a diameter of 2 mm. The electrode distance is 4 mm. The calculation area of the model is a trapezoid, and the length of the bottom surface is consistent with the diameter of the cathode spot jet. The two sides are free boundaries. The cathode is at the bottom, and the anode is at the top. The initial incidence angle of the cathode jet is  $\alpha$ , which is the angle between the side boundary and the perpendicular line of the cathode surface.

### 2.2 Modeling Assumptions

In the model of this article, the following assumptions were made:

- (1) Assuming that the single-cathode spot jet is not affected by others;
- (2) Assuming the AMF in the calculated area during the simulation process is a constant value;
- (3) Assuming that the model is an axisymmetric model;
- (4) The plasma in the calculated region is highly ionized, containing only ions and electrons;

- (5) Assuming that the plasma in the calculated area meets the quasi-neutral condition;
- (6) Assuming that the vacuum arc satisfies fluid theory to describe;
- (7) Ions and electrons are regarded as ideal gas;
- (8) Assuming that both ions and electrons follow the Maxwell distribution;
- (9) The anode is not yet active and passively receives ions and electrons that arrive at the anode.

### 2.3 Boundary Conditions

The single-cathode spot jet can be regarded as a vacuum arc in which ions are in a supersonic state. For the boundary of the cathode, base on previous experimental data, the velocity of ion that near the cathode  $u = 10^4$  m/s, the electron temperature  $T_e = 1.5$  eV, the ion temperature  $T_i = 0.3$  eV, and the average charge of ion  $z_i = 1.85$ . Assuming a uniform distribution of axial current density on the cathode side.

The boundary condition on the anode side of the equation of electron energy conservation is:

$$2.5n_e k v_z T_e + q_{ez} = n_e v_z e \cdot \left( \frac{2kT_e}{e} - \varphi_{sh} \right) \quad (1)$$

$n_e$  is the electron number density;  $k$  is the Boltzmann constant;  $v_z$  is the electron axial velocity;  $T_e$  is the electron temperature;  $\varphi_{sh}$  is the potential of the anode sheath.

Assuming that the electron energy conservation equation is adiabatic on the side boundary, that is:

$$\partial T_e / \partial n = 0 \quad (2)$$

The boundary condition of the magnetic transport equation on the cathode side is:

$$B_\theta = \frac{\mu_0 I(t)}{\pi R^2} \cdot \frac{x}{2} \quad (3)$$

$B_\theta$  is the azimuthal magnetic field;  $R$  is the radius of the column of arc,  $x$  is the  $x$ -axis coordinate value of the grid of the cathode side.

The boundary condition of the magnetic transport equation at the side boundary is:

$$B_\theta = \frac{\mu_0 I(t)}{2\pi r} \quad (4)$$

$r$  is the distance between the grid of the side boundary and the axis of the arc column.

$$\frac{\partial B_{\theta}}{\partial z} = -\mu_0\sigma(-v_z B_{\theta} - \frac{1}{n_e e} j_{\theta} B_z + \frac{1}{n_e e} \frac{\partial P_e}{\partial r} + g_t \frac{k}{e} \cdot \frac{\partial T_e}{\partial r} + \frac{\partial \varphi_{sh}}{\partial r}) \quad (5)$$

$j_{\theta}$  is the azimuthal current density;  $B_z$  is the strength of the axial magnetic field;  $p_e$  is the electron pressure;  $g_t$  is the thermodynamic constant.

### 3 Simulation Results and Discussion

The Simulation condition is that the current of single-cathode spot jet drops from 200 to 50 A within 15  $\mu$ s. The initial calculation time is 20  $\mu$ s before the current crosses zero. During the rapid current falling phase, the variation of the AMF lags significantly behind that of current. Meanwhile the simulation calculation time is very short, and the simulation area is very small, so the AMF in the calculated area during the simulation process sets as a constant value of 100 mT. Due to the large current drop rate during the rapid current falling phase, the arc current can be approximately considered as a linear decrease. The simulation model is a transient model, and time step of this simulation is 0.5  $\mu$ s. In this paper, the simulation results of the characteristics of single-cathode spot jet at four different time (the corresponding arc current value at four different time is 200, 150, 100 and 50 A respectively) are taken for analysis. The simulation results are as follows.

#### 3.1 Ion Number Density

Figures 2 and 3 indicate that as the current decreases, the ion number density decreases significantly. Before the current close to zero, due to the small current carried by a single jet, the plasma in arc column is distributed in a diffuse manner. At the corresponding time of each arc current value, the ion number density decreases gradually from cathode to anode, and also decreases from the center of the arc column along the radial direction to the edge. Comparing the distribution of ion number density at the corresponding moments of different arc current values, it is found that as the current decreases, the overall ion number density decreases, and the diffusion degree of the jet gradually weakens. The reason is that the decrease of ion number density will lead to the decrease of radial pressure gradient, and then the radial diffusion velocity of plasma decreases, so the overall diffusion of the single-cathode spot jet weakens.

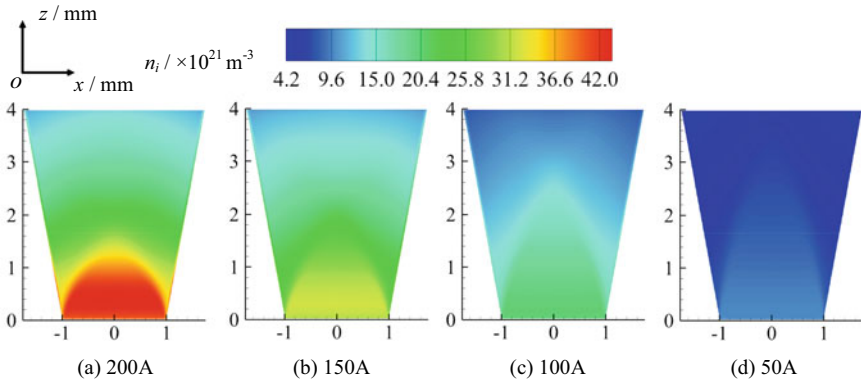
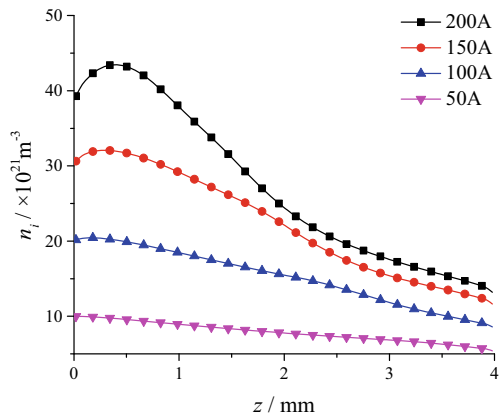


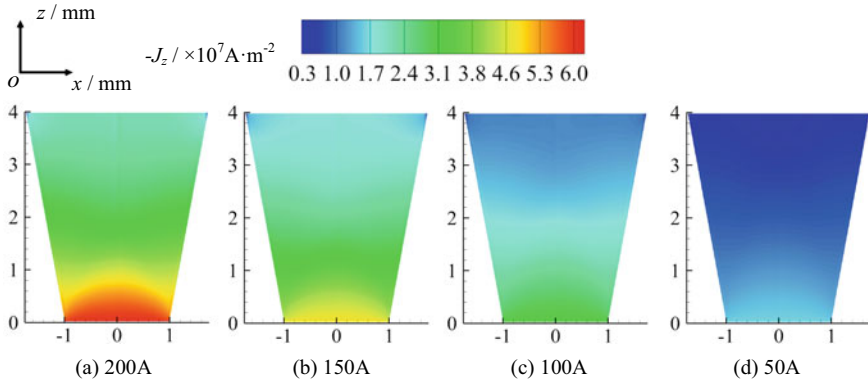
Fig. 2 Distribution of the ion number density (cathode at the bottom, anode at the top)

Fig. 3 Distribution of the ion number density on the arc column centre axis (cathode is at  $z = 0$  mm, anode is at  $z = 4$  mm)



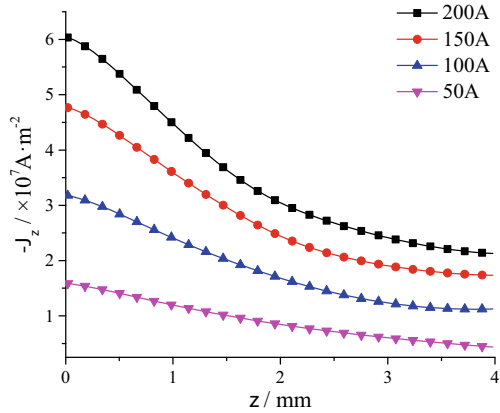
### 3.2 Axial Current Density

Figures 4 and 5 show that as the current decreases, the axial current density of the jet also decreases. At the corresponding time of each arc current value, the axial current density and its gradient gradually decrease from the cathode to the anode. This is because in a low current diffusion state arc, the pinch force generated by the self-generated magnetic field on the ions is smaller than the ion pressure. So the distribution of the axial current density is consistent with the ion number density.



**Fig. 4** Distribution of the axial current density

**Fig. 5** Distribution of the axial current density on the arc column centre axis

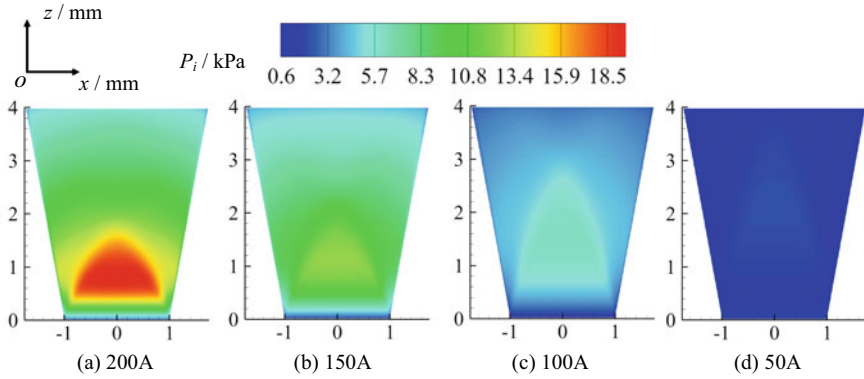


### 3.3 Ion Pressure

Figures 6 and 7 demonstrate that as the current decreases, the ion pressure decreases. As shown in Fig. 7, the ion pressure at the central axis increases first and then decreases. The peak value of ion pressure is not on the cathode, but above the cathode. As the current decreases, the peak position of the ion pressure is farther away from the cathode, which is quite different from the distribution of the ion number density.

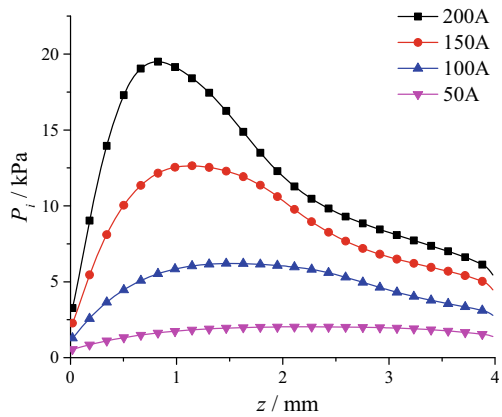
### 3.4 Ion Temperature

Figures 8 and 9 show that as the current decreases, the ion temperature decreases. The main reasons are as follows: Firstly, with the decrease of the current, the generated



**Fig. 6** Distribution of the ion pressure

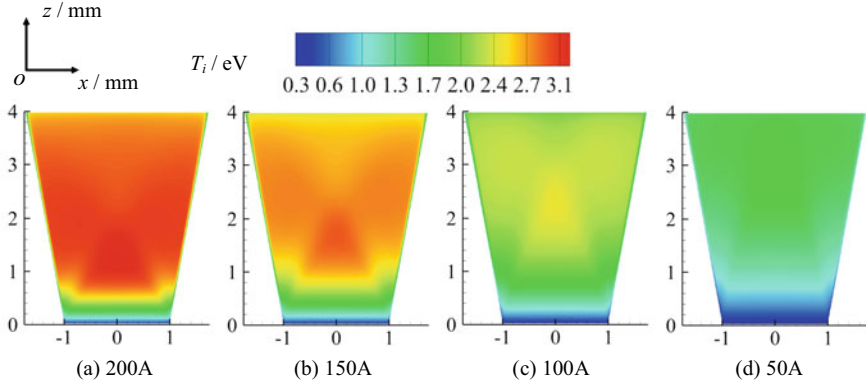
**Fig. 7** Distribution of the ion pressure on the arc column centre axis



Joule heat decreases significantly, leading to the decrease of the electron temperature. The heat obtained by ions in the process of electron and ion heat exchange decreases, so the ion temperature decreases. Secondly, as the current decreases, the deceleration of ions by the radial current and the azimuthal magnetic field weakens, so the kinetic energy of the ions converted into internal energy decreases, causing the ion temperature to decrease.

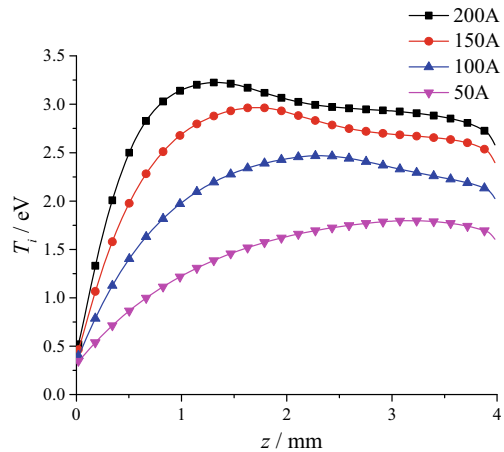
### 3.5 Electron Temperature

Figures 10 and 11 indicate that as the current decreases, the electron temperature decreases. Compared with the ion temperature, the electron temperature is higher. The distribution of the electron temperature from cathode to anode increases first and then decreases, which is like that of the ion temperature. The reason why the



**Fig. 8** Distribution of the ion temperature

**Fig. 9** Distribution of the ion temperature on the arc column centre axis



electron temperature close to the anode will decrease is that the electron consumes energy during the process of passing through the anode sheath.

## 4 Conclusions

This article establishes a 2D transient MHD model to simulate the dynamic properties of VA during DC breaking process based on artificial current zero when the current approaches zero. The following conclusions are obtained:

- (1) The ion density, the axial current density, the ion pressure, the ion temperature and the electron temperature in the region of the arc column decrease as the arc current decreases.



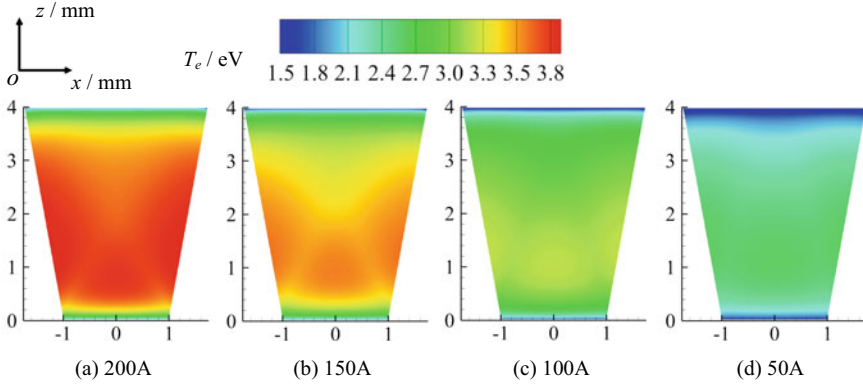
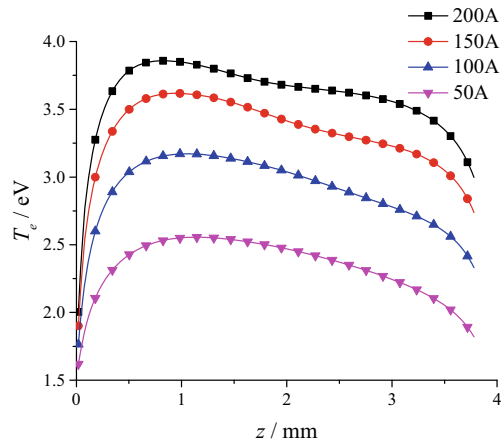


Fig. 10 Distribution of the electron temperature

Fig. 11 Distribution of the electron temperature on the arc column centre axis



(2) As the current decreases, the diffusion degree of plasma weakens.

**Acknowledgements** This work was funded by the Science and Technology Program of China Southern Power Grid (Intelligent Individual Soldier Patrol and Inspection Device for the Distribution Grid, 082100KK58200002).

### References

1. Tang G, Luo X, Wei X (2013) The technology of Multi-terminal HVDC transmission and DC power grid. Proc CSEE 33(10):8–17 (in Chinese)
2. Shi Z, Jia S (2015) Review of research on high-voltage DC circuit breaker. High Volt Appar 51(11):1–9 (in Chinese)

3. Boxman R (1977) Magnetic constriction effects in high-current vacuum arcs prior to the release of anode vapor. *J Appl Phys* 48(6):2338
4. Keidar M, Beilis I, Boxman R et al (1996) 2D expansion of the low-density interelectrode vacuum arc plasma jet in an axial magnetic field. *J Phys D-Appl Phys* 29(7):1973–1983
5. Beilis I, Keidar M, Boxman R et al (1998) Theoretical study of plasma expansion in a magnetic field in a disk anode vacuum arc. *J Appl Phys* 83(2):709
6. Beilis I, Keidar M (2002) Electron temperature in the expanding cathode plasma jet in a vacuum arc. In: 20th international symposium on discharges and electrical insulation in vacuum. IEEE, Tours, France, pp 535–538
7. Schade E, Shmelev D, Sfv E et al (2002) Numerical modeling of plasma behavior and heat flux to contacts of vacuum arcs with and without external axial magnetic field (AMF). In: 20th international symposium on discharges and electrical insulation in vacuum, pp 44–51. IEEE, France
8. Schade E, Shmelev D (2003) Numerical simulation of high-current vacuum arcs with an external axial magnetic field. *IEEE Trans Plasma Sci* 31(5):890–901
9. Wang L, Jia S, Shi Z et al (2005) Simulation research of magnetic constriction effect and controlling by axial magnetic field of vacuum arc. *Plasma Sci Technol* 7(1):2687–2692
10. Wang L, Jia S, Shi Z et al (2006) High-current vacuum arc under axial magnetic field: numerical simulation and comparisons with experiments. *J Appl Phys* 100(11):113304
11. Wang L, Luo M, Deng J et al (2021) Numerical simulation of multi-species vacuum arc subjected to actual spatial magnetic fields. *IEEE Trans Plasma Sci* 49(11):3652–3662
12. Qian Z, Wang L, Jia S et al (2015) The 3D simulation of high-current vacuum arc under combined effect of actual magnetic field and external transverse magnetic field. *IEEE Trans Plasma Sci* 43(8):2275–2282
13. Qian Z, Wang L, Jia S et al (2014) 3-D simulation of plasma's rotation behavior in high current vacuum arcs under realistic spatial magnetic field profile. *IEEE Trans Plasma Sci* 42(10):2708–2709
14. Shmelev D, Uimanov I (2014) Hybrid computational model of diffuse high-current vacuum arc. In: 26th international symposium on discharges and electrical insulation in vacuum, pp 269–272. IEEE, Mumbai, India
15. Childs S, Greenwood A (1980) A model for DC interruption in diffuse vacuum arcs. *IEEE Trans Plasma Sci* 8(4):289–294
16. Jadidian J (2009) A compact design for high voltage direct current circuit breaker. *IEEE Trans Plasma Sci* 37(6):1084–1091
17. Liu X, Liu C, Zou J (2015) Comparative analysis of AC and DC vacuum arc plasma characteristics. *J Vac Sci Technol* 35(10):1203–1208 (in Chinese)
18. Hashemi E, Niayesh K (2020) DC current interruption based on vacuum arc impacted by ultra-fast transverse magnetic field. *Energies* 13(18):4644
19. Wang L, Zhang Z, Chen J et al (2022) 3D transient MHD simulation of DC breaking vacuum arc based on artificial current zero. *J Appl Phys* 132(6):063301
20. Wang L, Zhang Z, Yang Z et al (2022) 3-D dynamic simulation of the initial expansion process of vacuum arc plasma in DC interruption. *IEEE Trans Plasma Sci* 50(5):1301–1312
21. Zhang L, Jia S, Wang L et al (2011) Simulation of vacuum arc characteristics under four kinds of AMFs and comparison with experimental results. *Plasma Sci Technol* 13(4):462–469

# Design and Simulation Analysis of a New Cylindrical Permanent Magnet Linear Motor for Vortex-Induced Vibration Ocean Current Power Generation



Liguo Fan, Guoqiang Liu, Xianjin Song, Wenwei Zhang, Tongyang Jin, Lipeng Wu, and Hui Xia

**Abstract** Aiming at the disadvantages of rotating generators' low electrical energy conversion efficiency and poor system stability in eddy vibration sea current energy generation systems, this paper proposes a radially magnetized cylindrical permanent magnet linear generator, which simplifies the intermediate transmission device and improves the stability of system operation. The Ansys program was used to investigate the relationship between the magnetization technique, pole arc coefficient, permanent magnet thickness, back iron thickness, and the linear motor. The air gap magnetic density and no-load-induced electric potential waveform curves were also provided. The results demonstrate that the maximum generating power can be reached by analyzing the load characteristics when the polar arc coefficient is 0.75, the amplitude of the no-load induced electromotive force generated by the radial magnetization drum permanent magnet linear motor is the largest, and the waveform sinusoidal is the best.

**Keywords** Ocean current energy · Vortex-induced vibration · Cylindrical permanent magnet linear motor · Finite element simulation analysis

---

L. Fan · X. Song · L. Wu  
School of Electric Power and Architecture, Shanxi University, Taiyuan 030006, China

L. Fan · G. Liu · W. Zhang · T. Jin · H. Xia (✉)  
Institute of Electrical Engineering, Chinese Academy of Sciences, Beijing 100190, China  
e-mail: [xiahui@mail.iee.ac.cn](mailto:xiahui@mail.iee.ac.cn)

© Beijing Paiké Culture Commu. Co., Ltd. 2024  
X. Dong and L. Cai (eds.), *The Proceedings of 2023 4th International Symposium on Insulation and Discharge Computation for Power Equipment (IDCOMPU2023)*, Lecture Notes in Electrical Engineering 1103, [https://doi.org/10.1007/978-981-99-7413-9\\_19](https://doi.org/10.1007/978-981-99-7413-9_19)

## 1 Introduction

With China's "double carbon" plan entering a critical period, to achieve low carbon emissions and reduce the impact of fossil fuels on the environment, humanity is actively exploring new renewable and clean energy, and current sea energy as a green renewable energy has attracted much attention, how to improve the utilization rate of ocean current energy is to be solved [1].

The vortex vibration aquatic clean energy device, created by Professor Bernitsas et al. in 2008, is the most well-known sea current energy generation device. It uses the flow to impact the vibrating cylinder to generate vortex vibration energy, which drives the rotating motor to generate electricity [2]. In 2022 Zhang et al. designed pool experiments to measure eddy excitation response and found that high damping suppresses eddy excitation vibration amplitude [3]. In 2022, Wu et al. used a one-way clutch to achieve energy capture for the periodic motion of the obtuse body. They explored the optimal parameters in terms of mass ratio and obtuse body diameter, respectively [4]. The traditional rotating generator has a complicated intermediate transmission structure and low energy conversion efficiency. The linear motor simplifies the transmission structure of the rotary motor, converts mechanical energy directly into electrical energy, and realizes the efficient conversion of current sea energy [5].

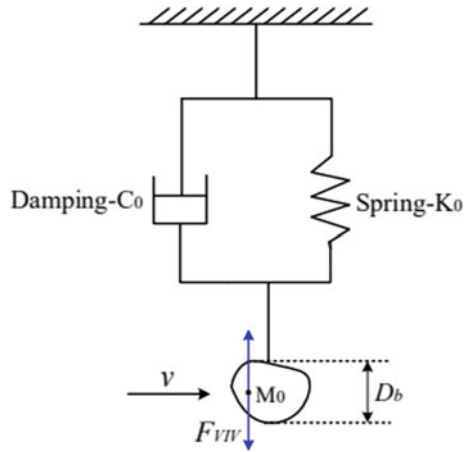
In this paper, a two-dimensional finite element model of a linear motor is constructed by Ansys software to elaborate the design method of a linear cartridge motor applicable to eddy vibration sea current energy generation. Firstly, the secondary permanent magnet array is simulated and the trend of air gap magnetic density is observed by changing the magnetization method and magnet structure; secondly, the primary iron core is added for simulation to give the no-load induction potential and positioning force waveforms of the motor under different parameters; finally, the load characteristics are analyzed to verify that the motor can achieve the rated power generation of 150 W.

## 2 Principle of Vortex-Excited Vibration Power Generation

### 2.1 *Vortex-Excited Vibration Energy Capture Principle*

When the obtuse body is placed in a certain velocity of water, the water impacts the obtuse body to form an alternating shedding vortex at its tail, which triggers the periodic vibration of the obtuse body to realize the conversion of current sea energy to mechanical energy. The vibration amplitude reaches the maximum when the vortex shedding frequency is close to the intrinsic frequency of the cylinder [6] (Fig. 1).

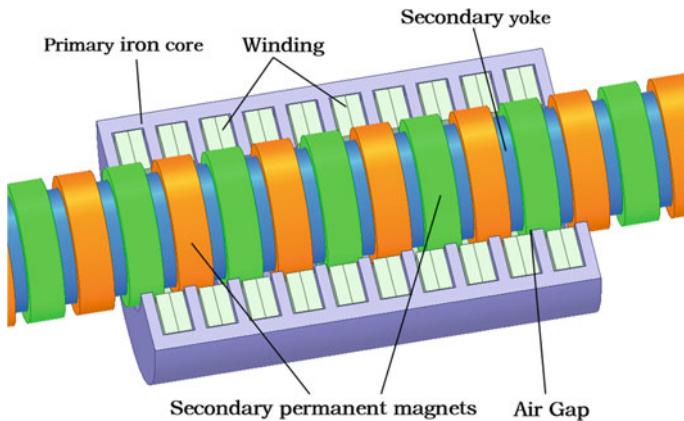
**Fig. 1** Vortex-excited vibration energy capture principle



## 2.2 Structure and Principle of Cylindrical Permanent Magnet Linear Generator

The Tubular Permanent Magnet Linear Generator (TPMLG) consists of a primary core and a secondary permanent magnet, which has a simple structure and no transverse side end effect, reducing the inherent losses of conventional motors [7] (Fig. 2).

The current energy generation system based on the cylindrical permanent magnet linear generator comprises a vortex-induced vibration energy acquisition device and a cylindrical linear generator. Its working principle is as follows: the secondary



**Fig. 2** Vortex-excited vibration energy capture principle

permanent magnet moves linearly and periodically under the push of the vortex-induced vibration blunt body, forming a traveling wave magnetic field in the air gap and cutting the primary coil to generate induced electromotive force [8].

### 3 Secondary Permanent Magnet Array Without Primary

#### 3.1 Permanent Magnet Magnetization Mode

The critical factor affecting the performance of cylindrical permanent magnet linear motor is the size of the air gap magnetic field, which differs from one magnetizing structure to another. The main magnetization methods commonly used in linear motors are axial magnetization structure and radial magnetization structure, as shown in Fig. 3 [9, 10].

As shown in Fig. 4, the magnetic line distribution at the air gap of the axial magnetization structure is sparse and the magnetic field utilization is not high; the magnetic line density at the inner side of the radial magnetization structure is more intensive and the permanent magnet utilization is high.

The linear motor air gap magnetic field determines the generator's output power. It is seen from Fig. 5 that the radial air gap magnetic density of the two magnetizing structures are 0.207 T and 0.3621 T respectively, indicating that the output power of the radial magnetizing structure is greater than that of the axial magnetizing structure under the same structural parameters.

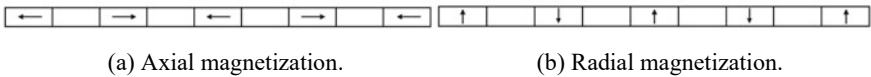


Fig. 3 Structure diagram of magnetizing

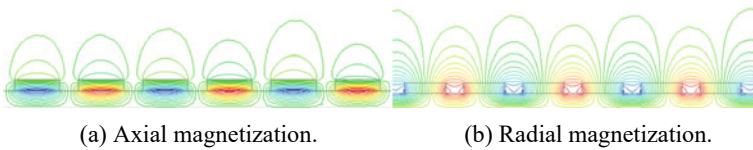


Fig. 4 Distribution of magnetic lines without primary side

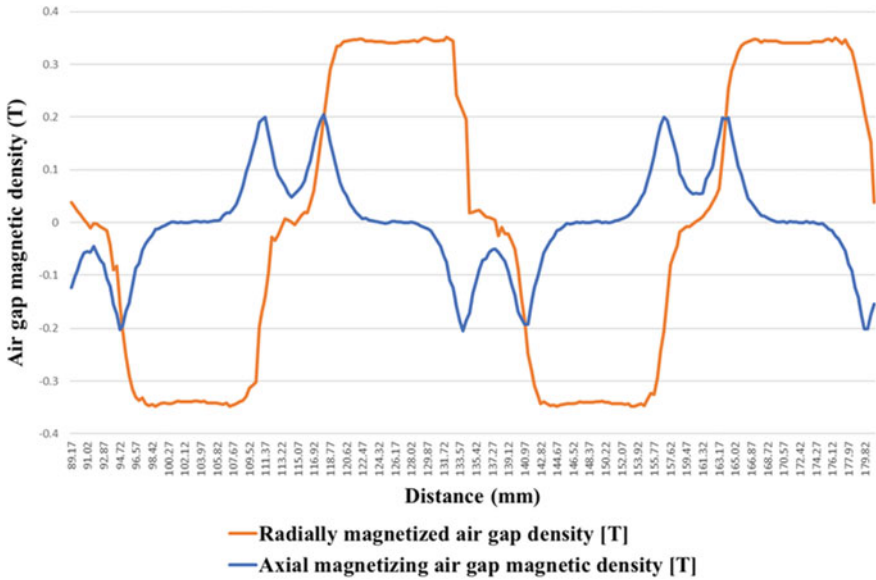


Fig. 5 Without primary  $\delta = 1$  mm air gap magnetic density curve

### 3.2 Effect of Polar Arc Coefficient on Air Gap Magnetic Field

The polar arc coefficient is a coefficient describing the distribution of the air gap magnetic field, which is taken from 0.5 to 0.8 for finite element analysis to explore the variation law of the air gap magnetic field, as shown in Fig. 6.

From the above curve can be seen: the larger the air gap distance, the smaller the air gap magnetic density; when the pole arc coefficient is 0.7, the air gap magnetic density exists a great value of 0.2293 T, and the total harmonic distortion rate is small.

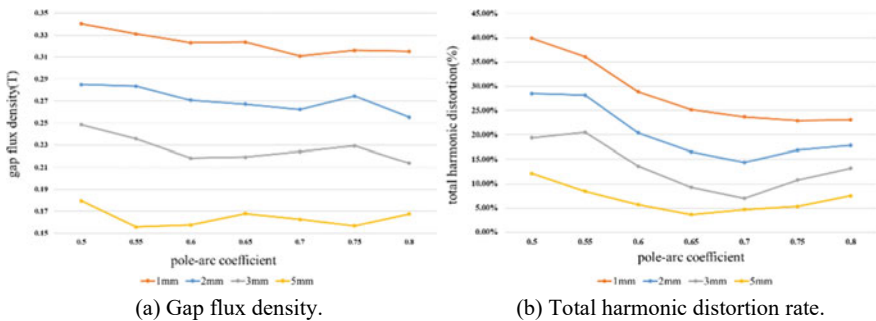


Fig. 6 Curve of the effect of polar arc coefficient on air gap magnetic field

### 3.3 Effect of Permanent Magnet Thickness on Air Gap Magnetic Field

Based on the optimal pole-arc coefficient, the air-gap magnetic density is increased by adjusting the thickness of the permanent magnet, and the results are shown in Fig. 7. With the increase of the permanent magnet thickness, the air gap magnetic density fundamental wave content shows a linear growth trend, and the air gap magnetic density has a great value point at 6 mm.

## 4 Linear Motor Model with Primary Core

Ansys finite element simulation software is used to construct a two-dimensional axisymmetric model of the cylindrical permanent magnet linear motor. The relevant parameters of the motor are shown in Table 1.

As can be seen from the curves in Fig. 8, the air-gap magnetic field density of the radially magnetized structure with the addition of the primary core is significantly improved, and the magnetic density curve has better sinusoidal.

In order to verify the effect of different magnetization structures on the output electrical energy, the three-phase no-load induced electromotive force of the two magnetization structures is shown in Fig. 9 when the generator secondary is given a synchronous speed excitation of 0.58 m/s.

Analysis of the curves shows a high amplitude of no-load electric potential for radial magnetization with good sinusoidal, which matches the results without the addition of the primary side (Fig. 10).

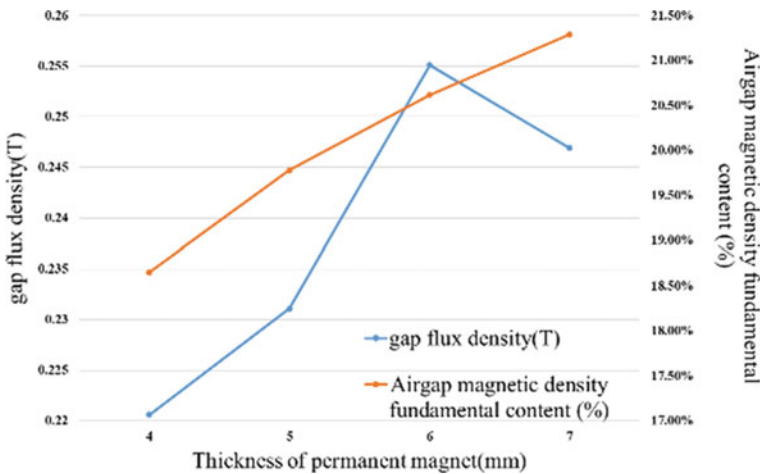
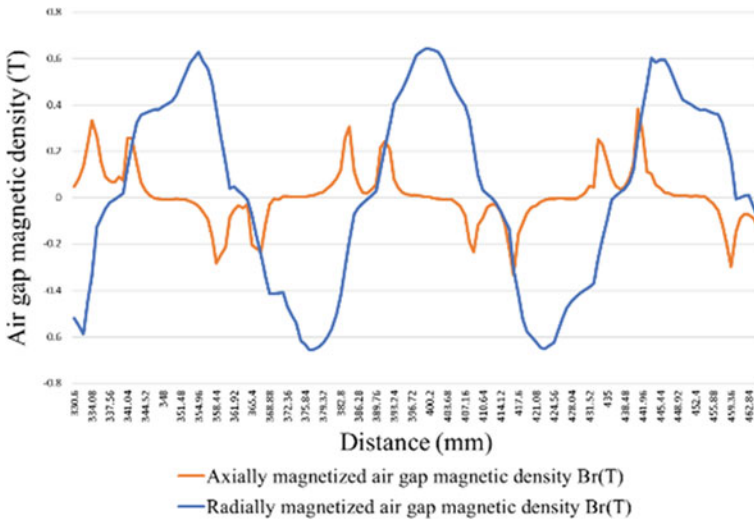


Fig. 7 Influence curve of different permanent magnet thickness on air gap magnetic density

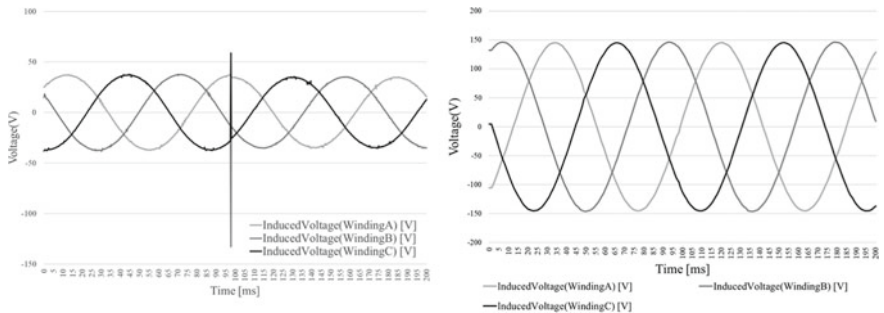


**Table 1** Key structural parameters of the generator

Parameters	Numerical value	Unit
Rated power	150	W
Nominal velocity	0.58	m/s
Outside diameter of machine	150	mm
Effective length	225	mm
Internal diameter of machine	70	mm
Polar distance	25	mm
Groove height	28	mm
Groove width	16.076	mm



**Fig. 8** Air gap density curve with primary side



(a) Axially magnetized electromotive force. (b) Radially magnetized electromotive force.

**Fig. 9** No-load induction electromotive force curve

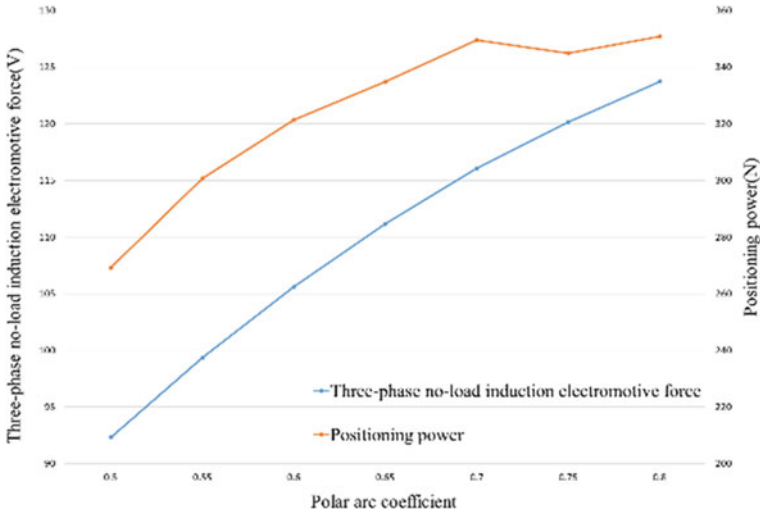


Fig. 10 Three-phase no-load induced electromotive force and positioning force curve

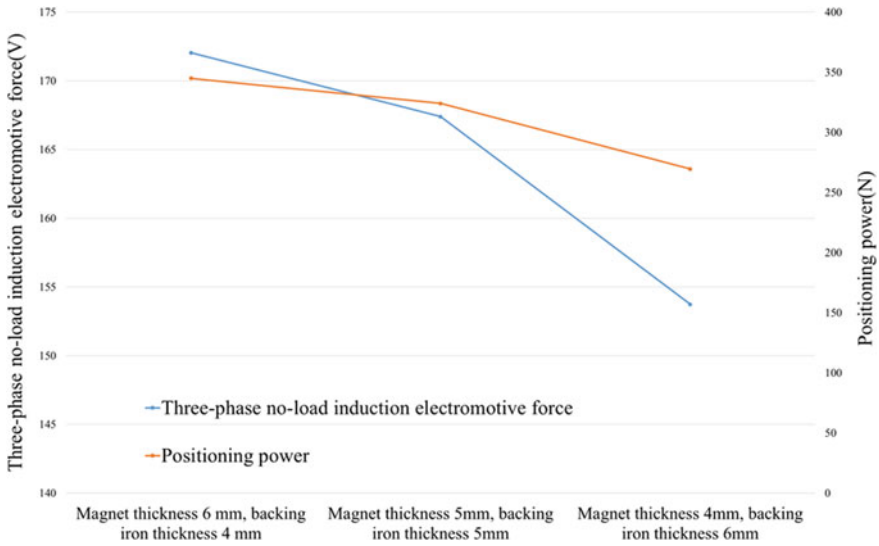
### 4.1 Influence of the Pole Arc Factor on Linear Motors After the Addition of Primary Motors

The finite element simulation is carried out by taking the pole arc coefficients from 0.5 to 0.8 without changing the other parameters of the linear motor.

From the above curve, with the increase of the pole arc coefficient, the amplitude of the three-phase no-load induction potential increases, and when the pole arc coefficient is 0.75, the positioning force appears to be a minimal value point.

### 4.2 Effect of Permanent Magnet Thickness and Backing Iron Thickness on Linear Motors

When the outer diameter of the primary core is determined, the magnet thickness increases and the primary slot area decreases instead of reducing the electrical load. Fixed linear motor primary inner diameter, the pole arc coefficient is selected as 0.75. As seen from the curve in Fig. 11, the three-phase induced electric potential has a larger value when the permanent magnet thickness is larger; the motor positioning force is smaller when the back iron thickness is wider.

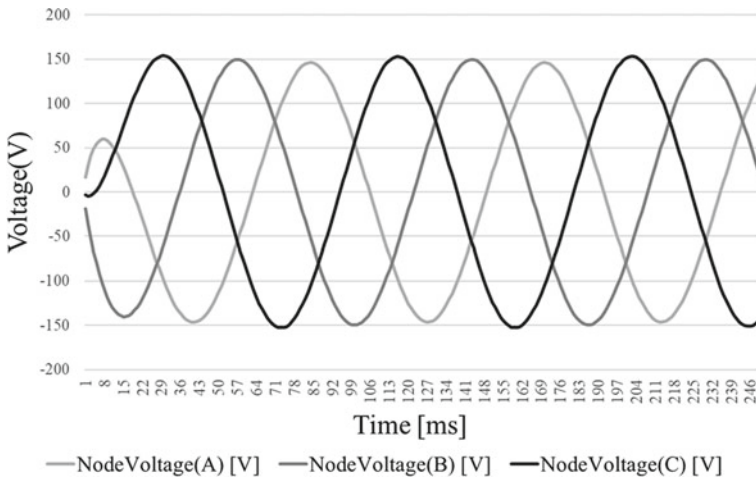


**Fig. 11** Electromotive force and positioning force curves for different magnet and back iron thicknesses

### 5 Load Characteristics of Linear Motors

The load characteristic is the ability of the motor to bear the load during operation and is also one of the essential parameters of the motor. When the voltage waveform across the load is obtained by applying an external circuit in series with a 100 Ω resistor, as shown in Fig. 12.

The phase voltage amplitude, current amplitude and three-phase output power under varying load conditions are shown in Table 2. As the load resistance increases, the output voltage becomes larger and the output current decreases. When the load resistance is 50 Ω, the maximum three-phase output power can reach 364.201 W.



**Fig. 12** Voltage waveform curves at both ends of the load

**Table 2** A-phase voltage, current and three-phase output power at different loads

Load resistance ( $\Omega$ )	Output current amplitude (A)	Output voltage amplitude (V)	Three-phase output power (W)
10	3.253	32.528	182.499
30	2.86	85.784	345.38
50	2.321	116.04	364.201
100	1.463	146.343	278.676

## 6 Conclusion

In this paper, a cylindrical permanent magnet linear generator for an eddy-vibration sea current energy generation system is proposed, and the main conclusions from the simulation model analysis study include:

- (1) The analysis of the permanent magnet array shows that the radially magnetized structure has a denser distribution of magnetic lines at the air gap, and the air gap magnetic density of the radially magnetized structure is significantly improved after the addition of the primary core.
- (2) Under the condition that the main dimensions of the generator are determined, the influence of the pole arc coefficient on the magnetic field strength is more obvious, and the pole arc coefficient of 0.75 is the optimal value; secondly, the generator is optimized from the reasonable combination of the magnet and back iron thickness, and the three-phase no-load induction potential amplitude and positioning force under each optimized parameter is analyzed to obtain the optimal motor design dimensions.

- (3) Through the generator load characteristics analysis, the maximum three-phase output power of the generator can reach 364.201 W when a 50  $\Omega$  resistive load is connected to the external circuit, which meets the requirements of the expected rated power 150 W motor.

**Acknowledgements** This work was funded by the Strategic Pioneer Science and Technology Special Project (Class A) of the Chinese Academy of Sciences (XDA22010401).

## References

1. Curto D, Franzitta V, Guercio A et al (2022) An experimental comparison between an ironless and a traditional permanent magnet linear generator for wave energy conversion. *Energies* 15(7):2387
2. Bernitsas MM, Raghavan K, Ben-Simon Y et al (2008) VIVACE (vortex induced vibration aquatic clean energy): a new concept in generation of clean and renewable energy from fluid flow. *J Offshore Mechan Arct Eng* 130(4)
3. Zhang B, Li B, Fu S et al (2022) Experimental investigation of the effect of high damping on the VIV energy converter near the free surface. *Energy* 244:122677
4. Wu Z, Chang Y, Zhao W et al (2022) Research on power generation performance of three-stable electromagnetic vortex-induced vibration energy harvesting device. *J Vib Shock* 41(13):26–33 (in Chinese)
5. Yu Haitao SHI, Xueqing HUM et al (2012) Performance analysis of cylindrical permanent magnet linear generator for ocean wave power generation. *Mar Technol* 31(04):79–82 (in Chinese)
6. Wise M, Albadri M, Loeffler B et al (2021) A novel vertically oscillating hydrokinetic energy harvester. In: *Proceedings of the 2021 IEEE conference on technologies for sustainability (SusTech)*, pp 22–24
7. Fuli W (2020) Design and research of cylindrical permanent magnet linear generator for wave power generation. Guangdong University of Technology (in Chinese)
8. Rao D (2020) Design of cylindrical permanent magnet linear generator with composite transformer. Shenyang University of Technology (in Chinese)
9. Tao X (2019) Research on optimization design and control of cylindrical linear motor for direct drive wave power generation. Southeast University (in Chinese)
10. Liu C, Dong R, Ye B-L (2022) Comprehensive sensitivity analysis and multi-objective optimization on a permanent magnet linear generator for wave energy conversion. *Renew Energy* 198:841–850

# 3D Pic-Mcc Simulation of Particles Expansion for Straight Curved Contact and Butt Contact in the Post-arc Phase



Tong Ziang, Wu Shengxiu, Qin Enyao, Shen Zhengbin, Wu Jianwen, Shi Shengsheng, Zhang Liyan, and Sun Weili

**Abstract** Straight curved contact is a vacuum interrupter contact structure with excellent interrupting performance. The process of post arc dielectric recovery during the disconnection process is not yet clear. However, one-dimensional and two-dimensional Particle-In-Cell/Monte Carlo (Pic-Mcc) models cannot accurately describe this process. This article establishes a three-dimensional Pic-Mcc model for the dielectric recovery process after vacuum arc of curved contacts. Taking the butt contact as a reference, the particle diffusion process and particle characteristics of curved contact in the post-arc phase were compared and analyzed. The results indicate that the curved electrode structure and larger electrode surface area are the main factors affecting the post arc particle diffusion process.

**Keywords** 3D Pic-Mcc · Curved contact · Post-arc · Particles expansion

---

T. Ziang (✉) · W. Jianwen  
Beihang University, Beijing 100191, China  
e-mail: [tzahdh@163.com](mailto:tzahdh@163.com)

W. Shengxiu  
Guizhou Tianyi Electrical Co., Ltd., Zunyi 563002, China

Q. Enyao · S. Shengsheng  
Kushan Guoli Electronic Technology, Kushan 215333, China

S. Zhengbin  
Chengdu Aircraft Design & Research Institute, Aviation Industry Corporation of China, Chengdu 610091, China

Z. Liyan  
Dalian University of Technology, Dalian 116024, Liaoning, China

S. Weili  
Beijing Yanshan Yulong Pec Co., Ltd., Beijing 102500, China

## 1 Introduction

Among the existing arc-extinguishing measures, vacuum arc-extinguishing technology has strong arc-extinguishing ability and high insulation strength, and has extremely strong aviation applicability [1]. For vacuum switches, the contact is an important carrier for circuit connection and arc interruption. Magnetic control contact, represented by transverse magnetic and longitudinal magnetic, is currently the mainstream contact structure [2, 3]. Domestic and foreign scholars have conducted in-depth research on the anode phenomenon, breakdown characteristics, and magnetic fluid modeling of magnetic control contacts in 50 Hz vacuum arc-extinguishing [4–6]. However, for 360–800 Hz variable frequency systems, the magnetic field lag effect caused by the increase in frequency will cause the arc control of magnetic control contacts to fail during arc ignition and zero-crossing moments [7, 8], resulting in the inability of the arc interruption capability of magnetic control contacts to be further improved.

In this context, the curved surface contact vacuum arc-extinguishing structure emerged [9], and its design concept is to obtain a larger contact surface area through the curved surface under a limited contact diameter, in order to reduce the erosion effect during arc ignition and enhance the dissipation process of the remaining plasma after zero-crossing. Experimental results show that in medium-to-high frequency vacuum arc interruption experiments, curved surface contacts show significant advantages in limiting breaking current and erosion resistance compared to traditional magnetic control contacts and butt contacts [10, 11]. However, the parameter design lacks theoretical support.

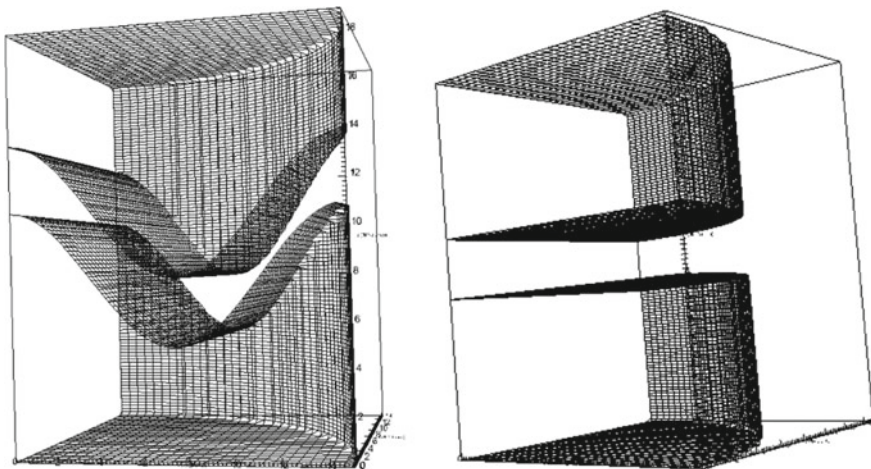
Scholars have done a lot of research work on the particle simulation of plasma in vacuum arc. They usually use methods such as molecular dynamics and Monte Carlo to simulate the particle motion in plasma. Through these simulations, they can study the particle behavior, particle–particle interactions, physical properties of plasma, and other related issues. These studies are of great significance for a deeper understanding of the nature and characteristics of plasma in vacuum arc, as well as for optimizing the design and operation of vacuum arc equipment. Andrew and others [12] proposed a continuous variation model based on the Poisson equation, continuity equation and momentum equation, and simulated the development process of the sheath of a semi-infinite and collisionless plasma. Sarrailh and others established a hybrid model and particle model to simulate the development of the post-arc sheath and the process of post-arc re-striking in vacuum arc [13, 14]. Wang Zhenxing established one-dimensional and two-dimensional PIC/MCC models to simulate the diffusion and re-striking process of post-arc plasma, and analyzed the effects of longitudinal and transverse magnetic fields on the recovery of post-arc insulation materials in the post-arc stage [15]. A model of metal vapor breakdown after arc is established, and its development process is simulated in two-dimensional space and three-dimensional velocity [16]. Mo Yongpeng, Wang Dan established a two-dimensional PIC model to analyze the effects of the initial temperature and drift velocity of charged particles

on the development of the post-arc sheath under different metal vapor effects, and obtained the distribution of electron density [17, 18].

The analyzed straight and curved contact tips in this paper are a non-centrosymmetric structure in space. Therefore, one-dimensional or two-dimensional models cannot accurately describe its post-arc particle diffusion process. To address this issue, a three-dimensional PIC/MCC model for curved contact tips was established in this paper, and the post-arc particle diffusion process and particle characteristics were analyzed.

## 2 Simulation Models

The three-dimensional physical model of simulation is shown in Fig. 1. In order to improve the computing efficiency, a 1/4 symmetric model is adopted. The radius of the two electrodes is 15 mm, and the gap distance between them is 3 mm. The postarc anode is grounded with 0 V. The postarc cathode is connected to the instantaneous recovery voltage, and the rate of change is  $-1 \text{ kV}/\mu\text{s}$ . The surfaces of the two electrodes are the first type of boundary condition and are absorptive, that is, when particles reach the surface of the electrode, they are removed from the computing area. Set the upper, left, and front boundaries of the simulation domain as second-class boundary conditions, and set the lower, right, and back boundaries as first-class boundary conditions. Here, the left and front boundaries are actually the symmetrical cross-sections of the electrode, in order to simulate particle number balance on the boundary, particles will bounce back when they come into contact with the left or front boundary.



**Fig. 1** Curved contact physical object and 1/4 simulation model



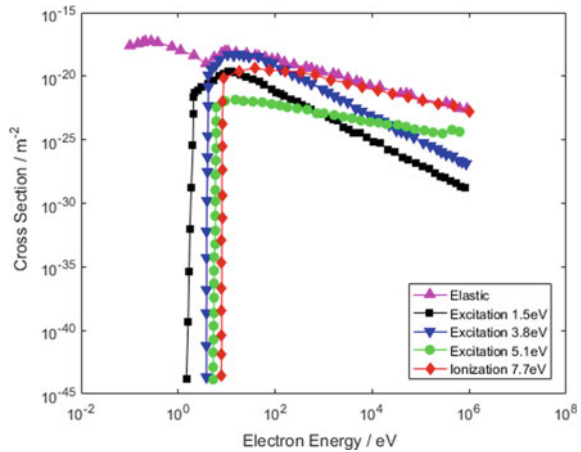
**Table 1** Collision reaction

Type of the reaction	Reaction	Energy loss/eV
Elastic	$\text{Cu} + e \rightarrow e + \text{Cu}$	0
Excitation	$\text{Cu} + e \rightarrow \text{Cu}^* + e$	1.5
Excitation	$\text{Cu} + e \rightarrow \text{Cu}^* + e$	3.8
Excitation	$\text{Cu} + e \rightarrow \text{Cu}^* + e$	5.1
Ionization	$\text{Cu} + e \rightarrow \text{Cu}^+ + 2e$	7.7

At the beginning of the simulation, the remaining plasma during the arcing process is uniformly distributed in the middle area of the electrode with a radius of 15 mm. The density is  $10^{17} \text{ m}^{-3}$  and the ions are singly charged copper ions ( $\text{Cu}^+$ ). The initial temperature of the ions is 2 eV, and the initial temperature of the electrons is 3 eV. Assuming the distribution area of copper vapor is the same as the initial distribution area of the remaining plasma, with a density of  $10^{21}$  and uniform distribution, at a temperature of copper’s boiling point, 2835 K.

The collision process in this model includes elastic collision, collisional excitation and collision ionization between electrons and background metal vapor Cu. It also includes charge exchange and momentum exchange between copper ion  $\text{Cu}^+$  and background metal vapor. The specific reaction types and collision interface data are shown in Table 1 and Fig. 2. These collisions are processed using Monte Carlo collision models.

**Fig. 2** Cross sections of various collision reactions



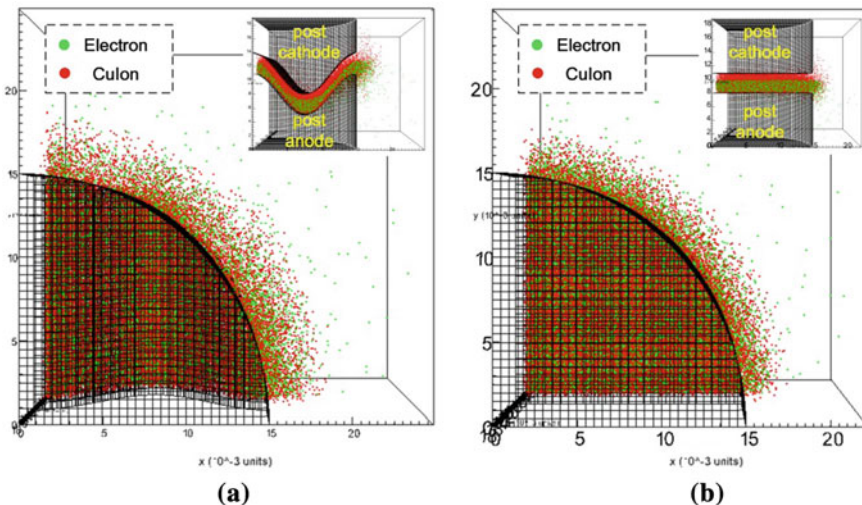
### 3 Results and Discussion

Arcing particle distribution results of the butt and curved contacts within  $0.8 \mu\text{s}$  were obtained based on the model settings described above. Under the effect of recovery voltage, electrons move towards the post-arc anode and are mainly absorbed by it in the vertical direction. In the horizontal direction, electrons tend to move towards both boundaries, as they act as shields with zero potential. Due to the much larger mass of copper ions compared to electrons, ion motion is relatively slower.

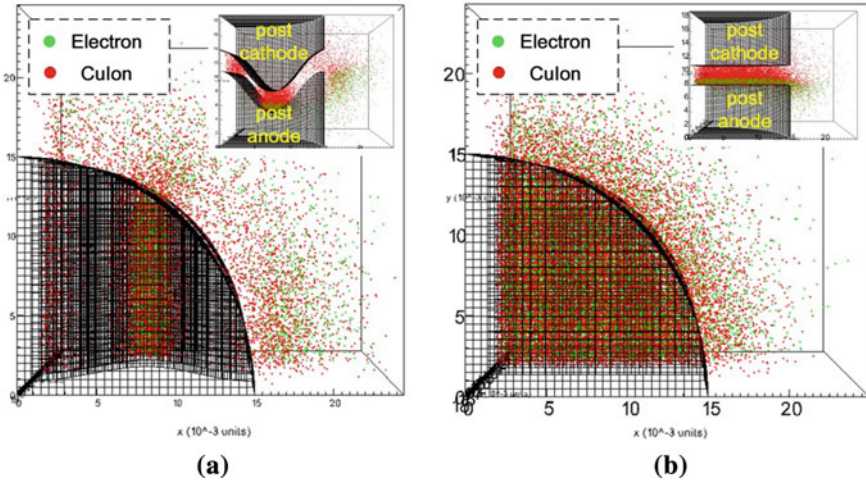
At the time of  $0.2 \mu\text{s}$ , it can be observed that an ion sheath layer appeared on the cathode side after the arc due to the absorption of electrons near the anode after the arc shown in Fig. 3. The sheath layer is distributed more evenly on the butt contact surface, while an uneven distribution of the sheath layer occurs on the curved contact surface. Some electrons and ions have already moved outside the perpendicular gap of the contact.

At  $0.4 \mu\text{s}$ , the length of the sheath layer on the butt contact surface continues to grow, and its distribution remains relatively uniform. In the gap between curved contact surfaces, there is still a sheath layer remaining in the valley position of the curved surface wave, while the unevenly distributed residual ions form quasi-vacuum conditions in some areas of the gap shown in Fig. 4.

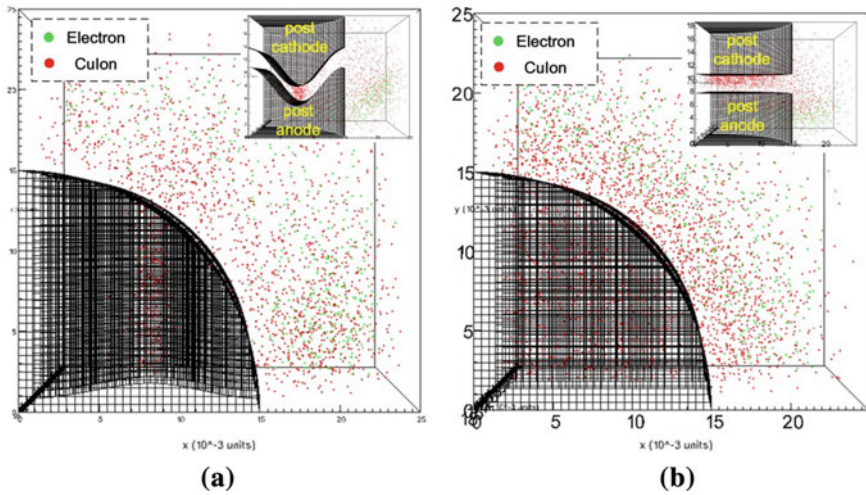
At  $0.6 \mu\text{s}$ , The ions in the gap are gradually absorbed by the post-arc cathode, and the absorption rate of the curved contact is significantly faster than that of the butt contact. As shown in Fig. 5, there are small amounts of residual ions in the gaps of the butt and curved contacts, and most of the post-arc particles are distributed outside the perpendicular gap of the contact.



**Fig. 3** Particle distribution of curved contact and butt contact at  $0.2 \mu\text{s}$ . **a** Curved contact, **b** butt contact

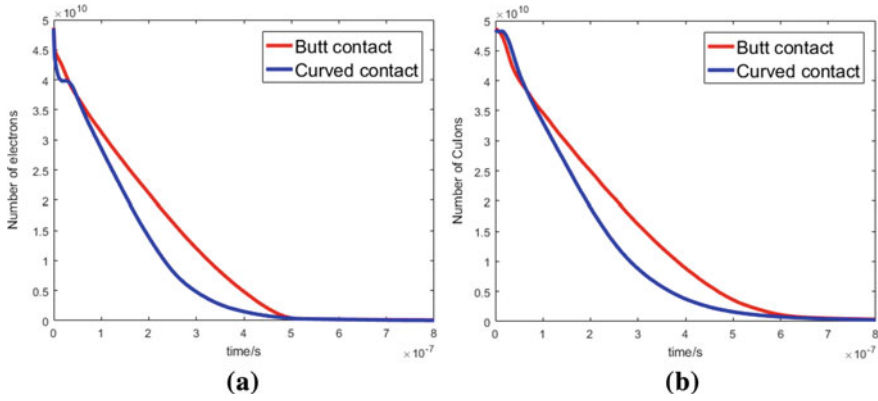


**Fig. 4** Particle distribution of curved contact and butt contact at 0.4  $\mu\text{s}$ . **a** Curved contact, **b** butt contact



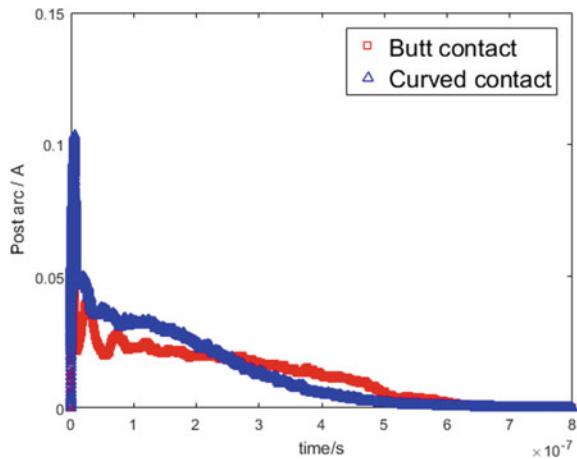
**Fig. 5** Particle distribution of curved contact and butt contact at 0.6  $\mu\text{s}$ . **a** Curved contact, **b** butt contact

Figure 6 shows the trends in the number of ions and electrons for both contacts, and it is evident that the curved contact absorbs post-arc particles faster. Figure 7 shows the trends in post-arc current for both types of contacts. The post-arc current of the curved contact is initially higher but quickly drops to zero, whereas the post-arc current of the butt contact is initially smaller but has larger fluctuations and lasts longer.



**Fig. 6** Particle distribution of curved contact and butt contact at 0.6  $\mu\text{s}$ . **a** Electron, **b** CuIon

**Fig. 7** The post-arc current variation of the curved contact and butt contact within 0.8  $\mu\text{s}$



The results above indicate that the curved electrode structure of the curved contact affect the diffusion process of post-arc particles and the amplitude changes of post-arc current. The main sources of these effects are the larger electrode surface area and the electric field distortion in the curved gap. The larger electrode surface area makes it easier for post-arc particles to be absorbed, while the uneven distribution of electric field in the gap leads to differences in the diffusion state of post-arc particles in localized areas. These two effects are acting simultaneously.

## 4 Conclusion

This article uses a 3D Pic-Mcc particle diffusion model to compare and analyze the sheath changes and particle distribution states of curved surface contacts and butt plate contacts during arc afterglow. The results show that compared with butt plate contacts, the sheath distribution of curved surface contacts is uneven and the particle dissipation rate is faster, resulting in a shorter arc afterglow current maintenance time.

**Acknowledgements** This research is supported by Beijing Natural Science Foundation (3232049) and China Postdoctoral Science Foundation (2022M720342).

## References

1. Jimei W (1986) Theory and application of vacuum switch. Xi'an Jiaotong University Press, Xi'an (in Chinese)
2. Jianhua W, Yingsan G, Zhiyuan L, Jing Y (2017) Vacuum interrupting technology for high voltage. *High Volt Appar* 53(03):1–11 (in Chinese)
3. Yanabu S, Kaneko E, Okumura H et al (1981) Novel electrode structure of vacuum interrupter and its practical application. *IEEE Trans Power Appar Syst PAS-100(4)*:1966–1974
4. Liao M, Duan X, Zou J (2007) Statistical characteristics of insulation breakdown in single and three series vacuum arc quenching chambers. *Proc CSEE* 12:97–102 (in Chinese)
5. Lijun W, Shenli J, Zongqian S, Mingzhe R (2005) Study on magnetic fluid dynamics model and simulation of vacuum arc. *Proc CSEE* 04:115–120 (in Chinese)
6. Miller HC (2017) Anode modes in vacuum arcs: update. *IEEE Trans Plasma Sci* 45:2366
7. Bin L, Wu J, Chao X (2014) Study on dynamic characteristic in force interrupted dc vacuum arc. *IEEE Trans Plasma Sci* 42:2382–2383
8. Jing W, Wu J (2009) Experimental study on medium frequency vacuum arc under longitudinal magnetic field. *Proc CSEE* 29(25):126–132 (in Chinese)
9. Tong Z, Wu J, Hui G et al (2019) Study on sinusoidal curved surface contact vacuum arc characteristics under medium frequency. *Proc CSEE* 39(21):6460–6471 (in Chinese)
10. Tong Z, Wu J, Li K et al (2022) Vacuum arc characteristics of a new type of curved-surface contact for high-frequency forced interruption in aero applications. *Vacuum* 196:110754
11. Tong Z, Wu J, Jin W et al (2020) Properties of intermediate frequency vacuum arc in sinusoidal curved contact and butt contact. *Plasma Sci Technol* 22(2)
12. Andrews JG, Varey RH (1971) Sheath growth in a low pressure plasma. *Phys Fluids* 14(2):339
13. Sarrailh P, Garrigues L, Hagelaar GJM et al (2009) Sheath expansion and plasma dynamics in the presence of electrode evaporation: application to a vacuum circuit breaker. *J Appl Phys* 106(5):053305
14. Sarrailh P, Garrigues L, Hagelaar GJM et al (2008) Two-dimensional simulation of the post-arc phase of a vacuum circuit breaker. *IEEE Trans Plasma Sci* 36(4):1046–1047
15. Wang Z, Tian Y, Hui MA (2015) Decay modes of anode surface temperature after current zero in vacuum arcs—Part II: theoretical study of dielectric recovery strength. *IEEE Trans Plasma Sci* 43(10):3734–3743
16. Yu Z, Fei Y, Hao S, Yi W, Niu C, Rong M (2021) Analysis of metal vapor breakdown process of vacuum DC circuit breaker after arc based on PIC-MCC method. *High Volt Eng* 47(6):2141–2148 (in Chinese)

17. Yongpeng MO, Zongqian SHI, Zhibin BAI (2016) Influence of residual plasma drift velocity on the post-arc sheath expansion of vacuum circuit breakers. *Phys Plasmas* 23(5):053506
18. Wang D, Wang L, Liu J (2020) Two dimensional kinetic simulation of plasma dynamics in the post-arc stage of vacuum circuit breakers. *Phys Plasma* 27(1):013501

# The Electric-Thermal Characteristics of 110 kV Transformer RIP Bushings Based on Electromagnetic-Thermal-Fluid Analysis



Sirui Zhao, Hao Yang, Wenxiu Hu, Jinpeng Chen, and Yimeng Duan

**Abstract** As the key electrical equipment of substation, it is necessary to study the electric heating characteristics of RIP bushing in order to ensure its safe and stable operation. In this paper, the multi-layer structure of the capacitor board is established by the calculation method of equal capacitance, and the distribution characteristics of the electric heating field of RIP bushing are determined by the finite element simulation software. The results show that at rated voltage, the internal electric field intensity of the capacitor core exhibits a U-shaped distribution. The surface field strength of the capacitor core near the guide bar is the highest, which is 1.69 kV/mm. Along the axial direction, the overall temperature of RIP bushing is high in the middle and lower parts and low at both ends. High in the middle and low at both ends along the radial direction. The highest temperature is 98°C, which appears in the middle and lower part of the central current-carrying guide rod. The design of air gap between the inner and outer guide bars can effectively reduce the temperature distribution. The research results can provide theoretical and practical basis for the optimal design of high voltage AC RIP bushing.

**Keywords** RIP · Capacitor core · Current-carrying tube

## 1 Introduction

Transformer is the key equipment to maintain the reliable operation of power system. Traditional oil-paper bushing is easy to cause fire and explosion accidents. The main insulating material of dry sleeve is epoxy resin impregnated insulating paper, which has the advantages of fire and explosion proof, easy installation, and has been widely used in urban power grid reconstruction [1].

High voltage bushings have withstood the test of complex environments such as electricity, heat, and machinery during long-term operation. Wang Qian et al. used

---

S. Zhao (✉) · H. Yang · W. Hu · J. Chen · Y. Duan  
Xi'an Polytechnic University, Xi'an 710048, China  
e-mail: 2920141152@qq.com

© Beijing Paiké Culture Commu. Co., Ltd. 2024  
X. Dong and L. Cai (eds.), *The Proceedings of 2023 4th International Symposium on Insulation and Discharge Computation for Power Equipment (IDCOMPU2023)*, Lecture Notes in Electrical Engineering 1103, [https://doi.org/10.1007/978-981-99-7413-9\\_21](https://doi.org/10.1007/978-981-99-7413-9_21)

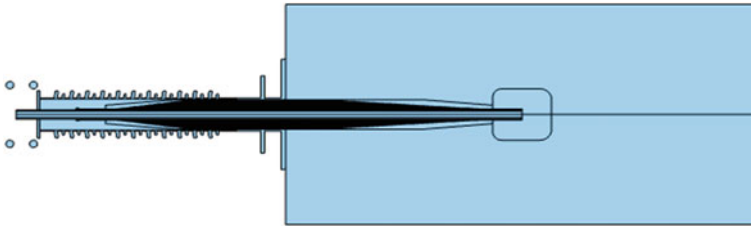
finite element simulation software to study and calculate the distribution characteristics of electric heating field and the influence law of temperature field on electric field distribution of valve side bushing of converter transformer [2]. Aiming at the problem of bushing temperature rise, based on the electrothermic coupling model of dry DC bushing, Shiling Zhang et al. found that the radial electric field distortion of bushing was serious under load conditions, but no effective improvement measures were proposed [3]. but no effective improvement measures were proposed. Qingyu Wang et al. propose a new structure is proposed to improve the bushing temperature distribution [4]. Liu et al. studied the fretting corrosion model and SF<sub>6</sub> decomposition process, and diagnosed the typical overheating failure caused by contact deterioration of RIP bushing [5]. Chi et al. calculating the relationship between insulation resistivity and relative dielectric constant of oiled paper and material moisture content and temperature [6]. The distribution of temperature and electric field of oil paper insulation under composite voltage is studied. At present, most studies on RIP bushing are based on UHV valve side bushing, and there are few studies on 110 kV high-voltage transformer bushing, and mainly on oil paper bushing. This article analyzes the electromagnetic heat flux, considering the actual working conditions, establish a 110 kV RIP bushing model using finite element software, and the electric heating characteristics of the bushing are simulated. It provides a basis for casing condition monitoring.

## 2 Simulation Model of RIP Bushing Electric Heating Field

The 110 kV RIP bushing model studied in this paper is established based on the Principles of Electrical Insulation Structure Design and the technical specifications of the national standards with the actual working conditions, as shown in Fig. 1. The main structure of the model consists of an inner central current-carrying guide rod, an outer conductor, connecting fittings, SF<sub>6</sub> gas, capacitor core, flange, top pressure balancing ring and bottom pressure balancing cover. The capacitor core in the bushing model is composed of aluminum foil and epoxy-impregnated paper. The multi-layer plate is designed by using the method of equal capacitance step size calculation to uniform the internal electric field intensity. The condenser core is the main insulating part of the casing. The lower part of the bushing is immersed in transformer oil, and SF<sub>6</sub> insulating gas fills the upper part of the core, which is used as auxiliary insulation of the RIP bushing with the outer silicone rubber composite insulator sheath.

The design of transformer bushing capacitor core is the key to the electrical design calculation of transformer bushing. This paper establishes the multi-layer plate structure of capacitor plate by means of the calculation method of equal step and so on. By determining the allowable field strength of the inner space of the bushing; Determine the appropriate size of each layer of pressure equalizing plate; Thus, the distribution of radial and axial electric fields is ensured to be even and reasonable [7]. In this paper, it is calculated zero sequence plate  $r_0 = 30$  and end plate  $r_{34} = 77$ . The design size of each layer plate of the capacitor core is obtained





**Fig. 1** Calculation model of RIP bushing

through layer by layer calculation and modification of the calculation result combined with the actual design and application requirements of the bushing.

The total length of RIP bushing sleeve of this model is 2870 mm. The length of the oil-immersed part is 1300 mm. The bushing model studied in this paper is BLC126/1250CJ. The inner diameter of the central current carrying conductor is 17.5 mm and the outer diameter is 25 mm. The air gap is designed to increase the heat dissipation capacity of the core. Inner diameter of outer conductor 27 mm, outer diameter 30 mm. Silicone rubber composite insulator adopts alternating umbrella design, parameters according to the national standard design.

### 3 Calculation Method of RIP Electric Heating Field

#### 3.1 Theoretical Analysis of Electric Field Calculation

The calculation of electric field is based on Maxwell equations. Since the calculation of electric field is a quasi-electrostatic field problem, the expression formula is as follows:

$$\nabla \times E \approx 0 \tag{1}$$

$$\nabla \times H = J_c + \frac{\partial D}{\partial t} \tag{2}$$

$$\nabla \times D = \rho \tag{3}$$

Among these,  $E$  is Electric field intensity, unit V/m;  $H$  is Magnetic field strength, unit A/m;  $J_c$  is Conduction current density, unit A/m<sup>2</sup>;  $\rho$  is Free charge density, unit C/m<sup>3</sup>.

The zero sequence plate and the central current carrying conductor as a whole and its connected metal parts are set as high potential, the outer guide rod does not participate in the current carrying, but is equal potential with the inner conductor;

The end plate, connecting flange and transformer oil tank are set to ground; Except for zero sequence plate and end plate, the remaining plates are set to suspension potential.

### 3.2 Theoretical Analysis of Thermal Field Calculation

There are two heat sources, Joule heat and dielectric loss, in the operation of RIP bushing [8]. The metal guide rod is used as the heat source of the whole model to apply heat. Dielectric loss and heating of insulating medium such as capacitor core and insulating sheath. According to Maxwell's equation, the governing equation of electromagnetic field is shown as follows:

$$\nabla \times \frac{1}{\mu} (\nabla \times A) = J_s - \sigma \frac{\partial A}{\partial t} \quad (4)$$

Among these,  $\mu$  is conductor magnetic permeability;  $A$  is magnetic vector position;  $J_s$  is current density;  $\sigma$  is conductivity.

After the unit volume loss of the above parts is obtained, it is introduced into the temperature field as a heat source for coupling calculation [9].

Heat transfer from capacitor core to insulating medium. The governing equation of heat conduction is as follows [10]:

$$\rho C \frac{\partial T}{\partial t} = \lambda \left( \frac{\partial^2 T}{\partial x^2} + \frac{\partial^2 T}{\partial y^2} + \frac{\partial^2 T}{\partial z^2} \right) + Q \quad (5)$$

Among these,  $T$  is temperature;  $C$  is specific heat capacity;  $\lambda$  for thermal conductivity;  $x$ ,  $y$  and  $z$  are coordinate values;  $\rho$  is density;  $t$  is time;  $Q$  is heating power per unit volume.

Both the transformer oil and the air on the outer surface of the bushing have natural convection heat transfer with the bushing. The governing equation of heat convection is as follows:

$$\frac{\partial v_x}{\partial x} + \frac{\partial v_y}{\partial y} + \frac{\partial v_z}{\partial z} = 0 \quad (6)$$

where,  $v_x$ ,  $v_y$  and  $v_z$  represent the velocity of the fluid along the  $x$ ,  $y$  and  $z$  axes.

The bushing surface also radiates heat to the external environment and absorbs heat radiated from the environment [11]. Stefan-boltzmann law can be used to describe the process of heat radiation between two surfaces, namely:

$$q_3 = \varepsilon \sigma (T_1^4 - T_2^4) \quad (7)$$

In the formula,  $\varepsilon$  is the surface blackness of surface 1,  $\sigma$  is Steffen-Boltzmann constant ( $\sigma = 5.67 \times 10^{-8}$ ).  $T_1$  and  $T_2$  are the temperatures of the two surfaces respectively.

In temperature field simulation, the air boundary is set at 20 °C and the temperature of transformer oil is set at 80 °C.

## 4 Electric Field Distribution Result

The multilayer design optimizes the electric field distribution of the core and avoids the sudden increase of the field intensity. As can be seen from the electric field distribution in Fig. 2, the strong electric field is confined between the plate regions, and the electric field outside the plate envelope weakens rapidly. And the increase of field intensity is distributed in the edge of each laminate, flange, pressure equalizing cover and other positions.

The overall electric field strength inside the capacitor core presents U-shaped distribution, and the maximum field strength of the core is 1.69 kV/mm, which meets the control requirements of the maximum radial field strength of RIP casing.

### 4.1 Temperature Field Distribution

In this paper, the rated current of 1250 A is applied to the central current-carrying conductor for electrothermal coupling simulation. By setting the boundary conditions of the temperature field, the temperature distribution results of the RIP bushing were obtained after several iterations on the basis of the calculated dielectric loss, as shown in Fig. 4.

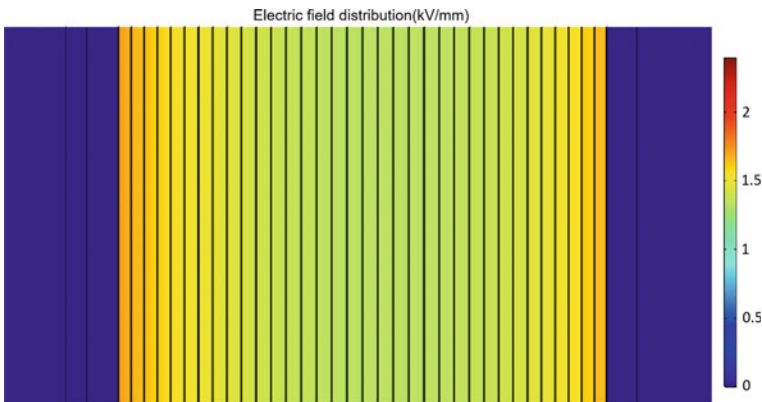
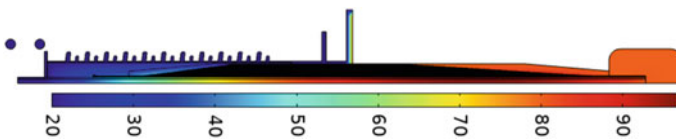
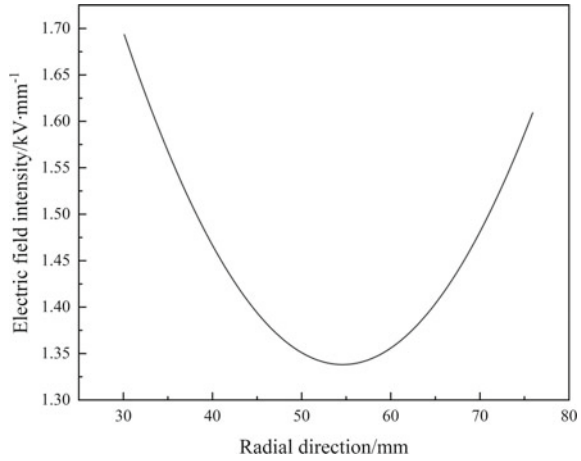


Fig. 2 Electric field distribution of RIP bushing capacitor core

**Fig. 3** Electric field intensity of core

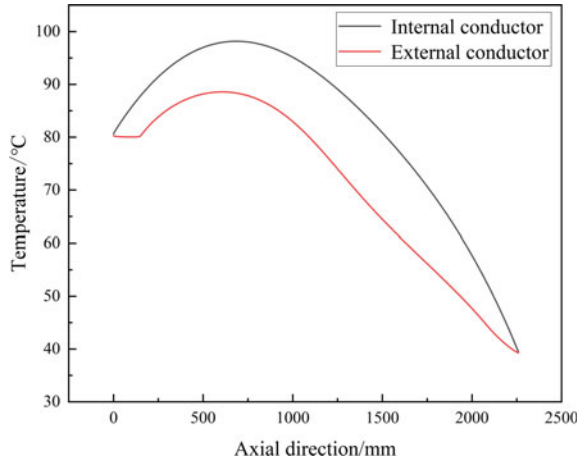


**Fig. 4** Overall temperature distribution of RIP bushing

According to Fig. 4, the middle and lower parts of the bushing are at a higher temperature, while the two ends are at a lower temperature. The highest temperature appears in the middle and lower part of the center current carrier guide rod, the temperature is 98 °C, the lowest temperature is located in the outer edge of the upper end of the bushing, the temperature is 20 °C, the highest temperature is 5 times the lowest temperature.

Extract the temperature of the outer surface of the inner guide rod and the outer guide rod, and draw the temperature distribution diagram as shown in Fig. 5. According to the heat conduction formula/Fourier Law, the greater the temperature difference, the better the heat transfer capacity. The bushing has sufficient heat transfer at the air end, so the upper part of the bushing is cooler than the lower part. Because the lower end of the casing is inserted into the transformer oil, the oil temperature is high, which is not conducive to heat dissipation. The axial temperature distribution characteristics of the bushing along the oil side of the transformer to the upper air side were analyzed. It was found that the temperature distribution of the internal and external pipes rose first and then decreased, and the highest temperature appeared in the middle and lower parts. The maximum temperature of the outer wall of the inner tube is 98 °C, and the maximum temperature of the outer wall of the outer tube is 88 °C. In addition, by comparing the outer surface temperature of the inner guide bar with that of the outer surface temperature of the outer guide bar, it is concluded that the air gap design can effectively reduce the temperature distribution.

**Fig. 5** Axial temperature distribution of different paths



Three radial transect lines (A, B and C) as shown in Fig. 6 are taken respectively to compare and analyze the temperature distribution rule inside the core at different positions.

The temperature distribution under different paths is shown in Fig. 7. The temperature distribution of the three paths showed a downward trend as a whole. The inner side of path A is guide rod, and the outer side is transformer oil. Because the lower end of the bushing is immersed in transformer oil, the temperature of transformer oil is 80 °C, and the heat dissipation capacity of oil is poor, the core hot spot temperature in this path is the highest. The inner side of path B is the guide bar, the outer side is the flange, the flange has high thermal conductivity, and the outer boundary is in direct contact with the air, close to the constant temperature of 20 °C air end, the heat dissipation ability is the best, so the temperature at the flange appears a rapid decline; The inside of path C is the guide bar, and the outside is the SF<sub>6</sub> filling area and the silicone rubber sheath area, which will produce certain medium loss. The outer sheath directly contacts the external 20 °C constant temperature air end, and the heat dissipation ability is good.

#### 4.2 Temperature Field Distribution Under Different Load Capacity

According to the survey, the rated current of 110 kV RIP bushing in actual operation is generally 630, 1250 and 2500 A. In this paper, the bushing temperature field under the above different load rates is simulated and analyzed.

The internal and external temperature distribution of the core along the axial direction is studied. The core inner axial temperature distribution increases first and then decreases, which is because the heat dissipation capacity in transformer oil is

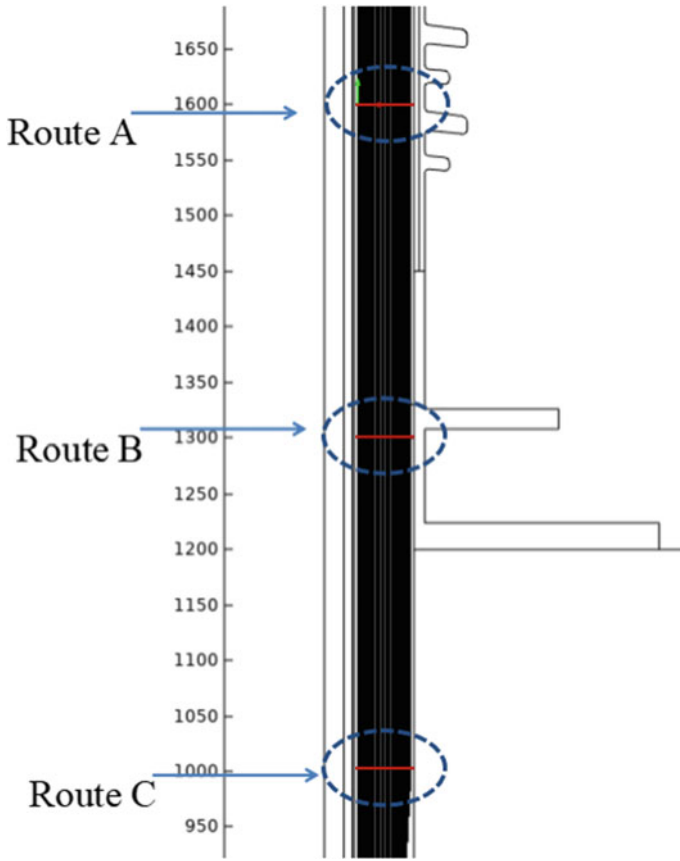
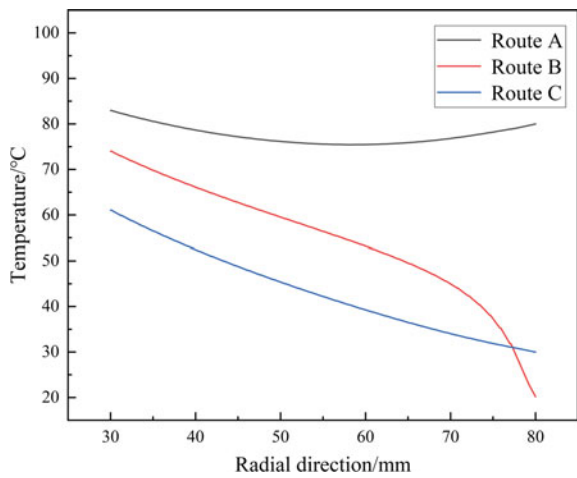


Fig. 6 Different route transversals

Fig. 7 Radial temperature distribution of different paths



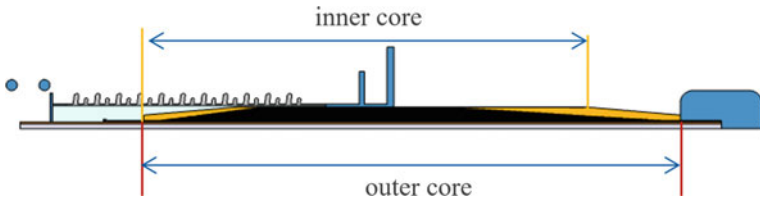


Fig. 8 Inner and outer core path

Fig. 9 Outer core temperature distribution

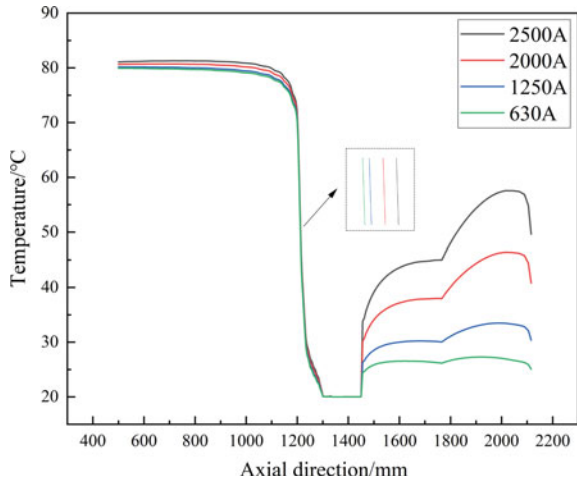
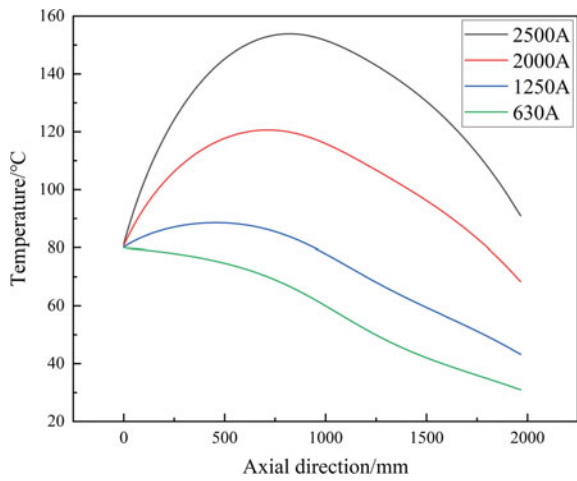
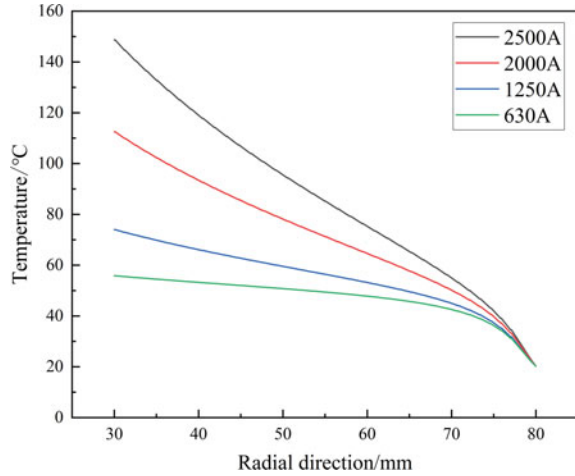


Fig. 10 Inner core temperature distribution



**Fig. 11** Comparison of temperature distribution under different load capacity



poor, and the core hot spot temperature is the highest. The outer core along the axial temperature distribution of sudden drop phenomenon, this is because one end of the flange contact with the core, and the other end directly contact the outside air, and the flange is metal, high thermal conductivity, play a good role in heat conduction.

Figure 11 shows the radial temperature distribution inside the capacitor core obtained through simulation calculation. The maximum temperature of 630, 1250 and 2000 A current is obviously lower than that of 2500 A current, and the overall distribution trend is consistent. With the increase of the carrying capacity, the bushing temperature presents an upward trend and the hot spot temperature increases. When the carrying capacity of the center guide rod increases and the carrying capacity of the center guide rod of the bushing reaches 2500 A, the hot spot temperature of the bushing exceeds the national standard. The national standard requires that when the temperature of the RIP bushing reaches stability, the maximum temperature of the center conductor is lower than 120 °C. In this study, when the bushing carrying rate is 2500 A, the temperature distribution inside the bushing does not meet the national standard, so the internal core structure of the high pressure bushing should be further optimized.

## 5 Conclusion

Taking 110 kV RIP bushing as the research object, the electric field distribution and temperature field distribution of RIP bushing were studied by electromagnetic, thermal and fluid coupling field analysis method. The main conclusions are as follows:



- (1) The design of multilayer boards has a uniform electric field effect on the RIP bushing, and the electric field intensity of the bushing capacitor core is distributed in a U-shape, with a maximum electric field intensity of 1.69 kV/mm, appearing near the guide rod.
- (2) The temperature distribution of the bushing is high in the middle and lower parts along the axial direction, and low at both ends. The radial direction is high in the middle and low at both ends. The highest temperature occurs in the middle and lower part of the central current-carrying guide bar. Due to the design of air gap, the temperature of the outer conductor is reduced by 10°C compared with that of the inner conductor.

## References

1. Xiang L (2022) Study on dynamic thermal characteristics model and temperature prediction of high pressure casing defects on the side of rheological valve. *Transformer* 59(10):48–54 (in Chinese)
2. Qian W (2020) Research on distribution characteristics and optimization method of electric heating field in valve side sleeve of UHV converter transformer. Tianjin University (in Chinese)
3. Zhang S (2021) Theoretical calculation model of insulation medium and eddy current heating under complex waveform of  $\pm 800$  kV convertor transformer RIP bushing used in valve side. *J Phys Conf Ser* 1906(1):012057
4. Wang Q (2017) A novel dissipating heat structure of converter transformer RIP bushings based on 3-D electromagnetic-fluid-thermal analysis. *IEEE Trans Dielectr Electr Insul* 24(3)
5. Liu P (2019) Research on the deterioration process of electrical contact structure inside the  $\pm 500$  kV converter transformer RIP bushings and its prediction strategy. *IET Gener Transm Distrib* 13(12)
6. Chen M (2020) Influence of material volume conductivity on electric field and surface charge of RIP valve-side bushing core under DC electrothermal coupling stress. *IEEE Trans Dielectr Electr Insul* 27(1):164–171
7. Qichang L (1981) Principles of electrical insulation structure design. Mechanical Industry Press, Beijing, vol 2 (in Chinese)
8. Yang H (2020) Dielectric and thermal conductivity characteristics of epoxy resin-impregnated H-BN/CNF-modified insulating paper. *Polymers* 12(9):2080
9. Jyothi NS (2010) Temperature distribution in resin impregnated paper insulation for transformer bushings. *IEEE Trans Dielectr Electr Insul* 17(3):931–938
10. Xie G (2022) Simulation and experimental analysis of three-dimensional temperature distribution of  $\pm 400$  kV converter transformer valve-side resin impregnated paper bushing under high current. *16(15):2989–3003*
11. Yang J, Three-dimensional simulation of electric field distribution in  $\pm 800$  kV converter transformer bushing. *Hydropower Energy Sci* 36(09):188–191 (in Chinese)

# Simulation Analysis of Mechanical Properties of Grafted Polypropylene Cable



Xinhua Dong, Yuxiao Zhou, Changlong Yang, Huajun Wu, Weigang Zheng, Tao Li, Xuchen Lu, and Jinliang He

**Abstract** Polypropylene (PP) is an excellent environmental-friendly cable insulation material with a high melting point, low density, excellent electrical insulation properties, and recyclability. The mechanical properties of PP have an essential influence on its application in cable insulation and play an important role in determining the use of cable. The mechanical properties of the material are usually evaluated using film samples, but they are significantly different from those of actual cable. This paper simulated and analyzed the mechanical properties of pure PP and grafted PP cable insulation materials to compare the mechanical properties of the two insulation materials in cable use. The simulation results showed that the stress and strain of different parts of the cable were different in the force process, and the stress distribution of cable insulation in different radial positions was uneven. The simulation has given a good indication of the stress on the various parts of the cable during deformation, with the surface layer requiring higher mechanical properties due to the more significant deformation. Considering the maximum deformation of the cable during manufacture and use, the stress on the cable was calculated for both insulation materials, and the distribution was analyzed. This study provides a good basis for the development and application of grafted PP cable.

**Keywords** Grafting modification · Polypropylene · Mechanical properties · Stress-strain · Simulation

---

X. Dong (✉) · J. He  
Tsinghua University, Beijing 100084, China  
e-mail: [dongxinhua@163.com](mailto:dongxinhua@163.com)

Y. Zhou · W. Zheng · X. Lu  
Electric Power Research Institute of State Grid Liaoning Electric Power Co., Ltd.,  
Shenyang 110006, Liaoning, China

C. Yang  
State Grid Shenyang Electric Power Supply Company, Shenyang 110003, Liaoning, China

H. Wu · T. Li  
State Grid Liaoning Electric Power Co., Ltd., Shenyang 110000, Liaoning, China

## 1 Introduction

Due to its advantages such as large transmission capacity, long distance, land saving, low loss, environmental friendliness, etc., high-voltage direct current (HVDC) cables have become an important development direction of power systems and have received more and more extensive applications and attention [1, 2]. Cross-linked polyethylene (XLPE) is currently the most widely used insulation material for HVDC cables. With the widespread application of XLPE HVDC cables, its problems have become increasingly prominent. As a thermosetting material, XLPE can only be incinerated after cable retirement, causing serious environmental pollution and not in line with the development concept of green environmental protection [3]. At the same time, XLPE cables will produce cross-linking by-products during the manufacturing process, forming impurities inside the material and reducing the insulation performance of the material. Therefore, developing a new type of cable insulation material that is recyclable and free of cross-linking to replace existing XLPE has become an important research direction for cable insulation.

Polypropylene (PP), as a thermoplastic material, has the advantages of no cross-linking and degassing treatment, no introduction of cross-linking by-products, and recyclability. At the same time, its excellent insulation performance and thermal performance have become a new type of environmentally friendly cable insulation material that can replace XLPE cable insulation. As a semi-crystalline polymer, PP has poor toughness and high rigidity. In order to improve the mechanical properties and insulation properties of materials, many modification methods have been adopted. The most commonly used methods currently include blending, doping and grafting [4–6]. Blending modification can improve the mechanical properties of PP but will cause a decrease in its insulation performance, and its melting temperature will also decrease, which is not conducive to use at high temperatures. Chemical grafting can improve the microstructure and charge transfer process of polymers by introducing polar groups, thereby improving the insulation performance of PP. Compared with nano-doping, grafted PP has more excellent insulation performance and no agglomeration problem. It is more suitable as a cable insulation material. Zheng et al. used ABAQUS finite element analysis software to simulate and analyze the crack propagation of metallurgical composite bimetallic pipes [7]. Zhang et al. simulated buried pipelines through ABAQUS finite element analysis software [8]. Currently, ABAQUS has been widely used in the analysis of complex mechanical systems [9–11].

Currently, research on PP mainly focuses on insulation performance, and research on mechanical properties is relatively rare. This article uses ABAQUS finite element software to analyze the maximum deformation bending of pure PP and styrene (St) grafted modified PP high-voltage cables during use. The stress–strain situation during the bending process of the two cables was compared by the ABAQUS four-point bending simulation model, and the stress situation in different parts was characterized and analyzed.

## 2 ABAQUS Analysis Model

### 2.1 Cable Simulation Model

Taking 110 kV cable as the research object, the conventional product size parameters that meet the standard ICS 29.060.20 are used. The conductor nominal radius is set to 20 mm, and the insulation nominal thickness is set to 18.5 mm. The bending radius is set to 15 times the cable diameter. This article mainly studies the mechanical properties of pure PP and St grafted PP insulation cables during bending. From the perspective of not affecting the analysis results and saving calculation time, the cable structure is reasonably simplified: the cable insulation core is equivalent to a solid copper column, and the conductor shield and insulation shield are incorporated into PP insulation. Three-point bending and four-point bending tests are commonly used to assess bending performance. The three-point bending test is simple to operate but has an obvious pressure head effect; in the four-point bending test, the ideal bending section is between the two heads, which can effectively reflect the real stress state of the cable. This article uses a four-point bending model to study the bending performance of PP cable insulation. As a result, the cable simulation model and structural parameters are shown in Fig. 1 and Table 1.

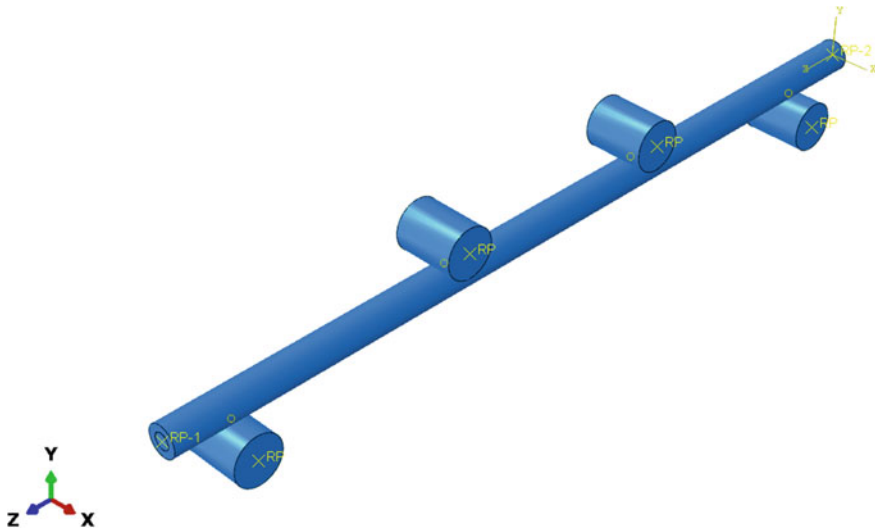


Fig. 1 Cable simulation model

**Table 1** Structural parameters of simulation model

	Structure	Thickness/(mm)	Outside diameter/(mm)	Length/(mm)
Simulation model	Cable core	–	20	2000
	PP insulation	18.5	37	2000

## 2.2 Mechanical Parameters of Materials

The elastic modulus and stress–strain relationship of pure PP and St grafted PP were obtained by tensile test, as shown in Table 2.

In order to eliminate the influence of cross-sectional changes of specimens during tensile testing, it is necessary to convert the engineering stress–strain data obtained from tensile testing into true yield stress–plastic strain data. The plastic parameters of pure PP and St-grafted modified PP are shown in Table 3.

**Table 2** Elastic parameters of materials

Materials	Elastic modulus/MPa	Elongation at break
Pure PP	1550.55	282.67
St grafted PP	389.69	1029.11

**Table 3** Plastic strain parameter

Material	True stress/MPa	True plastic strain	Material	True stress/MPa	True plastic strain
Pure PP	6.32	0	St grafted PP	4.720	0
	30.74	0.2559		20.04	0.1845
	38.13	0.4645		28.08	0.3516
	46.49	0.6349		32.41	0.4911
	56.07	0.7749		37.34	0.6094
	62.40	0.904		42.14	0.7127
	70.03	1.0141		46.81	0.8045
	78.11	1.112		51.19	0.8872
	86.12	1.2003		55.59	0.9618
	92.30	1.2818		60.07	1.0294

### 3 Finite Element Simulation and Analysis

ABAQUS/Standard is used to analyze the cable strain when the cable is at rated displacement. Figure 2 shows the deformation process of pure PP insulated cables. It can be seen that when there is no external force at the beginning, the cable is a symmetrical structure and is in a free state. After being subjected to pressure head action, the cable begins to bend downward. In the four-point bending test, there is still a pressure head effect, which causes large local deformation at that point; and the constant bending moment in the area between the two indenter can be regarded as the ideal bending section, so the deformation state of the ideal bending section of the cable is analyzed.

#### 3.1 Analysis of Strain Results

Equivalent plastic strain is used to measure the degree of insulation deformation during cable bending. Figure 3 shows the equivalent plastic strain distribution of pure PP under the specified bending radius and the variation of equivalent plastic strain with time at the position above and side of pure PP cable. It can be seen that the distribution of equivalent plastic strain of cable insulation during bending process of pure PP cable is uneven and wave-like. The maximum equivalent plastic strain is distributed on the compressed side above the cable and the tensile side below the cable, while the equivalent plastic strain on both sides of the cable is very small. The maximum value is located at the top of the cable, which is 0.045; The minimum value is located at the side position of the cable, which is 0.0072.

Simultaneously characterizes the degree of deformation of St-grafted modified PP cable during use. Figure 4 shows the equivalent plastic strain distribution of St grafted PP under the specified bending radius and the variation of equivalent plastic strain with time at the position above and side of pure PP cable. It can be seen that

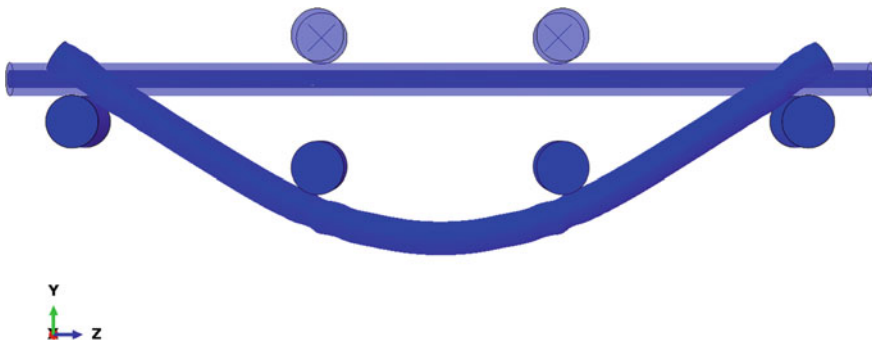


Fig. 2 Deformation process of four-point bending cable

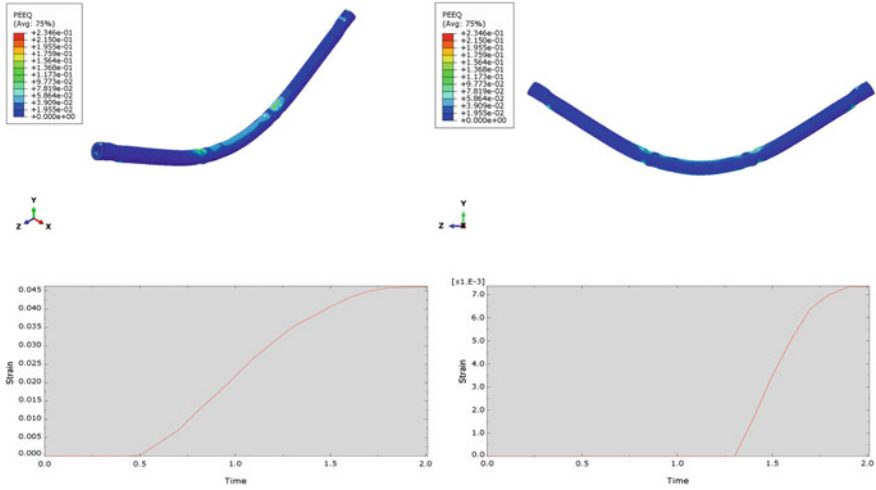


Fig. 3 Equivalent plastic strain of pure PP and variation with time

the distribution of equivalent plastic strain of cable insulation of St-grafted modified PP cable is also uneven and wave-like during the bending process. The maximum equivalent strain is distributed on the compressed side above the cable and the tensile side below it, while the equivalent plastic strain on both sides of the cable is very small. The maximum value is located at the top of the cable, which is 0.018; The minimum value is located at the side position of the cable, which is 0.0011. It indicates that in the bending process, the center part of St-grafted modified cable is also prone to deformation, and it is also the position where deformation is largest, which is the best position to characterize mechanical properties during cable use.

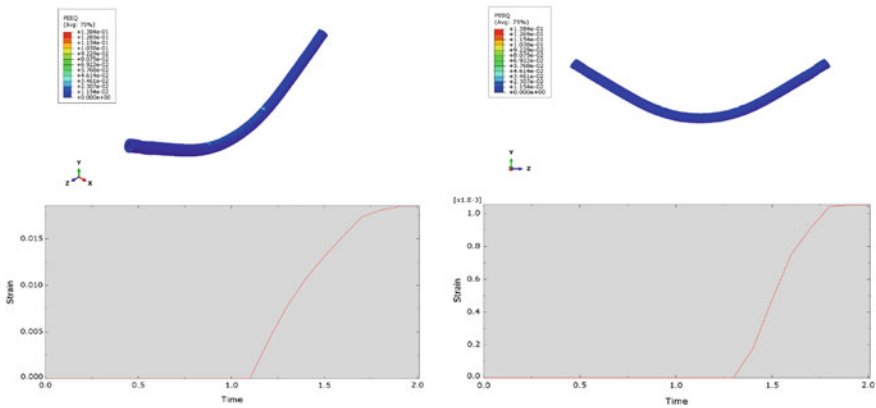
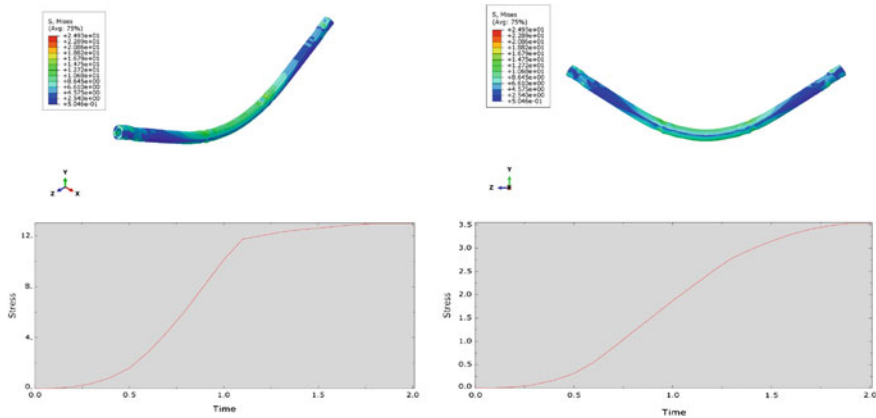


Fig. 4 Equivalent plastic strain of St grafted PP and variation with time



**Fig. 5** Equivalent stress of Pure PP and variation with time

### 3.2 Analysis of Stress Results

Use equivalent stress to measure the strength and usability of the insulation layer when the cable is bent. Figure 5 shows the equivalent stress of pure PP cable insulation under the specified bending radius and the equivalent stress changes with time at the position above and side of pure PP cable. It can be seen that the stress distribution of the cable insulation during bending of pure PP cable presents a wavy and uneven distribution. The maximum equivalent stress is distributed on the compressed side above the cable and the tensile side below the cable, while the equivalent stress on both sides of the cable is very small. The maximum value is located at the top of the cable, which is 14.5 MPa; The minimum value is located at the side position of the cable, which is 3.4 MPa.

At the same time, it characterizes equivalent stress in St-grafted modified PP use process. Figure 6 shows the equivalent stress of St grafted PP cable insulation under the specified bending radius and the equivalent stress changes with time at the position above and side of pure PP cable. It can be seen that during bending process, St-grafted modified PP cable insulation presents a wavy and uneven distribution of stress distribution. The maximum equivalent strain distribution is located on the compressed side above and tensile side below of cable, while equivalent stress on both sides of cable is very small. The maximum value is located at top of cable which is 11.5 MPa; The minimum value is located at side position of cable which is 1.8 MPa. It shows that in bending process, center part of St-grafted modified cable also becomes a stress concentration area, and is the best position to characterize mechanical properties during cable use.



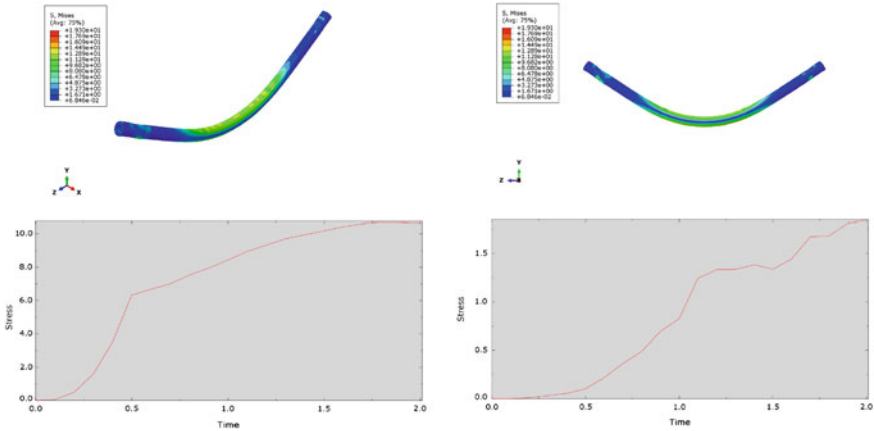


Fig. 6 Equivalent stress of St grafted PP and variation with time

### 4 Conclusion

The mechanical properties of polypropylene have an important influence on its application in cable insulation, and play a crucial role in the use of cables. Therefore, in order to further improve the mechanical and insulation properties of PP cables, it is necessary to study the mechanical properties of cables and the stress–strain situation under bending. In the analysis, ABAQUS finite element analysis software was used to analyze the bending of pure PP and St grafted PP cables. The maximum equivalent plastic strain of pure PP and St grafted PP cable is located above the cable, and the minimum value is located at the side of the cable. The maximum equivalent stress of pure PP and St grafted PP cable is also located above the cable, and the minimum value is located at the side of the cable. When St grafted PP cable is bent, its stress is smaller, which is more conducive to use and laying construction.

**Acknowledgements** This work was supported by the Science and Technology Project of State Grid Corporation of China under grant number 5500-202228113A-1-1-ZN.

### References

1. Zhou Y, Peng S, Hu J et al (2017) Polymeric insulation materials for HVDC cables: development, challenges and future perspective. *IEEE Trans Dielectr Electr Insul* 24(3):1308–1318
2. Chen G, Hao M, Xu Z et al (2015) Review of high voltage direct current cables. *CSEE J Power Energy Syst* 1(2):9–21
3. Dong X, Hu S, Huang S et al (2022) The radial gradient effect of grafting modified polypropylene cable in insulation properties. In: 2022 IEEE international conference on high voltage engineering and applications (ICHVE). IEEE, Chongqing, pp 1–4

4. Dang B, He J, Hu J et al (2016) Large improvement in trap level and space charge distribution of polypropylene by enhancing the crystalline-amorphous interface effect in blends. *Polym Int* 65(4):371–379
5. Zhou Y, Hu J, Dang B et al (2016) Mechanism of highly improved electrical properties in polypropylene by chemical modification of grafting maleic anhydride. *J Phys D-Appl Phys* 49(41):415301
6. Liang Y, Liu L, Zhang W et al (2020) Preparation and electrical properties of 4-acetoxystyrene grafted polypropylene for HVDC cable insulation. *J Mater Sci Mater Electron* 31(5):3890–3898
7. Zheng L, Li C, Zhao L et al (2010) Simulation and analysis on crack propagation of bimetallic tube based on ABAQUS. In: 2010 international conference on measuring technology and mechatronics automation. IEEE, Changsha, pp 358–361
8. Zhang W, Guo Y, Dai Y et al (2022) Research on seismic capacity of buried pipelines based on ABAQUS. In: IPEC2022: 2022 3rd Asia-Pacific conference on image processing, electronics and computers. IPEC, Dalian, pp 202–205
9. Zeng Y, Wang S, Xue X et al (2023) Fatigue life evaluation of orthotropic steel deck of steel bridges using experimental and numerical methods. *Sustainability* 15(7):5945
10. Zhang T, Li L, Du A et al (2022) Research on anchor damage and protection of three-core composite submarine cable considering impact angle. *Ocean Eng* 265(1):112668
11. Tian Y, You H, Li Z et al (2022) Analysis of nonlinear deformation relationship between steel-plastic grid and membrane structure based on Abaqus software. In: 2022 3rd international conference on computer vision, image and deep learning & international conference on computer engineering and applications (CVIDL & ICCEA). IEEE, Changchun, pp 1075–1078

# Analysis on Surge Characteristics and Protection for Wind Turbines Based on ATP-EMTP Simulation



Haoen Li, Ruanming Huang, Fei Fei, Shenhui Hua, Jiafeng Gu, and Zhenyu Pang

**Abstract** The surge generated by lightning strike blade will impact the electrical system of wind turbine. When the traditional voltage limiting surge protective device (SPD) is used in PWM wave instability and long cable effect, the frequent repeated temporary overvoltage will lead to the phenomenon of sharp reduction in the life of SPD. Therefore, the MW wind turbine is used as the simulation model to analyze the expected surge characteristics at the converter position of the fan electrical system under the condition of lightning strike fan blade. Based on ATP-EMTP simulation, the operation characteristics of the traditional voltage limited SPD selection scheme and the optimized selection scheme under the condition of harmonic oscillation are verified and compared. It is proved that the optimized scheme is feasible to realize fine protection and high tolerance in the case of repetitive transient.

**Keywords** Surge protection · Wind turbine generator · SPD · Transient interference

## 1 Introduction

With the depletion of traditional energy and environmental degradation, countries around the world are increasing their development of clean and renewable energy. Wind energy has the advantages of convenient access and high energy density, and plays an important role in new Energy development. For example, in recent years, China has implemented the “carbon neutral” plan after the “rush to install” on land and sea, wind turbines and photovoltaic power generation will play an important role in the future renewable energy field [1].

---

H. Li · R. Huang · F. Fei · S. Hua · J. Gu  
Planning Center State Grid Shanghai Municipal Electric Power Company, Shanghai, China

Z. Pang (✉)  
Shanghai University, Shanghai, China  
e-mail: [870521660@qq.com](mailto:870521660@qq.com)

Wind turbines are usually located in open areas or prominent areas to make better use of wind resources. Based on circuit theory, the lightning current distribution on the tower of a lightning struck wind turbine was studied, and the impact of lightning current on the spatial distribution of electromagnetic fields near the tower was considered. Analyzing the wave process of lightning waves invading the transformer by considering the self inductance of the internal windings and the distributed capacitance between them [2]. Lightning electromagnetic pulse will threaten sensitive electrical systems. Installing appropriate lightning arrester (SPD, also known as surge protective device) is the most economical and reasonable protection method at present, which can effectively protect power supply and communication systems.

Pulse width modulated (PWM) rectangular voltage produced by the converter's insulated grid bipolar transistor (IGBT), it is transmitted to the generator via a cable from the tower to the cabin [3, 4]. The high-frequency overvoltage damping oscillation (transient, usually kHz) with large peak value and steep rise times generated by the voltage reflection phenomenon will affect the generator, converter and other terminal equipment. According to the standard, the PWM peak value between L-PE [5] can reach 1.75 kV, the wind turbines of DFIG and PMSG types need to be considered under this transient [6, 7].

According to the existing research on SPD, metal oxide varistors (MOVs) are more likely to enter the safe failure mode under repeated transient conditions [8], resulting in the gradual degradation of MOVs, and eventually leading to flashover and other problems [9]. SPD is usually set at the junction of wind turbine lightning protection zones, and multi-level surge protection devices are installed for power and signal lines to shunt and clamp overvoltage, ultimately limiting overvoltage below the equipment's withstand overvoltage level. Existing conditions such as internal heat disconnection of the main power distribution circuit can be accepted to ensure SPD safety. Therefore, it is clearly required that when SPD is superimposed on the working voltage, the maximum continuous working voltage  $U_c$  should be selected to withstand the repeated transient stress [10]. Therefore, both  $U_c$  and  $U_p$  need to be considered when selecting SPD. Following the basic principles of the standard may make the lower life [11, 12].

The main focus of this article introduces typical wind machine blades are applied to the surging characteristics of the power supply system under the condition of lightning and hitting the current, explaining the surging distribution of different regions in different regions, analyzes difference of the function of surge protected of SPD use standard  $U_c$  and highly recommended  $U_c$  for repetitive transients, then puts forward suggestions on the selection of wind turbine SPD.

## 2 Wind Turbine and Surge Model

### 2.1 Wind Turbine Model

When the blade of the fan is attacked by lightning strikes, because the length of the leaves is much higher than the radius, it is equivalent to one drainage conductor during modeling. Not higher than the upper limit of the lightning current, as of 1/10 of the wavelength corresponding to the frequency. Considering that the rotation factor of the blades will affect the capacitors and inductance parameters in the  $\pi$ -type coupling circuit, according to the definition of wave resistance [13], the rotation of the paddle wave waves will also change with the rotation of the paddle. Therefore, in order to ensure the accuracy of the padget model, the rotation of the paddle, the height of the tower, and the length of the paddle leaves need to be considered.

When the paddle leaves are hit by lightning, the lightning current will pass along the paddling leaves to the tail, and then reach the tower through the main axle, brush, and slip ring flowing through the cabin. Due to the oil membrane effect produced by lightning current, the axis is capacity [14].

It can be considered that the tower is a vertical cylinder. Lightning current can be equivalent to the flow of spherical waves when passing through the tower, similar to the wave flow of the cone antenna [15]. LEMP transients are generated on transmission lines.

When designing a fan system grounding system, the method of calculating DC ground resistance or industrial -frequency ground resistance is used. The electrical resistance component in the resistance is zero or small. However, for the lightning current, due to the short duration and the high steepness of the current wave, it will cause a significant increase in electrical resistance, which makes the impact ground resistance value greater than DC and industrial-frequency ground resistance.

### 2.2 Surge Model

Heidler model [16] is a matching model to study the first return stroke process of a lightning stream. This location, which often occurs at the tip of the blade and carries the highest risk of direct lightning stroke, is usually defined as a Level 0 lightning protection zone.

$$i(t) = kI_m \frac{\left(\frac{t}{t_1}\right)^n}{1 + \left(\frac{t}{t_1}\right)^n} e^{\left(-\frac{t}{t_2}\right)} \quad (1)$$

Of these,  $I_m$  a peak current, the rough range is 2–300 kA,  $k$  is the modifiers of the current peak,  $t_1$  is the time of the time before the wave,  $t_2$  the time spent from 0 to the peak; The current attenuation to half of the peak values takes time. According to

the national standard GB 50,057–2010,  $n$  is the steepness factor of the current, and the general value is generally 2 or 10.

### 2.3 Mathematical Model of Surge Protective Device (SPD)

In order to simply compare the lightning protection effect of SPDs, this paper only analyzes the converter side of generator. The nonlinear properties of the piezoresistor are as follows [17]:

$$i_b = p \left( \frac{U}{U_{ref}} \right)^q \quad (2)$$

where,  $i_b$  represents pulse current, kA.  $p$  and  $q$  are character-fitting constants, excluding dimensions. The model is simpler than IEEE.

In order to better withstand the impact of repetitive transient overvoltage or interference spike, it is recommended to use SPD with higher  $U_c$  level. The existing test of 2.5 MW wind turbine converter and the comparative study of simulation results under different MOV levels show that the expected life of SPD at  $U_c = 750$  Vac is far lower than that at  $U_c = 1000$  Vac due to the influence of transient voltage.

## 3 Surge Characteristics of Wind Turbines When Lightning Strikes

The simulated lightning current of 200 kA applied on the blade meets the LPLI level of IEC61400-24, and the typical impact lightning current waveform is 10/350  $\mu$ s. The injection position is at the tip of any of the three blades, and the probe is set at the position of the shield wire and the tower base of the distribution line to monitor the surge characteristics.

In order to generate more accurate repetitive transient overvoltage on the power generation side of the converter, the circuit models of the converter and transformer with control are established respectively. The model includes the transient analysis of the output control unit of the control system (TACS), transformer, switch circuit object and line cable assembly (LCC).

### 3.1 Surge Characteristics Without SPD

The lightning current oscillation trend as a whole and gradually decreases, lasting about 0.8 ms before returning to a stable state. Each oscillating the waveform lasts

about 20 h. Many subsequent surges, close to  $8/20 \mu\text{s}$  Typical induced overvoltage of s current.

The tower base is the main discharge path of lightning current, and the shield wire and distribution line also have large surge current, but it is lower than the tower base. From the probe data.

The possible solutions are as follows: The typical mode of SPD protection for sensitive equipment selected should conform to the appropriate type 2 discharge current, corresponding to the nominal and maximum discharge capacity ( $I_n$  and  $I_{\text{max}}$ ) of SPD. Because the set value is 200 kA, the frequency of occurrence is very low (less than 1%), so 64.6 kA is also the extremely high expected current value in the converter. In general, the SPD's  $I_{\text{max}} = 40 \text{ kA}$  or even slightly lower is acceptable. The greater the  $I_n$  and  $I_{\text{max}}$ , the higher the safety factor.

Repeating transient is another important factor affecting SPD for surge protection of wind turbines. Under ideal modeling conditions of 0.1 and 1.5 s, the repetitive transient state of 1140 Vac power system can reach 1.5 kV. Based on system and monitoring data, the actual data can reach 2.5 kV or even higher peak value.

As mentioned above, SPDs with lower  $U_c$  will continue to suffer from repeated transient overvoltages, and their deterioration state will accelerate and rapidly change into failure mode. Therefore, consideration needs to be given to the introduction of  $U_c$  high SSDs to extend service life.

### ***3.2 Surge Characteristics of Installed SPD***

After setting a 3-pole SPD with  $U_c = 750 \text{ Vac}$  for each phase, the lightning current discharge detected at the SPD position reaches 63.5 kA, indicating SPD has become a major discharge path, and there is almost no current intrusion into the converter. Even if  $U_p$  is applied to the protection device, the impact current can be accepted to discharge according to the designed SPD path.

Because the higher the residual voltage is, the higher the  $U_p$  is. To achieve accurate protection, it is necessary to monitor the remaining voltage between the power supply and the ground. At a peak value 63.5 kA, the remaining voltage drops to 5.3 kV. The remaining voltage needs to be considered whether the inverter has been subjected to equipment anti-jamming test and pressure tolerance level. SPD reduces surge voltage by 68.3% compared to 16.7 kV without SPD protection.

### ***3.3 SPD Performance Under Repeated Transient Overvoltage***

The repetitive peak value of SPD can reach 1.5 kV, but the SPD with  $U_c = 750 \text{ Vac}$  usually degrades to a certain extent after withstanding the transient voltage of more than 1350 V. The higher the value or the longer the duration, the more serious the degradation, and eventually the SPD will soon enter the failure mode and end its life.

In order to have a better tolerance level under transient conditions, following the rules recommended by IEC standards, the SPD with  $U_c = 1000$  Vac. Set up two Series MOVs equivalent to “34S821K” or one with “34S162K” is located in the model, the leakage current presents a very low level, the max monitoring value is 16  $\mu$ A. Compared with low  $U_c$ , it can extend the expected service life of SPD (without considering lightning strike conditions).

## 4 Conclusions and Recommendations

Through systematic simulation, first of all, a typical lightning stroke is applied to the modeling blade of the wind turbine. Surge currents are distributed differently in different environment, and the waveform shows oscillation attenuation. The expected surge amplitude is simulated to further analyze the appropriate surge protection scheme. Secondly, the general SPD scheme and the optimized SPD scheme under repeated transient overvoltage are compared and analyzed, and the response characteristics and expected life of SPD are clarified, so that a more optimized SPD selection scheme can be realized through the simulation template of ATP-EMTP.

On the main control side of the wind power generator unit, the voltage is relatively stable and the interference is small. The voltage sensitive voltage of the SPD of the fan crew can be selected 690 V. On the side of the variable device, the voltage interference is large, and the voltage sensitivity of the SPD of the fan generator unit SPD The voltage can be selected 1053 V or 1225 V. During the design process of the SPD of the fan generator set, the length of the cable can be leaked by more energy at the first level of SPD to protect the back -end devices well, but The first -level SPD leaks too much energy will shorten the service life of the first -level SPD, so the length of the cable needs to be discounted during design.

## References

1. Du X, Xu T, Bao Y, Wu F, Ren X, Zhang J (2022) The analysis of the transient synchronization stability margin based on doubly-fed wind turbine. In: 2022 5th international conference on power and energy applications (ICPEA), Guangzhou, China, pp 190–195
2. Liang J, Qiao W, Harley RG (2009) Direct transient control of wind turbine driven DFIG for low voltage ride-through. In: 2009 IEEE power electronics and machines in wind applications, Lincoln, NE, USA, pp 1–7
3. Malcolm N, Aggarwal RK (2012) Transient overvoltage study of an Island wind farm. In: 2012 47th international universities power engineering conference (UPEC), Uxbridge, UK, pp 1–6
4. Mehrshad M, Effatnejad R, Mohammadpour A (2014) Transient simulation of fixed-speed wind turbine with grid fault variety in real wind farm. In: 2014 IEEE 23rd international symposium on industrial electronics (ISIE), Istanbul, Turkey, pp 248–253
5. EN CLC/TS (2010) Low-voltage surge protective devices—surge protective devices for specific application including d.c. In: Part 22: selection and application principles—wind turbine applications



6. Papadakis S, Perilla A, Torres JR, Ahmad Z, Meijden Mvd (2020) Real-time EMT simulation based comparative performance analysis of control strategies for wind turbine type 4 to support transient stability. In: 2020 IEEE power & energy society general meeting (PESGM), Montreal, QC, Canada, pp 1–5
7. Duong MQ, Sava GN (2017) Coordinated reactive power control of DFIG to improve LVRT characteristics of FSIG in wind turbine generation. In: 2017 international conference on electromechanical and power systems (SIELMEN), Iasi, Romania, pp 256–260
8. Liu Y, Wang F, Wu X (2014) Performance analysis of thermal fuses in SPD disconnector. *MeteorolSci Technol* 42(2):251–255
9. Matsui M, Sato M, Ito H, Yokoyama S, Michishita K (2012) Study on the soundness of SPD devices using data of Japanese lightning detection network. In: 2012 international conference on lightning protection (ICLP), Vienna, Austria, pp 1–5
10. Chen S, Shen L (2011) Analysis of two-stage cascade SPD coordination under the impact of lightning combination wave in 220V low-voltage distribution system. In: 2011 7th Asia-Pacific international conference on lightning, Chengdu, China, pp 335–340
11. Zhou Q, Xiao Y, Bian X, Zhang Y, Shen J, Ye J (2022) Studying of the operating mechanism of the triggering circuit inside a switching-type SPD. In: 2022 IEEE international conference on high voltage engineering and applications (ICHVE), Chongqing, China, pp 1–4
12. Sato A, Morii N, Sato H (2011) Overcurrent protection function for SPD disconnectors. In: 2011 7th Asia-Pacific international conference on lightning, Chengdu, China, pp 586–589
13. Dusonchet L, Massaro F, Telaretti E (2007) Transient stability simulation of a fixed speed wind turbine by Matlab/Simulink. In: 2007 international conference on clean electrical power, Capri, Italy, pp 651–655
14. Rongqi Z, Zhiliang T, Penghao X (2007) Research on conversion relation between square wave and ESD EMP in the electromagnetic damage of electronic devices. In: 2007 8th international conference on electronic measurement and instruments, Xi'an, China, pp 1-64–1-68
15. Soloot AH, Høidalen HK, Gustavsen B (2015) Influence of the winding design of wind turbine transformers for resonant overvoltage vulnerability. *IEEE Trans Dielectr Electr Insul* 22(2):1250–1257
16. Li W et al (2020) Transient characteristics of wind turbine grounding system in high soil resistivity area due to lightning strike In: 2020 IEEE international conference on high voltage engineering and application (ICHVE), Beijing, China, pp 1–4
17. Chinges T, Li Q, Zhao J (2022) The significance of mutual coupling on the lightning transient voltage and current of typical wind turbine under different lightning strokes. In: 2022 11th international conference on power science and engineering (ICPSE), Eskisehir, Turkey, pp 21–27

# Study on the Influence of Crosslinking By-Products on XLPE Breakdown Performance in XLPE Cables Based on the First-Principles and Band Gap Theory



Qiannan Zhao, Jin Liu, Yifei You, Shicheng Gao, and Wei Wang

**Abstract** When high voltage XLPE cables are cross-linked with dicumyl peroxide (DCP), the by-products generated by the decomposition of DCP can significantly reduce the intrinsic breakdown performance of XLPE dielectrics. To investigate the effect of crosslinking by-products on the breakdown performance of XLPE, the band gap of three typical crosslinking by-products,  $\alpha$ -methylstyrene, acetophenone and benzenemethanol, was calculated based on the first-principles and band gap theory, and the resulting data were fitted and analyzed. The results show that in the calculated field strength range, the band gap of all three decreases with increasing electric field strength, but at different rates; and the threshold values of electric field strength when the band gap of acetophenone,  $\alpha$ -methylstyrene, and benzenemethanol decreases to zero are 0.048, 0.065 and 0.068 a.u., respectively; at any electric field strength the band gap values of acetophenone are lower than the other two when the band gap decreases to zero, which has the greatest impact on breakdown and should be removed as a priority in the production process.

**Keywords** XLPE · Crosslinking by-products · The first-principles · Band gap

## 1 Introduction

In recent years, crosslinked polyethylene (XLPE) power cable is widely used because of its excellent electrical performance, processing, accessory joint making, easy installation, and other excellent characteristics [1, 2].

XLPE is crosslinked by polyethylene (PE). Dicumyl peroxide (DCP) is generally used to crosslink high-voltage XLPE cables [3, 4]. During the cross-linking process,

---

Q. Zhao · J. Liu · Y. You · S. Gao · W. Wang (✉)

School of Electrical and Electronic Engineering, North China Electric Power University, Beijing 102200, China

e-mail: [kingway@ncepu.edu.cn](mailto:kingway@ncepu.edu.cn)

© Beijing Paiké Culture Commu. Co., Ltd. 2024

X. Dong and L. Cai (eds.), *The Proceedings of 2023 4th International Symposium on Insulation and Discharge Computation for Power Equipment (IDCOMPU2023)*, Lecture Notes in Electrical Engineering 1103, [https://doi.org/10.1007/978-981-99-7413-9\\_24](https://doi.org/10.1007/978-981-99-7413-9_24)

265

DCP will decompose at high temperatures and form peroxide radicals, which, due to their high activity, will move rapidly within PE and, when they encounter the PE macromolecular chains, will seize the hydrogen atoms on the macromolecular chains, forming macromolecular chain radicals and crosslinking by-products [5]. The crosslinking by-products produced by the decomposition of DCP are usually present in the XLPE amorphous zone in the form of small molecules. The production of crosslinking by-products reduces the insulation performance of the cable and is detrimental to its reliable operation.

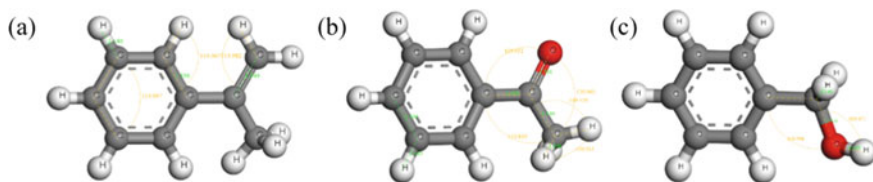
Much research has focused on the detection and reduction of crosslinking by-products, exploring the effects of crosslinking by-products on material properties from a macroscopic perspective, while there has been relatively little research on their microscopic perspective [6, 7]. With the development of recent years, molecular simulation techniques are gradually being used in the field of high voltage insulation to simulate insulating materials and to analyze their physical and chemical properties through microscopic mechanisms, mainly for the study of oil-paper insulation properties and polymer solid insulation properties [8–11]. This paper focuses on the molecular modeling of crosslinking by-products through simulation software and investigates their influence on the breakdown performance of XLPE based on the first-principles and band gap theory.

## 2 Calculation Model and Method

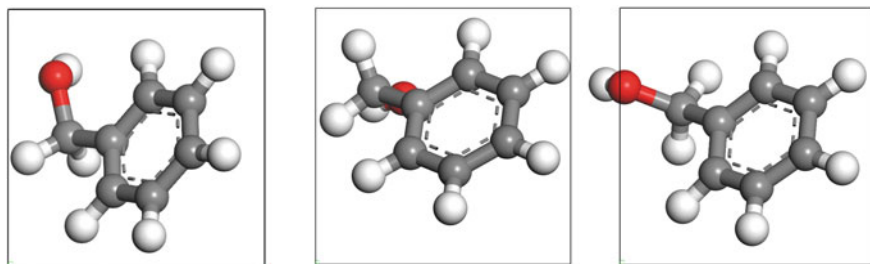
XLPE is a web-like polymer compound obtained by crosslinking quasi-one-dimensional material polyethylene in a linear structure. The insulation material of XLPE power cables is formulated by introducing small molecule additives such as crosslinking agents and anti-oxidants with a low-density polyethylene base material, so some by-products are inevitably produced during the cross-linking process.

Materials Studio is a materials science computing software that can simulate a wide range of materials such as molecules, crystals, and surfaces and provides molecular dynamics, quantum mechanics, and Monte Carlo algorithms for analyzing the physical, chemical, and mechanical properties of materials. The Visualizer module of the Materials Studio software platform was used to build a three-dimensional visual molecular model of the impurities in the amorphous zone, mainly including the molecular models of the main crosslinking by-products  $\alpha$ -methylstyrene, acetophenone, and benzenemethanol in XLPE, as shown in Fig. 1.

For the following crosslinking by-product molecules, the bond length of the C–C single bond is set to 1.54 Å and the bond length of the C–H single bond is set to 1.14 Å for the benzene ring and methyl portion shared by all three, and the symmetrical distribution of the chemical bonds in the methyl portion are all set to 110°; the bond length of the C=C double bond in  $\alpha$ -methylstyrene is set to 1.54 Å and the bond angles between the C=C double bond and the other chemical bonds are all set to 120°. The bond length of the C=O double bond in acetophenone was set to 1.51 Å



**Fig. 1** Molecular models of three typical crosslinking by-products of XLPE materials, **a**  $\alpha$ -methylstyrene, **b**, acetophenone **c**, benzenemethanol



**Fig. 2** X–Y plane views of the three amorphous cell models of benzenemethanol

and the angle between the C=O double bond and the other chemical bonds was set to  $120^\circ$ .

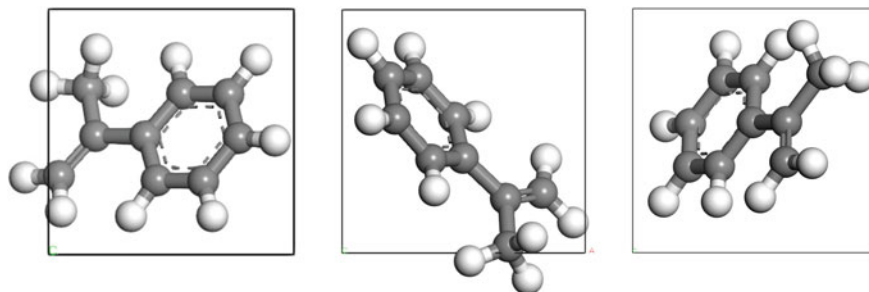
The Monte Carlo method is a numerical calculation method guided by probabilistic statistical theory, and in molecular simulation techniques the method is mainly used to simulate the random motion of molecules. By generating a molecular configuration randomly in space and then subjecting it to irregular changes and judging its acceptance or otherwise according to the Monte Carlo criterion, and so forth.

The Monte Carlo method was used to model the amorphous cells of each of the three crosslinking by-products, as shown below. In this regard, Figs. 2, 3, and 4 show three stochastic models of benzenemethanol,  $\alpha$ -methylstyrene, and acetophenone in X–Y plane view respectively.

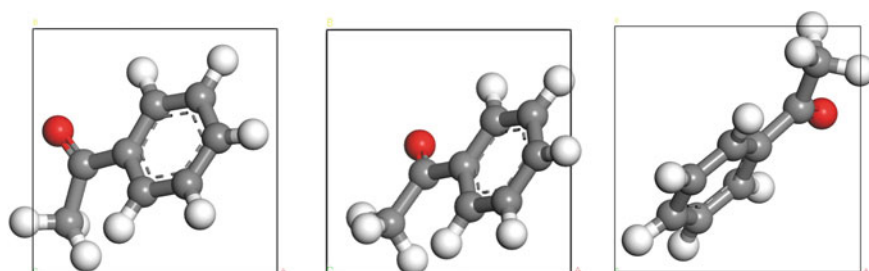
The electric field strength is then applied to the model in 0.001 a.u. steps along the z-axis and its geometry are optimized, setting the electric field strength in the range of 0.00–0.02 a.u.

### 3 Result in Analysis and Discussion

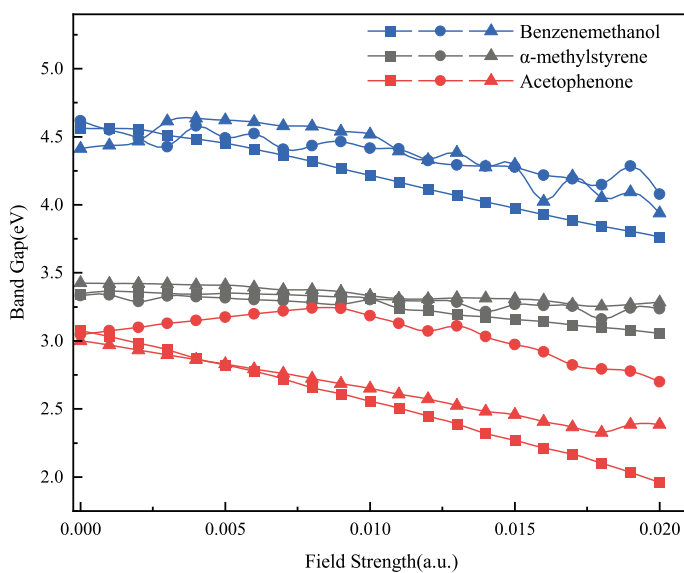
The band gap values for each crosslinking by-product in three random states were calculated separately under different electric field strengths based on the first-principles and the results are shown in Fig. 5.



**Fig. 3** X-Y plane views of the three amorphous cell models of  $\alpha$ -methylstyrene



**Fig. 4** X-Y plane views of the three amorphous cell models of acetophenone



**Fig. 5** Band gap values of three crosslinking by-products for different state models at different field strengths

For bound electrons in a solid to become free electrons or holes, they must gain enough energy to jump from the valence band to the conduction band. The energy range between the highest energy level of the valence band (top of the valence band) and the lowest energy level of the conduction band (bottom of the conduction band) is called the band gap [12]. The larger the band gap, the more difficult it is for electrons to be excited from the valence band to the conduction band, and the less conductive they are. For insulating materials, which usually have a high band gap, the magnitude of the band gap can also characterize the degree of breakdown. For example, the band gap value is zero which is when there is no energy difference between the valence band and the conduction band, the material is broken through.

When the electric field is not considered, that is the electric field strength is zero, the band gap values of the three crosslinking by-products differ significantly, with the smallest band gap value being that of acetophenone at about 3 eV; the largest band gap value being that of benzenemethanol at about 4.5 eV; and the band gap of  $\alpha$ -methylstyrene is not very different from that of acetophenone at about 3.3 eV. The forbidden bandwidth of XLPE cannot be obtained to an exact value because of its material chemical composition, degree of cross-linking, and other factors, but it often has a smaller forbidden bandwidth compared to PE. Using quantum chemistry or linear combinations of atomic orbitals, the forbidden band width of PE can be derived as 8–9 eV [13]. In contrast, the by-product acetophenone in XLPE is most likely to have an effect on breakdown.

According to the above graph, the band gap of the crosslinking by-products decreases as the electric field strength increases; and the band gap values of different molecular models of the same crosslinking by-products do not differ much in the absence of an electric field, but the rate of decrease of the band gap of different molecular models differs as the field strength increases, which may be due to the different angles between the cross-linked by-product molecules and the field strength in different molecular states. The angle between the two is also random in the actual material due to factors such as the disordered arrangement of molecules in the polymer.

Therefore, the model corresponding to the molecular state with the lowest band gap value is selected as the object of analysis, and the band gap variation curves of each of the three are fitted and analyzed at different field strengths. After fitting by the relevant software, it is found that the fitting using binomial is less error-prone. The values of the main parameters and measures of the fitted equations are shown in Table 1. The binomial fitting curves are shown in Fig. 6.

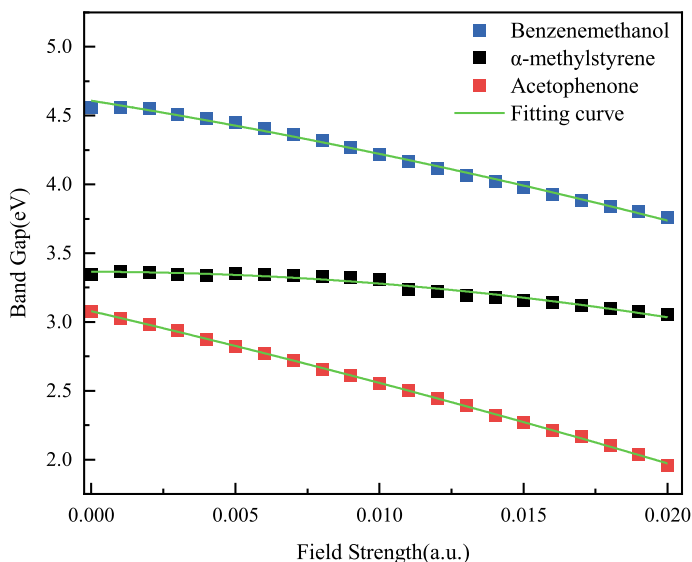
The COD is called the coefficient of determination or goodness of fit and ranges from 0 to 1. The larger the value, the better the fit. From the parameters in the above table, we can see that the OCD values of all three are close to 1 and the residuals are small.

In order to compare more intuitively the rate of change of band gap values with field strength for the three crosslinking by-products, a first-order derivative of the above-fitted curves was therefore carried out and the results are shown in Fig. 7.

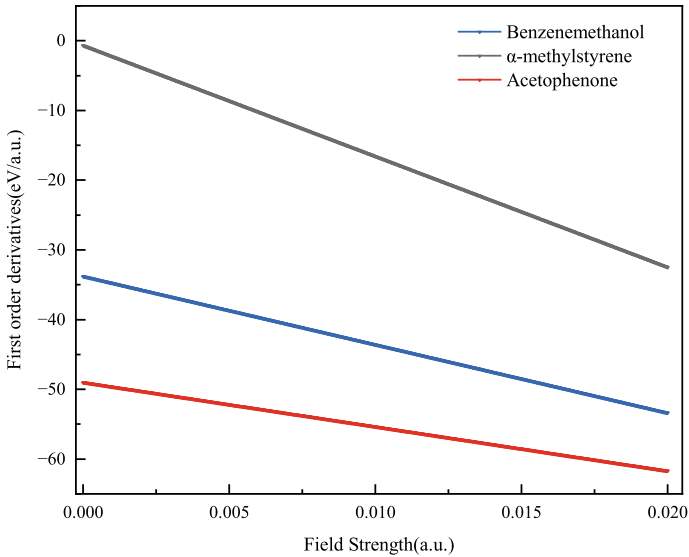
As can be seen from the above graphs, the first-order derivatives of the band gaps of the three crosslinking by-products with respect to field strength are all

**Table 1** Parameters of the binomial fit curve equation and evaluation parameters for three crosslinking by-products

Parameter	Benzenemethanol	$\alpha$ -methylstyrene	Acetophenone
Intercept	$4.6084 \pm 0.0118$	$3.3652 \pm 0.0118$	$3.0787 \pm 0.0040$
$B_1$	$-33.7702 \pm 2.7351$	$-0.6559 \pm 2.7323$	$-48.9884 \pm 0.9215$
$B_2$	$-489.8660 \pm 132.0332$	$-795.1945 \pm 131.8983$	$-317.5280 \pm 44.4811$
RSS	$7.04 \times 10^{-3}$	$7.02 \times 10^{-3}$	$7.99 \times 10^{-3}$
COD	0.9952	0.9698	0.9997

**Fig. 6** Band gap values of three crosslinking by-products at different field strengths and their fitted curves

negative over the calculated range of field strengths, meaning that the band gaps of all three decrease as the electric field strength increases. Calculations using the three fitted equations above show that the threshold values for the electric field intensity are 0.048, 0.065 and 0.068 a.u. for acetophenone,  $\alpha$ -methylstyrene and benzenemethanol, respectively, when the band gap is reduced to zero.



**Fig. 7** First-order derivatives of the fitted curves of the band gap of three crosslinking by-products with respect to field strength

## 4 Conclusion

The band gap value of acetophenone decreases the fastest and, as can be seen from Fig. 5, the band gap value of acetophenone is lower than that of  $\alpha$ -methylstyrene and benzenemethanol at zero electric field strength, that is, at any electric field strength, the band gap value of acetophenone is lower than that of  $\alpha$ -methylstyrene and benzenemethanol and, according to the above calculation, the electric field strength corresponding to a zero band gap value of acetophenone is the smallest among the three, so the removal of acetophenone should be given priority in the manufacturing process of cross-linked polyethylene.

The band gap value of  $\alpha$ -methylstyrene is much smaller than that of benzenemethanol when the electric field is not taken into account, but the band gap value of benzenemethanol decreases more rapidly and is smaller than that of  $\alpha$ -methylstyrene as the electric field strength increases. Therefore, in the manufacturing process, if the content of both cannot be reduced at the same time, the content of  $\alpha$ -methylstyrene should be reduced first to ensure that the XLPE dielectric is minimally affected.

## References

1. Liu M, Li X, Jiang X et al (2019) Study on cross-linked by-products of XLPE insulation materials for ultra-high voltage cables. *Shanghai Plast* 187(03):31–34 (in Chinese)



2. Ren H et al (2018) Influence of crosslinking byproducts on DC conductivity of HVDC XLPE cable insulation. In: IEEE conference on electrical insulation and dielectric phenomena
3. Zhang C, Wang T, Sun W, Li C et al (2021) Grafting of antioxidant onto polyethylene to improve DC dielectric and thermal aging properties. *IEEE Trans Dielectr Electr Insul* 28(02):541–549
4. Jin H, Zeng Y, Ma J et al (2019) Effect of degassing heat treatment on mechanical and dielectric properties of 110 kV AC XLPE. *Insul Mater* 52(08):24–31 (in Chinese)
5. Li F et al (2021) Electric field distribution considering the byproducts inhomogeneity of crosslinking insulation in HVDC cable. In: IEEE international conference on the properties and applications of dielectric materials
6. Zhang H, Chen M, Wang Y et al (2021) Interaction effects of three major crosslinking byproducts on space charge accumulation in polyethylene. *IEEE Trans Dielectr Electr Insul* 28(02):710–718
7. Chen M, Yin Y, Zhang H et al (2019) Effects of acetophenone on charge dynamics in low density polyethylene. In: IEEE electrical insulation conference, Calgary
8. Sun Y et al (2021) Effect of temperature varying rate on moisture migration in oil-paper insulation. In: International conference on advanced electrical equipment and reliable operation, pp 1–4
9. Liu C, Zhang H, Zhang Y et al (2023) Mechanism influence of low molecular acid on alcohol diffusion in oil–paper insulation based on molecular dynamics simulation. *IEEE Trans Dielectr Electr Insul* 30(02):744–751
10. Wang T, Li D, Hou Y et al (2020) Molecular dynamics simulation of key physical properties of graphene oxide/epoxy resin nanocomposite dielectrics. In: IEEE international conference on high voltage engineering and application (ICHVE), pp 1–4
11. Wang T, Li D, Zhang G (2021) Molecular dynamics simulations of interface properties and key physical properties of nanodielectrics manufactured with epoxy resin doped with metal nanoparticles. *IEEE Access* 9:34231–34239
12. Huang K, Han R (2018) Solid state physics. Higer Education Press (in Chinese)
13. Lei Q, Liu G (2018) How to understand the two basic physical processes of polarization and conductance in engineering dielectrics and scientific principles and methods of their measurement. *CSEE J Power Energy Syst* 38(23):6769–6789+7113 (in Chinese)

# Simulation Study on the Motion of Dust Particles in Traveling Wave Electric Curtain Photovoltaic Panel



Long Long Wang and Hai Jin

**Abstract** To reveal the mechanism of the directional transport of dust particles in the traveling wave electric field. In this paper, by establishing the mathematical model of the spatial electric field distribution above the electric curtain surface, giving the mathematical description of the spatial electric field distribution, studying the electric field distribution law of the traveling wave electric curtain, using COMSOL Multi-physics multi-physics field simulation software, coupling the results calculated in the AC/DC module to the fluid flow particle tracking module, using numerical simulation to track the particle motion, studying the effect of external applied voltage and particle diameter on particle motion is investigated. The trajectory of single particle motion at different starting positions and different electric field frequencies is studied, the conditions required for directional transport of dust particles are proposed, and the transport mechanism of traveling wave electric curtain is explained.

**Keywords** Dust particle · Traveling wave electric curtain · Particle tracking · Photovoltaic Panel

## 1 Introduction

Photovoltaic power plants are usually established in desert areas far from the crowd, where sand and dust pollution is serious, and it is easy to accumulate dust particles on the photovoltaic panels, which affects the photoelectric conversion capacity of solar photovoltaic panels and greatly reduces the power generation efficiency of photovoltaic systems [1]. At present, the main cleaning methods for dust particles on the surface of photovoltaic panels are manual cleaning method, mechanical dust removal method, robot dust removal method, self-cleaning coating method and electrostatic dust removal method, but all these cleaning methods have obvious disadvantages

---

L. L. Wang · H. Jin (✉)

College of Electrical Engineering and Information Engineering, Lanzhou University of Technology, Lanzhou 730050, China  
e-mail: [jinhai@lut.edu.cn](mailto:jinhai@lut.edu.cn)

© Beijing Paiké Culture Commu. Co., Ltd. 2024

X. Dong and L. Cai (eds.), *The Proceedings of 2023 4th International Symposium on Insulation and Discharge Computation for Power Equipment (IDCOMPU2023)*, Lecture Notes in Electrical Engineering 1103, [https://doi.org/10.1007/978-981-99-7413-9\\_25](https://doi.org/10.1007/978-981-99-7413-9_25)

273

[2]. The electric curtain dust removal technology was first proposed as a cleaning technology by Tatom et al. of NASA in 1967 for the spacecraft contaminated by moon dust in the lunar exploration project, and then NASA conducted a series of theoretical studies and test experiments to determine the feasibility of the technology [3–5].

Masuda et al. [6, 7] used a linear approximation of the equation of motion to decompose the motion of the particles into a slow motion component and a fast oscillatory motion component, and found that driven by the electric field force, the fine dust particles suspended in the air move back and forth without a net horizontal displacement and finally fall to the bottom under the action of gravity. For the traveling wave electric curtain, after the three-phase excitation source is connected, the suspended micro-dust particles have both reciprocal motion and horizontal net displacement from left to right, which confirms that the traveling wave electric curtain can effectively realize the directional transport of micro-dust particles.

Kawamoto et al. [8] used the Runge–Kutta method to solve the equations of motion and simulate the particle trajectories, and confirmed that the Coulomb force is the dominant force affecting the particle motion and that the direction of particle transport does not always coincide with the direction of traveling wave motion. Horenstein et al. [9] investigated the motion of particles of different sizes in a three-phase traveling wave curtain trajectories and observed that large particles are more prone to aggregation phenomena, while small particles move along the direction of the traveling waves, and changes in the initial position of the particles drastically alter their trajectories in the three-phase traveling wave curtain. The present study does not reveal the mechanism of the directional transport of dust particles in the traveling wave electric field.

In this paper, by establishing a mathematical model of the spatial electric field distribution above the electric curtain surface and giving a mathematical description of the spatial electric field distribution, the electric field distribution law of the traveling wave electric curtain is studied, and the results calculated in the AC/DC module are coupled to the fluid flow particle tracking module using COMSOL Multi-physics multi-physics simulation software, and the dust particle motion is tracked by numerical simulation. The effects of externally applied voltage and particle diameter on particle motion are investigated, the trajectories of single particles at different starting positions and different electric field frequencies are studied, the conditions required for the directional transport of dust particles are proposed, and the transport mechanism of the traveling wave electric curtain is explained.

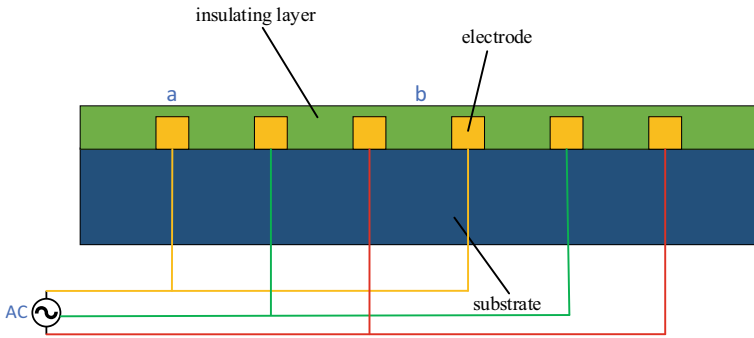


Fig. 1 Three-phase traveling wave electric curtain model structure

## 2 Traveling Wave Electric Curtain Model

### 2.1 The Traveling Wave Electric Curtain Studied

In this paper is composed of three sets of conductor electrodes etched on a dielectric substrate parallel to each other, and the traveling wave electric field is formed by connecting a three-phase alternating voltage excitation source on the electrodes. The two-dimensional model is shown in Fig. 1.  $a$  is the electrode width,  $b$  is the electrode spacing, the electrode height is  $h_1$ , the electrode surface is covered with an insulating layer, the distance from the upper surface of the insulating layer to the upper surface of the glass substrate is  $h_2$ , and the electrodes are all on the same horizontal line. From left to right, each of the three adjacent electrodes is connected to the three-phase power supply  $U, V$  and  $W$  in turn, forming a spatial cycle of the electric curtain.

### 2.2 Three-Phase Traveling Wave Electric Curtain Electric Field Distribution

As shown in Fig. 1. The  $x$ -axis is assumed to be perpendicular to the electrode axis, the  $y$ -axis is perpendicular to the plane where the electrodes are located, and the  $z$ -axis is located on the centerline of the electrodes, with the direction perpendicular to the paper facing inward. When the electrode is connected to the excitation voltage, the space free charge is distributed on the surface of the electrode, and the free charge in the outer area of the electrode is zero. The potential distribution of the electric curtain electrode excited in the external region can be expressed as:

$$\begin{aligned} \phi(x, y, t) = & U_0(\varphi(x, y) \cos(\omega t) + \varphi(x - \lambda/3, y) \cos(\omega t - 2\pi/3) \\ & + \varphi(x - 2\lambda/3, y) \cos(\omega t - 4\pi/3)) \end{aligned} \tag{1}$$

where,  $\varphi(x, y) = \sum_{n=0}^{+\infty} a_n \cos(n\alpha x) \exp(-n\alpha y)$ ,  $\omega = 2\pi f$ ,  $f$  is the frequency,  $p = a + b$ ,  $a_n$  is the coefficient of Fourier expansion and the expression of the electric field distribution generated in the upper half space is [9]:

$$E_x = -\frac{\partial\phi}{\partial x} = U_0(\cos(\omega t) + \varphi(x - \lambda/3, y) \cos(\omega t - 2\pi/3) + \varphi(x - 2\lambda/3, y) \cos(\omega t - 4\pi/3)) \sum_{n=1}^{+\infty} a_n n\alpha \cdot \sin(n\alpha x) \exp(-n\alpha y) \quad (2)$$

$$E_y = -\frac{\partial\phi}{\partial y} = U_0(\cos(\omega t) + \varphi(x - \lambda/3, y) \cos(\omega t - 2\pi/3) + \varphi(x - 2\lambda/3, y) \cos(\omega t - 4\pi/3)) \sum_{n=1}^{+\infty} a_n n\alpha \cdot \cos(n\alpha x) \exp(-n\alpha y) \quad (3)$$

### 2.3 Differential Equation of Motion of Dust Particles

In this paper, numerical simulation is used to analyze the particle motion, and in order to show the force of the particles on the surface of the electric curtain more intuitively, the figure is made assuming that the particles are regular spherical particles, and the force of their dust particles is shown in Fig. 2.

The gray sphere in the figure indicates the particle, the solid arrow indicates the direction of the force on the particle, and the dotted arrow indicates the direction of the electric field. The main forces on the particle in the alternating electric field are van der Waals force, gravity, Coulomb force, traction force, particle–particle interaction force and dielectrophoretic force, so the differential equation of particle

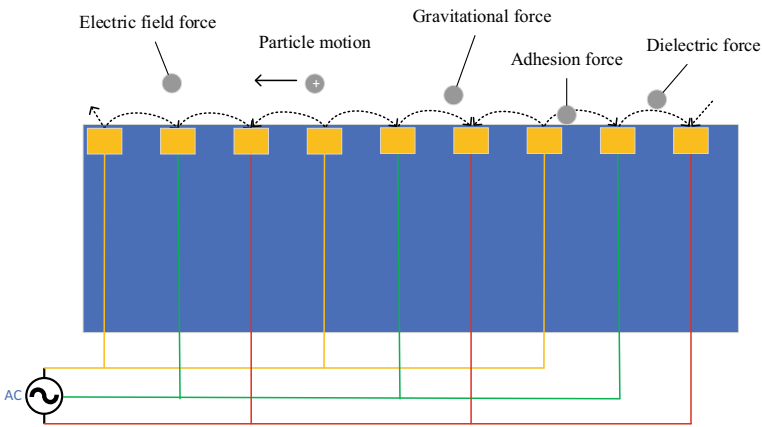


Fig. 2 Schematic diagram of the force on dust particles

motion can be calculated by Newton's second law as follows [9]:

$$\frac{d(mv)}{dt} = F_c + G + F_{drag} + F_{dep} + F_{vdw}$$

### 3 Simulation Analysis of Dust Particle Motion in Traveling Wave Electric Curtain

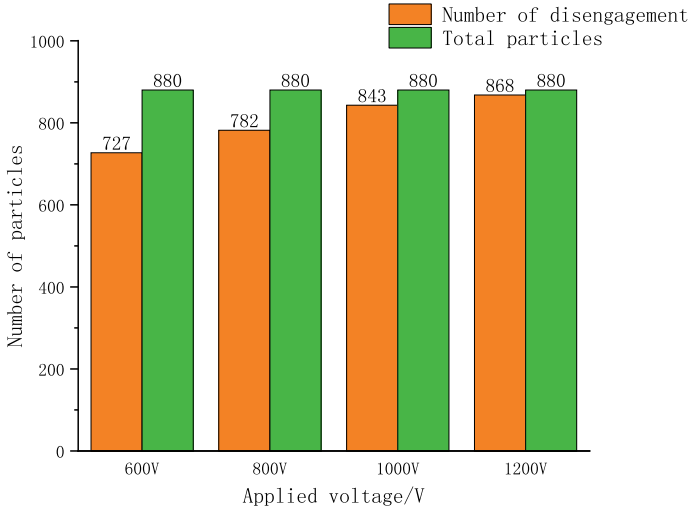
In this section, the fluid flow particle tracking module in COMSOL simulation software is introduced, and the AC/DC module and fluid flow particle tracking module in COMSOL simulation software described in the previous section are coupled with each other to analyze the force state and motion trajectory of the particles at a specific moment, and reveal the dynamic characteristics of the particles on the traveling wave electric curtain from the principle.

In COMSOL simulation software AC/DC module: electrode width  $a = 0.5$  mm, electrode spacing  $b = 1$  mm, electrode loading sine wave AC voltage signal, set AC signal frequency 50 Hz, amplitude 1000 V, phase difference  $120^\circ$ , electrical signal loading time 0–1 s. Introduce fluid flow particle tracking module: a line above the electric curtain surface is set as particle velocity entrance boundary conditions, wall conditions for crossing, dust particles uniformly distributed on the surface of the electric curtain, wall conditions on the surface of the electric curtain set to bounce, both sides and above the air domain set to particle exit boundary conditions, wall conditions for freezing, in 0–0.1 s time uniformly deposited on the surface of the electric curtain 880 velocity 0 particles, the calculation using transient solver, this section part of the parameter settings on references [2–4] have references.

#### 3.1 Effect of Voltage on Particle Movement

To investigate the effect of the applied voltage on the particle movement, the waveform is chosen as a sine wave with a frequency of 50 Hz in order to facilitate the application in engineering practice. the dust particles on the volt plate will be basically removed when the applied voltage reaches 1000 V. A simple increase in the applied voltage level in the electric curtain dust removal will additionally increase the risk of the electric curtain plate being penetrated [8] the applied voltage signals in this subsection are 600, 800, 1000, and 1200 V. the structure of the electric curtain is the same as that in Sect. 2.1, 800, 1000 and 1200 V AC voltage signals, and the electric curtain structure is the same as in Sect. 2.1.

Figure 3 counts the number of dust particles that are removed from the top of the PV panel at the moment  $t = 0.5$  s after applying voltages of different amplitudes, and the particles are considered to have been transported away from the surface of



**Fig. 3** Distribution of the number of detached particles at different voltages

the PV panel when they move to the set air domain exit (exit on both sides or above the air domain). Define the transport efficiency calculation formula:

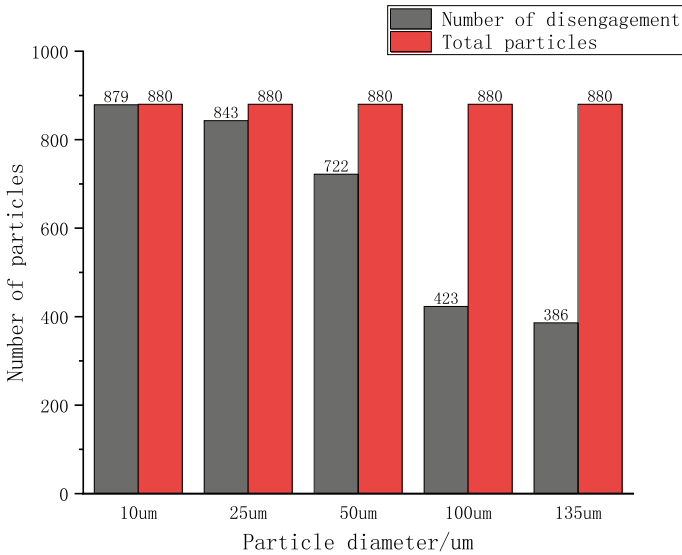
$$\zeta = n/N \times 100\% \tag{4}$$

where:  $N$  is the dust particles accumulated on the surface of the PV panel,  $n$  is the dust particles that have been removed from the outlet above the PV panel.

As the applied voltage level increases, the number of dust particles transported away from the top of the PV panel increases, and the number of particles transported away from the top of the PV panel with the applied voltage of 600 V is 727, and the transport efficiency is only 82.61%, which indicates that the electric field force formed by the applied voltage of 600 V is far from sufficient to transport all the dust particles away from the surface of the PV panel. When the applied voltage reaches 1000 V, the number of dust particles removed reaches 843, and the transmission efficiency reaches 95.80%, which indicates that the dust particles with particle diameter between 20 and 30  $\mu\text{m}$  are basically removed when the applied voltage of the traveling wave curtain reaches 1000 V.

### 3.2 *The Effect of Particle Diameter Diameter on Particle Motion*

Choose the particle diameter of 10, 25, 50, 100 and 135  $\mu\text{m}$  under five different sizes of particles to 0.1 times the positive saturation power for the initial charge of dust



**Fig. 4** Number of particles detached at different particle diameters

particles, for easy application in engineering practice, the applied voltage amplitude is taken as 1000 V, the frequency is 50 Hz, the electric curtain structure is the same as the above Sect. 2.1.

It can be seen from Fig. 4 that the number of dust particles transported away from the top of the PV panel gradually decreases as the particle diameter increases under the same conditions, and when the particle diameter is 25  $\mu\text{m}$ , the number of particles separated from the top of the PV panel is 843, and the transmission efficiency is 95.80%, while when the particle diameter is 135, the number of dust particles separated is only 386, and the transmission efficiency is only 43.86%. The above data surface in the traveling wave electric curtain when other conditions are the same, when the applied voltage is determined, the dust particles with a constant charge, with the increasing diameter of the particles, the number of particles transported away from the surface of the photovoltaic panel continues to decrease.

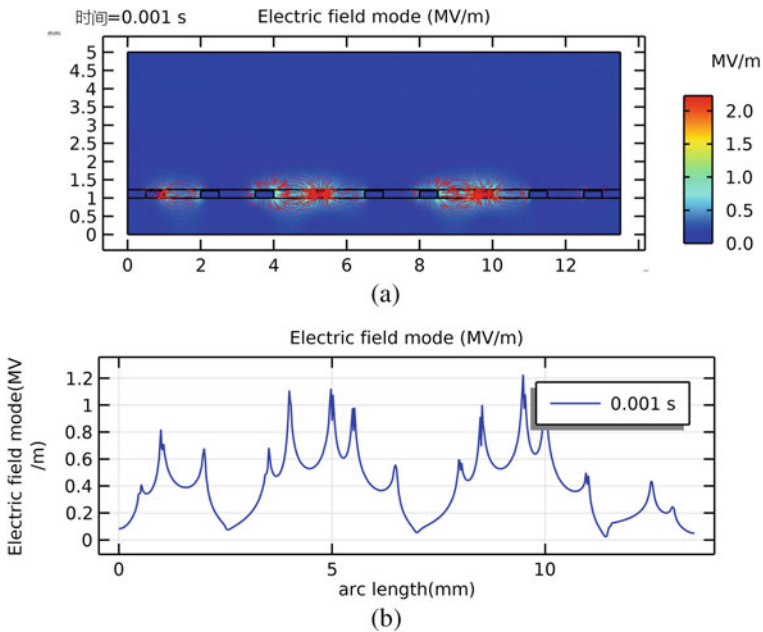
### 3.3 Effect of Initial Position on the Trajectory of Single Particle Motion

The dust particles are released at 0.001 s. Figure 5a, b shows the electric field diagram of the three-phase traveling wave electric curtain at 0.001 s and the electric field mode value diagram of the surface of the electric curtain plate, respectively. When the structure of the electric curtain is determined, the electric field mode size at different locations is different, with the electric field mode at the edge of the electrode being

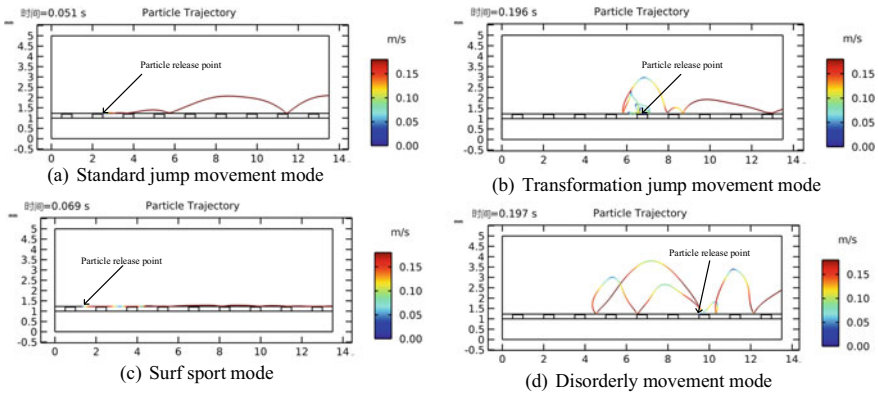


the largest, the electric field mode at the middle of the electrode being the second largest, and the electric field mode at the location between two adjacent electrodes being the smallest. As the electric field force is the only force driving the particle motion, the particles at different positions are subjected to different magnitudes and directions of the force, and therefore the particles obtain different initial velocities, resulting in different patterns of motion of the dust particles.

From Figs. 5 and 6, it can be seen that when the dust particles are released at the edge of the electrode and the electric field force direction is upward, the particles move in a standard jumping motion mode and the particles leave the top of the PV panel after 0.051 s. When the dust particles are released in the middle of the electrodes and the electric field force is directed upward at this time, the particles have a deformed jumping motion mode, and the particles leave the top of the PV panel after 0.196 s. When the particles are released from the middle of the two electrodes, a surfing motion mode occurs and the particles finally leave the surface of the PV panel after 0.069 s. The time spent in jumping mode and surfing mode is shorter, and the time spent in deformed jumping mode and disordered mode is longer.



**Fig. 5** **a** Electric field diagram of the three-phase traveling wave electric curtain. **b** Electric curtain plate surface electric field modulus diagram



**Fig. 6** Particle motion mode in traveling wave electric curtain

### 3.4 Effect of Frequency on the Trajectory of Single Particle Motion

In order to study the effect of frequency on the trajectory of dust particles, the frequencies  $f = 25 \text{ Hz}$ ,  $f = 50 \text{ Hz}$ ,  $f = 75 \text{ Hz}$  and  $f = 100 \text{ Hz}$  were selected, the applied voltage amplitude was taken as  $1000 \text{ V}$ , the particle inlets were selected consistently for comparative analysis, and the electric curtain structure was the same as in Sect. 2.1.

From Fig. 7, it can be seen that the motion pattern of dust particles released from the same point is a standard jumping motion when all other external conditions are the same, but the motion trajectory is completely different and the transport time off the top of the electric curtain is also different. As the frequency increases, the time to transport the dust particles released from the same point off the top of the electric curtain increases, increasing the time to remove dust from the traveling wave curtain.

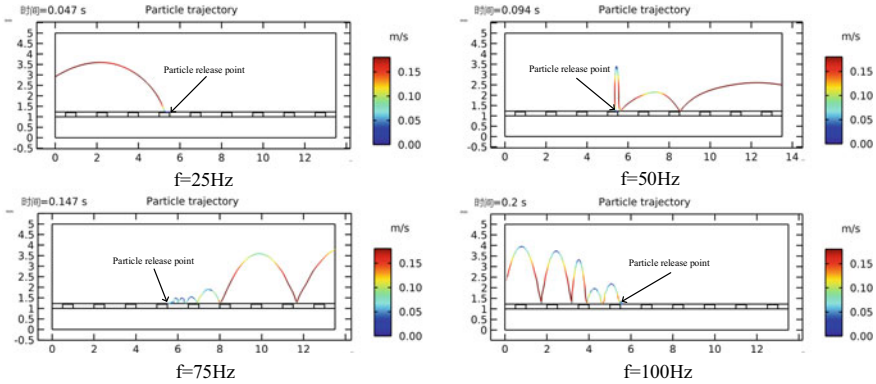


Fig. 7 Trajectories of particles at different frequencies

## 4 Conclusion

- (1) The greater the external voltage applied in the traveling wave curtain, the stronger the dust removal capacity of the traveling wave curtain, with a self-cleaning efficiency of more than 95% at a frequency of 50 Hz and an applied voltage of 1000 V;
- (2) When the charge of the dust particles in the traveling wave curtain is constant, the number of particles transported away from the surface of the photovoltaic panel continues to decrease as the particle diameter increases, and the efficiency of the electric curtain dust removal decreases;
- (3) The motion pattern of dust particles in the traveling wave curtain is complex; when the particles are released at the edges of the electrodes, the dust particles are transported in the standard jump mode; when the particles are released in the middle of the electrodes, the dust particles are transported in the deformed jump mode; when the particles are released in the middle of the two electrodes, the dust particles are transported in the surf mode;
- (4) When the particles are moving in the standard jumping motion mode and surfing motion mode, the time required for the transport to break away from the top of the electric curtain is shorter, and when the particles are moving in the deformed jumping motion mode and disordered motion mode, the time required for the transport to break away from the top of the electric curtain is longer;
- (5) The increase in the frequency of the applied voltage in the traveling wave curtain will increase the time required for dust particle transport out of the top of the electric curtain plate, increasing the dust removal time of the traveling wave curtain.

**Acknowledgements** This work is supported by the Natural Science Foundation of Gansu Province, China (Grant No.21JR7RA237).

This work was supported by Gansu Provincial Natural Science Foundation of China(21JR7RA237), Gansu Provincial Science and Technology Commissioner Special Project(22CX8GA11).

## References

1. Kong JH, Kim TH, Kim JH et al (2014) Highly flexible, transparent and self-cleanable superhydrophobic films prepared by a facile and scalable nanopillar formation technique. *Nanoscale* 6(3):1453–1461
2. Zhang J, Zhou C, Tang Y et al (2018) Criteria for particles to be levitated and to move continuously on traveling-wave electric curtain for dust mitigation on solar panels. *Renew Energy* 119(APR):410–420
3. Adams JG, Cline BL, Contaxes NA et al (1967) Lunar dust degradation effects and removal prevention concepts. In: Summary final report, vol 1
4. Calle CI, Buhler CR, Johansen MR et al (2011) Active dust control and mitigation technology for lunar and Martian exploration. *Acta Astronaut* 69(11–12):1082–1088
5. Calle CI, Buhler CR, Mcfall JL et al (2009) Particle removal by electrostatic and dielectrophoretic forces for dust control during lunar exploration missions. *J Electrostat* 67(2):89–92
6. Masuda S, Fujibayashi K, Ishida K et al (2010) Confinement and transportation of charged aerosol clouds via electric curtain. *Electr Eng Jpn* 92(1):43–52
7. Masuda S, Matsumoto Y (1973) Theoretical characteristics of standing-wave electric curtains. Wiley Subscription Services, Inc. A Wiley Company, vol 93, no 1, pp 71–77
8. Kawamoto H, Seki K, Kuromiya N (2006) Mechanism of travelling-wave transport of particles. *J Phys Appl Phys* 39:1249
9. Sun Q, Yang N, Xiao Z et al (2012) Experimental study on the dust removal efficiency of standing wave electric curtain. *Spacecr Eng* 21(003):72–79; JonesTB (1995) *Electromechanics of particles*. Cambridge University Press, Cambridge (in Chinese)

# Study on the Influence of Wildfire on Streamer Discharge in Transmission Line Gap



Maoqiang Bi, Shijun Zhang, Chensihao Jiang, Xiong Wang, Shaolan Lei, and Tianyan Jiang

**Abstract** In order to explore the influence of wildfire on the streamer discharge of transmission line gap, combined with the characteristics of the high temperature environment and the change of air gas composition ratio caused by wildfire, based on the theory of plasma hydrodynamics, this paper establishes a streamer discharge model with a rod-plane gap of 5 mm under wildfire conditions, and conducts two-dimensional numerical simulation of the streamer discharge process. Air is regarded as a mixture of  $N_2$ ,  $O_2$  and  $CO_2$ , and different  $CO_2$  concentrations and temperature are set to simulate the transmission line environment under wildfire conditions. The simulation results show that under standard atmospheric pressure, the development rate of streamer increases with the increase of temperature and the increase of  $CO_2$  concentration. Compared with the influence of the two on the gap streamer discharge, temperature plays a decisive role.

**Keywords** Streamer discharge · Plasma · Temperature ·  $CO_2$  concentration

## 1 Introduction

Overhead transmission lines of various voltage levels need to cross the vast mountain forest land to complete the cross-regional power transmission task, which will inevitably be disturbed by wildfires and other natural disasters [1]. When a forest fire breaks out near the high-voltage transmission line, the flame and the resulting smoke spiral up to the transmission line gap, causing the transmission line gap discharge, and even leading to large-scale line outage failure.

Many scholars have designed and built the simulation model of streamer discharge. Dawson et al. applied the Raether-Meek criterion for the conversion of electron avalanches to flow injection by assuming that the flow injection head contains small

---

M. Bi (✉) · S. Zhang · C. Jiang · X. Wang · S. Lei · T. Jiang  
School of Electrical and Electronic Engineering, Chongqing University of Technology,  
Chongqing 400054, China  
e-mail: [bimaoqiang@cqut.edu.cn](mailto:bimaoqiang@cqut.edu.cn)

spherical regions of positive charge, and developed the first analytical model for positive flow injection in an air inhomogeneous electric field [2]. Gallimberti developed a model for the development of positive flow injection based on the energy balance theorem for the development of a secondary electron avalanche at the head of the flow injection [3].

At present, the model of streamer discharge in transmission line gap caused by wildfire is not perfect. For some special conditions, the factors considered are single, and the combined influence of different factors on streamer discharge is not analyzed. Based on the variation characteristics of temperature and gas composition ratio caused by wildfire, this paper further improves the simulation model and provides a reliable reference for studying the influence mechanism of wildfire on gap streamer discharge of transmission lines.

## 2 Simulation Model

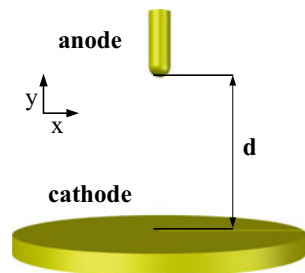
### 2.1 Physical Model

The model framework for building a bar-plate gap inhomogeneous electric field is shown in Fig. 1. The anode is a copper rod, the cathode is a copper disc, the spacing  $d$  is 5 mm, the air pressure  $P$  is 101 kPa and the ambient temperature is set to  $T$ . In a two-dimensional Cartesian coordinate system, the anode (with a voltage of  $+U = 3$  kV) is located at  $y = 5$  mm and the cathode (grounded) is at  $y = 0$ .

To better describe the shape of the initial ionized region, two ionized seeds satisfying a Gaussian distribution are superimposed to form a whole, assuming that the maximum value of particles (species electrons and positive ions) present before the discharge is  $10^{16} \text{ m}^{-3}$ , and the Gaussian formula describing the whole is

$$n_e\{x, y\}|_{t_0} = n_0 \exp \left[ - \left( \frac{x - x_0}{\sqrt{2}s_0} \right)^2 - \left( \frac{y - y_0}{\sqrt{2}s_0} \right)^2 \right] \quad (1)$$

Fig. 1 Rod-plane model



**Table 1** Chemical reaction equations and rates

S. no.	Reaction equation	Rate factor
1	$\text{CO}_2 + e \rightarrow 2e + \text{CO}_2^+$	$f(\varepsilon)$
2	$\text{CO}_2 + e \rightarrow \text{CO} + \text{O}^-$	$f(\varepsilon)$
3	$\text{CO}_2 + \text{CO}^+ \rightarrow \text{CO}_2^+ + \text{CO}$	$1.0 \times 10^{-15}$
4	$\text{O}_2 + \text{CO}_2^+ \rightarrow \text{O}_2^+ + \text{CO}_2$	$5.3 \times 10^{-17}$
5	$\text{O} + \text{CO}_2 \rightarrow \text{O}_2 + \text{CO}$	$2.46 \times 10^{-17}$
6	$\text{O}^- + \text{CO}_2^+ \rightarrow \text{O} + \text{CO}_2$	$3.48 \times 10^{-14}$

where  $n_e\{x, y\}|_{t_0}$  is the density distribution function of positive ions and electrons,  $n_0 = 10^{16} \text{ m}^{-3}$ ,  $x_0 = 0 \text{ }\mu\text{m}$ ,  $s_0 = 25 \text{ }\mu\text{m}$ ,  $y_0$  is the position of the tip of the bar. The initial conditions have been shown to only accelerate the formation of the pulse and do not change the discharge characteristics [4].

## 2.2 Chemical Reaction Models

Most of the existing literature treats air in a simplified way, treating it as a nitrogen-oxygen mixture, but in the special environment where hill fires occur, the large number of combustion reactions can cause a significant increase in  $\text{CO}_2$  concentration near the transmission line, so this paper adds reactions involving  $\text{CO}_2$  to the overall reaction system on the basis of the existing literature, and selects representative types of these reactions, as shown in Table 1.

The reaction rate of ionization collision and elastic collision are calculated by solving the Boltzmann dynamic equation with BOLSIG + software. The surface reaction involved is represented by setting the reaction adhesion coefficient in the simulation model, and the newly added reaction equation rate coefficient is obtained by querying the QuantemolDB database [5].

## 2.3 Boundary Condition Setting

This paper uses a conventional fluid dynamics model, which consists of a Poisson equation for the continuity of particles (also known as the convective diffusion equation) coupled with a Poisson equation for the electric potential.

The applied voltage  $+U = 3 \text{ kV}$  is applied directly to the anode, the plate electrode is set to zero potential and for the open boundary Farouk's voltage zero discharge boundary condition is used [6]:

$$\mathbf{n} \cdot (\varepsilon \nabla \varphi) = 0 \quad (2)$$

The boundary conditions for the electron flux at the cathode and anode are:

$$\begin{aligned} \Gamma_e \cdot \mathbf{n} = & \frac{1 - \gamma_e}{1 + \gamma_e} \left[ -(2\alpha_e - 1)n_e \mu_e \mathbf{E} \cdot \mathbf{n} + \frac{1}{2} v_{th,e} n_e - \frac{1}{2} v_{th,e} n_\gamma \right] \\ & - \frac{2}{1 + \gamma_e} (1 - \alpha_e) \sum_p \gamma_p \cdot \mathbf{n}_e \end{aligned} \quad (3)$$

$$v_{th} = \left( \frac{8k_B T_e}{\pi m_e} \right)^{1/2} \quad (4)$$

$$\begin{aligned} n_\gamma = & (1 - \alpha_e) \frac{1}{\mu_e} \sum_p \gamma_p \frac{1 + \gamma_p}{1 + \gamma_p} \\ & \left[ (2\alpha_p - 1) \text{sgn}(q_p) + \frac{1}{2} \left( \frac{8(m_p + m_s)m_s}{\pi(5m_p + 3m_s)m_p} \right)^{\frac{1}{2}} \right] \mu_p n_p \end{aligned} \quad (5)$$

$$\alpha_{e,p} = \begin{cases} 1, & \text{sgn}(q_{e,p}) n_{e,p} \mu_{e,p} \mathbf{E} \cdot \mathbf{n} > 0 \\ 0, & \text{sgn}(q_{e,p}) n_{e,p} \mu_{e,p} \mathbf{E} \cdot \mathbf{n} \leq 0 \end{cases} \quad (6)$$

The density fluxes of all particles in open conditions are:

$$\mathbf{n} \cdot (\varepsilon \nabla n_k) = 0 \quad (7)$$

In the above equation,  $\mathbf{n}$  is the boundary normal vector,  $\Gamma_e$  is the electron density fluxes,  $v_{t,e}$  is the electron heat rates, and  $m_e$ ,  $m_p$  and  $m_g$  are the electron, positive ion and gas molecular masses respectively.  $n_\gamma$  is the electron density in the region where the electrons hit the electrode and are not bounced back into the discharge region,  $\gamma_e$  is the secondary electron emission coefficient,  $\gamma_p$  is the emission coefficient of the secondary electrons produced by heavy particles hitting the surface of the electrode,  $q_i$  represents the charge of the ion,  $\mu_i$  is the ion mobility, and  $n_i$  is the ion number density.

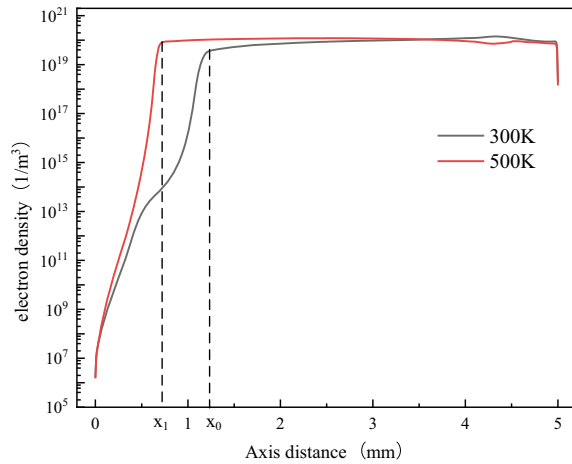
### 3 Analysis and Discussion of Simulation Results

#### 3.1 Effect of High Flame Temperatures on Flow Injection Discharge

Temperature affects both the average thermal movement velocity of the included air and the average free travel of the ions, which in turn affects the mobility of the ions [7, 8]. In this paper, the ambient temperature at room temperature is set to 300 K, the ambient temperature around the transmission line during a simulated hill fire is 500 K



**Fig. 2** Axial electron density at the same time at different temperatures



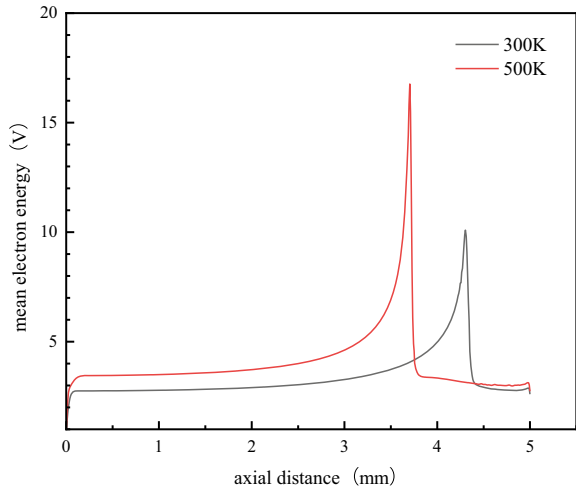
and the gap distance is set to 5 mm to compare the effect of increased temperature only on the flow injection discharge.

Figure 2 shows the axial electron density of two different temperatures at 16 ns. The maximum electron density at each time appears at  $x$  near the anode. The electron density of the streamer head ( $x_0, x_1$ ) is equivalent to the electron density at the anode, and the streamer develops more forward at 500 K. Obviously, the increase of temperature accelerates the development rate of the streamer.

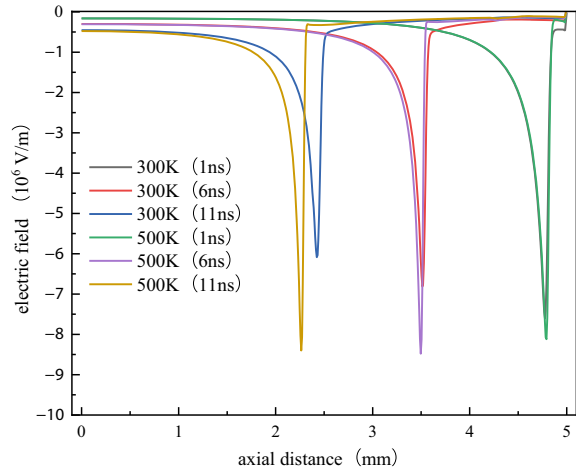
As shown in Fig. 3, the average electron energy of the entire gap at the same temperature remains basically constant and is lowest at both poles, with the maximum average electron energy concentrated at the head of the flow injection. As the temperature rises, the average electron energy across the gap increases, and the maximum average electron energy increases from 10.092 V at 300 K to 16.761 V at 500 K. Therefore, the average electron energy and temperature are positively correlated, and the increase in temperature accelerates the migration rate of ions, thus increasing the current in the gap injection channel and increasing the discharge intensity.

Analysis of the electric field strength can be informed of the strength of the development of the flow injection, from Fig. 4 can be seen, the same temperature electric field strength presents two poles electric field strength of 0, the middle of the peak, the electric field strength at the peak is the electric field strength of the head of the flow injection. Comparing the position of the peak at the two temperatures at the same moment, the position of the peak at 500 K is closer to the cathode, indicating that the rate of development of the flow injection is faster, and the peak electric field intensity at 500 K is higher than 300 K at the same moment, indicating that the increase in temperature accelerates the ionization process, generating more electrons and causing a greater degree of electric field distortion.

**Fig. 3** Mean electron energy



**Fig. 4** Comparison of electric field strength at different temperatures



### 3.2 Effect of CO<sub>2</sub> Molar Fraction Flow Injection Discharge

The concentration of CO<sub>2</sub> around the transmission line under wildfire conditions increases as the combustion reaction proceeds. The plasma discharge rate will change with the change of gas composition ratio [9]. The electron density at different moments was obtained by simulation, comparing the change in electron density at room temperature for a CO<sub>2</sub> molar fraction of 0.0004 and a CO<sub>2</sub> molar fraction of 0.01 at 5 ns and 10 ns of flow injection development, as shown in Fig. 5.

From Fig. 5, it can be seen that when the streamer develops to 10 ns, the mole fraction of CO<sub>2</sub> is 0.0004 and 0.01, which develops to 2.25 and 2.70 mm from the

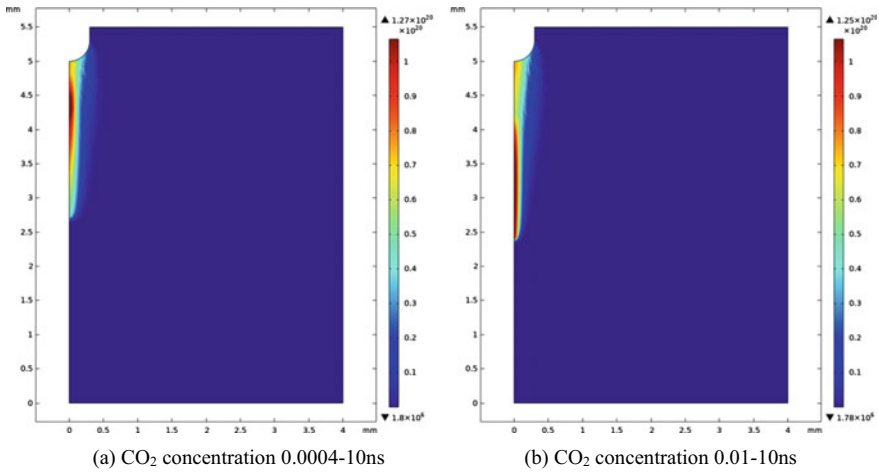
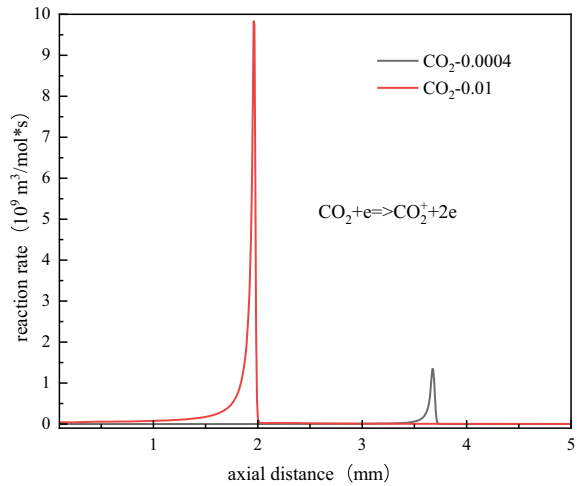


Fig. 5 Comparison of electron density of different CO<sub>2</sub> mole fraction

anode, respectively. The increase of CO<sub>2</sub> concentration obviously accelerates the rate of streamer development.

Comparing the reaction rate changes of CO<sub>2</sub> ionization under two different mole fractions, it can be seen from Fig. 6 that when the mole fraction of CO<sub>2</sub> increases from 0.0004 under normal conditions to 0.01 under wildfire conditions, the reaction rate also increases by nearly 5 times, and the streamer head is closer to the cathode position, indicating that the streamer develops forward more.

Fig. 6 Ionization reaction rate of CO<sub>2</sub>



### 3.3 Effect of Combined High Temperature and CO<sub>2</sub> Concentration on Flow Injection Discharge

Considering the effect of temperature on gap flow injection discharge alone is not sufficient to simulate the environment of a transmission line under hill fire conditions. The combustible materials in green plants are hydrocarbon-oxygen organic compounds that undergo chemical reactions to produce CO<sub>2</sub> as well as other hydrocarbons during combustion. In this paper, high flame temperatures and CO<sub>2</sub> concentrations are considered in the overall reaction system to investigate the effect of combined high temperatures and CO<sub>2</sub> concentrations on transmission line gap flow injection discharge. Simulation results at a temperature of 500 K and a CO<sub>2</sub> molar fraction of 0.01 are compared with those of the norm.

From Fig. 7 shows the two-dimensional distribution of the electric field intensity at the same moment, the rate of flow injection development is significantly faster under the combined effect of temperature and CO<sub>2</sub> concentration than under the norm, comparing the electric field intensity of the two flow injection heads, the electric field intensity is  $-6.84 \times 10^6$  V/m under the combined effect and  $-5.89 \times 10^6$  V/m under the norm, and the maximum value of the spatial electric field intensity increases from  $4.13 \times 10^5$  V/m under the norm to  $5.92 \times 10^5$  V/m, which shows that the combined effect of the two factors causes greater distortion of the spatial electric field.

The net space charge density distribution is a macroscopic reflection of the charged particles throughout the discharge process, from which the distribution of the flow injection head and discharge channel at each discharge instant can be clearly seen [10]. Figure 8 shows that most of the discharge gaps are electrically neutral, with

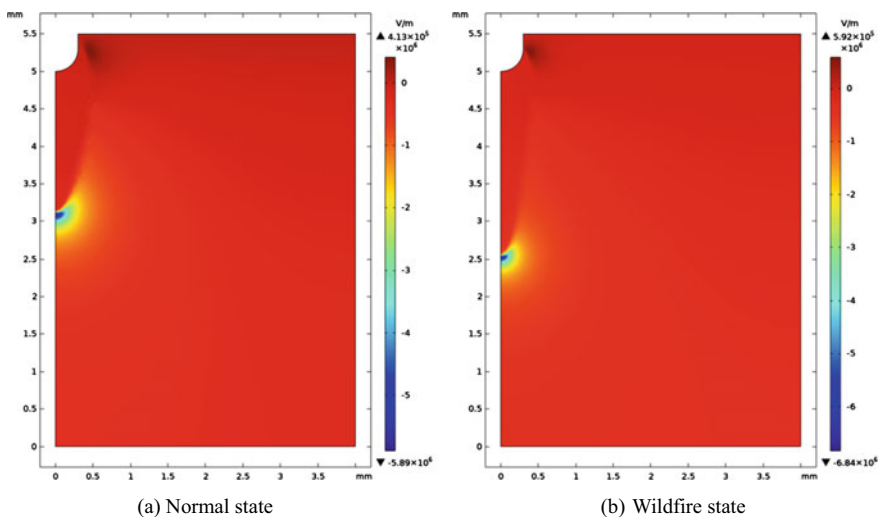
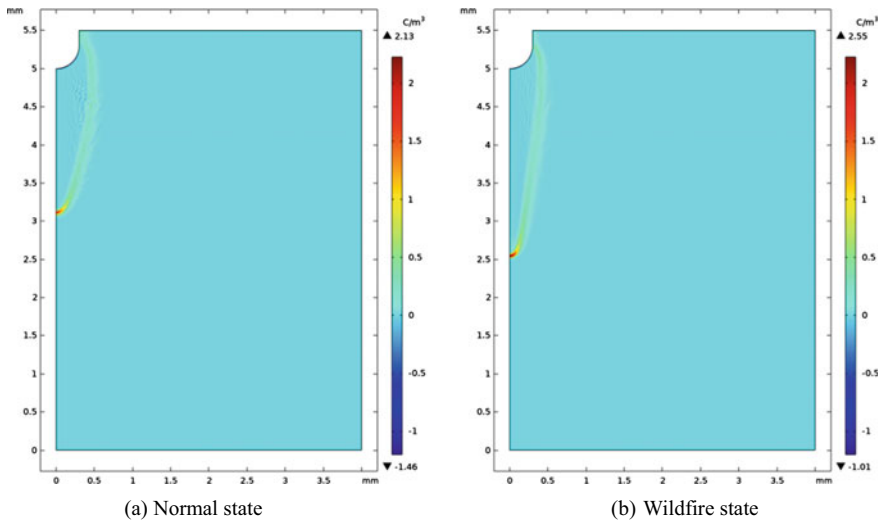


Fig. 7 Two-dimensional distribution of electric field intensity



**Fig. 8** Two-dimensional distribution of net space charge

only a positively charged plasma feature at the head of the flow injection. This is because the head of the flow injection is the most concentrated region in terms of field strength and collisional reflections occur mainly there, and the positive ions can be considered to remain almost motionless at the moment of discharge compared to the electron motion velocity, hence the region is electrically neutral. Comparing the two figures in Fig. 7, the net space charge density at the same moment of combined action reaches  $2.55 \text{ C/m}^3$ , compared to only  $2.13 \text{ C/m}^3$  at normal conditions, and the flow injection develops  $0.5 \text{ mm}$  further towards the cathode, indicating that the increase in temperature and  $\text{CO}_2$  concentration under wildfire conditions accelerates the formation process of flow injection channels in the transmission line gap.

In this paper, the method of plasma chemical reaction is used to describe the microscopic process of gas discharge, so the reaction rate coefficient of plasma reaction can be used as a characteristic quantity of the strength of this microscopic process, and the strength of air gap channel discharge can be characterized by comparing the magnitude of each reaction rate. Three types of electron collision reaction rates, ionization collision, elastic collision and attachment collision, are selected separately to compare the combined effect of high temperature and  $\text{CO}_2$  with that of the normal state.

As can be seen from Fig. 9, the reaction rate coefficient of ionization collisions at the same moment under combined action is 3.5–6 times higher than that under normal state, and the ionization rate of  $\text{CO}_2$  is higher than that of  $\text{N}_2$  and  $\text{O}_2$ , the reaction rate of elastic collision is 1 order of magnitude higher than that of ionization collision, while the attached collision is 3 orders of magnitude lower than that of ionization collision. The combined effect of flow injection towards the cathode is

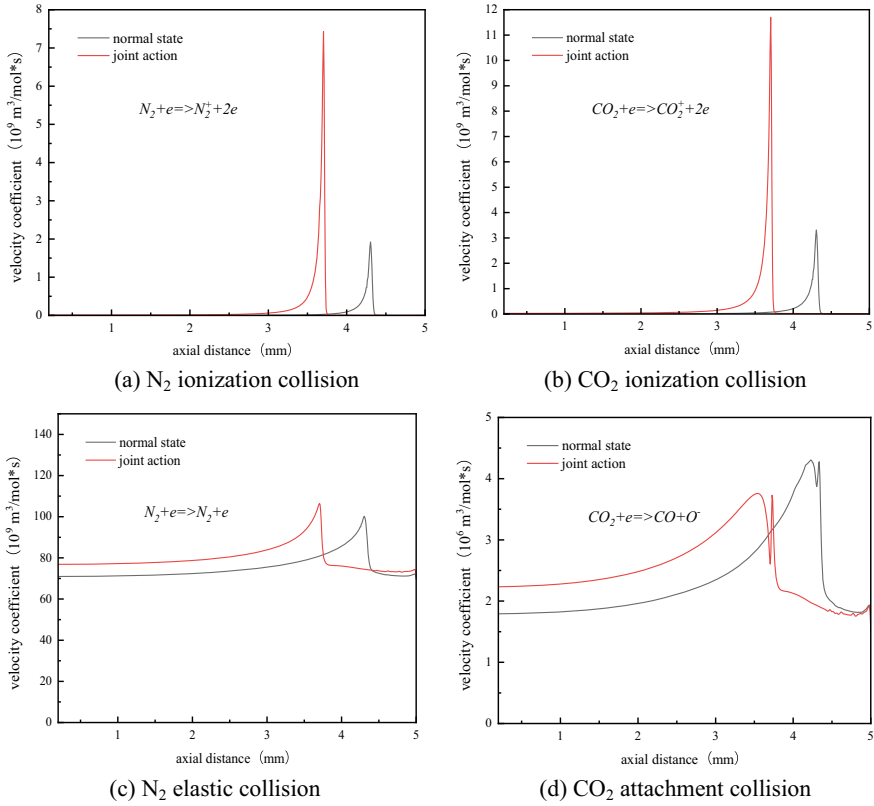


Fig. 9 Rate coefficients

faster, and the high temperature and  $CO_2$  concentration play a significant role in promoting the formation of discharge channels in the transmission gap.

### 4 Conclusion

In this paper, a plasma simulation model of the flow injection discharge between transmission lines is built for the typical characteristics of wildfires, and the corresponding boundary conditions are set. The electron density, average electron energy, electric field strength, space charge density and reaction rate are calculated through the simulation, and the effects of temperature,  $CO_2$  concentration and their combined effects on the flow injection discharge are compared and analyzed from various aspects. The simulation model in this paper improves the shortcomings of the simulation model of flow injection discharge under hill fire conditions, and provides an effective method

for investigating the effect of hill fire on the flow injection discharge in transmission lines.

**Acknowledgements** This research is supported by Chongqing Natural Science Foundation Project (CSTB2022NSCQ-MSX0267).

## References

1. Zhou E, Fan L, Huang D et al (2022) Breakdown characteristics of conductor-plate gap under vegetation fire at 2013m altitude. *High Volt Technol* 48(11):4316–4322 (in Chinese)
2. Dawson GA (1965) A model for streamer propagation. *J Phys* 182–183
3. Gallimberti I (1972) A computer model for streamer propagation. *J Phys D Appl Phys* 5(12):2179–2189
4. Wu F, Liao R, Wang K et al (2014) Numerical simulation of the characteristics of heavy particles in bar-plate DC positive corona discharge based on a hybrid model. *IEEE Trans Plasma Sci* 42(3):868–878
5. Quantemoldb. <https://www.quantemoldb.com>. Accessed 21 Jan 2023
6. Farouk T, Farouk B, Staack D et al (2006) Simulation of DC atmospheric pressure Argon micro glow-discharge. *Plasma Sources Sci Technol* 15(4):676–688
7. Wu D, Mei H, Meng X, Shao T, Tang W, Wang L (2022) Effect of temperature on positive streamer corona discharge characteristics in rod-plane gap. *High Volt Electr Appar* 58(02):50–59 (in Chinese)
8. Zhang Z, Song H, Dai J (2021) Simulation study on the effect of temperature on air gap flow injection discharge of needle plate under atmospheric pressure. *Chin J Electr Eng* 41(08):2929–2939 (in Chinese)
9. Mirpour S, Nijdam S (2022) Investigating CO<sub>2</sub> streamer inception in repetitive pulsed discharges. *Plasma Sources Sci Technol* 16(5):31
10. Dong X, Liu X (2022) Numerical simulation study on the effect of gas composition on atmospheric pressure Ar/O<sub>2</sub>/SiH<sub>4</sub> discharge. *J Vac Sci Technol* 42(12):952–961 (in Chinese)

# Influence of AC Voltage Frequency on Partial Discharge of Oil-Pressboard Insulation and Its Mechanism



Shuqi Li, Xinyi Sui, Mingsheng Wang, Penghong Guo, Yongwei Xu, Guodong Gu, Liangkai Wang, and Qingquan Li

**Abstract** The high frequency of harmonic voltage is more likely to cause partial discharge and insulation failure. The partial discharge experimental platform is built to study the partial discharge characteristics of oil-pressboard insulation under different frequency voltages. Based on the analysis of the obtained partial discharge information, it can be found that the spectrum changes with frequency. As the voltage frequency increases, the discharge quantity increases more steeply with the phase. The higher the voltage frequency, the larger the discharge quantity and discharge repetition rate, and the more serious the partial discharge. The accumulation and dissipation of residual charge have an important influence on the development of partial discharge. The higher the voltage frequency is, the slower the residual charge dissipation is, forming a residual electric field to promote partial discharge.

**Keywords** Oil-pressboard insulation · Voltage frequency · Residual charge

## 1 Introduction

The converter transformer is pivotal in the HVDC transmission system. With the long-term operation of the converter transformer, its insulation failures are becoming more and more prominent. According to the data of CIGRE, the insulation failures

---

S. Li · Q. Li (✉)

Shandong Provincial Key Laboratory of UHV Transmission Technology and Equipment, School of Electrical Engineering, Shandong University, Jinan 250061, China  
e-mail: [lqq@sdu.edu.cn](mailto:lqq@sdu.edu.cn)

X. Sui

Qingdao Electrical Engineering Installation Co., Ltd, Qingdao 266100, China

M. Wang · P. Guo · Y. Xu · G. Gu

Shandong Electric Power Equipment Co., Ltd, Jinan 250024, China

L. Wang

Yantai Power Supply Company of State Grid, Yantai 264001, China

© Beijing Paiké Culture Commu. Co., Ltd. 2024

X. Dong and L. Cai (eds.), *The Proceedings of 2023 4th International Symposium on Insulation and Discharge Computation for Power Equipment (IDCOMPU2023)*, Lecture Notes in Electrical Engineering 1103, [https://doi.org/10.1007/978-981-99-7413-9\\_27](https://doi.org/10.1007/978-981-99-7413-9_27)

297



accounts for more than half of the converter transformer accidents [1]. As the main insulation of the converter transformer, the state of the oil-pressboard insulation affects the normal operation of the power grid [2].

The main insulation on the valve side is subjected to complex voltages, including 50 Hz AC voltage, DC voltage, and a large number of harmonic voltages [3]. Harmonic voltage is AC voltage with the frequency that is a multiple of 50 Hz. The increase in voltage frequency affects the partial discharge process, accelerates the degradation of insulation medium, and threatens the insulation performance and operational safety of converter transformer. Partial discharge is not only the cause of insulation deterioration, but also the characteristic quantity to evaluate the insulation state [4]. Therefore it is essential to study the laws of partial discharge of oil-pressboard insulation under different frequency harmonic voltages.

The research on the affect of AC voltage frequency on partial discharge is still in its initial stage. Italian scholar Cavallini studied the affect of voltage frequency on partial discharge of air-gap model, and found that discharge pulses are mainly distributed near the zero-crossing point and rising edge of waveform, and the distribution phase is basically independent of voltage frequency [5]. Guangning Wu studied the characteristics of partial discharge of oil-pressboard insulation under superimposed inter-harmonic AC voltages, and found the addition of the inter-harmonic caused the discharge phase to change [6]. In addition, Florkowski studied the influence of high-voltage harmonics on the development of discharge [7, 8].

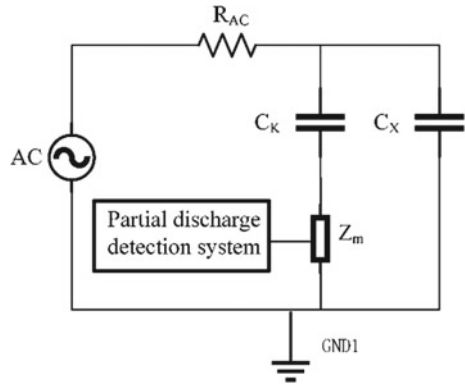
According to the previous discuss, scholars have attached importance to the affect of harmonic voltage on partial discharge, but did not quantitatively analyze the influence of different harmonic voltage frequencies on partial discharge. In addition, scholars have not made the in-depth explanation of the influence mechanism of voltage frequency. Therefore, it is urgent to study the partial discharge characteristics of oil-pressboard insulation under different frequency voltages.

## 2 Experimental Platform

The partial discharge experimental circuit diagram is shown in Fig. 1. AC power supply can provide harmonic voltages of different frequencies.  $C_x$  is an air-gap defect model. Partial discharge detection system can obtain discharge PRPD spectrum and other information. The partial discharge is detected by pulse current method. In order to avoid partial discharge in the experiment loop, the experiment equipment is connected with shielded wires, which are as short and straight as possible, and the ground points are wrapped with copper foil.

In the process of pretreatment, the cut insulating pressboard is placed in the vacuum condition of constant temperature 110 °C and pressure 50 Pa for 48 h, and the moisture content of the insulating pressboard is required to be less than 1% after pretreatment. Filter the test oil for 2 h using a vacuum oil filter device, and then put the dried insulating pressboard into the filtered transformer oil, and fully soak for 48 h in a vacuum drying oven with a pressure of 80 °C and less than 10 Pa. The

**Fig. 1** Experimental circuit diagram



transformer oil and insulating pressboard are fully cooled before the experiment. After pretreatment, the integral number of the gas body of the transformer oil is less than 2%, and the water content of the transformer oil is less than 10  $\mu\text{L/L}$ .

### 3 Partial Discharge Characteristics Under Different Frequency Harmonic Voltages

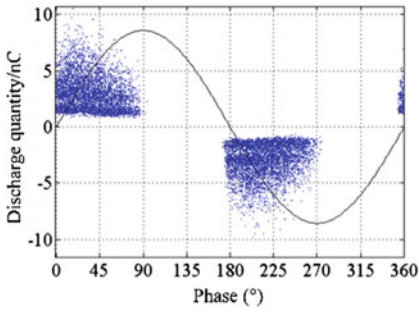
According to the simulation of HVDC transmission system, the harmonic components of the main insulation of the converter transformer valve side can be obtained: 50, 150, 250, 300, 350 Hz. These five harmonic voltage components account for the highest proportion. Therefore, the partial discharge characteristics under these five voltages are mainly studied.

The frequencies of the applied voltage were set to 50–350 Hz, and the voltage was slowly increased until partial discharge occurred to determine the partial discharge inception voltage  $U_{PDIV}$  at different frequencies. It is found that the frequency change has little effect on  $U_{PDIV}$ , and the root-mean-square value of  $U_{PDIV}$  at different frequency AC voltages remains at about 6.4 kV. In the partial discharge experiment of air-gap defect, the root-mean-square values of test voltage are set to 8 kV, 10 kV and 12 kV respectively. The partial discharge pulse signals under these three voltages are collected, and the characteristic parameters of partial discharge are extracted and compared.

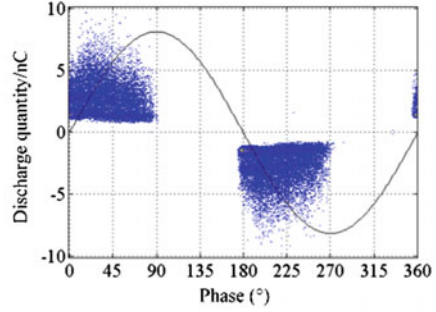
Figure 2 shows the partial discharge PRPD spectrum of the air-gap model when the voltage is 10 kV. It can be found that the positive and negative half cycles of the spectrum are basically symmetrically distributed, and the shape of the spectrum is different under different frequency voltages. When the voltage frequency is low, the spectrum is ‘peak-like’, and the discharge quantity changes slowly with the phase. When the voltage frequency is high, the discharge spectrum is ‘rabbit-ear-like’, and the discharge quantity increases steeply with the phase. The main discharge cluster

similar to ‘rabbit-ear-like’ appears on the rising edge, and as the discharge frequency increases, ‘rabbit-ear’ gradually becomes longer.

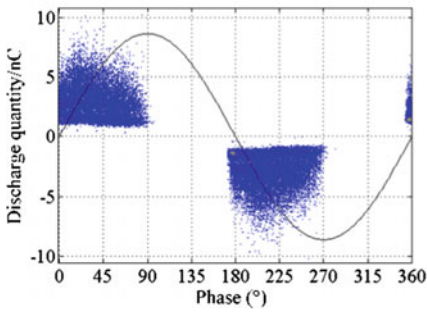
With the increase of AC frequency, the number of discharges increases obviously, and the discharge amplitude also increases. The partial discharge pulses are mainly



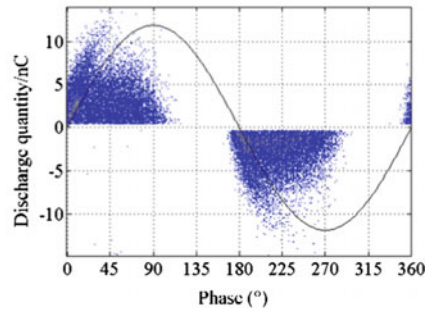
(a) 50Hz



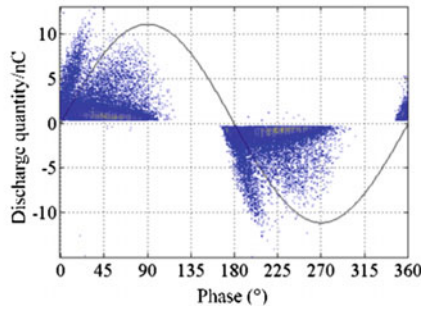
(b) 150Hz



(c) 250Hz



(d) 300Hz



(e) 350Hz

Fig. 2 Partial discharge PRPD spectrum under different frequency AC voltages

distributed in the voltage rising edge  $0^{\circ}$ – $90^{\circ}$  and  $180^{\circ}$ – $270^{\circ}$  phase interval, and the discharge quantity is not large near the voltage peak of  $90^{\circ}$  and  $270^{\circ}$ . In addition, with the increase of the frequency, the phase shift occurs, and the phase distribution of the discharge pulses moves forward to the zero-crossing point.

As shown in Fig. 3, the partial discharge characteristic parameters under different frequency AC voltages are counted, and the variation law is summarized.

When the applied voltage is the same, the characteristic parameters increase with the increase of frequency, among which the maximum discharge quantity and discharge repetition rate change most obviously, and the average discharge quantity increases little. When the voltage frequency is the same, the characteristic parameters increase with the increase of the applied voltage. The higher the voltage frequency, the greater the voltage amplitude, the larger the maximum discharge quantity, the more the number of discharges, and the more serious the insulation damage.

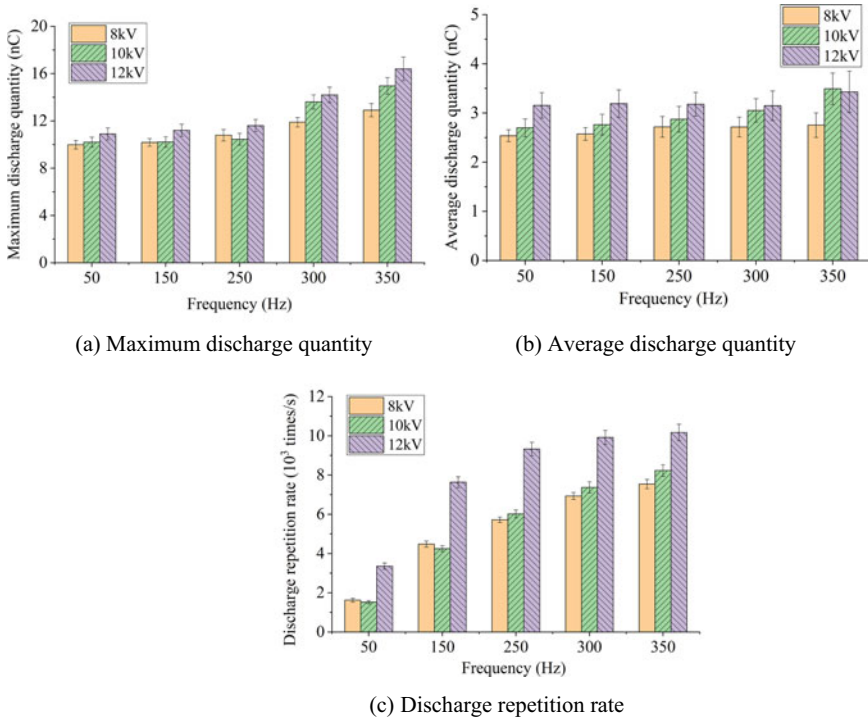


Fig. 3 Partial discharge characteristic parameters under different frequency AC voltages

## 4 Discussion

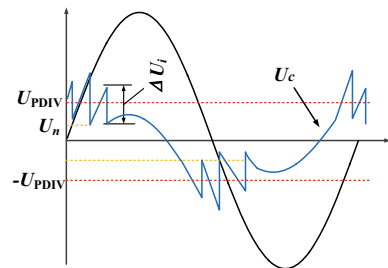
There are two conditions for partial discharge of air-gap defect: one is that there are enough free electrons in the defect to produce initial electron avalanche; secondly, the voltage of the air gap reaches its own minimum discharge voltage to maintain its own discharge. The initial electrons may come from field ionization, or from the residual space charge that has not dissipated completely after the last discharge [9]. After partial discharge appears, the positive and negative charges in the air gap move to the air gap wall, forming a residual electric field  $E_n$ . The electric field  $E_n$  is opposite to the applied electric field  $E_w$ , and the actual electric field  $E_c$  in the air gap is:

$$E_c = E_w - E_n \quad (1)$$

As shown in Fig. 4,  $U_c$  is the voltage of the air gap.  $U_{PDIV}$  is the partial discharge inception voltage.  $U_n$  is the residual voltage.  $\Delta U_i$  is the voltage difference before and after the  $i$ -th time discharge of the air gap. Under the action of external AC voltage, when  $U_c$  reaches  $U_{PDIV}$ , partial discharge will occur. Due to the instantaneous completion of discharge, the voltage of both ends of the air gap drops by  $\Delta U_i$ . Because  $U_n$  after discharge is lower than  $U_{PDIV}$ , the discharge is suspended. Then the voltage at both ends of the air gap increases with the increase of the applied voltage waveform until the next discharge occurs. Due to the existence of residual voltage, the residual electric field  $E_n$  will be established.  $E_n$  is opposite to the direction of  $E_w$  in the positive half cycle of AC, which weakens the air-gap discharge.  $E_n$  in the negative half cycle of AC is the same as the direction of  $E_w$ , thus promoting the occurrence of discharge.

The accumulation and dissipation process of residual charge is correlated with voltage frequency. The interfacial charge dissipation of the inner wall of the air gap shows an exponential decay trend [10]. The higher the voltage frequency, the less the charge decay, the more the residual charge, and the larger the residual electric field  $E_n$ . Therefore, the higher the voltage frequency, the more severe the partial discharge, and the ‘rabbit-ear-like’ discharge appears at the rising edge.

**Fig. 4** Partial discharge diagram of air-gap model under AC voltage



## 5 Conclusion

The conclusions are as follows:

- (a) When the voltage frequency is low, the spectrum is ‘peak-like’, and the discharge quantity changes slowly with the phase. When the voltage frequency is high, the discharge spectrum is ‘rabbit-ear-like’, and the discharge quantity increases steeply with the phase.
- (b) When the AC voltage frequency is higher and the voltage is larger, the maximum discharge quantity and the average discharge quantity become larger, the number of discharges increases, and the insulation damage is more serious.
- (c) The increase of the voltage frequency slows down the dissipation rate of the residual charge in the air gap wall. The charge accumulation forms a large residual electric field, which enhances the reverse partial discharge, so that the discharge quantity gradually increases, and the ‘rabbit-ear-like’ discharge appears at the rising edge of the voltage.

**Acknowledgements** This project was supported by the Central Guidance on Local Science and Technology Development Fund of Shandong Province (YDZX2022001).

## References

1. Liu H (2021) Simulation research on the discharge characteristics of converter transformer paperboard depression under composite AC-DC voltage. *Proceedings of the CSEE* 41(18):6461–6472 (in Chinese)
2. Zhao Z (2022) Molecular dynamics on cracking mechanism of oil-pressboard insulation under electric-thermal coupling. *IEEE Trans Dielectr Electr Insul* 29(5):1675–1684
3. Li S (2021) Characteristics of Creeping Discharge Caused by a Needle Electrode in Oil-Pressboard Insulation under plus DC Voltage. *IEEE Trans Dielectr Electr Insul* 28(1):215–222
4. Wang Y (2023) Study on object recognition method of multisource PD diagrams in oil-immersed power transformer. *Insulating Materials* 56(4):85–92 (in Chinese)
5. Cavallini A (2006) Effect of supply voltage frequency on testing of insulation system. *IEEE Trans Dielectr Electr Insul* 13(1):111–121
6. Li X (2020) Partial discharge characteristics of oil-paper insulation for on-board traction transformers under superposed inter-harmonic AC voltages. *IEEE Trans Dielectr Electr Insul* 27(1):240–248
7. Florkowski M (2013) Impact of high voltage harmonics on interpretation of partial discharge patterns. *IEEE Trans Dielectr Electr Insul* 20(6):2009–2016
8. Florkowski M (2020) Partial discharges in HVDC insulation with superimposed AC harmonics. *IEEE Trans Dielectr Electr Insul* 27(6):1906–1914
9. Zhang Q (2019) Influences of internal void defect dimension and position on partial discharge characteristics in the solid insulation. *High Voltage Engineering* 45(4):1313–1322 (in Chinese)
10. Kindersberger J (2008) Surface charge decay on insulators in air and sulfurhexafluorid-Part I: simulation. *IEEE Trans Dielectr Electr Insul* 15(4):941–948

# Study of Electrical Characteristics of Epoxy Resin Under Different Environmental Conditions of Condensation



Zhangang Yang, Yongguang Ji, Xiao Ma, Haonan Tan, Xiao Rao, and Maoqiang Bi

**Abstract** Currently, testing of epoxy resin insulation parameters yields good results; however, existing research results primarily focus on the influence of epoxy resin degradation on insulation characteristics, and there is a lack of research on the discharge characteristics of epoxy resin under condensation conditions with varying environmental factors and aging degrees. The electrical properties of epoxy resin are investigated in this work from two perspectives: environmental influences and corona aging effects. The results show that both environmental factors and hygrothermal corona aging can affect the condensation state and condensation discharge characteristics of an epoxy resin surface, but in different ways, with the former primarily changing the surface medium and the latter changing the material structure itself.

**Keywords** Epoxy resin · Condensation · Hygrothermal corona aging · Leakage current

## 1 Introduction

Switchgear is a basic component of the electric power network and plays an important role in opening and closing short-circuit currents and ensuring the stable operation of the electric power system [1]. Because of its superior chemical, electrical, and

---

Z. Yang · X. Ma

State Grid Chongqing Electric Power Company, Shibe Power Supply Branch,  
Chongqing 400054, China

Y. Ji

State Grid Chongqing Electric Power Company, Chongqing 400054, China

H. Tan · X. Rao · M. Bi (✉)

School of Electrical and Electronic Engineering, Chongqing University of Technology,  
Chongqing 400054, China

e-mail: [bimaoqiang@cqut.edu.cn](mailto:bimaoqiang@cqut.edu.cn)

© Beijing Paiké Culture Commu. Co., Ltd. 2024

X. Dong and L. Cai (eds.), *The Proceedings of 2023 4th International Symposium on Insulation and Discharge Computation for Power Equipment (IDCOMPU2023)*, Lecture Notes in Electrical Engineering 1103, [https://doi.org/10.1007/978-981-99-7413-9\\_28](https://doi.org/10.1007/978-981-99-7413-9_28)

305

mechanical properties [2], epoxy resin is widely employed in the electrical, electronic, construction, and material domains [2]. Recent studies on solid insulated switchgear have demonstrated that using epoxy resin as the main insulating medium and support body of the switchgear, as well as using epoxy resin to encase and mold busbars, vacuum interrupters, and other equipment in the switchgear, can not only meet the insulation requirements in the switchgear but also have the advantages of small size, strong environmental adaptability, and integral disassembly. It has the potential to replace gas insulated goods and has a fair chance of growth in medium and low distribution networks.

In the switchgear, as the switchgear has current passing through, the equipment will be heated, and the dielectric loss of insulation materials brought about by the alternating magnetic field generated by alternating current, as well as the hysteresis loss and eddy current effect brought about by the magnet will be dissipated in the switchgear in the form of heat energy. This not only makes the temperature of the power equipment rise, but also makes the ambient temperature inside the switchgear rise. When the temperature of the equipment reaches a certain level, it will lead to the mechanical strength of the metal of the power equipment and the insulation strength of the insulation material is reduced, and when the temperature is too high, it will also lead to insulation failure and other problems to reduce the service life of the equipment [3]. At the same time, the rise in ambient temperature will increase the saturation of water vapor in the air, when the hot saturated air and insulation surface, metal conductors, switch cabinet walls and other relatively low temperature interface contact, the water vapor in the air will precipitate in the contact surface due to the sudden drop in temperature to form a condensation phenomenon, resulting in corrosion and aging of metal equipment insulation equipment, partial discharge, leakage phenomenon, making the switchgear failure, seriously affecting the equipment's normal safe operation of the equipment. At present, the condensation phenomenon caused by the change of temperature and humidity in the switchgear is one of the main reasons for the failure of the electrical equipment in the switchgear [4].

The Xi'an Branch of China Academy of Space Technology has conducted thermal and oxygen aging tests on epoxy resin under different conditions, and the mathematical model of thermal and oxygen aging of epoxy resin was derived by detecting the changes of mechanical parameters of epoxy resin and analyzing the laws of parameter changes, and the service life of epoxy resin under certain environments was predicted by this model [5]. North China Electric Power University's State Key Laboratory of New Energy Power Systems investigated the characteristics of epoxy resin at various stages of electrothermal aging and discovered a difference in the effective onset electron production probability of epoxy resin insulation flaws [6]. The Guangzhou Power Supply Bureau conducted thermal aging tests on epoxy resins under different temperature conditions for thermal factors, and the results of the study showed that the increase in aging temperature would lead to a significant decrease in the dielectric properties of epoxy resins and more serious insulation degradation [7].

In summary, the insulation parameters of epoxy resins have been tested with good results, but the existing research results mainly focus on the influence of epoxy



resin degradation on insulation characteristics, and there is a lack of research on the discharge characteristics of epoxy resins under condensation conditions with different environmental factors and different aging degrees. In this paper, we mainly study the surface condensation discharge characteristics of epoxy resin from two aspects: environmental factors and corona aging factors. The influence of different condensation conditions on the surface leakage current of epoxy resin is investigated.

## **2 Test Method and Procedure**

### ***2.1 Experimental Sample Production***

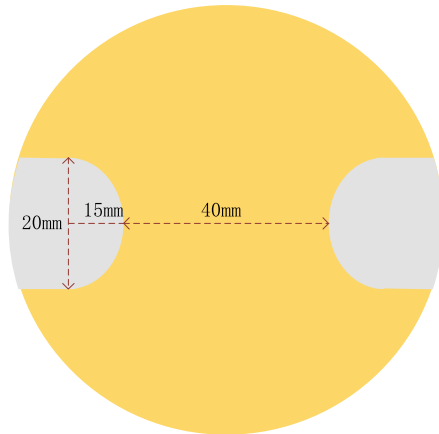
In this paper, the main raw materials used for making epoxy resin were bisphenol A epoxy resin (E-51), methyl tetrahydrodiphthalic anhydride (MTHPA) and 2,4,6-tris(dimethylaminomethyl)phenol (DMP-30). Teflon material was chosen as the epoxy resin casting mold, which not only can achieve efficient demoulding, but also the material of the mold is not much deformed by heat, and the epoxy resin is evenly heated, so there will be no bubbles and cracks inside the sample basically (Fig. 1).

### ***2.2 Condensation Environment Simulation***

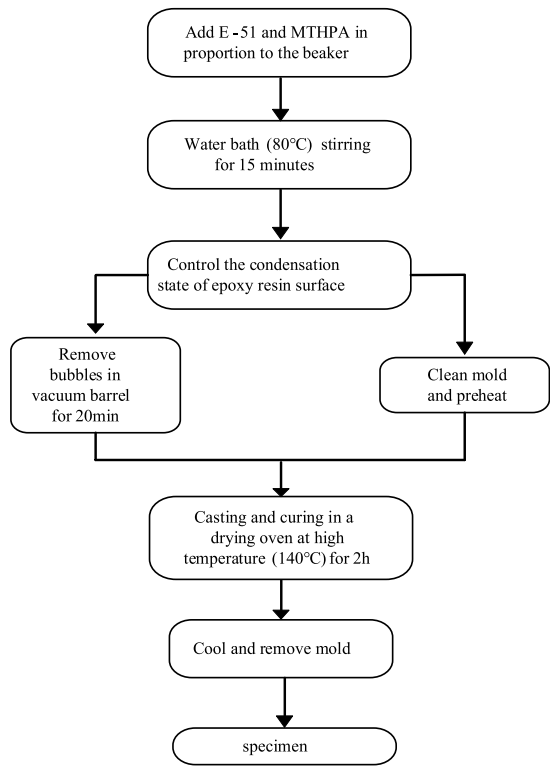
In this paper, we use ultrasonic fog generators, air compressors, and environmental chambers to build a condensation environment, and change the temperature and flow rate in the environmental chamber to achieve the effect of condensation. Since the condensation phenomenon is mainly due to the precipitation of water vapor in the air in liquid form when wet air with higher temperature meets objects with lower temperature, this paper uses the difference between the surface of the constructed sample and the ambient temperature to achieve the condensation effect.

After the condensation environment is simulated in the laboratory, it is necessary to monitor the condensation environment and control the relevant equipment based on the monitored data results to ensure that the generated environment is closer to the real condensation phenomenon. The main parameters of the condensation environment monitored in this paper are: temperature and relative humidity in the environmental chamber, in order to ensure the stability of temperature and humidity control in the environmental chamber.

**Fig. 1** a Epoxy resin samples; b epoxy resin preparation flow chart



(a)



(b)

### 2.3 Experimental Platform Construction

The main electrode of the needle-plate electrode is divided into two parts: upper and lower electrodes, both of which are made of pure copper. The upper electrode is a bowl-shaped electrode with a diameter of 28 mm, and 31 metal clamps with a radius of 4 mm are distributed inside the electrode for fixing the stainless steel needle electrode; the lower electrode is a pure copper metal plate with a thickness of 4 mm and a diameter of 140 mm, which is used for placing samples and used as a grounding electrode [8]. It was verified by simulation and test that the electrode can apply corona discharge to the sample uniformly and effectively, which meets the requirements of hygrothermal corona aging test [9] (Fig. 2).

After the experimental samples were made and the condensation environment was successfully simulated, the test equipment used in this paper are: NHSB-5kVA/50 kV transformer; EWS06-500W air compressor; air flow meter; TBS2000 SERIES oscilloscope, where the measurement resistance is 10 Ω non-inductive resistance. The test process is all done in the artificial environment box, and the test circuit is shown in Fig. 3 [10].

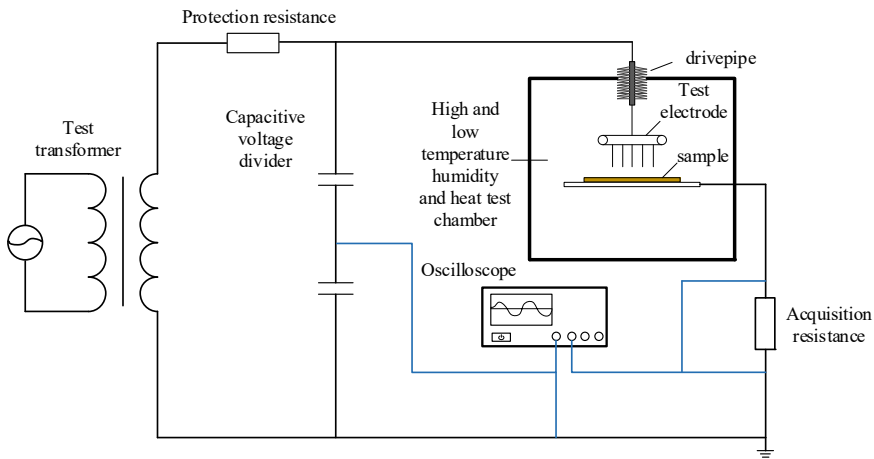


Fig. 2 Hygrothermal aging principle diagram

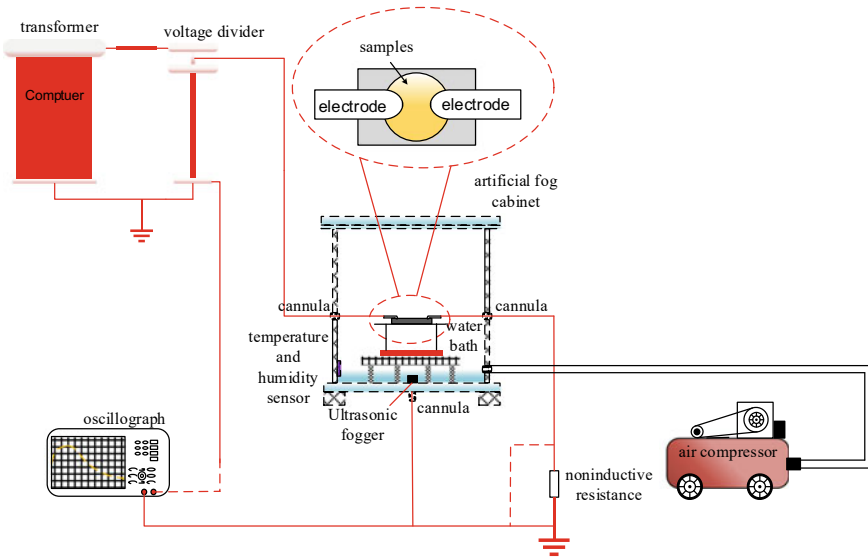


Fig. 3 Leakage current test device

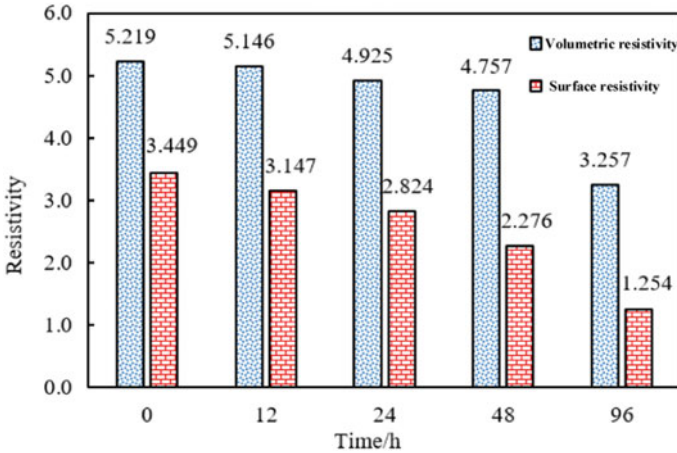
### 3 Results Analyse

#### 3.1 Volume and Surface Resistivity Test Results

Table 1 displays the results of tests conducted on both surface and volume resistivity. The test results demonstrated that the epoxy resin samples' volume and surface resistivity both reduced as aging time increased, with the surface resistivity decreasing more noticeably. For a more intuitive surface test result, the test results were converted into the bar graph in Fig. 4. It is obvious from the graph that the volume resistivity changes less when the aging time is less than 48 h, and only decreases by 8.85% compared with the unaged sample, while the aging time of 96 h decreases by 37.59%; the surface resistivity and volume resistivity change in a different trend, basically decreasing evenly with the increase of aging time, and is more obviously affected by the aging time of damp heat corona.

**Table 1** Volume and surface resistivity test results of samples with different aging time

Time/h	Resistivity / $10^{10}\Omega\cdot\text{cm}$	Surface resistivity / $10^{13}\Omega$
0	5.219	3.449
12	5.146	3.147
24	4.925	2.824
48	4.757	2.276
96	3.257	1.254



**Fig. 4** Volume and surface resistivity test results

It is analyzed that in the process of hygrothermal corona aging, the surface of epoxy resin is continuously bombarded by high-energy electron beam under the action of electric field, thus the surface structure is damaged, and the surface structure is damaged more seriously with the increase of time, so the surface resistivity of epoxy resin is further reduced. The volume resistivity decreases significantly after the aging time of 48 h, which may be caused by the hygroscopic property of epoxy resin, which is a hydrophilic material with hygroscopic property in the high temperature and high humidity environment. When the aging time reaches 96 h, the surface structure of epoxy resin is seriously damaged and the surface layer is loose, which promotes the process of physical and chemical moisture absorption, resulting in a more serious decrease of volume resistivity of epoxy resin material.

### ***3.2 Effect of Different Environmental Factors on Epoxy Resin Leakage Current***

Leakage currents were collected from the samples after the condensation test by means of an oscilloscope and a collection resistor. The voltage at both ends of the electrode was set to 2 kV, the sampling frequency was 12.5 k/s, and eight cycles were collected for analysis for each group of samples. By reading the literature and the test results, it can be seen that the influence of temperature and humidity on the leakage current of epoxy resin surface is mainly determined by the condensation quality of the surface, and the larger the condensation quality is, the larger the leakage current amplitude and the stronger the periodicity is. In order to study the influence of different environmental factors on the condensation leakage current, this test was conducted to measure the leakage current of clean sample, single salt dense sample,

single gray dense sample and dirty sample respectively, and the results are shown in Fig. 5.

The test results show that the leakage current of clean samples is the smallest and the leakage current of dirty samples is the largest. The value of leakage current of single salt-dense sample increased compared with clean sample due to the formation of conductive ions after the fusion of NaCl and water, and the distortion of waveform caused by partial discharge phenomenon on the sample surface during the collection process. Single gray dense samples due to gray dense can make the condensation increase, water molecules adsorbed on the insoluble diatomaceous earth, so the sample surface can not form discrete water beads, water molecules and diatomaceous earth together to build a conductive channel makes the sample surface

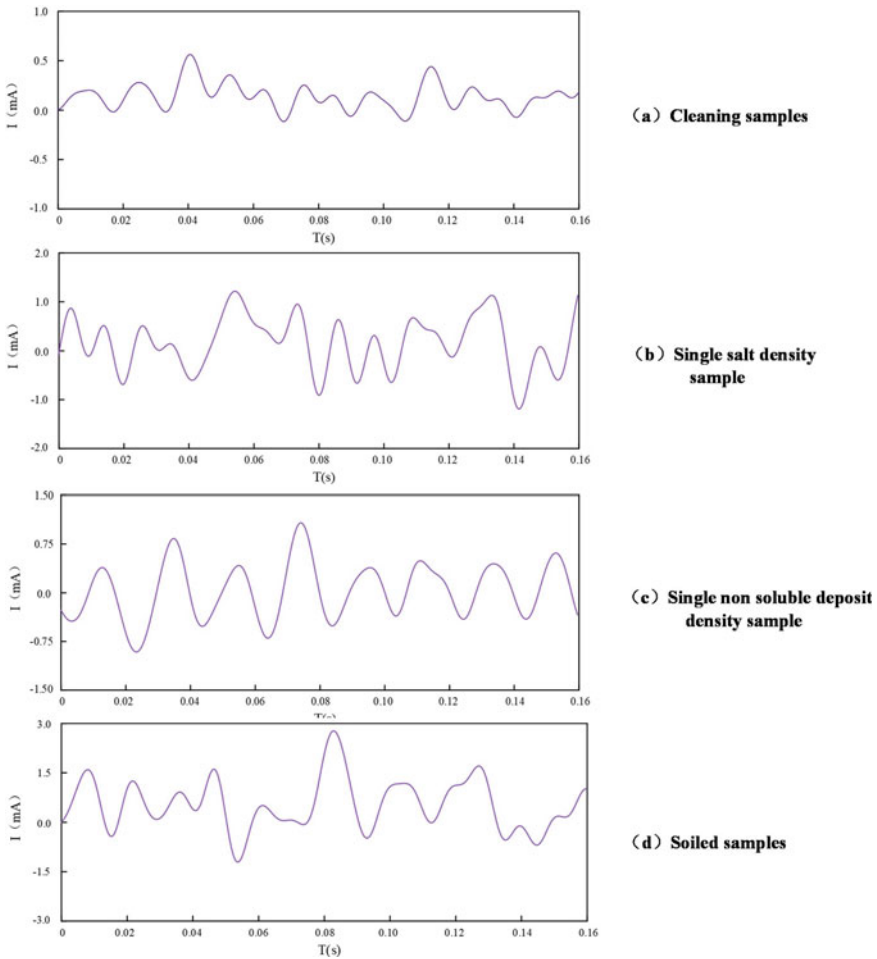


Fig. 5 Condensation leakage current for different environmental factors

leakage current is a regular loaded sine wave. The surface of dirty samples contains conductive ions and conductive channels built by dew droplets and diatomaceous earth, so the partial discharge phenomenon is more obvious in dirty samples during the collection process, the amplitude of waveform is larger and the shape is distorted by the influence of local discharge.

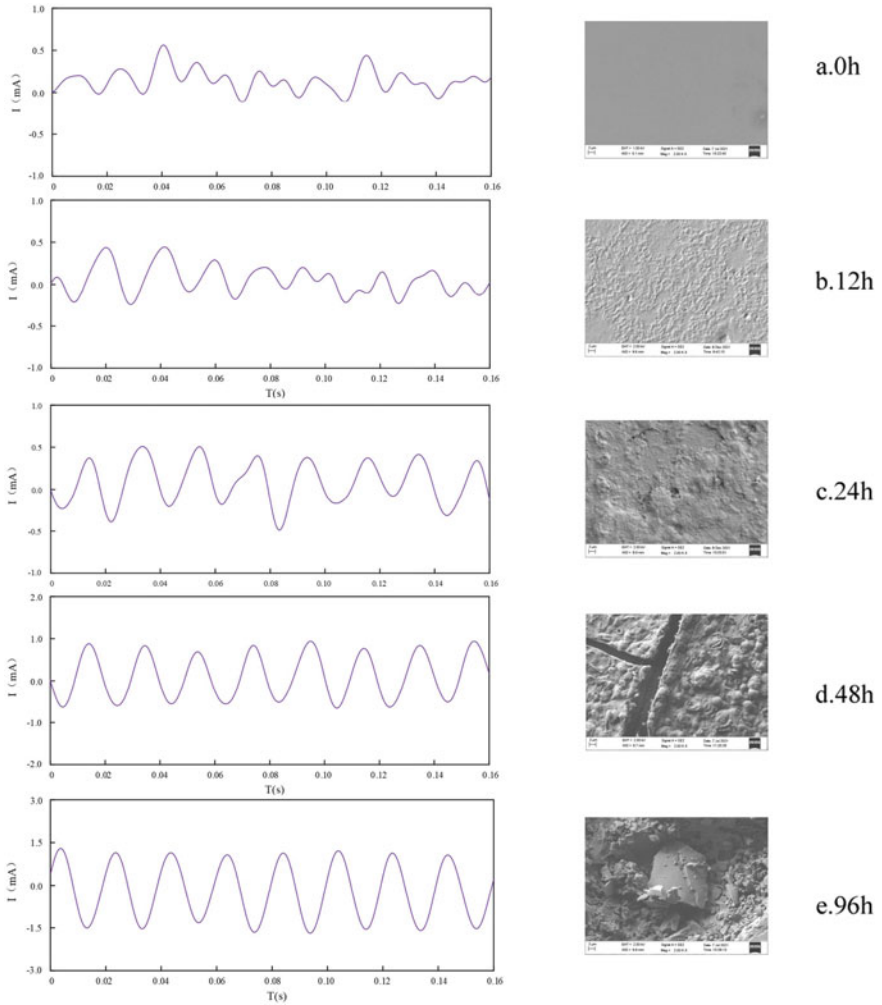
Different environmental factors have an effect on the leakage current after the epoxy resin surface condensation. The waveform of the leakage current of clean samples will appear local periodic due to the influence of condensation; diatomaceous earth can form a conductive channel with dew droplets to make the waveform of the leakage current of samples larger in amplitude and more periodic; NaCl will cause local discharge on the surface of samples and make the waveform of the leakage current distorted.

### ***3.3 Condensation Discharge Test for Different Time of Hygrothermal Aging Samples***

The leakage current was collected as above, and the samples were subjected to condensation test in the environmental chamber after aging. 2 kV was applied to both ends of the electrodes after the condensation was completed, and the leakage current was collected through the collection resistor. The leakage currents for different aging durations are shown in Fig. 6.

From the figure, it can be seen that the aging time has a great influence on the leakage current of epoxy resin under condensation, the greater the aging time, the larger the leakage current and the stronger the waveform periodicity, the effective values of leakage current of aging 48 and 96 h samples under condensation are 0.82 and 1.37 mA, compared with 0.24 mA of unaged samples, and the leakage current of aging samples has a significant increase. The waveform periodicity is not obvious, local periodic sine wave, while the aging 48, 96 h sample leakage current is very strong periodic sine wave. This indicates that there is no continuous conductive channel on the surface of the unaged samples in the condensation state, which leads to the irregularity of the leakage current waveform, while the more severe aging samples have continuous discharge channels on the surface after condensation. This phenomenon is the same as the law of change of the condensation flashover voltage, not aging or aging length of the sample, the surface hydrophobic not completely lost, the surface dew is evenly dispersed, for the formation of a large area of water film. The sample with more aging time, the surface damage is more serious loss of hydrophobic serious, resulting in a large number of continuous water film on its surface, forming a continuous conductive channel, the leakage current appears continuous regular sinusoidal wave.

After the aging of the sample surface cracks, holes, water repellency loss of its surface condensation is easy to appear after the formation of more obvious conductive channels by water, resulting in a rapid decline in the sample condensation flashover



**Fig. 6** Post-aging sample condensation test leakage current

voltage, condensation leakage current increases, and the greater the aging length of the sample surface condensation leakage current waveform is more periodic, the greater the amplitude tends to be closer to the sine wave.



## 4 Conclusion

This study examines how epoxy resin discharges during condensation, including how epoxy resin samples are prepared, how condensation environments are simulated, how condensation discharge tests are conducted, and how aging and environmental factors affect how epoxy resin discharges during condensation. The study's key findings include the following:

- (1) Different environmental factors affect the leakage current of the epoxy resin surface after condensation. The waveform of leakage current of clean sample will appear local periodicity due to the influence of condensation; diatomaceous earth can form a conductive channel with dew droplets to make the waveform of leakage current of sample larger in amplitude and stronger in periodicity; NaCl will cause local discharge on the surface of sample and make the waveform of leakage current distorted.
- (2) Epoxy resin leakage current under condensation is significantly influenced by aging time; the longer the aging time, the higher the leakage current and the more pronounced the waveform periodicity. After aging, the sample's surface develops cracks and holes, and its water repellency significantly decreases, making it easier for water to form conductive channels on the sample's surface after condensation. This causes the condensation flashover voltage to drop quickly and the condensation leakage current to rise.

**Acknowledgements** This work was supported by the State Grid Chongqing Electric Power Company Science and Technology Project, 2023 Yudian Science and Technology 50#.

## References

1. Cao Y, Zhu X, Tan Y (2018) Design of heat dissipation structure for high current medium voltage AC Gas-insulated metal-enclosed switchgear. *High Voltage Apparatus* 54(01):200–206 (in China)
2. Ning W, Lin X, Peng W, Suo W, Yuan H (2020) Research on the key technology of medium voltage environmental protection metal-enclosed switchgear. *E3S Web Conf* 185:04031
3. Degui C (2008) Progress in the thermal analysis of low voltage apparatus. *Low Voltage Appliances* 17:1–4 (in China)
4. Liu H, Xing Y, Li Wet al (2010) Corrosion on surface coating of electronic devices in hygrothermal environment. *Mater Eng* (2):58–63 (in China)
5. Liu Z, Zhang Z (2015) Investigation of thermal-oxidative accelerated aging mode for life prediction of epoxy resin pouring sealant. *Space Electron Technol* (05):77–82 (in China)
6. Li Q, Liu W Han S et al (2015) Analysis on partial discharge characteristics of epoxy resin insulation during high-frequency electrical-thermal aging. *High Voltage Eng* 41(02):389–395 (in China)
7. Huang Y, Yi L (2016) Effect of thermal ageing on dielectric property of epoxy resin for dry-type transformer. *Insulating mater* (09):53–56+60 (in China)

8. Bi M, Deng R, Jiang T et al (2022) Study on corona aging characteristics of silicone rubber material under different environmental conditions. *IEEE Trans Dielectr Electr Insul* 29(2):534–542
9. Bi MQ et al (2021) Simulation design of multi-needle-plate electrode corona aging device and experimental study on aging characteristics of silicone rubber. *J CQUT* 35(2):177–184 (in China)
10. Bi MQ et al (2020) The research on corona aging silicone rubber materials' NMR characteristics. *IEEE Access* 8:128407–128415

# Transformer Health Condition Assessment Method Based on Full Life Cycle Data



Linhong Xie, Zihao Jiang, Longji Feng, Chengbo Chu, Zhiyong Huang, and Xiaotian Liu

**Abstract** Existing transformer condition assessment methods cover too few condition indicators and the assessment process relies on expert experience, making it difficult to guide field maintenance work. To address these problems, this paper proposes a transformer health condition assessment method based on full life cycle data. The method uses multi-dimensional, multi-structured, full life cycle data such as transformer operation information, online monitoring data, offline test data and operations and maintenance records as feature quantities, analyses the correlation between different condition indicators and transformer health status, constructs a fuzzy inference-based transformer health index calculation method, realises the quantitative rating of transformer health status, and verifies the method with field example analysis. The feasibility and validity of the method were verified by combining with field cases. The results of the field application show that the method can effectively reflect the transformer operation status and has certain guiding significance for the field operation and maintenance decision.

**Keywords** Transformers · Health index · Condition assessment · Fuzzy logic · Health management

## 1 Introduction

Power transformers are a significant and expensive piece of high voltage equipment in power systems, often accounting for 60% of the total investment. However, in practice, many transformers in operation have exceeded this time limit but still show no signs of increasing failure rates or end of life, although transformers are often reliable equipment, they do fail and if an incident occurs causing a widespread

---

L. Xie · L. Feng · C. Chu  
State Grid Nanjing Power Supply Company, Nanjing 210000, China

Z. Jiang (✉) · Z. Huang · X. Liu  
Department of Energy and Electrical Engineering, Nanchang University, Nanchang 330031, China  
e-mail: 1981375284@qq.com

© Beijing Paiké Culture Commu. Co., Ltd. 2024  
X. Dong and L. Cai (eds.), *The Proceedings of 2023 4th International Symposium on Insulation and Discharge Computation for Power Equipment (IDCOMPU2023)*, Lecture Notes in Electrical Engineering 1103, [https://doi.org/10.1007/978-981-99-7413-9\\_29](https://doi.org/10.1007/978-981-99-7413-9_29)

power outage, it will seriously affect the lives of residents and social production, bringing huge losses. Therefore, it is important to keep track of the operating status of transformers in real time and to take effective countermeasures in time to ensure their safe and stable operation [1, 2].

At present, A great deal of research has been carried out on the condition assessment of power transformers by researchers both at home and abroad. The paper [3–5] applied information fusion combined with relevant test indicators to assess the condition of power transformers, but the assessment results varied greatly by choosing different condition characteristic quantities, and the accuracy of the assessment was difficult to guarantee; the paper [6] applied the application of stochastic fuzzy theory to predict the operating condition of transformers, and took an accurate subordinate function for each parameter, but the number of state quantities considered is too small, and the influence of operational information, maintenance records and other indicators is not considered; the paper [7] applies the health index theory combined with a large number of indicators to predict the health state of power transformers, but the assessment is more subjective and there is a possibility of masking the real condition of transformers; in addition, there are also papers using neural networks [8], support vector machines [9], topologic analysis [10], deep learning [11] and other intelligent algorithms combined with transformer diagnostic and routine tests, online monitoring devices, etc. to build transformer condition assessment models.

Although researchers have achieved fruitful theoretical results in the field of transformer condition assessment, there is still a lack of methods to effectively assess the condition of transformers in the field. This paper proposes a transformer condition assessment method based on the whole life cycle data of power transformers and the fuzzy comprehensive evaluation method, which can effectively solve the problem of small number of state quantities in the assessment model and ignore the influence of correlation between state quantities, improve the accuracy of the assessment results, enhance the confidence of asset managers in the assessment results, and provide more reliable decision-making advice for field operation and maintenance.

## 2 Health Assessment Indicator System

In this paper, by reviewing the relevant literature and referring to [12, 13], we analysis the characteristic parameters affecting transformer condition during the full life cycle of transformers and establish a multi-layer assessment index system, dividing the evaluation indexes are divided into four aspects: factory test, handover tests, online monitoring, O&M maintenance test.

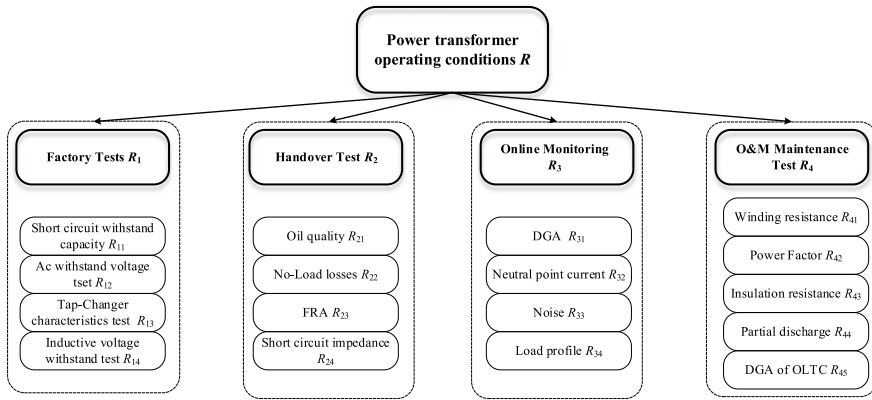


Fig. 1 Transformer condition assessment index system

### 2.1 Assessment Indicator System Establishment

The scientific and reasonable selection of evaluation indicators is a key element of condition assessment, and it is important to avoid redundancy of evaluation indicators while ensuring the integrity of the assessment system. The evaluation index system in this paper is shown in Fig. 1.

### 2.2 Quantification of Assessment Indicators

This paper introduces the concept of deterioration degree [14], which characterize the relative deterioration of the current actual state of a quantitative indicator compared to the fault state. Different values reflect different degrees of deterioration of the judged indicators. Each indicator is set according to the power industry standard for threshold value 1 and threshold value 2, and the specific calculation process refers to [15]. If there is no explicit threshold for one of the above state quantities or if a qualitative judgement is required, the degree of deterioration is given by the experts after discussion on the basis of the site conditions.

## 3 Multi-level Fuzzy Integrated Evaluation Method

Fuzzy comprehensive evaluation method is a comprehensive evaluation method based on fuzzy mathematics [16]. It can better solve fuzzy and difficult to quantify problems, and is suitable for various non-deterministic problems.

### 3.1 Multi-level Fuzzy Evaluation Model Development

**Fuzzy Factor Set.** According to the evaluation index system shown in Fig. 1, we have established a three-layer fuzzy evaluation model including target layer, criterion layer and indicator layer. The indicators established by the target layer are  $U = (U_1, U_2, U_3, U_4, U_5)$ ,  $U_i$  ( $i = 1, 2, 3, 4, 5$ ) is the  $i$ -th indicator of the criterion layer and is determined by all indicators of the indicator layer.

**Fuzzy Commentary Collection.** Set the rubric set  $Q = (\text{Very Good, Good, Fair, Poor, Very Poor}) = (v_1, v_2, v_3, v_4, v_5)$ .

**Fuzzy Judgment Matrix.** Let the  $i$ -th indicator  $u_i$  of a criterion layer element evaluate the state of the transformer, the indicator's affiliation to the element  $v_i$  in the comment set is  $r_{ij}$  ( $j = 1, 2, 3, 4, 5$ ), the evaluation result of  $u_i$  can then be represented by the affiliation set  $R_i, R_i = (r_{i1}, r_{i2}, r_{i3}, r_{i4}, r_{i5})$ , the affiliation set of all indicators in the criterion layer then constitutes its primary fuzzy evaluation matrix, the final evaluation matrix can be obtained after prioritization.

Similarly, the judgement matrix  $R$  of the target layer can be obtained from the fuzzy judgement of the criterion layer and then filtered by priority.

### 3.2 Weighting and Correction

In this paper, The analytic hierarchy process is chosen for weight determination. A reasonable judgment matrix is constructed to compare the importance of all state quantities with each other to obtain the evaluation index weights, which are calculated with reference to literature [17]. Referring to the relevant literature [12] and [18], summarize the common faults of power transformers with the corresponding diagnostic state quantities and modify the weights.

$$w_1 = w_0 \times A^k \quad (1)$$

$w_0$  is the weight before correction,  $w_1$  is the weight after correction,  $A$  is the correction constant,  $k$  is the correction factor, the value is determined by the health evaluation level of the state quantity with the most severe deterioration, the  $k$  value corresponds to 0–4 in order from healthy to severe. The final weights are obtained by normalizing the corrected weights.

The weight of each indicator in each layer can be determined according to the above weight determination method: criterion layer  $W = (W_1, W_2, W_3, W_4, W_5)$ , indicator layer  $w_i = (w_{i1}, w_{i2}, w_{i3}, \dots, w_{ij})$ .

**Table 1** Transformer health index assessment criteria

Health index	Health grade	Description of health condition
0.9–1	Very good	Slight ageing or slight deterioration of individual groups of components
0.7–0.9	Good	Minor deterioration of a few groups of components or significant deterioration of individual groups of components
0.5–0.7	Fair	Significant deterioration or minor defects in some group components
0.3–0.5	Poor	Significant deterioration or obvious defects in a large number of group components
0–0.3	Very poor	Serious defects or faults

### 3.3 Fuzzy Calculation and Health Indice

On the basis of the fuzzy evaluation matrix and the weight vector of each layer of the evaluation system, the overall state of the transformer is finally obtained by using the fuzzy comprehensive evaluation operator  $B = W \cdot R = (b_1, b_2, b_3, b_4, b_5)$ . The overall state is expressed in terms of a health index between (0,1), the closer to 1 the healthier it is, and is calculated as follows:

$$HI = 1 - \frac{\sum_{m=1}^5 b_m \times m}{5} \quad (2)$$

The health index assessment criteria are shown in Table 1.

### 3.4 Assessment of Indicator Affiliation Functions

In this paper, an improved triangular trapezoidal affiliation function is chosen to characterize the fuzzy comprehensive evaluation indicators, and the image of the improved triangular trapezoidal affiliation function is shown in Fig. 2. Based on the improved triangular trapezoidal affiliation function, the affiliation of the evaluation indicators can be calculated for each health class.

$\lambda_1 - \lambda_5$  in Fig. 3 are the fuzzy threshold values for each state rubric set indicator, calculated and analyzed with reference to standards [12] and [13] and years of data from the field, and evaluation indicators without clear fuzzy threshold values are analyzed jointly by multiple experts for their affiliation.

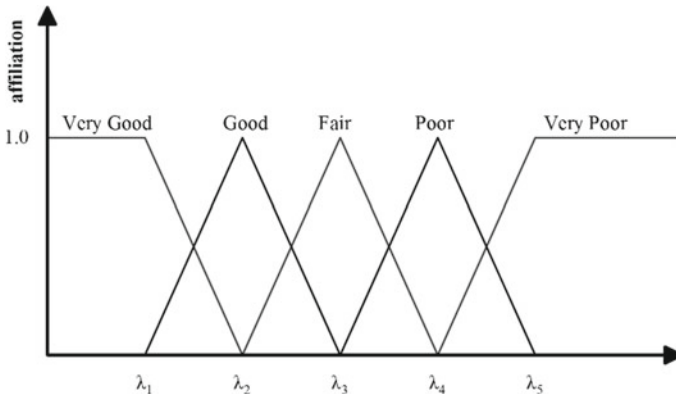


Fig. 2 Improved trigonometric subordinate function diagram

### 3.5 Transformer Health Status Assessment Framework

The complete assessment process in this paper can be divided into four steps, as shown below:

- (1) Establishment of health assessment index system, through the full life cycle data, a three-layer assessment index system is established.
- (2) Establishment of fuzzy evaluation model, establishing the corresponding fuzzy evaluation model according to the evaluation index system.
- (3) Acquisition and correction of weights, using hierarchical analysis to acquire weights and combining the interrelationship of state quantities for weight correction.
- (4) Combine the fuzzy evaluation results to calculate the health index, using fuzzy calculation to get the evaluation vector, and then carry out the calculation of health index and health state rating.

## 4 Case Studies

The algorithm is validated in the paper with data from a 500kV transformer at a substation in Jiangsu province, model ODFS-334000/500, commissioned in July 2012, with data up to June 2021, as shown in Table 2.

Through the experimental data, calculate the degradation degree and affiliation degree, can get the preliminary judgment matrix, and then after the priority screening, can get the final judgment matrix, this paper uses  $R_3$  as an example to calculate.

The primary evaluation matrix of  $R_3$  is shown below:



**Table 2** Transformer experimental data and weights

Guideline level indicators	Condition indicators	Value 1	Value 2	Measured values	Degradation	Weights
Factory tests $R_1$	$R_{11}$	–	–	–	0	0.1682
	$R_{12}$	0.5	0.8	0.45	0	0.2629
	$R_{13}$	–	–	–	0	0.3256
	$R_{14}$	0.5	0.8	0.39	0	0.2433
Handover test $R_2$	$R_{21}$	1.2	3	1.36	0.133	0.0463
	$R_{22}$	5	20	4.8	0	0.3672
	$R_{23}$	–	–	–	0	0.5521
	$R_{24}(\%)$	1	4	1.35	0.167	0.0344
Online monitoring $R_3$	$R_{31}$	1.2	3	2.6	0.778	0.4872
	$R_{32}(A)$	3	12	2.6	0.065	0.0228
	$R_{33}(dB)$	70	120	56	0	0.4876
	$R_{34}$	3.5	0.5	2.8	0.233	0.0024
O&M maintenance test $R_4$	$R_{41}(\%)$	1	5	1.26	0.065	0.0375
	$R_{42}$	0.003	0.01	0.0054	0.343	0.0248
	$R_{43}$	10,000	1000	10,800	0.089	0.0254
	$R_{44}(PC)$	0	300	241	0.8	0.0522
	$R_{45}$	1.2	3	1.15	0	0.8331

$$R_3 = \begin{bmatrix} 0 & 0 & 0 & 0.468 & 0.532 \\ 0.954 & 0.046 & 0 & 0 & 0 \\ 1 & 0 & 0 & 0 & 0 \\ 0.325 & 0.675 & 0 & 0 & 0 \end{bmatrix}$$

The priority filtered matrix is as follows:

$$R'_3 = [0 \ 0 \ 0 \ 0.468 \ 0.532]$$

Similarly, the judgment matrix of other indicators can be calculated, and combined with the weights obtained from the above calculation, we obtain the final result of the fuzzy calculation as shown in the following equation:

$$R = [0 \ 0 \ 0 \ 0.422 \ 0.578]$$

The calculation from Eq. (2) gives  $HI = 0.0844$ , which is serious. In fact, the main transformer was immediately taken out of service after analysis of the field data by the device alarm, and a routine, diagnostic test was carried out on the transformer, which was diagnosed as having a short circuit between the strands of the medium voltage coil, with a significantly hot core column and a very critical situation, and

the assessment was consistent with the actual results, verifying the validity of this paper.

## 5 Conclusion

- (1) The condition assessment of power transformers is a complex multi-indicator decision problem. This paper establishes a complete and scientific transformer operating condition assessment hierarchy based on transformer full life cycle data, mainly including factory tests, handover test, online monitoring, operation and maintenance record, and applies different methods to quantify each assessment index.
- (2) This paper uses the analytic hierarchy process to carry out the assignment of weights. The correlations between the evaluation indicators are also analysed and the resultant weights of the assignment are revised to make the assignment results more reasonable and realistic, and to introduce priority degrees to effectively overcome the problem that fuzzy calculations may conceal the true working conditions of transformers.
- (3) The transformer condition assessment method based on full life cycle data proposed in this paper can effectively overcome the problems of strong subjectivity, too little condition coverage and low evaluation accuracy compared to traditional methods. The effectiveness of the method is verified with practical cases, so that maintenance personnel can formulate reasonable maintenance plans and operation strategies.

## References

1. Thango BA, Akumu AO, Sikhosana LS, Nnachi AF, Jordaan JA (2021) Preventive maintenance of transformer health index through stray gassing: a case study. In: 2021 IEEE PES/IAS PowerAfrica, Nairobi, Kenya, 2021, pp 1–5. <https://doi.org/10.1109/PowerAfrica52236.2021.9543255>
2. Dorji T, Suwanasri T, Poonnoy N, Suwanasri C (2022) Fuzzy logic approach for power transformer condition assessment using health index. In: 2022 International conference on power, energy and innovations (ICPEI), Pattaya Chonburi, Thailand, 2022, pp 1–4. <https://doi.org/10.1109/ICPEI55293.2022.9986526>
3. Bardyk EI, Bolotnyi N (2022) Improved power transformer condition assessment under uncertainty using fuzzy logic. In: 2022 IEEE 8th International conference on energy smart systems (ESS), Kyiv, Ukraine, 2022, pp 53–58. <https://doi.org/10.1109/ESS57819.2022.9969327>
4. Milosavljevic S, Janjic A (2020) Power transformer health index estimation using evidential reasoning. *Facta Univ, Ser: Electron Energetics* 33(4):571–581
5. Yue Y, Shi C, Luyao L, Zheng G, Tao S (2021) Multi-dimensional information fusion and condition assessment of transformers based on improved D-S evidence theory. *Electr Technol* 22(06):66–72 (in Chinese)

6. Shi Y, Tan G, Zhao B, Zhang G (2022) A method of power transformer condition assessment based on fuzzy integrated assessment model and information fusion. *Power Syst Prot Control* 50(21):167–176. <https://doi.org/10.19783/J.CNKL.PSPC.220008> (in Chinese)
7. Scatiggio F, Pompili M (2013) Health index: the TERNA's practical approach for transformers fleet management. In: 2013 IEEE Electrical insulation conference (EIC), Ottawa, ON, Canada, 2013, pp 178–182. <https://doi.org/10.1109/EIC.2013.6554228>
8. Ballal MS, Jaiswal GC, Doorwar A, Venkatesh B (2019) Online condition assessment of power transformers using neural network. In: 2019 Innovations in power and advanced computing technologies (i-PACT), Vellore, India, 2019, pp 1–4. <https://doi.org/10.1109/i-PACT44901.2019.8960161>
9. Han X, Wang X, Han S, Zhang Y, Wang J (2021) A condition evaluation method for large power transformers based on integrated learning of unbalanced data. *Power Grid Technol* 45(01):107–114. <https://doi.org/10.13335/J.1000-3673.PST.2019.2180>. (in Chinese)
10. Liao R, Zhang Y, Huang F, Zheng H, Yang L (2012) Evaluation of the insulation status of power transformers based on the topological analysis method. *High Voltage Technol* 38(03):521–526 (in Chinese)
11. Su L, Chen L, Xu P, Lin J, Sheng Ge H, Jiang X (2021) Transformer operating condition analysis based on deep belief network. *High Voltage Electron* 57(02):56–62. <https://doi.org/10.13296/J.1001-1609.HVA.2021.02.009> (in Chinese)
12. DL/T 1685-2017 Guidelines for condition evaluation of oil-immersed transformers (reactors) (in Chinese)
13. DL/T 596-2021 Preventive test procedure for electric power equipment (in Chinese)
14. Li F, Hu YG, Tang Xianhu, Liu ZD (2010) Online operation status evaluation method for grid-connected wind turbines. *Chin J Electr Eng* 30(33):103–109. <https://doi.org/10.13334/J.0258-8013.PCSEE.2010.33.004> (in Chinese)
15. Ruijin L, Qian W, Sijia L, Yuxiang L, Caixin S (2008) A fuzzy integrated evaluation model for power transformer operating condition. *Power Syst Autom* 03:70–75 (in Chinese)
16. Zhao X, Zhao C, Jia X, Li G (2005) Fuzzy comprehensive evaluation of power quality based on variable weights. *Power Grid Technol* (06):11–16 (in Chinese)
17. Li N, He Z (2009) A comprehensive assessment of power quality by combining subjective and objective weights. *Power Grid Technol* 33(06):55–61 (in Chinese)
18. Xie L, Li L, Cheng Y, Lu M, Jiang L, Teng Y (2015) A transformer fault diagnosis method incorporating set-pair analysis and association rules. *Chin J Electr Eng* 35(02):277–286. <https://doi.org/10.13334/J.0258-8013.PCSEE.2015.02.003> (in Chinese)

# Effect of Positive Temperature Coefficient Materials on the AC Breakdown Strength and Dielectric Properties of Epoxy Composites



Chenyuan Teng, Shuo Li, Yuanxiang Zhou, Ling Zhang, Yunxiao Zhang, and Meng Huang

**Abstract** In operation, the negative temperature coefficient (NTC) electrical resistivity characteristics of polymeric insulating materials causes DC electric field distortion within power equipment insulation and lead to the failure. The doping of positive temperature coefficient (PTC) ceramic particles can suppress the NTC characteristics of the composites, but the electrical properties under AC voltages are unrevealed. In this paper, epoxy composites (0–20 wt%) doped with polydopamine-coated PTC particles were prepared, whose AC breakdown strength and dielectric properties were tested. The results shows that the decrease of AC dielectric strength is smaller than that under DC voltages after the doping PTC particles, and the coating of polydopamine can enhance the AC dielectric strength. As the doping content increases, the dielectric constant and  $\tan\delta$  of the epoxy composites increases, and the maximum increase of dielectric loss power is about 2% of the loss power caused by the current-carrying conductor. The research provides a theoretical basis for the optimization of the insulating performance of the equipment under the AC-DC composite voltages.

**Keywords** Temperature gradient · Resistivity-temperature properties · Positive temperature coefficient material · Epoxy resin · Polydopamine

---

C. Teng · S. Li  
College of Information Engineering, Zhejiang University of Technology, Hangzhou 310023, China

C. Teng · Y. Zhou (✉) · L. Zhang · Y. Zhang  
State Key Laboratory of Control and Simulation of Power Systems and Generation, Equipment Department of Electrical Engineering, Tsinghua University, Beijing 100084, China  
e-mail: [zhou-yx@tsinghua.edu.cn](mailto:zhou-yx@tsinghua.edu.cn)

C. Teng · M. Huang  
State Key Laboratory of Alternate Electrical Power System With Renewable Energy Sources, North China Electric Power University, Beijing 102206, China

## 1 Introduction

Both traditional fossil energy sources and new energy sources such as wind energy require high-voltage DC transmission technology to achieve long-distance and large-scale optimal allocation of energy [1]. Epoxy resin materials are widely used in DC electrical equipment such as bushings and insulators due to their excellent insulation, mechanical [2, 3]. During operation, a temperature gradient distribution inside the equipment insulation is inevitable due to the synergistic effect of heat generation from the current carrying conductor and heat dissipation from the environment [4]. The electrical resistivity of epoxy resin has a negative temperature coefficient (NTC) effect, i.e., it decreases with increasing temperature, resulting in a gradient distribution of electrical resistivity with temperature inside the equipment insulation as well [5]. Unlike AC electric fields, the distribution of DC electric fields is influenced by the electrical resistivity distribution. The temperature-dependent characteristics of electrical resistivity can lead to DC field distortion, which accelerates the aging of electrical equipment and even premature failure. Therefore, it is importance to optimize the electrical resistivity-temperature characteristics of epoxy resin materials.

In order to suppress the NTC effect of electrical resistivity of insulating materials, researchers usually use the doping of fillers such as  $\text{Al}_2\text{O}_3$ ,  $\text{MgO}$ , and graphene oxide to suppress the charge carrier migration behavior [6–8]. Since the temperature-dependent characteristics of common fillers are relatively fixed, it is difficult to meet the demand for directional regulation of electrical resistivity-temperature characteristics of different insulating materials under various operating conditions. Recent years, researchers have proposed the method of doping ceramic particles with positive temperature coefficient (PTC) electrical resistivity to suppress of NTC effect in epoxy resin materials and thus achieve a significant suppression of DC electrical field distortion [9]. Combined with the interfacial modification of polydopamine (PDA), the composites were able to obtain a high levels of DC breakdown strength [10]. However, bushings are also subjected to AC voltages simultaneously during operation, and the electrical properties such as AC breakdown affect the reliable operation of the device insulation, while the relevant research is lack.

Therefore, PTC particles with core-shell structure were constructed by PDA, and epoxy resin was selected as the matrix material to prepare epoxy resin composites with different mass fractions in this paper. The effect of PDA-coated PTC particles on the AC breakdown and dielectric properties of epoxy resin composites was studied to provide data and theoretical support for the reliable operation of the insulation under AC electric field.

## 2 Experimental

### 2.1 Experimental Materials and Preparation

In this paper, a bisphenol A type liquid epoxy resin was used. Methylhexahydrophthalic anhydride (MeHHPA) and N, N-dimethyl benzyl amine were selected as the curing agent and accelerator respectively. The mass ratio between epoxy resin, curing agent and accelerator was 100:85:2. Barium titanate based PTC ceramic (BT60) micron powder with a Curie temperature of 60 °C was used as a filler [11].

132 mL of Tris solution (10 mM, pH 8.5) was taken, and 1 g of BT60 particles were added and then ultrasonically shaken at room temperature for 30 min. Then 264 mg of dopamine hydrochloride powder was added and stirred magnetically at high speed in a water bath at 40 °C for 12 h. As the reaction proceeded, the solution gradually changed from yellow to dark brown [12]. After completion of the reaction, the mixture was washed three times by centrifuging with deionized water, and the waste solution was separated and removed using high-speed centrifugation. Finally, the coated BT60 particles were ground after being dried in oven at 70 °C for 24 h. The PDA-modified micron particles were denoted as BT60-PDA. In addition, a control group without the addition of dopamine hydrochloride, while being treated with the same steps was obtained and denoted as BT60-UN.

A certain amount of BT60-PDA, epoxy resin, curing agent and accelerator were mixed thoroughly and cured to prepare epoxy resin composite films. The mass fractions of BT60-PDA particles were 0 wt%, 2.5 wt%, 5 wt%, 10 wt% and 20 wt%, respectively, and were denoted as EP-0, pEP-2.5, pEP-5, pEP-10 and pEP-20. The BT60-UN doping mass fraction of 20 wt% is denoted as uEP-20. The thicknesses of the film are  $220 \pm 20 \mu\text{m}$  and 1 mm respectively, which are used to measure the AC breakdown and dielectric properties.

### 2.2 Characterization

The negative DC breakdown strength of the samples was tested according to the IEC 60243 Electric strength of insulating materials. Stainless steel ball plate electrodes and specimens were placed in transformer oil. The test temperature was controlled by an oven, which were 30 and 90 °C. 2h preheating was conducted before the test to ensure uniform temperature distribution. Resistance capacitance divider was used to show the real-time voltage values. The ramp-up rate was 1000 V/s. 21 measurements were performed for each group. The test results were expressed using a two-parameter Weibull distribution.

The dielectric properties of the specimens were measured using a CONCEPT 80 broadband dielectric spectrometer from Novocontrol, Germany. The measurement voltage was AC with an amplitude of 1 V and a frequency range of  $10^0$ – $10^6$  Hz. The measurement temperature range was 30–110 °C.

### 3 Results and Discussion

#### 3.1 AC Breakdown Characteristics

Taking valve-side bushings as an example, they are subjected to AC voltage during operation, so the AC breakdown strength characteristics cannot be ignored when optimizing the insulating materials. Figure 1 shows the Weibull distribution of AC breakdown test results. The calculated scale parameter  $\alpha$  and shape parameter  $\beta$  are shown in Table 1. The scale parameter  $\alpha$  represents the breakdown strength at a failure probability of 63.2% (usually called Weibull breakdown strength), and the shape parameter  $\beta$  represents the dispersion of the data.

From the test results, it is clearly to know that the AC breakdown strength of epoxy resin composites is much lower than the DC breakdown strength [11]. At AC voltage, the insulating material also has polarization loss, which leads to a more pronounced thermal effect during breakdown. The addition of BT60 particles

Fig. 1 Weibull distribution of AC breakdown test results

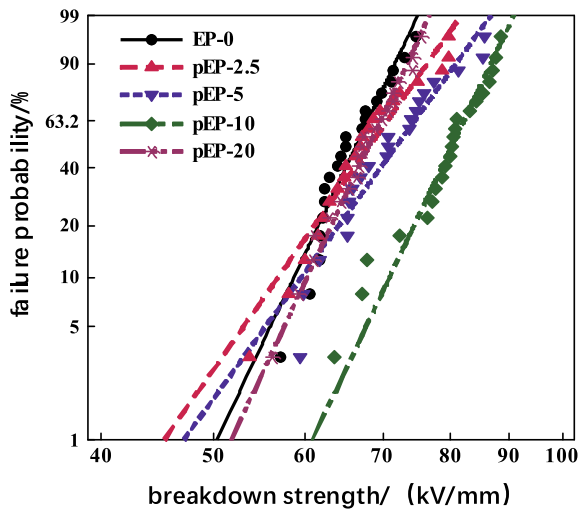
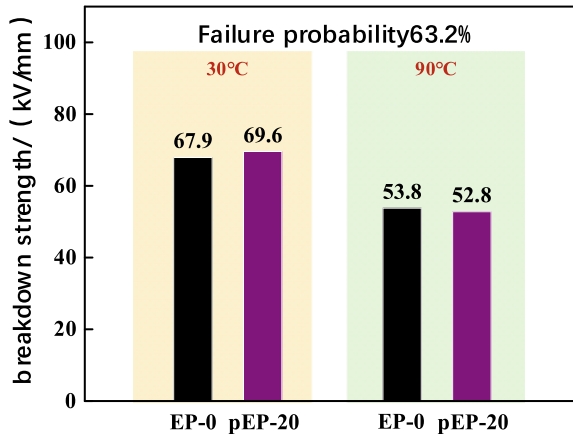


Table 1 Scale and shape parameters

Group	Doping quality (wt%)	Scale parameters/(kV/mm)	Percentage/%	Shape parameters
EP-0	0	67.9	100	15.3
pEP-2.5	2.5	70.5	103.8	10.4
pEP-5	5	74.5	109.7	10.0
pEP-10	10	82.1	120.9	15.3
pEP-20	20	69.6	102.5	15.5

**Fig. 2** Weibull AC breakdown strength of EP-0 and pEP-20 at 30 and 90 °C



improves the thermal conductivity of the epoxy composites. The increased dissipation of heat contributes to the AC breakdown strength. As the doping mass of BT60-PDA micron particles increases, the AC breakdown strength rises and then decreases. The breakdown strength of the pEP-10 group is the highest at 82.1 kV/mm, which is 120.9% (67.9 kV/mm) of the pure epoxy resin. pEP-20 group has the lowest breakdown strength of 69.6 kV/mm, but it is still higher than pure epoxy resin. It shows that epoxy composite with high doping content still have high AC breakdown strength at 30 °C.

Figure 2 shows the Weibull AC breakdown strengths of EP-0 and pEP-20 at 30 °C and 90 °C. As the temperature reaches to 90 °C, AC breakdown strength of EP-0 and pEP-20 decrease. The AC breakdown strength of EP-0 and pEP-20 at 90 °C were 53.8 kV/mm and 52.8 kV/mm respectively. It can be found that the difference between two groups is only 2.4%. Therefore, it can be concluded that the addition of BT60-PDA micron particles has little effect on the AC breakdown performance of the epoxy composites at high temperature in general. In contrast, the DC breakdown strength of pEP-20 was 92.7% of EP-0 at the same doping content [10], which indicates that the effect of BT60-PDA particles on the DC breakdown strength is greater than the AC breakdown strength.

### 3.2 Dielectric Properties

Figure 3a, b show the temperature spectra of the relative permittivity of the samples at 50 Hz and 10<sup>6</sup> Hz frequencies. Since the permittivity of BT60 particles is larger than that of the pure epoxy resin, it will increase the permittivity of the epoxy composites through the Maxwell–Wagner interfacial polarization. Therefore, the relative permittivity of the epoxy composites increase with the mass fraction of BT60-PDA particles. The relative permittivity of pEP-20 group is significantly higher than the



other groups due to the higher doping mass fraction. The relative permittivity of the pEP-20 group increases from 4.04 to 5.32 compared with EP-0 at 50 Hz. In addition, the relative permittivity of all groups increases with increasing temperature, and a turning point occurs near the glass transition temperature. Due to the difference of glass transition temperature among these groups is small, the temperature turning points showed in the temperature spectra are basically similar. After the temperature is higher than the glass transition temperature, the epoxy resin changes from the glassy state to the high-elastic state. At this stage, the motion of the molecular chain segments is enhanced, so the increase rate of the relative permittivity of all groups increases significantly.

Figure 3c, d show the frequency spectra of the relative permittivity of the samples before and after the Curie temperature of BT60 particles. It shows that the permittivity of the samples decreases with the frequency at both temperatures, while the decrease rate increases continuously. This is because the molecular structure of pure epoxy resin is tight, and the orientation of polymer molecules cannot keep up with the change of frequency. In contrast, the trend of the relative permittivity in the high frequency band of the epoxy composites indicates that the interface between the

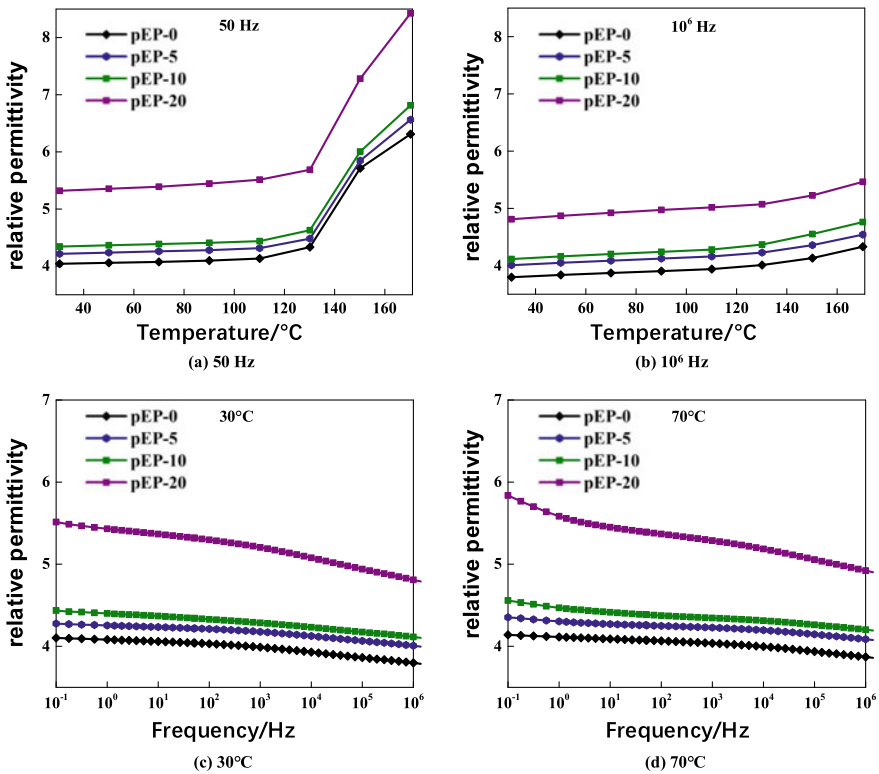


Fig. 3 Temperature and frequency spectra of dielectric constants

BT60 particles and the matrix is tightly bound by the polydopamine. On the other hand, the permittivity in the low frequency band are significantly different before and after the Curie temperature, indicating a temperature dependence of the internal interfacial state of the epoxy composite.

Under AC voltages, the dielectric has polarization loss in addition to leakage conduction loss. The loss is related to the heating of the insulating material. Therefore, the attention needs to be paid on the dielectric loss characteristics of insulating material at the same time. The dielectric loss angle tangent represents the loss of the material under AC voltages. In order to study the insulation loss during operation, the temperature spectrum of the loss angle tangent ( $\tan\delta$ ) of the samples at 50 Hz is given in Fig. 4. It shows that at lower temperatures,  $\tan\delta$  decreases and then increases as the doping mass of BT60-PDA particles increases. The  $\tan\delta$  of all groups decreases and then increases with the temperature. At 30 °C, the  $\tan\delta$  of EP-0 is about 0.006, while the pEP-20 is about 0.010. Although the  $\tan\delta$  of pEP-20 is higher than that of EP-0, it still meets the requirement of less than or equal to 0.01 as stipulated in the national standard IEC 60455 (Resin based reactive compounds used for electrical insulation).

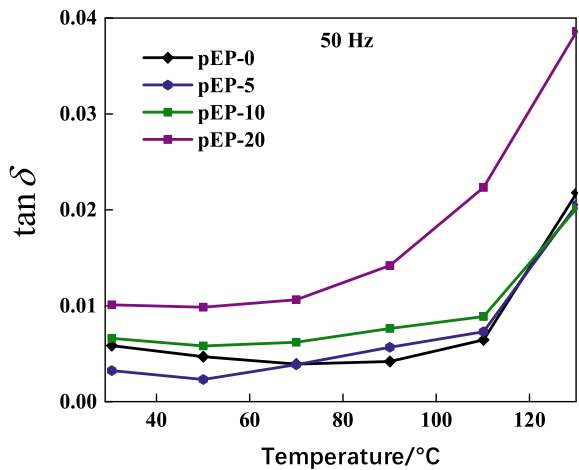
In order to study the influence on the loss power of the equipment induced by  $\tan\delta$ , the loss power calculation was carried out according to a 400 kV dry type valve-side bushing [13]. The loss power  $P$  can be obtained from the following equation [1]:

$$P = 2\pi fCU^2 \tan \delta \tag{1}$$

Equating the valve-side bushing insulation to the coaxial cylindrical capacitance, the capacitance value  $C$  can be calculated using the following equation [14]:

$$C = \frac{2\pi \varepsilon}{\ln(b/a)} \tag{2}$$

**Fig. 4** Dielectric loss frequency spectrum at 30 and 70 °C



where  $f$  is the frequency;  $U$  is the AC voltage rms;  $\epsilon$  is the permittivity, which is the product of vacuum permittivity and relative permittivity;  $b$  is the outer diameter;  $a$  is the inner diameter.

Combining the Eqs. 1 and 2, the loss power when insulated with EP-0 and pEP-20 can be calculated as 21 W and 48 W. Considering that the loss power of the current-carrying conductor of a 400 kV dry type valve-side bushing is 1534 W [13], it shows that the loss caused by BT60-PDA particles has a small effect on the temperature rise of bushing.

### 3.3 Effect of Polydopamine Coating

Figure 5 shows the AC breakdown results of EP-0, pEP-20 and uEP-20. Different from pEP-20, the doping of unmodified BT60 particles has a greater effect on the AC breakdown strength of the epoxy composite. The uEP-20 has a breakdown strength of 59.8 kV/mm, which is 88.1% of the pure epoxy resin (67.9 kV/mm). However, the decrease in AC breakdown strength is still less than that under DC voltages.

The AC breakdown strength of uEP-20 is 46.8 kV/mm at 90°C, which is 87% of EP-0, and this ratio is similar to that at 30°C. Since the surface of BT60-UN is unmodified, the interface formed is prone to form defects, resulting in a lower AC breakdown strength at both low and high temperatures compared with EP-0 (Fig. 6).

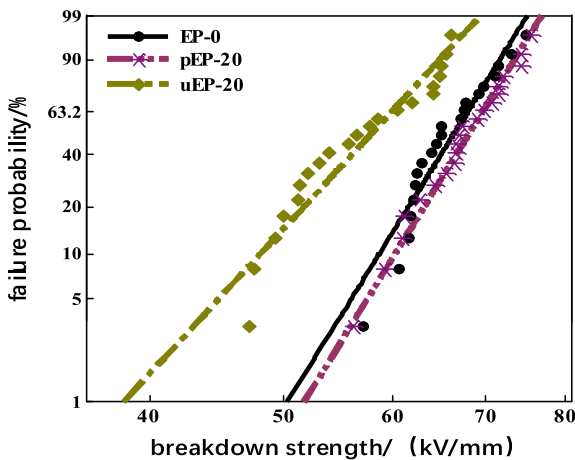
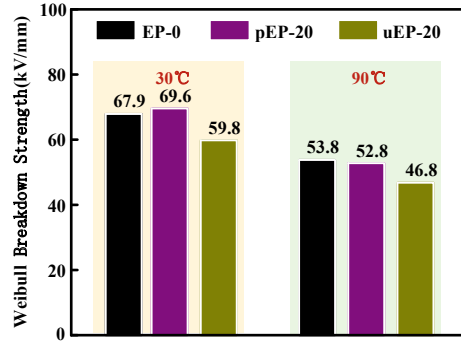


Fig. 5 Weibull distribution of AC breakdown strength

**Fig. 6** Weibull AC breakdown strength of EP-0, pEP-20 and uEP-20 at 30 and 90 °C



## 4 Conclusion

In this paper, epoxy resin composites doped with polydopamine-coated PTC particles were prepared, and experimental studies on their AC breakdown strength and dielectric properties were carried out, leading to the following conclusions:

- (1) Compared with the DC dielectric strength, the doping of positive temperature coefficient materials caused a smaller decrease in AC dielectric strength.
- (2) The AC breakdown strength of the epoxy composites doped with unmodified PTC particles decreases to 88.1% (30 °C) and 87% (90 °C) of the pure epoxy resin, while increases to 102.5% (30 °C) and 98.1% (90 °C) after modification with polydopamine.
- (3) The relative permittivity and  $\tan\delta$  of the epoxy composites increased with doping masses. When the doping mass fraction is 20 wt%, the  $\tan\delta$  increases from 0.006 to 0.010 at 30 °C, whose corresponding loss power increases about 2% of the current-carrying conductor.

**Acknowledgements** This study is supported by the State Key Laboratory of Alternate Electrical Power System with Renewable Energy Sources (Grant No.LAPS22013) and the National Natural Science Foundation of China (No.52207032).

## References

1. Liang XD, Zhou YX, Zeng R (2015) High voltage engineering, 2nd ed. Beijing: Tsinghua University Press (in Chinese)
2. Zhang CH, Zhang BY, Li MY (2023) Review of key insulation technologies of HVDC GIL. High Voltage Eng 49(3):920–936 (in Chinese)
3. Ding N, Mu HB, Liang ZJ et al (2022) Effect of moisture on the dielectric properties of epoxy resin impregnated paper for dry-type bushing. Trans China Electrotech Soc 37(11):2716–2724 (in Chinese)

4. Teng CY, Ding YC, Zhang YB et al (2022) Investigation on distribution of electrothermal coupling fields influenced by HVDC bushing insulation properties. *Front Energy Res* 10:1005470
5. El-Refaie AM (2019) Role of advanced materials in electrical machines. *CES Trans Electr Mach Syst* 3(2):124–132
6. Chen Y, Zhang DH, Wu XF et al (2017) Epoxy/ $\alpha$ -Alumina nanocomposite with high electrical insulation performance. *Prog Nat Sci-Mater Int* 27(5):574–581
7. Zhou Y, Yuan C, Li CY et al (2019) Temperature dependent electrical properties of thermo-plastic polypropylene nanocomposites for HVDC cable insulation. *IEEE Trans Dielectr Electr Insul* 26(5):1596–1604
8. Du BX, Sun HL, Kong XX et al (2020) Improved electric field distribution within bushing insulation by EP/GO nanocomposites with reduced temperature coefficient of conductivity. *IEEE Access* 8:176864–176872
9. Teng CY, Zhou YX, Li SH et al (2020) Regulation of temperature resistivity characteristics of insulating epoxy composite by incorporating positive temperature coefficient material. *IEEE Trans Dielectr Electr Insul* 27(1):512–520
10. Teng CY, Zhou YX, Zhang L et al (2022) Improved electrical resistivity-temperature characteristics of insulating epoxy composites filled with polydopamine-coated ceramic particles with positive temperature coefficient. *Compos Sci Technol* 221:109365
11. Zhou WJ, Teng CY, Zhou YX et al (2021) Regulation of DC electric field distribution within insulation via positive temperature coefficient material. *Trans China Electrotech Soc* 36(14):3063–3071
12. Li WB (2016) Study on the mechanism of the effect of graphene oxide reduction by polydopamine on the curing kinetics of epoxy resin and its mechanical properties. Beijing University of Chemical Technology, Beijing (in Chinese)
13. Wang QY, Yang X, Tian HD et al (2017) A novel dissipating heat structure of converter transformer RIP bushings based on 3-D electromagnetic-fluid-thermal analysis[J]. *IEEE Trans Dielectr Electr Insul* 24(3):1938–1946
14. Feng CZ, Ma XK (2000) Introduction to engineering electromagnetic fields. Higher Education Press, Beijing (in Chinese)

# Stage Recognition of Surface Discharge in Oil-Impregnated Paper Based on Convolutional Neural Network



Yuanxiang Zhou, Jianning Chen, and Yongyin Li

**Abstract** The stage recognition of surface discharge in oil-impregnated paper is of great significance to the safe and reliable operating of power transformer and the construction of digital twin system. Therefore, a convolutional neural network (CNN) method is proposed in this paper to identify the development stages of surface discharge. Firstly, the surface discharge experiment of oil-paper insulation was carried out by step-up voltage method. Then, according to the difference of phase-resolved partial discharge (PRPD), the surface discharge process could be divided into various stages. Finally, CNN was adopted to identify different stages of surface discharge, compared with support vector machine (SVM) and back propagation neural network (BPNN) based on 24-dimensional feature extraction. The results show that after 100 iterations, the recognition accuracy of CNN on surface discharge stage reaches 99.17%, while the overall accuracy of SVM and BPNN is only 91.04% and 87.29%, respectively. The CNN model proposed in this paper can automatically and effectively identify the PRPD patterns of different stages of surface discharge, with a higher recognition accuracy than the traditional methods such as SVM and BPNN.

**Keywords** Convolutional neural network · Oil-paper insulation · Surface discharge · Stage identification

---

Y. Zhou · J. Chen · Y. Li (✉)

State Key Laboratory of Power System and Generation Equipment, Department of Electrical Engineering, Tsinghua University, Beijing 100084, China

e-mail: [liyongyin0022zzu@163.com](mailto:liyongyin0022zzu@163.com)

Y. Zhou

e-mail: [zhou-yx@tsinghua.edu.cn](mailto:zhou-yx@tsinghua.edu.cn)

J. Chen

e-mail: [chen-jn18@mails.tsinghua.edu.cn](mailto:chen-jn18@mails.tsinghua.edu.cn)

© Beijing Paiké Culture Commu. Co., Ltd. 2024

X. Dong and L. Cai (eds.), *The Proceedings of 2023 4th International Symposium on Insulation and Discharge Computation for Power Equipment (IDCOMPU2023)*, Lecture Notes in Electrical Engineering 1103, [https://doi.org/10.1007/978-981-99-7413-9\\_31](https://doi.org/10.1007/978-981-99-7413-9_31)

337

## 1 Introduction

Oil-paper insulation system is the main part of oil-impregnated power transformer insulation. In the case of damp, mechanical deformation, partial discharge is easy to occur on the oil-paper interface. Surface discharge is considered as one of the most serious fault types of transformer due to its fast development speed and large insulation damage [1]. Surface discharge at different stages has different damage degrees to oil-paper insulation, so it is of great significance to carry out identification of development stages of surface discharge for safe operating of transformers and construction of digital twin [2, 3].

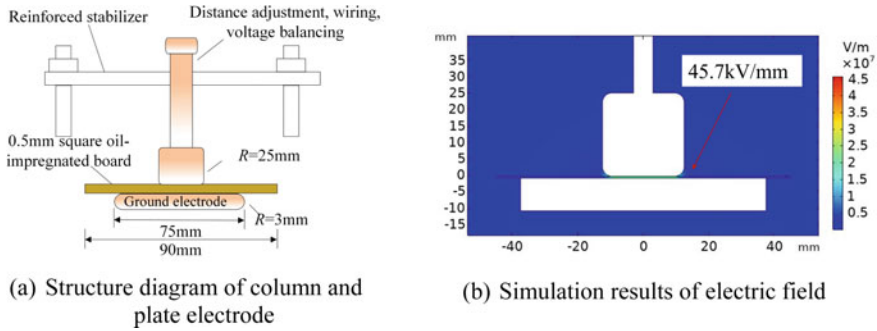
Scholars at home and abroad have carried out extensive research on the identification of partial discharge. Zhou divided the partial discharge stages according to the discharge characteristics, the gradient of the discharge pattern and other fingerprint parameters, combined with the gas production characteristics [4]. Li adopted the genetic optimization support vector machine (SVM) algorithm with feature selection to identify the three stages of surface discharge [5]. Sun and other scholars [6, 7] extracted 29 statistical parameters of phase-resolved partial discharge (PRPD). And the probabilistic neural network (PNN) algorithm was used to identify the development stages of oil-paper insulation discharge with different aging degrees. Compared with back propagation neural network (BPNN) model, it was found that its recognition accuracy was higher. Ren used a multi-spectral ratio feature and deep neural network (DNN) model to classify the severity of surface discharge with an accuracy of over 93% [8].

Most of the studies used the feature from artificial extraction to identify the stage of surface discharge of oil-paper insulation, requiring the combination of one or several aspects of statistical characteristics, which had a certain subjectivity and could not reflect all the characteristics of each stage of surface discharge, leading to poor generalization performance. In this paper, the convolutional neural network (CNN) is adopted to automatically extract the features from the PRPD pattern, and identify the different stages of surface discharge. The recognition accuracy is compared with that of traditional methods such as SVM and BPNN with manual feature extraction.

## 2 Experiment

### 2.1 Sample Preparation

Karamay KI25X was selected as the experimental insulating oil, and its processing process is as follows. The transformer oil is pumped into a 40 °C vacuum oil filter for filtering, drying and degassing, and impurities such as particulate matter and moisture in the oil are fully removed. The filtered transformer oil meets the relevant provisions in CIGRE 12.17, and then it is put into a beaker that is fully washed and dried by anhydrous ethanol and deionized water, and dried for more than 48 h in a



**Fig. 1** The structure diagram of column and plate electrode and its simulation results of electric field

vacuum drying oven. Carl Fischer instrument was used to measure the moisture and ensure that moisture content in oil meets national standards. The insulating paper of the experiment is 0.5 mm Nantong Zhongling insulating paper.

The processing process of the oil-impregnated paper is as follows. First, the insulating paper is uniformly placed in a vacuum drying oven with temperature of 105 °C and pressure of 100 Pa for 48 h. Then, transformer oil is soaked in the insulating paper at 80 °C in vacuum. After full impregnated, it was cooled to room temperature naturally, and then transferred to a vacuum oven to dry for more than 48 h. Before the experiment, the physicochemical test of the oil-impregnated board is carried out, satisfying the requirements of IEC 60641-2.

### 2.2 Defect Simulation

The column plate electrode is selected as defect model according to IEC 60243-1. Its height and diameter are both 25 mm. The schematic diagram of its structure and the simulation results of electric field are shown in Fig. 1. Between the high voltage electrode and the ground electrode of the defect model was 0.5 mm square oil-impregnated paper. Under the strong vertical electric field, there exists both surface discharges generated by parallel components along the oil-paper interface and oil gap discharges caused by vertical components. The maximum electric field was located at the junction of high voltage electrode, oil-impregnated paper and oil.

### 2.3 Construction of Partial Discharge Experimental Platform

In order to obtain PRPD pattern of different stages of surface discharge in oil-paper insulation under column and plate defect, the experimental platform was built, as



shown in Fig. 2, which met IEC 60270 partial discharge experimental standards. The experimental circuit consists of three parts, including the power supply part, sample loop part and signal acquisition part. The power supply mainly includes the programmable signal generator AFG 3011C and the high voltage power amplifier Trek model (50 kV/12 mA). The programmable signal generator is adopted to generate voltage waveform, and the high voltage power amplifier will amplify the generated signal at a fixed gain of 5000:1 and apply it to the sample. In the sample loop part, the sample to be tested is directly connected with the coupling capacitance and the measured impedance, which is connected with the coupling capacitance in series to convert the pulse current signal into the voltage signal. Signal acquisition part collect partial discharge signals from the measurement impedance through the partial discharge measurement unit MPD600, then transmitting data to the PC terminal for analysis and processing. Digital oscilloscope is used to monitor the output waveform of high voltage power amplifier. All components in the circuit are smoothed to prevent additional partial discharge.

After each calibration or sample replacement, it is necessary to carry out no-load experiment to ensure that no discharge occurs when loop voltage is boosted to 35 kV, with noise signal less than 8pC.

The applied voltage method of surface discharge experiment is stepped voltage boost, and the typical waveform is shown in Fig. 3. The step-up method can ensure that more experimental data can be obtained in limited time. Before the experiment, it is necessary to measure the initial discharge voltage. During the PRPD experiment, the boost step and time interval remain unchanged. The step size is 0.4 kV AC and the interval is 20 min, and the PRPD pattern is collected.

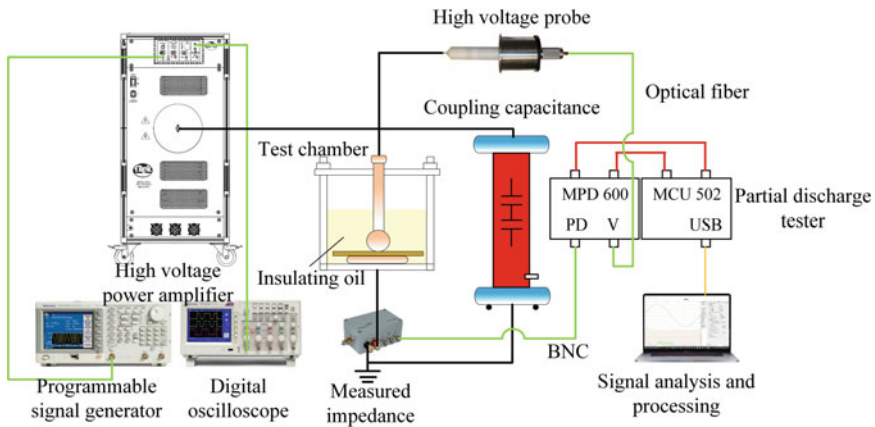
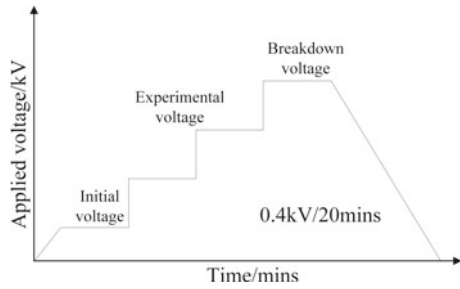


Fig. 2 Experimental platform of partial discharge

**Fig. 3** Applied voltage waveform



### 2.4 PRPD Pattern

According to the characteristics of PRPD pattern, the development process of surface discharge can be divided into the initial stage, the development stage, and the stage of near breakdown stage.

The PRPD pattern at the initial stage of surface discharge is shown in Fig. 4a. The discharge phase is mainly distributed in  $45^{\circ}$ – $90^{\circ}$  and  $210^{\circ}$ – $270^{\circ}$ . The positive half-cycle discharge pulse is evenly distributed between 0 and 3000pC, while the majority discharge under negative polarity is lower than 500pC. The discharge is mainly caused by high voltage electrode ionizing impurities and water in the oil, so the quantity is small and the development is slow, without large discharge appearing.

The PRPD pattern of the development stage of surface discharge is shown in Fig. 4b. The PRPD pattern presents a peak-like distribution, and the discharge amplitude slightly lags behind the peak applied voltage. Corona discharge at initial stage evolves into discharge along the oil-paper interface, and the discharge phase is mainly distributed in  $30^{\circ}$ – $120^{\circ}$  and  $180^{\circ}$ – $270^{\circ}$ , significantly extended compared with the discharge phase at initial stage. The maximum discharge quantity is also greatly increased to 10nC. The distortion electric field near the high voltage electrode cracks the transformer oil into  $H_2$ ,  $CH_4$  and other small molecules, further aging the insulation oil and aggravates the damage degree of oil-paper insulation.

The PRPD pattern near the breakdown stage of surface discharge is shown in Fig. 4c. The PRPD pattern is shaped like ‘rabbit ears’, that is, the front end of the discharge cluster protrudes, resembling rabbit ears, and there are many large value discharge pulses near the voltage peak. The discharge is distributed in the range of  $0^{\circ}$ – $360^{\circ}$ , and the discharge quantity increases to tens of nC. The discharge channel is formed perpendicular to the oil-impregnated paper, and the insulation is further aged. The aging of the paper and the growth of the distorted electric field at the defect promote each other, accelerating the development of discharge, finally leading to breakdown.

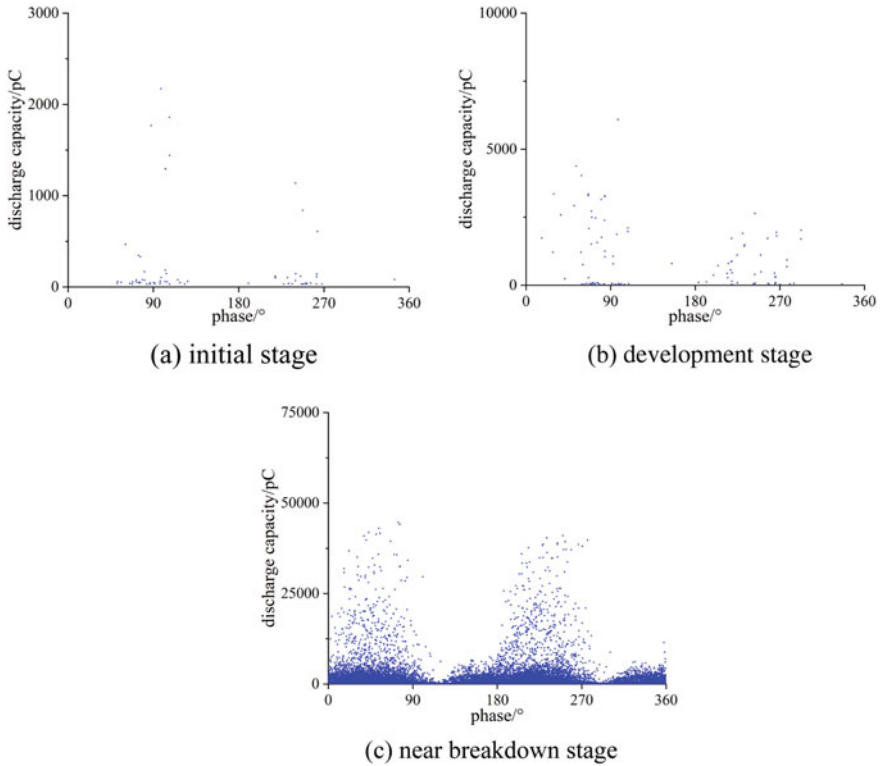
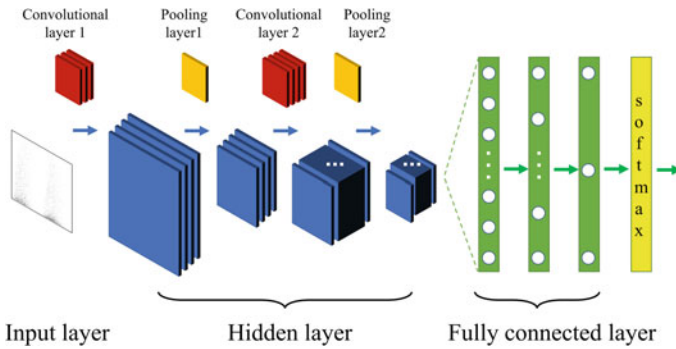


Fig. 4 PRPD pattern of surface discharge on various stages

### 3 Pattern Recognition

#### 3.1 Model Building

In this paper, two-dimensional convolutional neural network [9] is used for PRPD pattern recognition, whose basic structure includes input layer, convolutional layer, pooling layer, fully connected layer and output layer. The convolutional layer extracts feature information from the PRPD pattern and forms a new feature subgraph. Its convolutional kernel is essentially a filter to obtain features such as texture and edge of the image. Pooling layer is also known as the lower sampling layer, which is used to reduce the number of output parameters and represent the image with higher level features. As a classifier, the fully connected layer receives the features extracted after convolution pooling and maps them to a specific label such as 0, 1, and 2, corresponding to initial stage, development stage and near breakdown stage, respectively. Finally, the output is mapped to the probability distribution of 3 types of stage by the Softmax layer. The convolutional neural network structure established in this paper



**Fig. 5** Structure of convolutional neural network

is shown in Fig. 5, which includes 1 input layer, 2 convolutional pooling layers, 3 fully connected layers and 1 output layer. Among them, the first convolutional layer has a total of 4 convolutional kernels, and the second convolutional layer has a total of 16 convolutional kernels, with the size of  $3 \times 3$ . Maximum pooling was adopted. The number of units in the three fully connected layers is 96, 24 and 3, respectively.

### 3.2 Network Training

A total of 2400 PRPD pattern of different stages of surface discharge under column and plate defects were obtained by experiments, including 400 at the initial stage, 1000 at the development stage and 1000 at the near breakdown stage. 80% of the data is for training and 20% for testing.

The corresponding model is built in the server for training and testing. In the training process of convolutional neural network, cross entropy is used as a loss function to evaluate the training error, and the random gradient descent method is used to update the parameters. The training times are 100 times. Each iteration traverses the pictures of the training set once, and 20 iterations are carried out in each training cycle, for a total of 5 cycles. The initial learning rate is set at 0.001, with a 50% drop per cycle. The deep learning framework used in this paper is Pytorch and the programming language is Python3.9.

### 3.3 Recognition Accuracy Comparison

In order to evaluate the performance of the CNN model in stage recognition of surface discharge in oil-impregnated paper, its recognition accuracy was compared with the traditional machine learning models such as SVM and BPNN [10].

Statistical features extracted by SVM, BPNN and other methods include skew  $K_u$ , steepness  $S_k$ , peak number, asymmetry  $A_{sy}$ , correlation coefficient  $C_c$ , etc., as shown in Table 1. The definitions of each statistical parameter are detailed in literature [11].

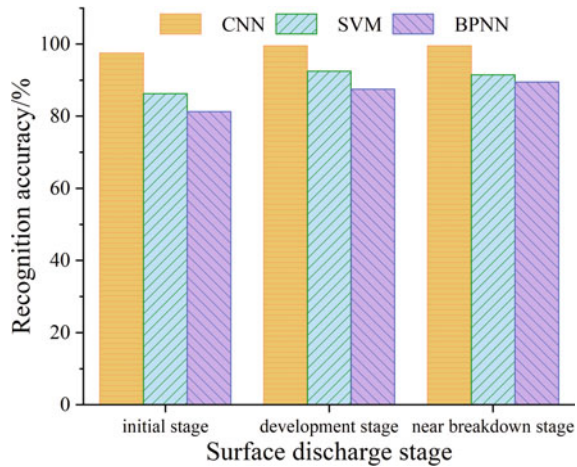
The recognition accuracy of three different models, CNN, SVM and BPNN, is shown in Fig. 6. According to Fig. 6, the recognition accuracy of CNN for each stage is higher than that of BPNN and SVM classifiers. After 100 iterations, the overall average recognition accuracy is 99.17%, while that of SVM and BPNN are 91.04% and 87.29%, respectively.

Since the features extracted by SVM and BPNN are based on the 24-dimensional statistical features of  $q_{max-\varphi}$ ,  $q_{ave-\varphi}$ ,  $n-\varphi$  pattern, which cannot accurately reflect all the statistical features of the pattern, resulting in worse performance in the stage identification of surface discharge. In the process of model training, convolutional neural network will automatically extract the features of the pattern. It can intelligently adjust the weight contribution of different spatial positions and different feature types to classification results, which has certain advantages over traditional manual feature extraction.

**Table 1** Statistical parameters of three characteristic pattern

Statistical characteristics	$q_{max-\varphi}$		$q_{ave-\varphi}$		$n-\varphi$	
	+	-	+	-	+	-
$K_u$	✓	✓	✓	✓	✓	✓
$S_k$	✓	✓	✓	✓	✓	✓
Peaks	✓	✓	✓	✓	✓	✓
$A_{sy}$	✓		✓		✓	
$C_c$	✓		✓		✓	

**Fig. 6** Comparison of recognition accuracy of different models



## 4 Conclusion

In this paper, by comparing the characteristics of PRPD pattern of oil-paper insulation along surface discharge in different development stages, a recognition method of oil-paper insulation along surface discharge development stage based on convolutional neural network is proposed. The recognition accuracy of this method is compared with SVM, BPNN and other methods to extract the statistical parameters of feature pattern, and the superiority of this method is verified. In the process of model training, convolutional neural network can automatically extract the features of the pattern and intelligently adjust the weight contribution of different spatial positions and different feature types in the pattern to classification results. Therefore, CNN-based classifier has more advantages than SVM and BPNN based on manual feature extraction. The overall average classification accuracy can be improved from 91.04% and 87.29% to 99.17%. Therefore, the convolutional neural network model proposed in this paper can provide effective method support for stage identification of transformer surface discharge.

**Acknowledgements** This work is supported by Science and Technology Project of State Grid Co., Ltd. (Research on the Improvement of Explosion Proof Design Technology for Oil Tanks and Components of UHV Transformer Equipment, 5500-202056464A-0-0-00).

## References

1. Raymond WJK, Illias HA, Mokhlis H (2015) Partial discharge classifications: review of recent progress. *Measurement* 68:164–181
2. Liu Y, Dong M, Xing Y, Hu Y, Xi Y, Ren M et al (2023) Development law and stage characteristics of multi-physical signals of surface discharge in oil-paper insulation. *Proc CSEE* 43(04):1611–1622 (in Chinese)
3. Li X, Li J, Jiang T, Wang Y, Huang Z (2018) Analysis of surface discharges on oil-impregnated pressboard under combined AC and DC voltages. *IEEE Trans Dielectr Electr Insul* 25(6):2380–2388
4. Zhou Y, Zhou Z, Sha Y, Huang X, Nie H, Zeng X (2018) Assessment of stages of partial discharge process of typical oil-paper insulation defect under combined AC-DC voltage. *Adv Technol Electr Eng Energy* 37(06):50–57 (in Chinese)
5. Li G, Wang K, Zhang S, Zhao Z, Li J, Cheng H et al (2018) Evolution characteristics and stage recognition method of surface discharge defects of oil-paper insulation in transformer. *Power Syst Technol* 42(10):3451–3458 (in Chinese)
6. Sun C, Su X, Zhao Z, Li T, Wang C, Ma S et al (2020) Development stage identification of oil-paper insulation surface discharge based on LLE-PNN model. *Insulating Mater* 53(06):57–64 (in Chinese)
7. Sun C, Su X, Li T, Wang C, Ma S, Hang H (2022) Development stage recognition of partial discharge in oil-paper insulation based on probabilistic neural network. *High Voltage Apparatus* 58(01):138–147 (in Chinese)
8. Ren M, Xia C, Yu J, Li X, Dong M (2023) Multispectral pulse evolution laws of insulator surface discharges and its diagnosis approach. *Trans China Electrotech Soc* 38(03):806–817 (in Chinese)

9. Krizhevsky A, Sutskever I, Hinton GE (2017) Imagenet classification with deep convolutional neural networks. *Commun ACM* 60(6):84–90
10. Chen J, Zhou Y, Bai Z, Zhao Y, Zhang Y, Zhang L (2022) Pattern recognition method of partial discharge in oil-paper insulation based on multi-channel convolutional neural network. *High Voltage Eng* 48(05):1705–1715 (in Chinese)
11. Contin A, Montanari GC, Ferraro C (2000) PD source recognition by Weibull processing of pulse height distributions. *IEEE Trans Dielectr Electr Insul* 7(1):48–58

# Dynamic Behavior of Suspended Bubbles in Insulating Oil Correlation with Flow Field Distribution



Ning Zhang, Jian Hao, Shili Liu, Junyi Zhang, Houhe Chen, and Ruijin Liao

**Abstract** In recent years, arcing faults inside large oil-immersed power transformers have been frequent. Suspended bubbles, as the main product of high temperature, high humidity, material aging and cracking gas production inside transformers, are one of the main causes of arcing inside transformers. However, due to the complex structure of the oil channel and the large fluctuation of the internal flow field distribution, the resulting bubble morphology evolution and movement law is not clear. In this paper, the influence of the initial position of bubbles and the relative position between bubbles on the flow field distribution is fully considered, and the dynamic behavior of suspended bubbles in oil under two fluid forms of natural oil circulation and forced oil circulation is simulated and studied by combining laminar and turbulent flow models and bubble force control equations, and the correlation mechanism between suspended bubbles and flow field distribution characteristics is analyzed. The simulation results show that the flow field in the laminar state affects the bubble aggregation and trajectory, while the turbulent state affects the bubble distortion and motion time, and a reasonable model in the simulation of bubble dynamic behavior is more beneficial to improve the simulation accuracy.

**Keywords** Arcing fault · Transformer oil · Suspended bubble · Dynamic behavior · Fluid mode

---

N. Zhang (✉) · S. Liu · H. Chen

Key Laboratory of Modern Power System Simulation and Control & Renewable Energy Technology, Ministry of Education, Northeast Electric Power University, Jilin 132012, China  
e-mail: [z.ning@aliyun.com](mailto:z.ning@aliyun.com)

N. Zhang · J. Hao · J. Zhang · R. Liao

State Key Laboratory of Power Transmission Equipment & System Security and New Technology, Chongqing University, Chongqing 400044, China

© Beijing Paiké Culture Commu. Co., Ltd. 2024

X. Dong and L. Cai (eds.), *The Proceedings of 2023 4th International Symposium on Insulation and Discharge Computation for Power Equipment (IDCOMPU2023)*, Lecture Notes in Electrical Engineering 1103, [https://doi.org/10.1007/978-981-99-7413-9\\_32](https://doi.org/10.1007/978-981-99-7413-9_32)



## 1 Introduction

Large oil-immersed power transformers, as a core component of the transmission and transformer system, are directly related to the safe and stable operation of the power system in terms of their insulation performance [1, 2]. However, with the increase in capacity, equipment deflagration accidents caused by high-energy arc discharge inside transformers have occurred frequently, resulting in serious economic losses and adverse social impacts [3]. Suspended air bubbles, as the main product of aging, deterioration, and staining of the oil-paper insulation system, present extremely complex morphological evolution and movement patterns in the complex environment of the oil channel [4, 5], and the resulting partial discharge of air bubbles and subsequent arc breakdown of the oil channel has been one of the main factors threatening the insulation performance of large power transformers.

In recent years, with the wide application of numerical simulation technology in the study of transformer oil discharge characteristics, Professor Tang Torch of Wuhan University proposed the idea of bubble group fusion, which is believed to occur under specific conditions, multiple small bubbles will fuse into large bubbles, and also provides a theoretical basis for the formation of “bubble bridges” [6]; Professor Li Qingmin of North China Electric Power University Professor Qingmin Li used numerical simulations to study the characteristics of bubble migration paths, rates and distortions under different field strengths [7]; Professor Qiaogen Zhang of Xi’an Jiaotong University discussed the study of the dynamics of bubbles in insulating media based on the phase field method [8]; Professor Yunpeng Liu of North China Electric Power University studied the trajectories of bubbles at different locations in the electric field under AC voltage and found that the bubbles would vibration [9]; Dan Cai of National University of Defense Technology believed that the bubble deformation is determined by the joint action of electric field force, surface tension and gravity on the bubble surface, and simulated the bubble deformation process by the level set method [10]. Taken together, few scholars have studied the impact of the accuracy and applicability of the model of the flow field itself on the simulation results for the simulation of bubble dynamics behavior in transformer oil.

Based on the laminar flow model and turbulent flow model of computational fluid dynamics, this paper constructs a simulation model of the dynamic behavior of suspended bubbles in transformer oil that can simulate the characteristics of multiple flow fields by changing the initial position of bubbles in the oil channel and the relative position between two bubbles to simulate the random generation characteristics of bubbles, and then investigates the correlation mechanism between the dynamic behavior of suspended bubbles in the oil channel and the flow field distribution characteristics under two fluid forms: natural oil circulation and forced oil circulation, and explains the effects of different fluid models on the distortion of bubble motion by combining the fluid dynamics theory.

## 2 Simulation Model Construction of Dynamic Behavior of Suspended Bubbles in Oil

### 2.1 Controlling Equations for the Dynamic Behavior of Suspended Bubbles

When the transformer oil temperature reaches 70 °C, the transformer oil density  $\rho$  is 848 kg/m<sup>3</sup>, and the viscosity  $\mu$  is 0.004 Pa s, the average oil flow velocity is 0.038 m/s for transformers with natural oil circulation air-cooled [11], and the fluid state is mainly laminar; for transformers with forced oil circulation air-cooled, the average oil flow velocity is 0.45–0.6 m/s [12], and the transformer oil flow state can be considered as turbulent flow. Therefore, there are both laminar and turbulent flow patterns in the actual operating transformer internal flow field distribution, which in turn will have an impact on the dynamic behavior characteristics of suspended bubbles.

This paper assumes that transformer oil is an incompressible fluid, and establishes the transformer oil channel laminar flow model and turbulent flow model based on computational fluid dynamics theory, in which the laminar flow model should satisfy the Navier–Stokes equations (N-S equations) in the flow process, and the mathematical expressions are as follows:

$$\nabla \cdot \mathbf{u} = 0 \tag{1}$$

$$\rho \frac{\partial \mathbf{u}}{\partial t} + \rho(\mathbf{u} \cdot \nabla)\mathbf{u} = \mathbf{F} - \nabla p + \nabla \cdot \left( \mu(\nabla \mathbf{u} + (\nabla \mathbf{u})^T) - \frac{2}{3}\mu(\nabla \cdot \mathbf{u})\mathbf{I} \right) \tag{2}$$

where,  $\mathbf{u}$  is the fluid flow rate;  $\mu$  is the dynamic viscosity;  $\lambda$  is the viscosity index of the fluid, which is about 0.02–0.052;  $\mathbf{F}$  is the volume combined force on the fluid;  $p$  is the gas pressure;  $T$  denotes the temperature value of the oil flow, and the ambient temperature is chosen as 25 °C;  $i$  and  $j$  denote the subscripts of the components of the velocity and position vectors in different directions.

The turbulence model is calculated using the  $k$ - $\varepsilon$  turbulence two-equation model of the Reynolds-averaged N-S set of equations (RANS set of equations) model, where the  $k$  equation and the  $\varepsilon$  equation are as follows, respectively:

$$\begin{cases} \frac{\partial(\rho k)}{\partial t} + \frac{\partial(\rho k v_i)}{\partial x_i} = \frac{\partial}{\partial x_i} \left[ \left( \mu + \frac{\mu_t}{\sigma_k} \right) \frac{\partial k}{\partial x_i} \right] \\ + \rho p - \rho \varepsilon \\ \frac{\partial(\rho \varepsilon)}{\partial t} + \frac{\partial(\rho \varepsilon v_i)}{\partial x_i} = \frac{\partial}{\partial x_i} \left[ \left( \mu + \frac{\mu_t}{\sigma_\varepsilon} \right) \frac{\partial \varepsilon}{\partial x_i} \right] \\ + C_{\varepsilon_1} f_1 \frac{\rho p \varepsilon}{k} - C_{\varepsilon_2} f_2 \frac{\rho \varepsilon^2}{k} \end{cases} \tag{3}$$

$$\begin{cases} k = \frac{1}{2} \overline{\mathbf{v}_i \mathbf{v}_i} \\ \varepsilon = \frac{\mu}{\rho} \left( \frac{\partial \mathbf{v}_i}{\partial x_j} \frac{\partial \mathbf{v}_i}{\partial x_j} \right) \\ \mu_t = \rho C_\mu \frac{k^2}{\varepsilon} \end{cases} \quad (4)$$

where  $k$  denotes turbulent energy;  $\varepsilon$  denotes dissipation rate and  $\mu_t$  denotes turbulent viscosity, which can be expressed as a function of  $k$  and  $\varepsilon$ ; other parameters are taken as follows:  $\sigma_k = 1.0$ ,  $\sigma_\varepsilon = 1.3$ ,  $C_{\varepsilon 1} = 1.44$ ,  $C_{\varepsilon 2} = 1.92$  and  $C_\mu = 0.09$ .

The bubbles in oil are subjected to several forces during the motion, including electric field force, drag force, fluid drag force, buoyancy force, surface tension, gravity, and frictional resistance. The electric field force and surface tension cause the bubble deformation and act on the bubble surface; the drag force, fluid drag force, buoyancy force, surface tension, gravity, and frictional resistance cause the bubble to move and act on the bubble volume, so Maxwell's stress tensor is used to convert the electric field force into surface stress to study the bubble deformation, and Newton's second law is used to study the bubble trajectory, whose mathematical expressions are shown in Eqs. (5)–(6).

$$\mathbf{F}_e = \nabla \cdot \left[ \mathbf{E} \mathbf{D}^T - \frac{1}{2} (\mathbf{E} \cdot \mathbf{D}) \mathbf{I} \right] \quad (5)$$

$$m \mathbf{a} = \mathbf{F}_e + \mathbf{F}_{st} + \mathbf{F}_X + \mathbf{F}_D + \mathbf{F}_B + \mathbf{F}_G + \mathbf{F}_f \quad (6)$$

where  $\mathbf{E}$  and  $\mathbf{D}$  are the electric field strength and potential shift vector, respectively;  $\mathbf{F}_e$  is the electric field volume force on the bubble;  $\mathbf{F}_{st}$  is the surface tension;  $\mathbf{F}_X$  is the drag force;  $\mathbf{F}_D$  is the fluid drag force;  $\mathbf{F}_B$  is the buoyancy force;  $\mathbf{F}_G$  is the buoyancy force;  $\mathbf{F}_f$  is the frictional resistance.

## 2.2 Geometric Model and Simulation Parameters Setting

For the actual operation of large oil-immersed power transformers, the internal oil channel structure varies greatly in different locations, and the width of the oil channel varies from a few millimeters to more than a dozen millimeters. In this paper, a two-pole plate model with a width of 10 mm and a height of 30 mm (turbulence model), 50 mm (laminar model), respectively, are selected to simulate the real vertical oil channel structure of the transformer equivalently. The left pole plate is connected to high potential, set to 15 kV, and the right pole plate is grounded. The lower part is also set as the oil flow inlet and the upper part as the oil flow outlet, and bubbles are placed randomly between the pole plates. The initial parameters of the transformer oil and bubbles are shown in Table 1.

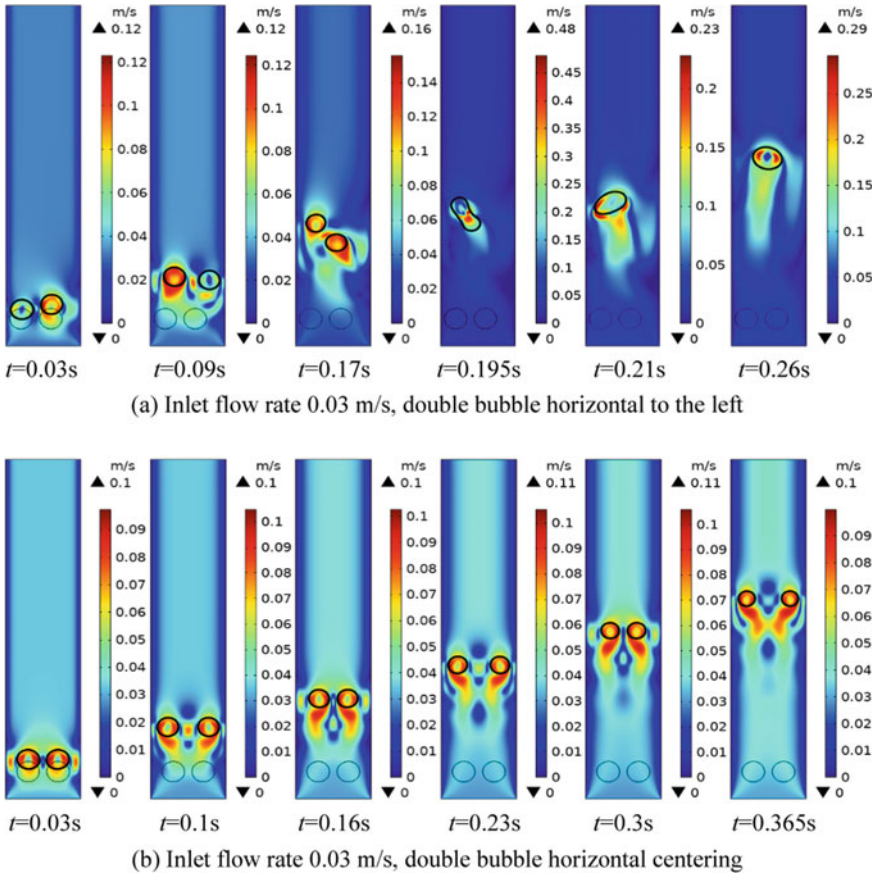
**Table 1** Transformer oil and bubble parameters

Properties	Size
Relative dielectric constant of bubbles $\varepsilon_b$ and Transformer oil $\varepsilon_l$	1/2.4
Bubble power viscosity $\mu_l$	2.05 Pa s
Bubble density $\rho_l$	1.29 kg/m <sup>3</sup>
Bubble radius $r_b$	1 mm
Transformer oil dynamic viscosity $\mu$	0.004 Pa s
Transformer oil density $\rho$	848 kg/m <sup>3</sup>
Transformer oil flow velocity $v$	0.55 m/s
Bubble surface tension coefficient $\sigma$	0.0725 N/m
Gravitational acceleration $g$	9.8 m/s
Drag force coefficient A	0.0125 N/m <sup>2</sup>

### 3 Simulation Results and Analysis Discussion

During the transformer operation, the change in oil flow velocity will make the fluid morphology in the oil channel change, which may affect the time of bubble agglomeration, the trajectory, and the degree of distortion. Keeping other conditions unchanged, this paper sets the oil flow velocity as 0.03 and 0.5 m/s to simulate the laminar flow state of natural oil circulation and the turbulent flow state of forced oil circulation and changes the initial position of bubbles (left, center, and right) and the relative position relationship (horizontal and vertical), the trajectory and distortion shape of bubbles obtained from simulation are shown in Figs. 1, 2, 3 and 4, because the bubbles are left and right geometric symmetry, so only the left-centered results are shown.

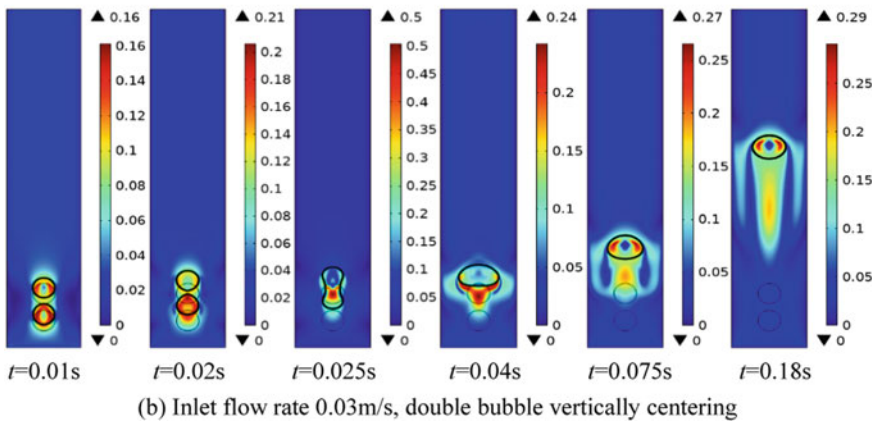
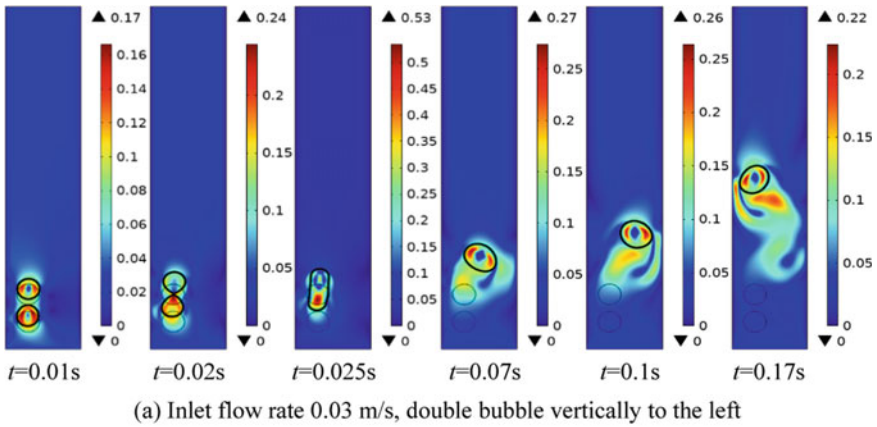
From the simulation results, it can be seen that the initial position of the bubble will have a great influence on the time of bubble convergence, the time required to flow out of the oil channel, the degree of distortion, and the trajectory when the relationship between the inlet flow rate and the relative position of the bubble is kept constant. From Figs. 1 and 2, it can be seen that for the laminar flow state, the horizontal bubbles located at the left and right edges of the oil channel have a later time to merge, about 0.2 s after the bubbles are generated, and the degree of distortion is smaller, and the new bubbles formed by aggregation are in S-shaped trajectory out of the oil channel, which takes a longer time, about 1 s; in the middle position, the two bubbles affect each other, constantly attract and repel each other, do not merge but accelerate the When in the middle position, the two bubbles interacted with each other and kept attracting and repelling each other, but accelerated the movement speed of the bubbles, and the time taken to flow out of the oil channel was shorter, around 0.6 s. The vertical bubbles were rapidly combined in about 0.02 s after generation, and also showed an S-shaped movement trajectory when located at the left and right edges of the oil channel, and rose vertically when located in the middle position, and the time required to flow out of the oil channel was reduced compared with the horizontal



**Fig. 1** Horizontal distribution of double bubbles under natural oil circulation laminar flow model conditions

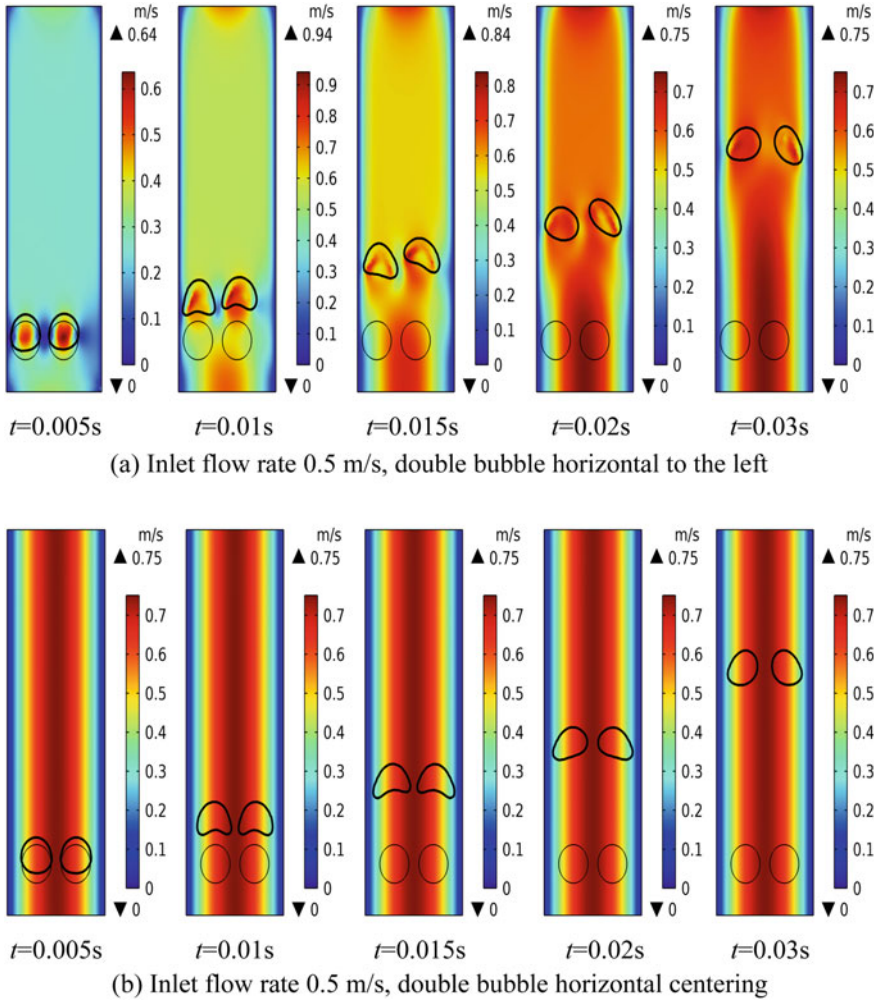
state. From Figs. 3 and 4, it can be seen that the distortion of horizontal and vertical bubbles is more serious for the turbulent state, showing the lower depression, narrow state, and even easy to appear the possibility of bubble splitting or breaking, and it is not easy to occur aggregation and flow out of the oil channel at a faster speed, which takes about 0.05 s.

Therefore, a comprehensive analysis shows that the laminar flow state affects the bubble aggregation and trajectory, while the turbulent flow state affects the bubble distortion degree and movement time. The intrinsic reason is that when the inlet velocity is normal to the velocity distribution, the motion of the bubble will generate a certain vortex field around it, especially a certain wake will be formed, so that the whole oil channel velocity field will be changed in the bubble flow through the region. When the initial distribution of bubbles for the edge of the position, it will make the flow field distribution not uniform, the side of the flow velocity will make the bubble

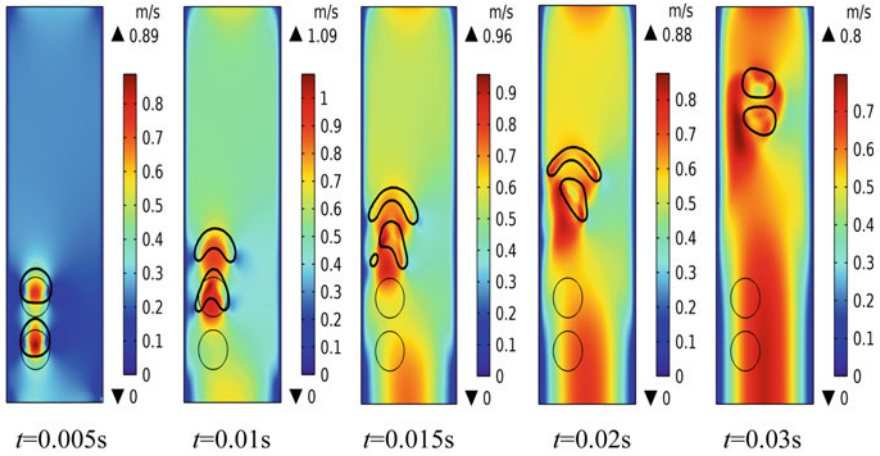


**Fig. 2** Vertical distribution of double bubbles under natural oil circulation laminar flow model conditions

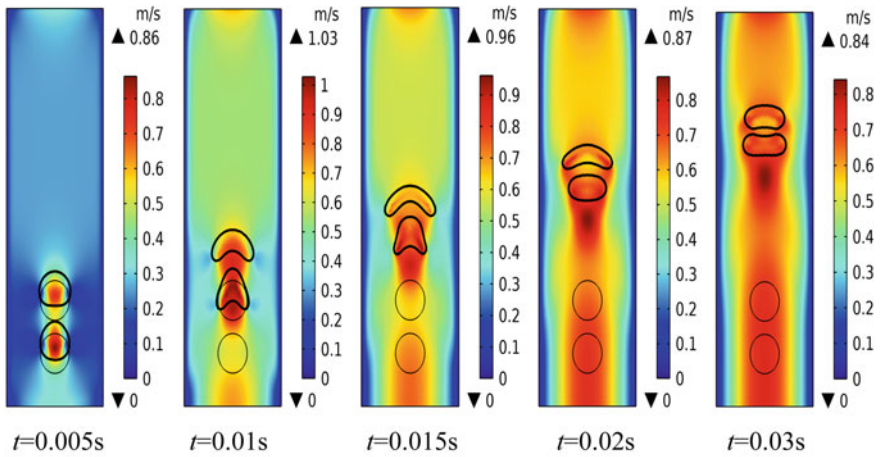
quickly float, and the smaller side of the relatively slow movement. When the larger bubble overtakes the smaller bubble by a distance, the wake behind it will make the smaller bubble accelerate upward, resulting in the fusion of the two contacts. When the initial distribution of bubbles for the middle position, the bubbles on both sides of the flow field distribution is uniform, the two-movement trend is the same, whether it can be gathered and depends on the role of the background velocity field force on the two bubbles when the flow velocity is larger, the force of the disorder is more prominent, so that the bubbles are not easy to gather when the flow velocity is small, the bubbles are less disturbed, easy to gather.



**Fig. 3** Horizontal distribution of double bubbles under forced oil circulation turbulent flow model conditions



(a) Inlet flow rate 0.5 m/s, double bubbles vertically to the left



(b) Inlet flow rate 0.5 m/s, double bubbles vertically centering

**Fig. 4** Vertical distribution of double bubbles under forced oil circulation turbulent flow model conditions

## 4 Conclusion

The bubble discharge in transformer oil is one of the key factors threatening the insulation performance of transformer oil paper, and the complex morphological evolution and movement law of suspended bubbles in the flow field directly determines its existence form in the oil channel. In this paper, the kinetic behavior of bubbles and the correlation characteristics of the flow field distribution are studied.



The simulation of the kinetic behavior of bubbles should be based on the actual operation of the transformer, and a suitable fluid model should be selected for calculation. Therefore, a reasonable flow control model can improve the simulation accuracy and discover new phenomena and new laws.

**Acknowledgements** This work was supported by the National Natural Science Foundation of China, “Structure Performance Analysis of Multivariate Mixed Insulating Oil “Structure-Component-Performance” and Study on the Synergistic Mechanism of Oil Paper System” (No. 52077015).

## References

1. Zhang R, Zhang QG, Guo C, He XH, Wu ZC, Wen T (2022) Bubbles in transformer oil: dynamic behavior, internal discharge, and triggered liquid breakdown. *IEEE Trans Dielectr Electr Insul* 29(1):86–94
2. Zhang R, Zhang Q, Guo C, Zhang Z, Wu Z, Wen T (2022) Effects of thermally induced bubbles on the discharge characteristics of oil-impregnated pressboard. *IEEE Trans Dielectr Electr Insul* 29(3):1191–1199
3. Liao RJ, Lin YD, Yang LJ, Zhao XT (2017) Effects and correction of temperature, moisture and aging on furfural content in insulating oil and aging assessment of insulation paper. *Proc CSEE* 37(10):3037–3044 (in Chinese)
4. Gao M, Zhang QG, Ding YQ, Wang TL, Ni HL, Yuan WX (2018) Characteristics of thermal-induced bubble formation in oil-impregnated paper insulation. *High Voltage Eng* 44(11):3634–3640 (in Chinese)
5. Zhang N, Liu SL, Hao J, Chen HH (2023) Review on partial discharge characteristics of bubble impurity phase in transformer oil. *Trans China Electrotech Soc.* <https://doi.org/10.19595/j.cnki.1000-6753.tces.211978> (in Chinese)
6. Zhang YZ, Tang J, Pan C, Luo XY (2020) Effects of temperature on partial discharge characteristics induced by suspended bubbles in flowing transformer oil and the mechanism. *Trans China Electrotech Soc* 35(6):1357–1367 (in Chinese)
7. Liu QS, Li QM, Ladislav NE, Li YP, Wu XW, Wu J (2022) Bubble dynamics and migration mechanism in insulation oil under extremely inhomogeneous electric field. *Proc CSEE* 42(9):3460–3470 (in Chinese)
8. Zhang R, Zhang QG, Chen M, Guo C, Wu ZC, Liu HY, Zhao Y, Wen T (2020) A phase field model for bubble dynamics in dielectric liquid. In: 2020 IEEE International conference on high voltage engineering and application, IEEE, Beijing, pp 1–4
9. Zhao T, Liu YP, Lv FC, Liu S (2016) Bubble dynamics simulation in transformer oil under AC electric field. *J Syst Simul* 28(12):3081–3086, 3094 (in Chinese)
10. Cai D, Liu L (2011) Effect of bubble deformation on liquid insulation under strong electric field. *High Power Laser Part Beams* 23(11):2966–2970 (in Chinese)
11. Tang J, Zhang YZ, Pan C, Zhou R, Wang DB, Li XX (2018) Impact of oil velocity on partial discharge characteristics induced by bubbles in transformer oil. *IEEE Trans Dielectr Electr Insul* 25(5):1605–1613
12. Liu YP, Chao NJ, Zhao T, Tong YX, Jia CH (2020) Mechanism and numerical model of bubble effect in oil-paper insulation based on microtubule model. *IEEE Trans Dielectr Electr Insul* 27(5):1529–1537

# Study on the External Insulation Characteristics of Epoxy Resin After Corona Aging Under Hygrothermal Coupling Effect



Yongliang Ji, Zhangang Yang, Liang Xie, Xiao Rao, Haonan Tan, and Maoqiang Bi

**Abstract** Epoxy resin has the characteristics of high adhesion and insulation, excellent dielectric properties, mechanical properties and heat resistance, good chemical stability and easy processing. However, in hygrothermal, epoxy resin generally has insulation aging phenomenon, which seriously affects the reliability and service life of equipment operation. In this paper, a hydrothermal corona aging platform was first built, and then the samples were subjected to artificial accelerated aging for up to 5 days under different hydrothermal environments, and the leakage current and flash-over voltage of the samples after aging were tested. The results show that the wet flash-over voltage of the epoxy resin aged samples affected by different temperatures is larger than that of the aged samples affected by different humidity, and the flash-over voltage is smaller. The higher the relative humidity of the aging sample, the greater the effective value of the leakage current, and the stronger the waveform periodicity. However, compared with the influence of different temperatures, the insulation performance of low humidity aging samples is less damaged.

**Keywords** Epoxy resin · Hygrothermal · Corona aging · Leakage current · Flash-over voltage

---

Y. Ji  
State Grid Chongqing Electric Power Company, Chongqing 400014, China

Z. Yang · L. Xie  
State Grid Chongqing Electric Power Company of SHIBEI, Chongqing 400015, China

X. Rao · H. Tan · M. Bi (✉)  
School of Electrical and Electronic Engineering, Chongqing University of Technology,  
Chongqing 400054, China  
e-mail: [bimaoqiang@cqut.edu.cn](mailto:bimaoqiang@cqut.edu.cn)

## 1 Introduction

Epoxy resin has the characteristics of high insulation strength, excellent chemical properties and good mechanical properties, which makes it widely used in high high-voltage electrical switches, such as bushings, contact boxes, and supporting insulators [1–3].

Analysis of the aging properties of insulating materials and the causes of damage, may be affected by moisture, internal air gap and installation methods do not meet and other factors caused. However, the root cause is actually the heat load generated by the insulation material during operation, and this load involves thermal, mechanical and electrical properties as well as the surrounding environmental factors in the material work [4, 5]. The surrounding environment refers to the influence of moisture, high temperature and corona discharge, which leads to the aging of epoxy resin and even the loss of insulation ability [6]. Therefore, it is urgent to study the aging properties of epoxy resin materials under hygrothermal corona aging.

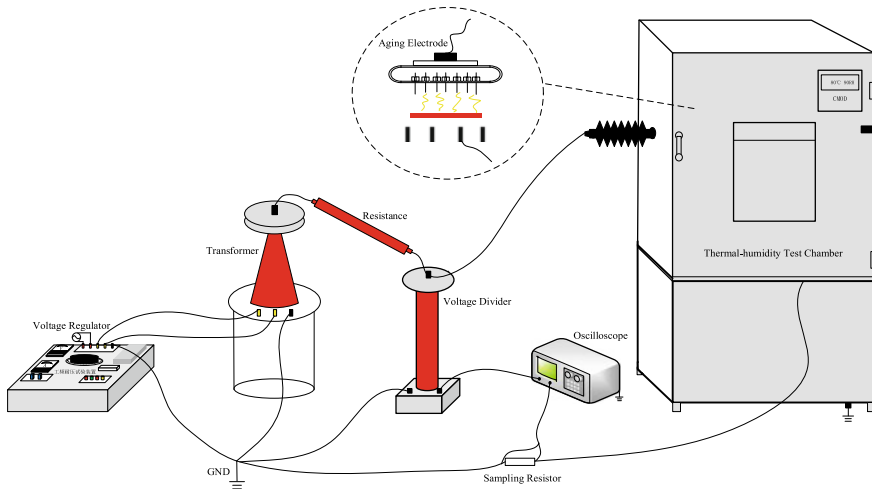
At present, scholars at home and abroad have studied the hygrothermal aging characteristics of epoxy resin. Xie et al. [7] have shown that the flash-over voltage of epoxy resin under extremely non-uniform electric field is lower than that under slightly non-uniform electric field. The dispersion of flash-over channel and flash-over voltage in vacuum is greater than that in air, and the surface flash-over voltage under asymmetric electric field has obvious polarity effect. Yongji [8] et al. carried out a pressure test on epoxy resin and studied the growth of electrical trees of epoxy resin under electric field. Ouyang et al. [9] studied the flexural properties and dynamic mechanical properties of epoxy resin after thermal aging. The results showed that the epoxy resin matrix had deboned with the fiber and the matrix was also broken, which indicated that the epoxy resin matrix could not transfer stress more efficiently.

In this paper, epoxy resin materials were prepared, and an experimental platform was built to simulate the experimental environment. The effects of corona aging on the leakage current and flash-over voltage of epoxy resin in different hygrothermal environments were studied.

## 2 Test Method and Procedure

### 2.1 Preparation of Sample

The volume ratio of the epoxy resin matrix chosen for this study was E51, MTHPA, and DMP30 during sample preparation. Using PTFE mold, the diameter of the sample prepared is 10 mm, the thickness is 3 mm.



**Fig. 1** Aging platform

## 2.2 Test Platform Construction

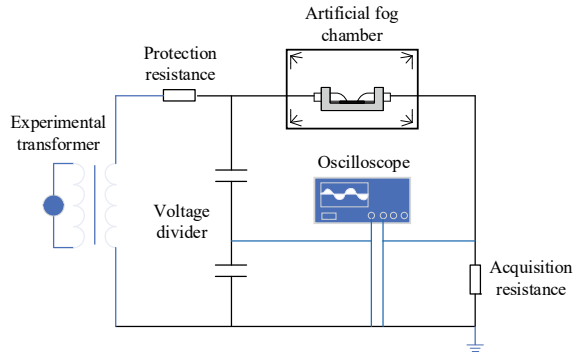
The corona aging test was conducted in this experiment at high temperatures with varying humidity and at high temperatures with varying humidity as variables. 10 kV of industrial frequency AC voltage was then applied to analyze the aged samples in order to learn more about the corona aging of epoxy resin in these various environments. The aging platform is depicted in Fig. 1.

Figure 2 illustrates the test schematic. The test environment was controlled by constructing an artificial fog chamber in the lab [10]. Water was atomized using an ultrasonic fog generator, and the air inlet of a fog generator was connected to the water's atomizer to modify the relative humidity of the atmosphere, the concentration of atomized water is altered. By adjusting the electrode discharge distance of 1 cm, the flash voltage and leakage current are gathered in this article, and the discharge voltage is read in real time through 1000:1 capacitive voltage divider, and the actual leakage current through the material surface is derived by collecting the voltage across the non-inductive resistor  $R_2$ . The acquisition frequency of the oscilloscope is set to 12.5 k for this acquisition, and the sample is 20 cycles [11, 12].

## 2.3 Test Procedure

- (1) The corona aging test platform for epoxy resin samples was built in accordance with the test schematic presented in this work prior to the test. Alcohol was used to clean the epoxy resin sample's surface before it was inserted in the multi-pin plate electrode and ready for testing.

**Fig. 2** Flash-over voltage/leakage current collection device



- (2) Using a high and low temperature humidity and heat test chamber, manage the environment during the test by adjusting the temperature for high humidity and the humidity for high temperature.
- (3) To determine the flash-over voltage and leakage current of epoxy resin corona aging, aging evaluation tests are performed on samples of epoxy resin corona aging in various temperature and humidity settings.

### 3 Testing Measure

The test was started after the relative humidity in the artificial fog chamber reached 100% after waiting for 10 min and the environment reached a stable state [13]. The finger electrode with epoxy resin sample was placed into the artificial fog chamber, and then the switch of the ultrasonic fog generator with deionized water was activated to make the deionized water atomized and blown into the fog.

#### 3.1 Flash-Over Voltage Test Procedure

- (1) After removing the grounding rod, raise the voltage on the finger-shaped electrode by turning the regulator's voltage button at a rate of 0.5 kV/s, and then check the voltage reading on the voltage divider.
- (2) Record the value of the flash-over voltage as soon as flash-over happens on the epoxy resin sample's surface by quickly rotating the regulator to reset the voltage to zero and discharging with a grounding device.
- (3) Take three samples for testing, give each sample five flashes, and use the test sample flash voltage to calculate the average test flash voltage. The computation is displayed in (Eq. 1).

$$U_f = \frac{\sum_{i=1}^n U_i}{n} \quad (1)$$

where  $n$  denotes the quantity of test flash-over voltages,  $U_f$  denotes the average flash-over voltage,  $U_i$  denotes the test flash-over voltage, and  $n = 15$ .

### 3.2 Leakage Current Test Procedure

- (1) After removing the grounding rod, switch on the regulator at a rate of 0.5 kV/s, activate the finger-shaped electrode for boosting, and stop pressurization when the predetermined applied voltage is reached.
- (2) This leakage current collection are data are collected after 1 min of pressurization, to be applied after 1 min of pressurization oscilloscope leakage current collection on both ends of R<sub>2</sub>.

## 4 Results Analyse

### 4.1 Influence of Temperature and Humidity on Leakage Current of Epoxy Resin Corona Aging

The surface resistance of the various aged samples varied as a result of the various degrees of damage to the epoxy resin surface after aging when the epoxy resin samples were subjected to the corona aging procedure at various ambient temperatures. Figure 3 displays the leaking currents of samples of unexposed epoxy resin. Figure 4 displays the leakage current patterns of the samples aged at various temperatures.

Figure 5 illustrates the variation in leakage current of epoxy resin samples after corona aging at various degrees of temperature. The greater the relative humidity

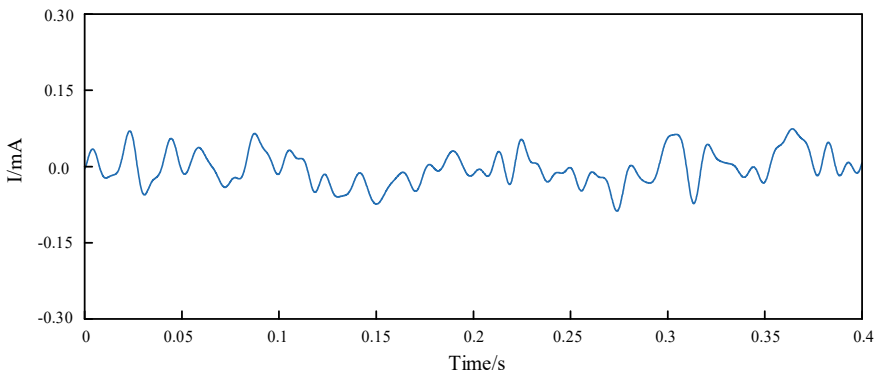
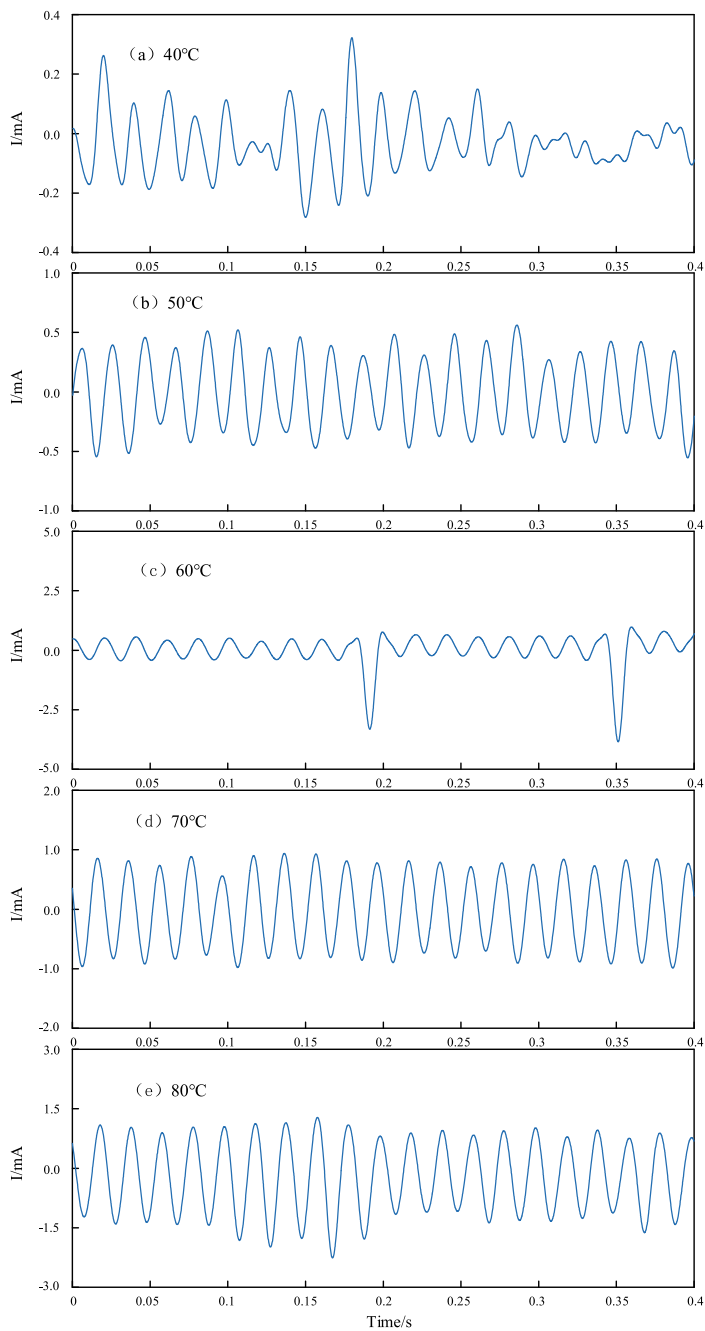


Fig. 3 Leakage current waveform of unaged sample



**Fig. 4** Leakage current wave of aging samples under different temperature environments

of aging samples, the greater the RMS value of leakage current, and the more periodic the waveform. The insulation performance of the low humidity aging samples, however, is less compromised than the impact of various temperatures. The effective leakage current values for samples aged at 55RH% and 65RH% are essentially the same, respectively, with a significant increase in leakage currents compared to the unaged samples, and the effective values for samples aged at 65RH% and 95RH% are nearly identical. The effective values of leakage currents for samples aged at 55RH% and 65RH% are basically the same, 0.07 mA and 0.08 mA respectively, with a significant increase in leakage currents compared to the unaged samples, and the waveforms are also irregular, the same as the unaged samples. The surface of the epoxy resin material is, however, more severely damaged as the relative humidity rises, which affects its surface resistance and, when the voltage is applied to both ends of the epoxy resin sample, the leakage current flowing through the surface, changes more noticeably. The leaking current appeared to be periodic in the aging samples with aging humidity between 75 and 95 RH%, and their effective values also reached 0.32, 0.64, and 1.23 mA, respectively.

#### ***4.2 Influence of Temperature and Humidity on Flash-Over Voltage of Epoxy Resin Corona Aging***

When the relative humidity of the environment reaches 70%RH, the flash test is conducted, and the voltage value obtained at this time is the dry flash voltage value. Results of the flash voltage test are shown in Table 1. The dry flash voltage drops from 9.32 to 8.34 kV when the temperature hits 80 °C. The aging sample's dry flash voltage and moist flash voltage, respectively, are 9.32 and 5.43 kV at 40 °C. The wet flash voltage value drops to 3.92 kV at temperatures higher than or equal to 60 °C. The wet flash voltage changes more as the aging temperature rises; when the temperature hits a maximum of 80 °C, the voltage is 3.78 kV.

The dry flash voltage of the epoxy resin samples aged by corona at a temperature of 80 °C changes by 0.98 kV, which is because the samples are suffering the most severe damage at this point in the aging process. Indicating that when the air humidity was higher, water molecules would enter the interior of the samples through the cracks and grooves of the epoxy resin samples, resulting in more loose structure and decreasing the wet flash voltage value. The wet flash voltage was smaller than the dry flash voltage, and the voltage value of the aging samples decreased with the increase in temperature.

When the ambient relative humidity was 70 RH% and 100 RH%, respectively, the flash test was conducted along the surface of the epoxy resin samples aged by corona, and the voltage values obtained at this time were the dry flash voltage and wet flash voltage values. The outcomes are displayed in Table 2. Dry flash voltage is greater than 9 kV before the relative humidity is less than or equal to 85%, but drops



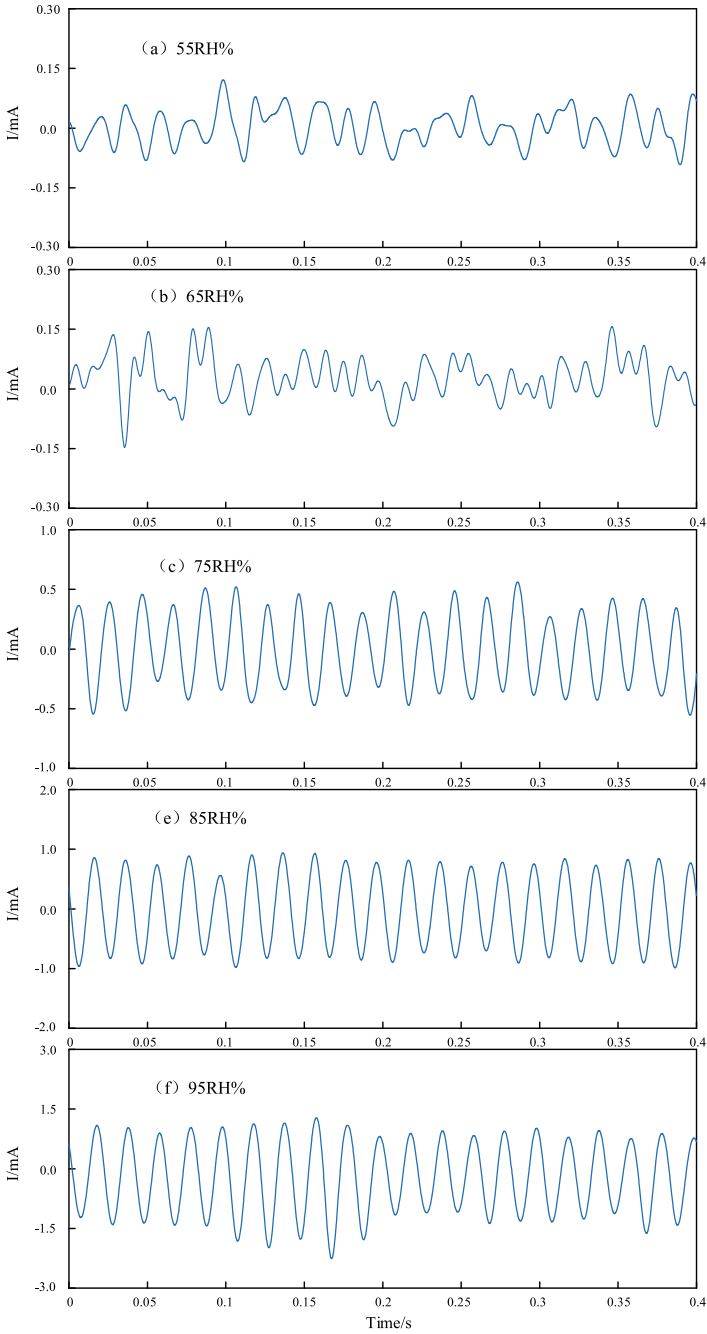


Fig. 5 Leakage current waveform of aging samples under different humidity

**Table 1** Flash-over voltage values of epoxy resin aging samples at different temperatures

Temperature/°C	Dry flash-over voltage /kV	Wet flash-over voltage /kV
40	9.42	5.43
50	9.24	5.21
60	8.87	3.92
70	8.56	3.89
80	8.34	3.78

**Table 2** Flash-over voltage values of epoxy resin aging samples under different humidity

Humidity/RH% (%)	Dry flash-over voltage /kV	Wet flash-over voltage /kV
55	9.53	7.62
65	9.51	6.88
75	9.23	5.56
85	9.14	4.79
95	8.34	3.78

to 8.34 kV when the relative humidity is 95%, demonstrating that the influence of aging samples' exposure to increased environmental humidity is somewhat stronger.

The table shows that the change in dry flash voltage value with increased humidity in the aging environment is not obvious, whereas the overall decrease in wet flash voltage is greater than the decrease in dry flash voltage, indicating that higher environmental humidity has a greater impact on the flash voltage value of aging samples.

## 5 Conclusion

The aging degree of epoxy resin samples increases with temperature and humidity, increasing the conductive material on the surface of the material and decreasing insulation performance. As a result, the flash-over voltage of epoxy resin aging samples obtained in different temperature and humidity environments decreases with temperature and humidity, and the wet flash-over voltage is lower.

With aging temperature and relative humidity, the leakage currents of epoxy resin samples rose. The surface structure of epoxy resin can be damaged more quickly when the temperature and humidity rise with age. The leakage current waveform is more periodic and closer to a sine wave the older the sample is, the more extreme the aging circumstances, and the greater the leakage current change.

**Acknowledgements** This work is supported by Technology project of State Grid Chongqing Electric Power Company(2023 Yudian Technology50#).

## References

1. Kim J-K, Lebbai M, Minglam Y et al (2005) Effects of moisture and temperature ageing on reliability of interfacial adhesion with black copper oxide substrate. *J Adhes Sci Technol* 19(6):427–444
2. Lyons J, Laub D, Giurgiutiu V et al (2002) Effect of hygrothermal aging on the fracture of composite overlays on concrete. *J Reinf Plast Compos* 21(4):293–309
3. Yu Y, Li P, Sui G et al (2010) Effects of hygrothermal aging on the thermal–mechanical properties of vinyl ester resin and its pultruded carbon fiber composites. *Polym Compos* 30(10):1458–1464
4. Dunn AS, Campbell PG, Marra KG (2001) The influence of polymer blend composition on the degradation of polymer/hydroxyapatite biomaterials. *J Mater Sci—Mater Med* 12(8):673–677
5. Wang Y, Liu Y, Xiao K et al (2018) The effect of hygrothermal aging on the properties of epoxy resin. *J Electr Eng Technol* 13(2):892–901
6. Kim J-K, Lebbai M, Woo RC (2005) Effects of hygrothermal ageing and thermal shock on reliability of interfacial adhesion between black oxide coated copper substrate and epoxy resin. *Compos Interfaces* 12(8–9):739–756
7. Zeghloul T, Dascalescu L, – Fellow, et al. Tribocharging phenomena in sliding contacts between polymeric materials. [C]// Industry Applications Society Meeting. IEEE, 2014.
8. Yongji G, Han Y, Fei X (2000) Experimental study on thermal oxidative aging of epoxy resin[J]. *Journal of Tsinghua University: Natural Science Edition* 40(7):1–3 (in Chinese)
9. Yang Y, Xian G, Li H et al (2015) Thermal aging of an anhydride-cured epoxy resin[J]. *Polym Degrad Stab* 118:111–119
10. Ivanov H, Leitgeb E (2022) Artificial Generation of Mie Scattering Conditions for FSO Fog Chambers. In: 2022 13th International symposium on communication systems, networks and digital signal processing (CSNDSP), Porto, Portugal, 2022, pp 54–58. <https://doi.org/10.1109/CSNDSP54353.2022.9907979>
11. Bi M, Deng R, Jiang T, Chen X, Pan A, Zhu L (2022) Study on Corona Aging Characteristics of Silicone Rubber Material Under Different Environmental Conditions. *IEEE Trans Dielectr Electr Insul* 29(2):534–542. <https://doi.org/10.1109/TDEI.2022.3163792>
12. Bi MQ et al (2020) The research on corona aging silicone rubber materials” NMR characteristics. *IEEE Access* 8:128407–128415. <https://doi.org/10.1109/ACCESS.2020.3008785>
13. Hu JI et al (2020) Influence of the thickness of room temperature vulcanized silicone rubber coating on the aging characteristics of corona. *High Voltage Eng* 46(4):1328–1336

# Design and Optimization of 6.5 kV SiC MOSFET Device Termination



Chuxuan Ma, Zhaocheng Liu, Xuebao Li, Zhibin Zhao, and Peng Sun

**Abstract** For high-voltage SiC MOSFET power devices, the breakdown voltage is a key parameter in device design, but the cylindrical junction can affect the withstand voltage capability of the device. Aiming at the problem of uneven electric field distribution and high electric field intensity on the surface of SiC MOSFET devices, a new 6.5 kV SiC terminal structure of field limiting rings is designed in this paper. The termination is optimized by adjusting the field limiting ring spacing and adding field plates, achieving the goal of 8.9 kV breakdown voltage. The termination reduces the junction surface effect to a certain extent, and greatly improves the electric field distribution on the chip surface.

**Keywords** High voltage SiC MOSFET power devices · Breakdown voltage · Field limiting rings · Field plates

---

C. Ma · Z. Liu · X. Li (✉) · Z. Zhao · P. Sun  
State Key Laboratory of Alternate Electrical Power System with Renewable Energy Sources,  
(North China Electric Power University), Changping District, Beijing 102206, China  
e-mail: [lx08357x@ncepu.edu.cn](mailto:lx08357x@ncepu.edu.cn)

C. Ma  
e-mail: [120212201562@ncepu.edu.cn](mailto:120212201562@ncepu.edu.cn)

Z. Liu  
e-mail: [zc.liu@ncepu.edu.cn](mailto:zc.liu@ncepu.edu.cn)

Z. Zhao  
e-mail: [zhaozhibin@ncepu.edu.cn](mailto:zhaozhibin@ncepu.edu.cn)

P. Sun  
e-mail: [sunpeng@ncepu.edu.cn](mailto:sunpeng@ncepu.edu.cn)

## 1 Introduction

SiC MOSFET power devices have many advantages such as conduction characteristics, switching characteristics, Excellent loss, high operating frequency and simple driving, so it has great development prospects in motor drive, locomotive traction and power grid system [1].

For high-voltage SiC MOSFET power devices, the breakdown voltage is a key parameter for termination design. Without considering the effect of junction curvature, the breakdown voltage is only determined by thickness and concentration of the epitaxial layer. However, the junction is cylindrical or spherical in process so that its edge will cause electric field concentration and reduce the withstand voltage capability of the device. In order to prevent the influence of the junction curvature effect, it is necessary to design a suitable terminal structure to improve the electric field distribution and increase the breakdown voltage [2].

The common termination structures include Field Limiting Ring (FLR), Field Plate (FP) and JTE [3–5]. The field limiting ring can expand the width of the depletion region to share the voltage of main junction, achieving the goal of improving the withstand voltage capability of the chip. Due to the simple process and high reliability of the field limiting ring, it is frequently used as the main termination in the design of the high-voltage device. Field plate is also a common termination structure, which can reduce the surface electric field to increase the breakdown voltage of the device. In the process of termination design, the field limiting ring and field plate are often combined to greatly improve the electric field distribution of the device. In addition, the semiconductor material in the terminal area of the silicon carbide chip is generally covered with silicon dioxide insulator, which serves as a passivation layer to shield external contamination and protect the chip termination. Cui Xiang's team established a chip semiconductor-insulator coupling electric field model for IGBT devices, and gave a mechanism explanation of the impact of external packaging insulation on the terminal electric field, providing a reference for the design of chip termination [6].

At present, there are few studies on the field limit ring of 6.5 kV SiC MOSFET. Therefore, based on the field limit ring structure, this paper analyzes the influence of the passivation layer on the chip termination, and then adopts a method of adjusting the field limit ring spacing and adding field plates, which optimizes the electric field distribution on the terminal surface and increases the breakdown voltage of the device.

## 2 Design of SiC MOSFET Device Termination

### 2.1 Design of Field Limiting Ring Termination

The field limiting ring is the most commonly used terminal structure. When the chip withstand reverse bias voltage, the depletion formed by the main junction and field limiting ring will continue to expand as the voltage increases. The field limiting ring can be implanted at the same time as the main junction without additional process steps, so the doping concentration and junction depth of the field limiting ring are exactly equal to those of the main junction.

In general, the breakdown voltage will enhance when the number of field limiting rings increase. For 14.5 kV SiC IGBT device, it requires 120 field limiting rings [7]. In addition, the main factors affecting the breakdown voltage include junction depth, ring width, ring spacing and ring spacing change rate. These variables affect each other, which bring great difficulties to the design and optimization of the termination [8]. The degree of parameter change affecting the withstand voltage capability was analyzed by DOE method. In the way, the change rate of ring number, ring width and ring spacing were regarded as the most important parameters in the optimization of termination. In the multi-field-limited ring terminal structure, the common ring spacing optimization criteria include equal spacing type, increasing spacing type, and decreasing spacing type, among which the incremental optimization criterion can better improve the breakdown voltage of the multi-field-limited ring termination. In the design of the structure, a linear incremental method is usually used to design different ring spacings, so as to achieve the aim of improving the electric field distribution.

### 2.2 Design of Field Plate-Field Limiting Ring Termination

In the oxidation process, the interface charge have a great impact on the breakdown voltage of the device, and even cause device failure. As mature technology, the field plate can well suppress the interface charge to greatly improve the withstand voltage capability of the device. Field plates are mainly divided into two categories: metal field plates and resistive field plates. The metal field plate can generally be a composite structure of polysilicon or metal, which is usually connected to a fixed potential and covered on the insulation of the chip; the resistive field plate is directly in contact with the chip surface, which can make the surface electric field more evenly distributed, it can also solve some problems caused by fixed charges in the oxide layer [9].

In practice, a field plate-field limiting ring compound structure can greatly increase the breakdown voltage and improve the surface electric field distribution to achieve the purpose of optimizing the termination. Wanji and others used a terminal structure combining field plate and field limiting ring for high voltage devices, which improved

the breakdown voltage of a single field limiting ring terminal structure<sup>10</sup>; In 2020, T. Hirao proposed a field plate-field-limiting ring structure, which suppressed the surface charges of the chip well, so that the breakdown voltage of the device is hardly affected by the charges [10].

Therefore, on the basis of the field limiting ring terminal structure, this paper make a optimization by using a field plate-field limiting ring structure to greatly increase the breakdown voltage of the chip and improve surface electric field distribution.

### 3 Simulation Results and Optimization

#### 3.1 Simulation of 6.5 kV SiC MOSFET Termination

For 6.5 kV SiC MOSFET device, this paper design a field-limiting ring structure (model A) with Sentaurus TCAD software, as shown in Fig. 1.

The terminal width is set to 700 μm, the lightly doped N-type drift region is 60 μm, the doping concentration is  $1 \times 10^{14} \text{ cm}^{-3}$ , the field limiting ring width is 5 μm, and the junction depth is 1.27 μm. The ring spacing of the structure follows the principle of linear increasing type:

$$S_M = S_1 + (M - 1) \times k \tag{1}$$

$S_M$  is the Mth spacing, and k is the increment coefficient. In this structure,  $S_1$  takes 0.3 μm, and k takes 0.02.

In order to analyze the influence of the passivation layer and the electric field distribution of the field limiting ring structure, this paper also established a branch electric field model of the SiC MOSFET device, as shown in Fig. 2.

The equations for the potential and charge of the insulator and the semiconductor region can be expressed as:

$$-\nabla \cdot (\epsilon_i \nabla \phi_i) = 0 \tag{2}$$

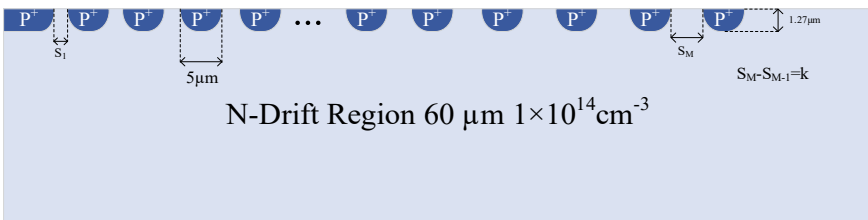
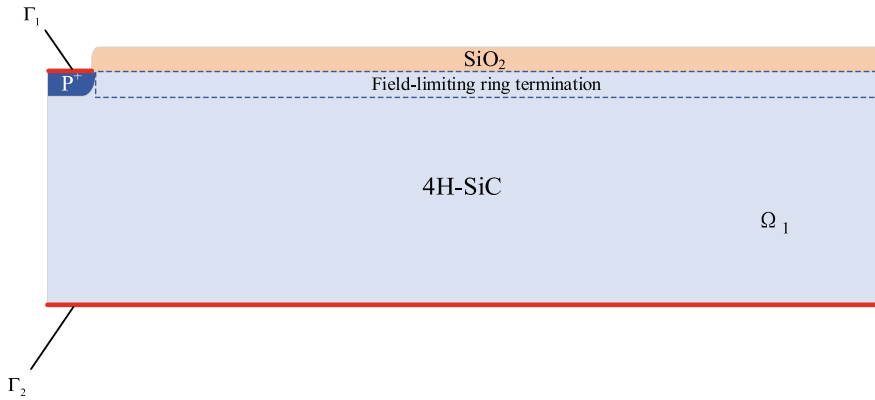


Fig. 1 Field limiting ring termination structure



**Fig. 2** Schematic diagram of electric field calculation model

$$-\nabla \cdot (\varepsilon_s \nabla \phi_1) = q(p - n + N_D - N_A) \quad (3)$$

$$\nabla \cdot (n\mu_n \nabla \phi_1 + D_n \nabla n) = R \quad (4)$$

$$\nabla \cdot (p\mu_p \nabla \phi_1 + D_p \nabla p) = -R \quad (5)$$

where  $\varepsilon_i$  and  $\phi_i$  are the dielectric constant and potential of the SiO<sub>2</sub> region,  $\varepsilon_s$  and  $\phi_1$  are the dielectric constant and potential of the 4H-SiC region.  $N_D$  and  $N_A$  are the donor and acceptor doping concentration,  $n$  and  $p$  are the electron and hole carrier concentrations.  $\mu_{n,p}$  and  $D_{n,p}$  are the mobility and diffusion coefficients of electrons and holes, respectively.

For the semiconductor termination area, the boundaries  $\Gamma_1$  and  $\Gamma_2$  are set as ohmic contact boundary condition:

$$\phi|_{\Gamma_1, \Gamma_2} = \phi_A + \frac{kT}{q} a \sin h \left( \frac{N_D - N_A}{2n_i} \right) \quad (6)$$

$$n|_{\Gamma_1, \Gamma_2} = \frac{1}{2}(N_D^+ - N_A^-) + \frac{1}{2} \sqrt{(N_D^+ - N_A^-)^2 + 4n_i^2} \quad (7)$$

$$p|_{\Gamma_1, \Gamma_2} = -\frac{1}{2}(N_D^+ - N_A^-) + \frac{1}{2} \sqrt{(N_D^+ - N_A^-)^2 + 4n_i^2} \quad (8)$$

In the formula,  $k$  is Boltzman's constant, which  $T$  is temperature,  $q$  is electronic power, and  $n_i$  is the semiconductor electronic concentrations.

Figure 3 shows the simulation of blocking characteristic curve of model A. It can be clearly seen that when  $S1 = 0.3 \mu\text{m}$  and  $k = 0.02$ , the breakdown voltage of the chip can reach about 7.7 kV.



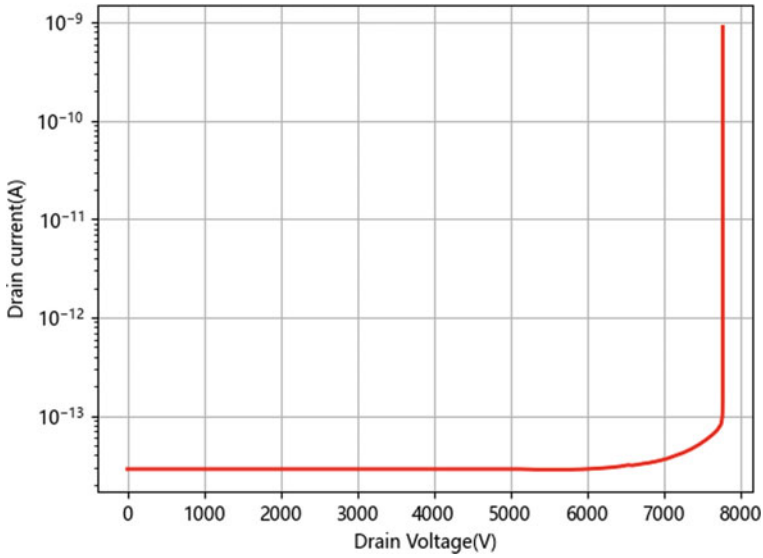


Fig. 3 Blocking voltage characteristic of model A

Figure 4 is the simulation of surface electric field distribution of model A. It can be seen from the figure shows an obvious downward trend, and the electric field strength of the main junction exceeds  $2 \times 10^6$  MV/cm, which easily lead to premature breakdown.

Figure 5 is the surface electric field distribution diagram after considering the passivation layer on the basis of model A. The figure shows that the electric field distribution at the terminal of the field limiting ring decreases as a whole, however, the electric field intensity of the last field limiting ring will increase greatly, making it difficult to increase the blocking voltage of this terminal structure.

### 3.2 6.5 kV SiC MOSFET Field Limiting Ring Termination Optimization

On the basis of model A, an attempt was made to increase the increment coefficients of the first 20 rings. The increment coefficients  $k$  selected for simulation were 0.03, 0.04, 0.05, and 0.06. When  $k$  exceeds 0.04, the electric field intensity of the last 60 rings drops sharply, and the electric field distribution on the termination is very non-uniform, as shown in Fig. 6.

After simulating and summarizing the regularity of multiple groups of experiment, this paper designs an improved field-limiting ring structure. The specific improvements are as follows: dividing 80 field-limiting rings into 5 groups, the number of rings in the first group is 4, the number of rings in the second group is 6, the number

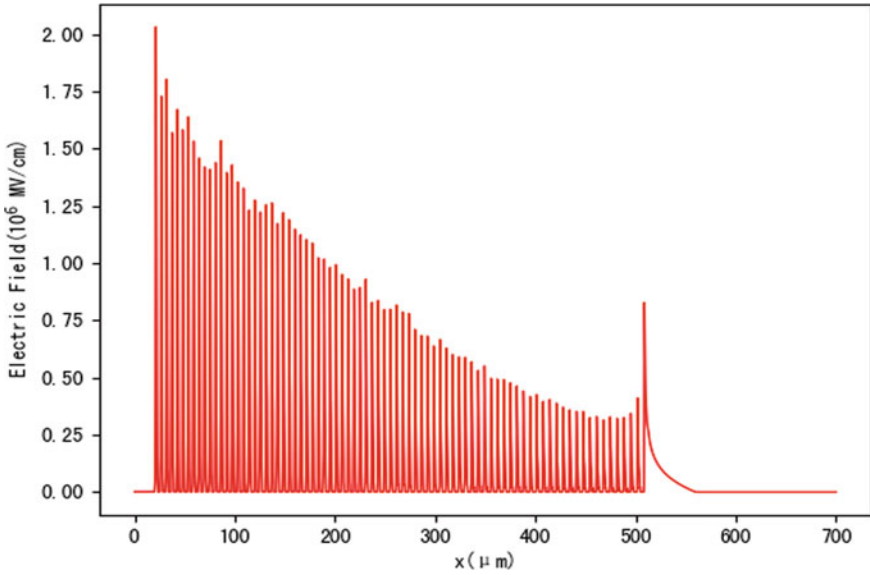


Fig. 4 Electric field distribution of models A

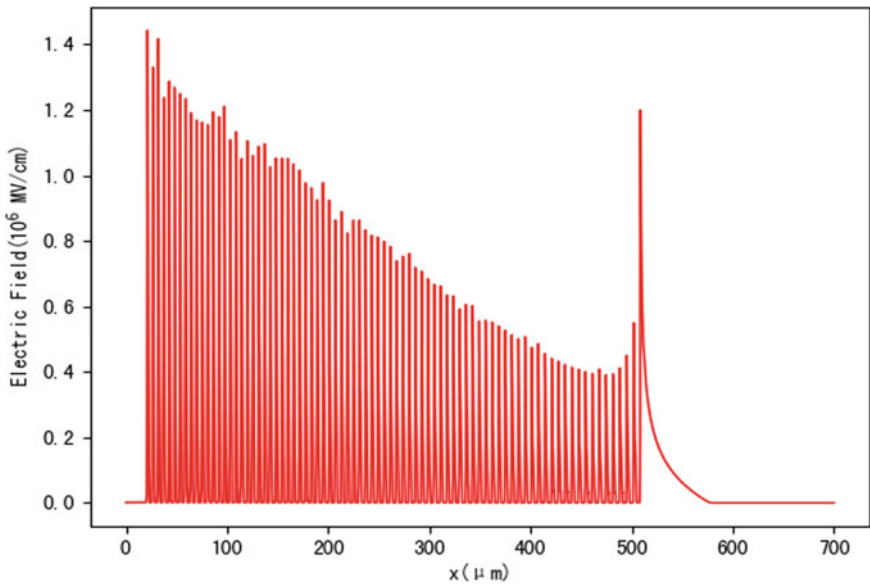
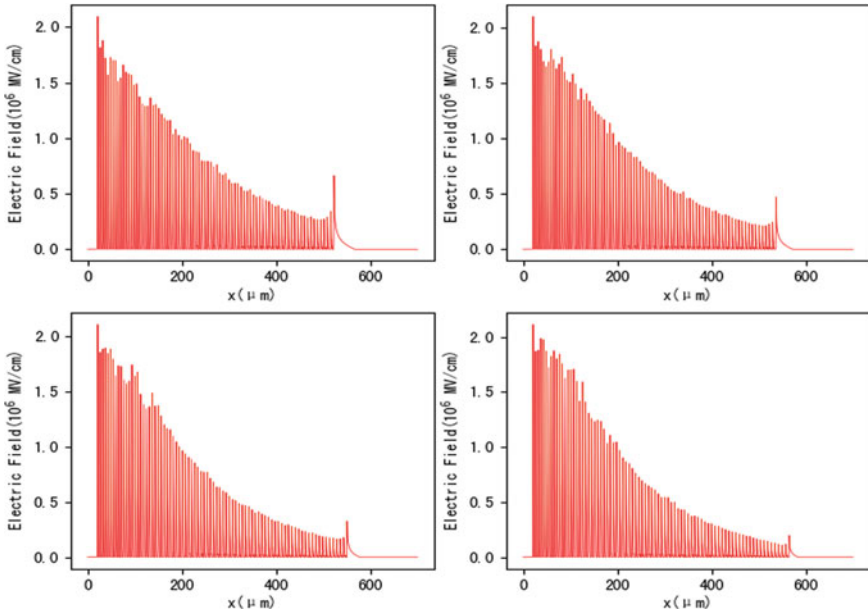


Fig. 5 Electric field distribution (considering passivation layer)



**Fig. 6** Electric field distribution ( $k_{20} = 0.03$ ,  $k_{20} = 0.04$ ,  $k_{20} = 0.05$ ,  $k_{20} = 0.06$ )

of rings in the third group is 10, the number of rings in the fourth group is 40, and the number of rings in the fifth group is 20. The increment coefficients  $k$  are 0.04, 0.05, 0.07 and 0.01 respectively, and the other parameters remain unchanged.

The simulation results of adjusted field-limiting ring structure are shown in Fig. 7. The figure shows that under the precondition of ensuring that the breakdown voltage of the chip is almost constant, the electric field intensity of the first 30 field limiting rings decreases, which indicate that the subsequent field limiting rings share more voltage, so that the electric field strength has increased.

However, the overall surface electric field distribution of the field limiting ring structure is still uneven, and the electric field intensity of the main junction remains high, so a field plate is added to further optimize electric field distribution. The field plate-field limiting ring terminal structure (model B) is shown in Fig. 8.

Figure 9 is the simulated blocking characteristic curve of model B. It can be seen from the figure that the breakdown voltage of the chip reaches 8.9 kV, which is about 13% higher than the original termination.

Figure 10 is the surface electric field distribution diagram of model B. The figure shows that the electric field distribution of the first 20 field limiting rings is more uniform. The field-limiting ring structure of the junction, and the field plate-field-limiting ring termination make the device less prone to premature breakdown.

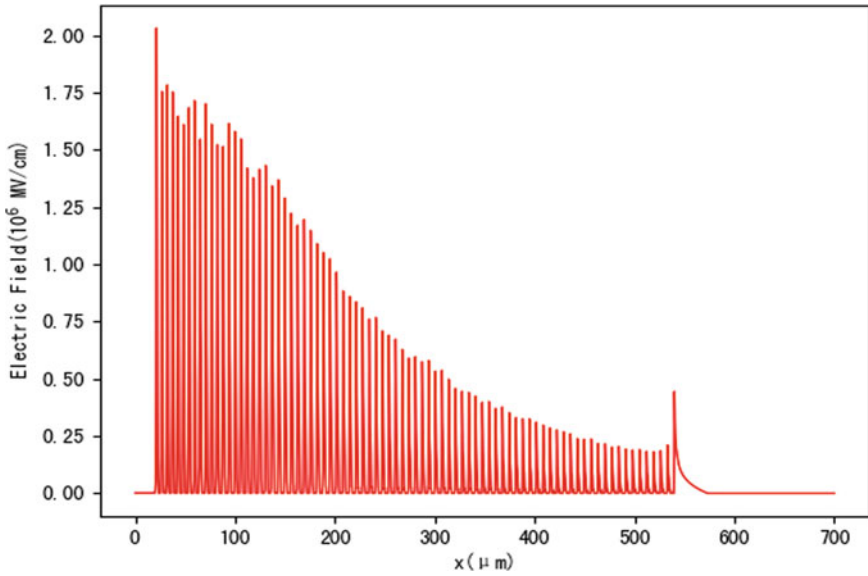


Fig. 7 Electric field distribution (after adjusting distance of field limiting ring)

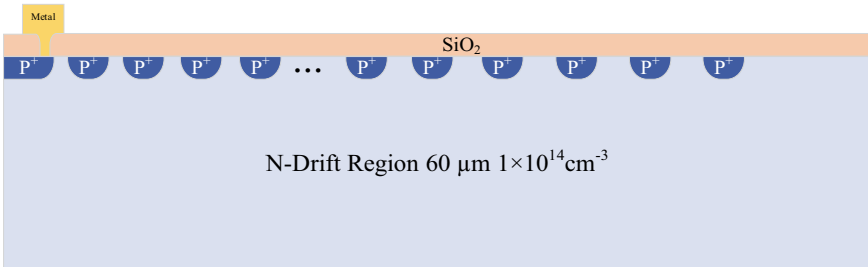


Fig. 8 Field plate-field limiting ring termination structure

In addition, Fig. 11 shows the potential comparison diagram of model A and model B. It can be seen that in the last 60 rings, the potential of model A is lower than that of the same ring in model B, which leads to the voltage of the last field-limited ring of model A is much greater than that of model B.

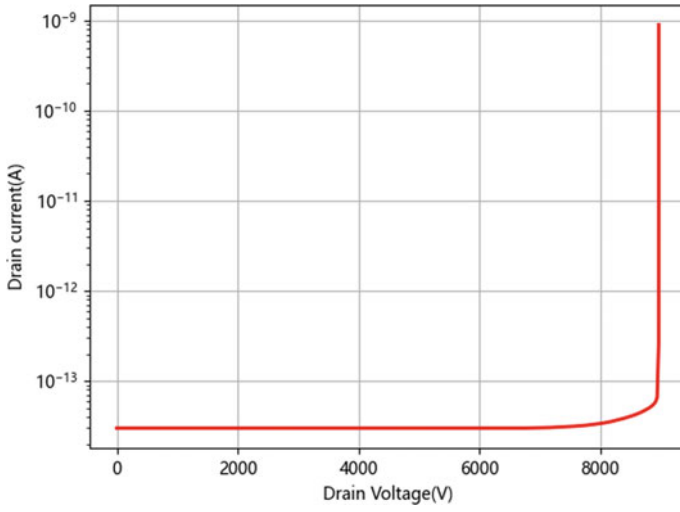


Fig. 9 Blocking voltage characteristic of models B

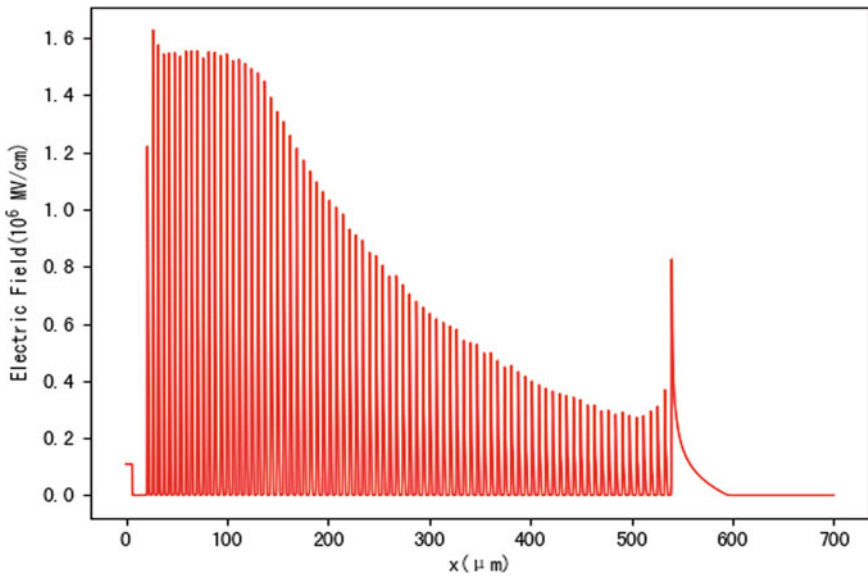


Fig. 10 Electric field distribution of models B

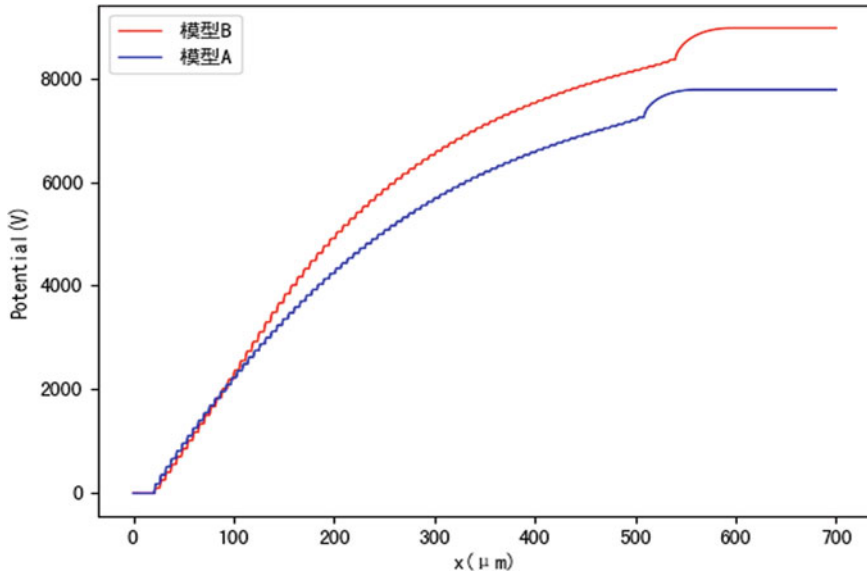


Fig. 11 Comparison of potential of model A and model B

## 4 Conclusion

In this paper, a termination using a fieldlimiting ring structure is designed for a 6.5 kV SiC MOSFET device with Sentaurus TCAD. In order to increase the breakdown voltage of the structure and improve surface electric field distribution, we make an optimization by adjusting the spacing of field limiting rings and adding field plates. The simulation results show that the breakdown voltage of the field plate and field-limiting ring terminal structure can reach 8.9 kV, which is 13% higher than that of the field-limiting ring structure; the maximum electric field intensity on the surface drops to about  $1.5 \times 10^6$  MV/cm, and the position of the maximum electric field is shifted from the main junction to the first field limiting ring, which improves the withstand voltage capability and the electric field distribution well.

## References

1. Ji SQ, Zhang ZY, Wang F (2017) Overview of highvoltage SiC power semiconductor devices: development and application. *CES Trans Electr Mach Syst* 1(3):254–264
2. Baliga BJ (2019) *Fundamentals of power semiconductor devices*. Springer International Publishing, Cham
3. Xingbi C (1988) A simple theory of floating field limiting rings. *Acta Electron Sin* 3:6–10 (in Chinese)
4. Chung S-K (2004) Analytic model for field-plate-edge breakdown of planar devices terminated with field plate and semiresistive layer. *IEE Proc—Sci, Meas Technol* 151(1):21–24

5. Johannesson D, Nawaz M, Nee H-P (2021) Assessment of junction termination extension structures for ultrahigh-voltage silicon carbide pin-diodes; a simulation study. *IEEE Open J Power Electron* 2:304–314
6. Zhaocheng LIU, Xiang CUI, Xuebao LI et al (2023) Influence analysis of packaging on electric field of chip in elastic press-pack IGBT Device. *Proc CSEE* 43(01):274–284 (in Chinese)
7. Wang F, Xinyu L, Xiaoli T et al (2023) Optimal design and fabrication of termination structure for 10 kV P-channel SiC IGBT. *J Power Supple* 21(1):202–207 (in Chinese)
8. Jung ES, Kyoung S-S, Chung H et al (2014) A study of field-ring design using a variety of analysis method in insulated gate bipolar transistor (IGBT). *J Electr Eng Technol* 9(6):1995–2003
9. Zhang B, Luo X, Li Z (2015) Electric field optimization technology for power semiconductor devices. The University of Electronic Science and Technology Press, Chengdu (in Chinese)
10. Hirao T, Onose H, Yasui K et al (2020) Edge termination with enhanced field-limiting rings insensitive to surface charge for high-voltage SiC power devices. *IEEE Trans Electron Devices* 67(7):2850–2853
11. Jiqing W, Diping C (1996) Design of high-voltage device of shallow planar junction with combination of field limiting ring and field plate. *Microfab Technol* 2:49–53 (in Chinese)

# Research on Factors Affecting Audible Noise of 500 kV Double-Circuit Straight-Line Tower AC Transmission Line



Xiaosen Zhou and Shengsuo Niu

**Abstract** To address the growing public concern over the issue of audible noise from overhead transmission lines, this paper focuses on the 500 kV AC double-circuit transmission line on the same tower. Using a controlled variable method under rated conditions, the paper analyzes the factors that affect audible noise, including different subconductor radii, minimum ground clearances, and phase-to-phase distances. The primary methods used in the study are the COMSOL finite element simulation software and MATLAB formula calculation, combined with the calculation of audible noise levels 1.5 m above the ground directly beneath the transmission line. The goal of the study is to identify the main factors affecting audible noise and provide feasible suggestions and measures to reduce audible noise levels from transmission lines.

**Keywords** Radio frequency interference (RFI) · Audible noise · 500 kV AC transmission line · Suppression measures

## 1 Introduction

The corona discharge phenomenon in electrical engineering primarily results in corona losses, electromagnetic interference, and audible noise. Research on audible noise began in the late 1960s. With the commissioning of ultra-high voltage AC transmission lines in North America, residents around the corridor began to complain and file complaints. Several 500 and 765 kV AC transmission lines built in the early United States were rebuilt due to audible noise issues. Currently, in the design and practice of overhead transmission lines at voltage levels of 500 kV and above, audible noise has surpassed electromagnetic interference as a control factor for the electromagnetic environment assessment of transmission lines, while corona losses and electromagnetic interference are only considered as verification factors [1–3].

---

X. Zhou · S. Niu (✉)  
North China Electric Power University, Baoding 071000, China  
e-mail: [1525513851@qq.com](mailto:1525513851@qq.com)

© Beijing Paiké Culture Commu. Co., Ltd. 2024  
X. Dong and L. Cai (eds.), *The Proceedings of 2023 4th International Symposium on Insulation and Discharge Computation for Power Equipment (IDCOMPU2023)*, Lecture Notes in Electrical Engineering 1103, [https://doi.org/10.1007/978-981-99-7413-9\\_35](https://doi.org/10.1007/978-981-99-7413-9_35)



This article is based on a 500 kV double-circuit transmission tower in Hami North, and aims to study the surface potential gradient of the transmission line using Comsol finite element software. Further, MATLAB programming is used to solve the actual audible noise value using the formula method, and to draw the trend of audible noise under different conditions. Based on the results, practical and feasible methods and measures to reduce audible noise are summarized for different conditions [4, 5].

## 2 Calculation Methods and Processes

A The formula for predicting audible noise for high-voltage transmission lines recommended in the United States is as follows [6, 7]:

$$SLA = 10 \lg \sum_{i=1}^Z \lg^{-1} \left[ \frac{PWL(i) - 11.4 \lg(R_i) - 5.8}{10} \right] \quad (1)$$

In the formula:  $SLA$ —A-weighted sound level;  $R_i$ —distance from measurement point to the measured phase  $i$  conductor;  $Z$ —number of phases;  $PWL(i)$ —sound power level of the  $i$ -phase conductor;  $PWL(i)$  Calculate according to the following formula:

$$PWL(i) = -164.6 + 120 \lg E + 55 \lg deq \quad (2)$$

In the formula:  $E$ —surface potential gradient of the conductor (kV/cm);  $deq$ —equivalent radius of the conductor;  $deq = 0.58n^{0.48}d$  (mm);  $n$ —wire split number;  $d$ —subconductor diameter (mm).

The predictive formula is applicable to conventional symmetric split conductors with a splitting distance ranging from 30 to 50 cm and a surface potential gradient ranging from 10 to 25 kV/cm. The calculation process diagram is shown in Fig. 1 [8–10].

The research method employed in this article is the method of controlled variables. The study focuses on the tower type and data as shown in Fig. 2, where the radius of the sub-conductor, the minimum height above ground level, the spacing between conductors, and the phase sequence of the conductors were modified while keeping other variables constant.

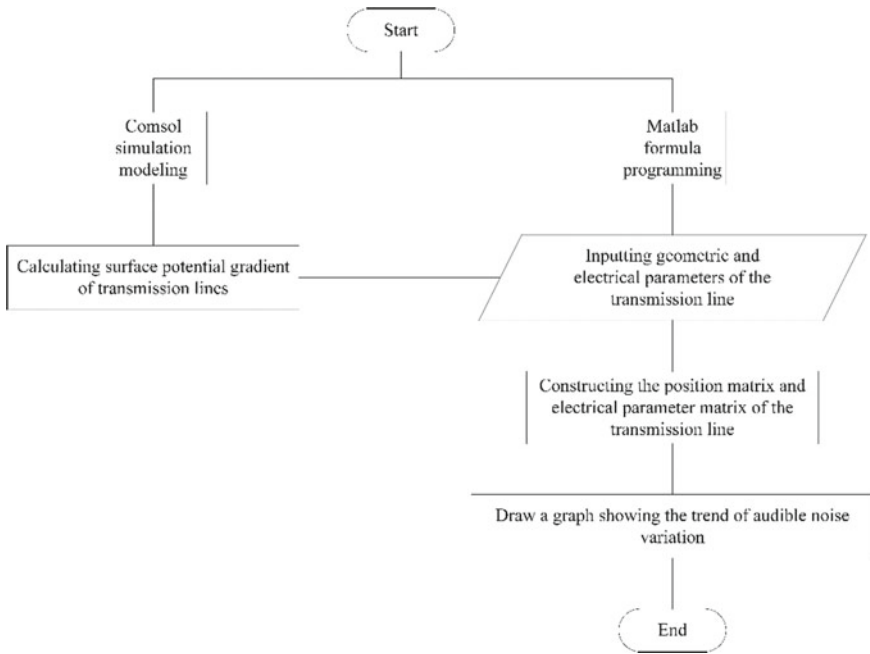
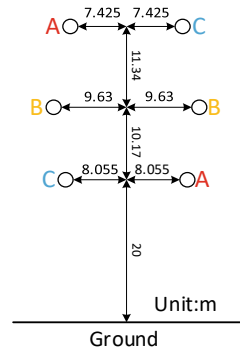


Fig. 1 Computational flowchart

Fig. 2 500 kV double-circuit transmission tower



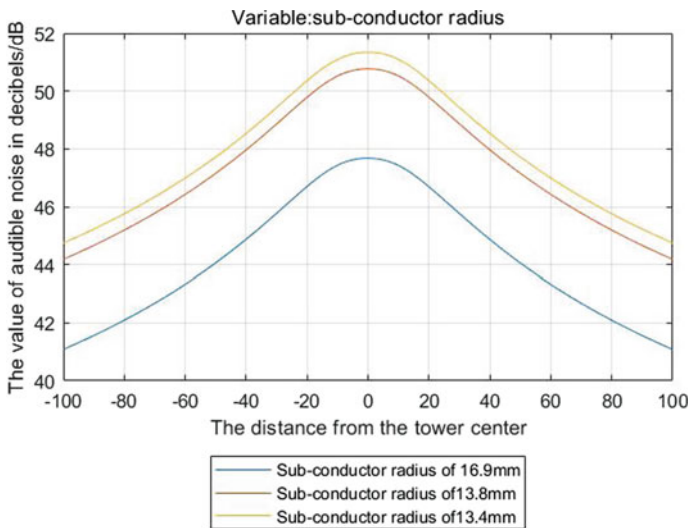
### 3 The Study of Factors Affecting Audible Noise

#### 3.1 The Effect of Sub-conductor Radius on Audible Noise

The maximum surface potential gradient on the conductors of the double-circuit transmission tower is shown in Table 1.

**Table 1** The surface potential gradient on the conductors

Sub-conductor radius, mm	The maximum surface potential gradient on the conductors, kV/cm (arranged from top to bottom, left to right)					
16.9	13.74	13.51	13.49	13.47	13.51	13.49
13.4	16.22	16.29	16.23	16.22	16.29	16.23
13.8	15.82	15.87	15.8	15.82	15.87	15.8



**Fig. 3** Trend graph of audible noise variation for the double-circuit transmission tower

The trend graph of audible noise variation for the double-circuit transmission tower is shown in Fig. 3

As the sub-conductor radius increases, the surface potential gradient on the conductors will decrease significantly. Therefore, the audible noise below the transmission line will also decrease significantly.

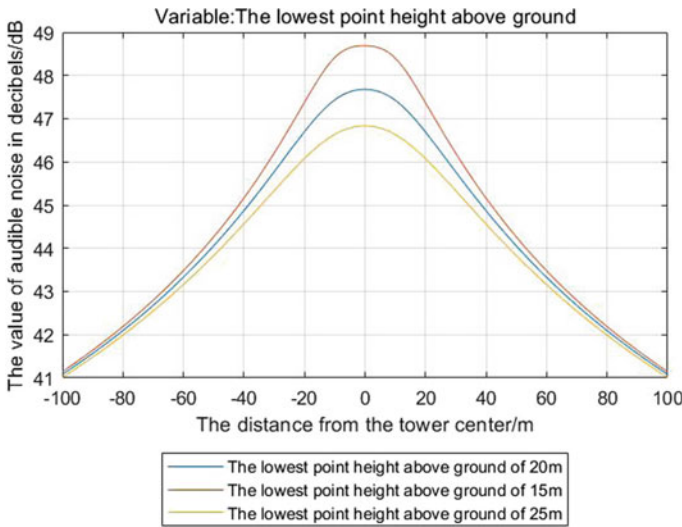
### 3.2 The Impact of Minimum Height to Ground on Audible Noise

Since raising the entire conductor without changing its relative position does not affect the surface potential gradient on the conductor, the initial potential gradient of the conductor is used.

The maximum surface potential gradient on the conductors of the double-circuit transmission tower is shown in Table 2.

**Table 2** The surface potential gradient on the conductors

Minimum height to ground, m	The maximum surface potential gradient on the conductors, kV/cm (arranged from top to bottom, left to right)					
20	13.74	13.51	13.49	13.47	13.51	13.49



**Fig. 4** Trend graph of audible noise variation for the double-circuit transmission tower

The trend graph of audible noise variation for the double-circuit transmission tower is shown in Fig. 4.

By analyzing the change trend, it can be observed that the higher the lowest point height above the ground, the lower the audible noise. However, this reduction trend is mainly concentrated near the conductor. The farther away from the conductor, the less impact it has on the audible noise level.

### 3.3 The Influence of Phase Spacing on Audible Noise

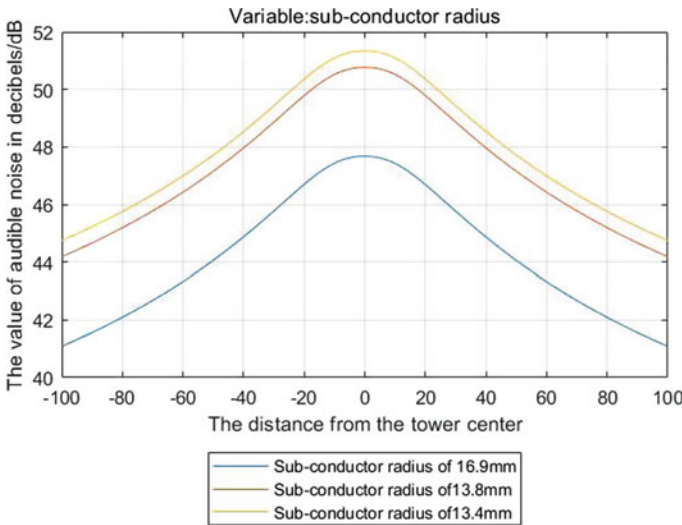
The maximum surface potential gradient on the conductors of the double-circuit transmission tower is shown in Table 3.

The trend graph of audible noise variation for the double-circuit transmission tower is shown in Fig. 5.

Increasing the phase spacing leads to a decrease in the value of audible noise, as it reduces the overall surface potential gradient of the transmission line, which in turn reduces the audible noise.

**Table 3** The surface potential gradient on the conductors

Phase spacing (outermost), m	The maximum surface potential gradient on the conductors, kV/cm (arranged from top to bottom, left to right)					
19.26	13.74	13.51	13.49	13.47	13.51	13.49
14.26	14.12	13.26	14	14.12	13.26	14
24.26	13.13	13.63	13.19	13.13	13.63	13.19



**Fig. 5** Trend graph of audible noise variation for the double-circuit transmission tower

### 4 Conclusion

Overall, the main influencing factor is the subconductor radius, because it can greatly affect the surface potential gradient of the conductor. Secondly, increasing the phase spacing should also be considered, as a larger phase spacing will result in a smaller overall potential gradient and thus a smaller audible noise level. The lowest point to ground height mainly affects the audible noise level near the tower. Therefore, to reduce audible noise, the subconductor radius should be increased and the phase spacing should be appropriately expanded.

### References

1. Meng C, Kong X, Wang Y, Li Q, Li Y, Jiang X (2023) Review on the research of audible noise from extra high voltage and ultra high voltage AC/DC transmission lines. Southern Power System Technology. <http://kns.cnki.net/kcms/detail/44.1643.TK.20230423.1128.006.html> (in

Chinese)

2. Zhang H, Wu H, Hu Q, He G, Shu L (2022) Review of audible noise of overhead transmission lines. *High Voltage Apparatus*, 1–6 (in Chinese)
3. Tarko R, Kochanowicz K, Nowak W, Szpyra W, Wszótek T (2021) Reduction of the environmental impact of electric field generated by high voltage power transmission lines. *Energies* 2021(14):6388. <https://doi.org/10.3390/en14196388>
4. Lertsawat K (2019) ISO1996-2:2017 acoustics-description, measurement and assessment of environmental noise-part 2: determination of sound pressure levels
5. Rozman I, Becan M, Babuder M, Vertacnik B (2016) Corona noise comparison of the standard and surface treated conductors obtained with monitoring of the newly erected 400 kV line and with corona testing in high-voltage laboratory. CIGRE Session
6. Li Q, Rowland SM, Shuttleworth R (2015) Calculating the surface potential gradient of overhead line conductors. *IEEE Trans Power Del* 30:43–52
7. Song F, Lv X (2022) Research on the influencing factors of electric field under AC transmission line crossover area. *Electric Mach Control* 26(06):40–52 (in Chinese)
8. Xie G, Fu W, He W, Lan L, Wan B, Zhang Y (2019) Calculation and research of audible noise of AC transmission lines (I)—three-dimensional distribution. *High Voltage Eng* 45(09):2990–2998 (in Chinese)
9. Fu W, He W, Xie G, Liang Q, Lan L, Chen Y (2019). Calculation and research of audible noise of AC transmission lines (II) distribution under crossing erection. *High Voltage Eng* 45(12):4070–4078 (in Chinese)
10. Wang X (2011). Study on electromagnetic environment of ultra-high voltage AC transmission lines, Dissertation. Shandong University (in Chinese)

# Transmission Ampacity Improvement of EHV Submarine Cable



Hao Zhang, Guoqing Ma, Pengfei Li, Youcong Huang, Tongtong He, and Yuesheng Zheng

**Abstract** The improvement of the transmission capacity of the line of EHV submarine cable has become urgent issues that need to be addressed. The transmission capacity of the EHV submarine cable is mainly determined by the operating temperature of the submarine cable. Therefore, several cooling schemes are compared to analyze their cooling effect on the cable core temperature in this paper. For the water pipe cooling scheme, the cooling effect is the most significant when the velocity of the cooling water is slower than 0.1 m/s, increasing the number of cooling water pipes can effectively reduce the cable core temperature. For the wind cooling scheme, the cooling effect is the most significant when the velocity of the air is slower than 0.1 m/s, and the cooling effect is more significant with the air velocity. For the backfill soil cooling scheme, the cooling effect is more significant with the thermal conductivity of the backfill soil.

**Keywords** EHV submarine cable · Cable trench · Cooling scheme · Cable core temperature

---

H. Zhang · G. Ma · P. Li  
Shandong Province, State Grid Shandong Electric Power Research Institute, Jinan 250001, P. R. China  
e-mail: [sdqzjh@163.com](mailto:sdqzjh@163.com)

G. Ma  
e-mail: [mgq198601@163.com](mailto:mgq198601@163.com)

P. Li  
e-mail: [lpfeng93@qq.com](mailto:lpfeng93@qq.com)

Y. Huang  
Fujian Province, State Grid Fujian Electric Power Research Institute, Fuzhou 350007, P. R. China

T. He (✉) · Y. Zheng  
College of Electrical Engineering and Automation, Fujian Province, Fuzhou University, Fuzhou 350108, P. R. China  
e-mail: [hett@fzu.edu.cn](mailto:hett@fzu.edu.cn)

Y. Zheng  
e-mail: [yueshengzheng@fzu.edu.cn](mailto:yueshengzheng@fzu.edu.cn)

## 1 Introduction

The transmission capacity of the EHV submarine cable plays a key role in the island power supply and other sea-crossing projects [1]. The bottleneck section of the transmission ampacity of EHV submarine cable not only limits the transmission ampacity but also reduces the efficiency of the EHV submarine cable usage [2–4]. Therefore, removing the bottleneck section of the transmission ampacity of EHV submarine cable line have become urgent issues that need to be addressed.

The research on improving the transmission ampacity of EHV submarine cables mainly focuses on reducing the self-losses of submarine cable and promoting the heat dispersion to the environment. For example, some researchers reduced the eddy current losses and the hysteresis losses of the cable by directly stripping the armored steel wire, or reduced the conductor losses by extending the area of the cable [5]. However, these methods are not applicable to the submarine cables that have already been put into production. Therefore, promoting the heat dissipation of submarine cables to the surrounding environment is currently the most reliable way to increase the transmission ampacity of submarine cables.

The way to promote the heat dissipation of submarine cables to the surrounding environment mainly depends on setting the submarine cable in the environment of low thermal resistance materials or cooling the cable by fluid medium. For example, Ming et al. proposed filling a mixture of low thermal resistance materials such as bentonite and fine sand into the submarine cable protection pipeline, and it was shown that the transmission capacity increased by 14.5% [6]. De Leon et al. studied the effect of backfill soil cross-sectional area, backfill depth, and other factors on improving the ampacity of the submarine cables [7]. Fluid medium cooling means that the fluid material in the layout environment is forced to flow at a certain velocity, for the purpose of taking away the heat. The use of fluid air cooling or fluid water cooling can significantly increase the ampacity of the cables. Yongming et al. built a three-dimensional simulation model to study the cooling effect of the fluid air on the improvement of the ampacity of the submarine cable [8]. Yu et al. built a simulation model to study the effect of arranging indirect cooling water pipes around cables on the improvement of the ampacity, and the results showed that the ampacity of the cables increased by 22% [9]. With the development of the wind power in China, the voltage level of submarine cables has reached 500 kV, but there is little research on improving the transmission ampacity of 500 kV submarine cables.

The landing section of the submarine cable is the bottleneck section of the transmission ampacity. In this study, a finite element model for 500 kV cross-linked polyethylene (XLPE) submarine cables was established. The cooling effects of water pipes, fluid wind and backfill soil on the landing section of the EHV submarine cable in the cable trench layout environment were studied.



## 2 Methodology

With the increasing demand for the transmission ampacity of the EHV submarine cables, the voltage level of submarine cables is increased from 220 to 500 kV. However, there is little research on the calculation of the transmission ampacity of 500 kV EHV submarine cables. Therefore, the research object in this study is 500 kV XLPE EHV submarine cables, and the structure of the EHV submarine cables can be seen in Fig. 1.

The finite element multi-physical field coupling model for the submarine cable consists the modules of magnetic field and heat transfer. The governing equations and the set of the boundaries can be found in our previous study [10].

The topology structure of the model can be seen in Fig. 2. The submarine cable length is 0.5 m, the cable trench height is 3 m. In the model, the submarine cable is placed in the bottom of the cable trench. Due to the limitation of the computing resources, the computational domain is reduced and only the cooling effect is discussed. The sets of magnetic field module, fluid module and heat transfer module are as follows.

- (1) Magnetic field module: Apply 1500 A current to the conductor of the submarine cable, and the cable temperature is observed while taking different cooling schemes.
- (2) Fluid module: The fluid module mainly serves as the air domain within the cable trench, with no slip on the cable trench walls and does not serve as an inflow or outflow boundary.

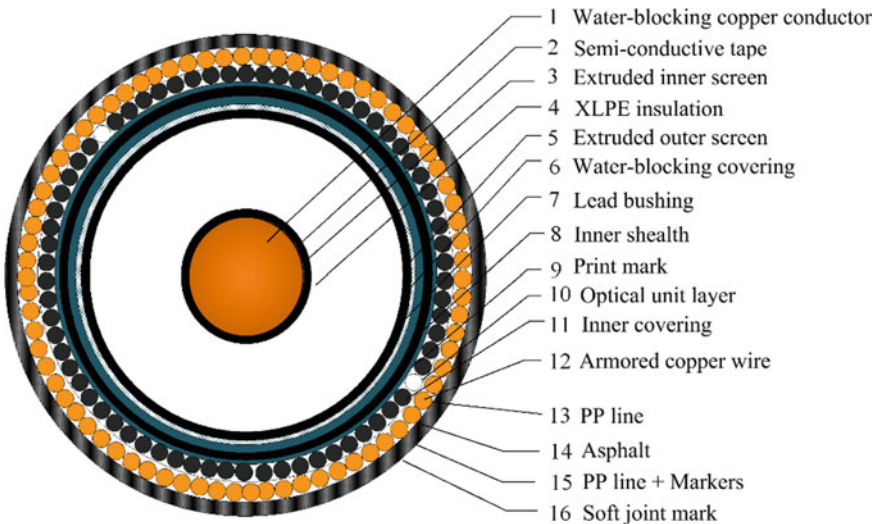
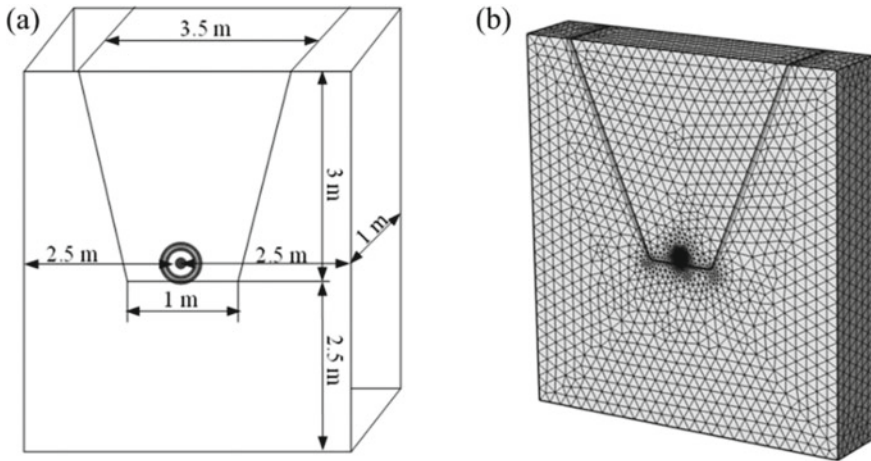


Fig. 1 The structure of the 500 kV XLPE EHV submarine cables



**Fig. 2** **a** Topological structure of the model. **b** Mesh dissection of the model

- (3) Heat transfer module: The thermal conductivity coefficient of soil is set as  $1 \text{ W}\cdot\text{m}^{-1}\cdot\text{K}^{-1}$ , the temperature of upper soil boundary condition is 308 K, the heat transfer coefficient is 8, and the temperature of lower soil boundary is 298 K. The overall model boundary of the submarine cable layout environment is the thermal type 2 boundary condition, which means the horizontal temperature gradient is 0.

When no cooling schemes are taken, the distribution of temperature of the whole cable trench can be seen in Fig. 3. It is shown that due to the increase of the temperature of the cable core, the temperature of the air and soil increases to varying degrees. The thermal conductivity of the air is much lower than the soil, hence the air temperature above the cable is slightly higher than that of the soil below the cable. It can be seen that the temperature distribution in the cable trench is relatively uniform, with an average temperature of  $55^\circ\text{C}$  throughout the cable trench. Due to the natural flow of air, the temperature difference in the entire air domain does not exceed  $5^\circ\text{C}$ .

### 3 Results and Discussions

#### 3.1 Water Pipe Cooling

The cooling effect of different cooling water pipe diameters, water flow velocities, water pipe numbers, and water flow directions on the submarine cable can be calculated. The positions of the water pipe and submarine cables can be seen in Fig. 4. The pipe is placed parallel to the submarine cable, 0.1 m from the submarine cable. For comparison, the cooling effect of the cooling water pipe with different outer

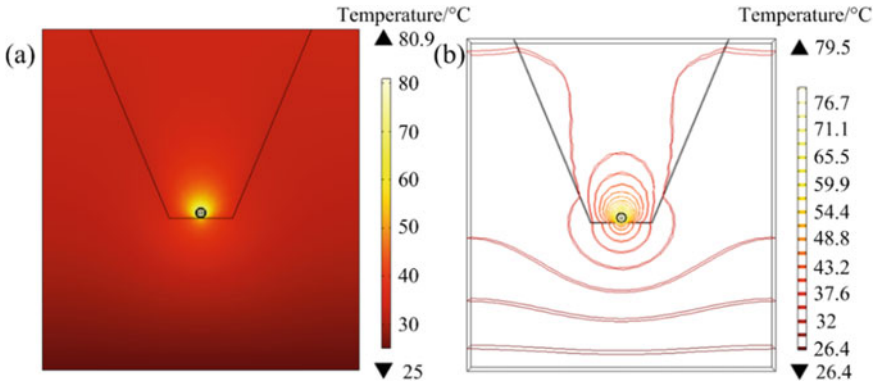


Fig. 3 The temperature distribution in the cable trench without cooling schemes

diameters and different water pipe numbers are studied. The diameters of the pipe are taken as 20 and 30 mm. The initial temperature of the water is set as 20 °C.

The cooling effects of cooling water pipes with a diameter of 30 and 20 mm on the submarine cable core temperature at a water velocity of 0–1 m/s can be seen in Fig. 5. It can be seen that for water pipes with a diameter of 30 mm, when the water velocity is slow, the cable core temperatures in the cases with one cooling water pipe and two water pipes both decrease the fastest when the water velocity is slower than 0.1 m/s. It is shown that the cooling effect of two water pipes is always better than that of the case with one water pipe. When two water pipes are used, the cooling effect of the pipes with the same water direction is slightly higher than that of the water pipes with the opposite water flow direction. When the water velocity increases to 0.25–1 m/s, the cooling effect is gradually not affected by the change of water flow rate.

For cooling water pipes with a diameter of 20 mm, when the water velocity is slow, the cable core temperatures in the cases with one cooling water pipe and two water pipes both decrease the fastest when the water velocity is slower than 0.1 m/

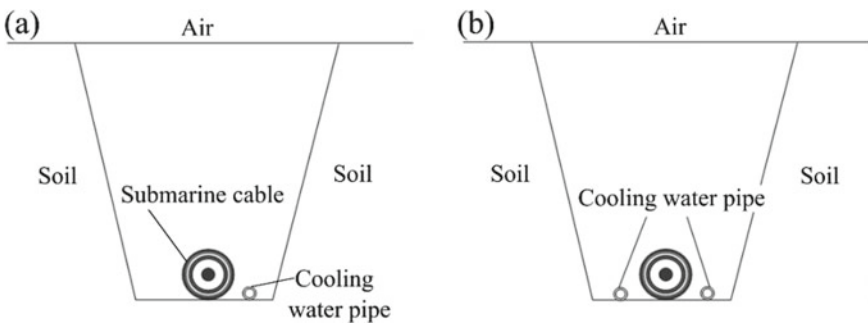
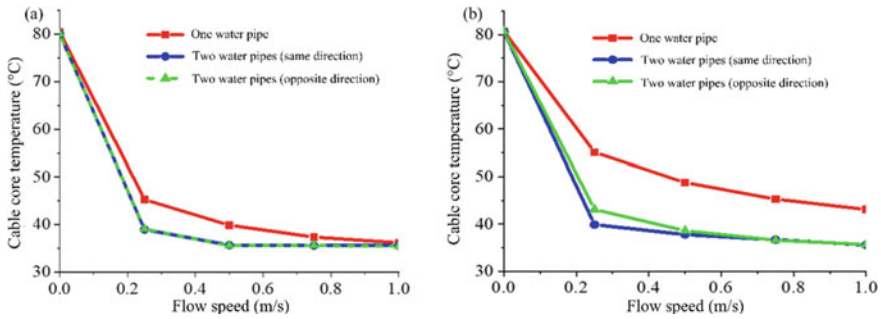


Fig. 4 Location diagram of the water pipe. a One pipe. b Two pipes



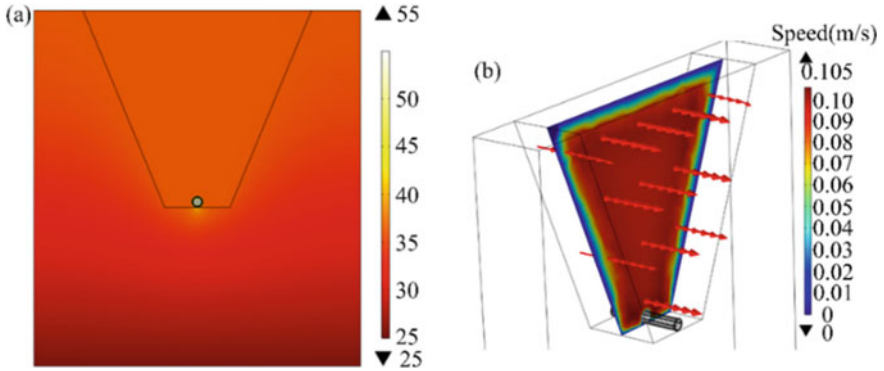
**Fig. 5** Cooling effect of the water pipe. **a** One pipe. **b** Two pipes

s. The core temperature decreases more significantly when the two water pipes are used, and the cooling effect of the pipes with the opposite water direction is slightly higher than that of the water pipes with the same water flow direction. When the water velocity increases to 0.25–1 m/s, the cooling effect is gradually not affected by the change of water velocity.

### 3.2 Wind Cooling

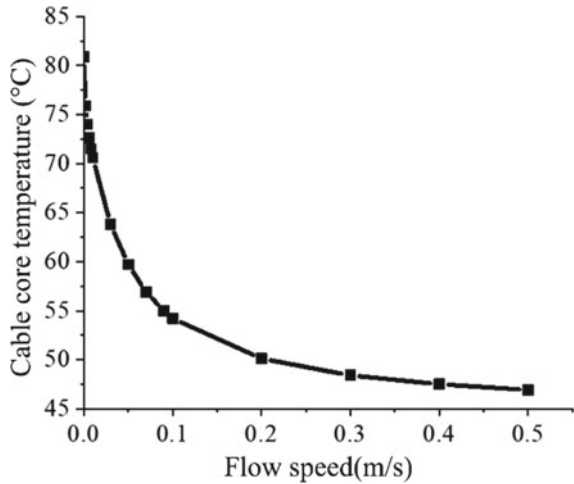
The distribution of the temperature of the whole cable trench in the case of wind cooling with the air velocity of 0.09 m/s can be seen in Fig. 6. The maximum temperature is the cable core, which is 55 °C. The heat distribution of the trench is relatively uniform, which is about 40 °C. The air flow velocity distribution can be seen in Fig. 6b, the red arrow represents the air flow direction, and the length of the arrow is proportional to the air flow velocity. The air flow velocity distribution of the cable trench is relatively uniform. As the cable heats up, the air density of the cable trench decreases, so the maximum air velocity can reach to 0.105 m/s, which is slightly higher than the given air velocity.

The cooling effect of the wind cooling scheme can be seen in Fig. 7, the core temperature decreases with the air flow velocity. When the air flow velocity increases from 0 to 0.1 m/s, the core temperature decreases by ~25 °C. It is shown that with a certain range of air flow velocity (such as 0.1 m/s), the air flow fully exerts its heat dissipation effect and has a significant cooling effect. The higher the air flow velocity, the faster the heat transfer. The reduction of heat accumulation can effectively cool the submarine cable.



**Fig. 6** a Temperature distribution of the cable trench. b Wind velocity distribution of the cable trench

**Fig. 7** Cooling effect of the wind

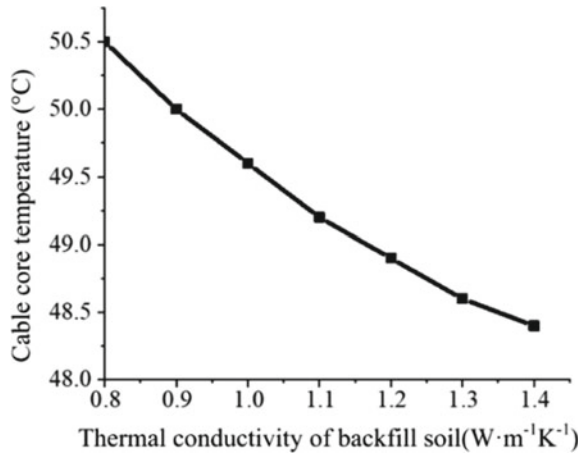


### 3.3 Backfill Soil Cooling

When the submarine cable is in the cable trench layout environment, the transmission ampacity is limited by the poor thermal conductivity of the air. Therefore, backfill soil with higher thermal conductivity can be used to improve the transmission ampacity of the submarine cable.

The cooling effect of the backfill soil can be seen in Fig. 8. When the soil has a thermal conductivity coefficient of  $0.8 \text{ W}\cdot\text{m}^{-1}\cdot\text{K}^{-1}$ , the thermal conductivity is more than 30 times that of the air, so the cooling effect of backfill soil is very significant. The temperature of the cable core decreases from 80.9 to 50.5 °C. When the thermal conductivity of backfill soil increases from 0.8 to  $1.4 \text{ W}\cdot\text{m}^{-1}\cdot\text{K}^{-1}$ , the temperature of the cable core decreases almost linearly.

**Fig. 8** Cooling effect of the backfill soil



## 4 Conclusion

This paper establishes a three-dimensional simulation model for the submarine cable in the cable trench layout environment, and several cooling schemes are used to analyze their cooling effect on the submarine cable core.

For the water pipe cooling scheme, the cooling effect is the most significant when the water velocity is less than 0.1 m/s. Increasing the number of cooling water pipes can effectively cool the submarine cable. The cooling effects of the water pipe with the same and opposite water flow directions are almost identical.

For the wind cooling scheme, the cooling effect is the most significant when the air velocity is less than 0.1 m/s, the cable core temperature decreases almost linearly with the air velocity. When the air velocity is faster than 0.1 m/s, the cooling effect is almost not affected by the air velocity.

For the backfill soil cooling scheme, the cooling effect is more significant with the thermal conductivity of the backfill soil.

**Acknowledgements** This research was supported by the Science & Technology Projects of State Grid Corporation of China (Grant No. 52060021006H).

## References

1. Dong T, Brakelmann H, Anders GJ (2023) Analysis method for the design of long submarine cables. *Renew Sustain Energy Rev* 171:113029
2. Zhang YY, Chen XM, Zhang H et al (2020) Analysis on the temperature field and the ampacity of XLPE submarine HV cable based on electro-therm al-flow multiphysics coupling simulation. *Polymers* 12(4):952
3. Chen ZX, Le YJ, Liu H et al (2019) Study of temperature field and ampacity of 110kV AC submarine cables under different laying conditions. *J Phys Conferen Series* 1346:012037

4. Duraisamy N, Gooi H, Ukil A (2020) Ampacity estimation for submarine power cables installed in saturated seabed-experimental studies. *IEEE Transact Industr Appl* 56(6):6229–6237
5. He XT, Ma XD, Yan XP (2011) Research on power loss reduction measures for landing parts of high voltage submarine power cables. *Zhejiang Electric Power* 10:29–31 (in Chinese)
6. Zhang M, Fan YB, Liu SH et al (2016) Improvement in power cables ampacity in ducts by using low thermal resistivity backfill material. *High Volt Eng* 42(8):2394–2398 (in Chinese)
7. De LF, Anders GJ (2008) Effects of Backfilling on cable ampacity analyzed with the finite element method. *IEEE Transact Power Deliv* 23(2):537–543
8. Yang YM, Cheng P, Chen J et al (2013) Current-carrying capacity calculation based on coupling fields for cable in ventilated trench and its influencing factors. *Electric Power Automat Equip* 33(7):139–143 (in Chinese)
9. Meng Y, Wang JH et al (2010) Increasing transmission capacity of cables by water cooling system. *Electric Power Constr* 31(11):54–56 (in Chinese)
10. Zhang H, Ma GQ, Li PF et al (2023) Overload capacity analysis of extra high voltage AC XLPE submarine cable. *Front Energy Res* 11:1178059

# Multi-Physics Field Simulation Analysis of GIS Disconnect Switch Contact Temperature Considering Contact Anomalies



Ziqi Zhang, Jiangjun Ruan, Shengwen Shu, Qiaofeng Chen, Chen Zhang, and Yongqing Deng

**Abstract** The thermal faults of GIS (Gas Insulated Switchgear) disconnect switch can lead to serious electrical accidents, and the temperature of the contacts is an important indicator for effectively detecting thermal faults. Therefore, conducting temperature field calculations for GIS is of great significance. In this paper, a multi-physics simulation calculation model is established for a 110 kV GIS disconnect switch. Firstly, electromagnetic simulation calculations are carried out to obtain the distribution of losses. Then, the calculated losses are coupled as heat sources to the temperature fluid field to obtain the temperature and flow field distribution. Based on this, temperature field analysis is further carried out for different contact resistance values in abnormal contact conditions. The results show that the temperature hotspots of the GIS disconnect switch are concentrated on the upper contacts of the disconnect switch. In the case of poor contact, the highest temperature point is 42.06% higher than that under normal working conditions.

**Keywords** GIS · Multi-physical fields · Temperature analysis · Contact anomalies

## 1 Introduction

With the rapid development of the economy, the demand for electricity in society has also increased significantly, promoting the construction and development of power grids. The GIS (Gas Insulated Switchgear), which uses SF<sub>6</sub> gas to combine some of the high-voltage components of the electrical system, has become an important operating equipment for substations [1, 2].

---

Z. Zhang (✉) · S. Shu  
College of Electrical Engineering and Automation, Fuzhou University, Fuzhou 350000, China  
e-mail: [1761599332@qq.com](mailto:1761599332@qq.com)

J. Ruan · Q. Chen · C. Zhang · Y. Deng  
School of Electrical Engineering and Automation, Wuhan University, Wuhan 430072, China



Although GIS has many advantages, with the increase in voltage level and operational life, GIS can experience various faults. Among them, thermal faults are an important part of GIS faults and one of the main forms of fault performance [3, 4]. Once a fault occurs, SF<sub>6</sub> repair work is more difficult to implement [5]. About 78% of the GIS faults classified as occurring from 2006 to 2015 are known to manifest as heat generation [4] eventually. If heat generation in GIS equipment is not detected and dealt with in a timely manner, it may lead to a series of serious electrical accidents [6].

At present, Researchers at home and abroad have carried out a lot of research on the thermal analysis of GIS disconnect switches, with the main methods being the finite element method and the thermal circuit method. Liu [7] points to establish an equivalent heat path model for 252 kV to effectively calculate the temperature rise of the focal node, but simplified the conditions and there is a gap with the actual working conditions. The multi-physical field coupling calculation method is widely used at home and abroad to calculate the temperature rise of power equipment. In one dimension, the paper [8] establishes a mathematical model of the temperature and flow fields, the model is too simple to accurately reflect the actual temperature rise of the equipment. The model is also too simple in two dimensions to obtain accurate calculation accuracy. And in three dimensions, where Pawar et al. used the finite element method to carry out eddy current field loss calculations for SF<sub>6</sub> high-voltage circuit breakers, and then used the CFX platform to calculate the circuit breaker temperature rise [9]; Song et al. [10] used a multi-physical field coupling method to calculate the temperature rise of a three-phase GIS considering skin and proximity effects.

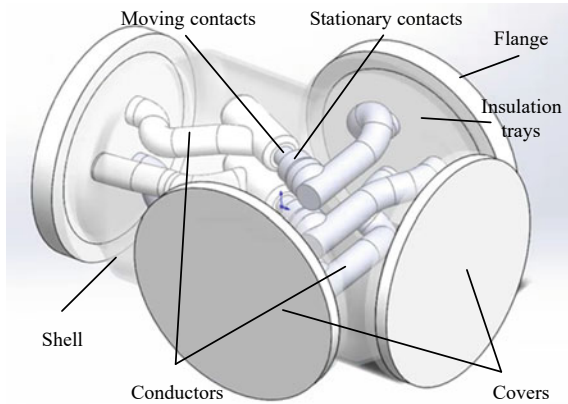
It is clear that research into the analysis of GIS disconnect switch heat generation has developed in the direction of finite element multi-physics field coupling. However, the research on refined modelling and the analysis of contact resistance under consideration of abnormal conditions is still not comprehensive enough and there are areas where further improvements can be made. Therefore, a multi-physics field coupling simulation study is carried out for 110kV GIS disconnect switch, and a temperature field calculation analysis under abnormal conditions is also carried out to investigate the influence of contact resistance on the temperature of GIS disconnect switch.

## 2 Building Physical Models

### 2.1 Geometric Models

The 110 kV GIS disconnect switch model ZF12B-126 is chosen for the simulation and is modelled in Fig. 1. In order to maintain the accuracy of the solution results and to facilitate modelling and simulation calculations, the simulation model simplified from the actual physical model as follows:

**Fig. 1.** 110 kV GIS disconnect switch model



Structures such as gearing rods, gears and inter-phase insulators that have less influence on the results of multi-physics field calculations are ignored and the remaining components are retained.

The stationary contacts, moving contacts and through-current conductors are retained, as well as the peripheral cover, insulating disc, flange and shell, but the details of these components have been simplified.

The large number of sharp corners, chamfers and rounded corners present in the model are simplified.

## 2.2 Material Parameters

In the multi-physics field coupling simulation of GIS disconnect switch, the accurate simulation of electrical contact determines the accuracy of the simulation calculation results. For GIS disconnect switch, the electrical contact exists between the moving contact and stationary contact finger positions and between the stationary contact finger and stationary contact base. In order not to affect the calculation of heat generation power and temperature rise, and to reduce the calculation difficulty, the complex structure of a large number of contacts in the plum touch finger is simplified to a circular entity, normal contact resistance is taken as  $3.5 \mu\Omega$ , where thermal conductivity can be derived from Eqs. (1) respectively

$$\frac{\lambda}{\sigma} = L \cdot T \quad (1)$$

where  $\lambda$  is the thermal conductivity,  $\sigma$  is the resistivity,  $L$  is the Lorentz number and  $T$  is the absolute temperature.

The material of the GIS disconnect switch current conductor, shell, flange and cover is aluminium alloy, the material of the moving and stationary contact fingers is

**Table 1** GIS disconnecter material electromagnetic parameters

Structure	Materials	Relative magnetic permeability	Resistivity ( $\times 10^{-8} \Omega \cdot m$ )
Covers\shell\flange	Aluminium alloy	1	2.80
Conductors	Aluminium alloy	1	2.80
Moving\stationary contacts	Copper	1	1.76
Insulation trays	Epoxy resin	1	–
Internal gases	Air	1	–

**Table 2** Thermal flow field parameters for GIS disconnecter materials

Materials	Parameters	Numerical values
Aluminium alloy	Density/ $g \cdot cm^{-3}$	2.68
	Specific heat capacity/ $J \cdot kg^{-1} \cdot K^{-1}$	963
	Thermal conductivity/ $W \cdot m^{-1} \cdot K^{-1}$	150
Epoxy resin	Density/ $g \cdot cm^{-3}$	1.6
	Specific heat capacity/ $J \cdot kg^{-1} \cdot K^{-1}$	550
	Thermal conductivity/ $W \cdot m^{-1} \cdot K^{-1}$	1

copper, where the material of the insulating disc is epoxy resin. Because the thermal conductivity of the metal shell is much higher than that of the epoxy resin insulating disc, the insulating disc dissipates relatively little heat and is therefore set as an adiabatic boundary. The entire GIS disconnect switch cavity is internally filled with air, with an air pressure of 0.1 MPa. In the simulation it is assumed that the resistance magnitude is constant and does not change with temperature, and that the material relative permeability of the equipment part of the structure is 1. The electromagnetic parameters and thermal flow field parameters of the specific materials are shown in Tables 1 and 2 respectively.

### 3 Building Mathematical Models

#### 3.1 Electromagnetic Fields

The source of heat generation in GIS barriers is Joule heat and eddy current losses, specifically Joule heat generated by the current flowing through the conductors and the contact resistance. At the same time, AC (alternating current) causes alternating magnetic fields, and structures such as shells, covers and flanges are affected by alternating magnetic fields to generate induction currents, which are the source of eddy current losses. The insulating material of the insulating discs produces small

losses at voltages of 110 kV and below and can therefore be ignored in the solution of the electromagnetic field.

The current-carrying conductor of a GIS disconnecter generates DC (direct current) losses and additional losses due to the skin and proximity effects caused by AC. The eddy current effect, proximity effect and skin effect are therefore taken into account in the loss calculation in this paper. The skin depth is calculated as shown in (2).

$$d = \sqrt{\frac{2}{\omega\mu\gamma}} \tag{2}$$

where  $\omega$  is the current frequency;  $\gamma$  is the material conductivity;  $d$  is the skin depth;  $\mu$  is the material magnetic permeability.

### 3.2 Thermal- Fluid Field

The heat transfer mechanism of the temperature fluid field includes heat conduction, heat convection and heat radiation. The losses generated by the conductors and contacts act as the heat source and the internal air undergoes convective heat transfer to the GIS disconnect switch shell. Where air is a weakly incompressible fluid, pressure work and viscous dissipation can be neglected, at which point the temperature field control equation is formulated as follows:

$$\rho_v C_p \frac{\partial T}{\partial t} + \rho_v C_p u \cdot \nabla T + \nabla \cdot (-k \nabla T) = Q \tag{3}$$

where  $\rho_v$  is the density,  $C_p$  is the constant pressure heat capacity,  $u$  convection velocity,  $k$  is the heat transfer coefficient and  $Q$  is the loss i.e. the heat source.

The fluid field control equations follow the equations of conservation of mass, conservation of momentum and conservation of energy, as follows:

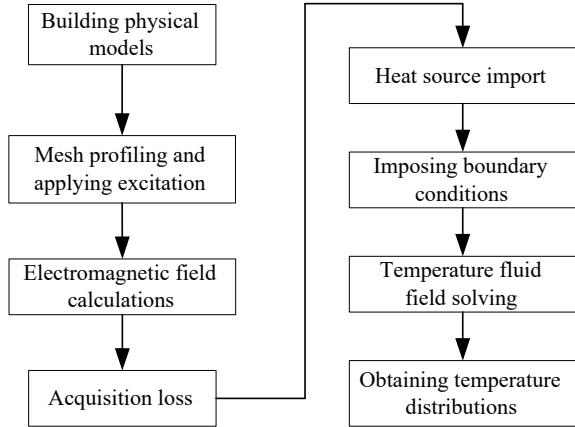
$$\nabla \cdot \mathbf{v} = 0 \tag{4}$$

$$\frac{\partial(\rho\mathbf{v})}{\partial t} + \rho\mathbf{v}\nabla\mathbf{v} = \rho\mathbf{f} - \nabla p + u\nabla^2\mathbf{v} \tag{5}$$

$$\frac{\partial(\rho)}{\partial t} + \nabla \cdot (\rho\mathbf{v}) = \rho\mathbf{q} - \nabla(k\nabla T) + \mathbf{q} \tag{6}$$

where  $\rho$  is the density of the air,  $\mathbf{v}$  is the flow rate of the air,  $\mathbf{f}$  is the fluid volume force,  $\mathbf{q}$  is the volumetric heat source of the fluid and  $c$  is the specific heat capacity.

**Fig. 2** Multi-physics field technical route

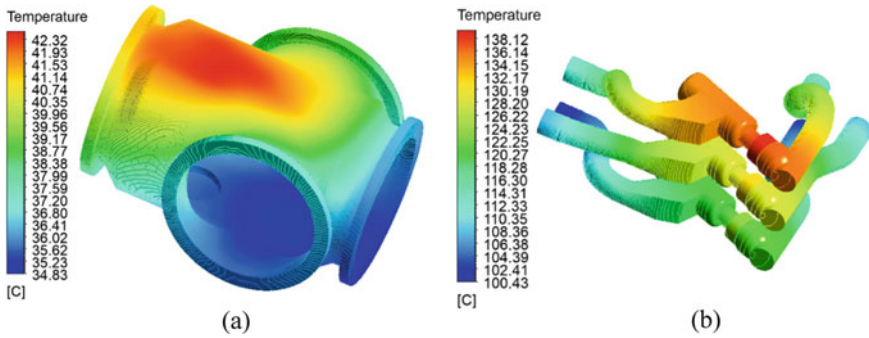


### 3.3 Multi-Physical Field Coupling

In this paper, the multi-physical field is coupled indirectly by adding a rated three-phase current with a frequency of 50 Hz, a three-phase lag of 120° and a size of 3150 A to the GIS disconnector for solving the electromagnetic field and obtaining the losses of its components. The losses are then introduced into the temperature fluid field as a heat source to calculate the temperature field distribution. The  $k-\epsilon$  turbulence model is used in the steady-state calculation of the thermal field, the heat transfer coefficient of the GIS disconnect switch surface is taken as  $9.90 \text{ W}\cdot\text{m}^{-1}\cdot\text{K}^{-1}$  and the flow-solid boundary is set as a no-slip boundary condition, i.e. the flow velocity of the fluid near the junction with the wall is 0 and the temperature of the fluid immediately adjacent to the wall is the same as the temperature of the wall. The technical route is shown in Fig. 2.

## 4 Analysis of Simulation Results

The results of the GIS disconnect switch electromagnetic field are obtained by solving for the eddy current field. because of the presence of electromagnetic induction, induced currents are generated on the GIS disconnect switch shell, and eddy currents are formed that are larger the closer the conductor is. The current distribution on the current-carrying conductor also receives proximity and skin effects, where it can be seen that the current density at the contact resistance is significantly greater than that of the current-carrying conductor. At the same time, the contact resistance is smaller in size and has a greater density of eddy current losses. The distance between the conductors is smaller and the proximity effect is more pronounced, so this part of the heat generation accounts for a higher percentage. The maximum loss of the



**Fig. 3** Temperature distribution of GIS disconnect switch **a** shell, **b** conductors

conductor can be calculated as 557.27 W, the contact resistance and contact finger loss is 116.19 W, the shell loss is 31.87 W, and the remaining loss is 3.62 W.

The calculated losses are coupled into the temperature-fluid field for solution, and the ambient temperature is set to 25 °C to obtain the temperature and flow field distribution. As shown in Fig. 3a for the shell temperature distribution, the highest temperature rise can be obtained at 17.32 °C and the lowest at 9.83 °C. The temperature distribution of the GIS disconnect switch conductor and contacts is shown in Fig. 3b and it can be seen that the highest temperature is concentrated at the contacts, approximately 138.12 °C. This is due to the large losses in the contacts and the volume of the contacts. This is due to the larger and smaller contact losses, which are more likely to generate high temperatures. As the gas is affected by the heat flowing upwards, it can be seen that the top shell temperature is higher. The temperature hot spot of the GIS disconnect switch is concentrated in the upper contact of the disconnect switch is also affected by the hot air flow.

## 5 Comparison of Abnormal States

The circuit resistance becomes greater when the GIS disconnect switch is in abnormal contact, with the specific resistance increasing in part to the contact resistance. In this paper, the contact resistance is increased by 10 μΩ to simulate the circuit resistance in the abnormal contact condition, keeping other conditions constant. The loss in contact resistance is calculated to be 400.33W through the electromagnetic field and coupled into the thermal-fluid field, the temperature distribution of the Fig. 4 can be obtained. It can be calculated that the maximum contact temperature in the abnormal state is 42.06% higher than under normal conditions, and the maximum shell temperature is 20.32% higher. The results show that the temperature of the GIS disconnect switch contacts increases significantly in the abnormal contact state. The heat dissipation conditions within the GIS disconnect switch are poor, which can easily lead to thermal failures or even accidents such as burnout.

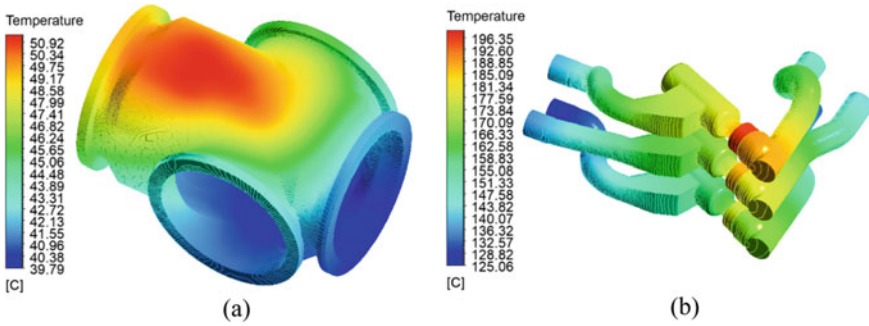


Fig. 4 Temperature distribution of GIS disconnect switch under abnormal contact a shell, b conductors

### 6 Conclusion

This paper takes the 110 kV GIS disconnect switch as the research object, starting from the actual physical model, the model is reasonably simplified and equivalent, and a multi-physics field simulation calculation model is established. Firstly, the eddy current electromagnetic field is calculated to obtain the loss of each part of the GIS disconnect switch, and then the loss is coupled into the thermal- fluid field to obtain the temperature distribution. In addition, the contact resistance is increased to simulate the abnormal contact condition of the GIS disconnect switch, and the temperature distribution under the abnormal contact condition is obtained and compared with the normal working condition. The following conclusions are obtained:

1. By multi-physical field coupling simulation of the GIS disconnect switch, the maximum temperature of the GIS disconnect switch shell is 42.32°C, which occurs at the top of the shell, and the maximum temperature of the contact is 138.12°C at the upper contact, in the normal working condition with rated current of 3150 A and ambient temperature of 25°C.
2. Keeping other working conditions same, the contact resistance of the GIS disconnect switch increases by 10 μΩ, the maximum contact temperature increases by 42.06% more than the normal working condition, and the maximum shell temperature increases by 20.32%. As a result, the contact temperature rises significantly when the contact is abnormal, while the shell temperature rises slightly.

### References

1. Yoo WJ et al (2008) Infrared fiber-optic sensor for non-contact temperature measurements. In: 2008 3rd International Conference on Sensing Technology, IEEE, Taipei, Taiwan, pp 500–503

2. Sijia H (2020) Research on the characteristics of contact overheating defects of GIS equipment disconnect switches and detection technology. In: South China University of Technology (in Chinese)
3. Song H et al (2017) Application of computational fluid dynamics to predict the temperature-rise of gas insulated switchgears. In: 2017 4th international conference on electric power equipment—switching technology, IEEE, Xi'an, China, pp 694–697
4. Mengdan H, Chun X, Zhining Y et al (2020) Advances in the study of heat generation in GIS equipment. *High Volt Applian* 56(12):24–33 (in Chinese)
5. Xiaoxing Z, Zhen W, Torch T et al (2010) UHF online monitoring system for partial discharge in gas insulated transformers. *High Volt Technol* 36(7):1692–1697 (in Chinese)
6. Li QM, Cong HX, Xing JY et al (2014) Online temperature monitoring of the GIS contacts based on infrared sensing technology. *Proceed CSEE* 9(4):1385–1393
7. Fen L, Gang L, Xiaoyu Q et al (2020) The use of equivalent thermal paths in the calculation of temperature rise of common box disconnect switches. *High Volt Technol* 56(8):211–216 (in Chinese)
8. Ye T, Zhen L, Yong Z et al (2018) Online monitoring of GIS switch contact temperature based on infrared sensing. In 13th IEEE conference on industrial electronics and applications (ICIEA), IEEE, Wuhan, China, pp 2187–2191
9. Pawar S et al (2011) Application of computational fluid dynamics to reduce the new product development cycle time of therm SF<sub>6</sub> gas circuit breaker. *IEEE Transact Pow Deliv* 27(1):156–163
10. Song YH, Wang W, Huang QD et al (2019) Influence of current-carrying conductor proximity and skin effect and current frequency on the temperature rise of a three-phase common box GIS. *High Volt Applian* 55(9):97–102 (in Chinese)



# Finite Element Analysis of Physical Properties of New Transformer Core Materials



Dong Zhao, Yang Wang, Yonggang Jia, Yan Du, Qingdong Zhu,  
and Bo Zhang

**Abstract** Power transformer is the core equipment which transmits and distributes electric energy in power system. Power grid performance is directly influenced by the performance of the transformer, and the transformer core losses account for the vast majority of the total losses. As a result, the choice of transformer core materials has a significant impact on the overall efficiency of the grid. The objective of this paper was to develop a three-dimensional model of a three-coherent transformer using ANSYS Electronics Desktop software, with PC95 as the core material and a multi-physical field coupling calculation simulation using the finite element mesh method for obtaining the physical parameters of the dynamic change characteristics, thereby enabling the visualization of transformer parameters. The magnetic field distribution and core loss of the transformer were simulated and compared with those of different core materials (PC44). According to the results of the study, the permeability of PC95 material is much greater, the loss of transformer core is much lower, and the temperature adaptability is greater than that of PC44 material. And it is more adaptable to the effects of temperature change, the optimization design of

---

D. Zhao · Y. Wang · Y. Jia · Y. Du · B. Zhang (✉)

School of Electronics and Information, Xi'an Polytechnic University, Xi'an, China

e-mail: [zhangbo@xpu.edu.cn](mailto:zhangbo@xpu.edu.cn)

Xi'an Key Laboratory of Interconnected Sensing and Intelligent Diagnosis for Electrical Equipment, Xi'an, China

D. Zhao

e-mail: [zhaodong2022@stu.xpu.edu.cn](mailto:zhaodong2022@stu.xpu.edu.cn)

Y. Wang

e-mail: [wangyang@xpu.edu.cn](mailto:wangyang@xpu.edu.cn)

Y. Jia

e-mail: [xpu.18700195710@163.com](mailto:xpu.18700195710@163.com)

Y. Du

e-mail: [duyan@xpu.edu.cn](mailto:duyan@xpu.edu.cn)

Q. Zhu

State Grid Shandong Electric Power Company Electric Power Research Institute, Beijing, China

e-mail: [165671795@qq.com](mailto:165671795@qq.com)

© Beijing Paiké Culture Commu. Co., Ltd. 2024

X. Dong and L. Cai (eds.), *The Proceedings of 2023 4th International Symposium on Insulation and Discharge Computation for Power Equipment (IDCOMPU2023)*, Lecture Notes in Electrical Engineering 1103, [https://doi.org/10.1007/978-981-99-7413-9\\_38](https://doi.org/10.1007/978-981-99-7413-9_38)

transformer in the environment of large temperature difference provides theoretical basis, so as to improve the efficiency of the transformer more effectively.

**Keywords** Core material · Finite element · Multi-physics coupling · PC95 · Dry-type transformer

## 1 Introduction

In recent years, the demand for electric energy has been increasing rapidly both in various industries and in residential electricity consumption. Electric energy was first discovered and proposed by American scientist Franklin in 1752 [1]. In order to reduce the power loss and impedance voltage drop of the transmission line, the transformer is required to increase the voltage before transmitting electric energy [2, 3]. Therefore, the transformer becomes an important part of the transmission system.

In the actual transformer, the electric energy is transferred from one system to another without any relative motion within each component through magnetic coupling, and loss is bound to occur in this process [5, 6]. Transformer is an indispensable part of power transmission system, but its loss is unavoidable. Therefore, scholars from all walks of life and major manufacturers have made a lot of efforts in transformer loss optimization, considering all aspects of the transformer to reduce the loss generated in the transformer work as much as possible [7].

Sibel Zorlu Partal et al. proposed a plug-in type iron core structure and compared it with EI type iron core. The results showed that the new type iron core could not only reduce the loss to a certain extent, but also greatly shorten the manufacturing process and time of iron core, thus improving the production efficiency [8]. Gaurav Upadhyay et al. proposed an open-core structure, which can also reduce certain losses [9]. On this issue, some researchers also used ANSYS Electronics Desktop software to build a transformer model, and made corresponding simulation of the new core material Mo.Me<sup>6</sup>. Compared with the commonly used core material, the new material has the advantages of low loss and high working efficiency [10]. Sarpreet Kaur et al. also proposed a kind of nanocrystalline material Finemet and Vitroperm for simulation and comparison, and built a model simulation using ANSYS Maxwell. The results also had a certain optimization effect on transformer core loss [11].

Therefore, this paper proposes a new material PC95 produced by TDK in Japan as the iron core of the transformer. B-H curve parameters of the material are input into Maxwell program, and three-phase excitation voltage equation is added to the windings. In particular, grid encryption was carried out for the solution parts, and certain boundary conditions were set and the step size was solved for simulation calculation. The superiority of the material was obtained by comparing the calculation of the principle equation with the simulation results.

## 2 Maxwell Equations

Maxwell is an open-source software that captures MySQL change data written in Java by Zendesk. Maxwell is used to analyze and calculate data based on finite element meshes. With the popularity of ANSYS Maxwell software, many scholars around the world have verified the software in different experiments and in different ways. Governing equation of electromagnetic field.

$$\begin{cases} \nabla \times H = J = J_s + J_c \\ \nabla \times E = -j\omega B \\ \nabla \cdot B = 0 \\ \nabla \cdot D = \rho \end{cases} \quad (1)$$

where  $H$  is the magnetic field intensity vector (A/m),  $E$  is the electric field intensity vector (V/m),  $B$  is the magnetic induction intensity vector (Wb/m<sup>2</sup>),  $D$  is the electric displacement vector (C/m<sup>2</sup>),  $J$  is the current density (A/m<sup>2</sup>),  $J_s$  is the source current density,  $J_c$  is the induced eddy current density,  $\rho$  is the charge density (C/m<sup>2</sup>). The constitutive relation of correlation vector is as follows:

$$\begin{cases} J_c = \gamma E \\ D = \varepsilon E \\ B = \mu H \end{cases} \quad (2)$$

where,  $\gamma$  is the electrical conductivity (S/m),  $\varepsilon$  is the dielectric constant (F/m) of the medium, and  $\mu$  is the permeability (H/m). It is difficult to solve for  $E$  and  $H$  using (1) and (2). The magnetic potential vector  $A$  is usually introduced to help with the solution, where it satisfies the following relation.

$$B = \nabla \times A \quad (3)$$

In a static magnetic field, here is an equation for the magnetic potential  $A$  of a vector. When solving the electromagnetic field problem, Eq. (4) is first used to solve the vector magnetic potential  $A$ , and then the magnetic flux density  $B$  is obtained from (3).

$$\nabla \times \left( \frac{1}{\mu} \nabla \times A \right) + \gamma \frac{\partial A}{\partial t} = J_s \quad (4)$$

### 3 Model Establishment

Figure 1 respectively show the front view and top view of the three-dimensional transformer model, the grid lines in the background provide a dimensional reference for the model builder. It can be seen that what this paper studies is the double-winding core transformer. The model is built in ANSYS Maxwell, and the basic transformer model framework is provided for scholars in the software.

#### 3.1 Winding Excitation Equation

A-phase excitation voltage:

$$V^{peak} \cdot (1 - e^{(-60 \times time)}) \cdot \cos(2 \cdot \pi \cdot 50 \cdot time) \tag{5}$$

B-phase excitation voltage:

$$V^{peak} \cdot (1 - e^{(-60 \times time)}) \cdot \cos(2 \cdot \pi \cdot 50 \cdot time + \frac{2}{3} \cdot time) \tag{6}$$

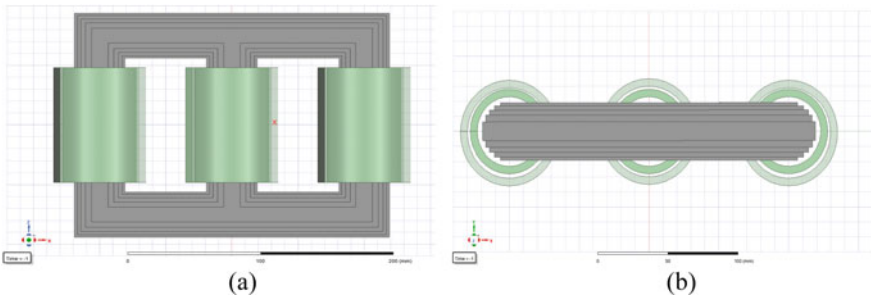
C-phase excitation voltage:

$$V^{peak} \cdot (1 - e^{(-60 \times time)}) \cdot \cos(2 \cdot \pi \cdot 50 \cdot time + \frac{4}{3} \cdot time) \tag{7}$$

Peak voltage:

$$V^{peak} = Rating \times \frac{Sqrt(2)}{Sqrt(3)} \tag{8}$$

Here  $V^{peak}$  stands for peak voltage and Rating stands for voltage rating.



**Fig. 1** Front view of three coherent transformer 3D model, Front view (a) and top view (b) of three-dimensional model of three-coherent transformer

### 3.2 Iron Core Material

In this paper, the simulation calculation of PC95 material as transformer core is proposed, The B-H curve and other related parameters of PC material are obtained through Mag web magnetic material platform. In order to make a method to verify the properties of materials, we must add various materials to the actual experiment for analysis. However, using ANSYS Maxwell simulation software can save a lot of costs. The platform of magnetization curve provides B-H parameters at different temperatures, which is because the material characteristics will slightly change with the temperature. However, considering the temperature characteristics of the transformer when it works, the following is the parameter change of PC95 material at 100°C.

It can be seen from Fig. 2 that the B-H curve of PC95 material is a non-linear curve. The magnetic flux density B is in the unit of tesla and H is in the unit of amperage meter. It is observed from the curve that PC95 material has the characteristics of low loss flux and high saturation of iron core. It is a kind of transformer that can maximize its characteristics in a wide temperature range.

In order to highlight the characteristics of PC95 material, this paper takes PC44 material and common ferrite material as reference, selects the same temperature working conditions, and changes the characteristics of the iron core material under the condition that the model and other parameters of the simulation are consistent, so as to compare the final simulation results of different iron core materials. Figure 3 show the B-H curve and B-P curve of PC44 material respectively (curve parameters are obtained by MAGWEB platform) (Table 1):

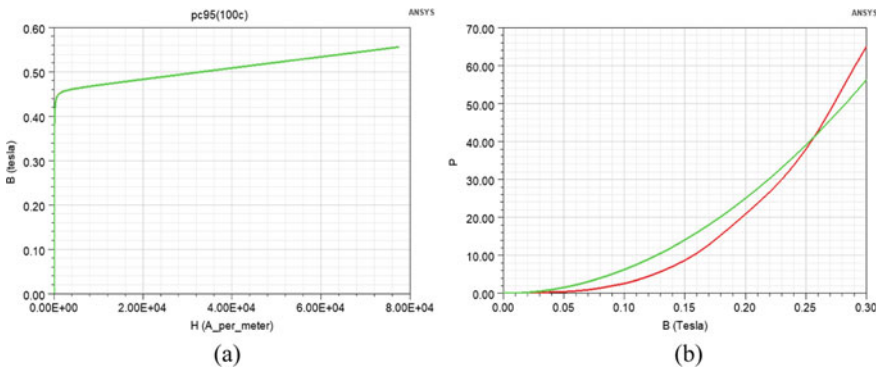
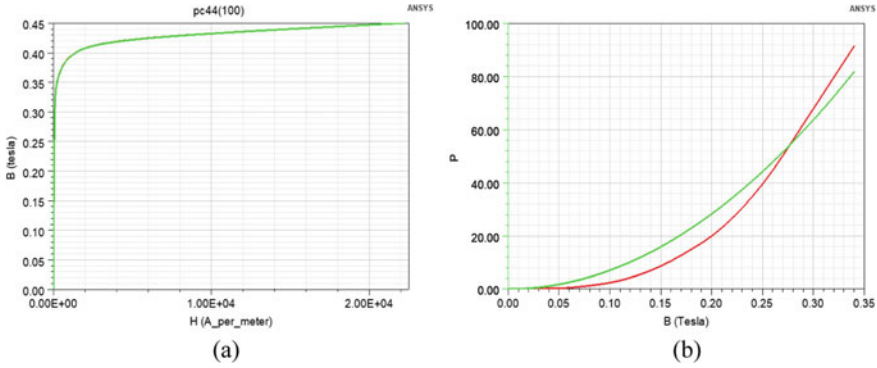


Fig. 2 B-H curve (a) and B-P curve (b) of PC95 material



**Fig. 3** B-H curve (a) and B-P curve (b) of PC44 material

**Table 1** Main parameters of transformer

Model	Thickness	Initial permeability	Frequency	Mass density
Performance	0.01778 mm	3300 S/m	50 Hz	4800 kg/m <sup>3</sup>

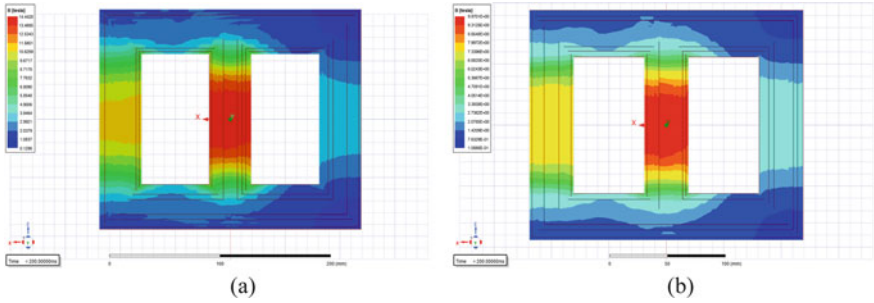
## 4 Analysis of Simulation Results

Based on the above model information, ANSYS Maxwell software was used to conduct electromagnetic simulation for the model, and the simulation calculation was established in Maxwell equations. These include Gauss’s law, which describes the relationship between electric field and charge distribution in space, faraday’s law of induction, which describes how a time-varying magnetic field can induce an electric field, Gauss’s law of magnetism, which describes that there is no problem with magnetic monopoles, and Maxwell-Ampere’s law, which describes two different methods of generating magnetic fields, which combine different physical calculations to produce a comprehensive physical field. The simulation calculation time process is from 0 to 1 s, and the calculation time step takes every 0.5 ms as a calculation time point.

### 4.1 Flux Density Distribution

In order to compare the physical characteristics of different iron core materials, the simulation results of two different materials used as transformer iron cores are shown in the Fig. 4:

As can be seen from the cloud Fig. 4 of magnetic induction intensity, when other conditions remain unchanged, PC95 material makes the distribution of magnetic flux density in the core more uniform.



**Fig. 4** Cloud map of magnetic flux density distribution of PC44 (a) and PC95 (b) core material (PC44,  $t = 200$  ms,  $B_{max} = 14.4428$  T; PC95,  $t = 200$  ms,  $B_{max} = 9.9701$  T)

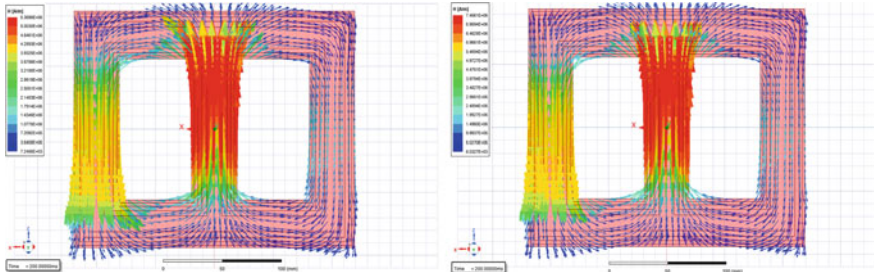
At the same time, its peak value is smaller than that of PC44 material, and the higher the peak value is, the higher the heat will be generated, thus accelerating the aging of insulation.

As can be seen from Fig. 4, the transformer core of PC95 material reaches a maximum flux density of about 9.97 T in a highly saturated state, and will fall on the three core columns in an even and alternating manner according to the phase difference of the input three-phase current value. The maximum magnetic flux density is distributed in the middle position of the magnetic core column and decreases to both sides successively, which indicates that the magnetic field generated in the middle position is the largest.

Therefore, during transformer operation or overload operation, the heat generated in the middle position of the transformer core column is the most. Therefore, in the design of transformer core materials, the quality of the middle position should be more strict requirements. When the magnetic induction intensity  $B$  is stronger overall, it also indicates that the permeability of ferromagnetic material  $\mu$  value is larger, so the area occupied by the iron core is smaller in the actual situation, and the transformer size and overall occupied space will also be smaller. This conclusion is mainly based on Eq. (9):

$$B = \mu \cdot H = \frac{\Phi}{A} \tag{9}$$

In the equation,  $B$  is the magnetic flux density of the iron core in the unit of Tesla (T),  $\mu$  is the permeability of the iron core material in the unit of Henry per meter,  $H$  is the magnetic flux intensity (A/m), with the diameter of magnetic flux in the unit of Wb,  $A$  is the surface area of the iron core in the unit of  $m^2$ .



**Fig. 5** Vector distribution cloud of magnetic field intensity of PC44 and PC95 iron core material (PC44:  $t = 200$  ms,  $H_{\max} = 5.3598E + 06A/m$ ; PC95:  $t = 200$  ms,  $H_{\max} = 7.4661E + 06A/m$ )

## 4.2 Magnetic Field Intensity Distribution

Maxwell software can accurately calculate the physical fields inside a transformer. The maxwell software can calculate the physical field distribution inside a transformer. Based on the calculated results, Maxwell can better analyze the physical characteristics of a transformer and even predict possible faults. In addition, Maxwell can provide effective data for preventing faults. It can be seen from Fig. 5 that the overall magnetic field intensity of PC95 is higher than that of PC44 by comparing the two materials when other conditions remain unchanged.

If the three core columns are divided into pillars A, B and C from left to right, and the corresponding winding phases are phases a, b and c, it can be seen from Fig. 5 that at  $t = 200$  ms, the maximum magnetic field intensity is distributed on the middle column, that is, pillar B, then phase b should reach the maximum value in the three-phase current waveform generated at this time. Therefore, based on such a data, you can further calculate its other parameter changes. The density of the magnetic field passing through pillar a and pillar c is different. This is because the magnetic field passing through pillar a reached its maximum value in the previous period, and the domain in the core still retained its original direction. On this basis, pillar A was greater than the magnetic field intensity of pillar C at 200 ms.

## 4.3 Core Loss

Through the simulation calculation of ANSYS Maxwell software, the loss waveform of iron core can be calculated (Fig. 6). It can be seen from Fig. 7 that the loss of PC95 material is relatively low and will reach a stable state around 60 ms. The maximum statistical value of loss is 18.5736W, which has been greatly optimized compared with that of PC44 material. Transformer loss is we continue to deepen the exploration of the problem, and different ferromagnetic materials often have different electrical and magnetic characteristics, the optimization of ferromagnetic materials according



to its characteristics are used in different working environments, so as to reduce the loss, save costs, and even extend the life of the transformer.

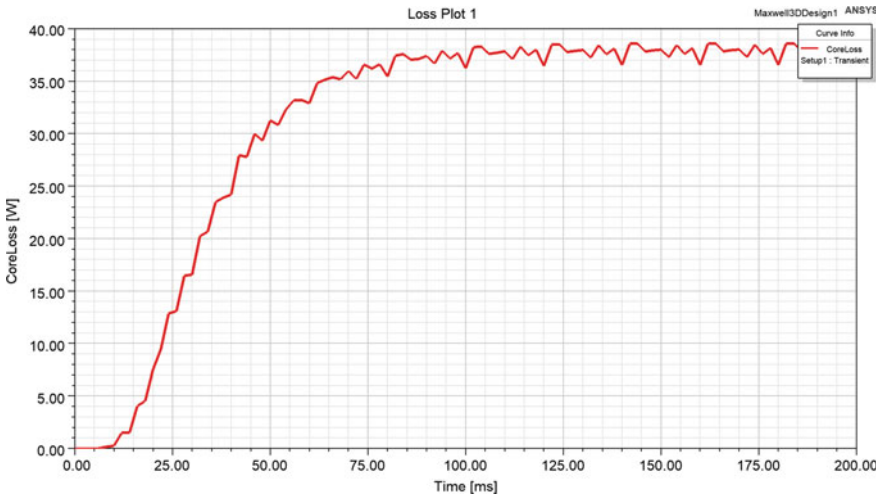


Fig. 6 Core loss of PC44 core material (t = 0 ~ 200 ms)

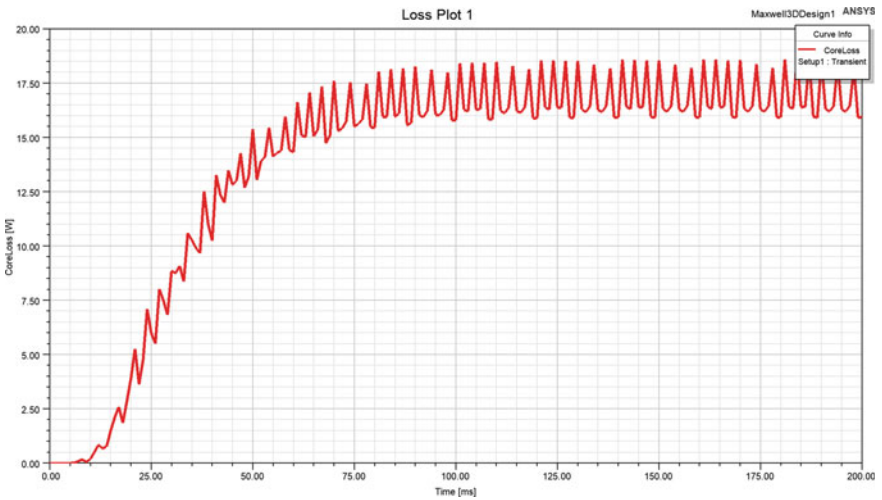


Fig. 7 Core loss of PC95 core material (t = 0 ~ 200 ms)

## 5 Conclusion

In this paper, ANSYS Electronics Desktop software was used to model and simulate the three-coherent transformer. PC95 material produced by TDK company in Japan was set as the transformer core. The parameters of material curve are obtained in the magnetic curve platform, and the physical influence of the material on the transformer was simulated. This paper introduced the simulated magnetic field distribution diagram in the iron core. It is concluded that when PC95 material works in the transformer, the distribution of magnetic flux density is relatively uniform, and less heat is generated during the operation of the transformer, which can reduce the speed of insulation aging. The loss of iron core is also smaller than that of PC44 material, which indicates that among transformer iron core materials, PC95 has the characteristic of low loss, which can provide reference for future material optimization and development. In addition, under the excitation of three-phase alternating voltage, it shows the same characteristics as the common iron core. Combined with the ambient temperature of the transformer, the influence of PC95 material in the environment of 100°C is minimized. This advantage can be combined with the transformer in the special temperature environment to provide reference value.

## References

1. Mehta HD (2014) A review on transformer design optimization and performance analysis using artificial intelligence techniques. *Int J Sci Res*
2. Dhonge D, Swami PS, Thosar AG (2015) Developing artificial neural network ANN model for fault diagnosis of power transformer. *Int J Scientific Eng Res* 1127–1132
3. Wang S, Wang SH, Zhang NM et al (2019) Calculation and analysis of mechanical characteristics of transformer windings under short-circuit condition. *IEEE Trans Magn* 55(7):8401804
4. Enokizono M, Soda N (1999) Core loss analysis of transformer by improved FEM. *J Magn Magn Mater* 196–197:910–912
5. Salam M, Quazi M et al (2016) Transformer principles and practice. McGraw-Hill Book Company, p 49–99
6. Wiszniewske A, Rebizant W, Schiel L (2009) New algorithms for power transformer inter-turn fault protection. *Electric Pow Syst Res* 79(10):1454–1461
7. Mustafa S, Anees A, Hameed B et al (2019) Effect of fin geometry on natural convection heat transfer in electrical distribution transformer: numerical study and experimental validation. *Therm Sci Eng Progr* 14:2451–9049
8. Zorlu P, Sibel S et al (2022) A novel plug-in core design for three-phase transformers. *IEEE Canad J Electric Comput Eng* 45:42–49
9. Kebriti R, Hossieni SMH (2022) 3D modeling of winding hot spot temperature in oil-immersed transformers. *Electric Eng* 3325–3338
10. Shabana S, Tanya T (2020) Optimal design of power transformer with advance core material using ANSYS technique. *Euro J Electric Eng Comput Sci* 4
11. Sarpreet K, Damanjeet K (2021) Finite element method (FEM) based design and simulation of practical transformer with nano-crystalline core using ANSYS. 1033:012038

# Research on Current Limiting Protection Method of Short Circuit Faults in Medium Voltage DC Integrated Power Systems



Beibei Wang

**Abstract** The problem of short-circuit fault limitation and protection is a big challenge in the development of medium voltage DC integrated power system. The traditional current–time protection principle cannot limit the fast rising short-circuit current, which will have a serious impact on the system. It is an effective protection idea to install fault current limiter in the power system. In this paper, the network structure and basic parameters of a medium voltage DC integrated power system are given, and the short-circuit fault characteristics and protection requirements are analyzed. Then, a protection strategy based on a new liquid metal current limiter is proposed, and the optimal configuration scheme and characteristics of the current limiter are analyzed, thereby achieving fast limitation of short circuit faults and rapid support of bus voltage, significantly reducing the system’s requirements for circuit breaker breaking capacity and speed.

**Keywords** Integrated power system · Liquid metal fault current limiter · Shipboard · Short-circuit protection

## 1 Introduction

The rated current of medium voltage DC integrated power systems is large, and the short circuit current rises rapidly and has a high amplitude, which seriously threatens the safe and stable operation of the system [1]. Due to the short transmission distance of ships, the amplitude difference between the upstream and downstream short-circuit currents of the same line is very small, resulting in the inability of the upper and lower circuit breakers to be set according to the current principle and can only be set according to the time principle. The short-circuit current at the power outlet cannot

---

B. Wang (✉)

Department of Electrical Engineering, Shanghai Jiao Tong University, Shanghai 200240, China  
e-mail: [wangbeibei@seari.com.cn](mailto:wangbeibei@seari.com.cn)

Shanghai Electrical Apparatus Research Institute (Group) Co., Ltd, Shanghai 200063, China

© Beijing Paiké Culture Commu. Co., Ltd. 2024

X. Dong and L. Cai (eds.), *The Proceedings of 2023 4th International Symposium on Insulation and Discharge Computation for Power Equipment (IDCOMPU2023)*, Lecture Notes in Electrical Engineering 1103, [https://doi.org/10.1007/978-981-99-7413-9\\_39](https://doi.org/10.1007/978-981-99-7413-9_39)

417

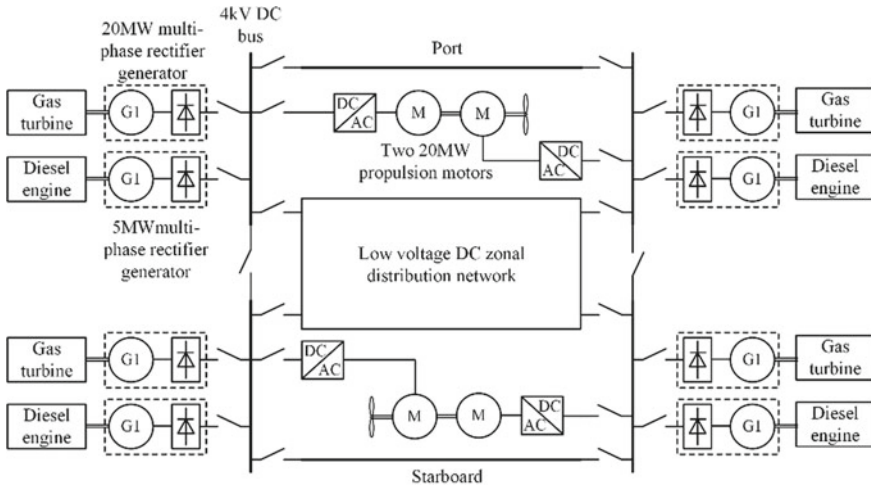
be effectively limited. When a short circuit fault occurs in the system, it will cause the voltage of the bus connected to the short circuit point to drop instantly, expanding the fault range. In addition, because DC current does not have a natural zero crossing, its breaking difficulty is much greater than AC current, and relying solely on circuit breakers for protection cannot balance selectivity and speed.

Current limiter is a promising protective component with great application prospects [2]. Installing a current limiter in the medium voltage DC integrated power system to limit the peak value of short-circuit current, and then using a circuit breaker for breaking can not only reduce the impact of short-circuit current on the line and equipment, greatly reduce the breaking burden of the circuit breaker, but also quickly support the bus voltage in non-fault areas and improve the selectivity of protection. As a new type of self-recovery current limiter, liquid metal current limiters have the characteristics of simple structure, fully enclosed, maintenance free, low on state loss, and strong current limiting ability, making them suitable for ship environments. This article will study the current limiting protection method for short circuit faults in medium voltage DC integrated power systems with liquid metal current limiters.

## **2 Short-Circuit Protection Requirements for Medium Voltage DC Integrated Power Systems**

### ***2.1 Network Structure***

The shipboard DC integrated power system mainly includes two structures: radial and ring network [3]. The former evolved from traditional AC systems and is generally powered by centralized distribution centers to the load. There are a large number of cables passing through the cabin, making the installation and maintenance of the system more difficult, and the fault self-healing performance is poor. The latter distributes electrical energy to the load centers of each area through the shipboard DC bus that runs through the entire ship, with a simple design and flexible power supply. A typical ring network second-generation integrated power system structure is shown in Fig. 1 [4], mainly composed of modules such as power generation, transmission and distribution, transformation and distribution, electricity consumption, and energy storage. The power generation module adopts high-speed multi-phase medium voltage rectifier generator set, including 20 MW gas generator and 5 MW diesel generator; The transmission and distribution module adopts a 4 kV medium voltage DC main network; The power transformation and distribution module adopts low-voltage DC zonal distribution, and achieves voltage transformation from 4 kV to 700 V through four 4 MW DC converters; The hotel load of the entire ship is powered by eight 1 MW inverters, each of which is simultaneously connected to the low voltage DC bus on the port and starboard sides, converting the DC 700 V voltage into the AC 400 V voltage. In addition, the main propulsion motor is planned to use variable frequency permanent magnet or high-temperature superconducting motors,



**Fig. 1** Network structure of a typical medium voltage DC integrated power system

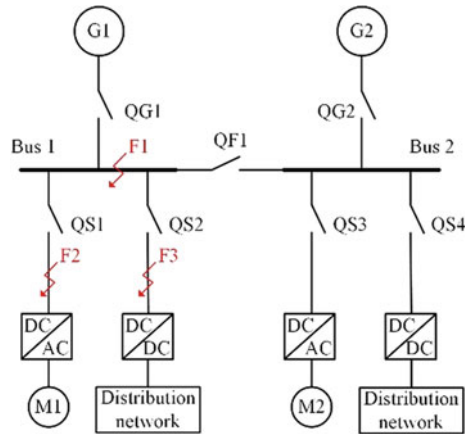
while the energy storage module is planned to use super capacitors, integrated inertial energy storage, or composite energy storage.

### 2.2 Short Circuit Fault Characteristics

The medium voltage DC system shown in Fig. 1 is powered by two power plants, each consisting of two units. Each unit consists of a 20 MW level main generator and a 5 MW level auxiliary generator. A single power plant can maintain normal power supply for the entire ship while working. In order to simplify the analysis and keep without loss of generality, this section takes a power station as the research object, and each unit only considers the main generator of 20 MW level. The network structure is shown in Fig. 2. Among them, G1 and G2 represent the medium voltage rectifier generator, and M1 and M2 represent the propulsion motor. The left and right power supply areas are connected through the bus circuit breaker QF1. QG1 and QG2 represent the generator outlet circuit breaker, QS1–QS4 represent the load branch circuit breaker, and F1–F3 represent typical short-circuit fault points.

When a short circuit occurs at the main distribution bus 1, F1, in Fig. 2, G1 and G2 simultaneously feed current to the fault point. If the short circuit current output by each generator is  $i$ , then the current flowing through QG1, QG2, and QF1 is  $i$ . At this point, the voltage of the two main distribution buses rapidly drops, affecting both the left and right power supply areas. It is necessary to disconnect QF1 as soon as possible, cut off the connection between the two buses, and ensure normal power supply to the non-fault area on the right. Due to the limited capacitance support time on the input side of the frequency converter and DC converter, QF1 is generally

**Fig. 2** Simplified structure and fault points diagram



required to complete the disconnection within 5 ms. When a short circuit occurs at the load branch such as F2, G1 and G2 simultaneously feed current to the fault point. At this time, the short-circuit current flowing through QS1 is  $2i$ , and the voltage of both main distribution buses drops. QF1 still needs to be disconnected as soon as possible. The situation when a short circuit occurs at F3 is similar to that at F2.

In order to obtain the peak value of short-circuit current  $i$ , it is necessary to model the medium voltage rectifier generators G1 and G2. This generator consists of a twelve phase synchronous AC generator with a diode uncontrolled rectifier system, and the basic principle is shown in Fig. 3 [5]. This article uses the equivalent decoupling method to equivalent a 4 kV/20 MW twelve phase rectifier generator to four three-phase synchronous generators with uncontrolled rectifier bridges. By using the universal components in MATLAB/SIMULINK, a simulation model is established, where the excitation voltage is set to a constant DC voltage and the short-circuit impedance is set to  $0.01 \Omega$  and  $10 \mu\text{H}$ . The short-circuit time is 0.1 s, and the simulation results show that the waveform of the short-circuit current and voltage output by the generator is shown in Fig. 4. After the short circuit occurs, the voltage rapidly drops from 4 kV to close to zero, and the current  $i$  rapidly increases, with an initial rate of increase of about  $23 \text{ A}/\mu\text{s}$ . After a short circuit occurs, it reaches a peak of 69.3 kA within 5 ms, decays to about 30 kA after 100 ms, and decays to about 25 kA after 200 ms. So, when there is a short circuit at F1, the peak current flowing through QG1, QG2, and QF1 is 69.3 kA. When there is a short circuit at F2, the peak short-circuit current flowing through QS1 is 138.6 kA.

### 2.3 Protection Needs and Difficulties

Considering the fast and selective requirements of short circuit protection, when a short circuit occurs at F1 in Fig. 2, QF1 should open first and break within 5 ms. At

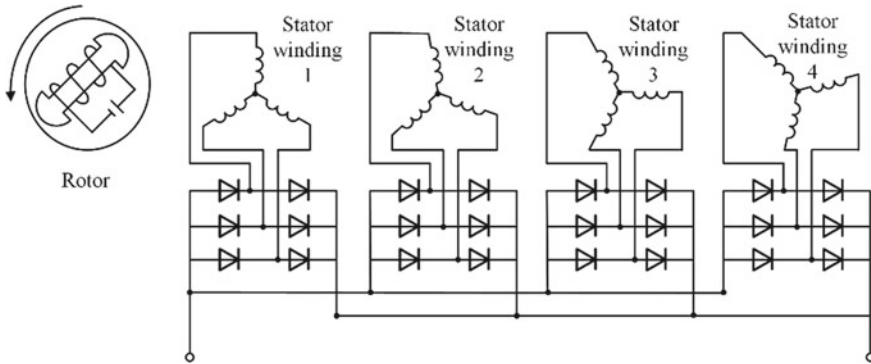
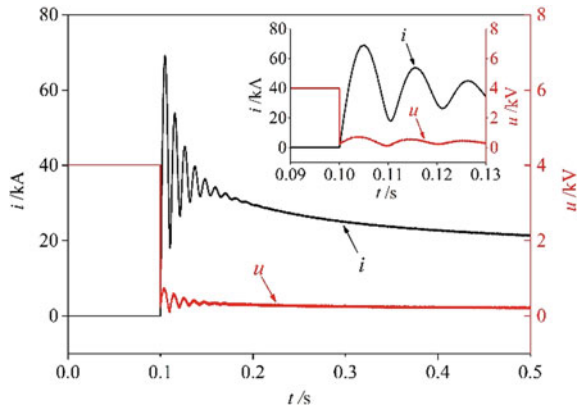


Fig. 3 Schematic diagram of a twelve phase synchronous rectification generator

Fig. 4 Simulation waveform of short circuit current and voltage output of a twelve phase synchronous rectifier generator



the same time, QG2 should not be disconnected, while QG1 should be disconnected. When a short circuit occurs at F2, QS1 should be separated first, while QF1, QG1, and QG2 should not be separated. Based on the above fault characteristics and protection requirements, it can be concluded that there are the following protection difficulties for short circuit faults in the shipboard medium voltage DC main network.

First, the breaking capacity of existing DC circuit breakers is difficult to meet the requirements. The peak current flowing through QS1 during a short circuit at F2 is 138.6 kA. Currently, there are no publicly reported DC circuit breakers that have reached this breaking capacity at 4 kV voltage.

Second, the existing DC circuit breakers are difficult to meet the quick action requirements of QF1. The full breaking time of air arc extinguishing circuit breakers is relatively long, usually over 10 ms [6], which clearly cannot meet the requirements. The full breaking time of current transfer circuit breakers can be shortened to less than 3 ms, but they have the disadvantages of complex structure and high cost, and are not suitable for use in medium and low voltage fields.

Third, the selectivity and rapidity of protection are difficult to meet simultaneously. Due to the short transmission distance of the ship's power system, the short-circuit currents at the generator outlet, main distribution bus, and load incoming line are not significantly different, resulting in the circuit breaker being unable to be set according to the current principle and can only be set according to the time principle. The commonly used practice is to not set instantaneous action for QG1 and QG2, but only set a short delay of 0.2–0.5 s [7]. Obviously, this will sacrifice the quick action of QG1 when short circuited at F1. For this reason, differential protection methods are generally adopted for bus, which to some extent shortens the action time of QG1 [8, 9]. However, for QF1, the strict speed requirements make it unable to form selective protection with QS1. When there is a short circuit at F2, QF1 still inevitably acts.

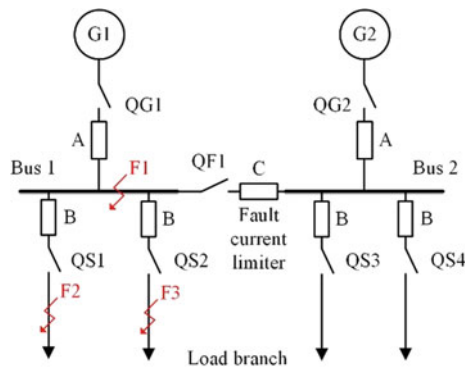
### 3 Current Limiting Protection Method

#### 3.1 Configuration Scheme of Fault Current Limiters

In response to the characteristics and protection difficulties of short-circuit faults mentioned above, this article proposes the installation of fault current limiters in the medium voltage DC main network as a short-circuit protection method. Specifically, the possible installation positions of the fault current limiter are shown in Fig. 5 at the outlet A of the generator, connected in series with QG1 and QG2; at the incoming line B of the load branch, connected in series with QS1 ~ QS4; at the bus connection C, connected in series with QF1.

Liquid metal current limiter is a type of current limiter based on resistive components, which fully utilizes the conductive fluid properties of liquid metal and relies on metal vapor arc to achieve current limiting and energy consumption functions. It has the characteristics of fully enclosed, maintenance free, no movable components, self-trigger and self-recovery. According to the mathematical model of liquid metal units in reference [10], 10 units with a channel diameter of 8 mm and a channel length

Fig. 5 Simplified structure and fault points of medium voltage DC network





of 20 mm are connected in series to form a fault current limiter model. The model is placed at position A and its short-circuit fault limiting characteristics are simulated. If the number of liquid metal units in series increases, the current limiting coefficient decreases, but it also leads to an increase in the volume and conduction losses of the current limiting device. The principle for selecting the number of the liquid metal units in this article is to ensure that the peak short-circuit current limiting coefficient of the generator output is less than 0.5, and to minimize the number of units as much as possible.

### 3.2 Current Limiting Protection Characteristics

Table 1 compares the configuration schemes of fault current limiters in the medium voltage DC main network, and provides the peak current flowing through each circuit breaker during short circuits at F1 and F2, as well as the voltage support of non-fault buses. It can be seen that if the current limiter is installed at the generator outlet, it can reduce the prospected short-circuit current of the entire system. However, the current limiter cannot support the voltage of the non-fault bus, and QF1 still needs to act quickly in case of a short-circuit fault. If the current limiter is installed at the incoming line of the load branch, it can only limit the short circuit fault at F2, and cannot limit the short circuit fault at F1. In comparison, installing a current limiter at the bus connection not only reduces the breaking burden of QF1 and QS1, but also supports the non-fault bus voltage in the event of a short circuit. QF1 does not require instantaneous action, so QS1, QF1, and QG1 can be adjusted according to the principle of time in conjunction with differential protection to minimize the fault power outage range. Therefore, installing a current limiter at the bus connection is the most reasonable solution. At present, the maximum breaking capacity of air arc extinguishing DC circuit breakers can reach 5 kV/90 kA, and the full breaking time is about 20 ms [11]. After installing the current limiter, the selection of air arc extinguishing DC circuit breakers for each circuit breaker in Fig. 5 can meet the requirements.

## 4 Conclusions

- (1) This article proposes a current limiting protection method for shipboard DC integrated power systems with liquid metal current limiters, which can achieve fast limitation of short circuit faults and rapid support of bus voltage, significantly reducing the requirements for the breaking capacity and speed of DC circuit breakers.
- (2) In the medium voltage DC network, installing a liquid metal current limiter at the bus connection can limit the short-circuit current at the outlet of the rectifier generator from the prospective peak of 69.3 kA to below 35 kA, and

**Table 1** Different configuration schemes of the fault current limiters

Location of fault current limiters		Without fault current limiters	At generator outlet (A)	At incoming line of load branch (B)	At bus connection (C)
Short circuit fault at F1	QG1/QG2	69.3/69.3 kA	34.6/34.6 kA	69.3/69.3 kA	69.3/34.6 kA
	QF1	69.3 kA	34.6 kA	69.3 kA	34.6 kA
	QS1	0 kA	0 kA	0 kA	0 kA
	Bus voltage	Drop	Drop	Drop	Support
Short circuit fault at F2	QG1/QG2	69.3/69.3 kA	34.6/34.6 kA	69.3/69.3 kA	69.3/34.6 kA
	QF1	69.3 kA	34.6 kA	69.3 kA	34.6 kA
	QS1	138.6 kA	69.2 kA	60.8 kA	77 kA
	Bus voltage	Drop	Drop	Support	Support

the short-circuit current of the load branch from the prospective peak of 138.6–77 kA, within the breaking capacity range of the air arc extinguishing DC circuit breaker.

- (3) The use of fault current limiters to limit short-circuit current and coordinate with circuit breakers to isolate faults is an effective protection scheme. It can maximize the selectivity and speed of protection, improve the continuity and reliability of the power supply.

**Acknowledgements** This work was sponsored by Shanghai Sailing Program (No. 21YF1415200).

## References

- Xu L, Guerrero JM, Lashab A et al (2022) A review of DC shipboard microgrids—part II: control architectures, stability analysis, and protection schemes. *IEEE Trans Power Electron* 37(4):4105–4120
- Shen B, Yang J, Tian M et al (2021) Saturated iron-core superconducting fault current limiter for VSC network: system modeling with loss analysis. *IEEE Trans Appl Superconductiv* 31(8):1–4
- IEEE Standards Association (2010) IEEE Std 1709™-2010. IEEE recommended practice for 1 kV to 35 kV medium-voltage DC power systems on ships. IEEE, New York, pp 5–9
- Ma WM (2011) Development of vessel integrated power system. In: 2011 international conference on electrical machines and systems. IEEE, Beijing, pp 1–12
- Ji F, Wang G, Fu L et al (2012) Study on equivalent reduced model of twelve-phase synchronous generator. *Pow Syst Protect Control* 40(2):28–33 (in Chinese)
- Chen W, Zeng R, He J et al (2021) Development and prospect of direct current circuit breaker in China. *High Voltage* 6(1):1–15
- Yang Y, Zhong C, Zhang Y et al (2016) Protection technology for marine electric power systems with multiple power supply modes. *Chinese J Ship Res* 11(5):113–119 (in Chinese)

8. Ye Z, Fang M, Wang G et al (2011) A layer-coordinated protection strategy for naval vessel power system. In: 2011 international conference on advanced power system automation and protection. IEEE, Beijing, pp 720–723
9. Li LQ, Antoniazzi A, Raciti L et al (2017) Design of solid state circuit breaker based protection for DC shipboard power systems. *IEEE J Emerg Select Topics Power Electron* 5(1):260–268
10. He HL, Wu Y, Yang Z et al (2018) Study of liquid metal fault current limiter for medium-voltage dc power systems. *IEEE Trans Comp Pack Manufact Technol* 8(8):1391–1400
11. Ma Z, Peng Z, Zhao C et al (2020) Research and development of 5 kV high-speed medium-voltage DC air circuit breaker. *High Voltage Eng* 46(1):312–318 (in Chinese)

# Structural, Magnetic, Relaxor Ferroelectric and Magnetoelectric Coupling Properties in Aurivillius Phase $\text{Bi}_6\text{La}_3\text{Ti}_3\text{Fe}_5\text{O}_{27}$



Maosong Wu, Long Xiao, Feng Deng, and Shengquan Zheng

**Abstract** Polycrystalline ceramics of  $\text{Bi}_6\text{La}_3\text{Ti}_3\text{Fe}_5\text{O}_{27}$  (BLTF) were prepared by a sol-gel method. Structural, magnetic, relaxor ferroelectric and magnetoelectric coupling properties were investigated. Studies indicate that the prepared sample has a plate-like shape structure with a thickness of 160–170 nm and a diameter of 2  $\mu\text{m}$ . La substitution has been shown to effectively induce the room temperature combining of ferroelectricity and ferromagnetism, thus indicating a promising way for improving multiferroic properties of antiferromagnetic  $\text{Bi}_9\text{Ti}_3\text{Fe}_5\text{O}_{27}$ . Two dielectric relaxations were observed in the temperature ranges of 500–590 and 600–650 K in BLTF ceramics. In addition, the magnetoelectric coupling effect between charge and spin ordering was determined by measuring the relative change of the ferroelectric polarization and dielectric constant in external magnetic field.

**Keywords** Ferroelectric property · Dielectric property · Magnetoelectric-coupling

## 1 Introduction

Multiferroic materials that combine ferroelectricity with magnetic ordering have showed great concern for the technological applications and the underlying physical mechanism [1]. Unfortunately, the multiferroics are rare because the condition required for magnetism in the ferroelectrics is far too difficult to meet [2]. Also, in general multiferroics (single phase) have a lower Néel temperature of magnetic transition, which constricts the application future enormously. The perovskite  $\text{BiFeO}_3$  is one of the well known single phase multiferroics with ferroelectric (FE) transition ( $T_C = 830\text{ }^\circ\text{C}$ ) and antiferromagnetic (AFM) transition ( $T_N = 370\text{ }^\circ\text{C}$ ) [3]. In spite

---

M. Wu · L. Xiao · F. Deng · S. Zheng (✉)

Science and Technology on Electromagnetic Compatibility Laboratory, China Ship Development and Design Center, Wuhan 430064, China  
e-mail: [752477472@qq.com](mailto:752477472@qq.com)

L. Xiao

e-mail: [xiaolong@tsinghua.org.cn](mailto:xiaolong@tsinghua.org.cn)

© Beijing Paiké Culture Commu. Co., Ltd. 2024

X. Dong and L. Cai (eds.), *The Proceedings of 2023 4th International Symposium on Insulation and Discharge Computation for Power Equipment (IDCOMPU2023)*, Lecture Notes in Electrical Engineering 1103, [https://doi.org/10.1007/978-981-99-7413-9\\_40](https://doi.org/10.1007/978-981-99-7413-9_40)

of the above nature is very prospective in view of practical value, BiFeO<sub>3</sub> has some inherent problems, such as high leakage current, weak ferromagnetism in bulk, lower magnetoelectric coupling output, and a wide difference in ferroic transition temperatures. In order to solve these problems, there are several reports on (a) rare-earth ions substitution at the A-site or ions cosubstitution at the A-/B-sites [4–7], (b) a solid solution with other perovskite materials such as PbTiO<sub>3</sub> and BaTiO<sub>3</sub> [8, 9], in which FE polarization together with ferromagnetism can be observed at room temperature. At present, BiFeO<sub>3</sub>-based materials and BiMnO<sub>3</sub> are the most concerned about multiferroics, providing the spin and charge orders in the higher temperature [4–10].

Another option is layered bismuth titanates with a well-known Aurivillius, which have been addressed [11, 12]. The Bi<sub>4</sub>Ti<sub>3</sub>O<sub>12–m</sub>BiFeO<sub>3</sub> system with a general formula of Bi<sub>*m*+1</sub>Fe<sub>*m*–3</sub>Ti<sub>3</sub>O<sub>3*m*+3</sub> have been seen as a candidate since they may present multiferroicity and magnetoelectric coupling effect. Moreover, these compounds have shown interesting dielectric anomalies at high temperatures. Among the compounds, Bi<sub>*m*+1</sub>Fe<sub>*m*–3</sub>Ti<sub>3</sub>O<sub>3*m*+3</sub> (*m* = 8) with an orthorhombically distorted perovskite-type structure is one such Aurivillius multiferroics with an eight-layered pseudo-perovskite [Bi<sub>7</sub>Ti<sub>3</sub>Fe<sub>5</sub>O<sub>25</sub>]<sup>2–</sup> sandwiched in between the [Bi<sub>2</sub>O<sub>2</sub>]<sup>2+</sup> in the *c* direction. Bi<sub>9</sub>Ti<sub>3</sub>Fe<sub>5</sub>O<sub>27</sub> exhibits AFM (*T*<sub>N</sub> = 127 °C) [12] and FE (*T*<sub>C</sub> = 584 °C) properties, which appears to have the best potential applications. Jartych et al. [13] studied the Mössbauer spectroscopy of the Bi<sub>9</sub>Ti<sub>3</sub>Fe<sub>5</sub>O<sub>27</sub> and reported that its *T*<sub>N</sub> is lower than 300 K, and that Fe<sup>3+</sup> may hold tetrahedral and octahedral sites. Besides the above reports, an obvious negative temperature coefficient effect has also been observed by Patri et al. in Bi<sub>9</sub>Ti<sub>3</sub>Fe<sub>5</sub>O<sub>27</sub> sample [14]. As noted above, BLTF is essentially AFM rather than FM and generally inhibits the emergence of the linear magnetoelectric coupling. The above compounds can be viewed as inserting the well-known multiferroic BiFeO<sub>3</sub> unit into the typical perovskite Bi<sub>4</sub>Ti<sub>3</sub>O<sub>12</sub>. It has been reported that La doping can improve its FE property of bismuth-layered perovskite Bi<sub>4</sub>Ti<sub>3</sub>O<sub>12</sub> [15]. Moreover, the doping of La<sup>3+</sup> for Bi<sup>3+</sup> breaks the space magnetic structure and obtain a certain net magnetization [16]. In this paper, the substitution of rare-earth cation (*i.e.*, La<sup>3+</sup> ion) for Bi-site in the Bi<sub>9</sub>Ti<sub>3</sub>Fe<sub>5</sub>O<sub>27</sub> compound is expected to change the spiral spin structure and improve ferromagnetism, while the substitution of La<sup>3+</sup> for Bi<sup>3+</sup> could enhance the ferroelectricity and thus induce strong magnetoelectric coupling effect. In this work, we study the magnetic, FE, dielectric and magnetoelectric coupling behaviors of La-substituted Bi<sub>9</sub>Ti<sub>3</sub>Fe<sub>5</sub>O<sub>27</sub> ceramics.

## 2 Experimental Procedure

BLTF ceramics have been prepared using a variation of the sol–gel procedure. Using Ti(C<sub>4</sub>H<sub>9</sub>O)<sub>4</sub>, Fe(NO<sub>3</sub>)<sub>3</sub>, Bi(NO<sub>3</sub>)<sub>3</sub> and La(NO<sub>3</sub>)<sub>3</sub> as starting materials. The samples were sintered at 850 °C for 1 h. The detailed procedure has been described in [17].

BLTF samples were obtained by XRD. The morphology of the samples was examined by a Sirion-200 FE-SEM. The high-resolution image was acquired using a JEOL 2010F TEM. Specimens for HRTEM were obtained by dispersing the products

in alcohol followed by ultrasonic treatment. Magnetic measurements were examined using a physical property measurement system (PPMS, Quantum Design). The FE behaviors were acquired by a Precision Premier II FE tester. The dielectric properties were measured by a Wayne Kerr 6500B precision impedance analyzer.

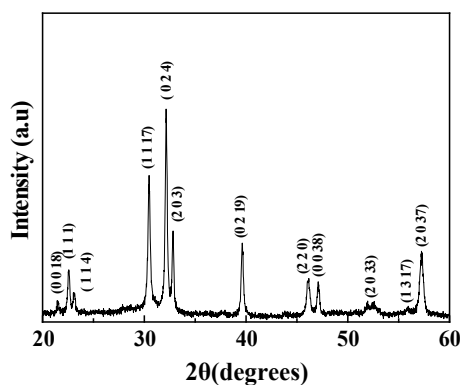
### 3 Results and Discussion

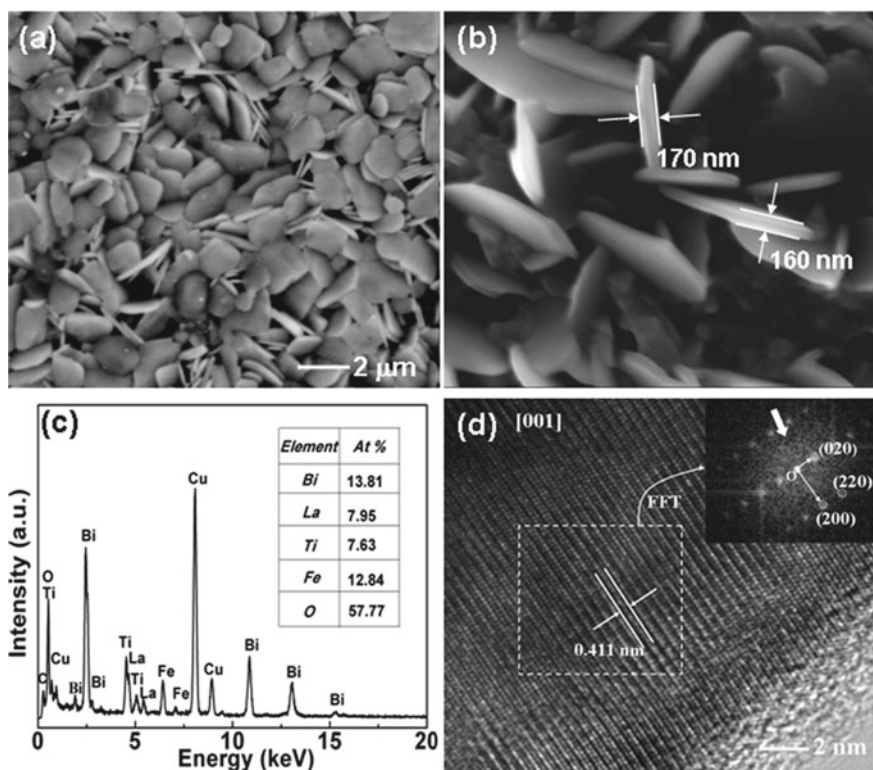
It can be seen from Fig. 1, no detectable secondary phase is observed in the pattern. This result illustrates that the pure BLTF phase has been formed. The BLTF sample has an orthorhombic ( $Fmm2$ ) space group, with unit cell dimensions  $a = 5.4932$ ,  $b = 5.6105$ , and  $c = 73.3491$  Å. The value of  $b/a$  ratio (orthorhombicity) was found to be 1.021 which is comparable to that of other Aurivillius systems [11, 18].

SEM and HRTEM images (Fig. 2a, b) demonstrate that the pure phase BLTF sample mainly consists of plate-like shape with a thickness of 160–170 nm and a diameter of 2  $\mu\text{m}$  which is attributed to the lower surface energy in the  $a$ - $b$  planes and rapid growth of (0 0 1) planes [19]. The EDS analysis confirms that the chemical composition BLTF agrees with the nominal ratio (Fig. 2c). In Fig. 2d we have shown the HRTEM image where we could notice well pronounced lattice stripes indicating very good crystalline nature of the BLTF ceramics. It is possible to identify the {001} family of planes with a uniform interplanar spacing of 0.411 nm. Figure 2d also reveals that all regions have a homogeneity microstructure with no trace of any other growth defects, such as dislocation, stacking faults, and intergrowth defect. The corresponding fast Fourier transform (FFT) image presented in the inset of Fig. 2d, showing a nice dot pattern, again clearly reveals the high crystallinity of BLTF sample.

Temperature dependence of magnetization measurements of polycrystalline BLTF sample were obtained at 1 kOe (Fig. 3a). The extremely low Curie-type increase toward 0 K definitively signals an almost impurity-free magnetic material. The magnetization measured in the field-cooled (FC) mode is not so different compared to that of zero-field-cooled (ZFC) excluding any kind of spin-glass-like state in BLTF.

**Fig. 1** XRD spectrum of BLTF ceramics

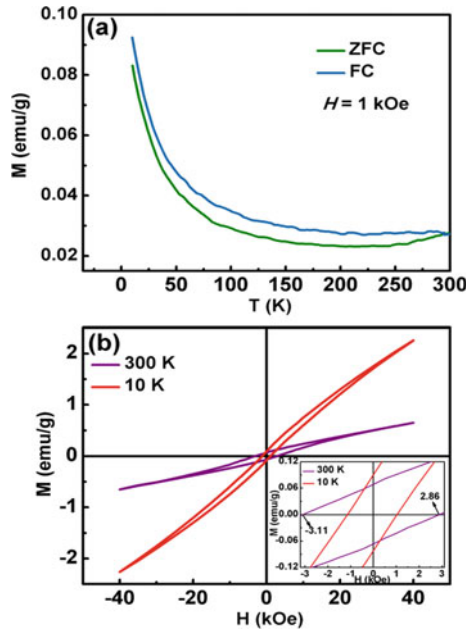




**Fig. 2** **a** Surface SEM image of the as-prepared BLTF and **b** magnified SEM image of the plate-like grain structure. **c** EDS spectrum shows that the as-prepared BLTF. **d** HRTEM image of BLTF. Inset shows the corresponding FFT pattern

However, the sample exhibits a distinct abruptness which may be due to the existence of a weak FM response, as confirmed by the magnetic  $M-H$  loop displayed in Fig. 3b. The magnetic field dependent magnetization at 10 K and 300 K are shown in Fig. 3b. At 300 K, the  $M-H$  loop reveals a weak FM behavior in the sample. Moreover, the magnetization increases with increasing magnetic field, but does not saturate even at a field of 4 T, indicating the basic AFM nature of the sample. Its remnant magnetization ( $2M_r$ ) and the coercive field ( $2H_c$ ) are determined to be  $\sim 0.14$  emu/g and 6.0 kOe. The enhancement of ferromagnetism can be explained as follows: Considering that the ionic radius difference between bismuth and lanthanum [ $r(\text{Bi}^{3+}) = 1.03 \text{ \AA}$ ,  $r(\text{La}^{3+}) = 1.06 \text{ \AA}$ ] is  $\sim 3\%$ , with partial substitution of La ions for A-site Bi ions, inducing lattice distortion as reflected in the change of  $\text{Fe}^{3+}-\text{O}-\text{Fe}^{3+}$  bond angles, and then releasing the large latent magnetization locked in the AFM state in the material by affecting the interactions of  $\text{Fe}^{3+}-\text{O}-\text{Fe}^{3+}$ . In addition, the local FM Fe-O clusters may also lead to ferromagnetism. It should be noted that there is no evidence to confirm or exclude its contribution to the FM nature of BLTF. The  $M-H$  loop measured at 10 K exhibits a larger  $M_{\text{max}}$  of 1.3 emu/g at 4 T than that measured

**Fig. 3.** **a** FC and ZFC curves of BLTF. **b**  $M$ – $H$  loops of BLTF ceramics measured at 10 and 300 K. Inset shows the magnified  $M$ – $H$  loops



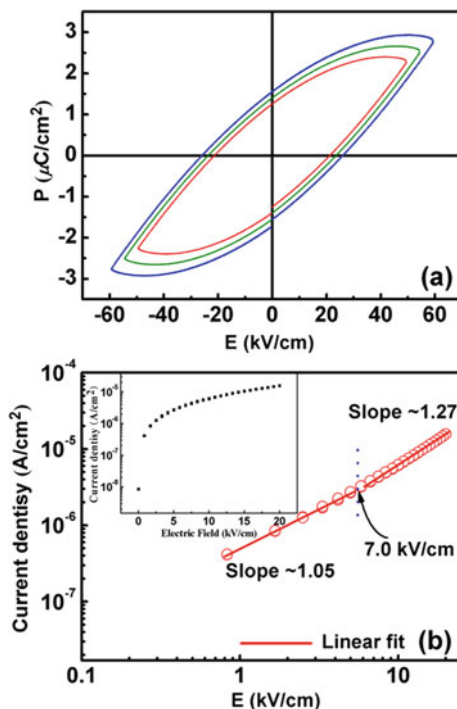
at 300 K. Meanwhile, the coercivity is reduced to  $\sim 1/3$  of the  $H_c$  value measured at 300 K. A similar decrease in coercivity also takes place in a rare-earth doped bismuth ferrite,  $\text{Bi}_{0.9-x}\text{La}_{0.1}\text{Pr}_x\text{FeO}_3$ , and this has been interpreted as the change in magnetic anisotropy at low temperatures [4].

From the inset of Fig. 3b, one may clearly notice a shift of the  $M$ – $H$  loop indicating the occurrence of the exchange bias. In general, the presence of exchange bias implies the existence of strong exchange interaction between FM and AFM interfaces [20]. In this case, the Fe–O octahedral FM clusters embedded randomly in AFM matrix result in the exchange interaction at FM shells and AFM cores interfaces, eventually leading to the exchange bias effect observed here.

Fig. 4a shows the  $P$ – $E$  loops of the sample, measured at different applied electric fields, giving a typical FE nature of the BLTF. The remnant polarization ( $2P_r$ ) value obtained from the  $P$ – $E$  loop is about  $3.11 \mu\text{C}/\text{cm}$  at  $60 \text{ kV}/\text{cm}$  and the corresponding coercive field is  $25.95 \text{ kV}/\text{cm}$ . Although the FE remnant polarization is not very high, the loops with partial saturation represent the presence of ferroelectricity in the ceramics. Very similar curve shape has been reported in other multiferroics, such as  $\text{Bi}_{1-x}\text{Gd}_x\text{FeO}_3$  [5] and  $(\text{PLZT})_{0.3}(\text{BiFeO}_3)_{0.7}$  [21]. It is known that the oxygen vacancies combined with micropores (see Fig. 2a) would lead to relatively high conductivity. Meanwhile, oxygen-ion vacancies and possible lattice defects in BLTF could prevent the FE domain switching, leading to a lower value of  $P_r$ . To get insight into the conduction mechanism in BLTF,  $J$ – $E$  curve was measured. In Fig. 4b, we plot the  $\log(J)$ – $\log(E)$  curve. The curve slope  $\alpha$  which are obtained by fitting the  $\log(J)$ – $\log(E)$  data in region I and region II have the values of  $\sim 1.05$  and  $\sim 1.27$ ,



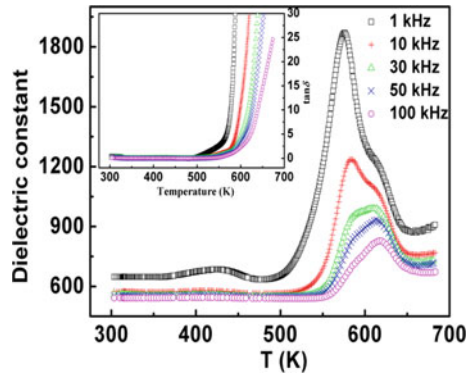
**Fig. 4.** **a** P–E loops of BLTF ceramics. **b**  $\log(J)$ – $\log(E)$  curve of BLTF. Inset shows the  $\log(J)$ – $E$  curve



respectively. Therefore, the dominant transport mechanism in BLTF is Ohmic. The  $\log(J)$ – $E$  curve (inset of Fig. 4b), demonstrates a nonlinear increase with increasing applied field and the conductivity calculated from the  $\log(J)$ – $E$  curve is  $\sim 7.8 \times 10^{-10} / \Omega\text{-cm}$  at 20 kV/cm, which confirms well with the unsaturated FE hysteresis loops.

Figure 5 shows FE behavior of BLTF ceramics with temperature at selected frequencies. The dielectric constant appears to be stable below 370 K and then increases slowly to high value with a hump around 425 K. This hump is attributed to the change of conductive model. Surprisingly, two dielectric anomalies, which have broad peaks, are observed in the present ceramics at 500–590 K and 600–650 K. The disorder in the distribution of  $\text{La}^{3+}$  and  $\text{Bi}^{3+}$  in the  $[\text{Bi}_2\text{O}_2]^{2+}$  layers may lead to the broad peaks. A dielectric peak at 500–590 K is observed and it disappears at high frequencies. This dielectric relaxation should be related to the point defects such as  $\text{Vo}^{**}$  and electron hopping between  $\text{Fe}^{3+}$  and  $\text{Fe}^{2+}$ , which are commonly formed during sintering in air. In the 600–650 K, the dielectric transition temperature shifts toward higher temperature with further increasing  $f$  which signifies the relaxor behavior. This dielectric anomaly may be assumed to be related to FE to paraelectric phase transition. Similar results are also found for Aurivillius phases such as La-doped  $\text{SrBi}_2\text{Nb}_2\text{O}_9$  [22] and  $\text{Bi}_4\text{Ti}_3\text{O}_{12}$  [23] and can be explained by the macroscopic disorder induced by  $\text{La}^{3+}$  cations. Additionally, it is observed from the inset of Fig. 5 that the  $\tan\delta$  values increase rapidly above 550 K. This behavior can be attributed to the thermally activated transport and some defects.

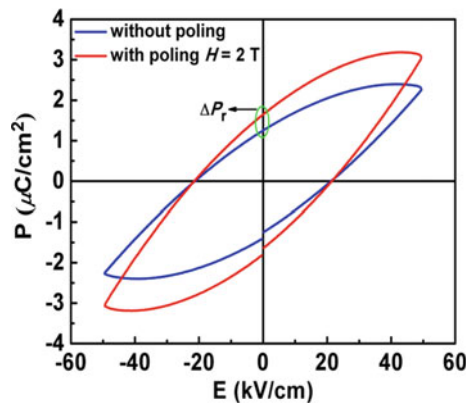
**Fig. 5.** Temperature dependences of the dielectric constant. Inset shows the dielectric loss of BLTF



To investigate possible magnetoelectric coupling in BLTF compound, the coupling effect between magnetization and polarization at room temperature is shown in Fig. 6, obtained by measuring the magnetic field dependence of electrical polarization. By poling the sample at 2 T for 1 h, the FE hysteresis loop becomes more typical and shows a marked enhancement in the remnant polarization (denoted as  $\Delta P_r$ ). Comparing to the as-sintered sample, the coercive field remains practically unchanged, whereas the remnant polarization is improved by approximately 33%. The magnetic field effect at present can be regarded as a novel magnetoelectric effect, where the significant change in  $P$  ( $\Delta P_r \approx 0.41 \mu\text{C cm}^{-2}$ ) is caused by the spin reorientation-induced switching of the FE polarization through the ferroelastic domains to affect the interaction between FE orderings, demonstrating the multiferroic magnetoelectric nature of the sample. Therefore, magnetoelectric interaction exists in multiferroic BLTF bulk.

Recent magnetodielectric (MD) investigation, which has been reported for a wide range of materials [24], on multiferroics reveals the importance of magnetoelectric coupling in this ceramics. The induced modulation of the dielectric constant of a material by applying an external magnetic field is described by the MD coefficient and

**Fig. 6.** P–E loops of BLTF ceramics without poling (blue) and after poling (red) at  $H = 2$  T DC magnetic field



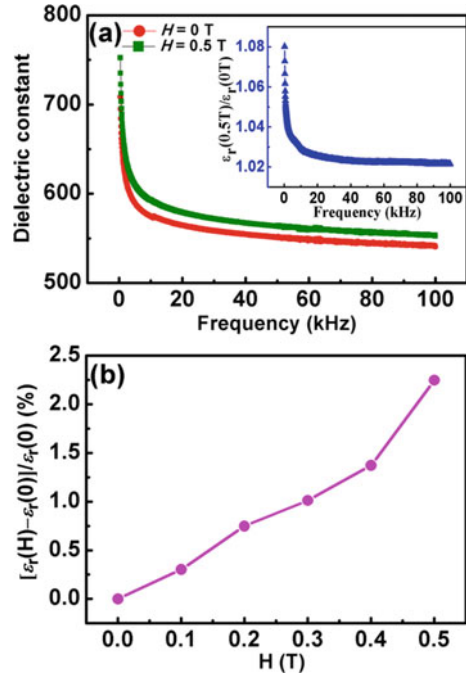
defined as  $MD = [\varepsilon_r(H) - \varepsilon_r(0)] / \varepsilon_r(0)$ , where  $\varepsilon_r(0)$  and  $\varepsilon_r(H)$  are dielectric constants measured under zero and nonzero magnetic fields, respectively. Figure 7a shows the dielectric constant as a function of frequency measured at 0 and 0.5 T at room temperature. The dielectric constant decreases as frequency increases and gradually tends to reach a saturation value at selected magnetic fields since polarization of ferroelectromagnet relaxation is mainly decided by dipole orient polarization wherein at low frequency the dipoles are able to follow the frequency of the applied field. In addition, another notable feature is the frequency dependence of the dielectric constant ratio between 0 and 0.5 T defined as  $\varepsilon_r(0.5 \text{ T}) / \varepsilon_r(0 \text{ T})$ , as clarified in the inset of Fig. 7a. Upon increasing from 100 Hz up to 100 kHz,  $\varepsilon_r(0.5 \text{ T}) / \varepsilon_r(0 \text{ T})$  value decreases and then becomes nearly constant ( $\sim 1.02$ ) above 20 kHz, corresponding to the conductivity cut-off of the charge carrier to an external electric field predicted by Catalan et al. [25, 26]. The maximum value of the dielectric constant ratio as defined by  $[\varepsilon_r(0.5 \text{ T}) / \varepsilon_r(0 \text{ T})]_{\max}$  reaches values as large as  $\sim 1.08$  near 100 Hz. For deeper insight into the magnetoelectric properties of the sample, the variation of dielectric constant at 50 kHz with the applied magnetic field was carried out (Fig. 7b). With increasing field, both dielectric constant and MD value increase, reflecting strong magnetic field dependence of dielectric constant, which may be responsible for the complicated spin structure arising from the addition of various ions (*i.e.*,  $\text{La}^{3+}$ ,  $\text{Bi}^{3+}$ , and  $\text{Fe}^{3+}$  doping into  $\text{Bi}_4\text{Ti}_3\text{O}_{12}$  at Bi/Ti sites) since BLTF can be regarded as a solid solution of  $\text{Bi}_4\text{Ti}_3\text{O}_{12}$ - $\text{BiFeO}_3$ - $\text{LaFeO}_3$ . When  $\Delta H = 0.2$  and 0.5 T at room temperature, the values of MD effect are 0.78% and 2.25%, respectively. Similar behaviors were also observed in Pb-substituted  $\text{BiFeO}_3$  [27] and we obtained larger values of MD than for Pb-substituted  $\text{BiFeO}_3$  ceramics. The measuring applied field dependent MD behaviors (*i.e.*, the change in dielectric constant with applied magnetic field) suggest that magnetoelectric coupling between electrical polarization and spin does indeed exist in this compound. Therefore, our results also suggest that the substitution of rare-earth ions for  $\text{Bi}^{3+}$  in  $\text{Bi}_9\text{Ti}_3\text{Fe}_5\text{O}_{27}$  ceramics implies a path to new magnetoelectric applications at low magnetic field.

Taking account of results of a former magnetization-induced enhanced electric polarization study, the MD behavior can be explained as follows. In multiferroics, the dielectric constant of a material is directly related to the electric polarization. Application of an external magnetic field to the sample, it will be strained: this in turn, induces stress which subsequently generates an electric field on the FE domains. Owing to the reorientation of FE domains, the polarization will enhance, what would lead to a change in dielectric constant.

## 4 Conclusions

In summary, phase pure BLTF sample have been successfully synthesized using a sol-gel method. It was found that BLTF ceramics exhibit a combining of ferromagnetic and ferroelectric behaviors as confirmed by the appearance of magnetic and electric polarization loops. The conduction mechanism in BLTF was found to be

**Fig. 7** **a** Frequency dependence of the dielectric constant of BLTF ceramics measured at  $H = 0$  and 0.5 T. Inset shows the frequency dependence of dielectric constant ratio  $\epsilon_r(0.5\text{ T})/\epsilon_r(0\text{ T})$ . **b** Magnetic field dependence of magnetodielectric effect at room temperature



dominantly Ohmic. The nature of relaxor behavior of the sample is related to the macroscopic disorder, resulting from  $\text{La}^{3+}$  doping on the A-site. Moreover, the change in dielectric constant and  $P$ - $E$  loops upon the application of magnetic fields suggests the existence of magnetoelectric coupling effect in this material. Considering that the multiferroic and magnetoelectric behaviors, the studied material demonstrates its potential applications in magnetic field controllable devices or magnetoelectric transducers.

**Acknowledgements** This research was partially funded by the Major Basic Scientific Research Project under grant 2019207029.

## References

1. Fiebig M, Lottermoser T, Fröhlich D, Goltsev AV, Pisarev RV (2002) Observation of coupled magnetic and electric domains. *Nature* 419:818–820
2. Rao C, Serrao CR (2007) New routes to multiferroics. *J Mater Chem* 17(47):4931–4938
3. Smolenskii GA, Chupis I (1982) Ferroelectromagnets. *Soviet Physics Uspekhi* 25:1475–1493
4. Lu YS, Dai JQ (2022) Enhanced electrical properties of (Zn, Mn)-modified  $\text{BiFeO}_3$ - $\text{BaTiO}_3$  lead-free ceramics prepared via sol-gel method and two-step sintering. *J Alloy Compd* 899:163387–163387

5. Li K, Zhang W, Guo K et al (2022) Modulating light absorption and multiferroic properties of BiFeO<sub>3</sub>-based ferroelectric films by the introduction of ZnO layer. *Mater Res Exp* (2022)
6. Koo BH (2022) Effect of Mn concentration on the structural, ferroelectric, optical, and magnetic properties of BiFeO<sub>3</sub> nanoparticles. *Crystals* 12
7. Ma ZZ, Li JQ, Chen ZP et al (2014) Multiferroic properties and exchange bias in Bi<sub>1-x</sub>Sr<sub>x</sub>FeO<sub>3</sub> (x=0–0.6) ceramics. *Chinese Phys B* 23(9):097505–097510
8. Tuboltsev V, Savin A, Sakamoto W et al (2012) Nanomagnetism in nanocrystalline multiferroic bismuth ferrite lead titanate film. *J Nanopart Res* 13(11):5603–5613
9. Pikula TB et al (2016) Composition-driven structural and magnetic transitions in mechanically activated(1-x)BiFeO<sub>3</sub>-(x)BaTiO<sub>3</sub> solid solutions. *Solid State Commun* 47:246
10. Hill NA, Rabe KM (1999) First-principles investigation of ferromagnetism and ferroelectricity in bismuth manganite. *Phys Rev B* 59(13):8759–8769
11. Ramana EV, Suryanarayana SV, BSankaram TB (2006) Ac impedance studies on ferroelectromagnetic SrBi<sub>5-x</sub>La<sub>x</sub>Ti<sub>4</sub>FeO<sub>18</sub> ceramic. *Mater Res Bull* 41(6):1077–1088
12. Zuo XZ, Yang J, Yuan B, et al (2015) Enhanced multiferroic properties of Aurivillius Bi<sub>6</sub>Fe<sub>1.4</sub>Co<sub>0.6</sub>Ti<sub>3</sub>O<sub>18</sub> thin films by magnetic field annealing. *Appl Phys Lett* 107(22):759
13. Jartych E et al (2010) Hyperfine interactions in some aurivillius Bi<sub>m+1</sub>Ti<sub>3</sub>Fe<sub>m3</sub>O<sub>3m+3</sub> compounds. *J Magn Magn Mater* 322(1):51–55
14. Patri SK, Choudhary RNP, Samantaray B (2008) Studies of structural, dielectric and impedance properties of Bi<sub>9</sub>Fe<sub>5</sub>Ti<sub>3</sub>O<sub>27</sub> ceramics. *J Electroceram* 20(2):119–126
15. Kojima T, Watanabe T, Funakubo H et al (2003) Ferroelectric properties of lanthanide-substituted Bi<sub>4</sub>Ti<sub>3</sub>O<sub>12</sub> epitaxial thin films grown by metalorganic chemical vapor deposition. *J Appl Phys* 93(3):1707–1712
16. Lin PT, Li X, Li Z et al (2014) La-doped BiFeO<sub>3</sub>: synthesis and multiferroic property study. *Chin Phys B* 4:6
17. Wu MS, Huang ZB, Han CX et al (2012) Enhanced multiferroic properties of BiFeO<sub>3</sub> ceramics by Ba and high-valence Nb co-doping. *Solid State Commun* 152(24):2142–2146
18. Singh RS, Bhimasankaram T, Kumar GS et al (1994) Dielectric and magnetoelectric properties of Bi<sub>5</sub>FeTi<sub>3</sub>O<sub>15</sub>. *Solid State Commun* 91(7):567–569
19. Horn JA, Zhang SC, Selvaraj U et al (1999) Fabrication of textured Bi<sub>4</sub>Ti<sub>3</sub>O<sub>12</sub> by templated grain growth. *J Am Ceram Soc* 82:921–926
20. Punnoose A, Morales EH, Lederman D et al (2003) X and Q-band ferromagnetic resonance studies of exchange biased Co/MnPt bilayers. *J Appl Phys* 93:771
21. Kanai T, Ohkoshi S, Nakajima A et al (2001) A ferroelectric ferromagnet composed of (PLZT)<sub>x</sub>(BiFeO<sub>3</sub>)<sub>1-x</sub> solid solution. *Adv Mater* 13(7):485–487
22. Chen XB, Hui R, Zhu J et al (2004) Relaxor properties of lanthanum-doped bismuth layer-structured ferroelectrics. *J Appl Phys* 96(10):5697–5700
23. SHuang S, Sun L, Feng C et al (2006) Relaxor behavior of layer structured SrBi<sub>(1.65)</sub>La<sub>(0.35)</sub>Nb<sub>2</sub>O<sub>9</sub>. *J Appl Phys* 99(7):076104.1–076104.3
24. Freitas RS, Mitchell JF, Schiffer P (2005) Magnetodielectric consequences of phase separation in the colossal magnetoresistance manganite Pr<sub>0.7</sub>Ca<sub>0.3</sub>MnO<sub>3</sub>. *Phys Rev B* 72:144429
25. Catalan G (2006) Magnetocapacitance without magnetoelectric coupling. *Appl Phys Lett* 88:102902–112902
26. Catalan G, Scott JF (2007) Magnetoelectrics: Is CdCr<sub>2</sub>S<sub>4</sub> a multiferroic relaxor? *Nature* 448(7156):E4–5
27. Zhang XQ, Sui Y, Wang XJ, Tang JK et al (2009) Influence of diamagnetic Pb doping on the crystal structure and multiferroic properties of the BiFeO<sub>3</sub> perovskite. *J Appl Phys* 105(7):07D918–07D921

# Electric Field Optimization of Optical Fiber Insulator Based on Random Focus Search Algorithm



Yanjie Cui, Wenhao Lu, Qian Chen, Yang Feng, Liang Liu, Shengtao Li, Wei Xiao, and Senlin Zhao

**Abstract** Optical fiber is widely used in power systems, and partial discharge of optical fiber occasionally occurs during normal operation, resulting in signal transmission interruption and insulation performance degradation. In this paper, the electric field simulation analysis is carried out for the structure of the end flange of the optical fiber insulator, indicates that the electrical strength inside the flange reaches 0.48 kV/mm, higher than the average electrical field strength of 0.15 kV/mm. The electric field distribution in the flange of materials with different resistivity and size is studied, and the electric field strength of the interface between the materials inside the flange is taken as the optimization goal. By using Random Focus Search Algorithm, electrical field strength is reduced to 0.12 kV/mm, and the optimal resistivity material parameters and flange size structure of the optical fiber insulator are obtained.

**Keywords** Finite element method · DC electric field · Optical fiber insulator · Random focus search algorithm

---

Y. Cui (✉) · W. Lu · Q. Chen  
Electric Power Research Institute, CSG EHV Power Transmission Company, Guangzhou 510663, Guangdong, China  
e-mail: [542824948@qq.com](mailto:542824948@qq.com)

Y. Feng · S. Li  
State Key Laboratory of Electrical Insulation and Power Equipment, Xi'an Jiaotong University, Xi'an 710049, Shaanxi, China  
e-mail: [fengyang@xjtu.edu.cn](mailto:fengyang@xjtu.edu.cn)

L. Liu  
NR Electric Power Electronics Co.Ltd, Changzhou 213100, Jiangsu, China  
e-mail: [liuliang@mail.iv.nari.cn](mailto:liuliang@mail.iv.nari.cn)

W. Xiao  
Electric Power Research Institute, CSG, Guangzhou 510663, Guangdong, China  
e-mail: [xiaowei@mail.iv.csg.cn](mailto:xiaowei@mail.iv.csg.cn)

S. Zhao  
Nanjing Nari-Relays Electric Co, Ltd, Nanjing 211122, Jiangsu, China  
e-mail: [zhaosenlin@mail.iv.nari.cn](mailto:zhaosenlin@mail.iv.nari.cn)

## 1 Introduction

Due to its excellent transmission characteristics and capacity, optical fiber is widely used in power systems for signal transmission and measurement and sensing [1, 2]. However, partial discharge of optical fiber occasionally occurs during normal operation, resulting in signal transmission interruption and insulation performance degradation [3–5]. Partial discharge in optical fiber is mainly caused by that the resistivity of the multilayer insulation material inside the optical fiber is not matched. Leading to electrical field distortion under DC voltage, eventually causing breakdown [6–8]. Therefore, the selection of appropriate insulation material parameters and size structure is very important for the normal operation of optical fiber [9]. In this paper, the electric field simulation analysis is carried out for the structure of the end flange of the optical fiber insulator which partial discharge, the electric field distribution in the flange of materials with different resistivity and size is studied, and the electric field strength of the interface between the materials inside the flange is taken as the optimization goal, and the optimal resistivity material parameters and flange size structure of the optical fiber insulator are obtained by random focus search algorithm.

## 2 Methodology

### 2.1 Simulation Model of Optical Fiber Insulator

A 3D simulation model of optical fiber insulator is utilized to study the effect of material characteristics on the electric field distribution, as shown in Fig. 1. Flanges are assembled at the ends on both sides of the epoxy hollow insulator and is equipped with an external equalizing ring. Hollow insulator is filled with an insulating grease, through which the optical fiber passes (see Fig. 2). Optical fiber consists of sheath layer and fiber core. Materials and electrical parameters are shown in Table 1.

**Fig. 1.** 3D simulation model of the optical fiber insulator



**Fig. 2** Optical fiber inside the flange



**Table 1** Structures and electrical parameters of insulation materials

Structure	Material	Conductivity (S/m)
Shed	Silicone rubber	$3.57 \times 10^{-14}$
Epoxy tube	Epoxy resin	$1.30 \times 10^{-13}$
Insulating grease	Multicomponent mixture	$1.00 \times 10^{-13}$
Optical fiber sheath	TPU	$1.33 \times 10^{-10}$
Optical fiber core	Silica glass	$1.00 \times 10^{-14}$

## 2.2 Fundamental Physics Equations

Optical fiber insulator operates under DC voltage, according to the constant current field calculation principle, Maxwell’s equations can be simplified as follows,

$$\begin{cases} \nabla \cdot \mathbf{J} = Q \\ \mathbf{E} = -\nabla V \end{cases} \tag{1}$$

where  $\mathbf{J}$  is current density,  $Q$  is electric charge,  $\mathbf{E}$  is electric field strength,  $V$  is potential.

For isotropic media, the constitutive relations are as follows,

$$\mathbf{J} = \sigma \mathbf{E} \tag{2}$$

where  $\sigma$  is conductivity of insulation material.

These quantities must obey the principles followed with boundary conditions. The boundary of the simulation domain is electrically insulating, which can be expressed as follows,

$$\begin{cases} \mathbf{n} \cdot \mathbf{J} = 0 \\ V_{boundary} = 0 \end{cases} \tag{3}$$



where  $n$  is normal vector.

Considering the operating conditions of optical fiber insulator, flanges at the high-voltage terminal  $V_H$  and at the low-voltage terminal  $V_L$  are set to 400 kV and 0 kV, respectively.

$$\begin{cases} V_H = 400 \text{ kV} \\ V_L = 0 \end{cases} \quad (4)$$

Simulation model is meshed into free tetrahedrals for 3D finite element calculation based on the above equations and boundary conditions. The electric field distribution is calculated by solving the partial differential equation for the 3-D domain.

### 3 Results and Analysis

#### 3.1 Electric Field Distribution of Optical Fiber Insulator

Electric field distribution of optical fiber insulator is shown in Fig. 3. There are a variety of insulating materials inside the insulator, and the maximum field strength appears in the insulating grease between the optical fiber and the epoxy resin inside the flange, and the maximum field strength is 0.48 kV/mm.

Since resistivity of sheath layer on the surface of the optical fiber is low, and its surface potential decays quickly, while the potential of the epoxy inner wall of the hollow insulator drops slowly, resulting in a large potential difference appears inside the flange, as shown in Fig. 4.

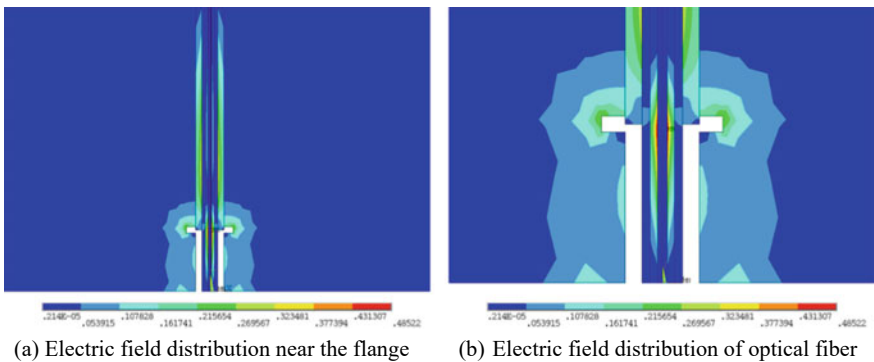
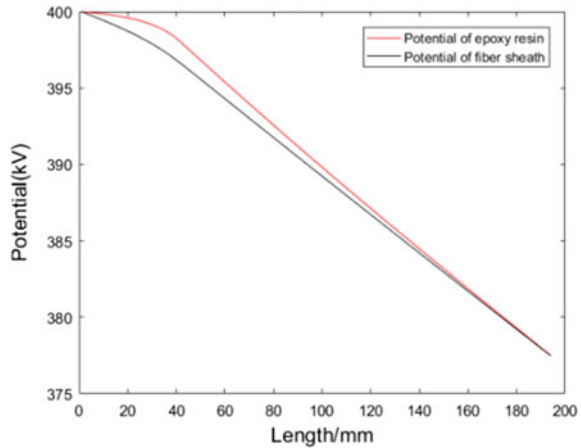


Fig. 3 Electric field simulation results near the flange

**Fig. 4** Potential distribution along interface



### 3.2 Influencing Factors of Electric Field Strength

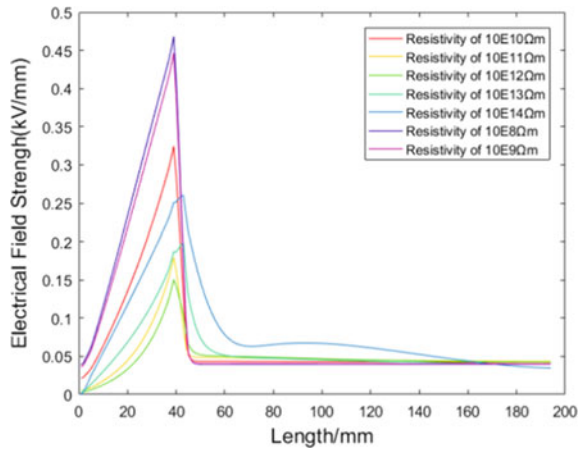
Simulation result shows that the electric field distribution under DC voltage depends on the resistance of material layers. If there is an interface from high resistance to low resistance inside the insulating material, the potential distribution on both sides will be quite different. Higher electric field strengths may occur inside highly resistive material layer. Therefore, when designing DC power equipment, all parameters that may affect the insulation resistance should be considered. In this paper, the parameters that mainly affect the insulation resistance include resistivity and layer thickness are analyzed.

Figure 5 shows the variation of the maximum electric field inside the insulator with the resistivity of insulating grease. Simulation results show that when the resistivity of insulating grease reaches  $10^8 \Omega\text{m}$ , the maximum electric field strength is  $0.48 \text{ kV/mm}$ , which is the highest. As the resistivity of the insulating paste increases, the electric field strength on the surface of optical fiber sheath will also begin to decrease. When the resistivity increases to  $10^{13} \Omega\text{m}$ , the electric field distribution becomes more uniform, and the maximum electric field strength drops to  $0.15 \text{ kV/mm}$ , close to the average electric field strength of  $0.05 \text{ kV/mm}$ .

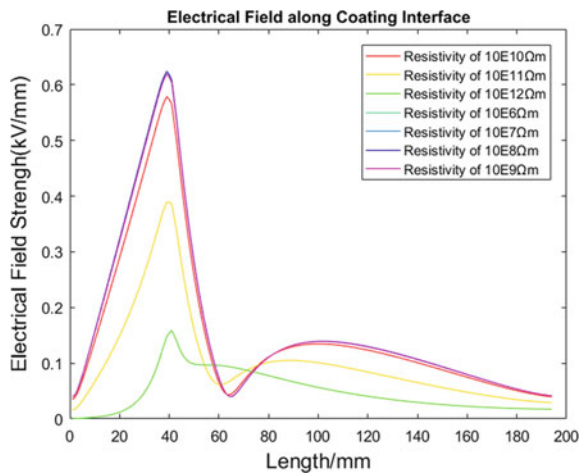
Figure 6 shows the variation of the maximum electric field strength inside the insulator with the resistivity of the fiber sheath. Simulation results show that when the resistivity of the fiber sheath is lower than  $10^9 \Omega\text{m}$ , the maximum electric field strength is higher than  $0.5 \text{ kV/mm}$ . As the resistivity of the optical fiber sheath increases, the electric field strength on the surface of optical fiber sheath decrease. When the resistivity increases to  $10^{12} \Omega\text{m}$ , which is close to that of the filling paste, the electric field distribution becomes more uniform, and the maximum electric field strength drops to  $0.15 \text{ kV/mm}$ , much lower than that of the low-resistivity case.

Figure 7 shows the variation of the maximum electric field strength inside the insulator with the thickness of the optical fiber sheath. Simulation result shows that

**Fig. 5** Influence of length of insulation grease resistivity on electric field distribution



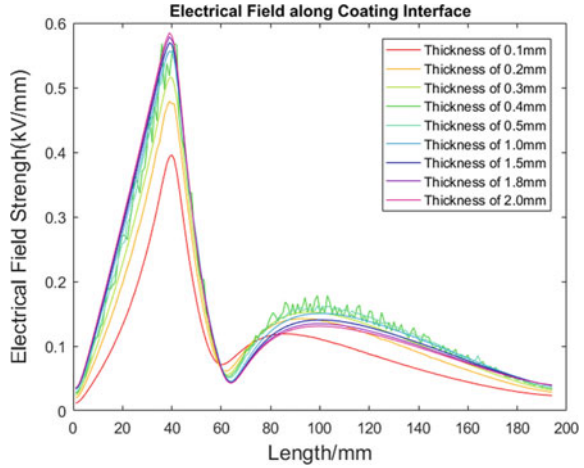
**Fig. 6** Influence of length of sheath resistivity on electric field distribution



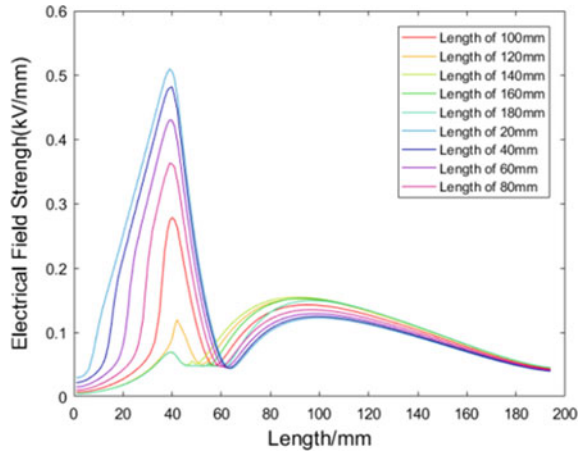
when the thickness of the fiber sheath is higher than 0.3 mm, the maximum electric field strength is higher than 0.5 kV/mm. As thickness of optical fiber sheath decreases, the electric field strength on the surface of the sheath decrease, mainly due to the decrease of insulation resistance value of fiber sheath. When the sheath thickness is reduced to 0.1 mm, the maximum electric field strength drops to 0.38 kV/mm.

During the manufacture, since the hollow insulator is very long, the volume of insulating grease will change continuously under the temperature cycling, so an air column is generally reserved at the end of the hollow insulator. Figure 8 shows the effect of the air column length on the electric field distribution. When the air column length is 20 mm, the maximum electric field strength is higher than 0.5 kV/mm. As the length of the air column further increases, the electric field strength on the surface

**Fig. 7** Influence of length of sheath thickness on electric field distribution



**Fig. 8** Influence of length of air column on electric field distribution

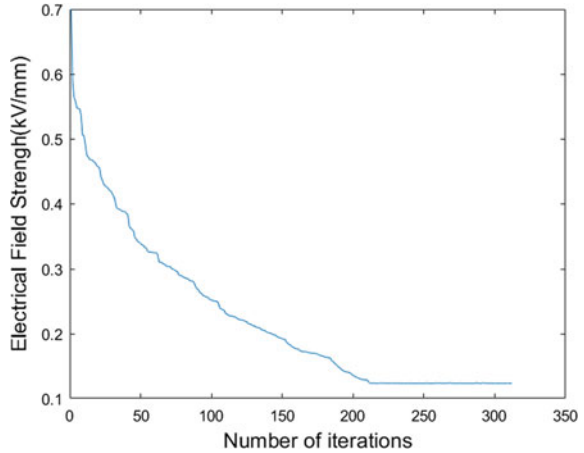


of the sheath will also decrease. When the air column length is greater than 120 mm, the maximum electric field strength will drop below 0.1 kV/mm.

### 3.3 Random Focus Search Algorithm

The Stochastic Focusing Search (SFS) algorithm imitates human search behavior and its randomness in the search process, selects appropriate neighborhood space parameters, and can efficiently search for the global optimal value while avoiding convergence to the local optimal value [10]. In this paper, the maximum electric field strength is set as the optimization goal, the influence factor of resistivity, thickness,

**Fig. 9** Convergence curve of random focus search algorithm



and air column length are studied by fitting the simulation results, and the optimal result of the minimum electric field strength of 0.12 kV/mm is obtained, as shown in Fig. 9.

## 4 Conclusion

In this paper, the electric field simulation research on the optical fiber insulator is carried out, and the electric field distribution law at the flange is obtained under different resistivity, sheath thickness, and cavity length. The electric field strength is reduced from 0.46 to 0.12 kV/mm. Results are as follows:

- (1) The electric field distribution of power equipment under DC is determined by the resistance. The potential distribution of low-resistivity materials is determined by itself, which may be quite different from the potential distribution of adjacent high-resistivity materials, causing field strength distortion inside the high-resistivity medium, resulting in discharge.
- (2) The resistivity and structural size parameters of insulating materials may affect the insulation resistance. By optimizing the insulation resistance value of materials, the internal field strength of power equipment under DC can be effectively reduced and the risk of abnormal discharge can be reduced.

**Acknowledgements** This work was supported by CSG EHV Power Transmission Company (CGYKJXM20210330). It was also supported by State Key Laboratory of Electrical Insulation and Power Equipment, Xi'an Jiaotong University.

## References

1. Liu H, Li S (2016) Application of optical fiber communication technology in power system. *Automat Applicat* 1(4):99–101
2. Guo S, Han L, Xu, L (2016) Review of research progress of optical fiber sensors in partial discharge detection. *Adv Technol Electric Eng Energy* 35(3):47–53
3. Zhu L, Xiao Y, Ni R (2015) Analysis on discharge of optical fiber in valve tower of nanqiao converter station. *Power Energy* 1(2):272–276
4. Xiao Y, Ni R (2015) Analysis on discharge of optical fiber in valve tower of converter station. *Shanghai Electric Power* 1(3):20–23
5. Li S, Jiao S, Zhang J (2023) Research on internal discharge mechanism of fiber optic insulator of DC optical current transformer. *Electric Eng* 1(30):216–220
6. Wang Y, Ding Y, Yuan Z (2021) Space-charge accumulation and its impact on high-voltage power module partial discharge under DC and PWM waves: Testing and modeling. *IEEE Trans Power Electron* 36(10):11097–11108
7. Gu X, He S, Xu Y (2018) Partial discharge detection on 320 kV VSC-HVDC XLPE cable with artificial defects under DC voltage. *IEEE Trans Dielectr Electr Insul* 25(3):939–946
8. Seri P, Cirioni L, Naderiallaf H (2019) Partial discharge inception voltage in DC insulation systems: a comparison with AC voltage supply. In: *IEEE electrical insulation conference (EIC)*. IEEE, pp 176–179
9. Kumara S, Xu X, Hammarström T (2020) Electrical characterization of a new crosslinked copolymer blend for DC cable insulation. *Energies* 13(6):1434–1440
10. Zheng Y, Chen W, Dai C (2009) Stochastic focused search optimization algorithm. *Control Theory Appl* 1(8):915–917

# Research on the Influence of Safety Film on the Thermal Field Distribution of Metallized Film Capacitors



Yanjie Cui, Yong Sun, Wenhao Lu, Cheng Yao, and Chunhong Zhou

**Abstract** Metallized film capacitors are widely applied in power electronics devices due to their large capacitance and high power density, such as support capacitors for flexible DC converter valves. In this paper, thermal resistance of the T-shaped safety film and the diamond-shaped safety film are simulated and calculated, and the power density of the film is calculated according to the equivalent resistance. The overall temperature rise of the capacitor is simulated and analyzed. Simulation results show that the ordinary metallized film has the lowest thermal resistance; the thermal resistance and equivalent resistance of the safety film mainly depend on the effective cross-sectional area of fuse. When the effective cross-sectional area is increased, the thermal resistance will become smaller, improving the heat dissipation capacity of the capacitor. The temperature rise of T-type safety film capacitors is the most serious, which is 15 K higher than that of ordinary metallized films.

**Keywords** Metalized capacitor · Safety metalized film · Temperature rise

## 1 Introduction

Metallized film capacitors are widely applied in power electronics devices due to their large capacitance and high power density, such as support capacitors for flexible DC converter valves. During normal operation, the metallized film capacitor will generate heat due to the polarization of the medium and the resistance of the metal plates, and

---

Y. Cui (✉) · Y. Sun · W. Lu

Electric Power Research Institute, CSG EHV Power Transmission Company, Guangzhou 510663, Guangdong, China

e-mail: [542824948@qq.com](mailto:542824948@qq.com)

C. Yao

Electric Power Research Institute, CSG, Guangzhou 510663, Guangdong, China

e-mail: [yaocheng@iv.em.csg](mailto:yaocheng@iv.em.csg)

C. Zhou

Guilin Electrical Capacitor Co., Ltd, Guilin 541000, Guangxi, China

© Beijing Paiké Culture Commu. Co., Ltd. 2024

X. Dong and L. Cai (eds.), *The Proceedings of 2023 4th International Symposium on Insulation and Discharge Computation for Power Equipment (IDCOMPU2023)*, Lecture Notes in Electrical Engineering 1103, [https://doi.org/10.1007/978-981-99-7413-9\\_42](https://doi.org/10.1007/978-981-99-7413-9_42)

the temperature of the hot spot is related to heat dissipation capacity of the capacitor. Different from general metallized film capacitors, the electrode shape of safety film capacitors is generally T-shaped or diamond-shaped, and the plate resistance as well as thermal conductivity are different, and the maximum temperature rise is also more serious.

Studies have been done on the thermal field simulation of metallized film capacitors, but there are few studies on capacitors using safety films. Li Haoyuan analyzed the heat generation of metallized film capacitor plates theoretically, and gave the calculation formula of heat generation power of plates with different thicknesses [1]. Yin Ting has conducted simulation and experimental research on the thermal field distribution of metallized film capacitors, and believes that the film width and thickness have a great influence on the thermal field distribution [2]. Chen Hongxiao conducted a thermal simulation on the capacitor discharge process, and believed that the hottest point generally appears in the middle of the capacitor, which is proportional to the charge and discharge frequency [3]. Yue Guohua conducted an electrothermal coupling simulation on the capacitor. The system considered the influence of the capacitor, lead wire and bushing, etc., and optimized the internal layout of the capacitor [4]. In terms of safety film research, Yin Ting calculated the equivalent series resistance of safety films of different shapes and gave the calculation formula [5]. Xu Menglei calculated the thermal field distribution of capacitors using T-shaped safety film, and the results show that the temperature rise of safety film capacitors is higher than that of general metallized film capacitors [6].

In this paper, thermal resistance of the T-shaped safety film and the diamond-shaped safety film are simulated and calculated, and the power density of the film is calculated according to the equivalent resistance. The overall temperature rise of the capacitor is simulated and analyzed. Simulation results show that the ordinary metallized film has the lowest thermal resistance; the thermal resistance and equivalent resistance of the safety film mainly depend on the effective cross-sectional area of fuse. When the effective cross-sectional area is increased, the thermal resistance will become smaller, improving the heat dissipation capacity of the capacitor. The temperature rise of T-type safety film capacitors is the most serious, which is 15 K higher than that of ordinary metallized films.

## 2 Safety Metallized Film

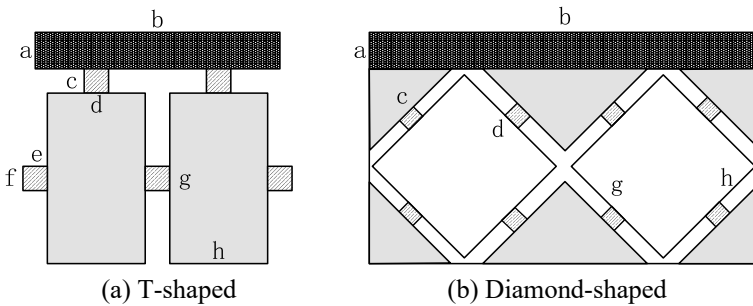
Metallized film is generally referred to a nano-scale thickness of zinc-aluminum alloy deposited on the surface of the organic film by vacuum evaporation technology, which has excellent properties of self-healing and large capacitance. However, when the self-healing energy is too large, the healing may fail, causing malfunction. Safety metallized film is manufactured by dividing the plate into multiple regular areas, using insulating gaps to separate the active layer of the plate from the thickened layer, and dividing the metallized plate into many squares with equal width film block by using multiple insulating gaps. Each plate is connected to each other by



a fuse composed of thin metal plates. When the self-healing energy is too large, a large current flows through the fuse and evaporates completely, preventing the self-healing failure process. The schematic diagram of the structure of the T-shaped and diamond-shaped metallized safety film is shown in Fig. 1.

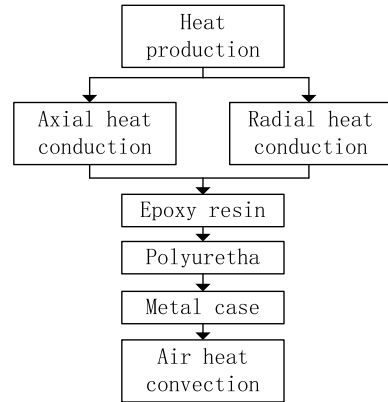
It can be seen from Fig. 1 that the safety film is composite of thickened layer, fuse, and active plates from the outside to the inside. The thickened layer is mainly used to reduce the field strength distortion at the end, and its width is  $a$  and its length is  $b$ . The width  $c$  of the fuse determines its operating current, and the length  $d$  determines its surface insulation level. Dimension  $g$  and  $h$  of the film block of the active layer determine the minimum capacitance loss after the fuse operates, and at the same time affect the equivalent thermal resistance of the metallized film. Therefore, the size of the fuse and the module determine the heat generation of the metallization film and capacitor.

Metallized film capacitors are generally composed of multiple elements. The element is manufactured by winding a multi-layer metallized film around an insulating mandrel, and the electrodes are drawn out by spraying gold at the end of the element. The gold spraying layers on the left and right sides are respectively connected to two metal electrodes. A plurality of capacitor elements is connected to the copper bar through welding leads, and are connected in series or parallel to form a capacitor core. Polyurethane is generally poured between the core and the capacitor shell under vacuum, so as to realize the insulation of the capacitor from the shell and assemble into a complete capacitor.



**Fig. 1** Schematic diagram of safety film structure

**Fig. 2** Heat dissipation process of metallized film capacitor



### 3 Analysis of Thermal Characteristics of Safety Metallized Film Capacitor

#### 3.1 Generation and Conduction of Heat Inside the Capacitor

The internal heat generation of the capacitor is mainly due to the dielectric loss of the insulating material under AC voltage and the Joule heating effect of the metal plate under DC voltage [7–9]. The heat dissipation process is shown in Fig. 2. After the capacitor element generates heat, it conducts axially and radially to the epoxy resin of the element casing. The polyurethane is covered with epoxy resin, and the heat is conducted to the metal shell through the polyurethane, and the heat exchange between the metal shell and the air belongs to air convection heat exchange. According to the heat dissipation process inside the capacitor, the structure of the safety film mainly affects the axial and radial heat conduction efficiency. Since the surface of the capacitor film is coated with a metal layer, the difference between the axial and radial thermal conductivity is relatively large. The metal coating thickness of the safety film is generally 20 nm, and the film thickness is generally 8  $\mu\text{m}$ , which has a large difference. Therefore, different film structures have little influence on the radial heat conduction efficiency, but have a greater influence on the axial heat conduction efficiency.

#### 3.2 Simulation Analysis of Equivalent Thermal Resistance of Safety Metallized Film

Thermal conductivity of the main materials of the safety metallized film capacitor is shown in Table 1. For a general metallized film, the thermal resistance of the metal coating and the polypropylene layer can be calculated according to the formula R

$= n/(\lambda S)$ , where  $R$  is the thermal resistance,  $n$  is the thickness of the material,  $\lambda$  is the thermal conductivity, and  $S$  is the material area [10]. The equivalent radial and axial thermal conductivity of the metallized film can be calculated according to the series-parallel thermal resistance of the metal coating and the polypropylene layer, respectively. However, the metal coating on the surface of the safety film is incomplete, so the calculation of its equivalent thermal conductivity needs to be calculated according to the actual heat conduction area.

(1) Equivalent thermal conductivity of T-shaped safety film.

The metal coating pattern of the T-shaped safety film is simple, thermal resistance can be directly calculated according to the coating area. It can be seen from Fig. 1 that when the metallized film conducts heat in the radial direction, its thermal resistance is calculated by:

$$R_1 = n_1 / (\lambda_1 (ab + cd * 2 + ef * 2 + gh * 2)) \tag{1}$$

When the polypropylene film conducts heat in the radial direction, its thermal resistance is calculated by:

$$R_2 = n_2 / (\lambda_2 [b(a + c + g)]) \tag{2}$$

The radial equivalent thermal conductivity of the safety film is calculated by:

$$\lambda = (n_2 + n_1) / [(R_1 + R_2)(b(a + c + g))] \tag{3}$$

Appropriate simplification can be made when calculating the axial equivalent thermal conductivity. It can be seen from the heat conduction law that the heat source is active layer, and heat is conducted from the active layer to the thickened layer. Temperature field distribution of each active layer can be considered as completely consistent, and the fuse between active layers has no effect on heat conduction and can be ignored in calculation. Therefore, when the metallized film conducts heat axially, its thermal resistance is calculated by:

$$R_1 = a / (\lambda_1 n_1 b) + c / (\lambda_1 n_1 d) + g / (\lambda_1 n_1 h) \tag{4}$$

**Table 1** Material property of capacitor

Material	Thermal conductivity/(W/(m·K))
Metal plating	128
Polypropylene film	0.22
Epoxy resin	0.28
Polyuretha	0.56
Metal case	17.5

When the polypropylene film conducts heat axially, its thermal resistance is calculated by:

$$R_2 = (a + c + g) / (\lambda_2 b n_2) \tag{5}$$

The axially equivalent thermal conductivity of the safety film is calculated by:

$$\lambda = (a + c + g) / [(R_1 + R_2)(b(n_2 + n_1))] \tag{6}$$

According to calculation, the radial equivalent thermal conductivity of the T-shaped safety film is 0.2202 W/(m·K), and the axial equivalent thermal conductivity is 0.2431 W/(m·K).

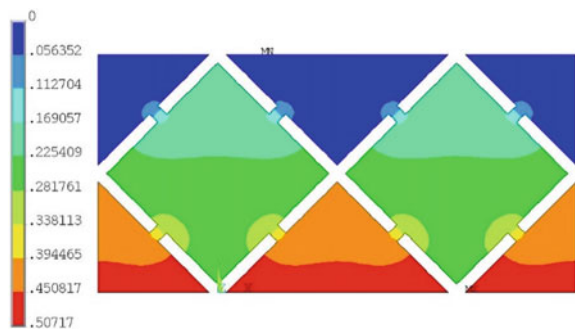
(2) Equivalent thermal conductivity of diamond-shaped safety film.

Calculate method of the radial equivalent thermal conductivity of the diamond-shaped safety film is the same as that of the T-shaped safety film. The thermal resistance is calculated according to the coating area, and the radial equivalent thermal resistance is calculated according to the series thermal resistance. However, when calculating the axial equivalent thermal conductivity, due to the irregular shape of the coating, it cannot be equivalent to a simple rectangle, and the calculation is difficult. In this paper, by establishing a simulation model, the temperature rise under a certain heat source power is obtained, and its equivalent thermal conductivity is obtained. The simulation results are shown in Fig. 3. At this time, the thermal energy density applied on the boundary of the metallized film is 109 W/m, and the temperature rise of the heat source is 0.507 K.

According to the thermal resistance calculation formula  $R = (T_2 - T_1) / P$ , the equivalent thermal resistance at this time is 6.9 MK/W. The formula for calculating the axial thermal resistance of polypropylene film is the same as that of T-type film. The radial equivalent thermal conductivity of the diamond-shaped safety film is 0.2202 W/(m·K), and the axial equivalent thermal conductivity is 0.2691 W/(m·K).

Calculation result shows that the radial equivalent thermal conductivity of safety films with different shapes is 0.2202 W/(m·K), which is basically the same as that of

**Fig. 3** Simulation results of temperature rise of diamond-shaped safety film



polypropylene film, indicating that the thermal conductivity of the safety film in the radial direction is poor. The axial equivalent thermal conductivity of the diamond-shaped safety film is higher than that of the T-shaped safety film, indicating that the arrangement of the fuse has a great influence on the thermal conductivity of the safety film: when the cross-sectional area of the fuse is large, its thermal conductivity also better.

### 3.3 Temperature Rise of Safe Metallized Film Capacitors

According to the equivalent thermal conductivity of different types of safety films, the simulation model of metallized film capacitors was established, and the temperature rise of the core and shell inside the capacitor was analyzed. The simulation results are shown in Fig. 4.

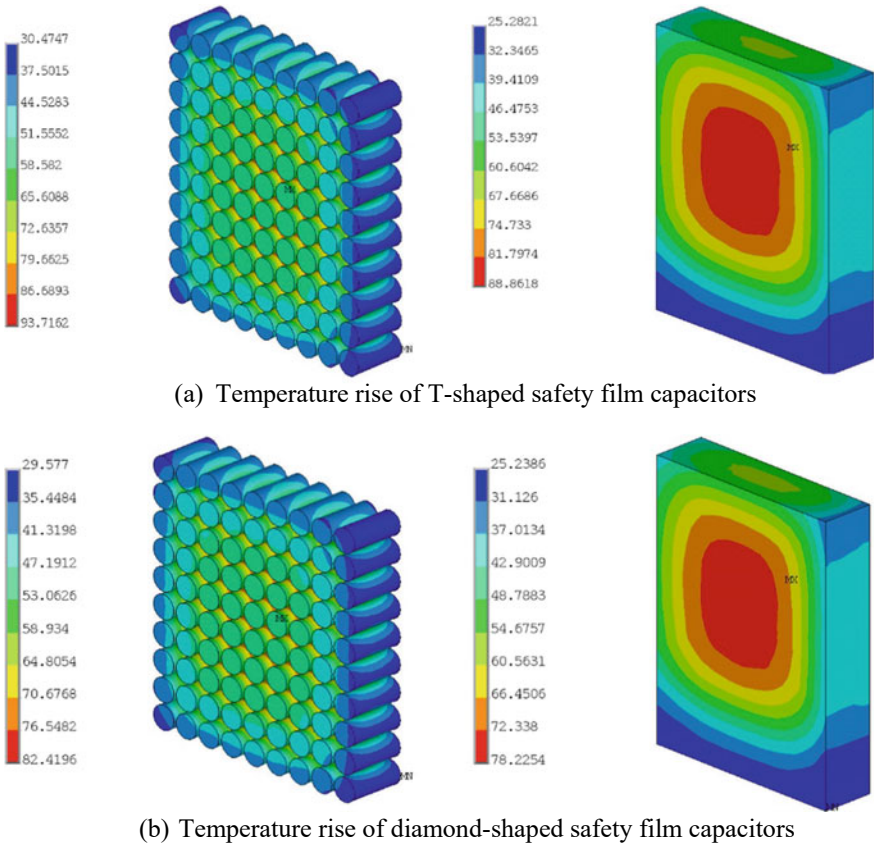


Fig. 4 Simulation results of temperature rise of different safety film capacitors

Simulation result shows that the type of safety film has little effect on the thermal field distribution of the capacitor. For different type of safety film capacitor, hot spots appear at the center of the core and the corresponding position of the shell. However, the temperature rise of hot spots of different safety film structures is quite different: when the ambient temperature is 25°C, the temperature rise of the core of the T-shaped safety film is up to 68 K, and the hottest spot is 93 °C; the highest temperature rise of the shell is 63 K, and the hottest spot is 88 °C. The axial heat conduction effect of the diamond-shaped safety film is better, and the internal core temperature rises to 57 K, and the hottest point is 82 °C; the maximum temperature rise of the shell is 53 K, and the hottest point is 78 °C, smaller than the T-shaped safety film. According to operating experience, the highest temperature rise of capacitors with non-safety film metallized film is generally around 50 K, and the hottest point will not exceed 75 °C. Therefore, attention should be paid to the heat dissipation of metallized film capacitors using safety films to avoid the high temperature of the internal insulating medium for a long time.

## 4 Conclusion

In this paper, equivalent thermal resistance of safety metallized films with different structures are analyzed, the axial and radial equivalent thermal conductivities of T-shaped and diamond-shaped safety films are calculated. The thermal field simulation model of metallized film capacitor was established, and the temperature rise of the internal components as well as the shell of the metallized film capacitor of different types of safety films is obtained. Result shows that:

- (1) For the shape of the safety film where it is difficult to directly obtain the equivalent thermal resistance according to the calculation formula, it is feasible to apply the heat density on the simulation model of the safety metallized film model and calculate the equivalent thermal resistance based on the simulation results.
- (2) The radial thermal conductivity of the diamond-shaped safety film and the T-shaped safety film are the same, but the radial thermal conductivity is quite different, indicating that the safety film with a larger effective cross-sectional area of the fuse has better radial heat conduction effect.
- (3) Temperature rise of metallized film capacitors using safety film is higher than that of general metallized film capacitors, especially the internal core temperature rise of T-type safety film capacitors can reach 68 K, which is much higher than 50 K of general metallized film capacitors. Safety film capacitors should pay attention to improve their heat dissipation efficiency.

## References

1. Li H, Yin T, Yan F (2015) Calculation of plate heating of metallized film capacitors. *Power Capacit React Power Compens* 36(5):4–12
2. Yin T, Yan F, Wang Z (2016) Temperature field analysis and optimal design of high voltage self-healing capacitor under typical AC conditions. *High Volt Technol* 42(12):3996–4004
3. Chen H, Liu X, Kong M (2020) Thermal simulation and analysis of metallized film pulse capacitor discharge process based on ANSYS. *Electron Comp Mater* 39(12):12–16
4. Yue G, Du Z, Meng S (2022) Analysis and optimization of non-uniform temperature rise distribution of dry-type DC capacitors based on electrothermal coupling[J]. *High Volt Technol* 48(12):10–22
5. Yin T, Yan F, Li H (2015) ESR calculation of metallized safety film capacitors. *Power Capacit React Power Compensat* 36(3):5–12
6. Xu M, Wang Z, Wang X (2018) Simulation of temperature field of T-shaped metallized safety film capacitor. *Power Capacit React Power Compensat* 39(3):7–12
7. El-Husseini M, Venet HP (2002) Thermal simulation for geometric optimization of metallized polypropylene film capacitors. *IEEE Transact Industr Applicat* 38(3):713–718
8. Kerrigan RM, Kropiewnicki B (2008) Film capacitor thermal strategies increase power density. *NWL Capacit Operat* 1(1):1–5
9. He Y, Wang F, Du G (2023) Revisiting the thermal ageing on the metallised polypropylene film capacitor: From device to dielectric film. *High Voltage* 8(2):305–314
10. BelKo V, Bondarenko P, Emelyanov O (2007) The dynamic characteristics of self-healing processes in metal film capacitors. *Russ Electr Eng* 78(3):33–38

# Research on Post-arc Recovery Characteristics of Sheath in Long-Gap Vacuum Circuit Breaker



Ying Feng, Dege Li, Jintao Zhang, Ziang Tong, and Jianwen Wu

**Abstract** Due to the proposal of China's the goals of carbon peaking and carbon neutrality, vacuum circuit breakers have become the best choice for SF6 replacement due to their advantages of zero carbon emissions and strong breaking capacity. However, there are only 126 kV and below single-break vacuum interrupters for high-voltage transmission levels, and 252 kV vacuum interrupters have not yet been put into use for commercial products. The 252 kV level vacuum switch has the characteristics of high withstand voltage level and long contact gap distance, and its breaking capacity is closely related to the recovery process of the back-arc medium. In this paper, the Continuous Transition Model (CTM) model of the back-arc sheath is adopted, and the transient recovery voltage of the 220 kV transmission line model is input as a parameter. Parameters, the curves of the length of the sheath, the surface electric field intensity of the new cathode, and the power density with time are obtained, and the time spent in the recovery phase of the back-arc sheath, the maximum value of the surface electric field intensity, and the maximum power density are obtained, which is high voltage level, long gap vacuum circuit breaker design provides theoretical support.

---

Y. Feng · J. Zhang · Z. Tong · J. Wu (✉)

School of Automation Science and Electrical Engineering, Beihang University, Beijing 100083, China

e-mail: [wujianwen@vip.sina.com](mailto:wujianwen@vip.sina.com)

Y. Feng

e-mail: [46236861@qq.com](mailto:46236861@qq.com)

J. Zhang

e-mail: [madchef@163.com](mailto:madchef@163.com)

Z. Tong

e-mail: [448341324@qq.com](mailto:448341324@qq.com)

Y. Feng · D. Li

China Electric Power Research Institute Co., Ltd, Beijing 100192, China

e-mail: [lidgege@epri.sgcc.com.cn](mailto:lidgege@epri.sgcc.com.cn)

© Beijing Paiké Culture Commu. Co., Ltd. 2024

X. Dong and L. Cai (eds.), *The Proceedings of 2023 4th International Symposium on Insulation and Discharge Computation for Power Equipment (IDCOMPU2023)*, Lecture Notes in Electrical Engineering 1103, [https://doi.org/10.1007/978-981-99-7413-9\\_43](https://doi.org/10.1007/978-981-99-7413-9_43)



**Keywords** 252 kV vacuum circuit breaker · Continuous transition model · Sheath · Post-arc recovery characteristics

## 1 Introduction

With the proposal of China's the goals of carbon peaking and carbon neutrality, vacuum circuit breakers have become a promising technology choice due to their outstanding advantages of strong breaking capacity and zero carbon emissions [1]. At present, SF<sub>6</sub> gas is still widely used as the arc extinguishing medium of circuit breakers with high voltage level for power transmission, which has a strong greenhouse effect. The rated voltage levels of commercial single-break vacuum interrupters are only 72 kV and 126/145 kV [2], and no mature commercial products have yet been put into use at the 252 kV level. Therefore, it is urgent to carry out research on key technologies of vacuum circuit breakers.

The advantage of using vacuum start technology is that the medium can be recovered quickly during the post-arc process [3]. The research on the post-arc process is of great significance for improving the breaking capacity of vacuum circuit breakers and adapting to the multiple rapid reclosing requirements of transmission and distribution networks. The sheath development stage is the first stage of the dielectric recovery process after the vacuum circuit breaker. The Child-Langmuir law gives a lower bound on the time of this process. Andrews and Varey further proposed the Continuous Transition Model (CTM) of post-arc growth of sheath, which can more accurately solve the relationship between post-arc sheath length and time [4]. Based on this, Orama and Glinkowski further proposed a method for solving the ion density and gave three breakdown criteria based on the calculations [5]. Bing L coupled the mathematical model of the key parameters of the residual plasma and metal vapor after the arc with the CTM equation set for a frequency 126 kV three-break tandem vacuum circuit breaker, so that the initial conditions for the solution of the post-arc sheath are expanded from constants to functions about time [6]. Liu studied the post-arc dielectric recovery process for multi-break DC vacuum circuit breakers, accounting for the effect of metal vapor density, and proposed that there are two types of particles, fast and slow, in the sheath growth process, and improved the CTM model [7]. Ding, Yuan and He conducted a study on the medium frequency circuit arc opening process of mechanical vacuum DC circuit breakers, accounting for the influence of the arc burning process to improve the CTM model [8]. They found that in the frequency range of 50–50,000 Hz, the sheath growth rate shows a non-linear relationship with the increase in frequency, while the slow particle dominance in the mid-frequency band leads to slow sheath growth, which is not conducive to arc breaking. There is also the Particle-in-cell (PIC) method for the study of post-arc particle motion. This method uses a numerical algorithm to calculate the microscopic motion of post-arc particles, which does not require assumption of parameters, but is too computationally intensive due to the extremely large number of particles. Sarrailh

[9] and Jadidian [10] have made improvements to the PIC model, trying to reduce the computational effort, but the solution is still difficult.

This paper investigates the effect of sheath growth on the post-arc process of long gap contacts at high voltage levels for the post-arc dielectric recovery process of 252 kV vacuum circuit breakers.

## 2 Continuous Transition Model of Post-arc Sheath

### 2.1 Bohm Sheath Model

The continuous transition model is used to describe the variation of the length of ion sheath with time in the post-arc process. This method is based on the assumption that the distribution of post-arc plasma satisfies the Bohm sheath model, that is, the sheath region can be divided into sheath, pre-sheath and plasma regions sequentially from the new cathode to the new anode.

Some assumptions of the Bohm sheath model are as follows.

1. The electron distribution follows a Boltzmann distribution. Electron temperature is  $T_e$ , in the plasma region.
2. The thermal motion of the ions is neglected, i.e., the temperature of the ions in the sheath is assumed to be zero in the sheath region. Thus, the ions in it are subjected to electric field forces only and make directional motion.
3. At the boundary between the sheath and the pre-sheath, the electron density is equal to the ion density.
4. The hypothesis of a pre-sheath region is introduced, and this region allows the directional acceleration of ions in the plasma region to Bohm velocity with a region thickness in the order of the Debye length. The Bohm speed is shown in the following equation:

$$v_{Bohm} = \left( \frac{kT_i}{m} \right)^{\frac{1}{2}} \quad (1)$$

### 2.2 Continuous Transition Model

The CTM model is shown in Eqs. (2–4) as follows:

The sheath length varies with time as follows:

$$l^2 = \frac{4\varepsilon_0 U_0}{9eZN_i} \left( \left( 1 + \frac{u(t)}{U_0} \right)^{3/2} + \frac{3u(t)}{U_0} - 1 \right) \quad (2)$$

The surface potential of the sheath is as follows:

$$U_0 = \frac{M_i}{2e} \left( v_i - \frac{dl}{dt} \right)^2 \quad (3)$$

The post-arc current is as follows:

$$i(t) = \frac{\pi D^2 Z N_i e}{4} \left( v_i - \frac{dl}{dt} \right) \quad (4)$$

The variables and constants are as follows:

$t$  is time, and time 0 is defined as the instant when the sheath begins to grow.  $l$  is the axial length of the sheath as a function of time.  $\varepsilon_0$  is the vacuum dielectric constant, which takes the value of  $8.85 \times 10^{-12}$  F/m.  $U_0$  is the surface potential of the sheath.  $e$  is the electronic charge, which takes the value of  $1.602 \times 10^{-19}$  C.  $Z$  is the average charge of the ion, which takes the value of 1.3–1.85 when the contact material is Cu.  $N_i$  is the ionic density in the plasma region.  $u(t)$  is the voltage at both ends of the gap, which takes the value of the transient recovery voltage (TRV) when applied to the circuit breaker.  $M_i$  is the ion mass, which takes the value of  $1.06 \times 10^{-25}$  kg for copper ion.  $v_i$  is the ion movement speed, which take the value of  $1 \times 10^3$ – $2 \times 10^4$  m/s for the copper ion in the vacuum interrupter.  $D$  is the effective diameter of the plasma. This parameter is the radial diameter of the plasma before the arc current crosses zero. In this paper, the cathode contact diameter is taken.

For long vacuum gap high current arc opening, if the arc is in the diffusion state, the initial plasma density is proportional to the rate of change of current at the current zero point.

The initial ion plasma density is as follows:

$$N_{i0} = \frac{4I_1}{v_i \pi D^2 Z e} \quad (5)$$

The ion density is as follows:

$$N_i = N_{i0} e^{-\frac{t-t_1}{\tau}} \left( 1 + \delta_{\text{AMP}} \frac{l^2}{l_{\text{gap}}^2} \right) \quad (6)$$

The variables and constants are as follows:

$t_1$  is the moment when the sheath starts to grow.  $I_1$  is the post-arc current at the moment the sheath starts to grow, i.e., the post-arc current at the initial moment of TRV.  $\tau$  is the time constant of plasma diffusion decay, generally taken as 0.5–10  $\mu$ s.  $\delta_{\text{AMP}}$  is the space charge distribution coefficient of ions in the gap, generally taken as 0–10.  $l_{\text{gap}}$  is the length of gap.

### 2.3 Breakdown Criteria in Vacuum Switches

The CTM model describes the dynamics of the post-arc plasma. However, it is still needed to indicate whether the interrupter will extinguish the current successfully or not. Therefore, three breakdown criteria have been proposed as follows.

$$E_c = 2\sqrt{\frac{eZN_i}{\epsilon_0} \left( \sqrt{u(t)U_0 + U_0^2} - U_0 \right)} \quad (7)$$

$$P_d = N_i v_i \left[ \frac{M_i v_i^2}{2} + u(t)eZ \right] \quad (8)$$

$$\left. \frac{dl}{dt} \right|_{l=0} < 0 \quad (9)$$

The three equations describe electrical breakdown, thermal breakdown, and breakdown caused by the reversal of the sheath, respectively. The occurrence of electrical breakdown is related to the sheath. The reason is that the post-arc sheath layer is not sufficient to withstand the recovery voltage and thus breakdown occurs. The occurrence of thermal breakdown is related to the electric field strength of the new cathode surface and the current power after the arc. When the surface electric field strength is too high or the current power is too high, the electrode evaporates a large amount of metal vapor. It cannot withstand the gap voltage and thus breakdown occurs. The third cause of breakdown is the return of the sheath length to zero. In this case, the plasma fills the gap again to the point that the conductive path is reconstructed and thus a breakdown occurs. If the direction of the sheath length increase is temporarily flipped while the length is not reduced to zero, the third breakdown theoretically does not occur.

## 3 Numerical Simulation of the Post-arc Sheath of 252 kV Vacuum Interrupter

### 3.1 Selection of Key Parameters of 252 kV Vacuum Interrupter

In this paper, the CTM model is used to study the development process of the post-arc sheath layer of the 252 kV vacuum interrupter. To simplify the model, a cylindrical flat contact of pure copper is selected as the material. The key parameters are selected as shown in Table 1.

**Table 1** The parameters of 252 kV vacuum arc interrupter

Parameter	Symbol/unit	Value
The average charge of the ion	$Z$	1.85
Ion mass	$M_i/\text{kg}$	$1.06 \times 10^{-25}$
Ion movement speed	$v_i/(\text{m/s})$	5000
Diffusion decay time constant of plasma	$\tau/\text{s}$	5
Space charge distribution factor of ion	$\delta_{\text{AMP}}$	5
The length of gap	$l_{\text{gap}}/\text{mm}$	100

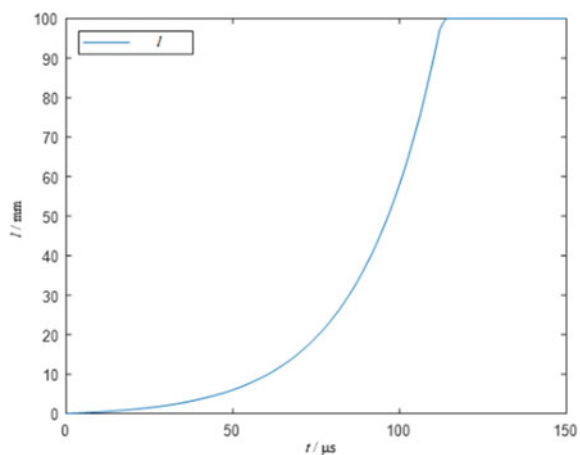
### 3.2 Sheath Growth Process Based on the CTM Model

In this paper, the CTM model is used to solve the development process of the post-arc sheath of the 252 kV vacuum interrupter.

The CTM model is a first-order higher-order implicit differential equation for the length  $l$  of the sheath of the variable to be solved. Therefore, it can be solved by using the ode45 function in MATLAB. The post-arc process and the growth of sheath of the obtained 252 kV vacuum interrupter are shown in Figs. 1, 2, and 3, which are the curves of sheath length, electric field strength of surface and power density with time, respectively.

Analysis of the above Fig. 1 shows that the post-arc sheath of the 252 kV vacuum interrupter initially grows very slowly. With the increase of recovery voltage and the decay of plasma density, the growth rate is gradually accelerated. Finally, the sheath grows to the new anode around 117  $\mu\text{s}$ . The growth time of the sheath is significantly longer than that of the low voltage, small spacing vacuum circuit breaker. The post-arc sheath recovery time is closely related to the plasma density and the ion velocity in the sheath. The spatial distribution of the plasma in the long gap will hinder

**Fig. 1** Relationship between the length of sheath and time



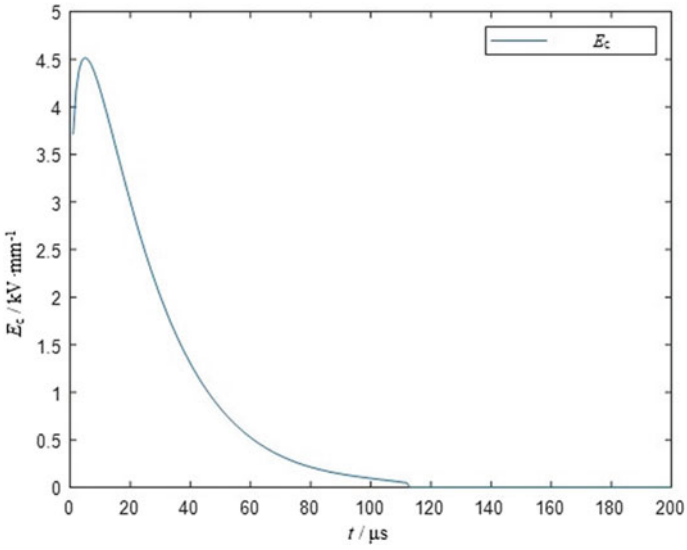


Fig. 2 Relationship between the electric field strength of the new cathode surface with time

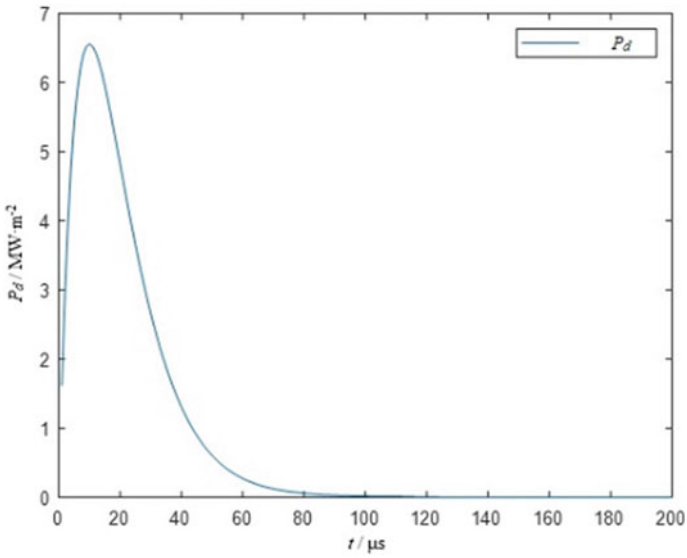


Fig. 3 Relationship between the power density of the new cathode surface with time

the growth of the post-arc sheath, which is harmful for the current breaking of the interrupter. Therefore, the effects of the characteristics of the post-arc plasma and the ions in the sheath should be further studied.

Analysis of Figs. 2 and 3 shows that the surface electric field strength and power density both increase first and then decrease. The maximum surface electric field strength is about 4.5 kV/mm. The maximum power density is about 6.5 MW/m<sup>2</sup>. Both peaks appear around the time constant of the plasma diffusion decay time constant (5 μs). This is basically the same trend as the previous research results at lower voltage levels and smaller opening distances. The maximum value of the surface electric field intensity and power density of the vacuum interrupter is affected by many factors such as the contact material and the structure of the interrupter. Moreover, the time constant of plasma diffusion decay also affects the judgment of restrike. Therefore, when designing a vacuum interrupter and selecting contacts, specific analysis should be combined with the actual situation.

## 4 Conclusion

In this paper, the 252 kV vacuum circuit breaker is taken as the research object, and the post-arc dielectric recovery characteristics of the long-gap vacuum circuit breaker are analyzed by using the post-arc CTM model. The development process of the sheath after the vacuum arc, as well as the evolution law of the electric field intensity and power density on the cathode surface were obtained. The recovery period of the post-arc sheath was found to be about 117 μs. The maximum surface electric field intensity was about 4.5 kV/mm. The maximum power density is about 6.5 MW/m<sup>2</sup>. The above research provides theoretical support for the design of high-voltage, long-gap vacuum circuit breakers.

**Acknowledgements** This work is supported by General Project of National Natural Science Foundation of China (KZ73-1171-01), State Grid Corporation of China Science and Technology Project (5500-202218392A-2-0-ZN) and China Postdoctoral Science Foundation (2022M720342).

## References

1. Zhang Z, Kang C (2022) Challenges and prospects of building a new power system under the goal of carbon neutrality. *Chinese J Electric Eng* 42(08):2806–2819 (in Chinese)
2. Jia S, Jia R, Zhu L (2022) Development status and trend of vacuum interrupting environmental protection GIS. *High Voltage Electric Appl* 58(09):1–12 (in Chinese)
3. Naeem S, Casey W, Jon R (2022) Advancements in clean air insulation technologies for switchgear and circuit breakers. *IEEE Power Energy Magaz* 20(2):132–138
4. Andrews G, Varey H (1971) Sheath growth in a low pressure plasma. *Phys Fluid* 14(2):339–343
5. Lionel O (1997) Numerical modeling of high-voltage circuit breaker arcs and their interaction with the power system. Rensselaer Polytechn Inst New York, USA

6. Bing L (2009) Research on equalization measures during breaking process of multi-fracture series vacuum circuit breaker. Wuhan University, Wuhan, China (in Chinese)
7. Liu L, Yuan Z, Chen L, Liu S, Wu K, He J, Pan Y (2021) Research on the current-zero period of vacuum arc interruption and equivalent model of post-arc gap. *J Phys D Appl Phys* 55(2):025202
8. Ding C, Yuan Z, He J (2020) Selection method of reverse current frequency of mechanical vacuum DC circuit breaker. *High Volt Technol* 46(08):2670–2676 (in Chinese)
9. Sarrailh P, Garrigues L, Hagelaar M, Jean-Pierre B, Gabriela S, Stephan R, Benoit J (2008) Two-dimensional simulation of the post-arc phase of a vacuum circuit breaker. *IEEE Trans Plasma Sci* 36(4):1046–1047
10. Soloot H, Jadidian J, Agheb E, Hans H (2010) Two dimensional simulation of post arc phenomenon in vacuum interrupter with axial magnetic field contacts. In: International symposium on discharges and electrical insulation in vacuum. Braunschweig, IEEE, Germany, pp 339–342



# Effect of Different Grounding Schemes on the Circulating Current of Gas-Insulated Transmission Lines



Zhiren Tian, Junqiang Gong, Zhen Xiang, Gen Li, and Yu Zheng

**Abstract** This paper quantitatively analyzes the impact of induced current and leakage current on GIL equipment by establishing a GIL shell circulating current calculation model. In addition, the GIL grounding system and shell circulation model were established. When the grounding spacing is less than 2000 m, the shell circulation and shell potential will increase significantly with the increase of grounding spacing, and the GIL shell potential shows a “U”-shaped distribution with low middle and high end. The potential can be reduced to a single digit to ensure the safety of staff.

**Keywords** Gas insulated transmission lines · Shell circulation · Induced voltage · Grounding system

## 1 Introduction

Gas insulated transmission line (GIL) is a new type of power transmission method [1, 2]. Compared with overhead lines, which are susceptible to atmospheric conditions, occupy large space, and have long insulation safety distances, GIL systems are increasingly used because they are insulated by pipe seals and are usually not affected by environmental factors such as harsh weather and special terrain, are not subject to external environmental interference, and are built underground without affecting urban surface municipal construction [3, 4].

---

Z. Tian · J. Gong · Z. Xiang  
Shenzhen Power Supply Company, Shenzhen 518048, China

G. Li (✉) · Y. Zheng  
Engineering Research Center of Ministry of Education for Lightning Protection and Grounding Technology, School of Electrical Engineering and Automation, Wuhan University,  
Wuhan 430072, China  
e-mail: [Leagren@whu.edu.cn](mailto:Leagren@whu.edu.cn)

School of Electrical Engineering and Automation, Wuhan University, Wuhan 430072, China

The metal shell and tubular conductors in GIL are arranged coaxially, and when current flows in the tubular conductors, induced currents are generated in the metal shell, i.e., shell circulating current [5, 6]. Firstly, it affects the transmission capacity of the system, and during normal operation, the shell circulating current value and the wire load current are basically of the same order of magnitude, resulting in large circulating current losses [7, 8]. Secondly, when the shell circulating current exceeds a certain value, the heat exceeds the thermal capacity of the shell, resulting in local heating and accelerating the aging of the insulation part, and there are many electronic devices in the GIL, whose working conditions are relatively harsh, and the high temperature environment will have a certain impact on its safe and stable operation [9, 10]. In order to reduce the effect of circulating currents, the outer casing of GIL is grounded, mainly at one point and multiple points. The grounding system configuration of the GIL inevitably affects the circulation, and few studies have been conducted in the literature to link the two.

In this paper, the GIL grounding system and shell circulation model are developed, the parameters of self-impedance and phase-to-phase mutual inductance of the circulating system are analyzed by the geometric model, and the circulating current of the GIL conductor shell is calculated to study the potential distribution pattern of the GIL conductor shell. Finally, the setting of the shorting row is discussed, the influence of the shorting row on the shell circulating current is analyzed, and reasonable structural parameters of the shorting row are proposed to provide a theoretical basis for the safe and stable operation of the GIL system.

## 2 Theoretical Model

According to the electromagnetic field theory, the magnetic fluxes generated by the three-phase conductive core currents of A, B and C on the surface of the metal shell of phase A are calculated as follows.

$$\varphi_{AA} = \frac{\mu_0 l}{2\pi} \ln \frac{r+h}{r} I_A \quad (1)$$

$$\varphi_{AB} = \frac{\mu_0 l}{4\pi} \ln \frac{(r+h)^2 + s_1^2}{s_1^2 + r^2} I_B \quad (2)$$

$$\varphi_{AC} = \frac{\mu_0 l}{4\pi} \ln \frac{(r+h)^2 + s_1^2}{s_1^2 + r^2} I_C \quad (3)$$

where:  $\varphi_{AA}$ ,  $\varphi_{AB}$ ,  $\varphi_{AC}$  are the magnetic fluxes generated by the A, B and C phase currents in the A phase metal shell, respectively.  $I_A$ ,  $I_B$ ,  $I_C$  are the operating currents flowing through the three phase wires of GIL, respectively;  $l$  is the length of the shell.  $h$  is the distance between the shell and the wall of each phase.  $r$  is the outer diameter of the shell.  $s_1$  is the spacing of the adjacent two phase line guide cores.  $s_2$  is the

spacing of the non-adjacent two phase guide cores.  $\mu_0$  is the magnetic permeability of free space,  $\mu_0 = 4\pi \times 10^{-7}$  H/m.

The calculation of the shell mutual inductance can be analogous to the coil mutual inductance, the core current in the metal shell of the flux generated by the core and the ratio of the current flowing through the core as the core and shell mutual inductance. B-phase shell and C-phase shell flux can be calculated by analogy to the formula (1–3). Due to the symmetrical spatial relationship, the size of A-phase and C-phase mutual inductance is the same, B-phase mutual inductance is slightly larger than A, C-phase mutual inductance, the specific calculation of mutual inductance formula is shown in Eqs. (4, 5).

$$M_A = M_C = \frac{\varphi_A}{I_A} = \frac{\varphi_{AA} + \varphi_{AB} + \varphi_{AC}}{I_A} \tag{4}$$

$$M_B = \frac{\varphi_B}{I_B} = \frac{\varphi_{BB} + \varphi_{BA} + \varphi_{BC}}{I_B} \tag{5}$$

where:  $M_A, M_B, M_C$  are the mutual inductance between the A, B, C phase conductors and the metal shell.  $\varphi_A, \varphi_B$  are the total magnetic flux of the A and B phase conductors respectively.  $\varphi_{BA}, \varphi_{BB}, \varphi_{BC}$  are the magnetic flux formed in the B phase metal shell by the A, B and C phase conductors respectively.  $Z_A, Z_B,$  and  $Z_C$  are the self-impedances of the A, B, and C phase conductors, respectively.

GIL transmission line shell and guide core are used aluminum alloy materials, three-phase shorting row and grounding copper row are used tinned copper, the structural parameters required for the calculation are shown in Table 1. The mutual inductance of the guide core and shell is calculated and obtained in Table 2.

**Table 1** The geometry parameters of 500 kV GIL

Parameters	Values
The external diameter of shell (mm)	542.0
The thickness of shell (mm)	8.0
The radius of conductor (mm)	177.8
Center-to-ground heights of conductors (mm)	700, 1700, 2700
Center distance between phases (mm)	1000
Distance of shell surface from wall (mm)	500
Shorting row specifications	Copper 70 × 6 mm
Grounding trunk specifications	Copper 70 × 6 mm
Main grounding wire specifications	Copper 50 × 5 mm

**Table 2** The electric parameters of 500 kV GIL

Parameters	Phase resistance per meter/ $\Omega$	Phase inductance per meter/H
Self-impedance of conductor	$8.01 \times 10^{-6}$	$3.34 \times 10^{-7}$
Self-impedance of shell	$4.23 \times 10^{-6}$	$2.97 \times 10^{-7}$
Self-impedance of Shorting row	$4.087 \times 10^{-6}$	$8.73 \times 10^{-7}$
Mutual inductance between the A-phase shell and the three-phase conductor		$2.60 \times 10^{-7}$
Mutual inductance between the B-phase shell and the three-phase conductor		$2.87 \times 10^{-7}$
Mutual inductance between the C-phase shell and the three-phase conductor		$2.60 \times 10^{-7}$

### 3 Results

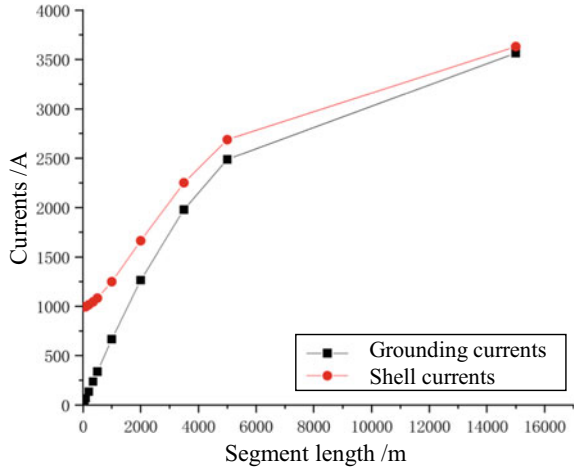
#### 3.1 GIL Single-Phase Segmented Circulation Model

According to the principle that the current in the GIL conductor core generates induced electric potential in the metal shell, the equivalence can be performed with a mutual coupling coil, and the analysis can be modeled in MATLAB for a section in a single-phase GIL segmented grounding with a length of 15 km based on the principle of mutual coupling coil equivalence circuit.

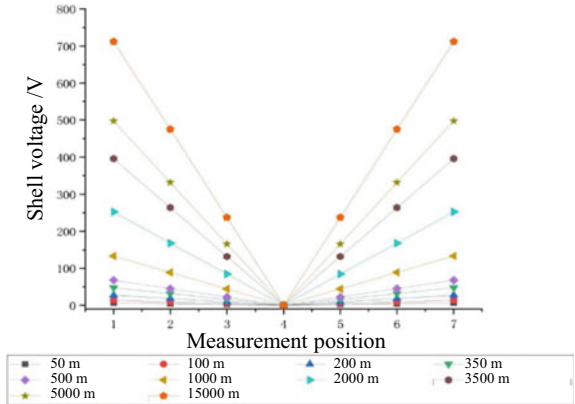
Adjust the load so that the conductor current is set to the rated value of 4000 A. The grounding network and the grounding lead impedance are combined and equivalent to the grounding lead impedance, the grounding network impedance is required to be less than 1  $\Omega$ , which is taken to be 0.2  $\Omega$  in this study. the case of grounding spacing of 50, 100, 200, 350, 500, 1000, 2000, 3500, and 5000 m is measured respectively. Loop current. At the same time, seven measurement points were set at equal intervals on the metal shell to measure the voltage to ground to analyze the shell potential distribution, where measurement points 1,7 are the shell potential at both ends and measurement point 4 is the shell potential at the middle point. Without considering the addition of a shorting row between the three phases, the simulation results are shown in the Fig. 1.

It is obvious from the Fig. 2 that the shell circulation and shell potential both increase as the grounding spacing increases, and the rate of increase becomes slower as the grounding spacing increases. In the single-phase grounding segment, the shell potential of GIL is V-shaped distribution, and the maximum shell potential between the two grounding leads appears at the contact point between the two grounding leads and the shell, so the main attention is paid to the shell potential at both ends in the subsequent simulation. The shell loop current reaches the maximum when only two ends are grounded, up to 3630 A. Since the mutual inductance of the middle phase

**Fig. 1** Variation of GIL single-phase shell circulating current with ground spacing



**Fig. 2** Variation of peak GIL single-phase shell potential with ground spacing



is slightly larger than that of the side phase, the shell current and shell potential of phase B will be slightly larger than those of phase A and phase C.

### 3.2 GIL Single-Phase Circulation Model

The whole section of GIL is segmented, multiple grounding leads are set, the grounding leads are connected to the trunk line of the grounded tinned copper row in the corridor, the tinned copper row is connected to the grounding grid at the two terminals. The figure shows the model diagram of single-phase shell circulating current for the entire 15 km GIL line divided into three sections at a grounding spacing of 5 km. For other grounding spacing models, the grounding lot is increased and the

**Table 3** The shell currents of 500 kV GIL

Grounding distances/m	Grounding currents/A	Shell currents/A	Shell voltages/V
5000	3564	3630	712.7
3000	3459	3540	691.8
1500	3564	3630	712.7
1000	3577	3641	715.5
500	3577	3641	715.5

distance between each section is reduced. 15 km GIL is modeled and the load is adjusted so that the conductive core current reaches the rated current of 4000 A. The incoming current and shell circulating current in each grounding spacing are counted and the maximum shell potential is shown in Table 3.

It can be found that the difference between the loop current data of the whole section of GIL with different grounding spacing is not significant, which is because the grounding network inside the corridor is not really grounded, and the magnitude of its loop current is mainly related to the overall length of GIL, and the measurement results are very close to the results of 15 km section in the single-phase section grounding simulation test. The potential distribution of the GIL shell in the line remains V-shaped. As the shell loop current enters the grounding network at both ends to form a circuit through the incoming current, the shell potential at both ends of the line is equal to the product of the incoming current and the grounding network impedance, which is always maintained at about 700 kV.

Therefore, to reduce the maximum shell potential, it is necessary to reduce the incoming current. The approach used in this paper is to achieve shunting by shorting the GIL three-phase shell by shorting the row to reduce the incoming current and shell potential.

### ***3.3 GIL Three-Phase Circulating Current Model with Shorting Row***

Shorting row material using  $70 \times 6$  mm tinned copper material, respectively, at both ends of the GIL line to three phase shell shorting. Because the impedance of the shorting row is much smaller than the impedance of the grounding network, most of the shell loop current will flow through the shorting row and flow through the shell in different phases, thus reducing the incoming current. Also, because the impedance in the loop is reduced, the size of the shell loop current will become larger.

A 15 km GIL circulation model with a short connection row added at 5 km segment spacing. Simulation tests are carried out for different segment spacing by adding segments and adjusting the length of each segment. The test results are shown in Table 4.

**Table 4** The shell currents of 500 kV GIL with shorting row

Grounding distances/m	Grounding currents/A	Shell currents/A	Shell voltages/V
5000	4.776/1.808	3914	0.955
3000	4.777/1.806	3914	0.9419
1500	4.776/1.808	3914	0.9431
1000	4.774/1.808	3914	0.952
500	4.776/1.808	3914	0.955

In the simulation test of different grounding spacing after connecting the shorting row at both ends of the shell, the measured current in the conduction row is 3913 A, and the current flowing through the shell is 3914 A, which is nearly 300 A higher than the shell circulating current without adding the shorting row. The maximum shell potential is reduced.

According to the calculation formula of contact voltage in the regulation, the safety range of contact voltage is calculated. According to the formula 5, set the human body resistance is  $1000 \Omega$ , from the strict estimate of the working environment ground resistivity is  $\rho_s = 100 \Omega \cdot \text{m}$ , the failure time to take the design value  $t_s = 3.0 \text{ s}$ , the surface attenuation coefficient  $C_s$  take the value range of (0, 1), can be calculated to obtain the critical value of the shell contact voltage  $E$  range of (100, 110) V.

According to the model calculation results, it can be seen that for 200 m and below, the maximum value of ground potential on the GIL shell is tens of volts, so under the condition of less than 200 m segment spacing, when a person contacts the shell inside the corridor, the maximum value of ground potential between the part of his hand touching the shell and the ground at the bottom of his feet meets the contact voltage safety requirements. However, for longer distance GIL equipment, in order to reduce the shell potential, it is recommended that additional shorting rows be installed at both ends of the line.

## 4 Conclusion

With the GIL line length increases, the maximum shell potential and shell loop current will increase, and its growth rate will also decrease, when the grounding distance is less than 2000 m, the shell loop current and shell potential will increase significantly with the increase in grounding distance. the shell potential distribution of the GIL shows the characteristics of low in the middle and high at the end, showing a V-shaped distribution. The size of the peak shell potential is mainly affected by the size of the incoming current, and the maximum shell-to-ground potential can be reduced to less than 1 V after shorting the three-phase shell at both ends of a 15 km GIL line. To meet the needs of safe operation, it is recommended that additional shorting rows be installed at both ends of the GIL line.

## References

1. Koch H, Schuette A (1998) Gas insulated transmission lines for high power transmission over long distance[J]. *Electric Power Syst Res* 44(1):69–74
2. Koch H (2012) Gas insulated transmission lines (GIL) [M]. Wiley-IEEE Press, Chichester, UK, pp 33–38
3. Memita N, Suzuki T, Itaka K et al (1984) Development and installation of 275 kV SF<sub>6</sub> gas-insulated transmission line [J]. *IEEE Trans Power Appar Syst* 103(4):691–698
4. Kuroyanagi Y, Toya A, Hayashi T et al (1990) Construction of 8 000 A class 275 kV gas insulated transmission line[J]. *IEEE Trans Power Deliv* 5(1):14–20
5. Benato R, Mario CD, Koch H (2007) High-capability applications of long gas-insulated lines in structures[J]. *IEEE Trans Power Deliv* 22(1):619–626
6. Benato R, Dughiero F (2003) Solution of coupled electromagnetic and thermal problems in gas-insulated transmission lines. *IEEE Trans Magn* 39:1741–1744
7. Cheng S et al (2022) Temperature rise prediction of gas-insulated transmission lines based on thermal network model considering contact fingers. In: 2022 IEEE 20th biennial conference on electromagnetic field computation (CEFC), pp 1–2
8. Liang R et al (2022) Gas-insulated transmission lines state classification and fault chamber location based on the divergence characteristics of temperature parameters. *Elect Power Syst Res*
9. Jörgens C et al (2022) Modeling of the electric field in high voltage direct current gas insulated transmission lines. In: 2022 IEEE 4th international conference on dielectrics (ICD), pp 134–137
10. Liu S, Li J, Du B, Liang H, Hao L, Wang Y (2021) Mechanical stress distribution and reliability analysis of GIL Tri-post insulator. *Int Conferen Electric Mater Power Equip (ICEMPE) 2021*:1–4



# Research on Digital Twin Analysis Technology of Electric Field in the Near Area of DC Grounding Electrode



Lei Jun, Li Xiaojuan, Li Shaoyu, Qi Weijian, Cao Bibo, and Xie Yankai

**Abstract** As an important part of HVDC transmission engineering, DC grounding electrode leads the fault current into the ground when the HVDC transmission fault occurs. DC grounding electrode will cause the ground electric field exceeding the standard, which will affect the normal operation of the power system and pipeline system nearby. This paper presents a digital twinning technology of ground electric field near DC grounding electrode, and deduces the basic theory and algorithm of horizontal layered ground space potential and electric field under the condition of unlimited layers. The paper presents a digital twinning algorithm of ground potential analysis based on 45-point linear filtering method, and a digital twinning algorithm of space electric field based on 47-point linear filtering method. The effectiveness of this method is proved by case analysis, and the results are compared with the complex image method, which proves the accuracy of this algorithm. The work of this paper can provide reference for the analysis of potential and electric field near DC grounding electrode Analytical work.

**Keywords** Digital twin analysis · Electric field · DC grounding electrode

## 1 Introduction

As an important component in HVDC transmission system, DC grounding electrode is an important task to clamp down the neutral overvoltage of converter valve and guide the fault current of DC system into the ground. Because of the high amplitude of single maximum return current in HVDC transmission project fault, DC grounding electrode has strict requirements on soil resistivity and heat dissipation parameters.

---

L. Jun (✉) · L. Xiaojuan · Q. Weijian · C. Bibo · X. Yankai  
Electric Power Research Institute of State Grid Gansu Electric Power Company, Lanzhou 730050, Gansu, China  
e-mail: [1250405107@qq.com](mailto:1250405107@qq.com)

L. Shaoyu  
State Grid Gansu Electric Power Company, Lanzhou 730050, Gansu, China

© Beijing Paiké Culture Commu. Co., Ltd. 2024  
X. Dong and L. Cai (eds.), *The Proceedings of 2023 4th International Symposium on Insulation and Discharge Computation for Power Equipment (IDCOMPU2023)*, Lecture Notes in Electrical Engineering 1103, [https://doi.org/10.1007/978-981-99-7413-9\\_45](https://doi.org/10.1007/978-981-99-7413-9_45)

DC grounding electrode is generally located in the area with low resistivity and good heat dissipation, and is generally far away from converter station to prevent grounding corrosion and DC magnetic bias caused by DC current entering the ground. At this time, DC grounding electrode may lead to additional corrosion risk of surrounding buried metals, thus affecting the normal operation of pipeline system or other systems.

There are a lot of literatures for reference on DC grounding and its adverse effects on peripheral systems. Li Wei et al. analyzes the distribution law of DC current in the earth considering deep earth resistivity [1]. The mutual resistance between substations is considered as an impact on DC current invading AC power grid, especially in the case of high earth resistivity, more currents will be intruded into the AC system [2]. Lu Hailing et al. have measured the stride potential difference between DC grounding and its vicinity, which can be approximated to the electric field in the ground [3]. B. Markovski, et al. have proposed a fast analysis method of impulse grounding resistance in layered soils [4]. Dan studied the numerical calculation method of Green's function in layered soils [4]. References [4, 5] provided an algorithm reference for the application of digital twinning technology. Charalambous et al. comprehensively introduced the related corrosion problems of buried metals [6–9]. Reference [6, 7] deals with the influence analysis of DC grounding electrode on pipeline, while [8] deals with the influence analysis of AC transmission line on pipeline system. Reference [9] gives an evaluation method for the life of buried metals.

Based on the current research, we find that there are still some problems in the analysis of the ground electric field near the DC grounding electrode. The existing methods are too complex and are not conducive to the application of digital twinning technology. Therefore, a simplified analysis method is proposed in this paper to form the digital twinning technology of the ground electric field near the DC grounding electrode, which provides technical support for the analysis of electromagnetic compatibility problems of the ground electric field near the DC grounding electrode.

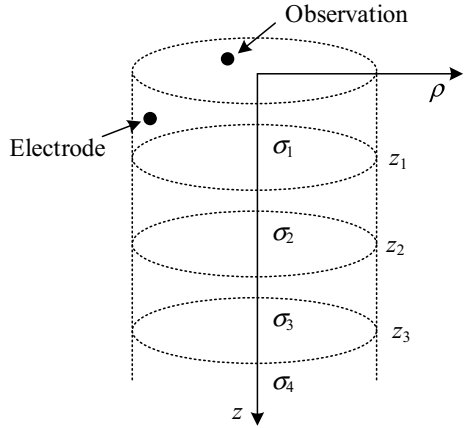
## 2 Digital Twinning Algorithm

In this paper, the following assumptions are made when studying the electric field in the near-ground area of DC grounding: the near-ground area is defined as the area far away from the size of the DC grounding electrode more than 5 times. In this case, the DC grounding electrode can be approximately a point current source located at the center of the electrode site.

The reference mathematical model of the ground electric field is closely related to the layered model of the earth. Figure 1 shows the horizontal layered earth model of the DC grounding pole site. The reference mathematical model of the ground electric field is expanded on the basis of Fig. 1. It should be noted that there is no limit to the number of layers in the digital twin model.

In the physical model of horizontal layered earth, each layer of soil corresponds to a conductivity. In addition to the conductivity, each layer has a thickness. The thickness

**Fig. 1** Physical model of horizontal layered earth



is determined by the z-axis boundary of each layer, and the z-axis coordinate between the boundaries of each layer is  $z_i$ . In the digital twinning algorithm, the potential  $V$  of the observation point is given by the following formula:

$$V_i(\rho, z_0, z) = \frac{1}{4\pi\sigma_i} \int_0^\infty [A_i(z, \lambda)e^{-\lambda(z_0-z)} + B_i(z, \lambda)e^{\lambda(z_0-z)}] J_0(\lambda\rho) d\lambda \quad (1)$$

where,  $A$  and  $B$  are the functions to be solved, subscript  $i$  is the number of the layer where the observation point is located,  $J_0$  is the first kind of zero-order Bessel function, and  $\lambda$  is the intermediate integral variable.

The formula is in the form of Bessel infinite integral, which is highly oscillatory. It is difficult to accurately solve the potential of the observation point by the general numerical integration method. In this paper, 47-point linear filtering method is used as the digital twinning algorithm for the potential of the observation point:

$$V_i(\rho, z_0, z) = \frac{1}{4\pi\sigma_i\rho} \sum_{k=1}^{45} W_{1k} \left[ A_i\left(z, \frac{\lambda_{1k}}{\rho}\right) e^{-\lambda_{1k}(z_0-z)} + B_i\left(z, \frac{\lambda_{1k}}{\rho}\right) e^{\lambda_{1k}(z_0-z)} \right] \quad (2)$$

Where  $\lambda_{1k} = \exp(-0.046339794 + (k-29)/6 \times \ln 10)$ ,  $W_{1k}$  is the weight which can be found in Table 1,  $k = 1, 2, \dots, 45$ .

The advantage of the digital twinning algorithm for the potential of observation point is that the integral can be calculated in the form of summation, thus reducing the difficulty of solving the problem.

For the physical model of horizontal layered earth shown in Fig. 1, the formula for calculating the electric field in the earth under the digital twin system is as follows

**Table 1** Weight value

k	1	2	3	4
W <sub>1k</sub>	8.442553E-05	-2.188238E-04	3.992356E-04	-4.902770E-04
k	5	6	7	8
W <sub>1k</sub>	5.924970E-04	-5.402089E-04	6.058318E-04	-4.291559E-04
k	9	10	11	12
W <sub>1k</sub>	5.710128E-04	-2.291581E-04	5.930441E-04	7.718970E-05
k	13	14	15	16
W <sub>1k</sub>	7.747867E-04	6.025228E-04	1.297029E-03	1.609243E-03
k	17	18	19	20
W <sub>1k</sub>	2.541381E-03	3.664201E-03	5.331464E-03	7.985009E-03
k	21	22	23	24
W <sub>1k</sub>	1.144405E-02	1.718604E-02	2.469615E-02	3.684803E-02
k	25	26	27	28
W <sub>1k</sub>	5.316417E-02	7.851667E-02	1.127491E-01	1.623984E-01
k	29	30	31	32
W <sub>1k</sub>	2.231669E-01	2.885882E-01	3.026171E-01	1.549609E-01
k	33	34	35	36
W <sub>1k</sub>	-3.194410E-01	-5.369178E-01	5.195257E-01	-1.976641E-01
k	37	38	39	40
W <sub>1k</sub>	5.580465E-02	-1.677557E-02	6.034991E-03	-2.466654E-03
k	41	42	43	44
W <sub>1k</sub>	1.056283E-03	-4.402132E-04	1.638434E-04	-4.736891E-05
k	45			
W <sub>1k</sub>	7.751497E-06			

$$\vec{E} = \nabla V = -\mathbf{e}_\rho \frac{\partial V}{\partial \rho} - \mathbf{e}_\phi \frac{\partial V}{\rho \partial \phi} - \mathbf{e}_z \frac{\partial V}{\partial z} = -\mathbf{e}_\rho \frac{\partial V}{\partial \rho} - \mathbf{e}_z \frac{\partial V}{\partial z} \tag{3}$$

Substituting (2) into (2)

$$\frac{\partial V}{\partial \rho} = \frac{1}{4\pi\sigma_i\rho} \sum_{k=1}^{47} W_{2k} \left[ A_i \left( z, \frac{\lambda_{2k}}{\rho} \right) e^{-\lambda_{2k}(z_0-z)} + B_i \left( z, \frac{\lambda_k}{\rho} \right) e^{\lambda_{2k}(z_0-z)} \right] \tag{4}$$

$$\frac{\partial V}{\partial z} = \frac{1}{4\pi\sigma_i\rho} \sum_{k=1}^{45} \lambda_{1k} W_{1k} \left[ A_i \left( z, \frac{\lambda_{1k}}{\rho} \right) e^{-\lambda_{1k}(z_0-z)} - B_i \left( z, \frac{\lambda_k}{\rho} \right) e^{\lambda_{1k}(z_0-z)} \right] \tag{5}$$

Where  $\lambda_{2k} = 10^{-3.050781876 + 0.11059901 k}$ ,  $W_{2k}$  is the weight which can be found in Table 2,  $k = 1, 2, \dots, 47$ .

**Table 2** Weight value

k	1	2	3	4
$W_{2k}$	1.0261945E-06	-6.0085885E-07	1.1827342E-06	-5.4755574E-07
k	5	6	7	8
$W_{2k}$	1.875566E-05	-1.465504E-05	1.537997E-05	-6.956283E-06
k	9	10	11	12
$W_{2k}$	1.418816E-05	3.414457E-06	2.139417E-05	2.349624E-05
k	13	14	15	16
$W_{2k}$	4.843403E-05	7.337330E-05	1.277038E-04	2.081200E-04
k	17	18	19	20
$W_{2k}$	3.498039E-04	5.791078E-04	9.658879E-04	1.604013E-03
k	21	22	23	24
$W_{2k}$	2.669038E-03	4.431116E-03	7.356317E-03	1.217828E-02
k	25	26	27	28
$W_{2k}$	2.010978E-02	3.300970E-02	5.371436E-02	8.605166E-02
k	29	30	31	32
$W_{2k}$	1.342676E-01	2.001250E-01	2.740275E-01	3.181687E-01
k	33	34	35	36
$W_{2k}$	2.416557E-01	-5.405492E-02	-4.469130E-01	-1.922319E-01
k	37	38	39	40
$W_{2k}$	5.523768E-01	-3.574290E-01	1.415105E-01	-4.614219E-02
k	41	42	43	44
$W_{2k}$	1.482738E-02	-5.074792E-03	1.838297E-03	-6.677428E-04
k	45	46	47	
$W_{2k}$	2.212775E-04	-5.662487E-05	7.882292E-06	

According to the above formula, the digital twinning of the ground electric field near the DC grounding electrode can be completed.

### 3 Case Analysis

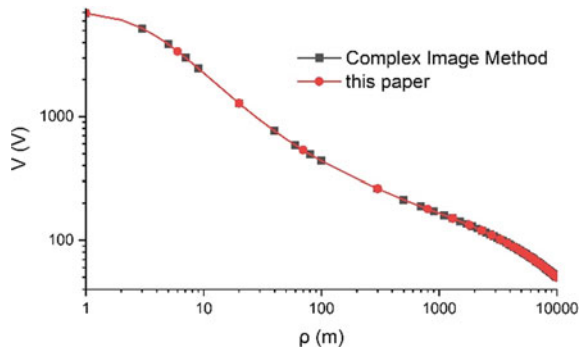
Take a 15-layer horizontal layered geodetic model, and the parameters are shown in Table 3. Assuming that the point current source is 5000A, which is located 3m below the origin, the variation law of surface potential and surface electric field is analyzed, and the results are shown in Figs. 2 and 3.

The comparison of surface potential distribution between complex image method and digital twinning method described in this paper is given in Fig. 2. From the calculation of the results in Fig. 3, it can be seen that the maximum deviation

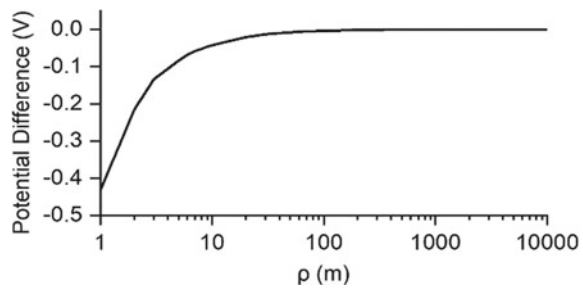
**Table 3** Layered soil parameters

$i$	$\rho_i$	$z_{i+1} - z_i$
1	26.5	97.5
2	66	242.5
3	29.5	175
4	257.5	197.5
5	1635	1997.5
6	1060	295
7	2046	1000
8	2833	1000
9	3744	2000
10	2481	1000
11	1395	1000
12	896.5	2000
13	579.5	2000
14	364.7	3000
15	209	ifinite

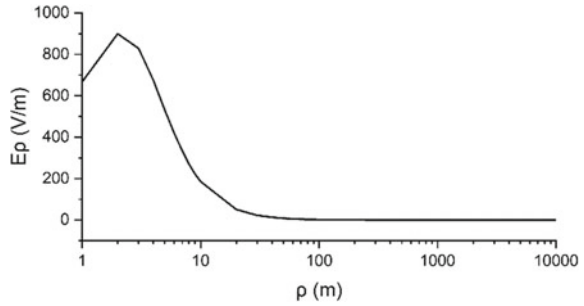
**Fig. 2** Ground potential distribution near DC grounding electrode



**Fig. 3** Ground potential difference between complex image method and this paper



**Fig. 4** Ground electric field distribution near DC grounding electrode



**Table 4** Surface electric field

Dis	Er/V/m
100	2.2898
500	0.1646
1000	0.05873
5000	0.00956
10,000	0.00413

between complex image method and this method is within 0.5 V, which proves the effectiveness of this method.

Figure 4 shows the variation of the surface electric field with the horizontal direction. It can be seen from the results that the amplitude of the surface electric field decays with the increase of the distance when the distance is greater than 10m, see the Table 4 for specific data.

It can be seen from the application of the case that the digital twinning algorithm proposed in this paper can effectively analyze the distribution of potential and electric field in the near region of DC grounding electrode, thus providing a powerful algorithm and tool for the analysis of electromagnetic compatibility of DC grounding electrode.

## 4 Conclusion

In this paper, a digital twinning algorithm has been proposed, which can effectively analyze the distribution of potential and electric field in the near region of DC grounding electrode. The conclusions are as follows:

- (1) Using digital twinning technology, the basic theory and algorithm of spatial potential and electric field of horizontal layered earth with unlimited number of layers are derived, which provides basic algorithm support for the work of this dissertation. The specific work of this dissertation is to propose a digital twinning algorithm for surface potential analysis based on 45-point linear filtering method

and a digital twinning algorithm for spatial electric field based on 47-point linear filtering method.

- (2) The effectiveness of the proposed method is analyzed by case study, and the results are compared with those of complex image method, which proves the accuracy of the proposed algorithm.
- (3) The work of this paper can provide reference for the analysis of potential and electric field in the near area of DC grounding electrode, which is helpful for the analysis of electromagnetic compatibility in the near area of DC grounding electrode.

## References

1. Pan Z, Zhang L, Wang X, Yao H, Zhu L, Liu Y, Wen X (2016) HVDC ground return current modeling in ac systems considering mutual resistances. *IEEE Transact Power Deliv* 31(1):165–173
2. Li W, Pan Z, Lu H, Chen X, Zhang L, Wen X (2017) Influence of deep earth resistivity on HVDC ground-return currents distribution. *IEEE Transact Power Deliv* 32(4):1844–1851
3. Lu H, Chen J, Tan B, Wang J, Chen W, Hu S, Xie S, Cai H, Li W, Wang S, Wen X (2022) Measurement and safety criteria of step voltage of high voltage direct current grounding electrode. *IEEE Transact Power Deliv* 37(1):423–430
4. Markovski B, Grcev L, Arnautovski-Toseva V (2021) Fast and accurate transient analysis of large grounding systems in multilayer soil. *IEEE Transact Power Deliv* 36(2):598–606
5. Dan Y, Zhang Z, Duanmu Z, Deng J, Li Y (2021) Segmented sampling least squares algorithm for Green's function of arbitrary layered soil. *IEEE Transact Power Deliv* 36(3):1482–1490
6. Charalambous CA (2021) Interference activity on pipeline systems from VSC-based HVDC cable networks with earth/sea return: an insightful review. *IEEE Transact Power Deliv* 36(3):1531–1541
7. Yu Z, Liu L, Wang Z, Li M, Wang X (2019) Evaluation of the interference effects of HVDC grounding current on a buried pipeline. *IEEE Transact Appl Superconduct* 29(2):1–5
8. Wang C, Liang X, Radons R (2020) Minimum separation distance between transmission lines and underground pipelines for inductive interference mitigation. *IEEE Transact Power Deliv* 35(3):1299–1309
9. Cai B, Shao X, Liu Y, Kong X, Wang H, Xu H, Ge W (2020) Remaining useful life estimation of structure systems under the influence of multiple causes: subsea pipelines as a case study. *IEEE Transact Industr Electron* 67(7):5737–5747



# Coupling Simulation and Experimental Verification of Partial Discharge Sound Field and External Optical Fiber in Insulation Air Gap of Cable Joint



Guo Tengjun , Qin Weiqi, Zhang Xiaolong, Wang Sihan, Hu Jing, and Ma Guoming

**Abstract** In this paper, the finite element model of the spike defect of the high-voltage conductor in the 10 kV cable joint is built, the propagation characteristics of the acoustic signal during the insulation air gap partial discharge are simulated, and the coupling function between the partial discharge acoustic wave of the cable joint and the external sensing fiber is established. The results indicate that for this type cable joint air gap partial discharge, it is most suitable to choose an external sensing fiber winding width of about 30 mm; When the external voltage of the cable joint is 19 kV and the partial discharge of the air gap defect is 250 pC, the maximum phase change of the corresponding sensing fiber is about 0.3 rad; The main component of sound waves received on optical fibers is within 2 kHz, and high-frequency signals rapidly decay. And a high-voltage testing system was built, and the phase change of the external optical fiber during partial discharge of the corresponding cable joint was measured using a coherent optical time-domain reflectometer. The correctness of the simulation results was verified through experiments. This analysis can provide basis for acoustic partial discharge detection of cable joints.

**Keywords** Cable joint · Partial discharge · Optical fiber · Acoustic wave · Cross-linked polyethylene

## 1 Introduction

Silicone rubber insulated prefabricated cable joints are currently the main type of medium and high voltage cross-linked polyethylene (XLPE) cable joints. However, during the production and installation process of prefabricated cable joints, there

---

G. Tengjun (✉) · Q. Weiqi · Z. Xiaolong · W. Sihan · H. Jing · M. Guoming  
State Key Laboratory of Alternate Electrical Power System With Renewable Energy Sources,  
North China Electric Power University, Beijing 102206, China  
e-mail: [guo.tengjun@foxmail.com](mailto:guo.tengjun@foxmail.com)

© Beijing Paiké Culture Commu. Co., Ltd. 2024  
X. Dong and L. Cai (eds.), *The Proceedings of 2023 4th International Symposium on Insulation and Discharge Computation for Power Equipment (IDCOMPU2023)*, Lecture Notes in Electrical Engineering 1103, [https://doi.org/10.1007/978-981-99-7413-9\\_46](https://doi.org/10.1007/978-981-99-7413-9_46)

are inevitably impurities or protrusions at the semiconductor layer, which can cause electric field concentration and insulation defects [1].

Partial discharge is an important characterization of insulation defects and one of the main reasons for insulation degradation. Therefore, partial discharge of measuring equipment can timely and accurately grasp the insulation status of equipment [2]. At present, the cable partial discharge detection methods mainly include pulse current method [3], ultra high frequency method [4], ultrasonic method [5], etc. Compared with electrical detection methods, ultrasonic detection method has strong anti electromagnetic interference ability and is very suitable for partial discharge detection of cables in complex electromagnetic environment.

In recent years, the research and application of distributed fiber optic sensing in the state detection of power cables have rapidly developed. In 2015, Rene Eisermann and Katerina Krebber, et al. of the German Federal Research and Test Institute for Materials, applied coherent optical time domain reflection (COTDR) to the partial discharge measurement of 40 kV cable intermediate joints, and successfully detected 1 nC level local emission signal [6]. In 2021, Xi'an Jiaotong University wound an optical fiber ring on the cable connector and detected 3.5 nC partial discharge signal in the experiment with COTDR [7]. The above research can indicate the broad application prospects of distributed fiber optic sensing technology in cable status detection. However, the coupling relationship between partial discharge acoustic wave and fiber deformation has not been concerned in the above research.

In terms of acoustic research on partial discharge, in 2015, Qi Weiqiang and others from Wuhan University established a transformer simulation model to study the propagation law and amplitude variation of local sound pressure in space [8]. In 2020, Hamidreza Karami et al. of the Swiss Federal Institute of Technology established a two-dimensional simulation model for transformers, using Gaussian pulses to simulate the inter turn partial discharge source of transformers [9]. In 2022, the Guoming Ma research group of North China Electric Power University simulated the radial propagation process of the partial discharge ultrasonic signal in the single-phase XLPE submarine cable, indicating that the strain of the fiber core caused by the partial discharge in the outer fiber unit is close to  $\mu\epsilon$  magnitude [10]. However, the middle joint of the cable differs from transformers, and submarine cables in terms of structural size, attenuation degree, etc. It is necessary to study the ultrasonic amplitude and characteristic frequency of the coupling of partial discharge sound waves from the cable joint to the optical fiber.

In order to understand the coupling relationship between the air gap partial discharge ultrasound of the cable joint and the external optical fiber, the finite element model of the high-voltage conductor spike defect of the cable joint was constructed in this paper. And a high-voltage testing system was built, and the phase changes of the external optical fibers during partial discharge of the corresponding cable joints were measured using a coherent optical time-domain reflectometer. Finally, the strain amplitude and characteristic frequency changes of the external optical fibers during partial discharge of the cable joints were obtained.

## 2 Acoustic Wave Propagation and Coupling Principle

### 2.1 Generation and Propagation of Partial Discharge Acoustic Waves

When an air gap occurs in the XLPE insulation medium of the cable joint, partial discharge may occur inside the air gap due to the concentration of field strength, and the heat generated by partial discharge will shrink and expand the air gap, eventually producing sound waves.

The calculation formula for sound waves on the air gap surface is:

$$\eta \cdot W_s = \frac{P_0^2}{\rho c} S \quad (1)$$

where  $S$  is the area where sound waves pass vertically, i.e. the circumferential area of the air gap ( $\text{m}^2$ ),  $\rho c$  is the acoustic impedance of the medium ( $\text{Pa} \cdot \text{s}/\text{m}$ ),  $P_0$  is the surface sound pressure of the air gap (Pa),  $\eta$  is the ratio of energy conversion from total partial discharge energy to sound wave energy,  $W_s$  is the power of the total energy of partial discharge,  $W_s = \frac{qU_s}{2t}$ ,  $q$  is the apparent discharge capacity (pC),  $U_s$  is the initial discharge voltage (V),  $t$  is the discharge duration (s).

When sound waves propagate in a medium, the absorption attenuation equation is:

$$P = P_0 \cdot e^{-\alpha d} \quad (2)$$

where  $P$  is the amplitude of the sound wave (Pa),  $P_0$  is the amplitude of the sound source sound wave (Pa),  $\alpha$  is the acoustic attenuation coefficient of the material (dB/m),  $d$  is the distance at which sound waves propagate in the medium (m).

The partial discharge acoustic wave of cable belongs to spherical wave. The farther the propagation distance is, the smaller its amplitude is. Its equation is:

$$P = \frac{P_0}{d} \quad (3)$$

When sound waves propagate to the interface of two media, refraction and reflection occur, and the equation is:

$$\begin{aligned} \alpha_{\text{transmission}} &= \frac{P_t}{P_i} = \frac{2Z_2}{Z_1 + Z_2} \\ \alpha_{\text{reflection}} &= \frac{P_r}{P_i} = \frac{Z_2 - Z_1}{Z_1 + Z_2} \end{aligned} \quad (4)$$

where  $P_i$  is the amplitude of the incident wave (Pa),  $P_t$  is the amplitude of the transmitted wave (Pa),  $P_r$  is the amplitude of the reflected wave (Pa),  $Z_1$  and  $Z_2$  are the wave impedance of two different media ( $Pa \cdot s/m$ ).

By combining the above equations, the propagation equation of the partial discharge sound wave from the cable joint partial discharge point to the external environment can be derived, and the sound pressure of each point on the propagation path of the partial discharge sound wave can be obtained.

## 2.2 Coupling of Sound Wave and Fiber Strain

The sound wave signal transmitted by the authorities through various layers can directly cause changes in the length (corresponding to the elastic deformation of the fiber) and refractive index (corresponding to the elastic optical effect of the fiber) of the sensing arm fiber in the interferometer, resulting in changes in the phase of the transmitted light in the fiber. The changes can be expressed as:

$$\frac{\Delta\varphi}{PL} = nk_0 \frac{2\mu}{E} + \frac{k_0}{2E} n^3 [(1 - \mu)P_{11} + (1 - 3\mu)P_{12}] \quad (5)$$

where  $P_{11}$  and  $P_{12}$  are the elastic optical coefficients of the optical fiber material,  $P$  is the sound pressure acting on the optical fiber (Pa),  $n$  is the refractive index of the optical fiber,  $k_0$  is the number of light waves,  $k_0 = 2\pi/\lambda$ ,  $\lambda$  is the wavelength of the light wave (m),  $E$  is the Young's modulus of the optical fiber (Pa),  $\mu$  is the Poisson's ratio of the optical fiber.

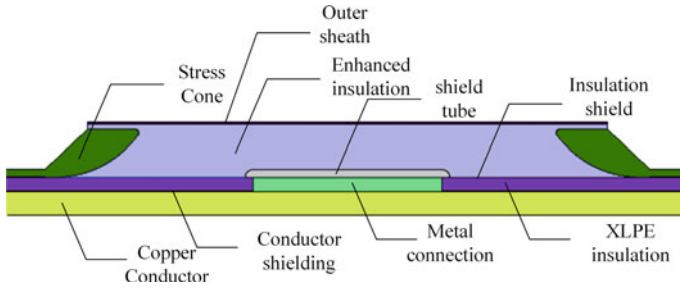
## 3 Ultrasonic Simulation of Air Gap PD in Cable Joints

### 3.1 Simulation Settings

This article takes the intermediate joint of JLS-10 kV fully cold shrinkable single core cable as the simulation object. The wire core cross-sectional area is 300 mm<sup>2</sup>, the conductor radius of 9.7 mm, the main insulation thickness of 5 mm, the joint length of 440 mm, and the silicone rubber insulation thickness of 13 mm. The overall structure is shown in Fig. 1.

Sound wave propagation in solid can be equivalent to stress wave, so the solid mechanics field simulation model of high-voltage cable intermediate joint is established.

To facilitate grid division, the conductor shielding layer and insulation shielding layer are classified as XLPE insulation layer. Due to the similarity in parameters between stress cones, shielding tubes, and reinforced insulation (silicone rubber)



**Fig. 1** Structural drawing of JLS-10 kV fully cold shrinkable single core cable joint

materials, they are considered as silicone rubber materials for simplified calculations. The structural materials and parameters of cable joints are shown in Table 1. The grid division is shown in Fig. 2.

Set an air gap defect with a radius of 0.5 mm in the XLPE insulation layer to simulate partial discharge acoustic signals. The Gaussian pulse is applied to the air gap boundary. The transfer function of the waveform is as follows:

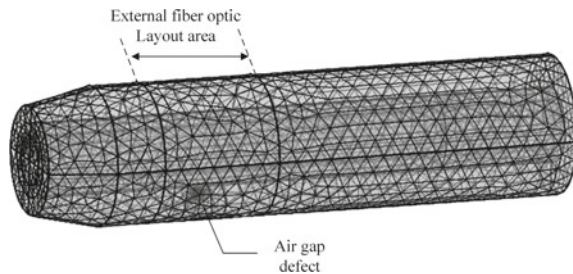
$$g(t) = \begin{cases} Ae^{-\pi^2 f_0^2 (t-\tau)^2}, & 0 < t < 2\tau \\ 0, & \text{else} \end{cases} \quad (6)$$

where  $A$  is the amplitude of the Gaussian pulse (Pa),  $f_0$  is the center frequency of the pulse (Hz),  $\tau$  is the time width of the pulse (s),  $\tau = 1/f_0$ .

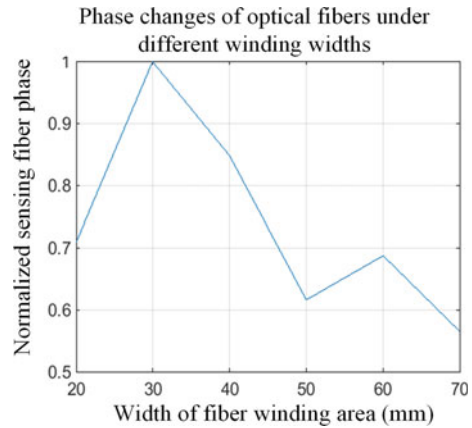
**Table 1** Acoustic parameters of cable joint materials

Material	Density	Poisson's ratio	Young's modulus
Copper	8630 kg/m <sup>3</sup>	0.35	127 GPa
XLPE	930 kg/m <sup>3</sup>	0.32	130 MPa
Silicone rubber	2230 kg/m <sup>3</sup>	0.45	1.95 MPa

**Fig. 2** Simulation grid diagram of fully cold shrinkable single core cable intermediate joint



**Fig. 3** Normalized phase change of optical fibers under different winding areas



### 3.2 Analysis of Simulation Results

The stress integral of the cylindrical outer surface of the cable joint directly above the partial discharge air gap is obtained, as shown in Fig. 2. Then, the related formulas are combined to obtain the phase change of the external sensing optical fiber.

(1)(1)(1) Analysis of the influence of different fiber winding areas on sensing fibers

When the external sensing fiber winding area changes from a width of 20 mm to a width of 70 mm, the maximum phase change is extracted, and the normalized phase of the fiber is shown in Fig. 3.

From this, it can be seen that for this type of cable joint air gap partial discharge, it is most suitable to choose an external sensing fiber winding width of about 30 mm.

(2)(2)(2) Correspondence between PD and phase of external sensing optical fibers

When the applied voltage of the cable joint is 19 kV and the local discharge of the air gap defect is 250 pC, the simulated phase time-domain waveform of the external sensing fiber is shown in Fig. 4.

From Fig. 4, it can be seen that when the external voltage of the cable joint is 19 kV and the local discharge of the air gap defect is 250 pC, the maximum phase change of the corresponding sensing fiber is around 0.3 rad, reaching its maximum value at 2 ms.

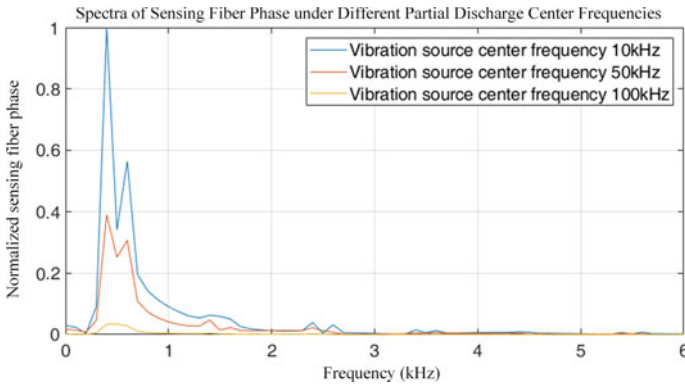
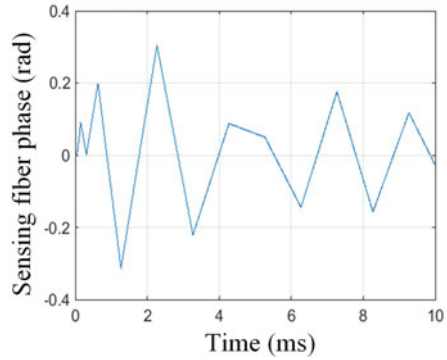
(3)(3)(3) Different partial discharge center frequencies

When the center frequencies of Gaussian partial discharge pulses are 10, 50, and 100 kHz, the fast Fourier transform spectrum of the sensing fiber phase is shown in Fig. 5.

Analysis of the spectrum shows that the main component of the frequency of the sound waves received on the optical fiber is within 2 kHz, and the high-frequency signal rapidly decays.

**Fig. 4** Simulated phase waveform of external sensing optical fiber

Simulated phase of external sensing optical fibers placed in the air gap of cables joints



**Fig. 5** Spectra of sensing fiber phase under different partial discharge center frequencies

### 4 Partial Discharge Sensing Experiment

The experimental arrangement of using the COTDR sensing system to detect the acoustic signal of cable joint partial discharge fault is shown in Fig. 6.

AC partial discharge test circuit is composed of power frequency test transformer ( $V$ ), protection resistance ( $R$ ) and coupling capacitance ( $C$ ). A high voltage conductor spike defect was artificially set inside the tested cable joint.

The external fiber optic ring is a single mode optic fiber with only a core and coating structure, wound at a specific position on the outer surface of the cable joint, just below which is the top of the high-voltage conductor spike. The phase disturbance on the optical fiber can be demodulated from the fluctuation of optical power, thereby detecting the partial discharge acoustic signal.

When the test voltage increases by 19 kV, the system generates repetitive partial discharge signals, with an average partial discharge of 250 pC. The COTDR sensing

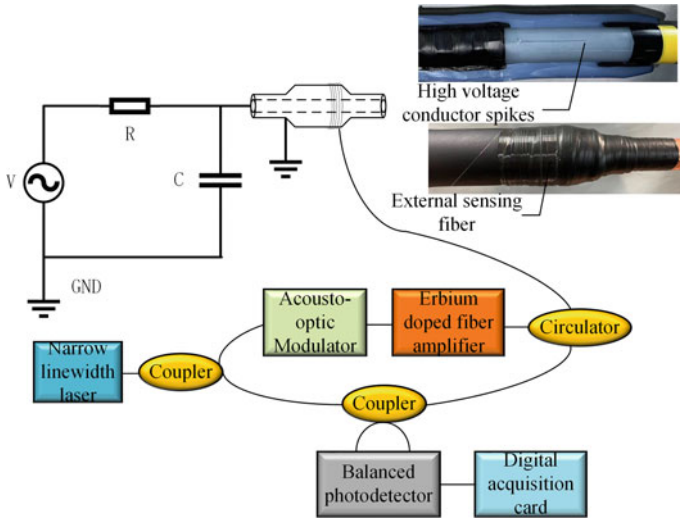


Fig. 6 Experimental arrangement for detecting PD faults in cable joint using COTDR system

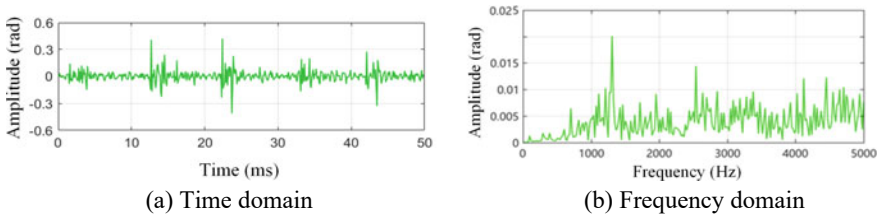


Fig. 7 Waveform of COTDR system for detecting PD faults in cable joints

system can observe obvious signals, and the demodulated phase time-domain and frequency-domain waveforms are shown in Fig. 7.

It can be seen from Fig. 7 that when partial discharge occurs to the prick defect of the high-voltage conductor, the maximum phase value of the external sensing optical fiber at the middle connector of the cable is about 0.3 rad, and the main component of the acoustic wave received is within 2 kHz.

It can be seen that the correctness of the simulation results has been verified through experiments. The reason for the difference in the high-frequency part is that the real partial discharge source and the simulated air gap partial discharge source cannot fully correspond, and the experimental measurement signal is prone to noise interference.



## 5 Conclusions

The results indicate that for this type of cable joint air gap partial discharge, it is most suitable to choose an external sensing fiber winding width of about 30 mm; When the external voltage of the cable joint is 19 kV and the partial discharge of the air gap defect is 250 pC, the maximum phase change of the corresponding sensing fiber is about 0.3 rad; The main component of sound waves received on optical fibers is within 2 kHz, and high-frequency signals rapidly decay. The correctness of the simulation results was verified through experiments. This analysis can provide basis for acoustic partial discharge detection of cable joints.

**Acknowledgements** This work was funded by Key Funding Project of Beijing Natural Science Foundation (3222058), Key Funding Project for Basic Research Business Fees of Central Universities (2022YQ003).

## References

1. Chang W, Li C, Su Q, Ge Z (2013) Study on the development process of partial discharge caused by sharp defects in cable joints. *Chin J Electr Eng* 33(7):192–201 (in Chinese)
2. Zhou Y, Zhao J, Liu R, Chen Z (2014) Analysis and prospect of key technologies for high voltage/ultra high voltage power cables. *High Voltage Technol* 40(9):2593–2612 (in Chinese)
3. Ilkhechi HD, Samimi MH (2021) Applications of the acoustic method in partial discharge measurement: a review. *IEEE Trans Dielectr Electr Insul* 28(1):42–51
4. Hicke K, Krebber K (2017) Towards efficient real-time submarine power cable monitoring using distributed fibre optic acoustic sensors. In: 2017 25th optical fiber sensors conference (OFS). IEEE, pp 1–4
5. Wijaya H, Rajeev P, Gad E (2021) Distributed optical fibre sensor for infrastructure monitoring: field applications. *Optical Fiber Technol* 64:102577
6. Rohwetter P, Eisermann R, Krebber K (2015) Distributed acoustic sensing: towards partial discharge monitoring. In: 24th International conference on optical fibre sensors, vol 9634. SPIE, pp 125–128
7. Chen H, Xu Y, Qian S et al (2021) Distributed fiber optic ultrasonic sensors are used to detect discharge faults in cable joints. *J Opt* 41(3):0306001 (in Chinese)
8. Qi W, Li J, Chen B et al (2015) Ultrasonic propagation characteristics in transformers based on COMSOL. *J Electrotech (S2)*:195–200 (in Chinese)
9. Karami H, Rachidi F, Azadifar M et al (2020) An acoustic time reversal technique to locate a partial discharge source: two-dimensional numerical validation. *IEEE Trans Dielectr Electr Insul* 27(6):2203–2205
10. Guo Z, Han D, Qin W et al (2022) Simulation study on the radial propagation process of partial discharge ultrasonic signals in single-phase XLPE submarine cables. *High Voltage Electr Appl* (in Chinese)

# Analysis of Safety for UAV Inspection of Electric Field in 220 kV Substation



Duanjiao Li, Ying Zhang, Yun Chen, Wenxing Sun, Ziran Jia, Wensheng Li, Lin Yi, and Yingyi Yang

**Abstract** As an emerging method of substation inspection, when unmanned aerial vehicle (UAV) is too close to the substation during the inspection process, it can cause interference to its normal operation, causing damage to the internal electrical structure of the drones or discharges. In order to analyze the safety of UAV substation inspection, we construct a simplified electric field simulation model for UAV and 220 kV substation, and use finite element method to simulate and analyze the changes in their electric field. The UAV inspection methods are divided into three types: UAV traverse insulation intervals for inspection, UAV conduct inspections near wires, and UAV patrol above insulation intervals, the variation of maximum surface field strength of unmanned aerial vehicles under three inspection methods is simulated and calculated separately. The maximum surface electric field strength of the UAV during the UAV conduct inspections near wires is 768 kV/m, less than air breakdown field strength (3000 kV/m). As a result, under the condition of only considering the influence of electric field, UAV is safe under these three inspection methods.

**Keywords** UAV inspection · 220 kV substation · Safety of electric field

## 1 Introduction

The traditional substation inspection is mainly based on manual inspection, relying mainly on the subjective judgment and experience of operation and maintenance personnel. Therefore, the traditional manual inspection is costly, inefficient and error-prone, and has failed to meet the needs of today's stability of substations [1]. The inspection method in some substations has been changed from traditional manual

---

D. Li · Y. Zhang · Y. Chen · W. Sun · Z. Jia  
Guangdong Power Grid Co. Ltd., Guangzhou 510080, China

W. Li (✉) · L. Yi · Y. Yang  
Guangdong Engineering Technology Research Center of Special Robots for Special Industries,  
China Southern Power Grid Technology Co. Ltd., Guangzhou 510080, China  
e-mail: [liwens@hotmail.com](mailto:liwens@hotmail.com)

inspection to intelligent robot inspection, which makes substation operation and maintenance more accurate and efficient [2]. However, the traditional intelligent robots have low vision and fixed inspection paths, and the distribution of each power equipment in the substation is very concentrated, so there are inevitably a series of visual blindness problems such as visual occlusion, which bring serious problems to the intelligent robots' inspection [3]. UAVs have the advantages of strong flight flexibility, high inspection efficiency and close observation distance, so the use of UAVs for inspection work in substations can well solve these problems [4].

As a highly integrated communication device, the UAV has many internal electromagnetic components, and the electromagnetic environment inside the substation is very complex, and the UAV will bring interference to the normal operation of the UAV when it is close to the substation for inspection [5], which may cause damage to the internal electrical structure of the UAV or discharge, and the occurrence of accidents such as "blowing up" and "hitting the tower" is increasing day by day with the expansion of UAV inspection operations.

For UAV inspection and substation inspection, domestic and foreign scholars have done various researches. Shen Y et al. propose an automatic framework for pylon detection by a hierarchical coarse-to-fine segmentation of powerline corridors from UAV laser scanning point clouds [6]. Wang et al. propose the design of a trackless robot with a robotic arm that can perform autonomous inspections in narrow and complex indoor substations [7]. Liu et al. analyze the electromagnetic field distribution around the drone inspection by establishing an electromagnetic simulation model of unmanned inspection of  $\pm 500$  kV DC transmission lines, and determined the safety distance when the drone inspected  $\pm 500$  kV DC transmission lines by combining the corresponding UAV inspection tests with the domestic safety technology of UAV inspection [8].

At present, people's research on substation inspection is mainly focused on inspection robots [9], and the research on drone inspection is mainly focused on transmission line inspection [10]. UAV substation inspection does not yet have more systematic and perfect safety inspection measures and programs, and operators can only guarantee the safety of UAV inspection operations based on the minimum safety distance and operating experience of UAV operations during line inspection. In this paper, by establishing the electric field simulation model of 220 kV substation drone inspection, the surface electric field distribution when the drone is located in different positions is calculated by finite element simulation, and then the safety of UAV inspection of 220 kV substation is derived.

## 2 Methods and Models

### 2.1 Finite Element Method

In this paper, finite element simulation is used to calculate the electric field of a 220 kV substation inspected by a UAV. The finite element method is a numerical calculation method based on the variational principle and the difference of profiles. Instead of solving the field directly, the finite element method uses the variational principle to transform the solved edge value problem into a variational problem taking extreme values, and derives the corresponding general function expressions by the variational method. The main steps of the solution using the finite element method are as follows:

- (1) Segmentation: The geometric object to be solved is partitioned and discrete into multiple small regular units. 3D solutions are generally divided into tetrahedra or polyhedra, and the fixed points of each unit are defined as nodes;
- (2) Cell analysis: the unknown function of any point in the segmentation cell is expanded with the shape function in the segmentation cell and the value of the function on the discrete grid points, that is, to establish a linear interpolation function;
- (3) Solution equation: The set of field functions formed by the division of multiple cells represents the field function of the object of study. Then according to the energy equation or weighted residual equation can be established a finite set of algebraic equations of the parameters to be determined, solve this discrete set of equations to obtain an approximate numerical solution.

### 2.2 UAV and 220 kV Substation Simulation Model

The research elephant in this paper is a quadrotor UAV manufactured by DJI, model Genie Phantom 4 Pro V2.044. The physical diagram and the simulation model is shown in the Fig. 1. The main components of the UAV are the fuselage, the four motors and wings, the landing gear, the integrated gimbal camera, and the control module inside the fuselage. The length of the UAV (including the wing spread) is 40 cm, the width is 30 cm, the height is 20 cm, and the wing length is 12 cm. According to the object for which the electric field distribution is to be calculated, the composition of the UAV is simplified by ignoring the screws, nuts, and other small parts on the UAV, and the UAV is made solid. According to the actual material composition of the UAV, the composition materials of the fuselage, wings and landing gear of the UAV are set as high dielectric materials, and the relative dielectric constant is set as 7. The four motors, the integrated gimbal camera and the internal control module of the UAV are set as metal materials, and the relative dielectric constant is set as 1.



**Fig. 1** Physical and simulation model drawings of the UAV

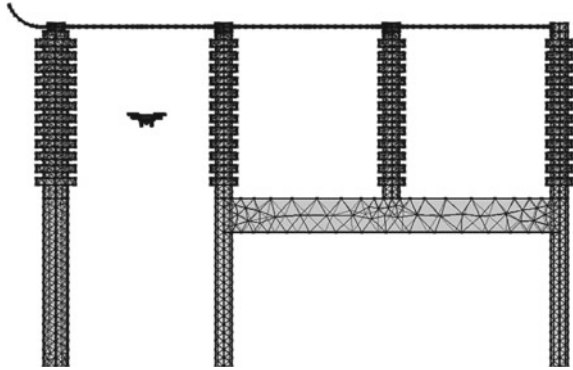
Considering that the electric field generated by the transmission conductor of the substation has a limited range of influence on the UAV, a part of it is selected as the simulation model of the substation, and the physical diagram of the selected 200 kV substation is shown in Fig. 2. The selected conductor is a one-phase conductor, the known line voltage is 220 kV, according to the symmetrical three-phase power supply, the relationship between phase voltage and line voltage, the maximum value of phase voltage on the conductor is taken as 179.6 kV. the cross-sectional area of the conductor is taken as 300mm<sup>2</sup>, the radius of the conductor is derived as 9.97 mm according to the formula  $S = \pi r^2$ , and the relative dielectric constant of the conductor is taken as 1. The isolation switch is seen as a closed and state, and the voltage on it is the same as the wire voltage. The insulator is a porcelain insulator with a relative dielectric constant of 2.6. The total length of the insulator string is 2 m. The height of the concrete column below is also 2 m. Since there is a wire grounded inside, it is treated as a grounded body with zero potential in the simulation calculation. The horizontal spacing of the two insulated columns is taken as 2 m, and the overall height of the conductor is about 4 m. Then the simulation model of the whole substation plus a large rectangular body as the air domain, the relative dielectric constant is set to 1.

After both models are successfully constructed, import the UAV into the substation model, pay attention to adjusting the corresponding ratio between the UAV and the substation, and after the corresponding electrostatic parameters are set, carry out grid dissection to obtain the computational model dissection shown in Fig. 3.

**Fig. 2** Physical drawings of the 220 kV substation



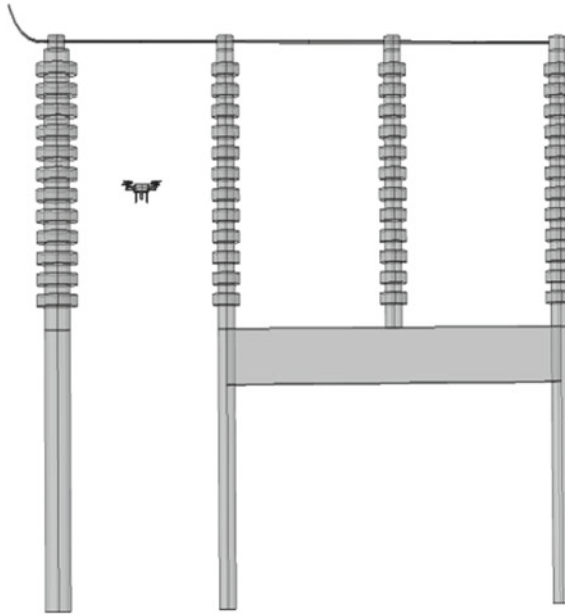
**Fig. 3** Simulation model profile of 220 kV substation UAV inspection



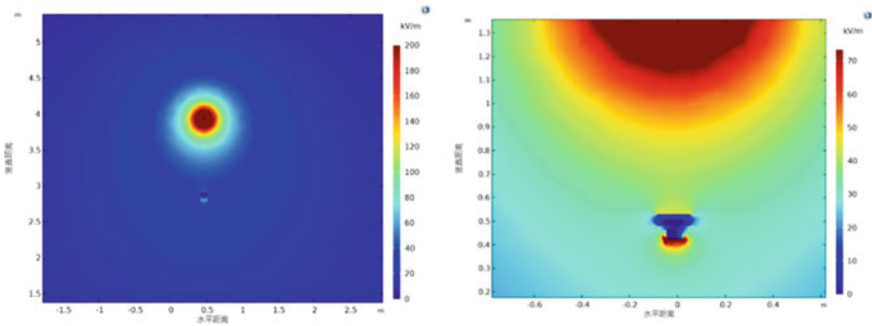
### 3 Calculation

The initial position of the drone machine across the insulated pillar inspection is shown in Fig. 4. The vertical distance between the drone and the ground is 3 m, and the vertical distance of the wire directly above is 1 m, in the middle of the two insulated pillar interval, simulation calculations to derive the electric field distribution around the wire cloud and local amplification of the electric field distribution near the drone as shown in Fig. 5, from the figure can be clearly seen that the field strength generated by the transmission line at the drone has Clear distortion at the UAV. Change the horizontal distance between the UAV and the insulated column in the order of 0, 0.5, 1, 1.5, 2, 2.5, 3, 3.5, 4 m for simulation calculations, and take out the change of the maximum field intensity on the surface of the UAV as shown in Table 1 and Fig. 6. It can be seen that when the UAV carries out inspection through the insulated pillar, the distance between the UAV and the insulated pillar is 0.5 m, and the maximum field strength on the surface of the UAV is 235 kV/m.

The initial position of the UAV near the wire inspection is shown in Fig. 7. The UAV is 4 m away from the ground and 0.5 m away from the wire, in the middle of the two insulated pillar interval, and the simulation calculation yields the electric field distribution near the UAV as shown in Fig. 8. We change the horizontal distance between the UAV and the wire in order for 0.5, 1, 1.5, 2, 2.5, 3, 3.5, 4 m, carry out the simulation calculation to obtain the change of the maximum field strength on the surface of the UAV as shown in Table 2 and Fig. 9. Shows. It can be seen that when the UAV is close to the transmission conductors for inspection, the maximum field strength on the surface of the UAV is 768 kV/m.



**Fig. 4** The initial position of the UAV when crossing the insulated interval for inspection



**Fig. 5** Electric field distribution around the UAV

**Table 1** The maximum electric field intensity on the surface of UAV

Horizontal distance (m)	0	0.5	1	1.5	2	2.5	3	3.5	4
Maximum electric field intensity (kV/m)	185.0	235.0	221.0	182.0	143.0	106.0	82.0	67.2	56.0

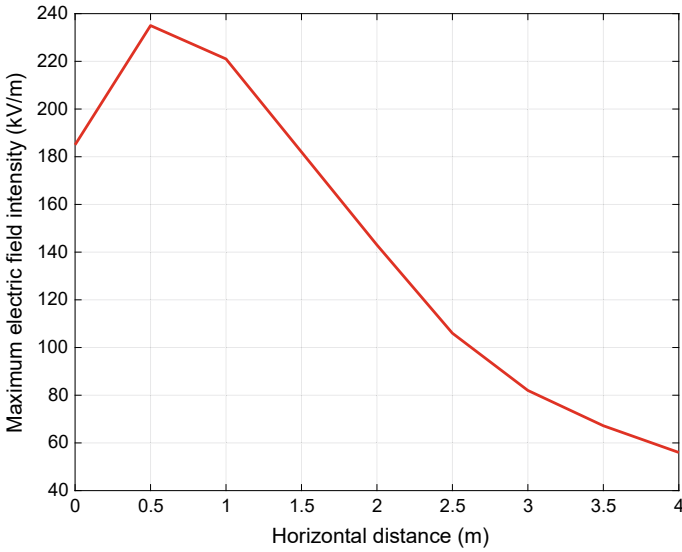


Fig. 6 The maximum electric field intensity on the surface of the UAV with distance

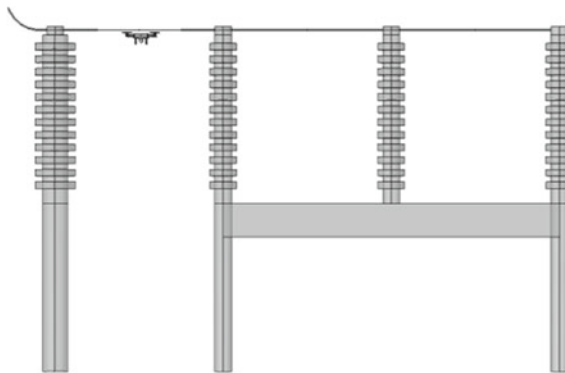


Fig. 7 The initial position of the UAV when close to the transmission conductor inspection

The initial position of the UAV inspecting above the insulation interval is shown in Fig. 10, which is 5 m away from the ground and 1 m away from the wire, located in the middle of the insulation interval, and the electric field distribution near the UAV is calculated by simulation as shown in Fig. 11. We change the height of the UAV above the wire in the order of 1, 1.5, 2, 2.5, 3, 3.5, 4 m, carry out the simulation calculation to obtain the maximum field strength of the UAV surface. The variations are shown in Table 3 and Fig. 12. It can be seen that when the UAV conducts inspection near the wire, when the UAV is 1 m above the wire, the maximum field strength of the UAV surface is 149 kV/m.



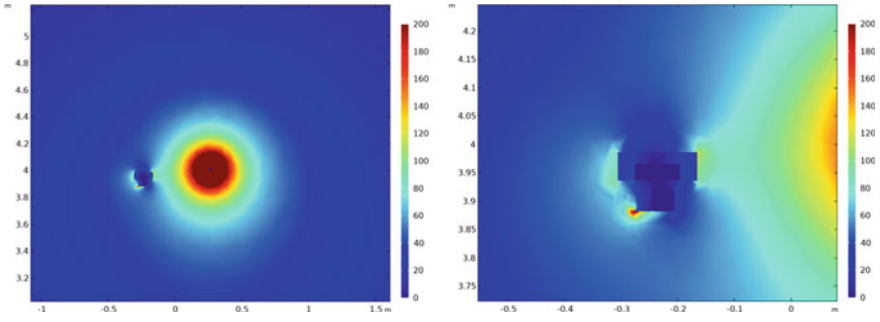


Fig. 8 Electric field distribution around the UAV

Table 2 The maximum electric field intensity on the surface of UAV

Horizontal distance (m)	0.5	1	1.5	2	2.5	3	3.5	4
Maximum electric field intensity (kV/m)	768.0	364.0	218.0	156.0	109.0	83.0	73.5	67.0

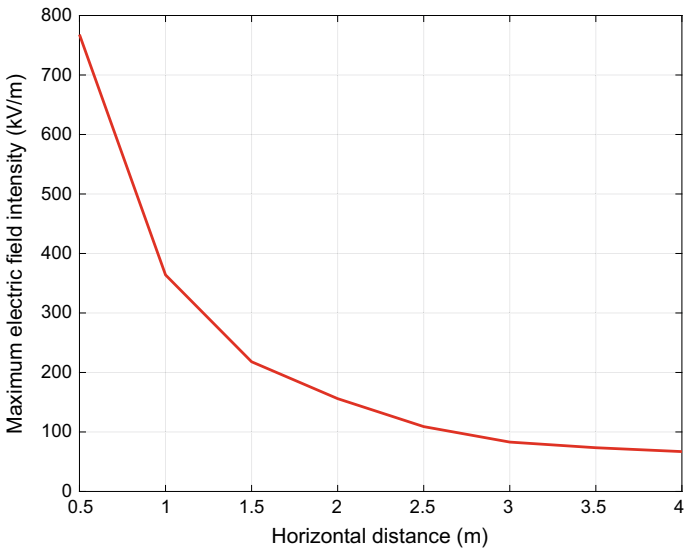
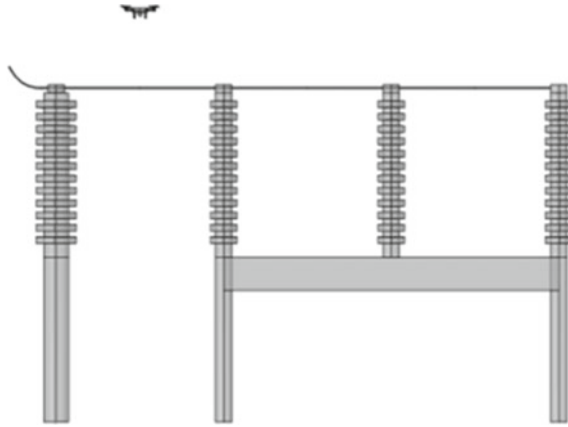
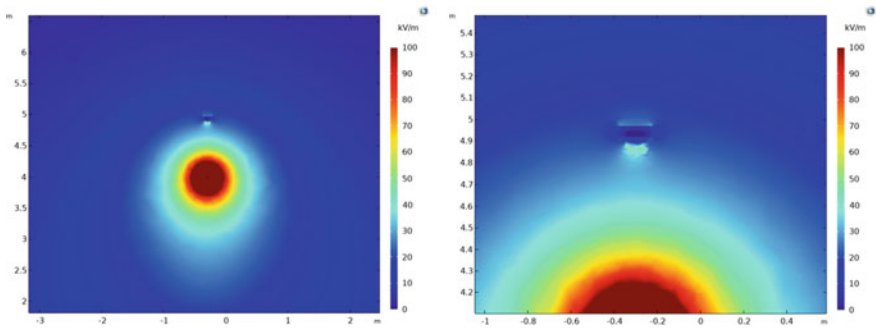


Fig. 9 The maximum electric field intensity on the surface of the UAV with distance



**Fig. 10** The initial position of the UAV during the inspection patrol above the insulation interval

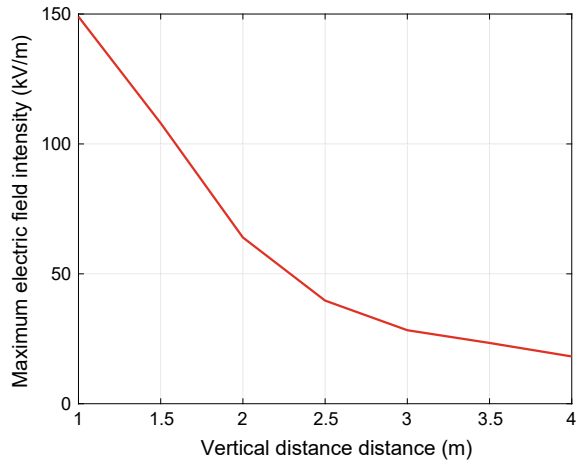


**Fig. 11** Electric field distribution around the UAV

**Table 3** The maximum electric field intensity on the surface of UAV

Vertical distance (m)	1	1.5	2	2.5	3	3.5	4
Maximum electric field intensity (kV/m)	149.0	108.0	64.0	39.7	28.3	23.4	18.2

**Fig. 12** The initial position of the UAV during the inspection patrol above the insulation interval



## 4 Conclusion

In this paper, we analyze the electric field distribution of the UAV in substation inspection operation, and simulate and calculate the electric field distribution of the UAV in three inspection modes: UAV crossing insulated pillar operation, UAV near conductor operation and operation above insulated pillar interval. In the three inspection methods, when the UAV is near the conductor, the maximum field strength of the UAV surface is 768 kV/m, which is smaller than the air breakdown field strength of 3000 kV/m. Under the condition that only the electric field influence is considered, the UAV is safe in the above three inspection methods.

**Acknowledgements** This work was financially supported by the China Southern Power Grid Corp funded science and technology project (GDKJXM20220879).

## References

1. Li MZ, Wang YP, Li XW, Wang F, Cai WF (2010) Analysis of intelligent substation and its technical characteristics. *Power Syst Prot Control* 38(18):59–62 (in Chinese)
2. Dong L, Chen N, Liang J et al (2023) A review of indoor-orbital electrical inspection robots in substations. *Ind Rob Int J Rob Res Appl* 50(2):337–352
3. Li J, Wang H, Zhao Y et al (2019) Application research of artificial intelligent technology in substation inspection tour. In: 8th joint international information technology and artificial intelligence conference. IEEE, Chongqing, pp 1097–1100
4. Zhang Y, Yuan X, Li W et al (2017) Automatic power line inspection using UAV images. *Remote Sens* 9(8):824
5. Zhang W, Ning Y, Suo C (2019) A method based on multi-sensor data fusion for UAV safety distance diagnosis. *Electronics* 8(12):1467

6. Shen Y, Huang J, Chen D et al (2023) An automatic framework for pylon detection by a hierarchical coarse-to-fine segmentation of powerline corridors from UAV LiDAR point clouds. *Int J Appl Earth Obs Geoinf* 118:103263
7. Wang C, Yin L, Zhao Q et al (2020) An intelligent robot for indoor substation inspection. *Ind Rob Int J Rob Res Appl* 47(5):705–712
8. Liu Z, Du Y, Chen Y et al (2019) Simulation and test of safe distance for UAV inspection of  $\pm 500\text{kV}$  DC transmission line straight tower. *High Voltage Technol* 45(02):426–432 (in Chinese)
9. Zhang H, Su B, Song H et al (2015) Development and implement of an inspection robot for power substation. In: 2015 IEEE intelligent vehicles symposium (IV). IEEE, Seoul, pp 121–125
10. Deng C, Wang S, Huang Z et al (2014) Unmanned aerial vehicles for power line inspection: a cooperative way in platforms and communications. *J Commun* 9(9):687–692

# Research on Electric Field Safety Distance of High-Voltage Equipment in Substations Inspected by UAV



Ying Zhang, Duanjiao Li, Yun Chen, Gao Liu, Daoqing Fan, Wensheng Li, Liqiang Zhong, and Xiaoming Mai

**Abstract** UAVs have the advantages of close observation, eliminating visual dead space, improving inspection speed and carrying a variety of inspection equipment in substation equipment inspection, which meet the needs of intelligent substation construction. But the complex electromagnetic environment in the substation, it is easy to cause electromagnetic interference to the UAV, while the UAV into the strong electric field environment there is also the possibility of triggering discharge. In this paper, we take the Genie 4 UAV commonly used for substation inspection as the research object, and study the safety distance when the UAV inspects the high-voltage equipment in the substation. By constructing the simulation model of the UAV and 220 kV substation, we simulate and calculate the electric field distribution when the UAV inspects different high-voltage equipment. Finally, the safety distance of the UAV inspection of high-voltage equipment in substations is analyzed by the simulation results, and provides data support for the subsequent research.

**Keywords** UAV inspection · High-voltage equipment · Safety distance

## 1 Introduction

After a long period of operation, the high-voltage equipment in the substation will have insulation aging damage, temperature abnormalities and other faults. But the equipment in the substation is dense, the conventional manual inspection speed is slow, labor-intensive, cannot achieve efficient and high-quality inspection of equipment fault defects [1]. As China continues to comprehensively promote the construction of intelligent power grid, the construction of intelligent substations is also

---

Y. Zhang · D. Li · Y. Chen · G. Liu · D. Fan  
Guangdong Power Grid Co. Ltd., Guangzhou 510080, China

W. Li (✉) · L. Zhong · X. Mai  
Guangdong Engineering Technology Research Center of Special Robots for Special Industries,  
China Southern Power Grid Technology Co. Ltd., Guangzhou 510080, China  
e-mail: [liwens@hotmail.com](mailto:liwens@hotmail.com)

steadily moving forward. The traditional substation inspection has been gradually replaced by the more automated and intelligent substation robot inspection [2]. However, the inspection perspective of the inspection robot is low, and the high-voltage equipment in the substation is dense and complex, leading to the inspection path of the robot has great limitations, and it is easy to have a blind spot, which affects the normal inspection work of the substation. In recent years, UAVs have been widely used in various industries by virtue of their high mobility and delicate airframe. UAVs have the advantages of close observation, eliminating visual dead spots, improving inspection speed and carrying a variety of inspection equipment in substation equipment inspection, which successfully solves the problems of traditional manual inspection and intelligent robot inspection [3]. However, the complex electromagnetic environment in the substation is easy to cause electromagnetic interference to the UAV, and there is also the possibility that the UAV enters the strong electric field environment to cause discharge [4]. In modern power systems, especially in high-voltage substations, the problem of electromagnetic safety is particularly prominent.

At present, a variety of studies have been conducted for the application of UAV inspection technology on transmission lines, and UAV line inspection technology has become mature and gradually applied UAV inspection technology to the construction of intelligent substations. Chen Dequan et al. established a finite element model for simulating the electromagnetic field of 500 kV catenary tower UAV inspection operation, combined with the average breakdown field strength of the bar-plate gap and the UAV electromagnetic compatibility limit to comprehensively determine the safety distance of UAV inspection in view of the widespread application of UAV (unmanned aerial vehicle) in transmission line inspection [5]. Carla Nardinocchi et al. proposed a new algorithm applied to fully automated point cloud analysis of transmission line corridors, enabling UAVs to automatically detect obstacles in transmission corridors [6]. Zheng et al. proposed a safety distance prediction formula using the tolerance values of electric and magnetic fields of UAV susceptible devices as the limit values, and conducted an example simulation analysis of the frequency electric and magnetic fields generated by 500 kV transmission lines [7]. Huang et al. conducted an electric field simulation study on the insulation level of typical 110 kV equipment gaps inspected by UAVs using electromagnetic field simulation software, which can provide reference for the distance control and path planning of UAV inspections in substations [8].

In general, the current research on the application of UAV inspection mainly focuses on the problems encountered by UAVs in transmission line inspection, such as the safety of UAV inspection, how to improve the autonomy of UAV inspection, and there is not too much in-depth research on the various problems encountered by UAVs in substation inspection, and there is a lack of test basis and mature safety distance setting methods [9, 10]. In this paper, by establishing the simulation calculation model of UAV and 220 kV substation, we studied the safety distance when UAV inspects different high-voltage equipment in 220 kV substation under the influence of substation electric field, and the research results can be used as a reference for the

safety distance of UAV inspection operation in substation, to promote the process of intelligent substation, and also to provide data support for the subsequent research.

## 2 Principle and Model

### 2.1 Principle of Electrostatic Field Simulation

In this paper, finite simulation software is used to analyze the change of electric field when the UAV inspects the substation. 220 kV substation generates an industrial frequency electric field with frequency ( $f$ ) of 50 Hz, and since the substation conductor length  $L$  is much less than  $6 \times 10^8$  m, it satisfies the static condition:

$$L \cdot f \ll c \tag{1}$$

where  $c$  is the electromagnetic wave propagation speed  $3 \times 10^8$  m/s. Therefore, we can regard the time-varying electric field generated by the substation as an electrostatic field. The electrostatic field is an active spinless field, satisfying Gauss's law, while introducing a scalar potential  $\varphi$  to represent the electric field strength:

$$\nabla \cdot \mathbf{D} = \rho \tag{2}$$

$$\mathbf{E} = -\nabla\varphi \tag{3}$$

where  $\mathbf{E}$  is the electric field strength,  $\mathbf{D}$  is the potential shift field. When the free charge density in the field is 0, the potential satisfies Laplace's equation:

$$\nabla^2\varphi = 0 \tag{4}$$

The corresponding Dirichlet boundary condition:

$$\varphi_{\text{line}} = V_{\text{line}} \tag{5}$$

$$\varphi_{\text{earth}} = \varphi_{\infty} = \varphi_{\text{tower}} = 0 \tag{6}$$

$\varphi_{\text{line}}$  is the transmission line potential,  $V_{\text{line}}$  is the transmission line voltage.  $\varphi_{\text{earth}}$  is the potential of the ground,  $\varphi_{\infty}$  is the potential at infinity, and  $\varphi_{\text{tower}}$  is the potential of the cement column, all of which are 0. The electric field distribution around the wire can be characterized by solving the above equations.



**Fig. 1** The physical and simulation models of UAV

## 2.2 Simulation Model

Small rotary-wing UAVs are often used in substation inspection. The small rotary-wing UAV selected in this paper is the Genie 4 UAV shown in Fig. 1, which is small in size, has high navigation accuracy and flexible flight operation, and is suitable for inspection in a narrow substation. The size of the Genie 4 UAV is  $270 \times 150 \times 90$  mm, mainly consisting of the fuselage, four motors and wings, landing gear, and an integrated gimbal camera. The simulation model shown in Fig. 1 is built by simplifying and solidifying the Genie 4 UAV.

The establishment of substation geometry model. Referring to the typical design of 220 kV substation, 220 kV substation generally includes 220 kV switchyard and 110 kV switchyard. Considering to ensure the electromagnetic safety of the UAV, we focus here on the electromagnetic field distribution when the UAV conducts inspection in the 220 kV switchyard. In order to simplify the calculation, the bus bar and the connecting line between the equipment are uniformly treated as a single conductor, equivalent to a finite length of a straight line segment or an arc segment connected to the composition, without considering any loss generated on the line. The main consideration is the external electromagnetic field generated by the conductors and high-voltage equipment in the station, so the internal structure of the high-voltage equipment can be simplified. Due to the very good shielding effect of the shell of the main transformer box, the external electromagnetic field generated is very small, and the electric field strength at a distance of about 1.5 m from the main transformer is less than 5 kV/m. When studying the electromagnetic field distribution in the substation, the effect of transformers and some components such as frames in the substation is ignored.

Based on the above simplification principle, a simulation model of 220 kV substation is established. The substation one-phase line is simplified to the transmission conductor through the disconnecting switch, current transformer, circuit breaker, voltage transformer and lightning arrester line as shown in Fig. 2. The final simulation model grid profile is established as shown in Fig. 3.



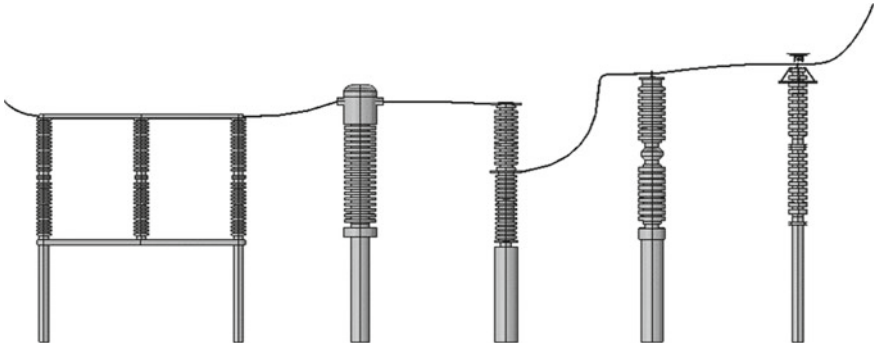


Fig. 2 The simulation models of 220 kV substation

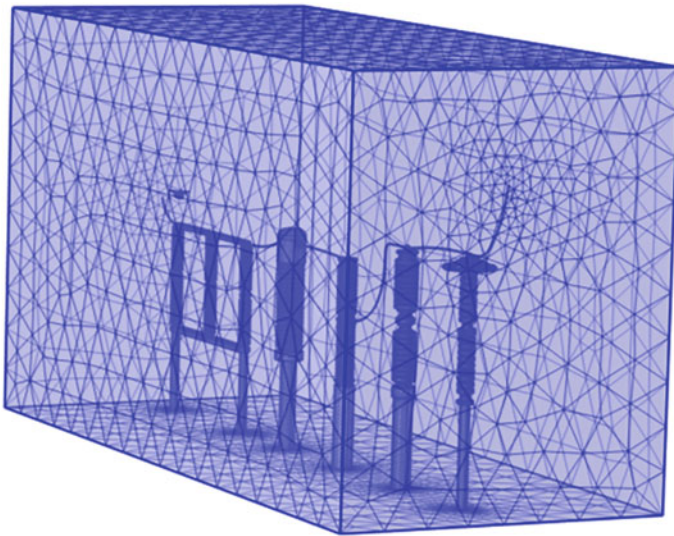


Fig. 3 The simulation model mesh profile

### 3 Simulation

When the UAV conducts substation inspection in accordance with the proximity inspection, it mainly inspects the single-phase high-voltage equipment, taking into account the limited range of influence of the electric field generated by the one-phase conductors in the substation, so the substation can be viewed as a single-phase line, and the corresponding inspection route can be simplified as shown in Fig. 4. In the proximity inspection route, the UAV flies at the same height as the transmission conductor, and the UAV keeps approaching the transmission conductor and high-voltage equipment during the flight.

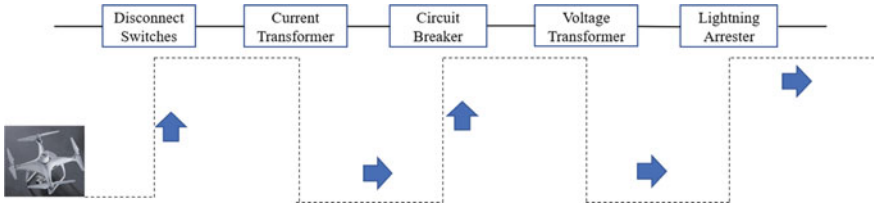


Fig. 4 The UAV inspection route diagram

The initial position of the UAV is located at the first insulated pillar of the disconnecting switch as shown in Fig. 5, keeping the horizontal distance between the UAV and the high-voltage equipment unchanged, the UAV flies from the disconnecting switch to the lightning arrester in turn, and gets the UAV and the high-voltage equipment distance of 0.5 m, the UAV surface field strength cloud map and the nearby field strength aberration map as shown in Figs. 6, 7, 8, 9, 10, 11 and 12.

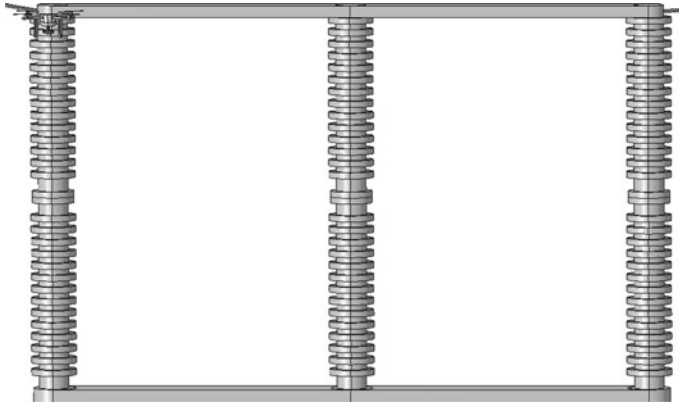


Fig. 5 The initial position of the UAV

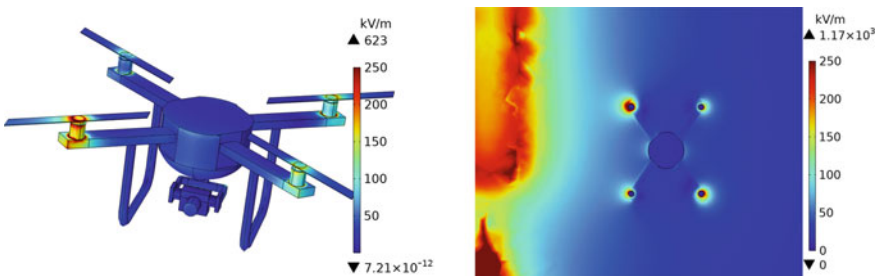


Fig. 6 The electric field distribution cloud map when the UAV inspects the first insulated pillar of the disconnect switch

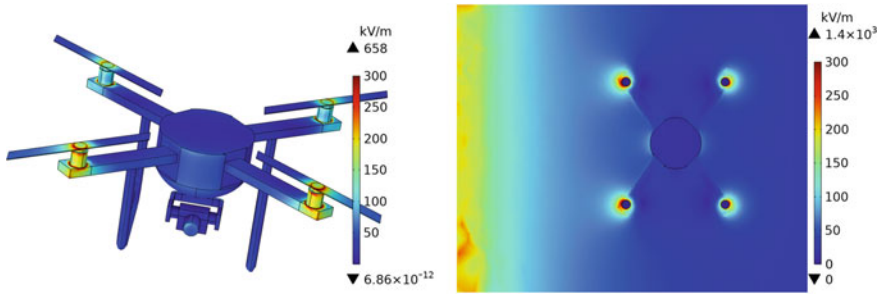


Fig. 7 The electric field distribution cloud map when the UAV inspects the second insulated pillar of the disconnect switch

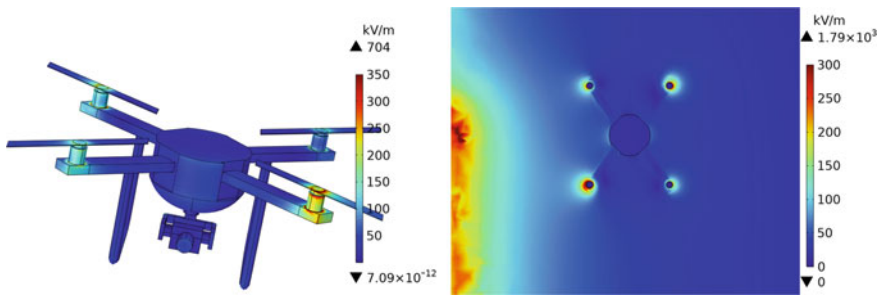


Fig. 8 The electric field distribution cloud map when the UAV inspects the third insulated pillar of the disconnect switch

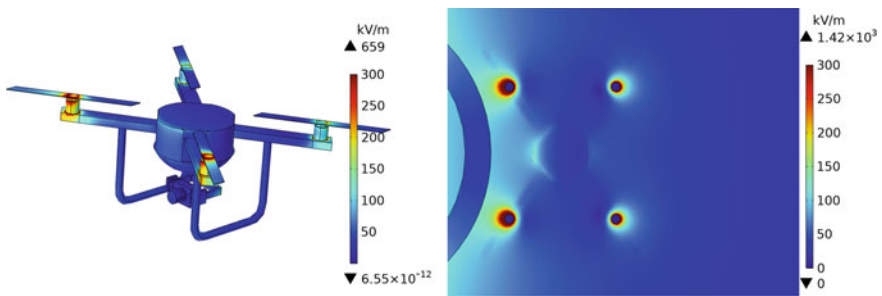


Fig. 9 The electric field distribution cloud map when the UAV inspects the current transformer

From Figs. 6, 7, 8, 9, 10, 11 and 12, it can be seen that the surface electric field distribution of the Genie 4 UAV during the inspection process is mainly concentrated near the four motors of the UAV and the center part of the four wings. The size of the distortion field in the space around the UAV is mainly between 100 and 300 kV/m, and the electric field distribution is consistent with the electric field distribution on the surface of the UAV.

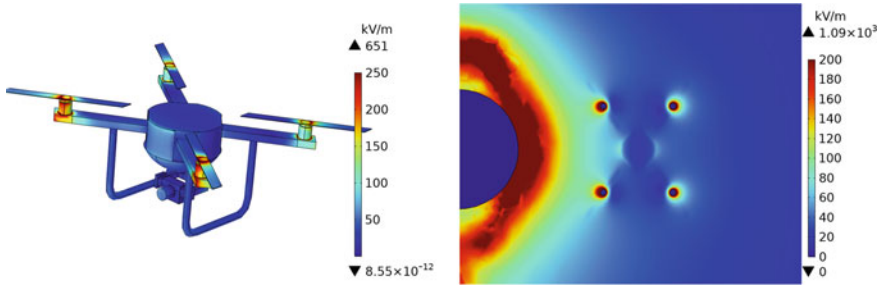


Fig. 10 The electric field distribution cloud map when the UAV inspects the circuit breaker

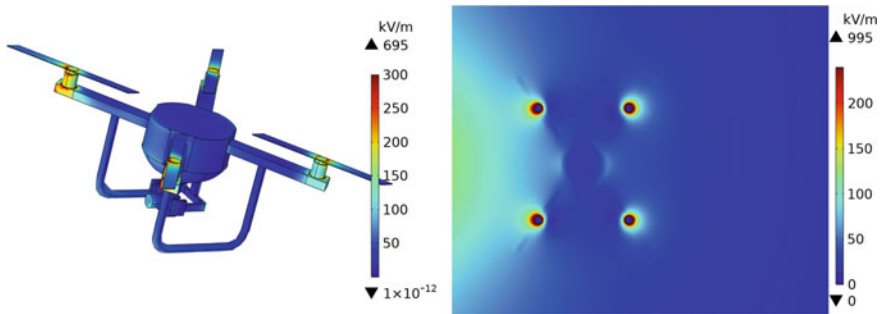


Fig. 11 The electric field distribution cloud map when the UAV inspects the voltage transformer

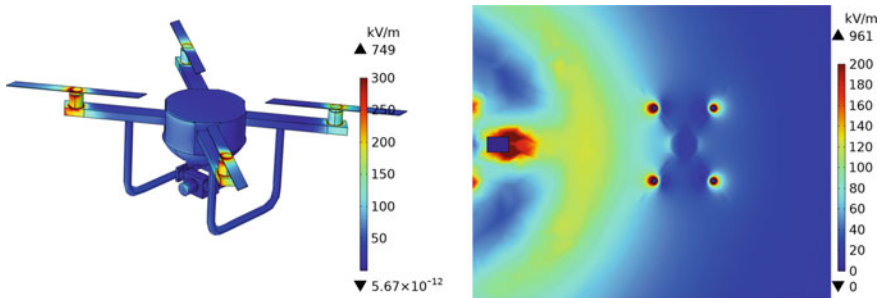


Fig. 12 The electric field distribution cloud map when the UAV inspects the lightning arrest

Genie 4 UAV in the lightning arrester near the inspection of the surface electric field strength is the largest, 749 kV/m, less than the air breakdown field strength. Under the condition of considering the influence of electric field, the UAV inspection is safe.

## 4 Conclusion

In this paper, we take the genie 4 UAV commonly used for substation inspection as the research object, and study the safety distance when the UAV inspects the high-voltage equipment of the substation, and analyze and calculate the electric field distribution when the UAV inspects different high-voltage equipment by constructing the simulation model of the UAV and 220 kV substation. From the simulation results, it can be seen that when the horizontal distance between the UAV and the high-voltage equipment is 0.5 m, the maximum surface electric field strength is 749 kV/m when inspecting near the arrester, which is smaller than the air breakdown field strength. Under the condition that only the electric field is considered, it is safe to keep a horizontal distance of 0.5 m between the UAV and the high-voltage equipment.

**Acknowledgements** This work was financially supported by the China Southern Power Grid Corp funded science and technology project (GDKJXM20220879).

## References

1. Zhen Z, Yun H, Hao H, Jia N, Zheng Y, Qi W (2023) Research on improving the inspection efficiency of substation based on big data analysis. *Electrica* 23(1):79–86 (in Chinese)
2. Yuan L, Zhang W, Zhang Z, Lin G (2022) Research on behaviour planning for power substation inspection robot based on fuzzy cognitive map. *J Phys Conf Ser* 2390(1):012116
3. Feng J, Luo RC, Wang F (2021) Analysis of electromagnetic environment effect of 110kV transmission line inspection UAV. *J Electric Power* 36(06):498–504
4. Li Z, Zhang Y, Wu H et al (2023) Design and application of a UAV autonomous inspection system for high-voltage power transmission lines. *Remote Sensing* 15(3):865
5. Chen D, Guo X, Huang P, Li F (2020) Safety distance analysis of 500 kV transmission line tower UAV patrol inspection. *IEEE Lett Electromagn Compat Pract Appl* 4(02):124–128
6. Diana S, Damira P, Mehdi B, Alex J (2020) IN-YOLO: real-time detection of outdoor high voltage insulators using UAV imaging. *IEEE Trans Power Delivery* 35(3):1599–1601
7. Zheng T, Sun L et al (2018) Determination method of safe flight area for UAV inspection for transmission line based on the electromagnetic field calculation. *Shandong Electric Power* 45(2):27–30
8. Li H, Huang D, Yang T et al (2022) Study on the insulation level of the gap between UAV and typical high voltage equipment in 110 kV substation. In: 2022 IEEE international conference on high voltage engineering and applications. IEEE, Chongqing, pp 01–04
9. Deng C, Wang S, Huang Z et al (2014) Unmanned aerial vehicles for power line inspection: a cooperative way in platforms and communications. *J Commun* 9(9):687–692
10. Jiang F, Song Q, Li C P et al (2023) Application of power ubiquitous Internet of Things technology in intelligent inspection of unattended substation. In: Second international conference on electronic information engineering and computer communication (EIECC 2022). SPIE, Xi'an, pp 37–42

# Performance of Annual Flashover Rate at Individual Poles in a Distribution Network Due to Indirect Lightning



Jinxin Cao, Jianguo Wang, Yaping Du, Amedeo Andreotti, Yuxuan Ding, Li Cai, Yadong Fan, and Mi Zhou

**Abstract** The complex distribution network has an obviously various lightning performance with that of the straight periodic lines, due to the uneven pole spans and feeder structure in the distribution network. In this paper, the lightning-induced flashover (FO) performance in a distribution network is investigated via a Monte Carlo method, based on the numerical PEEC-MTL method for line modeling and transient simulation. Different from the traditional indicator, i.e., the flashover rate of a total line, the annual FO number at individual poles is defined and concerned to reflect the distribution of the FO risk due to indirect lightning strikes. It is found that the in a part of an existing rural distribution network of concern if the terminal

---

J. Cao (✉) · J. Wang · L. Cai · Y. Fan · M. Zhou

Engineering Research Center of Ministry of Education for Lightning Protection and Grounding Technology, School of Electrical Engineering and Automation at, Wuhan University, Wuhan, China

e-mail: [jinxin.cao@connect.polyu.hk](mailto:jinxin.cao@connect.polyu.hk)

J. Wang

e-mail: [wjg@whu.edu.cn](mailto:wjg@whu.edu.cn)

L. Cai

e-mail: [caili@whu.edu.cn](mailto:caili@whu.edu.cn)

Y. Fan

e-mail: [ydfan@whu.edu.cn](mailto:ydfan@whu.edu.cn)

M. Zhou

e-mail: [zhoumi927@whu.edu.cn](mailto:zhoumi927@whu.edu.cn)

Y. Du · Y. Ding

Department of Building Energy and Environment Engineering, The Hong Kong Polytechnic University, Hong Kong, China

e-mail: [ya-ping.du@polyu.edu.hk](mailto:ya-ping.du@polyu.edu.hk)

Y. Ding

e-mail: [15903676r@connect.polyu.hk](mailto:15903676r@connect.polyu.hk)

A. Andreotti

Department of Electrical Engineering and Information Technology, University of Naples Federico II, Naples, Italy

e-mail: [andreot@unina.it](mailto:andreot@unina.it)

© Beijing Paiké Culture Commu. Co., Ltd. 2024

X. Dong and L. Cai (eds.), *The Proceedings of 2023 4th International Symposium on Insulation and Discharge Computation for Power Equipment (IDCOMPU2023)*, Lecture Notes in Electrical Engineering 1103, [https://doi.org/10.1007/978-981-99-7413-9\\_49](https://doi.org/10.1007/978-981-99-7413-9_49)

poles with distribution transformers located protected by surge arresters by default, the poles where the open area is around are more likely to have a higher annual FO number. The soil conductivity significantly affects the values of the annual FO number of individual poles, while there is no obvious change in its overall distribution characteristic of the distribution network, which is mainly determined by the line topology. Compared with the case without surge arresters besides the distribution transformers, it indicated the great significance of the protection for terminal poles with distribution transformers. The present work could provide a theoretical basis for differentiated protection against indirect lightning and more factors and conditions would be of concern in the following work.

**Keywords** Indirect lightning · Overhead distribution lines · Flashover · Monte Carlo method · Surge arrester

## 1 Introduction

Lightning-induced faults on the overhead distribution network are a critical issue of concern, especially in the area subject to severe lightning strikes. Nowadays, irregular overhead distribution line network is the main presentation form of distribution line systems in China. The flashover performance in complex distribution network should be firstly reasonably evaluated so that the regular periodic protection or differentiated protection could be implemented technical-reasonably [1–5].

For a complex distribution network, the flashover rate of a total line cannot well reflect the risk distribution. A more sensitive novel indicator, i.e., the annual flashover number at individual poles of the distribution network is set to get both the partial and overall lightning performance [1, 2]. The uneven pole spans and feeder structure of a distribution networks in most practice engineering results in an unevenly distributed stroke probability of both indirect and direct strokes. On the other hand, the peak-value distribution of the overvoltage and the rule of the surge propagation along the lines would be certainly different with that of the straight lines, subsequently causes the various flashover performance occurred at individual poles located at different positions.

Therefore, in this paper, the lightning-induced flashover (FO) performance in a distribution network is investigated via a Monte Carlo method. A part of the rural overhead distribution network located in southern China, which contains 56 poles and tens of feeder terminations with distribution transformers is adopted for the case study. Since lightning-induced overvoltage are the main risk that results in flashover for the distribution line system because of a generally low insulation strength [6], only the indirect lightning stroke is mainly concerned for investigation.

The paper is organized as follows. In Sect. 2, the Monte Carlo method, as well as the line configurations for the study are described. In Sect. 3, the assessment of the flashover performance under various line conditions is presented. The conclusion is finally summarized in Sect. 4.

## 2 Line Configurations and Monte Carlo Method

### 2.1 Line Configurations

Figure 1 shows the case of the overhead distribution network in the present study. It is part of an actual 10kV overhead distribution network located in southern China. The part of line networks contains the distribution transformers at the sub-feeder terminations, the surge arresters (SADT) for each transformer installed by default, and the poles with uneven spans. Other terminations of the network are represented with matching impedance, labelled as blue squares in Fig. 1.

In the distribution network, the parallel phase and shield wires are long wires and can be modelled with an MTL theory [7]. The metal components of poles, grounding lead, and grounding electrodes are short wires and are suitable for describing with the PEEC method [8, 9].

Transformers, insulators, and surge arresters in the network are modeled as widely used and recommended lumped circuits. The specific parameters could be found in [10]. A disruptive effect (DE) model [11] is adopted for the model of insulator flashover, with the verified parameters for the model via the curve fitting of the experimental data [10, 12].

An integrated PEEC-MTL model together with the lumped circuits for the mentioned electrical components yields a modified nodal analysis (MNA) matrix [9, 10]. Time-domain numerical simulation is then carried out for evaluation of the lightning surge and the status of flashovers at individual poles.

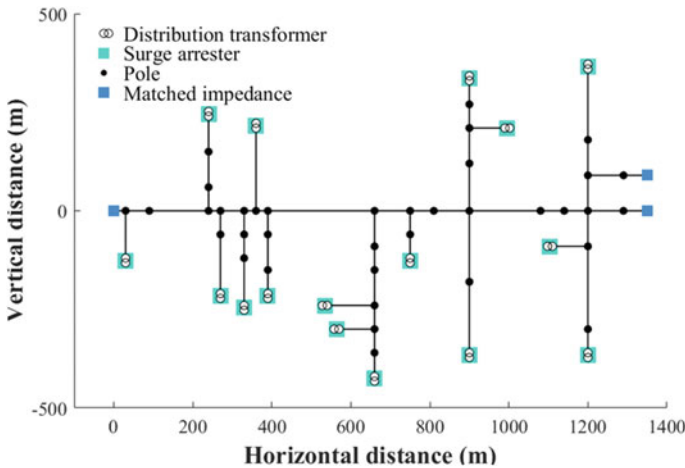


Fig. 1 Diagram of the part of distribution network for lightning assessment in this study



## 2.2 Monte Carlo Method for Indirect-Lightning Evaluation

To consider the natural randomness of lightning, a Monte Carlo procedure is adopted to determine the distribution of the lightning strokes in the area that covers the distribution network of concern as well as the LEMP effect on the lines. The widely used Electric Geometry Model (EGM) is adopted to distinguish the indirect and direct stroke for each occurrence of the lightning event.

The parameters of the Monte Carlo procedure are shown in Table 1, including the types of considered probabilistic parameters of lightning current, probabilistic functions, and the configurations as the reference case. Figure 2a–c respectively present the probabilistic distribution of amplitude  $I_{max}$ , wavefront  $t_r$ , correlation between  $I_{max}$  and  $t_r$  of the lightning current considered in the assessment.

Shown in Fig. 3 is the location of the randomly generated lightning indirect strokes (blue dots), and the normalized probability of the direct-stroke location along the distribution networks. In our previous work, the lightning performance due to the direct strokes has been comprehensively investigated [1, 2], thus in the present study, only the indirect stroke is of concern. With all the randomly generated indirect lightning events in the Monte Carlo procedure, the annual flashover rate at individual poles is calculated below:

$$AF O_p = \frac{n_{p-f}}{N_{total}} \cdot N_g \cdot A \tag{1}$$

where  $n_{p-f}$  is the number of lightning events that cause flashover at pole  $p$ , and  $N_{total}$  is the total number of the randomly generated events, adopted as 20,000 in the study.  $N_g$  is the annual lightning density in concern, with an area size of  $A$ . For simplicity, the  $N_g$  is adopted as a fixed value of 5.0.

**Table 1** Parameters for Monte Carlo method and the reference configurations for lightning assessment

Considered probabilistic parameters of lightning current	Probabilistic functions	Soil conductivity	Insulators	Surge arresters
Amplitude $I_{max}$ Wavefront $t_r$ Tail time to half value $t_d$	IEEE recommended functions and statistical values [13, 14]	0.01 S/m	PT-15	Besides the distribution transformers

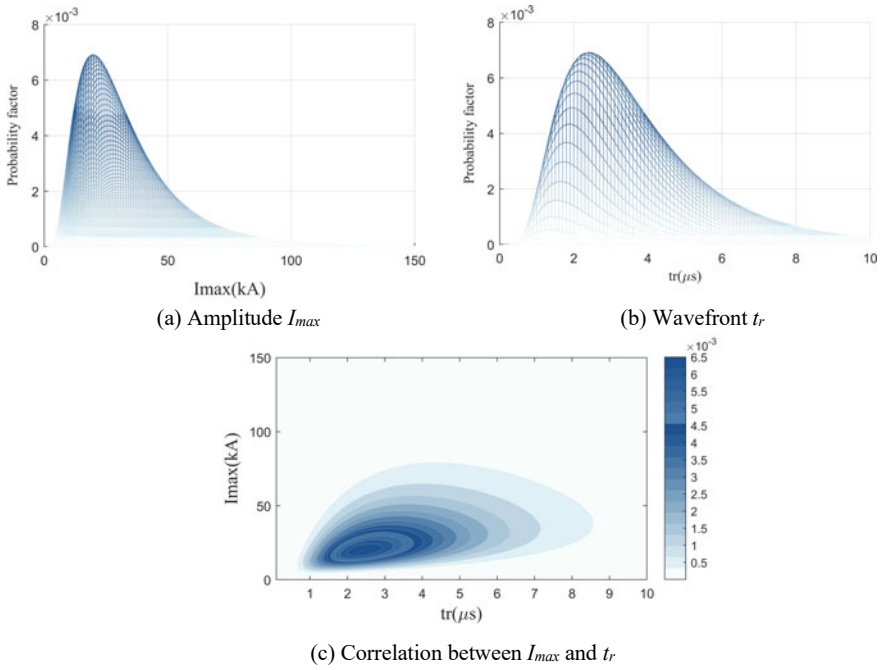


Fig. 2 Probabilistic distribution of parameters of lightning current in the assessment

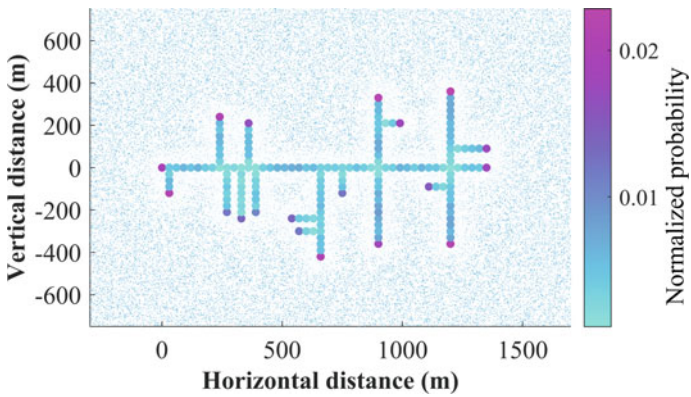


Fig. 3 Location of the randomly generated lightning indirect strokes (blue dots), and the normalized probability of the direct-stroke location along the distribution networks

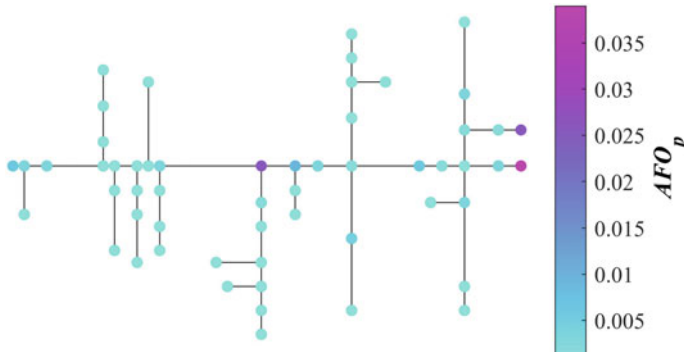


Fig. 4 Performance of lightning-induced annual flashover at individual poles

### 3 Lightning Performance Due to Indirect Lightning

#### 3.1 Flashover Performance Along the Distribution Lines

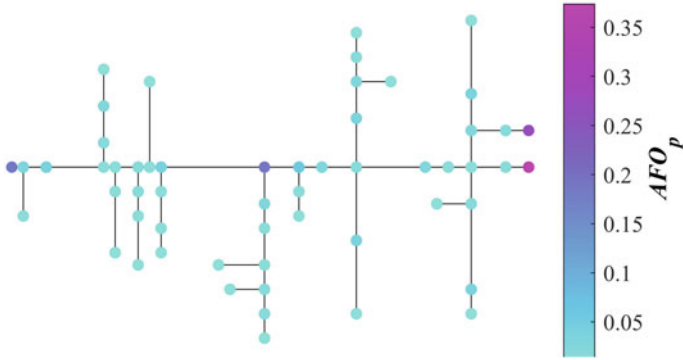
Shown in Fig. 4 is the performance of lightning-induced annual flashover  $AFO_p$  at individual poles, with the reference configurations shown in Table.1. The black lines represent the line topology of the distribution networks in the form of an overlook schematic. The colorful dots reflect the location of the poles and the value of  $AFO_p$ .

It is found that the poles with open areas around them have a relatively higher  $AFO_p$ . This phenomenon is related to the higher probability of the indirect return strokes terminating around. In other words, for the clustered poles with obviously shorter pole intervals and more dense sub-feeders, more direct lightning strikes would occur rather than indirect strokes. On the other hand, the nearby indirect lightning strikes would cause lightning-induced electromagnetic pulse with similar amplitude and time-delay effects, which may also be the main reasons why the clustered poles have shown a similar  $AFO_p$ . Note that in the reference configurations of concern, each distribution transformer has been protected by surge arresters, the protection effect of which could also be transferred to the nearby poles. Therefore, most of the poles have a relatively low  $AFO_p$ , except for the poles with open areas around them.

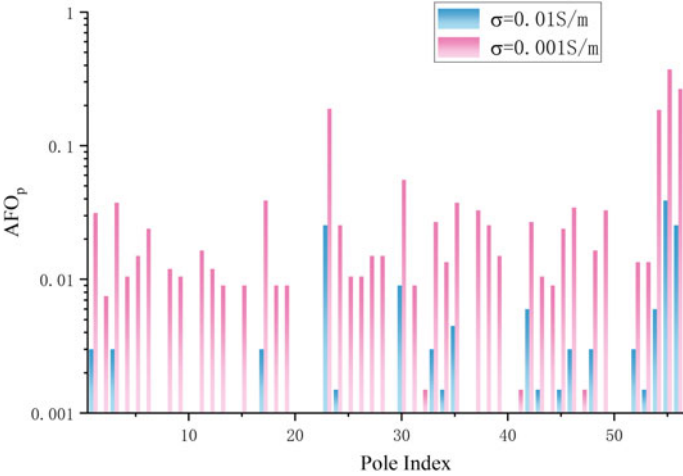
#### 3.2 Flashover Number at Individual Poles Versus the Soil Conductivity

Shown in Fig. 5 is the performance of  $AFO_p$  at individual poles, with the reference configurations shown in Table.1 but soil conductivity of 0.001 S/m. The distribution characteristics of  $AFO_p$  in the uneven distribution network is compared with that of 0.01 S/m as shown in Fig. 6, which indicates that the absolute values are increased

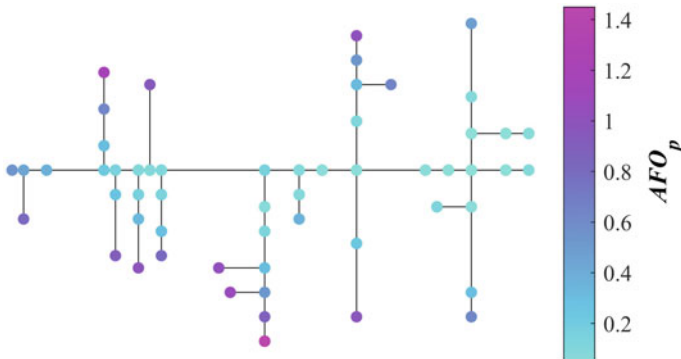
by about 8–10 times that with the soil conductivity of 0.01 S/m. This is because of the much higher LEMP with a lower soil conductivity [15]. The locations of the dangerous individual poles don't vary much, which is mainly determined by the line topology.



**Fig. 5** Performance of lightning-induced annual flashover at individual poles, with soil conductivity of 0.001 S/m



**Fig. 6** Comparison of the performance of lightning-induced annual flashover at individual poles under two conditions of soil conductivity

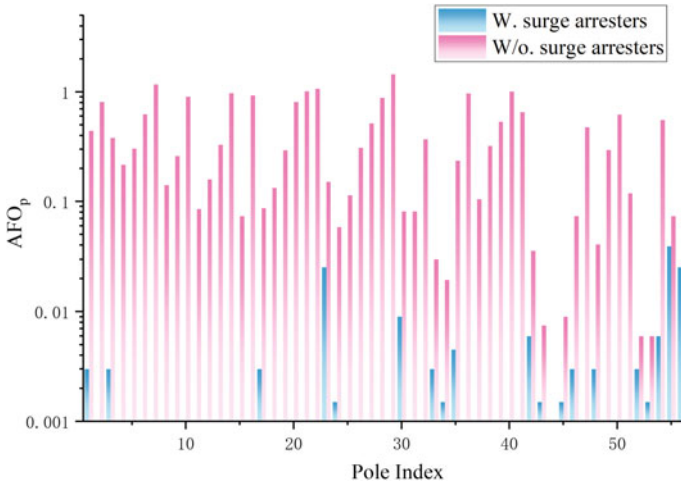


**Fig. 7** Performance of lightning-induced annual flashover  $AFOP_p$  at individual poles, without surge arresters besides the distribution transformers

### 3.3 Flashover Number at Individual Poles Without Surge Arresters

The results corresponding to Figs. 4 and 5 are the reference configurations with the surge arresters installed beside the distribution transformer by default. In this section the performance of  $AFOP_p$  without surge arresters (SAs) is assessed and presented in Fig. 7. The distribution characteristics of  $AFOP_p$  is compared with that of the reference case with SADT, as shown in Fig. 8. It is found that without the protection of SAs, the dangerous poles with the higher  $AFOP_p$  are generally located at the termination of the sub-feeders. This is because they always have a nearer distance from the open areas where the indirect return strikes are located in. This also indicates the great importance of SA protection for the poles with distribution transformers, which are likely to be exposed to a higher risk of LEMP initiated from indirect lightning.

The risk assessment of induction lightning, in fact, also depends mainly on the surrounding structures, which affects the distribution of indirect lightning because of the competitive relationship with the line conductors to attract the final termination of the step leader before the return-stroke channel. The influence of this factor on the assessed results of the  $AFOP_p$  distribution will be considered in subsequent work.



**Fig. 8** Comparison of the performance of lightning-induced annual flashover at individual poles with or without surge arresters beside the transformers (SADT)

## 4 Conclusion

This paper assesses the performance of lightning-induced flashover (FO) in a distribution network via a Monte Carlo method, based on the numerical simulation. The annual FO number at individual poles is defined and concerned to reflect the distribution of the FO risk. It is found that in a part of an actual rural distribution network of concern, if the terminal poles with distribution transformers located are protected by surge arresters by default, the poles where the open area is around are more likely to have a higher annual FO number. The soil conductivity significantly affects the values of the annual FO number of individual poles, while there is no obvious change in its overall distribution characteristic of the distribution network, which is mainly determined by the line topology. Compared with the case without surge arresters besides the distribution transformers, it is indicated the great significance of the protection for terminal poles with distribution transformers. The present work could provide a theoretical basis for differentiated protection against indirect lightning.

**Acknowledgements** The work leading to this paper was funded by grants from the Research Grants Council of the HKSAR (Project No. 15208019) and the science and technology project from China Southern Power Grid (Project No. 030600KK52220016).

## References

1. Cao J et al (2023) Lightning protection with a differentiated configuration of arresters in a distribution network. *IEEE Trans Power Delivery* 38(1):409–419
2. Cao J, Du Y, Ding Y et al, Lightning protection with a differentiated arrester configuration for distribution networks using a multi-objective optimization procedure. *IEEE Trans Power Deliv.* <https://doi.org/10.1109/TPWRD.2023.3240378>
3. Shariatinasab R, Safar JG, Falaghi H (2014) Optimization of arrester location in risk assessment in the distribution network. *IET Gener Transm Distrib* 8(1):151–159
4. Kamarposhti MA, Hejri AA (2021) Optimal location of surge arresters in distribution network considering reliability and technical and economic factors to reduce costs using ICA algorithm. *Int J Smart Electr Eng* 10(1):7–16
5. Barradas RPDS et al (2020) Methodology for analysis of electric distribution network criticality due to direct lightning discharges. *Energies* 13(7)
6. Cao J, Ding Y, Du Y et al, Comprehensive assessment of lightning protection schemes for 10 kV overhead distribution lines. *IEEE Trans Power Deliv.* <https://doi.org/10.1109/TPWRD.2021.3110248>
7. Paul CR (2008) *Analysis of multiconductor transmission lines*. Wiley-IEEE Press, pp 381–382
8. Qi R, Du YP, Chen M (2020) A full-wave PEEC model of thin-wire structures above the lossy ground. *IEEE Trans Electromagn Compat* 62(5):2055–2064
9. Cao J et al (2022) Lightning surge analysis of transmission line towers with a hybrid FDTD-PEEC method. *IEEE Trans Power Deliv* 37(2):1275–1284
10. Cao J, Ding Y, Du Y et al (2022) Practical schemes on lightning energy suppression in arresters for transformers on 10 kV overhead distribution lines. *IEEE Trans Power Deliv* 37(5):4272–4281
11. Darveniza M, Vlastos AE (1988) The generalized integration method for predicting impulse volt-time characteristics for non-standard wave shapes—a theoretical basis. *IEEE Trans Electr Insul* 23(3):373–381
12. Zhang X, Liu G, Chen RF (2015) Study on the V-t characteristics of lightning impulse of insulator in 10kV distribution network. *Electr Technol* 34(13):60–63
13. Short TA (2011) IEEE guide for improving the lightning performance of electric power overhead distribution lines. In: *IEEE Std.*, pp 1410–2010
14. Technical Brochure 839. *Procedures for Estimating the Lightning Performance of Transmission Lines—New Aspects*. CIGRE WG C4.23 (2021)
15. Rachidi F, Nucci A, Ianoz M, Mazzetti C (1996) Influence of a lossy ground on lightning-induced voltages on overhead lines. *IEEE Trans Electromagn Compat* 38(3):250–264

# Analysis of Induced Voltage of a Single-Point Grounded OPGW in 35 kV Distribution Lines



Yufei Chen, Jinxin Cao, Yong Wei, Xianchun Wang, Jiaju Zhang, Yadong Fan, Wenhao Zhang, and Jianguo Wang

**Abstract** The optical fiber composite overhead ground wire (OPGW) has been widely used in power transmission lines. It can not only serve as an overhead ground wire for lightning protection but also be used for information communication for power system as well as achieving functions such as online monitoring. There are two common grounding methods for OPGW: all-tower grounding and single-point grounding. Adopting a single-point grounding method can effectively reduce induction current and energy loss by 50 Hz power transmission, but may generate a larger induction voltage. This paper studied the induced voltage of insulated OPGW by single-point grounding on 35 kV single-circuit distribution lines. The conditions of segmented insulation and mid-point grounding are adopted for numerical simulation, and the influence of tower height and wire displacement on induction voltage was

---

Y. Chen · J. Cao (✉) · Y. Fan · W. Zhang · J. Wang  
School of Electrical Engineering and Automation, Wuhan University, Wuhan, China  
e-mail: [jinxin.cao@connect.polyu.hk](mailto:jinxin.cao@connect.polyu.hk)

Y. Chen  
e-mail: [2022282070095@whu.edu.cn](mailto:2022282070095@whu.edu.cn)

Y. Fan  
e-mail: [ydfan@whu.edu.cn](mailto:ydfan@whu.edu.cn)

W. Zhang  
e-mail: [2320059313@qq.com](mailto:2320059313@qq.com)

J. Wang  
e-mail: [wjg@whu.edu.cn](mailto:wjg@whu.edu.cn)

Y. Wei · J. Zhang  
State Grid Hebei Information & Telecommunication Branch, Shijiazhuang, China  
e-mail: [13398618998@163.com](mailto:13398618998@163.com)

J. Zhang  
e-mail: [zjiaz0@126.com](mailto:zjiaz0@126.com)

X. Wang  
State Grid Hengshui Electric Power Supply Company, Shijiazhuang, China  
e-mail: [zhangjianghui1974@126.com](mailto:zhangjianghui1974@126.com)

© Beijing Paiké Culture Commu. Co., Ltd. 2024

X. Dong and L. Cai (eds.), *The Proceedings of 2023 4th International Symposium on Insulation and Discharge Computation for Power Equipment (IDCOMPU2023)*, Lecture Notes in Electrical Engineering 1103, [https://doi.org/10.1007/978-981-99-7413-9\\_50](https://doi.org/10.1007/978-981-99-7413-9_50)



discussed. The results showed that tower height and wire displacement have almost no effect on the induced voltage.

**Keywords** OPGW · Induced voltage · 35 kV distribution lines · Single-point grounding · Segmented insulation

## 1 Introduction

In the current context of new power system construction, the recommended overhead ground wire is Optical Fiber Composite Overhead Ground Wire (OPGW) with dual functionality of ground wire and optical cable. OPGW has basic mechanical and electrical properties as lightning protection wires, and also has the advantages of high broadband capacity, large communication capacity, low transmission loss, and no electromagnetic interference as optical fiber communication. It can be used not only as an overhead ground wire for lightning protection [1, 2], but also as a high-frequency channel for relay protection, remote control signals, communication channels, and online fault monitoring within the power system [3, 4]. Nowadays, OPGW has been widely used in high-voltage transmission lines of 110 kV and above in China.

The mainstream grounding methods for OPGW are the all-tower grounding and single-point grounding. For the high-voltage transmission lines in China, OPGW has been operated with the former one, which can effectively distribute the surge current generated on the ground wire to both base towers on either side of the fault point when the line encounters a grounding short circuit or lightning strike. However, electromagnetic induction and electrostatic induction exist between the overhead ground wire and the conductor, and induction voltage imbalance caused by each phase conductor in the ground wire will form an induction current loop between the ground wire and the earth, causing power loss of the overhead ground wire. Single-point grounding of OPGW can effectively reduce induction current and energy loss, but when alternating current passes through the transmission line at high voltage, a large induction voltage will be generated on the ground wire. As transmission lines are mostly long-distance with high-amplitude currents, excessive induction voltage can cause breakdown discharge in the insulation gaps or insulators of OPGW, overvoltage risk to OPGW connection boxes and de-vices, even causing human safety in live operation. Adopting segmented insulation and single-point grounding can effectively suppress induction current while reducing induction voltage [5–8].

Currently, research on OPGW grounding methods mainly focuses on the application in transmission lines with the rate-voltage levels above 110 kV. However, research on OPGW grounding methods and induction voltage in 35 kV distribution lines with OPGW installation is limited. This paper mainly studies the ground wire induction voltage of a typical single-circuit tower under different heights and conductor replacement conditions in segmented insulation and midpoint grounding of OPGW in 35 kV distribution lines. It provides guidance for the safety of OPGW

installation in 35 kV distribution lines and future analysis of induction current and energy loss.

## 2 Data and Calculation Model

### 2.1 Mechanism of Ground Wire Induced Voltage Formation

When alternating current flows through a high-voltage transmission line, an alternating magnetic field is generated in space, and the induced electromotive force of the overhead grounding wire is mainly generated by electromagnetic induction [8]. The electromagnetic induced electromotive force per kilometer of the grounding wire can be calculated below:

$$E = j0.145 \sum_{i=1}^n I_{iA} \left( \alpha^2 \lg \frac{d_{lia}}{d_{lib}} + \alpha \lg \frac{d_{lia}}{d_{lic}} \right) \quad (1)$$

where  $I_{iA}$  is the A-phase's conductor current of the  $i$ -line,  $n$  is the number of circuits,  $d_{lia}$ ,  $d_{lib}$ ,  $d_{lic}$  are the distances between the ground wire and the  $i$ -line's three-phase conductor,  $\alpha = \angle 120^\circ$ ,  $E$  is the electromagnetic induction electromotive force per kilometer of ground wire [9].

It is noted that the existing formulas can only calculate the theoretical electromagnetic induced electromotive force per kilometer of ground wire, and cannot calculate the induced voltage under different grounding methods and operating parameters. Therefore, simulation is needed for further calculation and analysis when the rural configurations of grounding method, line configurations and operation configurations are of concern.

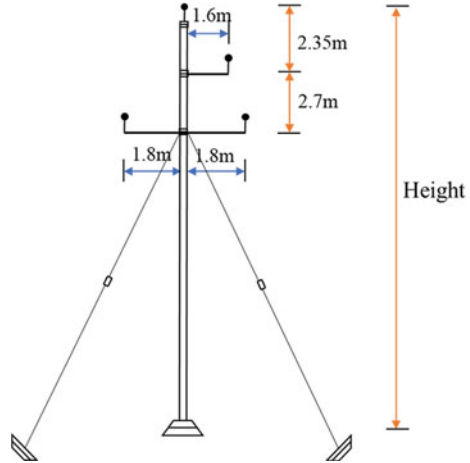
### 2.2 Tower Model and Parameters

According to the 2006 edition of "Typical Design of 35 kV Transmission Line Volume of State Grid Corporation of China" [10], there are a total of 42 modules and 262 types of towers in the typical design of 35 kV transmission lines. Among them, there are 8 modules and 48 types of concrete poles, 22 modules and 154 types of angle steel towers, and 12 modules and 60 types of steel pipe poles. Each type of tower also has multiple naming heights for selection during construction. Considering the meteorological conditions, engineering requirements, and the applicability of calculations, a representative model was selected from a single circuit concrete pole 35A02-Z4, the specific model and characteristics are shown in Table 1, and the schematic diagram of the typical design is shown in Fig. 1. Because OPGW has only been used in transmission lines in the past, there is no specialized OPGW for

**Table 1** Summary of 35 kV typical tower

Type	Feature	Wire	Span (m)	Height (m)
35A02-Z4	Single-circuit	LGJ-185/30	300	15, 18, 21

**Fig. 1** Typical single-circuit 35 kV transmission tower



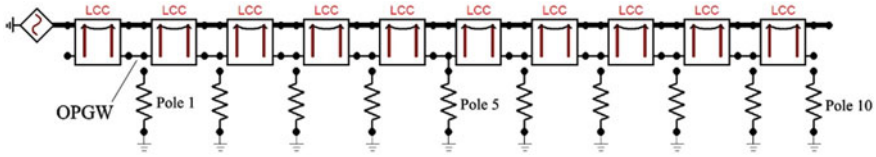
**Table 2** A35kV conductor models and specific parameters

Type	Calculation inside diameter (mm)	Calculation outside diameter (mm)	20 °C direct current resistance ( $\Omega$ /km)
LGJ-185/30	6.14	18.88	0.1592
OPGW-50-36-1-1	\	9.9	1.677

distribution networks on the market. According to the requirements for overhead ground wires in the “Typical Design of 35 kV Transmission Lines” volume of the “State Grid Corporation of China Transmission and Transformation Engineering Typical Design”, a single OPGW-50-36-1-1 is used for the ground wire, which is provided by the China Southern Power Grid Co., Ltd. enterprise standard data. The wire model and specific parameters used are listed in Table 2.

### 2.3 Line Model and Parameters

According to reference [5], the entire ground wire with the maximum induced voltage  $U$  is divided into  $n$  sections, and the maximum induced voltage becomes  $U/n$ . If grounded at the midpoint, the maximum induced voltage becomes  $U/2n$ . Therefore, in the simulated line, the ground wire is grounded at the midpoint with segmented insulation.



**Fig. 2** Segmented insulation and midpoint grounding conditions

The line model is built in ATP-EMTP based on the data in Sect. 2.2, and LCC model is used for tower calculation. The entire line consists of 40 towers, with substations at both ends and a span of 300 m. The line is divided into four sections, each consisting of 10 towers. The OPGW uses segmented insulation and is grounded at the midpoint, with grounding at the middle point of each section (at the 5th tower). The model diagram for the first section is shown in Fig. 2.

In the line model, the substations at both ends have a line current of 400 A, and the transmission current is simulated using a current source. The load impedance is 50.52 Ω. The double-circuit lines are arranged in the same phase sequence. The substation grounding resistance is 0.5 Ω, the earth resistivity is taken as 100 Ω/km, and according to the 2006 edition of “Typical Design of 35 kV Transmission Line Volume of State Grid Corporation of China”, the tower grounding resistance is taken as 15 Ω.

### 2.4 Operating Parameters of the Line

Common operating parameters of power lines include:

- (1) Tower height, which is referred to as the height parameter of the tower. Towers of the same model may have different heights due to different geographical environments and other factors.
- (2) Phase-conductor transposition, which is used to reduce the asymmetry of current and voltage caused by three-phase parameters during normal operation of the power line, and to limit the impact of the line on communication lines. The commonly used phase-conductor transposition method is ABC-BCA, as shown in Fig. 3.

The common ways of phase-conductor transposition can be divided into complete transposition and incomplete transposition. complete transposition means transposing the conductors at two thirds of the span, which in this line model is at towers 13 and 27 as shown in Fig. 3a. Incomplete transposition means transposing the conductors only at the midpoint, which in this model is at tower 20. Ground wire transposition refers to exchanging the positions of two ground wires.

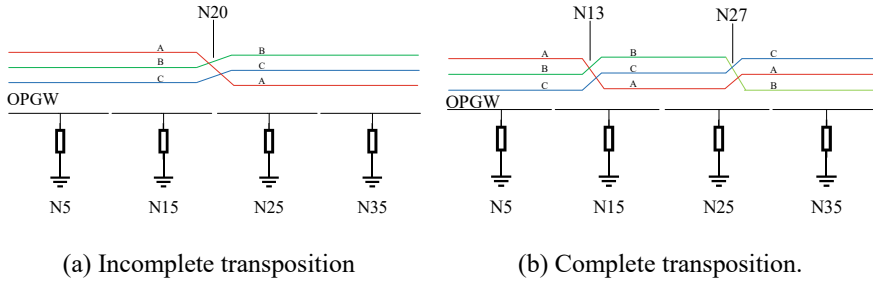


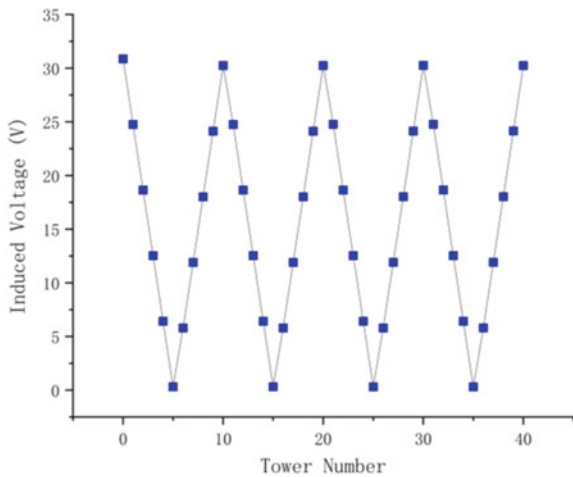
Fig. 3 Schematic diagram of phase-conductor transposition

### 3 The Distribution of Induced Voltage

The ground wire induced voltage distribution of a typical 35 kV single-circuit tower is shown in Fig. 4. In this section, the tower height is 15 m, and in the next section, the variation of ground wire induced voltage under different height and phase sequence conditions will be discussed. From Fig. 4, it can be seen that under the uniform use of segmented insulation and mid-point grounding, the distribution law of ground wire induced voltage is basically the same, with the highest value at the segmented tower and 0 at the grounding tower, showing a “V”-shaped distribution due to the equal length of each segment.

According to Fig. 4, for the 35 kV typical tower with ground wire divided into four sections, the maximum induced voltage of a single-phase circuit can reach 30.88 V, which is equivalent to an induced voltage of 10.29 V/km per kilometer.

Fig. 4 Distribution of induced voltage on ground wire of 35 kV typical tower



## 4 The Influence of Operating Parameters on Induced Voltage

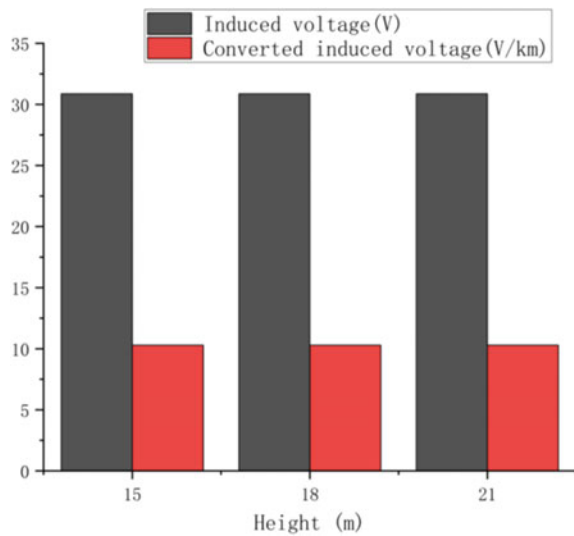
As discussed in the previous chapter, the distribution of induced voltage on the ground wire presents a “V” shape, so only the equivalent value of the maximum induced voltage per kilometer needs to be discussed.

### 4.1 The Influence of Tower Height on Induced Voltage

The concrete pole 35A02-Z4 has three nominal heights: 15, 18, and 21 m. Figure 5 shows the maximum induced voltage at different heights for the typical tower.

According to Fig. 5, it can be seen that the maximum induced voltage on the ground wire hardly changes at different heights. It can be considered that the height of the tower has almost no impact on the induced voltage on the ground wire. This is because the relative relationship between the conductors and the ground wire has not changed. According to Eq. (1), the electromagnetic induced electromotive force on the ground wire per kilometer has not changed. Therefore, for the same ground wire, under the same grounding method, the induced voltage remains unchanged.

**Fig. 5** The ground wire induction voltage at different heights



**Table 3** The induced voltage on the ground wire under conductor transposition

Transposition method	No transposition	Incomplete transposition	Complete transposition
Induced voltage (V)	30.88	30.87	30.88
Converted induced voltage (V/km)	10.29	10.29	10.29

## 4.2 The Influence of Conductor Transposition on Induced Voltage

Since there is only one ground wire in the 35 kV distribution line, there is no need to consider the factors of ground wire transposition. The common transposition method ABC-BCA was chosen in this article. Table 3 shows the ground wire induction voltage after conductor transposition.

According to Table 3, the two transposition methods of the single-circuit have almost no effect on the ground voltage induced by the wire. It can be inferred that transposition of the wires has almost no effect on the ground voltage induced by the single-circuit line, which is consistent with the research results of previous studies at other voltage levels [7]. Therefore, when transposing wires, there is no need to consider the impact on induced voltage.

## 5 Conclusion

This paper established a 35 kV transmission line model equipped with OPGW and analyzed the magnitude of the ground wire induced voltage for a typical single-circuit tower with segmented insulation and mid-point grounding.

The simulation results showed that the change in tower height and various wire transpositions do not affect the induced voltage under segmented insulation and mid-point grounding. Therefore, in future studies discussing the impact of these two factors on induced current and line loss, it is not necessary to consider their impact on induced voltage.

**Acknowledgements** This work was supported by the Science and Technology Project of State Grid Limited Headquarters (Project 5108-202218280A-2-418-XG).

## References

1. Snider WC, Moore RC, Erdman AJ, Doucet D, Charlton D (2021) Lightning-induced state of polarization change in OPGW using a transmission line model. In: Optical fiber communication conference. Optica Publishing Group, pp M3C-8
2. Santos JA, Moore RC, Snider WC, Doucet D, Charlton D (2022) Lightning-related ELF transients as a potential source of rapid state of polarization changes in shielded OPGW. In: 2022 optical fiber communications conference and exhibition (OFC). IEEE, pp 01–03
3. Ding ZW, Zhang XP, Zou NM, Xiong F, Song JY, Fang X, ..., Zhang YX (2021) Phi-OTDR based on-line monitoring of overhead power transmission line. *J Lightwave Technol* 39(15):5163–5169
4. Zhang L, Zheng H, Gao J, Li Y, Li Y, Kong X (2022) Fault diagnosis method for relay protection channel based on semantic web. In: International conference on electronic information engineering and computer communication (EIECC 2021), vol 12172. SPIE, pp 416–420
5. Wang J, Wang Y, Peng X, Li X, Xu X, Mao X (2014) Induced voltage of overhead ground wires in 50 0-kV single-circuit transmission lines. *IEEE Trans Power Deliv* 29(3):1054–1062
6. Sun Y, Zeng X, Zhang H, Xu Y, Qian M, Yin F, Wang L (2022) Analysis of induced voltage of ground wires in 1000kV transmission lines. In: 2022 IEEE international conference on high voltage engineering and applications (ICHVE). IEEE, pp 1–4
7. Fu ZX, Guo JM, Li YG (2016) Calculation of line parameters in different grounding modes of double earth wire. In: 2016 international symposium on computer, consumer and control (IS3C). IEEE, pp 148–151
8. Yuqun F, Liqun Q, Taishan H, Bo Z, Dongze X (2016) Analysis of the effect on induced voltage initiate by insulated ground wire transposition in double-circuit transmission line on the same tower. In: 2016 IEEE international conference on high voltage engineering and application (ICHVE). IEEE, pp 1–8
9. Diansheng Z (1999) Design handbook for high voltage power supply circuit of electric power engineering. China Electric Power Press 1999:156–161 (in Chinese)
10. Liu Z (2006) Typical design of state grid corporation's transmission and transformation projects: 35kV transmission lines. China Electric Power Press (in Chinese)



# Research on Pre-synchronization Control Strategy for the Integration of Individual Microgrid into Microgrid Clusters



Peng Yu, Rong Fu, Lihong Ma, Zaishun Feng, Mingjun Chen, Jinsong Li, and Xiangtao Zhuan

**Abstract** Tropical islands frequently face energy supply shortages due to limitations imposed by their natural environment. The utilization of a single microgrid structure often leads to power instability and even network-wide failures. Interconnecting multiple microgrids and operating them in a clustered manner can effectively enhance the reliability of power supply. However, during the process of integrating a specific microgrid into the cluster, voltage magnitude and phase imbalances at the common connection points can give rise to transient stability issues. To address the aforementioned challenges, a microgrid cluster synchronization and integration strategy based on pre-synchronization control is proposed. The voltage magnitude of inverter outputs and the voltage vector of the microgrid cluster are transformed into the rotational coordinate system using Clark and Park transformations, thereby obtaining the phase angle and magnitude deviations of the voltages. With PI control employed, compensatory values for grid frequency and grid voltage are individually determined to ensure consistent voltage phase and magnitude between the pre-synchronization side and the microgrid cluster side. This approach effectively resolves voltage and frequency fluctuations during mode transitions, enabling smooth switching between the islanded and grid-connected modes of microgrid operation. Finally, the effectiveness of the proposed control strategy is verified through simulation to be a feasible solution for the smooth integration of a microgrid into microgrid clusters.

---

P. Yu · R. Fu · Z. Feng · M. Chen  
Sansha Power Supply Bureau, Hainan Power Grid Co., Ltd., Sansha 573100, China  
e-mail: [al15370@126.com](mailto:al15370@126.com)

L. Ma  
Hainan Power Grid Co., Ltd., China Southern Power Grid, Haikou 570100, China

J. Li · X. Zhuan (✉)  
School of Electrical Engineering and Automation, Wuhan University, Wuhan 430000, China  
e-mail: [xtzhuan@whu.edu.cn](mailto:xtzhuan@whu.edu.cn)

J. Li  
e-mail: [2018302080116@whu.edu.cn](mailto:2018302080116@whu.edu.cn)

**Keywords** Microgrids · Pre-synchronization control · Virtual synchronous generator

## 1 Introduction

Energy is the driving force of social development. With the development of society and economy, the demand for energy is increasing. The significance of new energy sources, namely solar and wind power, has been on the rise due to their non-polluting, in-exhaustible, and renewable nature. Their importance is particularly pronounced in tropical island settings, where abundant solar energy resources are available. Therefore, distributed generation technology based on new energy sources has emerged. Distributed generation has the advantages of flexible control, low transmission loss, and low pollution [1]. However, as distributed generation is widely connected to the grid, its disadvantages have also been revealed. The cost of grid connection is high, and control is difficult. Improper operation may cause an impact on the power grid, seriously affecting its safety and stability [2].

In order to fully utilize the flexibility and efficiency of distributed generation and solve the grid connection problem of distributed generation, the US Consortium for Electric Reliability Technology Solutions (CERTS) proposed the concept of “microgrids” [3]. Microgrids integrate all distributed power sources in a region into a power network, turning the grid connection problem of multiple distributed power sources into a controllable unit, greatly reducing the adverse impact of distributed generation on the power grid.

However, in the power supply environment of islands, because they have been operating in an isolated island mode, using a single microgrid structure can easily result in unstable power supply or even a complete system collapse when equipment encounters faults or other emergencies [4]. Interconnecting multiple microgrids and running them in the form of a microgrid cluster can improve power supply stability [5]. However, the process of merging a single microgrid into a microgrid cluster faces various technical and management challenges, including effective power balance, coordinated control, and seamless switching [6].

Pre-synchronization strategy is a control strategy that achieves synchronization between a power generation unit and the grid in a power system. In the field of microgrids, it is mainly used for mode switching [7]. By adjusting the frequency and phase of distributed generation units in the microgrid, pre-synchronization is used to ensure that the microgrid is in a synchronized state with the main grid before switching to grid-connected mode. Currently, there are various pre-synchronization strategies proposed. For example, Zhong Q. proposed an inverter pre-synchronization method based on virtual current [8], and Xu H. used a phase-locked loop (PLL) to adjust the frequency in pre-synchronization and added it to the frequency control loop of the inverter [9]. Liang Meng, Can Su, Jiaqi Wu, Tian Ren, Zhenxiong Wang, and Hao Yi mainly studied the pre-synchronization method for multiple inverter grids and analyzed the effect of parameters on the pre-synchronization process [10].

However, the above research mainly focuses on the synchronization between microgrids and the external main grid, and there is little research on pre-synchronization between microgrids. This paper introduces the pre-synchronization control strategy and applies it to the process of merging a single microgrid into a microgrid cluster. By adjusting and matching the frequency, phase, and voltage parameters between microgrids in advance, stable voltage balance between microgrids is achieved, and the current impact and system oscillation during grid connection are reduced to ensure the stable operation of microgrids.

## 2 Modeling of Microgrid Clusters Based on VSG Control

The model of the microgrid cluster, as shown in Fig. 1, primarily comprises two microgrids, namely Microgrid A and Microgrid B. Microgrid A includes a distributed generation source, which is connected to the grid via an inverter used VSG control, as well as a local load denoted as  $Load_1$ . The distributed generation source, consisting of photovoltaics and energy storage, is represented by an ideal DC voltage source for the purpose of analytical convenience. Microgrid B is powered by conventional diesel generators and serves local loads, including an electric motor  $Load_2$  and a local  $Load_3$ . Microgrid A is interconnected with Microgrid B through the utility connection point (UCC).

Figure 2 depicts an inverter-interfaced circuit based on virtual synchronous generator (VSG) control, which consists of six major components, including the main circuit section, power calculation module, VSG control unit, voltage-current dual-loop control, space vector pulse width modulation (SPWM), and drive circuit. In the circuit,  $U_{DC}$  represents the DC source voltage,  $C_{DC}$  denotes the DC-side capacitance, and  $E_a, E_B, E_C$  represent the three-phase voltage output from the inverter.  $L$  denotes the AC-side filter capacitance,  $R$  represents the equivalent resistance of the LC filter and three-phase inverter,  $Z_t$  denotes the line impedance,  $C$  represents the filter capacitance.

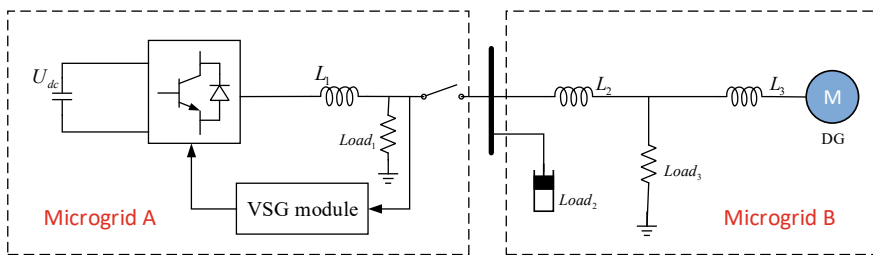


Fig. 1 Model of microgrid clusters

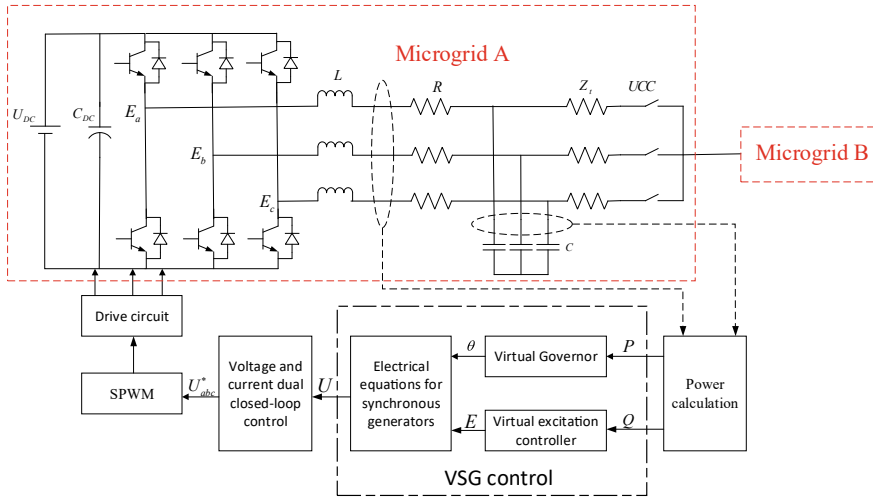


Fig. 2 Topology of microgrid A

The VSG main circuit employs a three-phase full-bridge inverter, and a DC power source is chosen to simulate the distributed generations, with a large capacitance connected in parallel on the DC side to stabilize the voltage. In low-voltage microgrids, the line impedance typically exhibits inductive resistance and can be represented as follows:

$$Z_t = R_t + jX_t \tag{1}$$

Set the polar logarithm of the virtual synchronous machine to 1 and use the second-order model, as follows:

$$\begin{cases} J \frac{d\Delta\omega}{dt} = T_m - T_e - D\Delta\omega = \frac{P_m}{\omega} - \frac{P_e}{\omega} - D(\omega - \omega_n) \\ \frac{d\delta}{dt} = \omega \\ E_0 = U + I(R_0 + jX_0) \end{cases} \tag{2}$$

In the given equation,  $J$  and  $D$  are the moment of inertia and damping coefficient, respectively;  $\omega$  is the angular velocity;  $T_m$ ,  $T_e$  refers to mechanical torque and electromagnetic torque respectively;  $P_m$ ,  $P_e$  refers to mechanical power and electromagnetic power respectively;  $\delta$  is the power angle;  $E_0$  is the excitation electromotive force of the synchronous generator;  $U$ ,  $I$  represents the armature voltage and armature current of the synchronous generator, respectively;  $R_0$ ,  $X_0$  represents the armature resistance and synchronous reactance, respectively.

The control module of VSG consists of three parts: virtual governor, virtual excitation controller, and electrical equation of synchronous motor. The virtual speed controller determines the reference voltage phase angle  $\theta$  based on the active power

$P$  calculated from a power sensor. Similarly, the virtual excitation controller determines the output voltage magnitude  $E$  of the VSG inverter bridge based on the reactive power  $Q$  calculated from the power sensor. The electrical equations for a synchronous machine can be used to obtain the reference voltage  $U$  by utilizing the  $\theta$  and  $E$  parameters. This reference voltage  $U$  serves as the input signal for the voltage-current double closed-loop control scheme.

### 3 Pre-synchronization Control Strategy in Microgrids

#### 3.1 Microgrid Mode Switching Stability Analysis

When using VSG control technology, transient instability may occur during mode switching in microgrids. In this paper, mode switching refers to the transient process of connecting microgrids with microgrid clusters.

The islanded operation mode of the microgrid refers to a mode of operation in which the microgrid independently controls the voltage and frequency inside the network to meet the load demand, without relying on the microgrid cluster. When the microgrid is operating in islanded mode, there is a certain voltage amplitude and phase difference between it and the microgrid cluster while maintaining the stability of the voltage and frequency within the network. During the process of connecting to the microgrid cluster, if there is a large difference in voltage amplitude and phase between the two, a large surge current will occur at the moment of connection. Surge currents not only cause connection failure and system crashes but damage power electronic devices. The potential impact of VSG transitioning to grid-connected mode can be mathematically verified in the equation using terminology from the electrical engineering field, as follows:

$$u_a = U \cos \omega t + \theta \quad (3)$$

$$u_{ga} = U_g \cos(\omega_g t + \theta_g) \quad (4)$$

In the equation,  $U$  and  $\theta$  representing the amplitude and phase of the output voltage of the VSG inverter respectively;  $U_g$  and  $\theta_g$  represents the voltage amplitude and phase at the UCC on the microgrid cluster side.

During the process of connecting a microgrid into the microgrid cluster, the difference between the output voltage of the VSG and the voltage at UCC can be expressed as  $\Delta u$ .

$$\Delta u = u - u_g = U \cos(\omega t + \theta) - U_g \cos(\omega_g t + \theta_g) \quad (5)$$

Under normal operating conditions, it can be approximately assumed that the output voltage amplitude of VSG is equal to the voltage amplitude on the microgrid group side,  $U \approx U_g$ , then Formula (5) can be rewritten as follows:

$$\Delta u_a \approx 2U \sin\left(\frac{\omega - \omega_g}{2} + \frac{\theta - \theta_g}{2}\right) \cos\left(\frac{\omega + \omega_g}{2} + \frac{\theta + \theta_g}{2}\right) \quad (6)$$

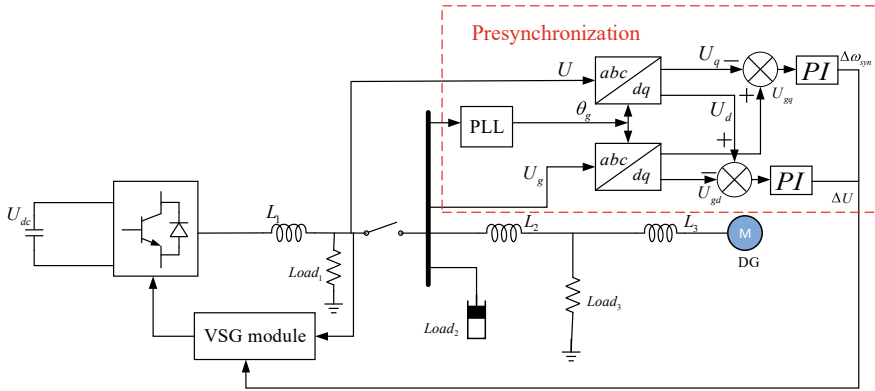
From Formula (6), it can be seen that the maximum voltage difference can reach  $2U$ . This will result in a large surge current, causing the failure of integrating the microgrid into the microgrid cluster. To address this stability issue, measures need to be taken to eliminate the phase and amplitude differences in voltage between the microgrid and the microgrids before the microgrid is merged into the microgrid cluster.

### 3.2 Pre-synchronization Control Strategy

When a microgrid is integrated into a microgrid cluster, there exists a certain voltage magnitude and phase difference between the microgrid and the cluster. As shown in Formula (6), without pre-synchronization of the voltage phase and magnitude, a large surge current will be generated during the grid connection moment, which may lead to a failed integration.

The pre-synchronization control strategy shown in Fig. 3 does not change the structure of the VSG control itself, but adds compensation for angular frequency and voltage in the control of the virtual speed governor and virtual excitation controller, thereby achieving pre-synchronization of voltage magnitude and phase before grid connection. The concrete operation steps are as follows: before grid connection, first replace the reference frequency  $\omega_n$  of the VSG with the frequency  $\omega_g$  of the microgrid cluster, and replace the reference voltage  $U_n$  of the VSG with the voltage magnitude  $U_g$  at the connection point. Then, turn on the pre-synchronization control switch. When the frequency and magnitude of the VSG output voltage are within the allowable error range comparing with UCC, pre-synchronization control can be considered as completed. At this time, turn on the grid connection switch to achieve the grid connection operation of the microgrid. After the grid connection is completed, turn off the pre-synchronization controller switch.

The control principle of pre-synchronization is shown in Fig. 3. Firstly, the frequency  $\omega_g$  of microgrid B is obtained by using the phase-locked loop as the reference frequency for microgrid A. Then, the output voltage  $U$  of the VSG is decomposed into the d-q axis with the phase  $\theta_g$  of the common connection point voltage as the reference. The d-axis and q-axis components of the voltage are  $U_d$  and  $U_q$ . Next, the reference voltage of the q-axis is set to zero, and the deviation value of  $U_q$  is sent to a PI controller, so that the synchronous compensation angular frequency  $\Delta\omega_{syn}$  can be obtained. By adding  $\Delta\omega_{syn}$  to the output angular frequency  $\omega$  of the active power control loop, the phase after pre-synchronization can be obtained. The



**Fig. 3** Pre synchronization control for microgrids

phase synchronization between the VSG output voltage and the common connection point voltage can be achieved.

When VSG is connected to the grid, the three-phase voltage  $u$  and voltage amplitude  $U_m$  the relationship between them is:

$$\begin{bmatrix} u_a \\ u_b \\ u_c \end{bmatrix} = \begin{bmatrix} U_m \cos \omega t \\ U_m \cos(\omega t - \frac{2\pi}{3}) \\ U_m \cos(\omega t + \frac{2\pi}{3}) \end{bmatrix} \tag{7}$$

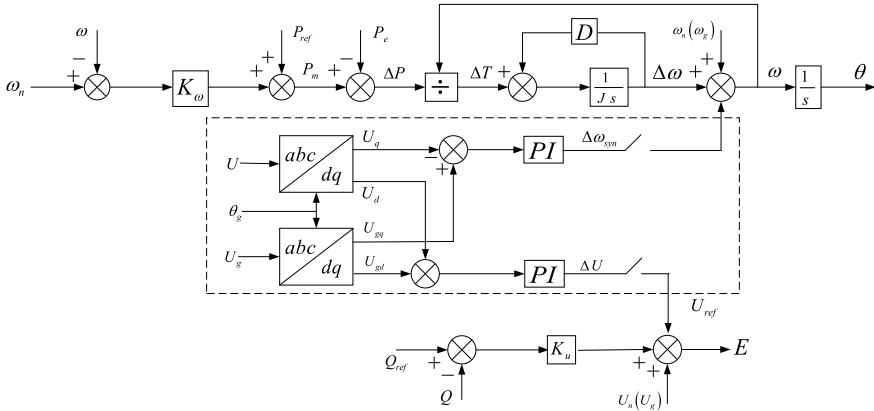
The formula for converting Formula (7) from the  $abc$  coordinate system to the  $dq$  coordinate system is as follows:

$$T_{abc \rightarrow dq} = \begin{bmatrix} \cos(\omega t) & \cos(\omega t - \frac{2\pi}{3}) & \cos(\omega t + \frac{2\pi}{3}) \\ -\sin(\omega t) & \sin(\omega t - \frac{2\pi}{3}) & -\sin(\omega t + \frac{2\pi}{3}) \end{bmatrix} \tag{8}$$

From Eqs. (6) and (7), it can be concluded that:

$$\begin{bmatrix} u_d \\ u_q \end{bmatrix} = T_{abc \rightarrow dq} \begin{bmatrix} u_a \\ u_b \\ u_c \end{bmatrix} = \begin{bmatrix} U_m \\ 0 \end{bmatrix} \tag{9}$$

From Eq. (8), it can be observed that after the  $dq$  transformation, the d-axis component of the terminal voltage is equal to the voltage magnitude  $U_m$ , while the q-axis component is 0. To achieve pre-synchronization of the voltage magnitude, it is necessary to make the voltage magnitude at the terminal equal to the d-axis component of the VSG output voltage. By achieving pre-synchronization of the voltage magnitude, we ensure that the voltage magnitude is equal.



**Fig. 4** Pre-synchronization controller

By combining the aforementioned pre-synchronization of voltage phase and magnitude, the pre-synchronization control strategy designed in this paper is obtained, as shown in Fig. 4.

### 4 Simulation Results and Validation

To validate the feasibility of the proposed pre-synchronization strategy in this paper, a simulation model was constructed using Matlab/Simulink, as depicted in Fig. 1. The system parameters were set according to Table 1.

The simulation experiment was set up as follows: A VSG-controlled microgrid operated in islanded mode with a constant impedance load of 14 kW. Simultaneously, the main microgrid, equipped with a diesel generator as the power generation unit, operated in islanded mode with a composite load comprising a constant impedance

**Table 1** Main parameters of simulation

Parameter	Value
Simulation time/s	10
Simulation step size/s	5e-05
Frequency adjustment coefficient $k_ω$	1/5.23e-04
Voltage adjustment coefficient $k_u$	0.001
Rated frequency $f_n/Hz$	50
Rotational inertia $J$	0.05
Damping coefficient $D$	5
Rated voltage $U_n/V$	220
DC side voltage $V_{dc}/V$	800

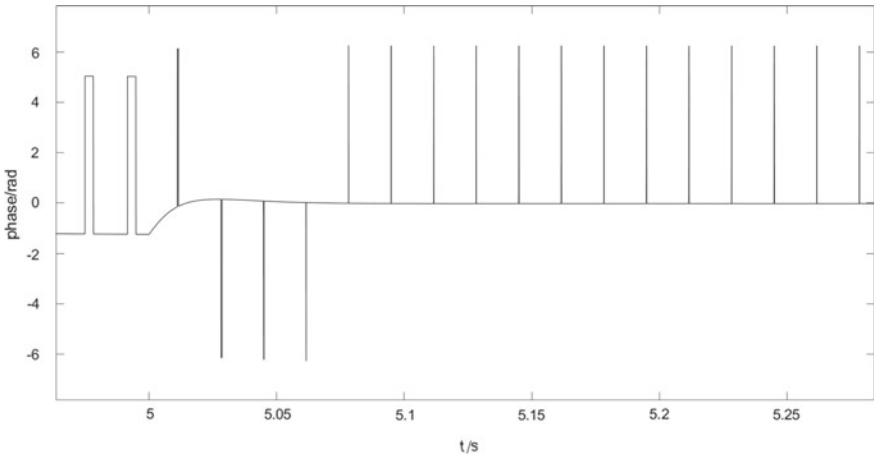


load of 450 kW and a motor load of 500 kW. The simulation duration in this study was set to 10 s. At the instant of the fifth second, the pre-synchronization switch was turned on to achieve pre-synchronization of voltage magnitude and phase. At the instant of the sixth second, the grid connection switch at the UCC was opened for grid integration. The reason for opening the pre-synchronization switch at 5 s is that both microgrids need to be in a stable state before performing the pre-synchronization operation. However, during the simulation, there is a startup time for the synchronous generator, during which the voltage and current of the microgrid exhibit decay oscillations until 5 s when the voltage and frequency reach a stable state, meeting the requirements for pre-synchronization.

At 5 s, the pre-synchronization switch is turned on, and the pre-synchronization controller starts operating. The voltage amplitude of the inverter output and the voltage vector of the microgrid cluster are transformed into the rotating coordinate system through Clark transformation and Park transformation, yielding the phase angle and amplitude deviation of the voltage. These values are adjusted through PI controllers to obtain compensating values for grid frequency and grid voltage. These values are then fed into the active and reactive power loops controlled by the VSG to ensure consistent phase and amplitude between the pre-synchronization side and the microgrid cluster side.

As shown in Fig. 5, the phase difference between two microgrids is depicted. Based on the image, it can be observed that prior to the activation of the pre-synchronization switch, there exists a phase difference of  $-1.32$  radians between them, accompanied by periodic step changes. This is attributed to slight frequency variations between the two microgrids before pre-synchronization, resulting from minor differences in regulating the synchronous generators. This leads to periodic phase jumps. After enabling the pre-synchronization switch, the phase begins to pre-synchronize, and from Fig. 5, it can be observed that the phase difference significantly reduces to almost zero after approximately 0.06 s, achieving pre-synchronization of the voltage phases on both sides. At 6 s, when the grid connection switch is turned on, the phase difference remains unchanged. This indicates that there is no instability problem during the integration of microgrids into microgrid clusters. In the graph, numerous pulse-like straight lines appear, corresponding to values around  $6.28$  radians, which is approximately  $2\pi$ , conforming to the requirements of grid phase synchronization.

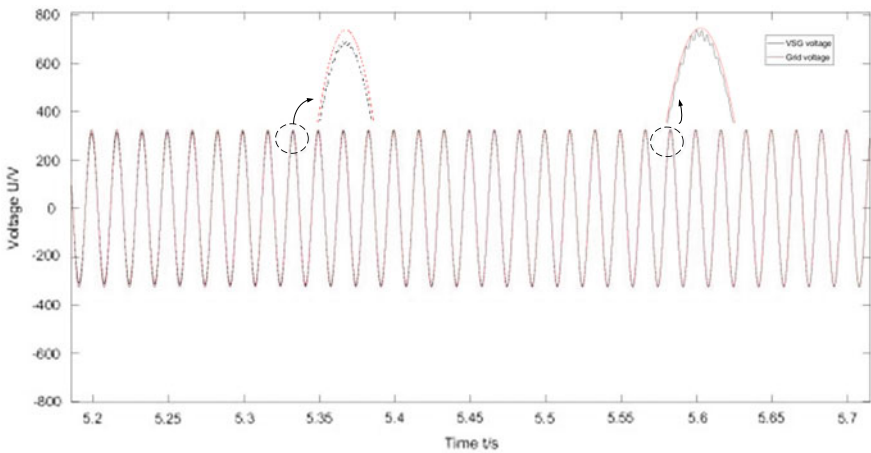
Figure 6 illustrates a comparison between the VSG output voltage and the microgrid bus voltage. The microgrid bus voltage is represented by the voltage at the UCC. The solid black line represents the VSG output voltage, while the red dashed line represents the microgrid bus voltage. Based on the comparison of the two curves, it can be observed that, prior to the operation of the 5-s pre-synchronization controller, there are significant phase and magnitude differences between the VSG output voltage and the microgrid bus voltage. However, after the closure of the 5-s pre-synchronization, the two curves gradually converge. The voltage difference between the microgrid bus voltage and the VSG output voltage at the same moment is depicted in Fig. 7. Prior to pre-synchronization, there is a noticeable voltage difference between the microgrid bus voltage and the VSG output voltage, reaching a maximum of 320 V. However, after the implementation of the pre-synchronization



**Fig. 5** Phase difference between the VSG output voltage and the UCC

controller, the voltage difference gradually decreases. At 5.6 s, the difference between the VSG output voltage and the UCC is within 10 V, which is below 5% and complies with the grid integration requirements. This achievement demonstrates the pre-synchronization of the VSG output voltage with the phase and magnitude of the grid voltage.

On the contrary, if grid connection is attempted without pre-synchronization, the system will become unstable. As shown in Fig. 8, it illustrates the variation of grid connection current when the pre-synchronization switch is not activated. It can be observed that when the grid connection switch is closed at 6 s, there is a phase and



**Fig. 6** Voltage of VSG and the UCC

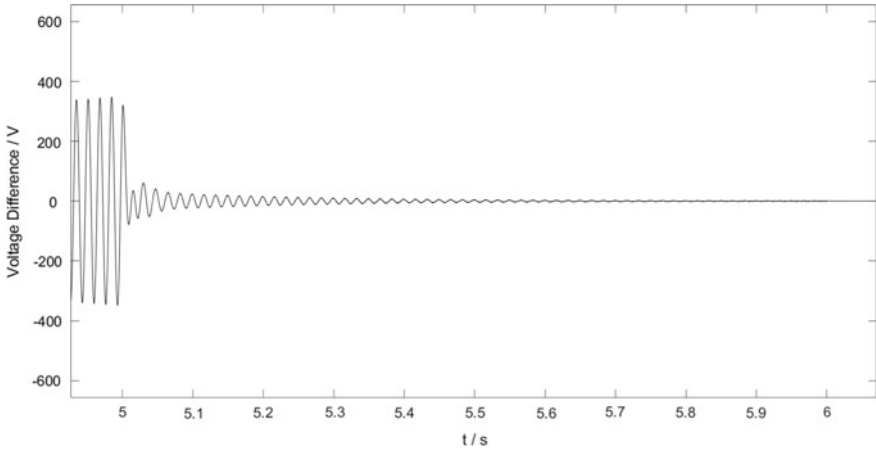


Fig. 7 Voltage difference between the VSG output voltage and the UCC

magnitude deviation between the VSG output voltage and the microgrid bus voltage. This deviation results in a maximum impulse current of up to 8 times the rated current, which can potentially damage power electronic devices and lead to grid connection failure.

The feasibility of the proposed pre-synchronization control strategy was validated by analyzing and comparing the VSG output voltage and microgrid bus voltage before and after pre-synchronization. By comparing the grid connection current with and without pre-synchronization control, it was confirmed that the pre-synchronization control strategy effectively suppresses the occurrence of impulse currents resulting

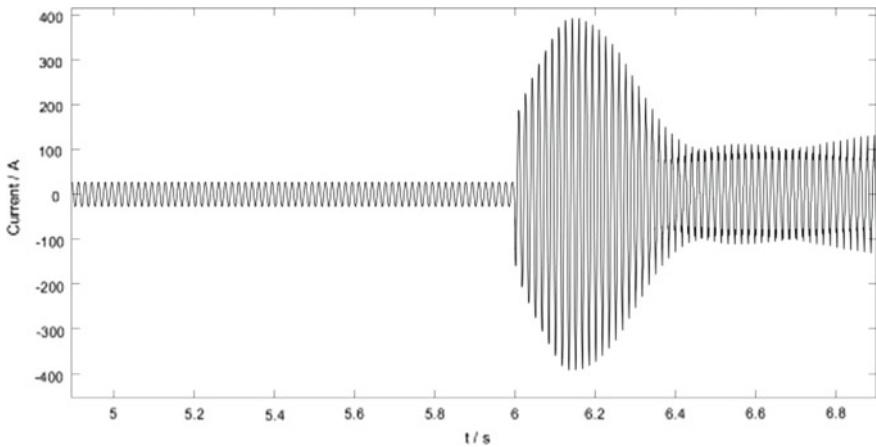


Fig. 8 Current on the VSG-side without pre-synchronization control

from grid connection, enabling a smooth transition of the microgrid integration into the existing microgrid cluster.

## 5 Conclusion

This paper proposes a microgrid cluster synchronization and integration strategy based on pre-synchronization control, enabling a seamless integration of a single microgrid into a cluster of microgrids. By compensating the frequency and voltage in the active power frequency loop and reactive voltage loop controlled by the VSG, the synchronization of voltage phase and magnitude among microgrids is achieved prior to grid connection. From the simulation results, it can be observed that compared to direct grid connection without pre-synchronization, this strategy effectively suppresses impulse currents and maintains stable operation of the microgrid cluster. These results validate the effectiveness of the proposed control strategy and provide a feasible solution for smooth integration of microgrids into a microgrid cluster.

## References

1. IEEE (2019) IEEE draft standard conformance test procedures for equipment interconnecting distributed energy resources with electric power systems and associated interfaces. IEEE Std 1547.1, 1-280
2. IEEE (2019) IEEE draft standard conformance test procedures for equipment interconnecting distributed energy resources with electric power systems and associated interfaces. IEEE Std 1547.1, 1-283
3. Nichols DK, Stevens J, Lasseter RH et al (2006) Validation of the CERTS microgrid concept the CEC/CERTS microgrid testbed. In: 2006 IEEE power engineering society general meeting. IEEE, Montreal, QC, Canada, p 3
4. Akula SK, Salehfar H (2021) Risk-based classical failure mode and effect analysis (FMEA) of microgrid cyber-physical energy systems. In: 2021 North American power symposium (NAPS). Arizona State University, TX, USA, pp 1–6
5. Movahednia M, Karimi H, Jadid S (2022) A cooperative game approach for energy management of interconnected microgrids. *Electric Power Syst Res* 213:108772
6. Yang W, Kang X, Wang X, Wang M (2023) MPC-based three-phase unbalanced power coordination control method for microgrid clusters. *Energy Rep* 9:1830–1841
7. Singh B, Pathak G, Panigrahi BK (2018) Seamless transfer of renewable-based microgrid between utility grid and diesel generator. *IEEE Trans Power Electron* 33(10):8427–8437
8. Zhong Q, Nguyen P, Ma Z et al (2014) Self-synchronized synchronverters: inverters without a dedicated synchronization unit. *IEEE Trans Power Electron* 29(2):617–630
9. Xu H, Zhang X, Liu F et al (2013) Synchronization strategy of microgrid from islanded to grid-connected mode seamless transfer. In: 2013 IEEE international conference of IEEE region 10. IEEE, Xi'an, pp 1–4
10. Meng L, Su C, Wu J, Ren T, Wang Z, Yi H (2022) Design and parameter analysis of an improved pre-synchronization method for multiple inverters based on virtual synchronization generator control in microgrid. *Energy Rep* 8:928–937

# Fault Identification of MOA Based on Infrared Thermal Imaging



Cheng Guokai, Weng Donglei, Zhou Qibo, Jiang Jiong, Zhang Rongwei, Sun Long, Shen Houming, and Wei Zhen

**Abstract** Metal oxide arrester (MOA), as an important device for limiting over-voltage in transmission lines, can ensure the safe and stable operation of the power system. The technology of using infrared instruments for troubleshooting arrester is relatively mature, but environmental factors can cause significant interference in infrared detection, and its accuracy is not high through visual observation. This article proposes an improved U-Net MOA segmentation algorithm to segment arresters in infrared images, and obtains temperature information from the images through operations such as dataset preprocessing, image segmentation, grayscale conversion, and temperature extraction. By combining the surface temperature method, the arrester in the infrared image can be diagnosed and the fault level and related treatment suggestions can be given.

**Keywords** Arrester · Convolutional neural network · Fault diagnosis

---

C. Guokai · W. Donglei · J. Jiong (✉) · S. Long  
State Grid Zhejiang Electric Power Co., Ltd, Ningbo Power Supply Company, Ningbo 315016,  
Zhejiang, China  
e-mail: [1158931790@qq.com](mailto:1158931790@qq.com)

Z. Qibo  
Ningbo Xinsheng Medium Voltage Electrical Appliance Co., Ltd, Ningbo 315020, Zhejiang,  
China

Z. Rongwei  
Ningbo Yongyao Power Investment Group Co., Ltd, Ningbo 315099, Zhejiang, China

S. Houming · W. Zhen  
Wuhan NARI Limited Liability Company, State Grid Electric Power Research Institute,  
Wuhan 430074, Hubei, China

© Beijing Paiké Culture Commu. Co., Ltd. 2024

X. Dong and L. Cai (eds.), *The Proceedings of 2023 4th International Symposium on Insulation and Discharge Computation for Power Equipment (IDCOMPU2023)*, Lecture Notes in Electrical Engineering 1103, [https://doi.org/10.1007/978-981-99-7413-9\\_52](https://doi.org/10.1007/978-981-99-7413-9_52)

547

## 1 Introduction

As the economic operation gradually improves, providing safe and stable electricity security is crucial. Metal oxide arrester (MOA), as an overvoltage protection device, has advantages such as strong energy absorption capacity, simple structure, and good stability. However, due to long-term exposure to nature, this device is prone to moisture, aging, short circuits, and surface pollution, resulting in thermal faults and power accidents [1]. Infrared thermal imaging technology is one of the important methods to determine whether power equipment is faulty. During the detection process, infrared detection equipment can avoid contact with the tested equipment, directly obtain the infrared image of the tested equipment without power outage, and then make fault diagnosis based on the operating temperature standards of the equipment. It has been widely used in power equipment monitoring and fault diagnosis.

The traditional manual fault diagnosis is to transmit the detected images or videos to the monitoring system through infrared instruments, and technical personnel can make judgments and diagnoses based on experience. Due to the large amount of data, the diagnosis process has characteristics such as long time consumption, large errors, high cost, and low efficiency [2, 3]. With the continuous expansion of the power grid and the increasing number of power equipment, how to effectively use infrared temperature measurement data for intelligent detection and recognition of target images in the face of massive monitoring data is the next urgent problem to be solved. It is a key link to achieve comprehensive power system intelligence and promote intelligent substations.

In recent years, the use of image processing technology and artificial intelligence technology to automatically detect and identify faults in power equipment has gradually become a development trend. Among them, deep learning has higher generalization ability compared to traditional machine learning and is widely used in image processing. Its biggest advantage is that it attempts to train images in an incremental manner, reducing subjective human interference factors, and can automatically extract network features.

This article proposes a diagnostic method based on surface temperature method for judging thermal faults of arresters; Then, an improved convolutional neural network object detection algorithm is used to achieve accurate automatic detection of arrester position and temperature, improving the ability to accurately locate and identify hidden danger points of arresters; Finally, a thermal fault diagnosis system for arresters was designed, which can quickly and effectively diagnose the health status of arresters and avoid unnecessary losses.

## 2 Principle of Fault Diagnosis

### 2.1 Principle of MOA Segmentation

At present, Convolutional Neural Networks (CNN) have been widely used in image semantic segmentation. Classic network models include FCN [4], SegNet [5], U-Net [6], Deeplab [7], and DANet [8]. In infrared image arrester fault diagnosis, there is a lack of public datasets and belongs to small sample object segmentation. Compared to other models, U-Net network structure is simpler and more effective. Therefore, this article utilizes an improved U-Net network to segment arrester devices in infrared images, and the algorithm framework is shown in Fig. 1.

In Fig. 1, the left half uses VGG16 as the backbone feature extraction network, with a total of 5 layers. The middle section introduces Effective Channel Attention (ECA) to achieve a non dimensionality reducing local cross channel interaction strategy, highlighting important features while addressing the issue of network performance and complexity, further enhancing detection accuracy [9]. The right part is to strengthen the feature extraction network, restore the image size, use the bilinear interpolation method for up sampling, perform four times of up sampling and convolution operations on the image, and splice and fuse with the features of the coding module to restore it to the original image size. Then, conduct channel adjustment on the image through convolution operation, and finally obtain the segmented image.

The algorithm for defining the fault area of arresters using convolutional neural networks requires a large amount of training dataset. However, there is currently no publicly available infrared database for arresters. Therefore, the experimental dataset in this article comes from typical infrared images of arresters taken in a certain substation and collected from the internet. In order to solve the problem of weak generalization ability of the model due to insufficient sample size in the infrared

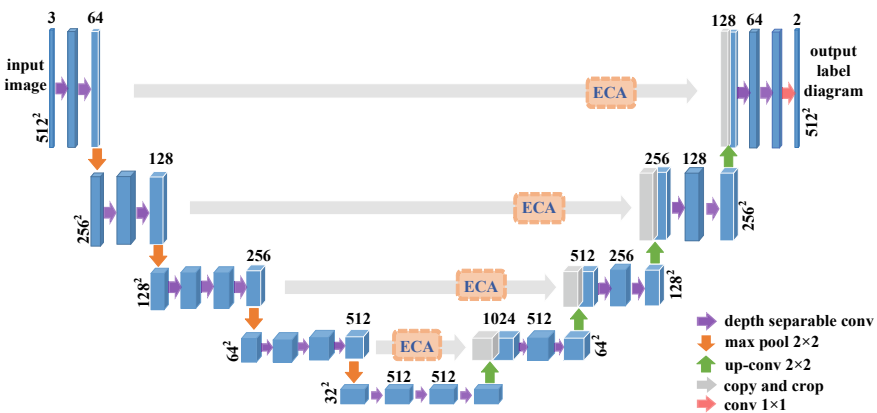
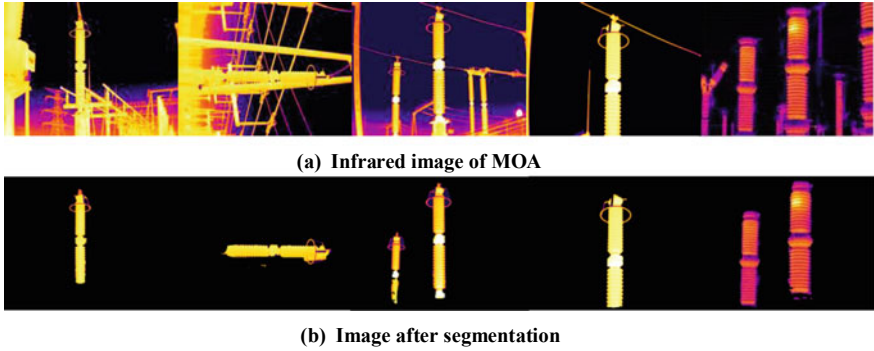


Fig. 1 Improved U-Net algorithm framework



**Fig. 2** U-Net segmentation effect

dataset, the original image of the arrester is horizontally flipped, randomly rotated, and stretched to expand the arrester dataset. The processed dataset contains a total of 830 device images, with a standardized image size of  $700 * 525$ .

The trained network using this dataset is used to segment the infrared image of the lightning arrester, and the results are shown in Fig. 2.

## 2.2 Principle of Temperature Extraction

In infrared images, the temperature of each pixel is stored in a matrix form. Due to the fact that the grayscale values of infrared image pixels can reflect the temperature level, that is, the larger the grayscale value, the higher the corresponding temperature. Therefore, this section obtains a grayscale matrix after identifying and locating the arrester equipment in the infrared image, and then extracts temperature values based on grayscale information.

A common method is to sum the three components of RGB and take the average value, but according to the importance of color, weighting the three components with different weights can obtain a more accurate grayscale image [10]. The formula for converting RGB images to grayscale images is:

$$\text{Gray} = R \times 0.299 + G \times 0.587 + B \times 0.144 \quad (1)$$

In the formula,  $R$ ,  $G$  and  $B$  represents the color intensity corresponding to red, green and blue in  $[0 \ 255]$ . Perform grayscale processing on the MOA identified in Fig. 2, some results are shown in Fig. 3.

In order to obtain the highest temperature value in the infrared image, it is necessary to determine the temperature distribution on the surface of the arrester. According to the gray image, the surface gray pixel matrix can be extracted, and the surface temperature distribution matrix of arrester can be obtained by constructing



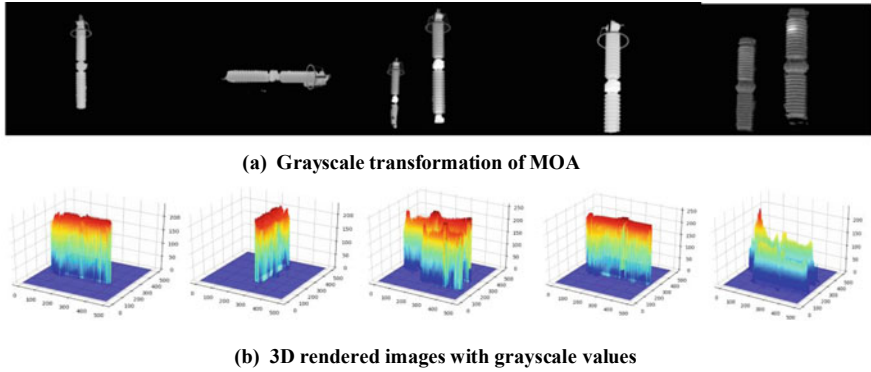


Fig. 3 Gray processing of arrester

the unary linear function of the temperature value in the image. The conversion formula between temperature and grayscale is as follows:

$$T = \frac{(T_1 - T_2)}{G_1 - G_2}G + (T_1 - \frac{(T_1 - T_2)}{G_1 - G_2}G_1) \tag{2}$$

In the formula,  $T$  represents the temperature value;  $G$  represents the grayscale value;  $T_1$  and  $T_2$  are the highest and lowest temperatures on the color bar in infrared images, while  $G_1$  and  $G_2$  are the maximum and minimum grayscale values after removing the background area in the image.

Therefore, the temperature distribution matrix of the MOA can be obtained, and the maximum and minimum values of the arrester surface temperature can be calculated. Finally, surface temperature method can be used to determine whether the arrester is faulty.

### 2.3 Principles of Fault Detection

Since the lightning arrester is a voltage-heated device, the surface temperature method is used to determine whether it is faulty or not. The formula for calculating surface temperature difference is as follows:

$$\Delta T = T_{\max} - T_{\min} \tag{3}$$

In the formula,  $\Delta T$  is the surface temperature difference,  $T_{\max}$  is the maximum surface temperature,  $T_{\min}$  is the minimum surface temperature.

After calculating the surface temperature difference, “Application rules of infrared diagnosis for live electrical equipment” is used to determine if the arrester is faulty and to diagnose its fault level.

### 3 Validation

This article selects 220 kV arresters as the research object. FLIR infrared thermal imager is used to capture infrared images of arresters at night. Based on infrared image preprocessing and positioning recognition algorithms, the main body of the arrester is separated from the background, and its grayscale information is converted into temperature information. Finally, surface temperature values are calculated to evaluate the operating status of MOA. If it is in a fault state, diagnostic suggestions are given. The diagnostic results are shown in Fig. 4.

As shown in Fig. 4d, there is obvious mutation in the temperature distribution of the arrester in the gray image, and the arrester may be faulty according to manual judgment; By using Eq. 3, the maximum temperature of this 220 kV arrester can be calculated as 10.86 °C, with a normal temperature of 9.97 °C and an ambient temperature of 8.9 °C. Ultimately, it can be concluded that the surface temperature difference is 0.89 °C, indicating that the arrester is faulty and requires attention from

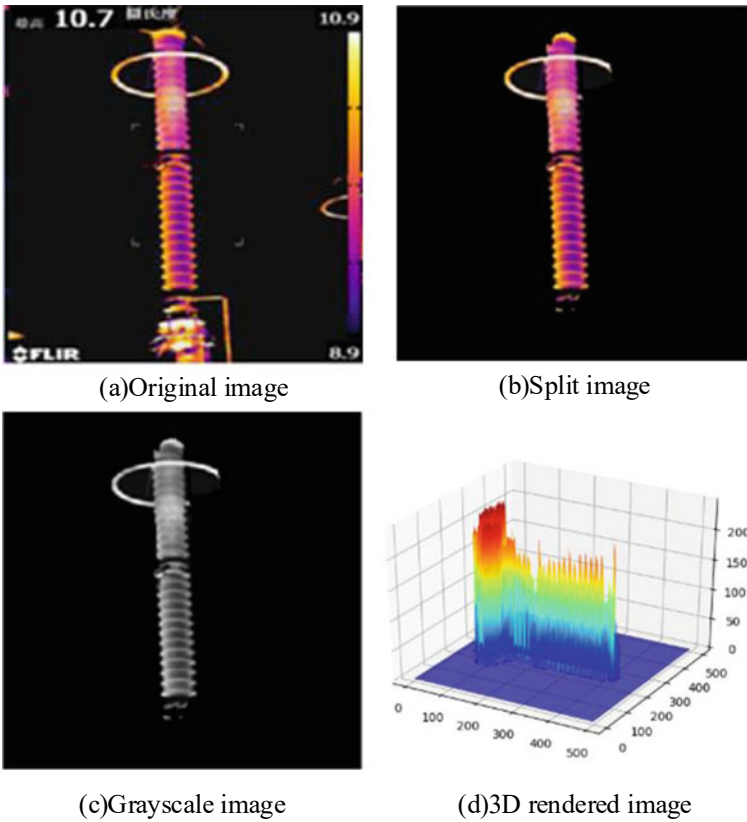


Fig. 4 Image of fault diagnosis results

the staff. It can be observed that the diagnostic system can accurately detect faults even when the surface heat of the arrester is relatively small.

## 4 Conclusion

- (1) On the basis of infrared arrester image preprocessing, further research was conducted on infrared image segmentation algorithms. An improved U-Net based MOA segmentation algorithm and device temperature value extraction algorithm were proposed. By replacing ordinary convolutions with deep separable convolutions and introducing efficient channel attention modules, the parameter and computational complexity were greatly reduced, and the computer operating memory was reduced, Enhance the learning rate of the network.
- (2) In order to achieve intelligent fault diagnosis and recognition of lightning arrester infrared images, this article realizes the conversion of grayscale information in infrared images into temperature information, and uses surface temperature difference method to diagnose lightning arrester faults in infrared images, providing fault levels and processing suggestions. This article verifies the reliability of an intelligent diagnosis system for infrared image faults. By loading a typical 220 kV lightning arrester infrared image, it can be found that the fault diagnosis system can effectively detect the highest temperature and fault level, and therefore can be used for online monitoring and diagnosis of lightning arrester equipment.

## References

1. Pan H, Du H, Ma YT et al (2022) Fault analysis on MOA used in an old 500 kV station. *Insulators and Surge Arresters* 310(06):45–51 (in Chinese)
2. Wang KX, Ren FJ, Ni HJ et al (2022) Temperature value recognition algorithm for the infrared image of power equipment. *CAAI Trans Intell Syst* 17(03):617–624 (in Chinese)
3. Wang JZ, Yin LJ, Xian RC et al (2021) Power equipment fault area segmentation method based on improved SLIC algorithm. *Comput Appl Softw* 38(01):222–226+237 (in Chinese)
4. Shelhamer E, Long J, Darrell T (2017) Fully convolutional networks for semantic segmentation. *IEEE Trans Pattern Anal Mach Intell* 39(4):640–651
5. Badrinarayanan V, Kendall A, Cipolla R (2017) SegNet: a deep convolutional encoder-decoder architecture for image segmentation. *IEEE Trans Pattern Anal Mach Intell* 39(12):2481–2495
6. Olaf R, Philipp F, Thomas B (2015) U-Net: convolutional networks for biomedical image segmentation. In: *International conference on medical image computing and computer-assisted intervention*, pp 234–241
7. Chen LC, Papandreou G, Kokkinos I, Murphy K, Yuille AL (2018) DeepLab: semantic image segmentation with deep convolutional nets, Atrous convolution, and fully connected CRFs. *IEEE Trans Pattern Anal Mach Intell* 40(4):834–848
8. Fu J, Liu J, Tian H et al (2019) Dual attention network for scene segmentation. In: *2019 IEEE/CVF conference on computer vision and pattern recognition (CVPR)*, IEEE, pp 3141–3149

9. Li X, Wang WH, Hu XL et al (2020) Selective Kernel Networks. In: Proceedings of 2019 IEEE/CVF conference on computer vision and pattern recognition. Long Beach, pp 510–519
10. Gu Z, Li XP, Zhou L et al (2022) Research on automatic insulation detection of power equipment based on infrared image recognition technology. *Manuf Autom* 44(10):174–178 (in Chinese)

# Research on Key Technologies of Intelligent Defect Image Detection for Substation Equipment in Complex Scenes



Ning Yang, Lihua Li, Yang Yang, Jiayun Zhu, and Wentong Shang

**Abstract** Image feature matching and image recognition are two important branches of image processing. In recent years, with the rapid development of artificial intelligence, big data and other information technology, as well as the technological breakthrough of computer computing ability, image analysis technology has been widely used in various industries. Daily inspection and defect detection of substation equipment is an important work of equipment operation and maintenance. Relying on image intelligent processing technology, it can greatly improve the efficiency of operation and maintenance, reduce the workload of operation and maintenance personnel, improve the detection probability of equipment defects and abnormalities, and ensure the safe and stable operation of power grid. Aiming at the complex defect scene of substation equipment, it has good research significance and application prospect to carry out the research of intelligent defect image detection technology. This paper described the basic principles and development of image feature matching technology and artificial intelligence image recognition technology, discussed the key problems and technical difficulties in the practical application of image processing technology, introduced the solutions and technical characteristics of key technologies, and put forward the image intelligent detection algorithm and multi-dimensional image comprehensive analysis method suitable for complex scenes. The verification results indicated that the method described in the article can effectively solve the problem of device multi scene defect detection.

**Keywords** Image feature registration · Image recognition · Artificial intelligence · Image detection · Substation equipment

---

N. Yang (✉) · L. Li · Y. Yang · J. Zhu · W. Shang  
China Electric Power Research Institute, 15 Xiaoying East Road, Haidian District, Beijing, China  
e-mail: [ynjackie@163.com](mailto:ynjackie@163.com)

© Beijing Paiké Culture Commu. Co., Ltd. 2024  
X. Dong and L. Cai (eds.), *The Proceedings of 2023 4th International Symposium on Insulation and Discharge Computation for Power Equipment (IDCOMPU2023)*, Lecture Notes in Electrical Engineering 1103, [https://doi.org/10.1007/978-981-99-7413-9\\_53](https://doi.org/10.1007/978-981-99-7413-9_53)

555

## 1 Introduction

The operation and maintenance of power grid equipment are fundamental to the entire process control and safety assurance of equipment. Daily equipment inspection is also the top priority of operation and maintenance work, and is an important means to obtain equipment operation status and provide operation and maintenance decisions. With the continuous advancement of the construction of the large power grid, the number of power grid equipment is rapidly increasing, and the operation of the large power grid also puts forward higher requirements for equipment operation safety. However, the number of power grid operation and maintenance personnel has remained relatively stable for a long time, and the operation and maintenance work of power grid equipment is facing a prominent contradiction between a surge in workload and a relative shortage of personnel. Therefore, it is urgent to carry out lean operation and maintenance control of power grid equipment, in order to improve the quality and efficiency of substation operation and maintenance work.

With the application of substation inspection robots and video monitoring devices, the inspection work of substation equipment can currently be assisted by inspection robots or video monitoring devices. However, a large number of inspection image samples require manual review to find equipment defects, which is inefficient and has a high rate of missed inspections. All of these cannot support the need for lean operation and maintenance control in substations, making it difficult to fundamentally reduce the workload of operation and maintenance personnel.

In recent years, computer computing power has been continuously improved, big data analysis technology has been continuously promoted and applied, and the new generation of artificial intelligence technology has also made breakthrough progress, providing strong technical support for artificial intelligence processing technologies such as image discrimination and recognition. The intelligent inspection technology for substations is developing towards intelligence, digitization, networking, and high-speed, providing feasible ways to solve the above problems.

Therefore, it is urgent to focus on the actual needs of substation operation and maintenance sites, research and establish image fusion analysis technology for substation equipment defects suitable for complex scenarios, improve the intelligence and practicality level of inspection equipment, completely release inspection personnel from daily heavy inspection tasks, achieve unmanned intelligent inspection of substations, and effectively improve the efficiency and quality of substation equipment inspection work.

## 2 Abnormal Image Discrimination Technology Based on SIFT

### 2.1 Basic Principles of SIFT Algorithm

Image matching technology originated in the 1970s and was first applied in the aerospace field, used for terminal guidance of military space vehicles and satellite map positioning in countries such as the United States. After the 1980s, the application scope gradually expanded to fields such as intelligent robots, computer vision, unmanned navigation, and medical assisted diagnosis [1, 2]. Early image matching methods were mostly corner matching algorithms, including Harris operator [3], FAST (features from accelerated segment test) operator [4], etc. In the late 1990s, David Lowe proposed the SIFT (scale invariant feature transform) method, which is a local feature algorithm. It maintains invariance for rotation, scale scaling, and brightness changes, and maintains a certain degree of stability for perspective changes, affine transformation, and noise, achieving good application results [5]. At present, image matching technology is mainly divided into grayscale based image matching methods and feature based image matching methods based on matching principles and convergence conditions [6].

The SIFT algorithm is a classic feature matching algorithm with high accuracy, strong adaptability, good robustness, easy implementation, and can be used for fast image matching. This article selects the SIFT algorithm for matching and comparing abnormal images of substation equipment.

The main implementation steps of the SIFT algorithm include five main steps: constructing feature scale space, detecting feature points, determining feature direction, calculating descriptors, and feature matching, as shown in Fig. 1.

#### (a) Constructing Feature Scale Space

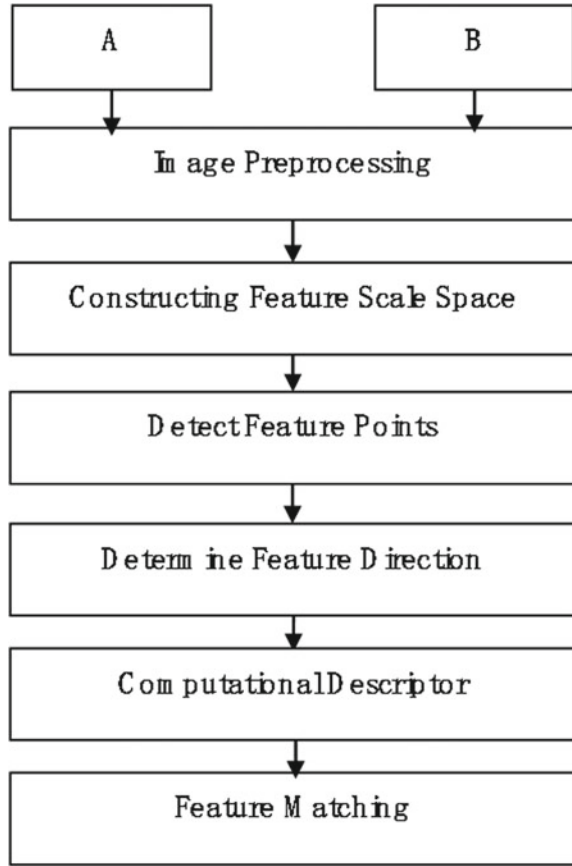
The feature scale space was proposed by Iijima et al. in 1962. Its core idea is to introduce scale factors and transform images into a set of image sequences at different scales through spatial transformation. SIFT algorithm uses Gaussian function convolution kernel  $G(x, y, \sigma)$  to building scale space  $L(x, y, \sigma)$ .

$$L(x, y, \sigma) = G(x, y, \sigma) * I(x, y). \quad (2-1)$$

The SIFT algorithm utilizes the Gaussian difference method DoG (Difference of Gaussian, DoG) to construct a pyramid image. The image in the DoG scale space is obtained by subtracting two adjacent Gaussian scale spaces

$$\begin{aligned} D(x, y, \sigma) &= [G(x, y, k\sigma) - G(x, y, \sigma)] * I(x, y) \\ &= L(x, y, k\sigma) - L(x, y, \sigma) \end{aligned} \quad (2-2)$$

Fig. 1 SIFT algorithm flowchart



The object of this article’s detection application is the equipment inspection images inside the substation, which are mostly collected using high-definition cameras. The image pixels are generally above 1080p, and the Gaussian pyramid has 10 layers, with each layer being half the size of the previous layer.

(b) Detect Feature Points

Find extreme points in the established DoG scale space, and perform extreme detection based on the size of each adjacent layer image pixel in the DoG space. Calculate the position of the extremum point based on Taylor expansion  $D(x, y, \sigma)$  and derivative  $\hat{X}$ .

$$\hat{X} = -\frac{\partial^2 D^{-1}}{\partial X^2} \frac{\partial D}{\partial X} \tag{2-3}$$

In the SIFT algorithm, a threshold is generally set to obtain the solution of the equation through interpolation. In the interpolation iteration, singular points and edge



response points that exceed the boundary conditions are continuously removed, and the removal of edge response points generally adopts a second-order Hessian matrix.

(c) Determine Feature Direction

Calculate the gradient value of adjacent pixels of image feature points and obtain the stable direction of each feature point.

$$m(x, y) = \sqrt{(L(x + 1, y) - L(x - 1, y))^2 + (L(x, y + 1) - L(x, y - 1))^2} \tag{2-4}$$

$$\theta(x, y) = \text{tg}^{-1}\left(\frac{L(x, y + 1) - L(x, y - 1)}{L(x + 1, y) - L(x - 1, y)}\right) \tag{2-5}$$

(d) Computational Descriptor

Descriptors are used to represent the position, scale, and direction of each feature point. When calculating the descriptor, the first step is to use a 4 \* 4 pixel area as a subunit, each subunit containing 8 directions, totaling 4 \* 4 \* 8 = 128 dimension vectors, which is the descriptor.

(e) Feature Matching

After obtaining the feature points and descriptors of the target image and the comparison image, the SIFT algorithm uses Euler distance to judge the matching relationship and similarity of the images.

$$E(A, B) = \sqrt{\sum_{i=1}^{128} (Des_A(i) - Des_B(i))^2} \tag{2-6}$$

## 2.2 A Method and Verification for Distinguishing Abnormal Images of Substation Equipment Based on SIFT

(a) Establish a standard image database and abnormal image dataset

The inspection images inside the substation are usually captured by robots, cameras, or maintenance personnel at fixed points. Based on the intelligent inspection terminals of the substation, a standard image library of substation equipment is constructed under different terminals, perspectives, and time dimensions, as a reference object for image matching and comparison; Establish inspection image discrimination scenarios, including three types of scenarios: oil leakage, suspended solids hanging in the air, and bird nests. Build inspection image datasets based on a single device, different terminals, different perspectives, and different time dimensions for different

defect scenarios. Provide data support for defect detection based on image matching and comparison technology (Table 1).

(b) Experimental verification




Firstly, construct an image scale space to extract multi-scale features of image data. Secondly, extreme points in the image scale space are detected to identify feature points in the image. Finally, filter the extracted feature points and eliminate any negative feature points that affect the matching effect, such as low contrast and unstable edge influence points.

This article selects 2624 feature points based on the abnormal image features of the substation equipment, which are used to compare the feature matching points of two images in a set of images, as shown in Fig. 2.

The verification results of each defect scenario are shown in Table 2, with detection accuracy of 80% for oil leakage and suspended solids, and 90% for bird nests.

An example of the validation results is shown in Figs. 3 and 4.

**Table 1** Identify defect scenario types

No.	Defect scenario	Sample
1	Oil leakage	
2	Hanging suspended solids	
3	Bird nest	

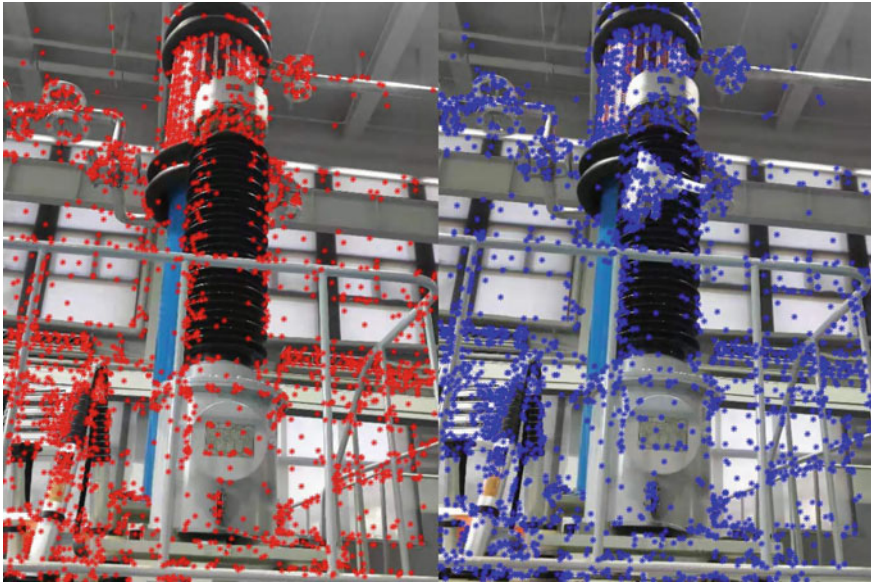


Fig. 2 Feature matching points

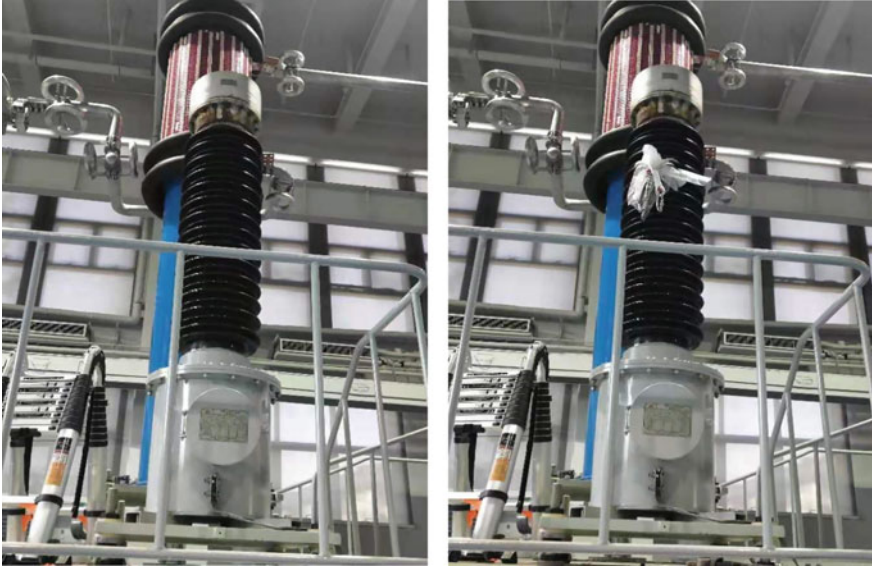
Table 2 Verification results of image discrimination algorithm

No.	Scene	Noise factor	Loss	Average calculation time (ms)
1	Oil leakage	0.2	0.1	327
2	Hanging suspended solids	0.2	0.1	345
3	Bird nest	0.1	0.1	289

### 3 Defect Image Recognition Technology Based on Faster RCNN

#### 3.1 Fundamentals of Faster RCNN

Image recognition technology refers to the use of techniques such as pattern recognition and machine learning to automatically recognize one or more semantic concepts present in an image. Image recognition technology can be traced back to the 1960s. Vapnik et al. proposed Support Vector Machine (SVM) in 1963 to solve pattern recognition problems. Over the following 50 years, through continuous improvement by Kimeldorf, Vapnik et al., it has developed into a theoretical system that includes algorithms such as least squares, decision trees, and hierarchical clustering. It is currently one of the important methods in image recognition [7, 8]. Another branch of image recognition technology is deep neural networks. As mentioned earlier, thanks to the



**Fig. 3** Reference image and comparison image

**Fig. 4** Experimental verification results



improvement of hardware computing power (GPU) and the accumulation and application of big data, deep neural networks have made significant progress in recent years. In some applications centered on deep learning, they have achieved the same or even better technical capabilities as humans in application scenarios that meet specific conditions. Krizhevsky et al. proposed in 2012 the use of convolutional neural networks (CNN) for large-scale image recognition tasks. The accuracy of image recognition tasks has rapidly increased, with Top5 accuracy exceeding 97% and 89% on representative datasets ImageNet and Place365, respectively [9, 10].

Faster RCNN has integrated the target region extraction layer, region screening layer, and target analysis layer into one network, greatly improving overall performance, especially in terms of detection speed. The end-to-end deep learning network architecture is trained through a large number of substation equipment and related defect samples, where the target area extraction layer and screening layer train the network layer parameters according to the marked result area, and the convolution layer and target analysis layer adjust according to the marked result loss function (Fig. 5).

Faster RCNN is mainly divided into four main network parts

- Conv layers: As a CNN network object detection method, Faster RCNN first uses a basic set of Conv + relu + pooling layers to extract feature maps of images. This feature map is shared for subsequent RPN layers and fully connected layers.
- Region Proposal Networks (RPN): RPN networks are used to generate candidate regions. This layer uses the softmax function to determine the anchor attributes, and then uses the bounding box regression algorithm to correct the anchors.
- RoI Pooling layer: This layer collects input feature maps and targets, extracts feature maps after synthesizing this information, and sends them to subsequent fully connected layers to determine target categories.

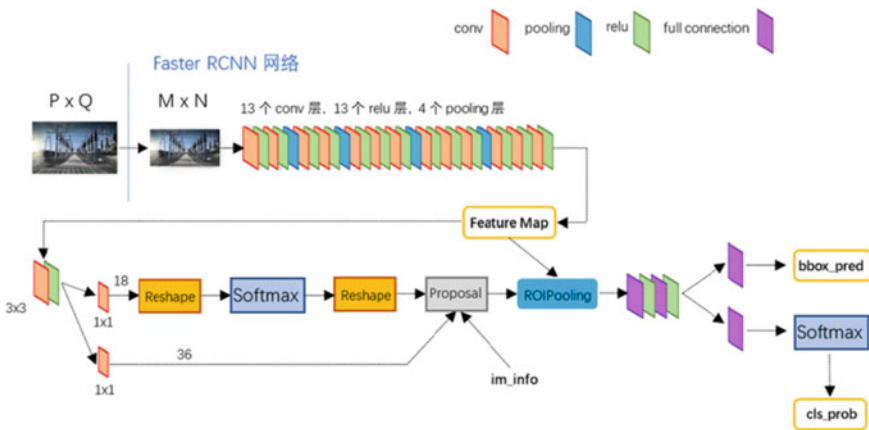


Fig. 5 Faster RCNN model method diagramy

- Classification: Use feature maps to calculate the category of the target, and use bounding box regression algorithm to obtain the final accurate position of the detection box.

### 3.2 Method and Verification of Transformer Equipment Defect Image Recognition Based on Faster RCNN


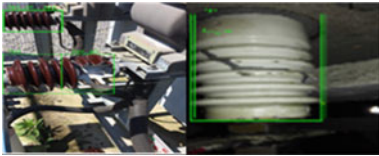
(a) Sample collection and labeling

Build a transformer equipment defect image sample library, collect and organize equipment image samples according to different equipment, components, and defect categories, establish the same labeling method for samples, and complete sample labeling. The defect samples should at least cover defect identification scenarios such as insulator damage and meter damage. There are a total of 1300 samples in this study, including 500 samples identified by the surface damage algorithm and 800 samples of insulator damage (Table 3).

The missed detection rate, false detection rate, and AP value of the identification results for each defect scenario are shown in Table 4. The recognition and verification results of the surface defect image are good, with an AP value greater than 0.9. The algorithm has a good regression effect on the samples, with an accuracy greater than 88%. Due to the large sample differences, the AP value of the insulator defect image is greater than 0.8, and the algorithm accuracy is greater than 65%.

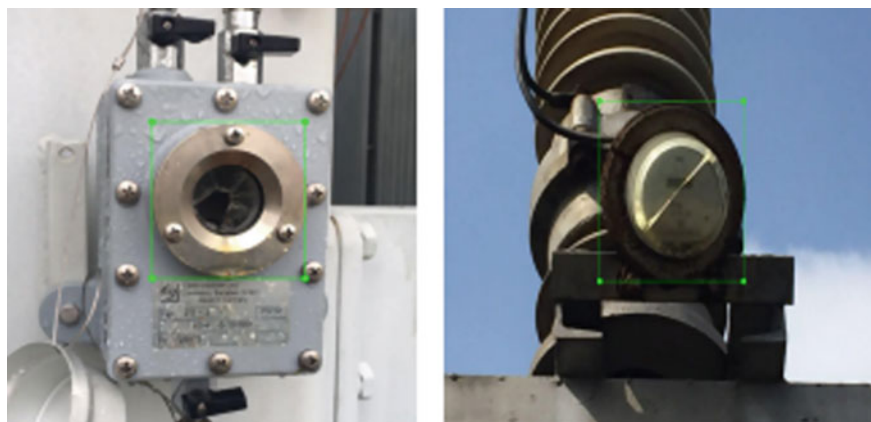
An example of the validation results is shown in Figs. 6 and Fig. 7.

**Table 3** Types of defect scenarios for meter damage identification

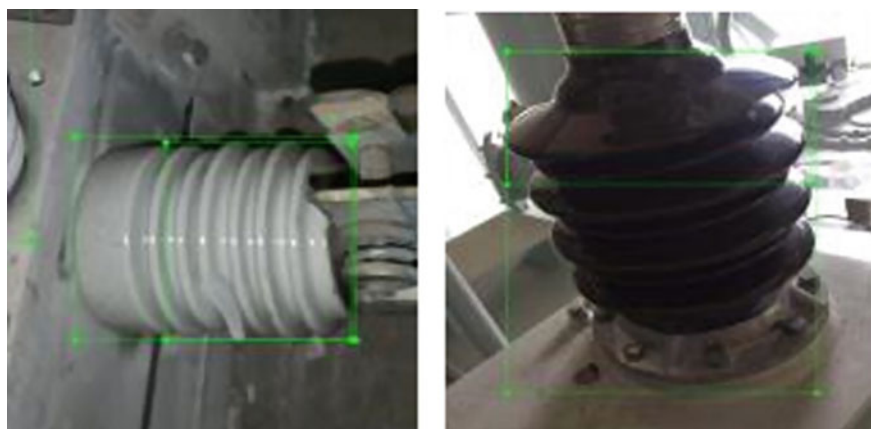
No.	Defect scene	Sample
1	Damaged meter	
2	Insulator damage	

**Table 4** Recognition results of each scene

No.	Defect scene	Noise factor	Loss	AP	Average calculation time (ms)
1	Damaged dial	0.22	0.15	0.92	329
2	Damaged cover plate	0.19	0.16	0.92	329
3	Shell damage	0.26	0.21	0.92	329
4	Insulator rupture	0.27	0.25	0.81	350
5	Insulator cracks	0.32	0.23	0.81	350



**Fig. 6** Table defect image detection results



**Fig. 7** Image detection results of insulator defects

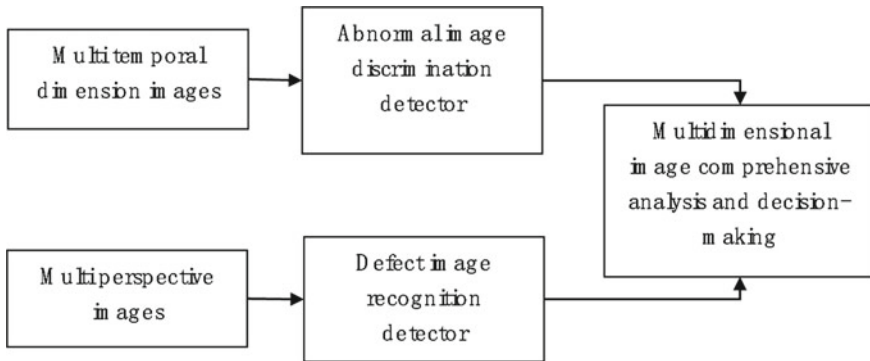


Fig. 8 Image comprehensive analysis method

### 3.3 *Multidimensional Image Comprehensive Analysis Technology for Substation Equipment*

Robots and video cameras collect device images at fixed preset positions, and can perform abnormal image discrimination analysis based on image samples from different time dimensions. For important equipment in substations, redundant image information collection is usually adopted, such as setting up surveillance cameras from multiple monitoring perspectives, or using surveillance cameras to collect real-time equipment appearance images, and using inspection robots to regularly collect equipment appearance images. This article establishes a comprehensive analysis method for anomaly and defect images using an image sample library with multiple time scales and multiple field of view angles (Fig. 8).

Multi time dimensional images and multi perspective images are processed through anomaly image discrimination detectors and defect image recognition detectors to determine equipment anomalies or defects, and the analysis results are sent to a multidimensional image comprehensive analysis decision model. Through weighted comprehensive analysis, accurate analysis of equipment anomalies and faults is achieved.

#### (a) Comprehensive Analysis of Multitemporal Dimensional Images

Extract device preset position information from the device image sample library and establish image sample sequences at the same location in different time dimensions. After conducting image normalization preprocessing, remove image influencing factors under different lighting and weather conditions. In the image sample sequence, select and set image benchmarks, and then use feature matching algorithms to distinguish abnormal images of substation equipment.

The judgment logic is as follows.

$$\lambda = \lambda_1 + \lambda_2 + \dots + \lambda_n \tag{4-1}$$



## (b) Comprehensive analysis of multi perspective images

Utilizing device appearance images from different perspectives for data fusion, eliminating external interference, improving the accuracy of temperature device defect image recognition, and avoiding false alarms, as shown in the following figure. At the same time, when one of the cameras or robots detects a suspected fault in the device image sample library from its perspective, they automatically call other devices for retesting and verification from different perspectives.

The judgment logic is as follows.

$$\lambda = \lambda_1 \cdot \lambda_2 \cdot \dots \cdot \lambda_n \quad (4-1)$$

## (c) Multidimensional image comprehensive analysis and decision-making

A multi-dimensional image comprehensive analysis decision-making model is used to comprehensively determine the results of abnormal image recognition detectors and defect image recognition detectors based on the confidence and weight of different defect image detection scenarios such as oil leakage, suspended solids, bird's nest, meter damage, and insulator damage.

## 4 Conclusion

This article analyzes and elaborates on image matching and comparison technology and image intelligent recognition technology, proposes abnormal image recognition methods based on SIFT and defect image recognition methods based on Faster RCNN, and establishes image discrimination and recognition models for 5 types of defect image detection scenarios in substations, including oil leakage, suspended solids, bird's nest and meter damage, and insulator damage. Through experimental verification, it has been proven that the algorithm model has good application effects and can meet the needs of intelligent defect image detection. This article proposes a multi-dimensional image comprehensive analysis method, which is based on anomaly image discrimination detector and defect image recognition detector. It achieves multi temporal dimension image comprehensive analysis and multi perspective image comprehensive analysis, and develops a multi-dimensional image intelligent detection comprehensive application, achieving intelligent analysis and automatic warning of substation robots, video surveillance, and manual inspection images. The main conclusions are:

- (a) The feature matching algorithm can effectively solve the detection problem of abnormal areas in a set of images, and is suitable for identifying abnormal images of different time scale image sample sets under fixed preset positions. It can achieve defect detection of substation equipment in specific scenarios such as oil leakage, suspended solids, bird nests, etc. Through experimental

verification, the detection effect is good, and it has engineering application conditions.

- (b) The deep learning algorithm can effectively solve the problem of image recognition for defects in substation equipment, and is suitable for image detection in specific scenarios such as meter damage and insulator damage. Experimental verification shows that the detection effect meets the engineering application conditions.
- (c) By integrating feature matching algorithms with deep learning algorithms through multidimensional image comprehensive analysis, comprehensive analysis is achieved for images with multiple time dimensions and perspectives, effectively improving image detection performance in complex scenes.

## References

1. Fan Y (2018) Research and application of several key techniques in image matching. University of Electronic Science and technology
2. Dai T, Zhu C, Hu S (2012) Overview of image matching technology (03):174–175
3. Harris C, Stephens M (1988) A combined corner and edge detector. In: Proceedings of the 4th Alvey vision conference. Manchester: AVC, pp 147–151
4. Rosten E, Drummond T (2006) Machine learning for high-speed corner detection. In: Proceedings of the 9th European conference on computer vision. Graz, Austria: Springer, pp 430–443
5. Lowe DG (2004) Distinctive image features from scale-invariant keypoints. *Int J Comput Vision* 60(2):91–110
6. Jia D, Zhu N, Yang N (2019) Overview of research on image matching methods. *J Image Graph* 24(05)
7. Zhang R, Wang Y (2016) Research on machine learning and its algorithms and development. *J Commun Univ China (Nat Sci Ed)*. 223(02):10–18
8. Zhang Z (2007) Artificial intelligence technology and its philosophical thinking. *Dev Innov Mech Electr Prod* (05):34–36
9. Yuan B, Zhang H, Cui M (2020) A safety management and control system for electric power infrastructure construction site based on deep learning. *Power Grid Clean Energy* 36(09):30–36
10. Saidi Think Tank (2017) Cross integration of intelligent technology and modern information technology. *Softw Integr Circuits* (09):50–59

# Calculation Analysis of Fast Motorised Crossing Devices for Transmission Line Erection



Wenzhuo Chen, Kai Li, Qiyun Han, Xianfeng Zhu, and Bo Tang

**Abstract** This article mainly describes a rapid motorized spanning device for transmission line erection development process. First of all, the article analyses the characteristics and difficulties of crossing power lines, kilometres, railways and other crossing constructions when erecting transmission lines and puts forward the functional requirements of the crossing frame. The structural form of the fast motorised crossing device is designed in combination with the functional requirements of the crossing frame. Finally, the focus of this paper is to use ANSYS structural analysis software to simulate the structure of the rapid motorized crossing device for various load conditions and analyse whether its load bearing capacity is satisfied.

**Keywords** Line erection · Crossover construction · Rapid motorized crossing device · ANSYS

## 1 Introduction

With the rapid development of social and economic development, the number of transmission lines and various traffic roads is growing rapidly [1]. Therefore, in the transmission line wire erection construction inevitably need to cross more power lines, kilometres, railways and other things to be crossed, increasing the workload and difficulty of the construction across. Existing across the construction method is commonly used to build across the frame and seal the network, this method is simple and feasible, but build across the frame need to take up a lot of construction time [2],

---

W. Chen · B. Tang (✉)

College of Electrical Engineering and New Energy, China Three Gorges University,  
Yichang 443002, China  
e-mail: [cwn\\_7007@163.com](mailto:cwn_7007@163.com)

Hubei Provincial Engineering Technology Research Center for Power Transmission Line, China  
Three Gorges University, Yichang 443002, China

K. Li · Q. Han · X. Zhu

Anhui Power Transmission and Transformation Engineering Co., Ltd, Hefei 230000, China

© Beijing Paiké Culture Commu. Co., Ltd. 2024

X. Dong and L. Cai (eds.), *The Proceedings of 2023 4th International Symposium on Insulation and Discharge Computation for Power Equipment (IDCOMPU2023)*, Lecture Notes in Electrical Engineering 1103, [https://doi.org/10.1007/978-981-99-7413-9\\_54](https://doi.org/10.1007/978-981-99-7413-9_54)

the quality of the erection of the frame body by the construction team level influence is larger [3]. For the case of construction time is urgent, the erection of the spanning frame will have a greater risk.

There are currently five main types of spanning frames at home and abroad [4] as follows:

The first, using bamboo, cedar wood poles or steel scaffolding set up across the frame, is also a relatively simple and often used across the construction method, usually across 10 kV, 35 kV and other lines used [5]. Main advantages: short and light individual components, simple erection operation, small risk, in small height difference terrain conditions, not restricted. The main disadvantages: the erection workload is high and takes a long time, requiring high construction costs. The span height is limited by the terrain and wind loads. The overall strength and stability of the span is low due to the small bending and compression capacity of the individual elements and the existence of certain dispersion.

The second type, the cableway type spanning frame, that is, in the tower on both sides of the thing to be crossed using high-strength insulated rope as a load-bearing rope. In the load-bearing rope according to the width of the crossed object laying the corresponding protection cable, so as to form a protection distance long enough safety channel [6]. The main advantages are: low influence by external terrain factors and height, light weight of the equipment and low damage to the surrounding vegetation. The main disadvantages: the distance between the two towers is large, the load-bearing cable is under great stress, the basic reliance on the roof net is not reliable, the width of the roof net is limited, the shielding effect is poor. In addition, when the cross angle is small, the tension of the roof net and the load-bearing ropes will increase sharply, which makes the construction of the net more difficult.

The third type, bridge type spanning frame, that is, in the crossed object on both sides of the pier, and then across the spanning object laying steel bridge, so that the guide, ground line can be directly from the bridge through, similar to the temporary overpass built above the crossed object [7]. Main advantages: stable structure, high load-bearing capacity, good safety during the discharge process. The main disadvantages: the bridge needs to be designed by professional units, professional units construction, bridge erection and demolition of high security risks, across the construction period, high cost, poor economy.

The fourth kind, across the tower, that is, in the crossed object on both sides of the group set up special across the tower, and in the two base across the tower set up between the capping network, as a line construction in the guide, ground line of the shield body [8]. Main advantages: tower stability, high mechanical strength, according to the span size and across the width of the line free design tower height and width of the cross-arms, by the professional design of the tower, can not hit the reverse pull line conditions, to withstand the construction of accidental superimposed load. The main disadvantage is that the foundation is poured, the construction period is long, the vegetation is damaged and it is difficult to replant.

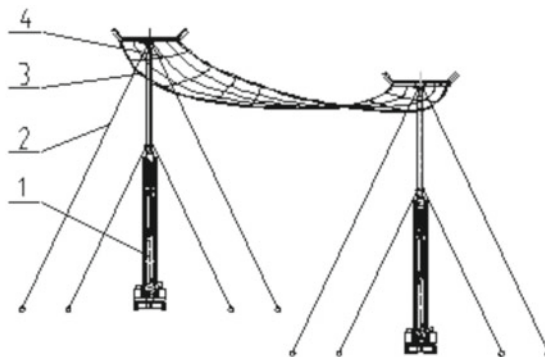
The fifth type, the crane spanning frame, is mainly composed of four cranes, crossbeams, load-bearing cables, pulling lines and capping nets and other parts [9]. The boom of the four cranes as well as the cross-elephant as the main body of the

spanning frame, through the four cranes (two on the large and two on the small side of the spanning object) synchronously support the boom, and then the two sides of the boom respectively support the cross-beam, which is used to bear the weight of the earth wire between the column and the tower. Lastly, the load-bearing ropes are placed between the beams on both sides and a capping net is laid to form a sheltering channel.

Although the above forms of equipment and construction methods are different, there is a general problem of large construction workload, long lead time, high costs and safety hazards. Therefore, it is necessary to develop a transmission line fast motorized spanning device, to meet the special circumstances of the spanning construction.

## 2 Crossover Device Design

In order to facilitate the construction and to meet the safety needs of the construction, a fast motorised crossing device has been designed as shown in Fig. 1, which is used in pairs during the construction of the crossing, using the crossbeams of both devices to complete the sealing function of the net during the crossing. The crossbeam is mainly supported by the independent main structure below, and the independent column is made up of a combination of three arms, which can be retracted into a horizontal mechanism. The lowermost part of the whole unit is an expandable support frame, fitted with wheels to enable manoeuvrability. The span must be equipped with diagonal lines to meet the horizontal force requirements of the frame when working.



1. Rapid motorized crossing device 2. Pulling the cord 3. Load-bearing cables  
4. Capping Network

**Fig. 1** Diagram of the main components of the rapid motorised crossing device

### 3 Modelling and Load Analysis

#### 3.1 Model Building

The basic height of the shelf platform is 20 m, the maximum telescopic height is 31 m, and the external dimensions of the equipment (approx.):  $13,000 \times 2300 \times 2700$  (mm). In order to ensure the safety and reliability of the use of the fast motorized spanning device and to verify the mechanical performance of the fast motorized spanning device, the finite element method is adopted and the international common large-scale structural analysis software ANSYS program is used for the overall stiffness, strength calculation and stability analysis of the structure. The main material of the first, second and third arm of the fast motorized crossing device is Q460, the basic arm is Q550, and the crossbeam part is HQ60. structural analysis principle [10]: the deformation in the fast motorized crossing device shall not exceed 200 mm, and the stability safety factor is 2.5.

As shown in Fig. 2, the main part of the rapid mobile span was simulated using BEAM188 beam unit with a customised beam section; the tension cables were simulated using LINK10.

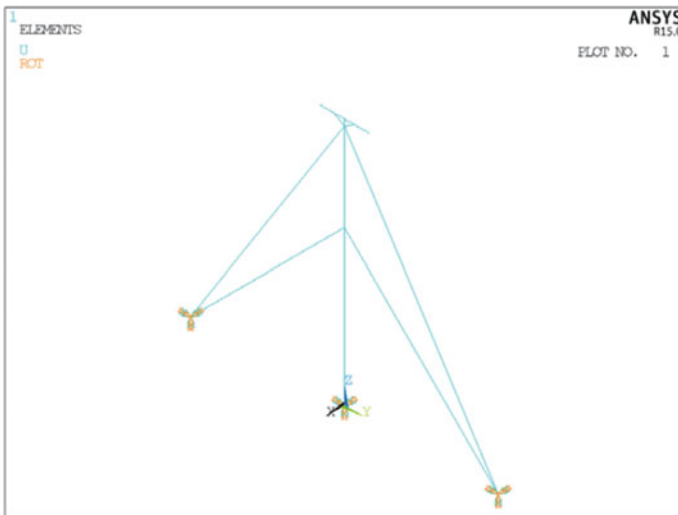


Fig. 2 Simplified model drawing of the overall rapid manoeuvring crossing

### 3.2 Load Calculation

Design load: 1.2 dead weight + 1.2 concentrated load + 1.4 wind load + 1.3 initial load on the cable + 1.2 tension on the capping net. The wind direction perpendicular to the basic arm is 0°, parallel to the basic arm is 90° and the direction of the angle bisector of the above is 45°. The design value of the load (the standard value of the load multiplied by the load division factor) shall be used for calculating the strength and stability of the structure or member; the standard value of the load shall be used for calculating the deformation in the limit state of normal use [11].

According to the relevant requirements, it is necessary to check the stiffness, strength and structural stability of the spanning device in the case of a double tie, an initial force of 200 kg for each tie, a beam width of 6 m and a force of 1 tonne at one end of the deflection, the following information on the working conditions is determined:

- Case 1: 1.0 dead weight + 1.0 concentrated load + 1.0 wind load (0°) + 1.0 initial load of ties + 1.0 capping net tension;
- Case 2: 1.0 dead weight + 1.0 concentrated load + 1.0 wind load (45°) + 1.0 initial load of ties + 1.0 capping net tension;
- Case 3: 1.0 dead weight + 1.0 concentrated load + 1.0 wind load (90°) + 1.0 initial load of ties + 1.0 capping net tension;
- Case 4: 1.2 dead weight + 1.2 concentrated load + 1.4 wind load (0°) + 1.3 initial cable load + 1.2 capping net tension;
- Case 5: 1.2 dead weight + 1.2 concentrated load + 1.4 wind load (45°) + 1.3 initial cable load + 1.2 capping net tension;
- Case 6: 1.2 dead weight + 1.2 concentrated load + 1.4 wind load (90°) + 1.3 initial load of cable + 1.2 capping net tension.

Maximum working height 30 m with Φ14 wire rope anchored to the ground.

According to the requirements of the relevant code [12], the self-weight and concentrated load can be simplified to 5kN vertical concentrated force at each end, and the wind load calculation results are shown in Table 1.

**Table 1** Table captions should be placed above the tables

Wind direction Location	0°	45°	90°	
Wind load	One-section arm	440	380	320
	Two-section arm	281	232	183
	Three-section arm	316	256	197
	Basic arm	718	862	718
	Crossbeam	0	70	139
	Total	1755	1800	1557

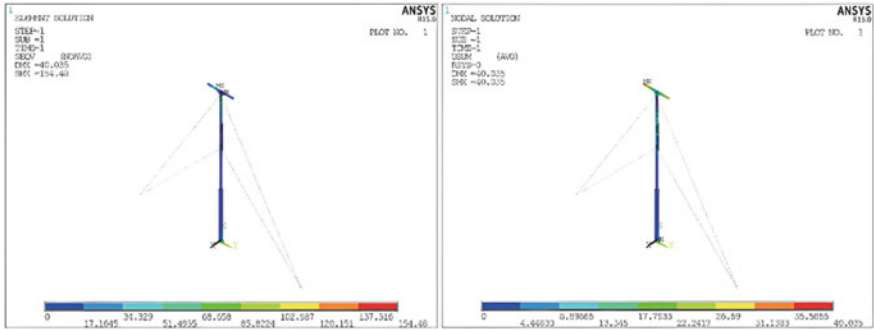


Fig. 3 Stress cloud under Case 1

Table 2 Summary of calculations for rapid motorized crossing devices

	State	Maximum stress (MPa)	Maximum displacement (mm)
Force analysis	Case 1	154.48	40.04
	Case 2	154.54	80.37
	Case 3	154.54	69.08
	Case 4	185.38	47.69
	Case 5	185.44	103.019
	Case 6	183.57	113.773

### 4 Force Simulation

The force simulation of the span device model was carried out in ANSYS under conditions 1 to 6, and the simulation results under condition 1 were obtained as shown in Fig. 3.

The simulation results for the various operating conditions are shown in Table 2.

### 5 Data Analysis

The maximum stress of the structure is 185.44 MPa, which does not exceed the strength design value of the given material; the maximum displacement is 80.37 mm for Case 2. The displacements in the X and Z directions in Case 2 are extracted as shown in Fig. 4 respectively. The maximum displacement in the Z-axis direction is 36.81 mm and the maximum displacement in the X-axis direction is 69.54 mm. According to the specification, the deformation does not exceed 200 mm. Therefore, under the conditions of double ties, initial force of 200 kg per tie, beam width of 6 m and force of 1 tonne at one end, the 6 sets of working conditions checked for the fast motorised crossing device all meet the requirements of stiffness and strength.



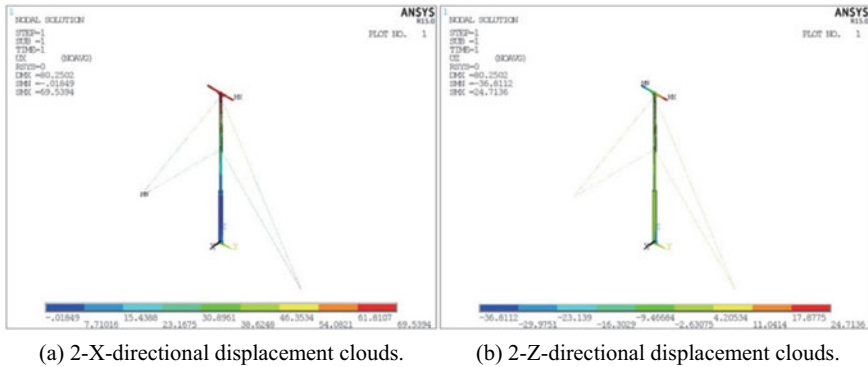


Fig. 4 Cross installation working conditions

## 6 Conclusion

This paper analyses the necessity of the development of the rapid mobile spanning device, and designs a spanning device with a column and a beam as the main structure, which can be rapidly manoeuvred, in combination with the construction characteristics. The strength, stiffness and stability of the structure of the spanning device under each working condition were checked through numerical finite element simulation analysis of the rapid mobile spanning device in each working condition, which showed that the spanning device meets the design requirements under the given working condition.

## References

1. Zapata S, Castaneda M, Herrera MM, Dyer I (2003) Investigating the concurrence of transmission grid expansion and the dissemination of renewables. *Energy* 276
2. Lv J, Meng S, Shan L (2008) Comparison and analysis of common methods of transmission lines with electric crossing. *Guangdong Power Transm Transformation Technol* 46(03):43–46 (in Chinese)
3. Zhang X, Niu H, Liu S, Yi Qi (2022) Anti-vibration measures of ultrahigh strength steel cored aluminum strand for long-span overhead line. *Int J Front Eng Technol* 4(10)
4. Ma Y, Jiang M, Xiong Z, Liu C, Meng F (2023) Solution algorithm and experimental verification on behavior of crossing frame impacted by conductor breaking. *J Phys: Conf Ser* 2433(1)
5. Yang X, Song JP (2020) Combined construction application of overhead transmission lines with and without span frame. *China Equipment Eng* 457(21):234–235 (in Chinese)
6. Wen F (2018) Technical research on the construction of ropeway type spanning power transmission line erection [J]. *Chinese and foreign entrepreneurs* 626(36):126–127 (in Chinese)
7. Zhou F, Chen Y, Li X et al (2019) Construction technology of double-side flat-turned bridge-type non-stop crossing. *Jiangxi Electric Power* 43(08):48–51+62 (in Chinese)
8. Shruthi CM, Namburi GNVV, Srinath SS, Vijay Vamsi G, Sudheer AP, Joy ML (2019) Android based control of transmission line robot for traversing through straight line and crossing of tower junctions. *Int J Innov Technol Explor Eng (IJITEE)* 8(6)

9. Tang Xiaobing, Wan Huaxiang, Zhong Wen, Li Yanjun, Yu Gang. Key technology for construction of important crossing of  $\pm 800$  kV Bai Zhe line. *Henan Science and Technology*, 2023, 42(10): 15–20. (in Chinese)
10. GB50135-2006 (2006) Regulations for the design of towering structures. Ministry of Construction of the People's Republic of China, Beijing (in Chinese)
11. GB50017-2017 (2017) Code for the design of steel structures. Ministry of Housing and Urban-Rural Development of the People's Republic of China, Beijing (in Chinese)
12. GB 50009-2001 (2001) Code for structural loading of buildings [S]. Ministry of Construction of the People's Republic of China, Beijing (in Chinese)

# Application of Portable Tower Arc Sag Observer in Transmission Line Engineering



Yushan Yao, Xianfeng Zhu, Kai Li, Jian Jiao, Bo Tang, and Qiyun Han

**Abstract** The arc sag is the key point of quality control in the erection of transmission lines, and the accuracy of its observation directly affects the operation safety of the line. The research status of arc sag observation of transmission lines is introduced, the theoretical and practical basis and structural and functional parameters of the arc sag observer on the convenient tower are analyzed, and the good results obtained by the arc sag observation of Anhui Shuangling-Transformer-Anqing 3500 kV transmission line project are introduced, which provides reference for similar projects.

**Keywords** Arc sag · Isometric method · Precision · Observation angle

## 1 Introduction

The arc sag of the transmission line is the main indicator of line design and operation, which is related to the operation safety of the line, so it must be controlled within the scope specified in the design. The isometric method usually adopts the visual inspection method tied to the vertical plate, which has the advantages of low cost, simple operation, and easy mastery by construction personnel, so it is widely used in transmission lines. With the gradual improvement of the voltage level of transmission lines, especially the construction of a large number of UHV projects, the line spacing is getting bigger and bigger, and the naked eye observation of lashing

---

Y. Yao (✉) · K. Li · B. Tang · Q. Han

College of Electrical Engineering and New Energy, China Three Gorges University, Yi Chang, Hubei Province, China

e-mail: [1663681954@qq.com](mailto:1663681954@qq.com)

X. Zhu

Anhui Power Transmission and Transformation Engineering Co., Ltd., He Fei, Anhui Province, China

J. Jiao

State Grid Yichang Electric Power Company, Yi Chang, Hubei Province, China

© Beijing Paiké Culture Commu. Co., Ltd. 2024

X. Dong and L. Cai (eds.), *The Proceedings of 2023 4th International Symposium on Insulation and Discharge Computation for Power Equipment (IDCOMPU2023)*, Lecture Notes in Electrical Engineering 1103, [https://doi.org/10.1007/978-981-99-7413-9\\_55](https://doi.org/10.1007/978-981-99-7413-9_55)

577

arc vertical plates requires higher and higher experience level of operators, affected by the observation accuracy, and the arc sag control results often exceed the allowable error of the design. Anhui Shuangling Transformer–Anqing Sanchang 500 kV transmission line project has a total length of 56.669 km, 136 new double-circuit angle steel towers, a total of 32 tensile sections, along the line there are many important crossings such as high-speed rail, general railway, high-speed railway, etc., with an average gear distance of about 420 m. In order to improve the quality of arc sag observation, reduce [1] the workload of tying arc vertical plates at height, and reduce safety risks, a tower arc observation device is specially designed in this project. The device is lightweight and portable, simple to operate, can be quickly fixed on the tower, adjust the vertical angle of the observatory to the calculated value, and use the cross wire in the telescope for arc sag observation.

## 2 Research Status of Arc Sag Observation of Transmission Lines

At present, there are two types of arc sag observation methods commonly used on transmission lines: isometric method and angle method. The isometric method adopts the method of lashing the arc vertical plate, which is simple to operate, low cost, not limited by terrain, and has low requirements for the measurement and calculation level of construction personnel, so it is widely used in construction, but the accuracy is not high, the amount of aerial work is large, and there are certain safety risks. The angle method adopts optical measuring instruments, which measures on the ground and has high precision, but the operation is complex, the cost is high, the equipment is heavy, the terrain is limited, and the construction personnel are required to have a certain level of measurement and calculation, so the application rate in arc vertical observation is not high. In order to combine the advantages of the two measurement methods, each company [2] has tried to find breakthroughs in the field of arc sag observation, as follows.

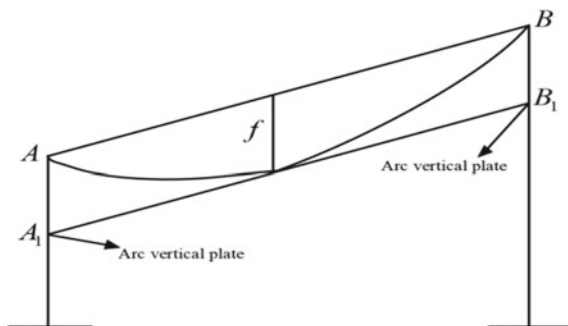
Try 1: Anhui Power Transmission and Transformation in the Sichuan cloud section developed based on GPS arc sag observation device, the device is non-optical observation arc sag, can solve the problem of dense fog, night arc sag observation, but the device needs to establish GPS differential base station and data transmission station, complex equipment non-professionals cannot operate, cannot solve the general problem.

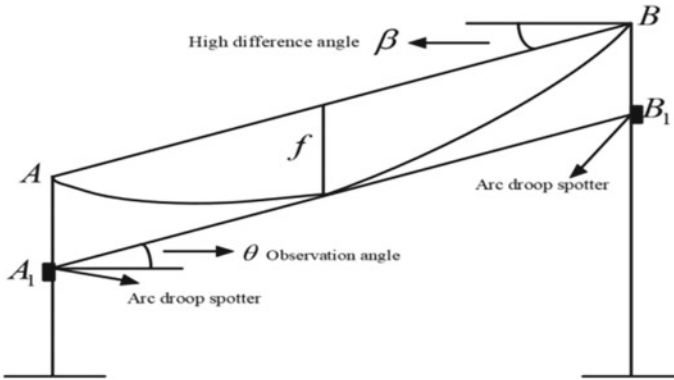
Try 2: An invention patent of Chengde Power Supply Company “a kind of iron tower ground wire.” Arc sag measuring device, the purpose of the utility model is to provide an iron tower ground guide arc sag measuring device [3], to solve the existing technology by tying the arc vertical plate on the iron tower [4] scheme requires manual multiple times to tie the arc vertical plate, the operation is cumbersome, the efficiency of arc vertical measurement is low [5].

### 3 Theoretical and Practical Basis of Portable Tower Arc Sag Observatory

From the current construction status of domestic transmission lines, the calculation level of construction personnel is generally low, and the arc sag observation method that can be popularized is still the isometric method. When the equal-length method is selected to observe the arc sag, the height of the hanging points of the pole towers at both ends of the observation file from the ground should be greater than the arc sag value, and the difference should meet the requirements of the operating height. The traditional isometric method to measure the arc sag is on the adjacent two towers of the observation file, from the overhead line suspension points A and B each downward measure the distance of the arc length  $f$ , and tie the arc vertical plate at the main material of the tower body of the contour line, using the principle of three points and one line, by adjusting the tightening device, visually make the connection of the plane of the two arc vertical plates tangent to the lowest point of the overhead line, so as to meet the design arc sag requirements. This method requires binding the arc vertical plate on both sides of the pole tower, so the amount of aerial work is large, especially in the mountainous pole position [6], and it takes a long time to hang the arc vertical plate. In addition, using the naked eye to observe, it is easy to produce observation deviations when the field of view is not clear due to large distances or weather factors. The portable tower arc sag observatory is improved for the traditional equal-length method to observe the lack of power in the arc sag. The instrument is fixed at one end of the observation file (the position of the original arc vertical plate) [7], and the observation angle  $\theta$  is obtained before use, according to the parallelogram principle, the observation angle is equal to the height difference angle of the hanging point. After fixing on the tower, the observation angle of the instrument is adjusted to the calculated value, and then the lowest point of the overhead line coincides with the cross wire in the telescope through the tightening device to achieve the design arc sag value [8]. The  $8\times$  telescope is used for observation by the portable tower arc observer, which greatly increases the accuracy of observation and improves the observation accuracy compared with the theodolite using the naked eye to observe the arc vertical point (Figs. 1 and 2).

**Fig. 1** Schematic diagram of the observation of the arc vertical plate of the lashing arc vertical plate





**Fig. 2** Arc sag observation by arc sagging observatory on portable tower

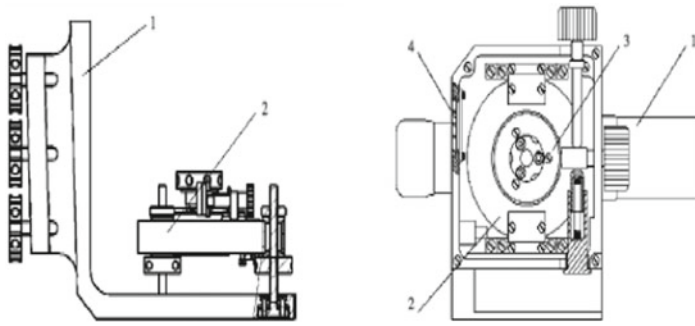
When calculating the height difference angle, the elevation of the observation file hanging point can be found from the design drawing [9]. Note that in the process of tightening the line, the linear tower ground guide line is in the trolley, and the elevation of the hanging point should be calculated according to the elevation of the trolley mouth, so the distance between the observation gear trolley mouth and the horizontal bearing point should be measured when hanging the trolley [10].

## 4 Structural and Functional Parameters of the Portable Tower Arc Droop Observatory

### 4.1 Constructed of a Portable Tower Arc Dip Observatory

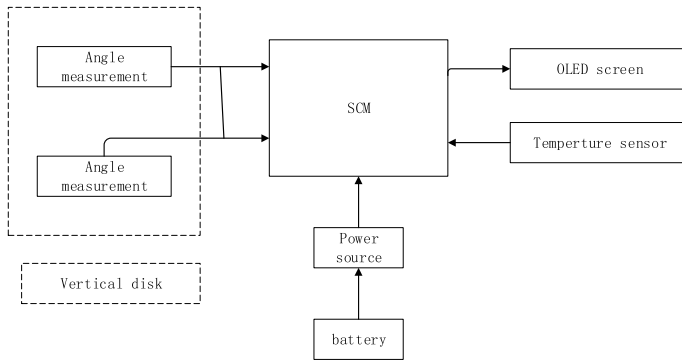
The portable tower arc sag observatory is composed of two parts: installation platform and observatory (Figs. 3 and 4).

Based on optical telescope and electronic display technology, the portable tower arc observation instrument is quickly connected to the iron tower through the tower clamping base, and the arc vertical installation base provides the installation platform of the arc dip observation instrument, which can realize the function of leveling and horizontal micro-movement. The observation device has a leveling and pitch scale, and uses the crosswire scale in the telescope to observe the arc on the tower. The instrument has only one vertical disk, using analog signal synthesis, coarse code processing after synthesis, and only a set of quadrature signals, so a single-CPU [11] design scheme is adopted, and the angle measurement, control, and display are all processed by this single-chip microcomputer (Fig. 4).



1—Clamping seat on the tower; 2—Arc mounting base  
 1—telescope assembly; 2—Goniometric components; 3—shafting; 4—Body frame and display parts

**Fig. 3** Installation and observatory platform



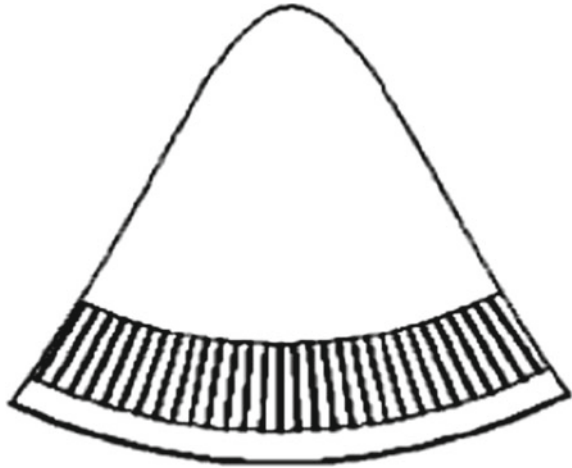
**Fig. 4** Electrical abridged block diagram

### 4.2 *Constructed of a Portable Tower Arc Dip Observatory*

The telescope assembly consists of an objective lens group, a orthographic prism group, a scribing plate group, an eyepiece group and related structural parts. The optical system is composed of an objective group, an Abbe orthographic prism, a scribe group, and an eyepiece. The object at infinity is turned into a positive image through the objective lens and orthogram prism on the scribing board, and the eyepiece group magnifies the image on the scribing board and images it to the pupil of the human eye, and the human eye can observe a clear object.

The goniometer assembly uses an incremental grating encoder for vertical angle measurement. The incremental grating encoder consists of a main and secondary grating disc and an infrared light-emitting tube and a photoelectric receiver tube

**Fig. 5** Schematic encoder structure



located on both sides. The main and secondary gratings are engraved with equal-width, equidistant raster lines. In the assembly process, a small gap (less than 0.1 mm) is maintained between the main and secondary gratings, and the grating line has a small angle  $\theta$ , and the formed Moiré fringes have an average effect on the grating error, weaken the influence of the grating error on the measurement results, and improve the measurement accuracy (Fig. 5).

The shaft drives the telescope to pitch and rotate. It is composed of horizontal shaft, bearing housing, steel ball, etc. The shafting system adopts dense bead type, the shafting structure is over-geometric, the balls are distributed spirally in the cylindrical surface, each ball rolls along its own track, and has high centering accuracy, so the error caused by the shafting shaking is negligible, and the plane surface in contact with the steel ball is extremely high, and the surface is hardened by quenching and other hardening treatment, with high hardness and strength. The shaft system has the advantages of high precision, low temperature influence, good vibration resistance, flexible low-temperature rotation, and not easy to jam. The body frame carries the body of all other components, and the main frame is connected to the mounting platform.

### **4.3** *Mainly Use the Function*

In order to improve the quality of arc sag observation, Anhui Power Transmission and Transformation Engineering Company proposed the first portable arc sag observation instrument in the Anhui Shuangling Transformer-Anqing Three Change 500 kV transmission line project. Taking the isometric method as the measurement principle, based on optical telescope and electronic display technology, combined with the field



usage, two optimizations and improvements were made in terms of fast connection fixation, horizontal alignment, angle fine-tuning, and seismic performance.

On September 13, 2018, the prototype was brought to the Anhui construction base for tower operation, and the following changes were made after integrating the opinions of the technical personnel of the power transmission and transformation company and the actual operation workers.

- (1) Observation device. Optical system optimization and improvement; The shafting system adds a micro-motion mechanism; The coarse sight was changed to a slender type, which is convenient for the operator to observe; Add “switch” and “zero” printing at the button; Battery compartment installation improvements.
- (2) Install the platform. The installation platform is divided into two types: the clamping base on the tower and the installation base of the arc droop; The clamping seat and mounting platform on the tower can be installed with 90° and 180° rotation; The installation base should extend 30 cm outside the tower to facilitate observation; Reserve the center screw hole at the bottom of the mounting base.

On December 12, 2018, the on-site operation record:

- (1) The installation of the clamping seat and tower in the installation platform can be completed within 1 min;
- (2) The leveling of the mounting base is controlled within 3 min. After the second improvement, the equipment is more convenient, flexible and efficient to apply on the construction site.

The optimized droop scanner completed 12 tensile segments of sag in this project Observation, in terms of measurement effect, the arc sag value is controlled in the design range ( $\pm 2.5\%$ ); In terms of use effect, the device is fixed, leveled quickly, simple and practical to operate, especially in mountainous areas to reduce the amount of arc vertical plate lashing, saving time, manpower, cost, and bringing a lot of economic benefits.

## 5 Conclusion

The development of the observatory, including engineering design and trial production, lasted for two stages More than 1 year. The manufactured prototype has been optimized three times, and the performance and indicators meet the requirements of use; In the development process, the requirements of generalization, serialization and combination are implemented, and the drawings and technical documents are complete, accurate, coordinated and standardized; The drawings and texts are consistent with the physical objects and meet the standardization requirements; The supply source of components and raw materials is stable and the quality is reliable. In practice, the practical activities of portable tower arc dip observer were carried out

in representative pole positions such as large height difference and large gear pitch of Anhui Shuangling Transformer–Anqing Three 500 kV transmission line project, and good arc droop control effect was achieved. Therefore, the on-site supply should be increased and continued to be optimized, so that the portable tower arc droop observer can be popularized and applied in the arc sagging observation of transmission line engineering of various voltage levels.

## References

1. Qingsong XU (2007) Real-time monitoring of arc sag of transmission lines. *High Volt Eng* 7:206–209
2. Peterl ZS, Volatl C, Farzaneh M et al (2008) Numerical investigations of a new thermal de-icing method for overhead conductors based on high current impulses. *IET Gener Transm Distrib* 2(5):666–675
3. Tao W (2017) Calculation of Arc sag change caused by suspension point height difference and control during construction. *Smart City* 12:39–40
4. Qingqing LIU, Lijun HAN, Lei REN et al (2017) High-precision angular displacement test method based on incremental grating encoder. *Aerosp Control* 3:58–61
5. Hall WS (2014) Selection of pull line and arc Drog observation files in transmission line construction. *Gansu Sci Technol* 30(3):8–50
6. Jiangang ZHU (2018) Arc sag observation and adjustment measures in transmission line tightening construction. *Commun World* 11:185–186
7. Luo K (2017) Observation and adjustment method of arc sag in transmission line tight line construction. *Sci Technol Innov Herald* 14(27):33, 35
8. Hao L, Wang G, Tan L (2006) Analysis of the relationship between large-load operation of transmission line and conductor sagg. *High Volt Eng* 32(1):107–109
9. Foss SD, Marajo RA (1990) Dynamic line rating in the operating environment. *IEEE Trans on PWRD* 5(2):1095–1105
10. Douglass DA, Edris AA, Pritchard GA (1997) Field application of a dynamic thermal circuit rating method. *IEEE Trans PWRD* 12(2):823–831
11. Li X, Zhou D, Jiang J (2013) Modeling of automatic defense system for icing of transmission lines and analysis of its impact on power grid. *High Volt Technol* 39(3):698–704

# Self-learning Diagnosis of Transmission Line Fault Type Based on Deep Forest and SMOTE



Xiao Tan, Guoji Chang, Gang Qiu, Jinjin Shi, Jie Chen, and Qiwei Wu

**Abstract** Accurately identifying the fault type of transmission lines is of great significance to the safe operation of transmission lines. In this paper, the distributed detection method is adopted to collect and classify transmission line fault data, while 15 time-domain features and 12 frequency-domain features are extracted from each fault waveform to build a transmission line fault database. Then, based on this database, study on classification and identification of faults by Deep Forest algorithm, and eliminate the imbalance of data by SMOTE, finally achieve intelligent diagnosis of fault types of transmission lines. The correctness rate of the proposed method is 92% in the binary diagnosis of lightning and non-lightning strike, and 79% in the full classification diagnosis. Compared with the traditional classification algorithm, the proposed method has higher accuracy and better generalization performance. The research has reference significance for the digital construction of transmission lines and the intelligent upgrading of power grid.

**Keywords** Transmission line · Fault diagnosis · Deep Forest · SMOTE

---

X. Tan (✉) · G. Qiu · J. Chen  
State Grid Jiangsu Electric Power Co., Ltd. Research Institute, Nanjing, China  
e-mail: [tanx2@foxmail.com](mailto:tanx2@foxmail.com)

J. Chen  
e-mail: [2008840320@163.com](mailto:2008840320@163.com)

G. Chang · J. Shi  
State Grid Jiangsu Electric Power Co., Ltd., Ultra High Voltage Branch, Nanjing, China

Q. Wu  
State Grid Jiangsu Electric Power Co., Nanjing, China

© Beijing Paiké Culture Commu. Co., Ltd. 2024  
X. Dong and L. Cai (eds.), *The Proceedings of 2023 4th International Symposium on Insulation and Discharge Computation for Power Equipment (IDCOMPU2023)*, Lecture Notes in Electrical Engineering 1103, [https://doi.org/10.1007/978-981-99-7413-9\\_56](https://doi.org/10.1007/978-981-99-7413-9_56)

## 1 Introduction

The electric power industry is an important basic industry and leading industry for the development of national economy, and transmission lines, as an important part of the electric power system, are the arteries of the electric power industry [1, 2]. Due to the large span of transmission lines and the complex landform, they are prone to be damaged by various natural or external factors. When a fault occurs, it is important to find out the fault type and location in time for the safe operation of transmission lines.

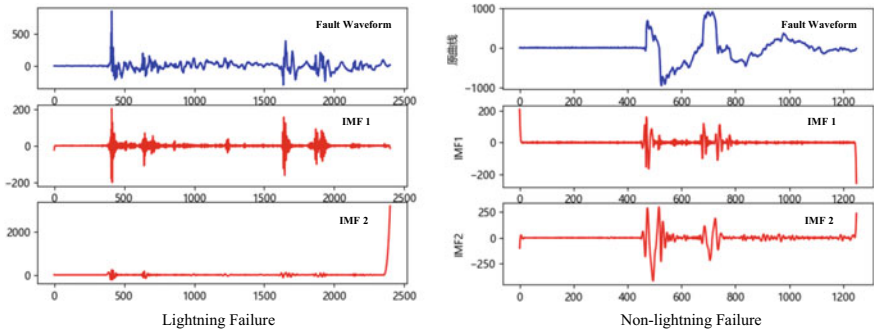
Because transmission line faults are similar in waveform characteristics. Such as lightning strike faults, wind bias faults and bird damage faults [3–5], which are mostly ground faults, will cause the phase voltage to drop and generate a large sinusoidal fault current after their occurrence. Therefore, the diagnosis of fault types largely depends on the experience of field operators. And it can't accurately intelligent identification of fault type or cause.

In order to improve the fault diagnosis ability of transmission lines, Guo Mofa et al. identified the corresponding fault phase through fuzzy kernel clustering algorithm based on the similarity of zero-sequence current waveforms of all lines after single-phase grounding [6]. In terms of identifying fault types, Peng Xiangyang's team adopted characteristics of line-wave to analyze the transient travelling wave current of lightning strike around, counterstrike and non-lightning strike faults, and identified the cause of the fault by observing the difference of its line-wave sign [7]. Dai Jiejie et al. determined whether the fault occurred in the line was a lightning strike or a non-lightning strike fault through the energy changes of different faults [8]. Liu Yilu's team identified line faults and positioned them by monitoring high-frequency waveforms on overhead lines [9]. Shao Wenquan et al. identified the fault type by applying high-frequency voltage disturbance to the fault line and detecting the waveform characteristics of the disturbance current, which could determine the instantaneous fault and permanent fault [10]. However, due to the distortion of traveling wave in line transmission and its susceptibility to external random interference, the accuracy of diagnosis needs to be further improved, and it is difficult to identify the cause of specific line faults.

Therefore, this paper will extract the time-domain and frequency-domain characteristics from the specific fault waveform detected on the distributed fault monitoring device and set up the database. By the combination of Deep Forest and SMOTE algorithm, diagnose the causes of many kinds of faults in the transmission line.

## 2 Typical Faults and Characteristic Extraction

To diagnose the causes of transmission line faults, it is necessary to know the types of line faults, which are mainly divided into lightning fault and non-lightning fault. First, the lightning fault includes two types: back flashover fault and shielding fault.



**Fig. 1** Lightning fault and non-lightning fault waveform

Non-lightning strike fault can be divided into bird damage, ice damage, wind damage, external force damage and other causes.

In the aspect of fault data acquisition, distributed fault monitoring device is used. The specific implementation method is to install a contact fault monitor every 30 km on the transmission line to directly measure the line information on the high voltage side [11]. In addition, empirical mode decomposition (EMD) method was used to extract the intrinsic mode function (IMF) of traveling wave to locate the fault. The specific fault waveform is shown in Fig. 1.

To diagnose the causes of transmission line faults, it is necessary to know the types of line faults, which are mainly divided into lightning faults and non-lightning faults. The essence of lightning strike fault of transmission lines is the overvoltage generated by lightning on the lines, which includes two types: lightning strike fault and lightning strike fault.

In order to identify and classify the obtained fault transient waveform, this paper will extract the characteristics of the transient waveform from the time domain and frequency domain respectively, so as to obtain the required characteristic values and save them, so as to facilitate the classification and recognition in the next step.

The characteristics of time domain mainly include 15 temporal characteristic parameters, such as waveform mean value, mean square error, root amplitude, peak value, skewness, peak factor and waveform factor, whose specific expressions are shown in Table 1, where  $a_1-a_4$  and  $a_8-a_{10}$  represent amplitude and energy of vibration in time domain.  $a_5-a_7$  and  $a_{11}-a_{15}$  represent the time series distribution of signals.

The characteristics of frequency domain mainly include 12 frequency domain characteristic parameters, including gravity center frequency, average frequency, frequency standard deviation, root mean square frequency, frequency domain spectral power, etc. The expression of frequency domain characteristic parameters is shown in Table 2, where  $b_1$  represents the magnitude of vibration energy in the frequency domain,  $b_2-b_4$ ,  $b_6$ ,  $b_{10}-b_{12}$  represents the concentration or dispersion degree of the spectrum.  $b_5$ ,  $b_7-b_9$  indicate the change of the position of the main frequency band.

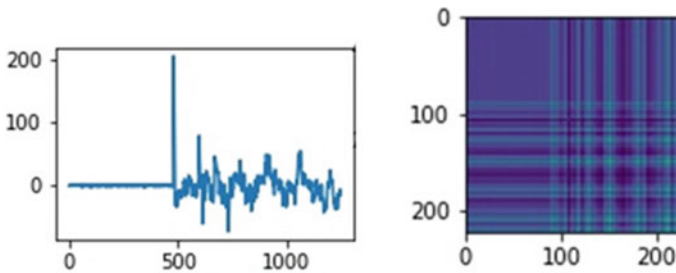
**Table 1** Expression of temporal characteristics

S. No.	Expression	S. No.	Expression	S. No.	Expression
1	$a_1 = \frac{\sum_{i=1}^N x(i)}{N}$	6	$a_6 = \frac{\sum_{i=1}^N (x(i)-a_1)^4}{N}$	11	$a_{11} = \frac{a_2}{a_4}$
2	$a_2 = \sqrt{\frac{\sum_{i=1}^N (x(i))^2}{N}}$	7	$a_7 = \frac{\sum_{i=1}^N (x(i)-a_1)^2}{N}$	12	$a_{12} = \frac{a_8}{a_2}$
3	$a_3 = (\frac{\sum_{i=1}^N \sqrt{ x(i) }}{N})^2$	8	$a_8 = \max x(i) $	13	$a_{13} = \frac{a_8}{a_4}$
4	$a_4 = \frac{\sum_{i=1}^N  x(i) }{N}$	9	$a_9 = \max x(i) $	14	$a_{14} = \frac{a_8}{a_3}$
5	$a_5 = \frac{\sum_{i=1}^N (x(i)-a_1)^3}{N}$	10	$a_{10} = a_8 - a_9$	15	$a_{15} = \frac{a_5}{a_7}$

**Table 2** Expression of frequency domain characteristics

S. No.	Expression	S. No.	Expression	S. No.	Expression
1	$b_1 = \frac{\sum_{n=1}^K s(n)}{K}$	5	$b_5 = \frac{\sum_{n=1}^K f_n s(n)}{\sum_{n=1}^K s(n)}$	9	$b_9 = \frac{\sum_{n=1}^K f_n^2 s(n)}{\sqrt{\sum_{n=1}^K s(n) \sum_{n=1}^K f_n^4 s(n)}}$
2	$b_2 = \frac{\sum_{n=1}^K (s(n)-b_1)^2}{K}$	6	$b_6 = \frac{1}{\sqrt{\frac{\sum_{n=1}^K (f_n-b_5)^2 s(n)}{K}}}$	10	$b_{10} = \frac{\sum_{n=1}^K (f_n-b_5)^3 s(n)}{b_6^3 K}$
3	$b_3 = \frac{\sum_{n=1}^K (s(n)-b_1)^3}{K b_2^{1.5}}$	7	$b_7 = \sqrt{\frac{\sum_{n=1}^K f_n^2 s(n)}{\sum_{n=1}^K s(n)}}$	11	$b_{11} = \frac{\sum_{n=1}^K (f_n-b_5)^4 s(n)}{b_6^4 K}$
4	$b_4 = \frac{\sum_{n=1}^K (s(n)-b_1)^4}{K b_2^2}$	8	$b_8 = \sqrt{\frac{\sum_{n=1}^K f_n^4 s(n)}{\sum_{n=1}^K f_n^2 s(n)}}$	12	$b_{12} = \frac{\sum_{n=1}^K \sqrt{ f_n-b_5 } s(n)}{\sqrt{b_6} K}$

In order to achieve rapid extraction of characteristic values of data waveform, the data waveform is first divided into overlapping  $n$  segments and converted into RGB images with  $256 \times 256$  resolution by GASF method [12], as shown in Fig. 2.



**Fig. 2** Example of waveform data visualization

Then, 3D Convolution Network is used to extract feature parameters from images. It is carried out on a  $3 * 3 * 3$  cube convolution kernel and output is obtained. Since the weight of convolution kernel in the whole cube is the same, that is, the same convolution kernel, multiple convolution kernel can be used for the same cube to extract multiple features [13].

### 3 Deep Forest and SMOTE Arithmetic

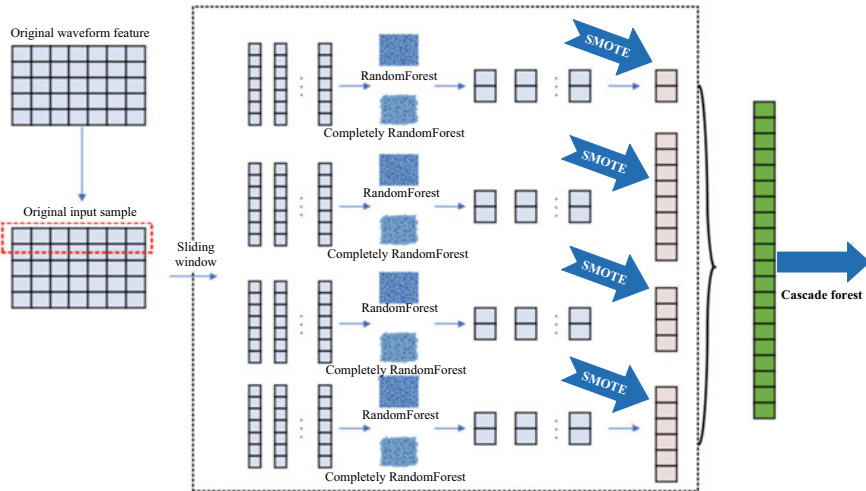
After determining the characteristic values of the data waveform, this paper uses the Deep Forest and SMOTE arithmetic to train the database, in order to achieve the role of identifying the fault type.

The essence of Deep Forest is to make prediction by virtue of the classification principle of decision tree. It takes the extracted data features as input and combines them into a training set, so as to train Random Forest and complete Random Forest. The output result of each tree model node is the proportion of samples of different categories, that is, the probability corresponding to each category. Subsequently, multiple results of multiple forests are spliced as new characteristic values and used as input of cascade forest module, and final prediction results are obtained to achieve high precision and robustness [14].

Input a given sample, where the red part indicates the path of the sample traversing to the leaf node, different shape marks represent different categories, each forest will calculate the training sample percentage of different categories in the relevant sample at the leaf node, and then calculate the average probability of categories generated by all trees in the forest, so as to generate an estimate of the distribution of categories. The estimated class distribution forms the class probability vector, which is then connected to the original feature vector input to the next level of the cascade.

However, due to the difference in the proportion of samples of different categories, it will affect the probability of final output categories, that is, there is imbalance. So we use SMOTE method, as shown in Fig. 3, increase the diversity of training set by generating synthetic samples of few classes. So that the model can learn the characteristics of few classes more easily. In addition, this method will not introduce noise or loss information to generate synthetic samples, improve the generalization ability of the model and reduce the overfitting phenomenon. And because SMOTE did not sample over the data space, but over the feature space, this will balance the class probability distribution with greater accuracy than the traditional method, further improving the recognition of the Deep Forest model.

The balanced category probability vector is fed into the next level forest module, which consists of a progressive, multi-level cascade forest with many layers. Each layer of the cascade forest is integrated by multiple forests, and each layer includes Random Forest and full Random Forest. In addition to the input vector directly used in the first layer, the input vector of each subsequent layer is the combination of the category probability vector output by the upper layer and the input vector, and every new level, the whole cascade forest will be evaluated through the verification set.



**Fig. 3** Schematic diagram of the Deep Forest algorithm with SMOTE

If the evaluation index is not improved compared with the model before the new level, the new level will be automatically deleted and the training will be terminated. Finally, the class probabilities of the output of the cascade forest in the last layer are added and then averaged, and the maximum probability is taken as the final prediction result.

Identifying the fault type of transmission lines for Deep Forest & SMOTE may be summarized as follows:

- (1) Filter the data meeting the conditions according to the categories and build the database.
- (2) Extract characteristic parameters such as time domain and frequency domain of waveform data, form new characteristic data and combine them into new data sets.
- (3) The characteristic data set is used as the input of classification model, and the data set is divided into training set and test set at 7:3.
- (4) Set parameters related to Deep Forest.
- (5) Input the data into the Deep Forest model.
- (6) The corresponding category probability of each input is obtained from the forest, and the distribution of each category probability is calculated.
- (7) For the unbalanced category, use SMOTE to balance, make the existing few categories balance, improve the performance of the model.
- (8) Input the connected class probability vector into the cascade forest module and iteratively learn layer by layer to obtain the final classification result.



## 4 Algorithm Application and Result Analysis

Based on the python3.8 language environment, a test platform was built with PyCharm as the compiler, and the transmission line fault waveform database was formed by using the State Grid historical fault information and marked labels after manual identification. There are 3701 samples of data in this database. Among them, lightning-strike fault data accounted for 1113 and non-lightning-strike fault data accounted for 2588. Among the fault types after screening, 199 ice damage date, 214 wind deviation damage date, 139 bird damage date, 416 external damage date and 70 others were detected for non-lightning strike faults. Lightning strike fault: 104 back flashover fault and 540 shielding fault.

This database is trained and detected by Deep Forest algorithm and other traditional machine learning methods such as Random Forest, Logistic regression, J48, Bagging. Comparing the accuracy of the above algorithms in diagnosing the fault categories of transmission lines, the results are shown in Tables 3 and 4.

From Tables 3 and 4, it can be seen that using Deep Forest-SMOTE method combined to diagnose the fault types of transmission line has the highest diagnostic accuracy.

In the LF/NF diagnosis, the accuracy of Deep Forest-SMOTE is 2.3% higher than that of Deep Forest, and 3.03% higher than Random Forest, which is the highest accuracy in traditional machine learning. In the full classification diagnosis, Deep Forest-SMOTE has 17.59% higher accuracy than the Deep Forest and 19.87% higher accuracy than Random Forest.

**Table 3** LF/NF diagnosis results

Name	Accuracy (%)	Name	Accuracy (%)
Ada boost	84.9550	Random Forest	89.6396
J48	87.2973	Deep Forest	90.3690
Logistic regression	88.0180	Deep Forest-SMOTE	92.6651

**Table 4** Total classification diagnosis results

Name	Accuracy (%)	Name	Accuracy (%)
Adaboost	48.7129	Random Forest	59.2079
J48	49.9010	Deep Forest	61.4850
Logistic regression	52.8713	Deep Forest-SMOTE	79.0784

## 5 Conclusion

In this paper, the transmission line fault will be summarized and classified according to the causes, and the fault waveform in accordance with the time domain and frequency domain characteristic quantity extraction, using Deep Forest and SMOTE algorithm combination, establish the fault type diagnosis model. The model is verified by using the historical data of State Grid to build the transmission line fault database. The results show that compared with the traditional machine learning algorithm, this model has a higher accuracy in the diagnosis of transmission line faults. The research in this paper can be applied to the abnormal state prediction, fault diagnosis and auxiliary operation and maintenance of transmission lines, and has great significance for supporting the construction of digital power grid and promoting the digital transformation of intelligent upgrading of power grid.

**Acknowledgements** This research is supported by Incubation Project of State Grid Jiangsu Electric Power Co. (Grant No. JF2022020)

## References

1. Almeida AR, Almeida OM, Junior BFS et al (2017) ICA feature extraction for the location and classification of faults in high-voltage transmission lines. *Electr Power Syst Res* 148:254–263
2. Zhang H, Che R (2015) Fault cause identification based on characteristics of transition resistances for transmission lines. In: 5th international conference on electric utility deregulation and restructuring and power technologies (DRPT). IEEE, pp 1405–1409
3. Zeng R, Zhuang C, Zhou X et al (2016) Survey of recent progress on lightning and lightning protection research. *High Volt* 1(1):2–10
4. Wang H, Wang S, Deng C et al (2018) Study on the flashover characteristics of bird droppings along 110 kV composite insulator. In: 2018 international conference on power system technology (POWERCON). IEEE, pp 2929–2933
5. Zhou Y, Zu G, Yao Y, Chen N (2022) Review on mechanism and preventive measures of overhead line dancing in distribution network. *J Electr Power Syst Autom* 34(04):83–89
6. Guo M, Yan M, Chen B, Yang G (2015) Fault line selection of resonant grounding system based on waveform time-domain feature clustering method. *Electr Power Autom Equip* 35(11):59–66+81
7. Peng X, Qian G, Li X, Gao F (2012) Intelligent diagnosis of overhead transmission line trip fault. *High Volt Technol* 38(08):1965–1972
8. Dai J, Liu Y, Jiang W, Liu Z, Shenggehobx, Yan Y, Jiang X (2016) Lightning strike type identification method for transmission lines based on time-domain characteristics of lightning traveling wave. *Trans China Electrotech Soc* 31(06):242–250
9. Liu Y, Liu C, Hou Y, Zhao C (2019) Fault diagnosis of feature quantity monitoring in high frequency waveform overhead circuit short circuit fault. *Electron Technol Softw Eng* 03:220–221
10. Shao W, He Y, Guan X, Luo X (2023) Phase-to-phase permanent fault identification method of distribution network based on multiple disturbance current waveform characteristics. *Power Syst Protect Control* 51(07):146–157
11. Chen K, Huang C, He J (2016) Fault detection, classification and location for transmission lines and distribution systems: review on the methods. *High Volt* 1(1):25–33

12. Fornás JG, Jaraba EH, Estopiñan AL et al (2022) Detection and classification of fault types in distribution lines by applying contrastive learning to GAN encoded time-series of pulse reflectometry signals. *IEEE Access* 10:110521–110536
13. Qiu Z, Zhu X (2022) Liao C: detection of bird species related to transmission line faults based on lightweight convolutional neural network. *IET Gener Transm Distrib* 16(5):869–881
14. Tian X, Liu Z, Liu J (2023) Identification of overhead line fault traveling wave and interference clutter based on convolution neural network and random forest fusion. *Energy Rep* 9:1531–1545

# Chemical Trap Orbital Analysis of Styrene-Grafted Polypropylene for HVDC Cable Insulation



Yuxiao Zhou, Changlong Yang, Shixun Hu , Huajun Wu, Weigang Zheng, Tao Li, Shangshi Huang , Xuchen Lu, Qi Li , and Jinliang He 

**Abstract** Polypropylene (PP) is regarded as a rather potential insulation material alternative for the next generation HVDC cable system. Grafting styrene is proved to be an effective method to further enhance the DC insulation properties especially under high temperature. The trap introduced by grafting modification is believed to be the key issue on such enhancement. In this paper, the quantum chemistry analysis based on DFT method is adopted to computationally investigate the chemical trap originating from grafting modification. The results indicate that grafting styrene introduces new trap orbitals within the HOMO–LUMO gap of PP, and the grafted aromatic ring, especially the delocalized Pi bond is responsible for it. Besides, the delocalized Pi bond can also lead to the local high negative electrostatic potential area on the PP chain, thus affecting the microscopic charge transportation in PP. This work is expected to provide a reference for investigating the mechanisms of charge transportation and macroscopic electrical properties enhancement of PP-based insulation for HVDC cables.

---

Y. Zhou · W. Zheng · X. Lu  
Electric Power Research Institute of State Grid Liaoning Electric Power Co., Ltd.,  
Shenyang 110006, Liaoning, China

C. Yang  
State Grid Shenyang Electric Power Supply Company, Shenyang 110003, Liaoning, China

S. Hu (✉) · S. Huang · Q. Li · J. He  
Department of Electrical Engineering, Tsinghua University, Haidian, Beijing 100084, China  
e-mail: [rugals@yeah.net](mailto:rugals@yeah.net)

Q. Li  
e-mail: [qili1020@tsinghua.edu.cn](mailto:qili1020@tsinghua.edu.cn)

J. He  
e-mail: [hejl@tsinghua.edu.cn](mailto:hejl@tsinghua.edu.cn)

H. Wu · T. Li  
State Grid Liaoning Electric Power Co., Ltd., Shenyang 110000, Liaoning, China  
e-mail: [whj747@126.com](mailto:whj747@126.com)

© Beijing Paiké Culture Commu. Co., Ltd. 2024

X. Dong and L. Cai (eds.), *The Proceedings of 2023 4th International Symposium on Insulation and Discharge Computation for Power Equipment (IDCOMPU2023)*, Lecture Notes in Electrical Engineering 1103, [https://doi.org/10.1007/978-981-99-7413-9\\_57](https://doi.org/10.1007/978-981-99-7413-9_57)

595

**Keywords** HVDC cable · Insulation material · Polypropylene · Grafting modification · Chemical trap

## 1 Introduction

Along with the continuously increasing transmission capacity and the “double-carbon” demand of the high voltage direct current (HVDC) cable system, the research and development of new-type high thermo-resistant, recyclable cable insulation materials has been extensively carried out, among which polypropylene (PP) is regarded as a promising alternative due to its strong insulation performance, high melting temperature, and recyclable nature. Especially compared with conventional cross-linked polyethylene (XLPE) insulation, PP-based insulation material shows satisfactory advantages for the application in the next generation recyclable cable network [1–4].

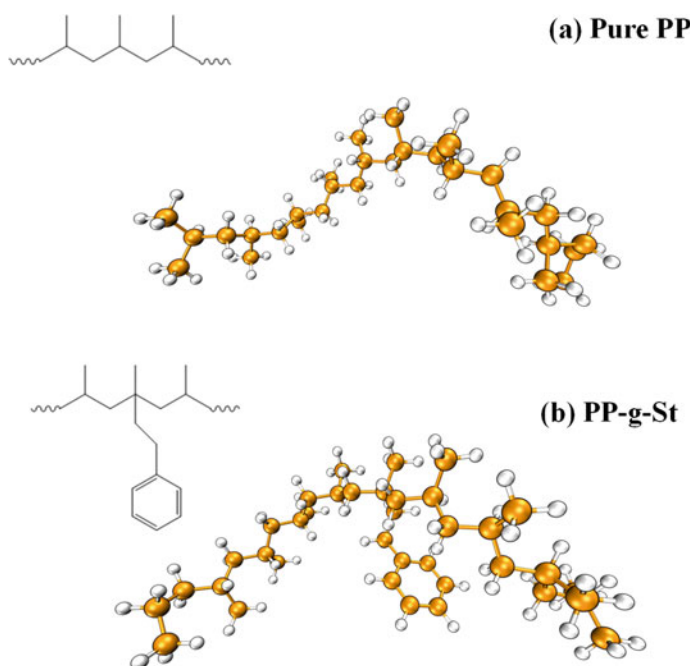
The insulation performances under high operating temperature (no less than 90 °C) of the cable insulation is rather important, on which PP still need to be improved. Many researches indicate that chemically grafting modification on PP is an effective method to enhance the insulation performances especially under high temperature [5, 6]. This modification technology is to microscopically graft functional chemical group onto the PP molecular chain by chemical reaction, in which the free radical-initiated grafting modification system is a commonly adopted method. The free radical of initiator can thermally decomposed and seize the hydrogen atom of PP molecular chain thus generating molecular chain radical. And the functional chemical group can additively react with the chain radical, finally realizing the grafting process [6]. By this molecular modification on the chemical structure of PP, the macroscopic electrical properties of PP can be enhanced. That is to say, this modification technology is more thorough and stable. Therefore, more suitable for industrial production and application.

With regard to the enhancement mechanism of PP-based grafting modification, some researchers have carried out pioneer and valuable investigations [6–9]. So far, it is commonly believed that grafting chemical groups onto the PP molecular chain can introduce deep traps into the modified PP material, which have been verified by experimental researches such as thermally stimulated depolarization current (TSDC) test [8, 9]. However, where do these deep traps come from, and what are the characteristics of these deep traps, are still not clear. Furthermore, because the grafting is a kind of chemical modification, the characteristics of the traps are hard to observe and investigate experimentally, hence becoming more troublesome. In this paper, to solve this problem, taking styrene-grafted PP as an example, the characteristics of the traps originated from grafting modification is analyzed entirely by quantum chemistry computation. The trap depth, trap type, and its electrostatic effect are discussed on the electron orbital level, radically and essentially. This work can act as a reference on the chemical mechanism of grafting modification to enhance the macroscopic electrical properties of PP-based HVDC cable insulation.

## 2 Computational Details

Styrene (St) is selected as the grafting monomer due to its significant enhancement on the DC electrical properties [6–8]. For the computation, the styrene-grafted PP fragment structure consisting of 10 propylene monomers and one grafted styrene group is established in GaussView6, named as PP-g-St. Based on the density functional theory (DFT), the geometric structure and single point energy are optimized and calculated at the function level of B3LYP-D3(BJ), with the basis function set of 6-31G(d). A PP fragment without grafted styrene group is also established and calculated at the same level, designated as pure PP, which can be regarded as the reference. Figure 1 shows the chemical structures of the both.

The ground state wavefunction of the two structures are obtained by aforementioned calculation, and the density of electron states (DOS) spectra are further calculated. Particularly, the partial DOS (PDOS) which describes the DOS contribution of specific atoms are calculated to analyze the DOS changes before and after the grafting modification, thus able to position the trap level orbitals. In addition, the electrostatic potential (ESP) distributions of the two structures are also calculated to analyze the grafting effect on the molecular electrostatic interaction [10].



**Fig. 1** Chemical structure of pure PP and PP-g-St

### 3 Results and Discussion

#### 3.1 Analysis on Trap Orbitals

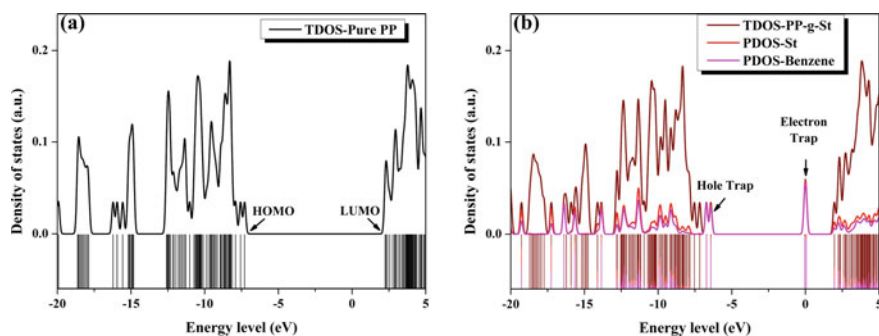
The trap levels and corresponding electron orbitals can be directly observed and investigated by the DOS spectrum. The DOS spectra of pure PP and PP-g-St are shown in Fig. 2.

It can be seen in Fig. 2a that the distance between the highest occupied molecular orbital (HOMO) and the lowest unoccupied molecular orbital (LUMO), which also can be designated as HOMO–LUMO gap, is approximately 10 eV, indicating that PP is a typical insulator. After grafting styrene, as shown in Fig. 2b, some new electron orbitals appear inside the HOMO–LUMO gap. Among them the new orbitals near the HOMO of pure PP correspond to the hole traps, while the orbitals near the LUMO of pure PP can be described as the electron traps. These results indicate that the hole and electron traps exist in styrene-grafted PP.

Regarding these trap orbitals in styrene-grafted PP, the DOS contributions of the atoms in grafted styrene groups are further calculated and exhibited in Fig. 2b in the form of partial DOS (PDOS), particularly focusing on the contribution of the grafted aromatic ring (benzene).

Comparing the two PDOS spectra with the TDOS of PP-g-St exhibited in Fig. 2b, it is easy to observe that the emerged hole and electron trap orbitals are almost contributed by the grafted St group, especially the aromatic ring—benzene. This result indicates that indeed the traps introduced by grafting modification originate from the grafted benzene structure. The depth of these introduced traps can be calculated by the trap energy level difference between the trap orbital and the HOMO or LUMO of pure PP. That is:

$$E_H = E_{\text{Hole trap}} - E_{\text{HOMO}} \quad (1)$$



**Fig. 2** Density of electron state (DOS) of **a** pure PP; **b** PP-g-St

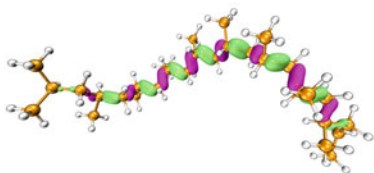
$$E_E = E_{LUMO} - E_{\text{Electron trap}} \quad (2)$$

where the  $E_H$  and  $E_E$  correspond to the depth of hole trap and electron trap, respectively.  $E_{HOMO}$  and  $E_{LUMO}$  are respectively the energy level of the HOMO and LUMO of pure PP fragment.  $E_{\text{Hole trap}}$  and  $E_{\text{Electron trap}}$  are the energy level of the trap orbitals. It can be calculated that the  $E_E$  is about 2.0 eV, while the  $E_H$  is approximately 1.0 eV. That is to say, grafting styrene can introduce hole and electron traps in the molecular structure of PP. The hole trap is shallow, while the electron trap, is of high depth.

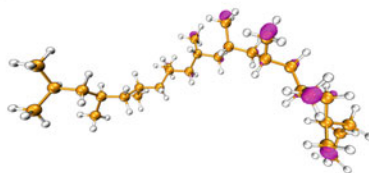
To make the trap orbitals visible, also for the convenience of a direct analysis, the orbitals distributions (electron clouds) in the chemical structures are depicted and shown in Fig. 3. In this figure, the magenta color orbitals correspond to the positive electron wavefunction, and the green color orbitals refer to the negative wavefunction.

It can be seen that the HOMO of pure PP fragment is distributed along the PP backbone, and the LUMO is near the methyl group ( $-\text{CH}_3$ ) of pure PP fragment. After grafting styrene, one can easily observe that the new HOMO and LUMO, which can

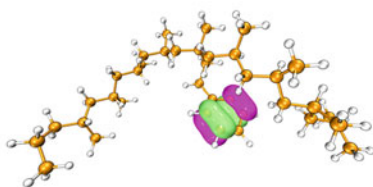
(a) Pure PP HOMO



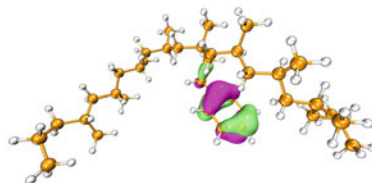
(b) Pure PP LUMO



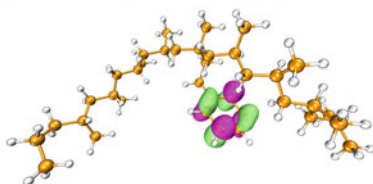
(c) PP-g-St HOMO-1 (Hole Trap1)



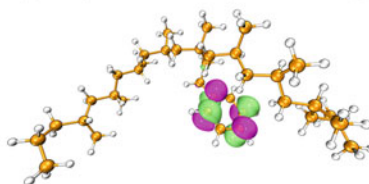
(d) PP-g-St HOMO (Hole Trap2)



(e) PP-g-St LUMO (Electron Trap1)



(f) PP-g-St LUMO+1 (Electron Trap2)



**Fig. 3** HOMO and LUMO of pure PP fragment. **a** HOMO; **b** LUMO; Hole trap orbitals of PP-g-St fragment (**c**, **d**); Electron trap orbitals of PP-g-St fragment (**e**, **f**)



also be regarded as hole and electron traps, are all distributed on the aromatic ring. This coincides with the PDOS results exhibited in Fig. 2b. Besides, according to the shape of the trap orbitals, these traps are strongly correlated to the delocalized  $\pi$  bond of the grafted aromatic ring. The transfer of electrons from the backbone or methyl of PP (i.e., HOMO or LUMO of PP) to the delocalized  $\pi$  bond of grafted aromatic ring (corresponding to the hole or electron trap of PP-g-St), can describe the trapping process in the styrene-grafted PP. The trapping process can capture the charge carriers in the material hence the charge mobility is reduced. Therefore, the macroscopic electrical properties, such as DC volume resistivity, and DC breakdown tolerance, can be significantly enhanced.

### 3.2 Analysis on Potential Well

The electrostatic potential (ESP) of the molecular structure can reflect the effect of grafted chemical group on the electron distribution of PP, which can in turn affect the transportation of the charge carriers. The ESP distribution are exhibited in Fig. 4.

**Fig. 4** Electrostatic potential of **a** pure PP and **b** PP-g-St

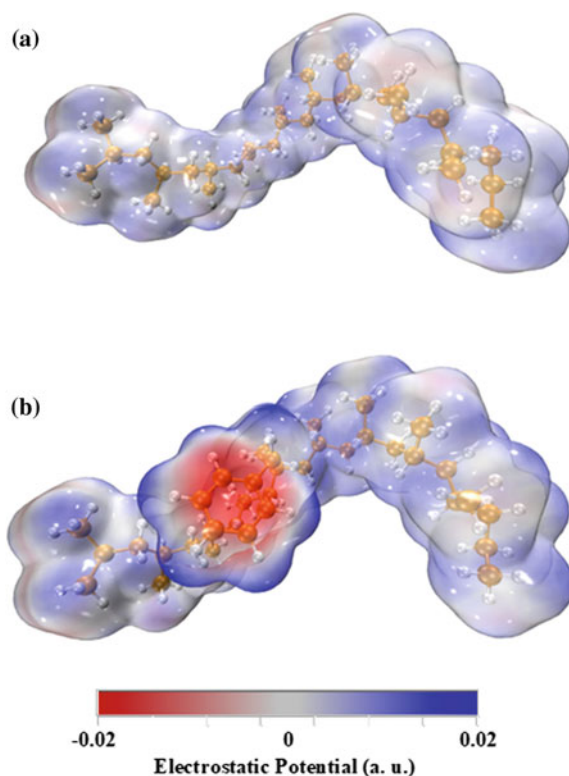


Figure 4 shows that the ESP of pure PP fragment is very gentle. This is easy to be comprehended due to the low polarity of PP itself. Whereas in PP-g-St, although styrene itself is of non-polarity, a highly negative potential area can be observed on the grafted aromatic ring, for which the contribution of delocalized Pi electrons should be responsible. This highly negative potential area can be regarded as a potential well that can affect the charge carrier transportation. Similar to the trapping effect of hole/electron trap orbitals, the mobility of charge carriers can be reduced, finally leading to the enhanced macroscopic electrical performances.

## 4 Conclusions

This paper calculates the influence on electron orbital structure and electrostatic potential of polypropylene-based grafting modification by styrene. The chemical trap orbitals are analyzed and discussed in depth. The results indicate that grafting styrene can introduce deep electron traps and shallow hole traps within the HOMO–LUMO gap of polypropylene. The delocalized Pi bond of grafted aromatic ring (benzene structure) is the origin of the trap orbitals. Besides, the grafted styrene can also introduce a deep negative electrostatic potential well which can affect the charge carrier transportation. Therefore, the charge carrier mobility can be reduced, and the macroscopic electrical properties can be enhanced. This work would be beneficial to the charge transportation mechanism investigation of grafting-modified thermoplastic materials for HVDC cable insulation.

**Acknowledgements** This work was supported by the Science and Technology Project of State Grid Corporation of China under grant number 5500-202228113A-1-1-ZN.

## References

1. Li CY, Yang Y, Xu GQ et al (2022) Insulating materials for realising carbon neutrality: opportunities, remaining issues and challenges. *High Volt* 7(4):610–632
2. Li ZL, Du BX (2018) Polymeric insulation for high-voltage dc extruded cables: challenges and development directions. *IEEE Electr Insul Mag* 34(6):30–43
3. Huang XY, Zhang J, Jiang PK et al (2020) Material progress toward recyclable insulation of power cables part 2: Polypropylene-based thermoplastic materials. *IEEE Electr Insul Mag* 36(1):8–18
4. Zhou Y, Hu SX, Yuan C et al (2020) Recyclable polypropylene-based insulation materials for HVDC cables: progress and perspective. *CSEE J Power Energy Syst Early Access* 1–10
5. Zha JW, Wu YH, Wang SJ et al (2016) Improvement of space charge suppression of polypropylene for potential application in HVDC cables. *IEEE Trans Dielectr Electr Insul* 23(4):2337–2343
6. Yuan H, Hu SX, Zhou Y et al (2021) Enhanced electrical properties of styrene-grafted polypropylene insulation for bulk power transmission HVDC cable. *CSEE J Power Energy Syst Early Access* 1–8

7. Hu SX, Zhang WJ, Wang W et al (2022) Comprehensive comparisons of grafting-modified different polypropylene as HVDC cable insulation material. *IEEE Trans Dielectr Electr Insul* 29(5):1865–1872
8. Yuan H, Zhou Y, Zhu YJ et al (2020) Origins and effects of deep traps in functional group grafted polymeric dielectric materials. *J Phys D Appl Phys* 53:475301
9. Hu SX, Yuan H, Zhang Q et al (2022) Deep trap origins, characteristics, and related mechanisms in chemically grafted polypropylene with enhanced direct current volume resistivity. *J Phys Chem C* 126:16280–16288
10. Lu T, Chen FW (2012) Multiwfn: a multifunctional wavefunction analyzer. *J Comput Chem* 33(5):580–592

# Numerical Simulation of Transient Temperature Rise on 110 kV/40 MVA Vehicle-Mounted Mobile Transformer



Zhijia Feng, Jinxin Cao, Hongling Zhou, Zhenpeng Tang, Jianguo Wang, Yadong Fan, Li Cai, and Mi Zhou

**Abstract** Vehicle-mounted mobile transformers are installed on mobile platforms, characterized by their compact structure and convenient transportation. It can be used as a temporary transformer when the capacity of the main transformer in a substation is insufficient or the power planning and construction do not meet the requirements. In order to analyze the temperature distribution in the compacted 110 kV/40 MVA mobile transformer at this voltage and capacity level, a single-phase axisymmetric 2-D finite element model of the mobile transformer was established, and transient temperature rise of the transformer was simulated using the short-circuit method. The results show that the maximum hotspot temperature reached 87.9 °C when the total losses were applied, while it reached 85.2 °C when the rated current was applied. The temperature rise satisfies the conditions for safe operation, indicating

---

Z. Feng · J. Cao (✉) · H. Zhou · J. Wang · Y. Fan · L. Cai · M. Zhou  
Engineering Research Center of Ministry of Education for Lightning Protection and Grounding Technology, School of Electrical Engineering and Automation, Wuhan University, Wuhan, China  
e-mail: [jinxin.cao@connect.polyu.hk](mailto:jinxin.cao@connect.polyu.hk)

Z. Feng  
e-mail: [2018302070201@whu.edu.cn](mailto:2018302070201@whu.edu.cn)

H. Zhou  
e-mail: [Zhouhl@whu.edu.cn](mailto:Zhouhl@whu.edu.cn)

J. Wang  
e-mail: [wjg@whu.edu.cn](mailto:wjg@whu.edu.cn)

Y. Fan  
e-mail: [ydfan@whu.edu.cn](mailto:ydfan@whu.edu.cn)

L. Cai  
e-mail: [cail@whu.edu.cn](mailto:cail@whu.edu.cn)

M. Zhou  
e-mail: [zhoumi927@whu.edu.cn](mailto:zhoumi927@whu.edu.cn)

Z. Tang  
Jiangmen Power Supply Bureau of Guangdong, Power Grid Co., Ltd., Jiangmen, China  
e-mail: [13702272352@139.com](mailto:13702272352@139.com)

that the transformer's structural design is reasonable and has good heat dissipation performance.

**Keywords** Mobile transformer · Temperature field · Numerical simulation

## 1 Introduction

With the rapid development of the economy, the demand for high-quality power and continuous electricity supply for power users is increasing. At the same time, the electricity load density is growing rapidly, leading to situations where conventional substations have the insufficient backup capacity and additional transformer capacity is required in the power system [1, 2]. Mobile substations have the configuration of a complete substation and can be quickly deployed for emergency power supply during fault repair, accident rescue, and other urgent situations, playing a role in emergency power supply [3–5]. The development of mobile substations is of great significance for improving the reliability of the power system.

At present, the research and application of mobile substations with a voltage level of 110 kV and above are currently limited, and the majority of 110 kV mobile substations have a capacity of 20 MVA or below [6]. Due to the restrictions imposed by road transportation regulations, conventional 110 kV transformers cannot meet the requirements. Therefore, it is necessary to reduce the mass of components such as windings and oil in the mobile transformer, adjust the cooling method, and optimize the arrangement of heat dissipation devices to reduce the equipment size [7]. However, reducing the size of the transformer may increase the load losses and temperature, posing a threat to its operational lifespan and affecting the reliability of the power supply [8]. Therefore, to evaluate the heat dissipation performance of the equipment, it is necessary to measure or analyze the internal temperature field of the transformer during operation. Analysis methods for the internal temperature of oil-immersed power transformers include direct measurement and indirect measurement [9]. Direct measurement methods mainly include fiber optic temperature sensing, thermocouple temperature sensing, and infrared temperature sensing [10]. Indirect measurement methods mainly include numerical calculation, thermal network method, empirical formula method, etc. [11]. In addition, methods based on artificial intelligence prediction are also being gradually applied in the field of transformer temperature rise calculation [12]. For numerical calculation methods, relevant equations are established based on heat transfer and fluid mechanics to calculate and solve for the temperature field and flow field distribution of the transformer. With the continuous progress in computer science, researchers commonly use finite element simulation software to calculate and analyze the temperature field of transformers [13].

Currently, temperature calculations for oil-immersed transformers mostly focus on conventional fixed transformers. There is still a lack of sufficient research on

temperature rise calculations for mobile transformers. To investigate the temperature field characteristics of a 110 kV/40 MVA mobile transformer, this study establishes a single-phase axisymmetric 2-D model of the transformer and utilizes the finite element simulation software to calculate the transient temperature rise of the transformer based on the short-circuit method. This aims to verify the rationality of the equipment’s structure and heat dissipation capability, providing a reference for future temperature field calculations and analysis of mobile transformers.

## 2 Mechanisms of Heat Generation and Dissipation

The heat generation in a transformer is primarily due to losses incurred during operation. Transformer losses are typically classified into three types. The first type is load losses, which refer to the ohmic losses generated by the current flowing through the windings. The second type is hysteresis losses, which occur when ferromagnetic materials are magnetized in an alternating magnetic field. The third type is stray losses, which are generated as leakage flux passes through components such as the tank walls and partitions.

The load losses of a transformer are proportional to the square of the direct current resistance and current. Under rated conditions, the load losses are given by (1).

$$P = 3I_{1Na}^2 r_{1.75^\circ\text{C}} + 3I_{2Na}^2 r_{2.75^\circ\text{C}} \tag{1}$$

where  $I_{1Na}$  is phase current of the primary winding (A);  $I_{2Na}$  is phase current of the secondary winding (A);  $r_{1.75^\circ\text{C}}$  is total resistance of the primary winding referred to 75 °C (Ω);  $r_{2.75^\circ\text{C}}$  is total resistance of the secondary winding referred to 75 °C (Ω).

The transformer core is made of silicon steel sheets, which are good conductors of electricity. The electromotive force generated by the electromagnetic induction phenomenon will form circulating currents within the core, resulting in eddy current losses. The expression for core losses is given by (2).

$$P_0 = K_0 G_{F_e} P_{1/50} (F/50)^\beta B_m^2 \tag{2}$$

where  $P_{1/50}$  is iron loss coefficient (W);  $P_0$  is basic loss (W);  $K_0$  is technological coefficient of the iron core loss;  $G_{F_e}$  is weight of the iron core (kg);  $P_c$  is iron loss per unit weight (W).

Transformer heat dissipation primarily occurs through three forms: conduction, convection, and radiation. Conduction refers to the heat transfer phenomenon that occurs through the movement of microscopic particles such as atoms and free electrons. Its mathematical expression is given by (3).

$$q = -\lambda \frac{\partial t}{\partial x} \vec{n} \tag{3}$$

where  $\lambda$  is coefficient of thermal conductivity ( $\text{W/m} \cdot \text{K}$ );  $q$  is heat flux ( $\text{W/m}^2$ ).

Convection refers to the heat transfer process that occurs due to the displacement of fluid during macroscopic motion. It only occurs within the fluid. Convection is always accompanied by conduction. Its mathematical expression is given by (4).

$$q = h(t_w - t_f) \quad (4)$$

where  $t_w$  and  $t_f$  are the temperatures of the wall plane and the fluid, respectively ( $^{\circ}\text{C}$ );  $h$  is surface heat transfer coefficient ( $\text{W/m}^2 \cdot \text{K}$ ).

Radiation refers to the phenomenon where an object transfers heat by emitting electromagnetic waves. The magnitude of radiation depends on the temperature and properties of the radiating surface. Its mathematical expression is given by (5).

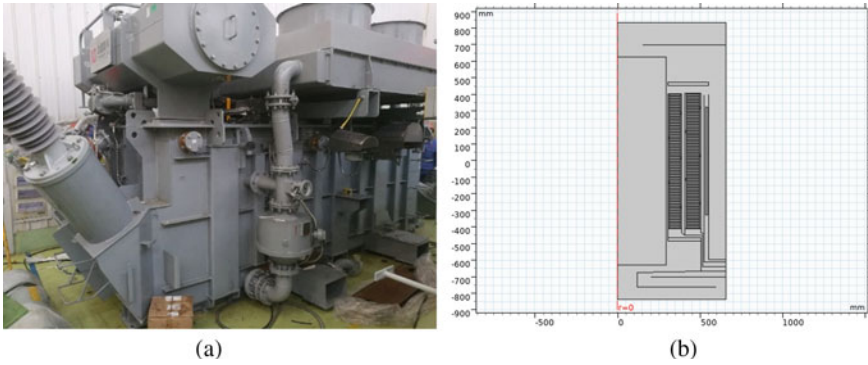
$$q = C_w \left[ \left( \frac{T_1}{100} \right)^4 - \left( \frac{T_2}{100} \right)^4 \right] A \quad (5)$$

where  $C_w$  is radiation coefficient;  $T_1$  and  $T_2$  are the temperatures of the two objects ( $^{\circ}\text{C}$ );  $A$  is radiation surface area of the radiator ( $\text{m}^2$ ).

### 3 Simulation Model and Method

The research object of this study is the SFPZ-40000/110 model transformer, and the physical representation of the equipment is shown in Fig. 1a. This equipment is currently the smallest size mobile transformer at this voltage and capacity level. The rated load loss and rated no-load loss of the transformer are 232.87 and 24.65 kW, respectively. The rated voltages on the high/low voltage sides are 110,000 and 10,500 V, with rated currents of 209.9 and 2199 A, respectively. The rated heat dissipation of the air cooler is 200 kW, and the rated air flow of the fan is 16,000  $\text{m}^3/\text{h}$ . The rated oil flow rate of the oil pump is 100  $\text{m}^3/\text{h}$ . The inner diameter/outer diameter/height of the low-voltage winding, high-voltage winding, and regulating winding are 626/836/1067, 762/995/1090, and 810/816/649 mm, respectively.

The fundamental principle of the finite element method (FEM) is to discretize continuous differential equations and solve them numerically. When using the FEM for temperature field calculations, the entire model is first divided into discrete elements composed of a finite number of nodes. The temperature characteristics of the continuous body are then considered as the linear sum of the temperature characteristics of each discrete element. Algebraic equations are established to describe the temperature relationships and solve them. In this study, finite element simulation software is used to model the 110 kV/40 MVA transformer. The three-phase geometry of the transformer is identical, and each phase is axially symmetric. To maximize computational speed and efficiency while ensuring accuracy, a single-phase



**Fig. 1** The transformer studied in this paper, **a** physical object, **b** simulation model

axisymmetric 2-D finite element model of the transformer is selected, as shown in Fig. 1b.

In the simulation model, the materials of the windings, core, and partitions are set as copper, steel, and epoxy resin, respectively. The parameters of the transformer oil are important for temperature rise calculations, so the physical properties and their relationship with temperature should be carefully considered. The parameters of several key materials are shown in Tables 1 and 2. The heat source in the simulation model is set as uniformly distributed, and the influence of thermal radiation is neglected. The thermal parameters of the transformer windings are set as shown in Table 3.

**Table 1** Property parameters of solid materials

Parameter	Copper	Steel	Epoxy resin
Specific heat capacity [J/(kg K)]	385	460	1000
Density [kg/m <sup>3</sup> ]	8700	7650	1850
Thermal conductivity [W/(m K)]	400	52	0.8

**Table 2** Property parameters of transformer oil

Temperature [°C]	Density [kg/m <sup>3</sup> ]	Thermal conductivity [W/(m K)]	Specific heat capacity [J/(kg K)]	Dynamic viscosity [Pa s]
30	876	0.1306	1890	0.0184
40	870	0.1299	1930	0.0121
50	864	0.1291	1975	0.0084
60	858	0.1283	2015	0.0060
70	852	0.1276	2060	0.0046



**Table 3** Thermal parameters of the windings

Position	Heat source [W]	Unit volume heat source parameter [W/m <sup>3</sup> ]
Core	43,065	11,000
LV winding	48,200	465,500
HV winding	2457	340,000
Regulating winding	0	93,000

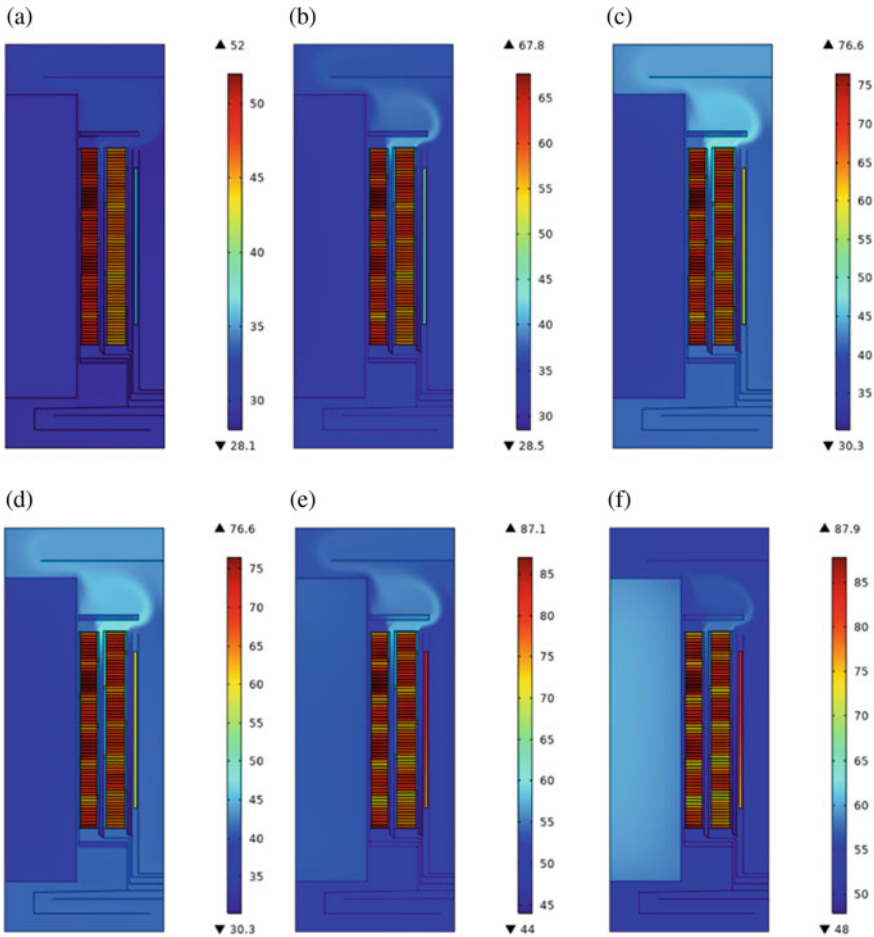
In this study, a short-circuit method is used for temperature rise simulation of the 110 kV/40 MVA mobile transformer, which utilizes the losses generated by the short circuit to raise the temperature of the transformer. The simulation is divided into two stages. In the first stage, a three-phase short circuit is applied to the low-voltage side of the transformer, and total losses are applied to the high-voltage side to measure the temperature rise of the transformer oil. The losses generated by the windings transfer heat to the transformer oil through heat exchange. When the rate of temperature rise at the top oil layer is less than 1 K/h, it is maintained for at least 3 h. In the second stage, the input power is reduced to make the winding current equal to the transformer's rated current, and the windings' temperature rise is measured. This process is maintained for at least 1 h. Finally, the power supply is cut off, the short circuit connection is opened, and the oil pump and cooling system continue to operate until the temperature of the transformer decreases to the ambient temperature over time.

## 4 Simulation Results

The proposed 110 kV/40 MVA mobile transformer model was subjected to temperature rise simulation using the short-circuit method in finite element analysis software. Firstly, the ambient temperature was set to 28 °C. The simulation for the first phase was performed by applying total losses to the model and maintaining it for 180 min. The transient temperature distribution cloud maps of the transformer at 5, 15, 30, 60, 120, and 180 min were obtained, as shown in Fig. 2.

In Fig. 2a, b, it can be observed that the temperature of the transformer rapidly changes within 0–15 min, resulting in a temperature rise of 39.8 K. During the time interval of 15–180 min, the hot-spot temperatures of the windings and the transformer oil gradually increase, eventually reaching a steady state. The hot-spot temperature of the low-voltage winding is 87.9 °C with a temperature rise of 59.9 K. The hot-spot temperature of the high-voltage winding is 84.5 °C with a temperature rise of 56.5 K. In this phase, the temperature difference between the low-voltage and high-voltage windings is small, remaining within 5 °C.

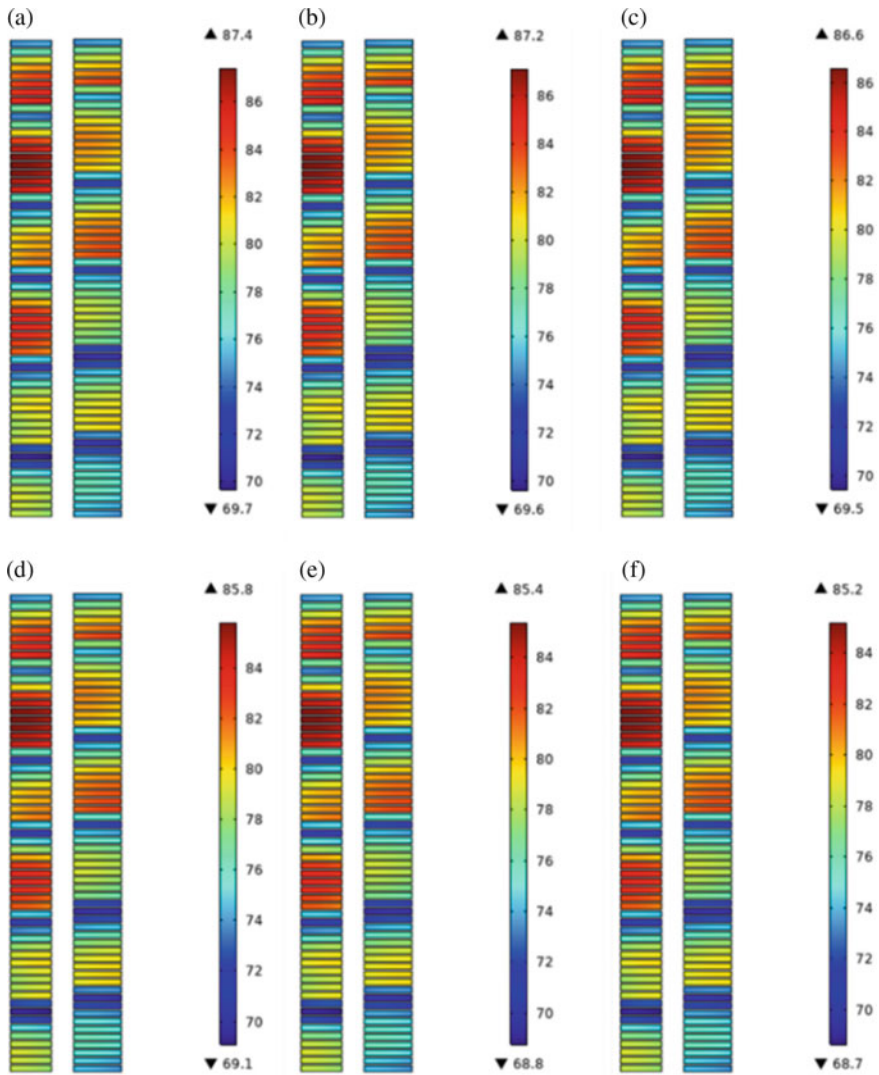
Subsequently, the second phase of the short-circuit method simulation was conducted. The volumetric heat source parameter values for the low-voltage, high-voltage, and regulating windings were modified to 426,400, 311,400, and 85,200 W/



**Fig. 2** Transient temperature field cloud when applying total losses. **a** 5 min, **b** 15 min, **c** 30 min, **d** 60 min, **e** 120 min, **f** 180 min

$m^3$ , respectively. The rated current was applied to the transformer model and maintained for 60 min. The transient temperature distribution cloud maps of the windings at 1, 2, 5, 15, 30, and 60 min were obtained, as shown in Fig. 3.

From Fig. 3, it can be observed that the distribution pattern of the winding temperature field when the rated current is applied is similar to the previous phase, but with slightly lower values. Within the 60-min timeframe, the hot-spot temperature gradually decreases, and the rate of temperature reduction decreases over time. After 30 min, the hot-spot temperature no longer significantly decreases, which is due to the low time constant of the windings. The maximum temperature of the transformer windings in this phase is 85.2 °C, ensuring safe operation within the specified temperature limits.



**Fig. 3** Transient temperature field cloud of windings when applying rated current. **a** 1 min, **b** 2 min, **c** 5 min, **d** 15 min, **e** 30 min, **f** 60 min

## 5 Conclusion

This paper presents a transient temperature rise simulation of a 110 kV/40 MVA mobile transformer, which is currently the smallest size and most compact vehicle-mounted transformer at this voltage and capacity level. Firstly, the physical mechanisms of heat generation and dissipation in the transformer are introduced. Then, based on the FEM, a single-phase axisymmetric 2-D finite element model of the

mobile transformer is established using simulation software. Finally, the transient temperature distribution of the transformer is obtained through simulation calculations based on the short-circuit method. The results show that when total losses are applied to the model, the hot spot is located on the low-voltage winding with a maximum temperature of 87.9 °C. When rated current is applied, the hot-spot temperature decreases by 2.7 °C within 30 min. Throughout the entire simulation process, the temperature rise does not exceed the limits of safe operation, indicating that the design of this mobile transformer is reasonably well-suited.

## References

1. Wu J et al (2021) Transportation monitoring of geo-location, speed, vibration, and shock acceleration for 110-kV vehicular mobile transformers. *IEEE Trans Instrum Meas* 70:1–10
2. Fan Y et al (2022) Transport vibration and shock characteristics of A 110 kV/40 MVA vehicular mobile transformer. *IEEJ Trans Electr Electron Eng* 17:1110–1120
3. Zhou L et al (2023) Transient characteristics of mobile transformer vehicle bypass operation. *Front Energy Res* 22:1–10
4. Tang Z et al (2019) Overview on technology progress in mobile substation. *Power Syst Technol* 43(9):3415–3423 (in Chinese)
5. Gao M (2021) Improving the comprehensive performance of mobile substation based on solid state transformer. *Trans China Electrotech Soc* 36(11):2315–2324 (in Chinese)
6. Yao R (2018) Modular integration scheme and electrical design of 110/10 kV-20 MVA vehicle-mounted mobile substation. *Electr Eng* 474(12):87–90 (in Chinese)
7. Zhou Y et al (2016) Influence factor and simulation of the loss of the converter transformer on-site testing. *High Volt Eng* 42(05):1608–1616 (in Chinese)
8. Dursun K et al (2013) Oil and winding temperature control in power transformers. In: 4th international conference on power engineering, energy and electrical drives. Istanbul, Turkey, pp 1631–1639
9. Liao C et al (2018) Review of study methods on hot-spot temperature of transformer. *High Volt Appar* 54(07):79–86 (in Chinese)
10. Jardini JA et al (2005) Power transformer temperature evaluation for overloading conditions. *IEEE Trans Power Deliv* 20(1):179–184
11. Susa D et al (2005) Dynamic thermal modelling of power transformers. *IEEE Trans Power Deliv* 20(1):197–204
12. Ippolito L et al (2004) Identification of Tagaki-Sugeno-Kang fuzzy model for power transformers predictive overload system. *IET Proc Gener Transm Distrib* 151(5):582–589
13. Santisteban A et al (2017) Numerical analysis of the hot-spot temperature of a power transformer with alternative dielectric liquids. *IEEE Trans Dielectr Electr Insul* 24(5):3226–3235

# Calculation of Distributed Photovoltaic Hosting Capacity in Distribution Network



Junwen Yang, Lei Shang, Xuzhu Dong, Huaimin Xia, Haiyan Zeng, Qing Duan, and Jie Zhao

**Abstract** If the scale of distributed photovoltaic exceeds the hosting capacity of the distribution network, the safe and stable operation of the distribution network will be seriously affected. To solve this problem, DIgSILENT/PowerFactory is used to calculate the hosting capacity of distributed photovoltaic in the distribution network. Firstly, a simulation model of low-voltage distribution network was established, and the influence mechanism and simulation analysis were used to explain the influence of distributed photovoltaic capacity and location on voltage, current, losses and harmonics. On this basis, the corresponding constraint conditions are constructed, and the hosting capacity of distributed photovoltaic in the distribution network is calculated to obtain the photovoltaic hosting capacity of each nodes, as well as the limiting factors and limiting elements.

**Keywords** Distributed photovoltaic · Hosting capacity · Distribution network · DIgSILENT

---

J. Yang · L. Shang (✉) · X. Dong · J. Zhao  
Center for AC/DC Intelligent Distribution Network, Hubei Engineering and Technology  
Research, Wuhan 430000, China  
e-mail: [shanglei@whu.edu.cn](mailto:shanglei@whu.edu.cn); [2018302070049@whu.edu.cn](mailto:2018302070049@whu.edu.cn)

School of Electrical and Automation, Wuhan University, Wuhan 430072, China

H. Xia · H. Zeng  
Wuhan Power Supply Company, Hubei Power Supply Company, State Grid, Wuhan 430024,  
China

Q. Duan  
China Electric Power Research Institute, Beijing 100192, China

© Beijing Paiké Culture Commu. Co., Ltd. 2024  
X. Dong and L. Cai (eds.), *The Proceedings of 2023 4th International Symposium on  
Insulation and Discharge Computation for Power Equipment (IDCOMPU2023)*, Lecture  
Notes in Electrical Engineering 1103, [https://doi.org/10.1007/978-981-99-7413-9\\_59](https://doi.org/10.1007/978-981-99-7413-9_59)

## 1 Introduction

The worsening environmental pollution and energy crisis, China's inherent requirements to achieve carbon peak and carbon neutral, and the continuous improvement of photovoltaic power generation technology and further cost reduction, continue to promote the development and use of distributed generation (DG), such as photovoltaic (PV), wind power. And the construction of decentralized energy production is being promoted. In 2021, China's new installed capacity of photovoltaic power generation reached 53 million kW. By the end of 2021, the installed capacity of PV power generation reached 306 million kW, and distributed PV reached 107.5 million kW, accounting for about one-third of the total installed capacity of PV power generation. Among the new PV power generation installations, distributed PV adds about 29 million kW, accounting for about 55% of all new PV power generation installations, and the development trend of centralized and distributed PV power generation is obvious [1]. With the accelerated construction of new power grids and the promotion of national whole-country PV plans, distribution networks, especially low-voltage distribution networks, will inevitably be connected to a large number of distributed PV power systems.

The large amount of distributed PV power generation will bring new problems and challenges to the distribution network. A large amount of distributed PV power generation will have a systemic impact on the distribution network. It changes the radiation network structure of the traditional distribution network and makes the distribution network appear multi-source. The tide of the distribution network will also be fundamentally changed, and the node voltage [2], line current [3], and system network loss [4] of the system will then be affected to varying degrees. At the same time, distributed PV systems as harmonic sources will also introduce more harmonic problems into the LV distribution network [5, 6].

The concepts of "hosting capacity" and "accommodation capacity" are often used to characterize the maximum bearing capability of the distribution network for DG in China and abroad [7–11]. According to the "Technical guidelines for evaluating power grid bearing capability of distributed resources connected to network", the bearing capability of the grid refers to the maximum capacity of the grid to accept power and load without continuously overloading of the grid equipment and without exceeding the voltage deviation, harmonics and other indicators [12]. Therefore, this paper adopts the concept of hosting capacity. Distributed PV will bring unpredictable risks to the distribution network if it is connected in a disorderly manner and exceeds the hosting capacity of the grid. Therefore, in order to ensure the normal access of distributed PV and the safe and effective operation of the distribution network, it is important to calculate and evaluate the PV hosting capacity of the distribution network. The literature [13] analyzed the overvoltage and voltage imbalance problems caused by distributed PV through a simplified Monte Carlo method to quantify the impact of several factors on the hosting capacity. Tan et al. [14] constructs an optimization model for the assessment of the hosting capacity of multi-DG access distribution networks using voltage offset, voltage fluctuation,

short-circuit current and relay protection technical indicators as constraints, and proposes a single-constraint and multi-constraint coordinated segmentation calculation method based on the sensitivity of the constraint indicators relative to the DG capacity. In [15], the index system for the comprehensive evaluation of the new distribution network hosting capacity is established by selecting appropriate evaluation indices for the comprehensive evaluation of the distribution grid after the new load and high proportion of distributed power sources are connected.

In this paper, in order to carry out the calculation of distributed PV hosting capacity of distribution network, firstly, the impact caused by distributed PV power sources access to distribution network is studied, and a typical PV system access to distribution network model is established by DIGSLIENT, and the PV hosting capacity and access location are changed to analyze and summarize the impact caused by PV access to distribution network power quality, line thermal stability and system network losses. As a result, the constraints required for the distribution network PV hosting capacity calculation are summarized, and the PV hosting capacity results are finally calculated.

## 2 Simulation Model Construction

In order to investigate the impact caused by distributed PV access to the distribution network, this paper uses a typical low-voltage distribution network topology [16], which is considered by CIGRE to be suitable for steady-state and transient simulations, to establish the model shown in Fig. 1. The distribution network is a 0.4 kV radial network, L1, L2, L3, L4 and L5 are both load nodes and nodes where distributed PV can be connected, and other nodes are main branch nodes and distribution nodes.

## 3 Impact of Distributed PV Access on Power Quality

### 3.1 Impact on Node Voltage

**Mechanistic Analysis.** A distribution network feeder line, as shown in Fig. 2, contains a total of  $N$  nodes.  $R_i + jX_i$  is the impedance between the  $i$ -1st node and the  $i$ -th node, and  $P_i + jQ_i$  is the load at the  $i$ -th node.  $U_0$  is the initial terminal voltage of the feeder, and  $U_i$  is the voltage at the  $i$ -th node. The distributed PV is connected at the  $p$ -th node with a capacity of  $P_{PV}$ .

The line losses are ignored due to their small magnitude. The direction of power flow to the load is assumed to be positive, and reactive power is neglected due to the small amount of reactive power required by the load in the actual distribution network. Thus, simplified values of the voltage at each node and the voltage-drop between the  $k$ -1st node and the  $k$ th node are given as

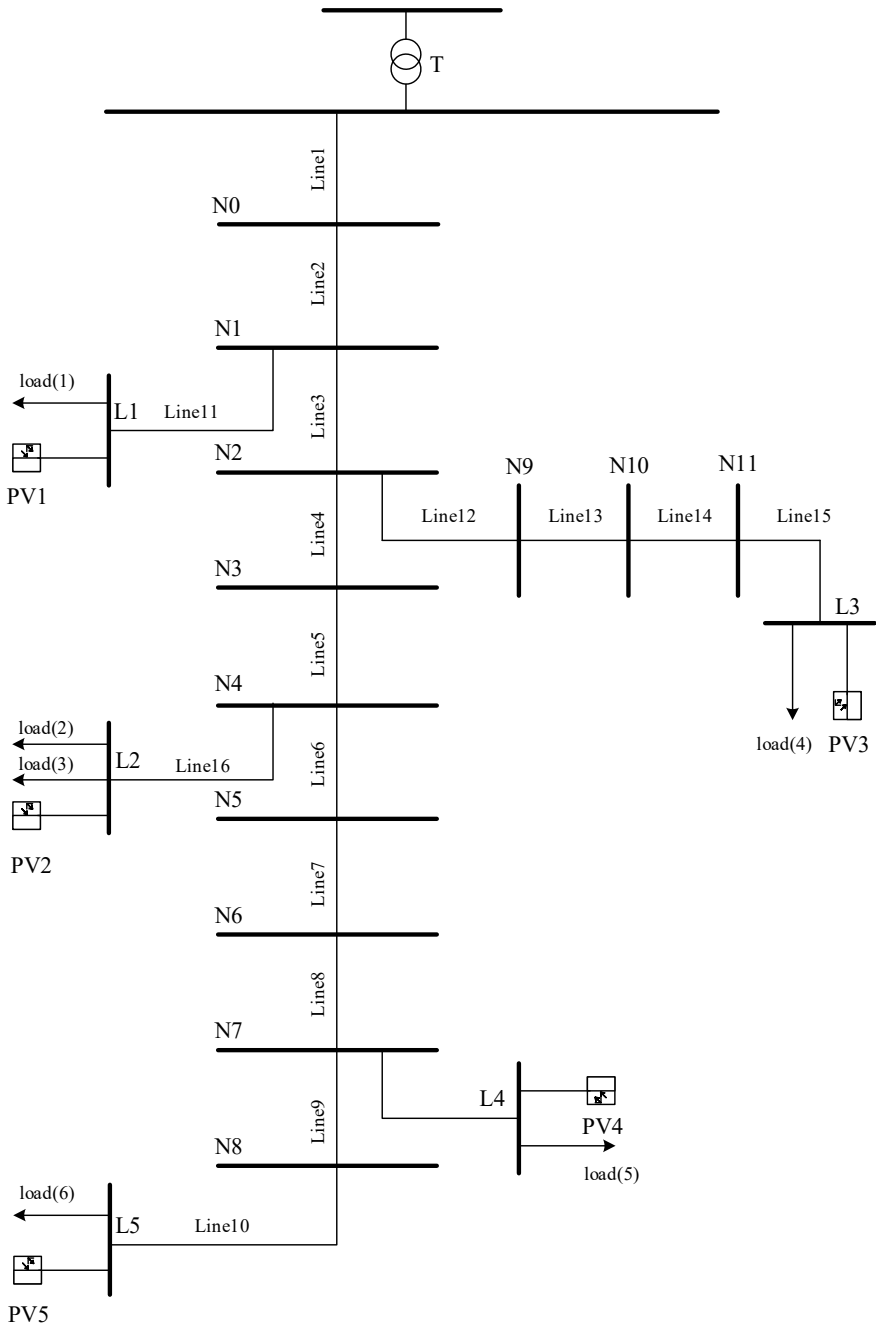
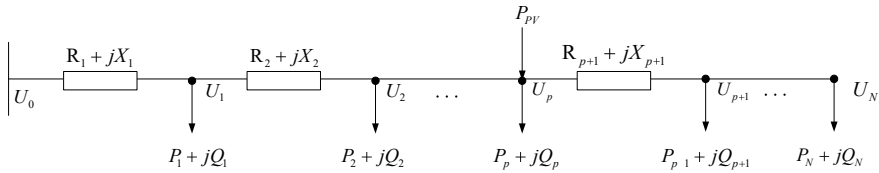


Fig. 1 A typical low-voltage distribution network





**Fig. 2** Single distributed PV connected to a radiant distribution network

$$U_i = U_0 - \sum_{k=1}^i \frac{\sum_{n=k}^N P_n R_k}{U_{k-1}} \tag{1}$$

$$\Delta U_k = \frac{\sum_{n=k}^N P_n R_k}{U_{k-1}} \tag{2}$$

And after access to distributed PV power generation, the node voltage will change, and it will be divided into two cases to discuss.

- (1) If the node is located before the point of connection (POC)  $p$ , i.e.  $0 < i < p$ , the voltage of the node and the voltage difference between the nodes is:

$$U_i = U_0 - \sum_{k=1}^i \frac{\left(\sum_{n=k}^N (P_n - P_{PV}) R_k\right)}{U_{k-1}} \tag{3}$$

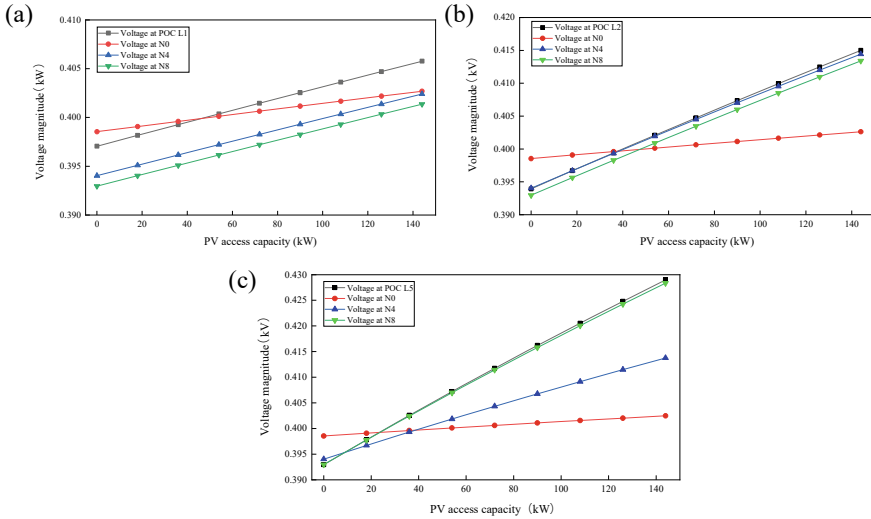
$$\Delta U_k = \frac{\left(\sum_{n=k}^N P_n - P_{PV}\right) R_k}{U_{k-1}} \tag{4}$$

- (2) If the node is located after the POC, i.e.  $i > p$ , the voltage at the node and the voltage difference between the nodes can be expressed as

$$U_i = U_0 - \sum_{k=1}^p \frac{\left(\sum_{n=k}^N (P_n - P_{PV}) R_k\right)}{U_{k-1}} - \sum_{k=p+1}^i \frac{\sum_{n=k}^N P_n R_k}{U_{k-1}} \tag{5}$$

$$\Delta U_k = \frac{\sum_{n=k}^N P_n R_k}{U_{k-1}} \tag{6}$$

Comparing the node voltages when the distributed PV is not connected, the node voltages all increase to some extent. For the node before the POC, if the sum of the power consumed by all the loads after this node is greater than the PV access capacity, the node voltage still decreases along the feeder. If the sum of the power consumed by all the loads after the node is less than the PV access capacity, the node voltage increases along the feeder instead. For the node after the access point, the voltage decreases along the feeder.



**Fig. 3** Voltage changes at different access capacities. **a** POC is L1, **b** POC is L2, **c** POC is L5

**Simulation Analysis.** The impact of distributed PV access on voltage deviation is analyzed from two perspectives: access capacity and access location. In the model, different capacities of PV are connected to load points L1, L2 and L5 at the beginning, middle and end of the line respectively, and the results are shown in Fig. 3. It can be seen that the system node voltages increase as the PV capacity increases. The magnitude of the effect of the capacity change on the nodes is also related to the location of the nodes. The magnitude of the voltage change near the end node and the grid connection point is greater than that of the first node.

For L1, L2, L3, L4 and L5, five POCs with increasing electrical distances from the busbar are connected to the PV, and the voltage changes at the POC and at each backbone node are shown in Fig. 4.

For the backbone nodes, the closer the access point is to the end of the feeder, the more pronounced the effect of the distributed PV generation on the voltage rise of the whole line. It can also be seen that at load point accesses L4 and L5, the node voltage appears to rise along the feeder direction behind node N4 for total load power less than the power provided by PV, confirming the previous related analysis.

### 3.2 Impact on Harmonics

**Mechanistic Analysis.** A brief analysis of the changes that occur when a distributed PV source is connected as a harmonic current source can be made using an equivalent circuit diagram [17] of the distribution network connected to a single distributed PV, as shown in Fig. 5. US is the external network equivalent to a voltage source, Zi is

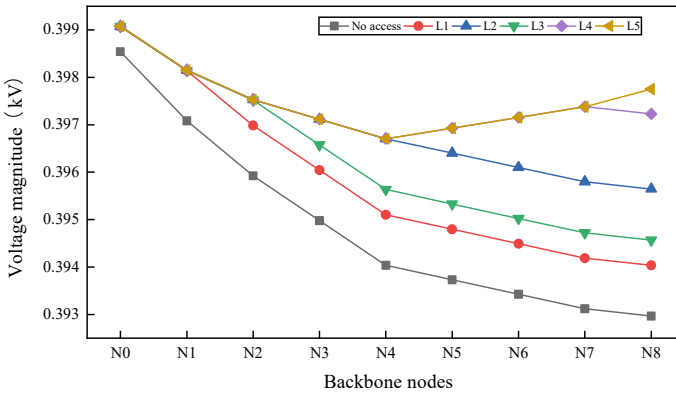


Fig. 4 Voltage changes at different access locations

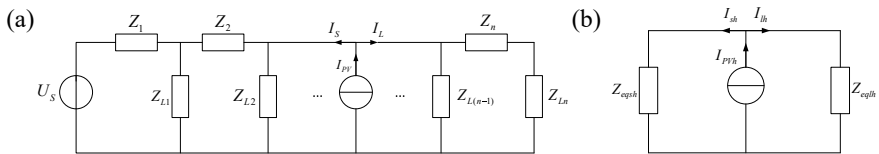


Fig. 5 The equivalent circuit harmonic analysis. **a** Equivalent circuit for a distribution network with a single distributed PV connection, **b** simplified equivalent circuit diagram

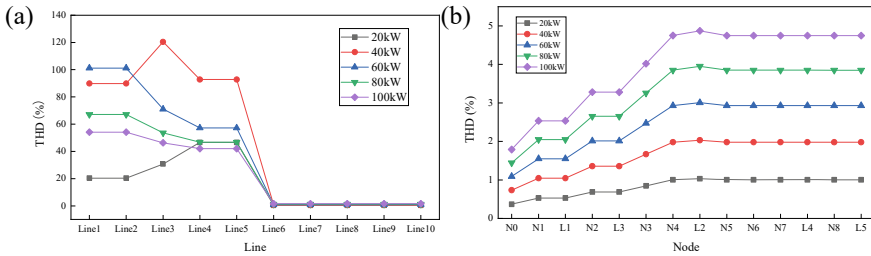
the line impedance of the *i*th branch and  $Z_{Li}$  is the impedance of the load at the *i*th node. The distributed PV power source is equivalent to a harmonic current source and the currents flowing to the system and load side are  $I_s$  and  $I_L$  respectively.

The current injected to the system side and the harmonic voltage at each node can be expressed as

$$I_{sh} = \frac{Z_{eqth}}{Z_{eqsh} + Z_{eqth}} I_{PVh} \approx I_{PVh} \tag{7}$$

$$U_{kh} \approx I_{PVh} Z_{eqsh} \tag{8}$$

From the above analysis, it can be concluded that the magnitude of the harmonic current generated by the PV system is related to the access capacity, while the magnitude of the harmonic current flowing to the system side and the load side is related to the line impedance, the external grid, the short-circuit capacity and the grid-connected location. From the perspective of both access capacity and access location, the larger the PV access capacity and the closer the access location is to the end of the line, the more severe the harmonic pollution and the worse the power quality. As can be seen from Eq. (7), most of the harmonic currents will flow to the system side, and the harmonic current content after the POC is very small. The harmonic voltage is



**Fig. 6** THD with different access capacities. **a** THD of line current, **b** THD of node voltage

generated by the harmonic current flowing through the impedance, so its magnitude is related to the magnitude of the harmonic current there and the magnitude of the equivalent impedance. The harmonic voltage before the POC should increase as the distance from the POC decreases, while the harmonic voltage at the node after the POC will remain approximately the same as at the POC due to the small harmonic current, with a slight decrease.

**Simulation analysis.** The relationship between harmonics and access capacity can be compared by connecting different capacities of PV to the same grid connection point. In the simulation, the load point L2 was selected as the POC, and different capacities of PV were connected to L2 for harmonic analysis, and the total harmonic distortion rate (THD) of the current was obtained as shown in Fig. 6a. It is clear that the harmonic content of the current on the line after Line5 is significantly reduced and close to zero. In contrast, the harmonic content on the line between the busbar and Line5 is higher and the harmonic current is larger. This indicates that a very small proportion of the harmonic currents flow to the load side. Furthermore, it can be noticed that due to the small equivalent impedance on the public grid side, most of the harmonic currents do not enter the distribution network, but flow from the PV connection points along the distribution network backbone to the public grid, with a very small part going to the end of the line.

For the harmonic voltage, THD of the voltage at the POC L2 is the largest, the THD of the voltage at the node after the POC is basically the same and slightly lower than at the POC, while the THD of the voltage at the node before the POC decreases rapidly towards the bus, and the THD of the voltage at the bus is the smallest. As the access capacity increases, the harmonic voltage continues to increase.

Distributed PV of the equal capacity is connected to each of the different load nodes and the results are obtained as shown in Fig. 7. Wherever the distributed PV is connected to the grid on the line, the harmonic level at the POC is higher than at other nodes. Comparing the harmonic voltages at different grid connection locations, it can be found that the overall harmonic voltage level is higher than other cases when the PV is connected at the far end of the line, L5, indicating that the harmonic voltage will be higher due to the greater equivalent impedance at the greater electrical distance, where the PV is more likely to cause power quality problems.

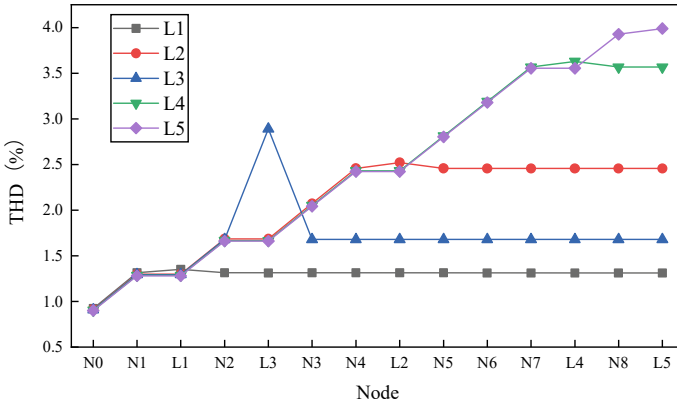


Fig. 7 THD of node voltage with different access locations

## 4 Impact of Distributed PV Access on Line Thermal Stability and Network Losses

### 4.1 Impact on Line Thermal Stability

As described in the mechanistic analysis in Sect. 3.1, the connection of distributed PV leads to a reduction in the line transmission power, a reduction in the voltage drop between the nodes and a corresponding impact on the line current.

In the simulation experiments, when PV is connected at the end load point L5, the current variation on Line10, the line connecting the POC to the backbone, is selected for study. If the PV capacity is less than the load at this point, the power delivered by the system to the load will decrease as the PV output increases, so the current will decrease as the capacity increases. If the access capacity is greater than the load at this point, the PV system not only supply the power required by the load, but also supply power to the system in the opposite direction, so that the current on Line10 reverse sand increases as the power transmitted through the line increases due to the increase in access capacity (Fig. 8).

### 4.2 Impact on Network Losses

For a system, the system losses and the network loss rate can be expressed by the following equation:

$$P_{\text{loss}} = \sum_{i=1}^n P_{i\text{loss}} \tag{9}$$

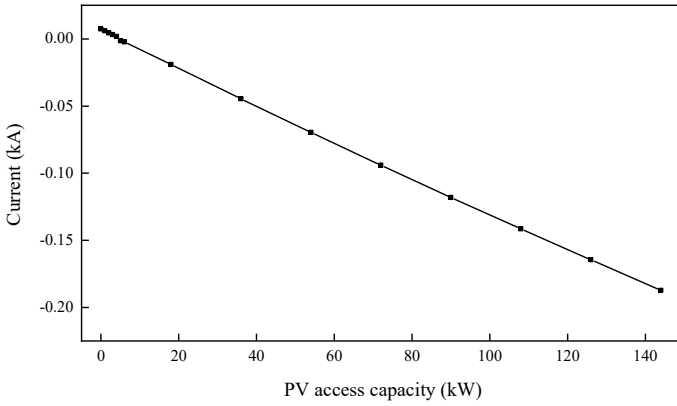


Fig. 8 Change of line current at different access capacities

$$\eta_{loss} = \frac{P_{loss}}{P_{load}} \times 100\% \tag{10}$$

$P_{i_{loss}}$  is the power loss on the  $i$ -th branch, and the sum of all the branch losses gives the total network loss  $P_{loss}$ , while  $P_{i_{load}}$  is the total supply load in the system.

In the different access scenarios, we can obtain the losses of each line by simulation, and from the above equation, we can obtain the system network loss rate. By comparing the variation of network loss under different scenarios, the relationship between system losses and PV access can be obtained as shown in Fig. 9.

It can be seen that as the access capacity increases, the system losses first decrease and then increase. Combined with the change in current with PV capacity, it can be concluded that the overall system network losses first decrease because the PV output

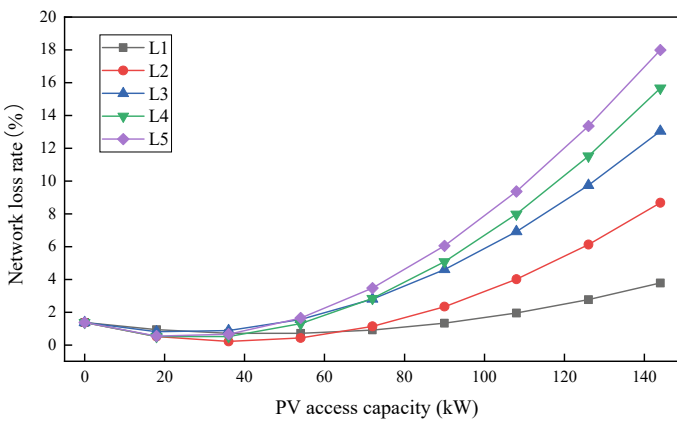


Fig. 9 System network losses varies with access capacity when access points vary

power reduces the amount of power the system has to provide to the load at that point, the current decreases and the losses then decrease. The lowest point of network losses is not when the PV power exactly matches the load at the POC, but when it is slightly greater than the load power. This is because not only is the power delivered from the system to the POC less, but the power delivered from the system to the other loads is also reduced, which in general greatly reduces the current transmitted through the line and reduces losses. When the PV output power to the grid is too high, the current will rise in the opposite direction and the losses will increase.

Comparing the difference between the network loss rates when the PV is connected at different access points, it can be found that when the PV is connected at L2, the heaviest of the load points, or at L5, the end of the line, the system losses are reduced to a greater extent when the PV is connected at the right capacity. This indicates that for heavy loads and for long electrical distances between the POC and the busbar, access to the right amount of PV can reduce the system losses to a greater extent.

## **5 Calculation of Distributed Photovoltaic Hosting Capacity of LV Distribution Networks**

### ***5.1 Distribution Network PV Hosting Capacity Constraints***

Based on the results of the previous analysis, it can be seen that the connection of distributed PV generation raises a number of problems. The distribution of the power flow in the system is significantly affected by the connection of distributed PV, and the distributed PV also injects harmonic currents into the system as the grid-connected PV inverter is a non-linear component. The power quality of the distribution network, the thermal stability of the lines and the losses of the system are all greatly affected.

Access to distributed PV power generation directly affects the system safety and power quality indicators that mentioned above, which are the limiting factors for distributed PV access. If the distributed PV hosting capacity of the distribution network is considered as a barrel, the various limiting factors are equivalent to the planks of different lengths on the barrel, and the distributed PV hosting capacity is limited because one of the factors has reached the maximum permissible limit [7]. The calculation of the PV hosting capacity of the distribution network must be based on certain constraints in order to be realised. Thus, based on the previous analysis of the impact caused by distributed power access and the constraints on the corresponding operational indicators in the system, this paper selects the corresponding constraints and establishes a distribution network distributed PV hosting capacity evaluation index system to provide an important basis for the calculation of distributed PV power hosting capacity in distribution network.

(1) Power flow constraint:

$$P_i = U_i \sum_{j=1}^n U_j (G_{ij} \cos \theta_{ij} + B_{ij} \sin \theta_{ij}) \quad (11)$$

$$Q_i = U_i \sum_{j=1}^n U_j (G_{ij} \sin \theta_{ij} - B_{ij} \cos \theta_{ij}) \quad (12)$$

When the hosting capacity is calculated, the system is in a normal operating state, so it needs to meet the power flow constraints for stable operation of the distribution network.

(2) Nodal voltage constraint:

$$U_{\min} \leq U_i \leq U_{\max} \quad (13)$$

where  $U_i$  is the voltage of node  $i$ ,  $U_{\max}$  and  $U_{\min}$  are the upper and lower voltage limits specified in the system operation respectively.

(3) Line thermal stability constraint:

$$I_i \% \leq I_{\max} \% \quad (14)$$

Too much current and too high a loading will cause the line to exceed its thermal stability limit, so the line thermal stability constraint is introduced, stipulating that the line loading should not exceed the line thermal stability limit. Where  $I_i \%$  is the loading of the line, then  $I_{\max} \%$  is the thermal stability limit of the line.

(4) THD of voltage constraint:

$$U_{THD} \leq U_{THD_{\max}} \quad (15)$$

where  $U_{THD}$  and  $U_{THD_{\max}}$  are the THD of the voltage at node  $i$  and its maximum permissible value, respectively.

## 5.2 Calculation of the PV Hosting Capacity of the Distribution Network

**Calculation Principles.** The hosting capacity calculation in DIGSILENT starts with a virtual connection of a distributed power source to the node that is the object of the hosting capacity calculation. The power of the connected distributed power source will continuously increase the capacity until the constraints are violated and the hosting capacity of the node is obtained. Then, the analysis continues with the next



node until all nodes have been processed. The complete hosting capacity calculation process is shown in Fig. 10.

**Calculation Results.** Based on the constraints constructed in the previous section and the relevant national regulations on the indicators, the constraints are set and DIGSILENT can be used to calculate the PV hosting capacity of the model, with the calculation range being all nodes in the system.

Table 1 shows the results of the PV hosting capacity calculations for this LV distribution network with the limiting factors for the PV hosting capacity of each node. As the algorithm calculates the hosting capacity of one node before calculating the next node, the calculated hosting capacity values for each node are independent. The column "Maximum accessible capacity" shows the PV hosting capacity of each node, i.e. the maximum capacity that can be connected to the PV at that point without violating any constraints. The column "Limiting element" indicates the corresponding element that limits the PV hosting capacity of the point, i.e. the element that has a problem of overstepping the limit if a PV capacity larger than the calculated capacity is connected to the point. The column "Reason for restriction" shows the specific overruns that can occur on the corresponding limiting element. An overloaded element means that the thermally stable limit of the line is exceeded, while an excessive harmonic means that the harmonic content at that point is too high and the THD of the voltage is too high.

In addition, Table 2 shows the calculation results of the corresponding constraint indicators in the PV hosting capacity calculation, i.e. the situation in the system when the PV capacity at the point reaches its maximum accessible capacity, including the maximum loading of the line, the maximum voltage at the node, the minimum voltage and the maximum THD.

By combining the results of the above calculations, it is also easy to see that the results of the distributed PV hosting capacity of the distribution network, as calculated by DIGSILENT, correspond to the results of the impact of the previous indicators. The results of the previous analyses all point to a greater impact on the voltage and harmonics of the system when PV is connected at the end. The results of the hosting capacity calculations show that nodes N8 and L5 at the corresponding ends also have the lowest PV load hosting capacity and can be connected to the smallest PV capacity.

## 6 Conclusion

In today's world of clean energy such as PV, the large number of distributed PV connections poses a great challenge to the economic and safe operation of the distribution network and the quality of power supply. Therefore, it is important to clarify which aspects of the distribution network are affected by distributed PV access and to assess the PV hosting capacity of the distribution network on this basis. This paper

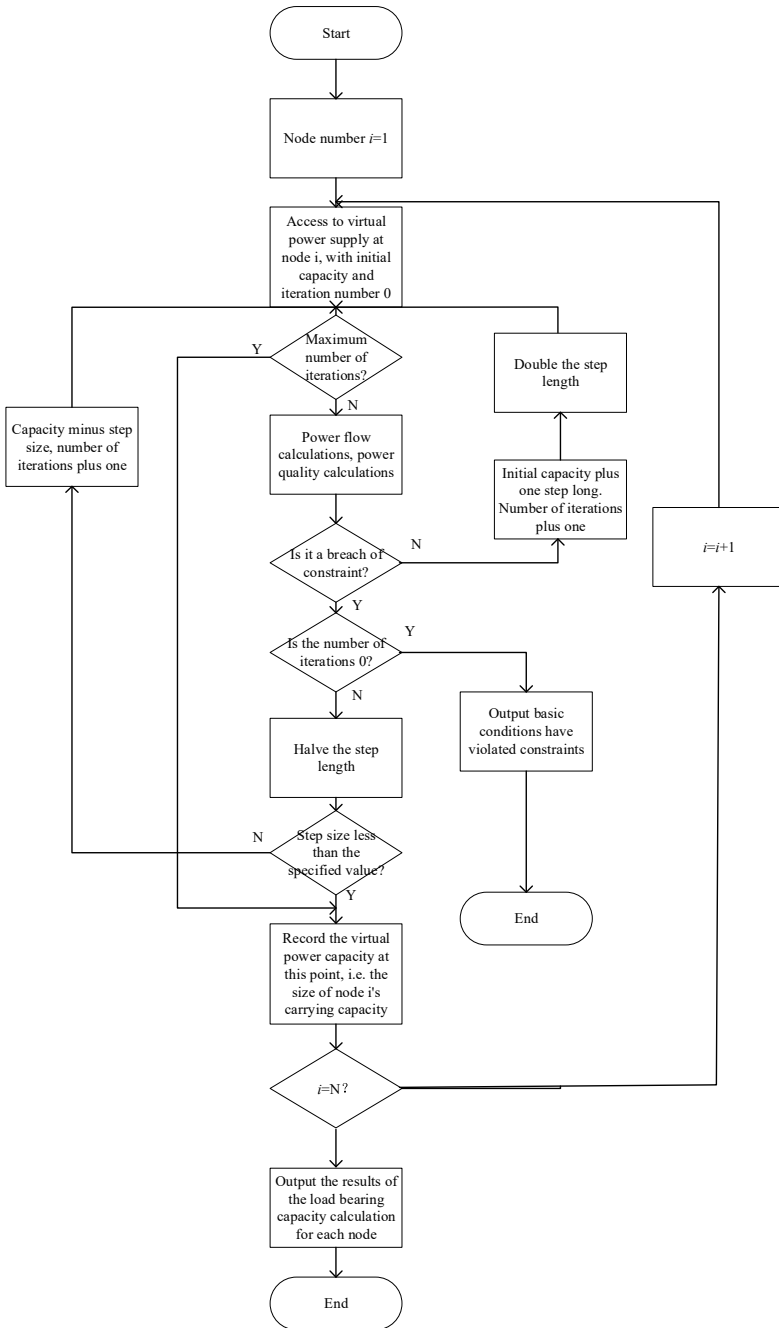


Fig. 10 A typical low-voltage distribution network

**Table 1** Calculation results of distributed photovoltaic capacity of distribution network and its limiting factors

Node	Maximum accessible capacity/MW	Limiting element	Reason for limiting
L1	0.11	Line11	Overload
L2	0.10	L2	Excessive harmonics
L3	0.09	L3	Excessive harmonics
L4	0.07	L4	Excessive harmonics
L5	0.06	L5	Excessive harmonics
N0	0.15	Line1	Overload
N1	0.15	Line1	Overload
N2	0.14	Line3	Overload
N3	0.12	L2	Excessive harmonics
N4	0.10	L2	Excessive harmonics
N5	0.09	L4	Excessive harmonics
N6	0.08	L4	Excessive harmonics
N7	0.07	L4	Excessive harmonics
N8	0.06	L5	Excessive harmonics
N9	0.11	Line12	Overload
N10	0.10	L3	Excessive harmonics
N11	0.09	L3	Excessive harmonics

investigates the calculation of the distributed PV hosting capacity of the distribution network based on DIgSILENT.

The paper investigates the impact of distributed PV power source access on power quality, line thermal stability and system losses. Based on a typical low-voltage distribution network model, the mechanism of the impact of distributed PV power generation on power quality is analysed, and the impact of the capacity and location of distributed PV access on voltage deviation, harmonics, line current and system losses is investigated by simulation. The results show that distributed PV access leads to higher node voltages, higher harmonic content, lower forward current and higher reverse current, and that access at the end of the line has a greater impact. Appropriate access to distributed PV can reduce the system losses.

Based on the study of the impact, this paper extracts the corresponding PV hosting capacity index of the distribution network. Combined with national standards, the constraints for the calculation of distributed PV hosting capacity of the distribution network are constructed. The PV hosting capacity of a typical distribution network is calculated by DIgSILENT, and the PV hosting capacity of each node of the system and the corresponding constraints are obtained, which is of reference significance for distributed power planning in distribution networks.

**Table 2** The calculation results of distributed PV hosting capacity constraint index in distribution network

Node	Maximum loading/%	Maximum voltage/p.u.	Maximum THD/%
L1	79.89	1.01	3.12
L2	59.88	1.02	4.99
L3	60.05	1.03	5.00
L4	47.86	1.03	5.00
L5	42.86	1.03	4.99
N0	79.87	1.01	2.85
N1	79.98	1.02	3.99
N2	79.87	1.02	4.80
N3	68.89	1.02	5.00
N4	54.55	1.02	4.99
N5	59.43	1.02	5.00
N6	51.35	1.03	4.99
N7	45.20	1.03	5.00
N8	43.63	1.03	4.99
N9	79.95	1.02	4.66
N10	71.98	1.03	5.00
N11	61.40	1.03	4.99

**Acknowledgements** The authors thank the Headquarter of State Grid Corporation of China for the financial support for this research. This research was supported by State Grid Corporation of China Project “Research and application of key technologies for distribution network adaptability enhancement under new power system”. Project code: 5400-202255150A-1-1-ZN.

## References

1. National Energy Administration (2023) China’s grid-connected photovoltaic power generation capacity exceeds 300 million kilowatts distributed development has become a new high-light. [http://www.nea.gov.cn/2022-01/20/c\\_1310432517.htm](http://www.nea.gov.cn/2022-01/20/c_1310432517.htm). Last accessed 13 May 2023 (in Chinese)
2. Wu Q, Wang F, Zhou T (2023) The impact and treatment methods of distributed photovoltaic power quality problems. *Electr Eng* 584(02):167–170+174 (in Chinese)
3. Liang Z, Xia J, Sun M (2020) Data driven assessment of distributed photovoltaic hosting capacity in distribution network. *Power Syst Technol* 44(07):2430–2439 (in Chinese)
4. Wu J (2022) Analysis on the influence of distributed photovoltaic grid connection on the line loss of 10 kV urban distribution network. *Electr Eng* 570(12):33–35 (in Chinese)
5. Ren M, Guan S, Tan J (2018) Configuration analysis of multi-node distributed photovoltaic generation considering harmonic constraints under optimal monitoring program. *Power Syst Protect Control* 46(08):73–79 (in Chinese)
6. Alam MJE, Muttaqi KM, Sutanto D (2014) An approach for online assessment of rooftop solar PV impacts on low-voltage distribution networks. *IEEE Trans Sustain Energy* 5(2):663–672

7. Dong Y, Wang S, Yan B (2019) Review on evaluation methods and improvement techniques of DG hosting capacity in distribution network. *Power Syst Technol* 43(7):2258–2266 (in Chinese)
8. Wen Y, Yang Y, Xing P (2023) Review on the new energy accommodation capability evaluation methods considering multi-dimensional factors. *Proc CSEE* 1–25, 24 5 2023 (in Chinese)
9. Li Z, Bao X, Shao Y (2018) Studying accommodation ability of distributed photovoltaic considering various voltage regulation measures. *Power Syst Protect Control* 46(08):10–16 (in Chinese)
10. Yao H, Du X, Li T (2019) Simulation of consumption capacity and voltage control strategy of distribution network with high penetration of photovoltaics. *Power Syst Technol* 43(02):462–469 (in Chinese)
11. Al-Saadi H, Zivanovic R, Al-Sarawi SF (2017) Probabilistic hosting capacity for active distribution networks. *IEEE Trans Industr Inf* 13(5):2519–2532
12. DL/T 2014–2019, Technical guideline for evaluating power grid bearing capacity of distributed resources connected to network (in Chinese)
13. Torquato R, Salles D, Oriente PC et al (2018) A comprehensive assessment of PV hosting capacity on low-voltage distribution systems. *IEEE Trans Power Deliv* 33(2):1002–1012
14. Tan X, Wang Z, LI Q et al (2020) Segmentation algorithm of maximum hosting capacity of distribution network with multiple distributed generators considering multiple constraints. *Autom Electr Power Syst* 44(04):72–80 (in Chinese)
15. Qu G, Wang C, Jin P (2019) Comprehensive evaluation of load hosting capacity of new load and distributed power connected to distribution network. *Electr Measur Instrum* 56(19):37–45+113 (in Chinese)
16. Papathanassiou S, Hatziaargyriou N, Strunz K (2005) A benchmark low voltage microgrid network. In: *Proceedings of the CIGRE symposium: power system with dispersed generation*, Athens, Greece
17. Chao N, Jun Y, Yongming Z (2022) Research on distribution network planning and design with distributed photovoltaic system. *J Electr Eng* 17(04):282–288 (in Chinese)

# Analysis of Induced Current of OPGW in 750 kV Transmission Lines



Yufei Chen, Yong Wei, Xianchun Wang, Jiaju Zhang, Wenzhao Liu, Xianglong Meng, Jinxin Cao, and Jianguo Wang

**Abstract** In recent years, the use of optical fiber composite overhead ground wires (OPGW), which are a combination of optical fibers and overhead ground wires, has become increasingly common due to the growing demand for reliable and secure communication links in power transmission and distribution systems. In high-voltage transmission lines, the all grounding method is commonly used for OPGW. Due to electromagnetic induction, there is an induced electromotive force on the ground wire, creating a loop between the towers and generating induced currents. These induced currents result in power losses. This study establishes a single-circuit model of a 750 kV transmission line using typical towers, with two OPGW cables employed and an all grounding configuration. The distribution of induced currents and ground currents along the line is investigated. Additionally, the effects of three operational parameters, namely, ground resistance, span distance, and conductor transposition,

---

Y. Chen · J. Cao (✉) · J. Wang

School of Electrical Engineering and Automation, Wuhan University, Wuhan, China  
e-mail: [jinxin.cao@connect.polyu.hk](mailto:jinxin.cao@connect.polyu.hk)

Y. Chen

e-mail: [2022282070095@whu.edu.cn](mailto:2022282070095@whu.edu.cn)

J. Wang

e-mail: [wjg@whu.edu.cn](mailto:wjg@whu.edu.cn)

Y. Wei · J. Zhang · W. Liu · X. Meng

State Grid Hebei Information & Telecommunication Company, Shijiazhuang, China  
e-mail: [13398618998@163.com](mailto:13398618998@163.com)

J. Zhang

e-mail: [zjiaz0@126.com](mailto:zjiaz0@126.com)

W. Liu

e-mail: [296899050@qq.com](mailto:296899050@qq.com)

X. Meng

e-mail: [mxl2008meng@163.com](mailto:mxl2008meng@163.com)

X. Wang

State Grid Hengshui Electric Power Supply Company, Shijiazhuang, China  
e-mail: [zhangjianghui1974@126.com](mailto:zhangjianghui1974@126.com)

© Beijing Paiké Culture Commu. Co., Ltd. 2024

X. Dong and L. Cai (eds.), *The Proceedings of 2023 4th International Symposium on Insulation and Discharge Computation for Power Equipment (IDCOMPU2023)*, Lecture Notes in Electrical Engineering 1103, [https://doi.org/10.1007/978-981-99-7413-9\\_60](https://doi.org/10.1007/978-981-99-7413-9_60)

on induced currents are discussed. The results indicate that span and ground resistance have a relatively small impact on ground-induced currents, while ground resistance has a more significant influence on ground currents. On the other hand, conductor transposition has a substantial effect on both induced currents along the ground wire and currents into the earth.

**Keywords** OPGW · Induced current · 750 V transmission lines · All grounding · Single-circuit

## 1 Introduction

Currently, in China, the optical fiber composite overhead ground wires (OPGW) are widely used in high-voltage and ultra-high-voltage transmission lines [1, 2]. In comparison to conventional ground wires, OPGW not only provides lightning protection but also serves as a secure and reliable communication line for the power system. Additionally, it enables real-time monitoring and control of the electrical grid [3, 4].

In high-voltage transmission lines in China, the mainstream grounding method for OPGW is the all grounding [5], which means that the ground wire is grounded at each tower. In this approach, when the line encounters a ground short-circuit or lightning strike, the overcurrent generated on the ground wire can quickly be diverted to both sides of the fault point, benefiting the protection of OPGW and the safety of the internal optical fibers. However, in the case of tower-by-tower grounding, the three-phase alternating current flowing in the phase conductors induces electromotive force on the ground wire, creating a current loop and resulting in losses.

Currently, research on OPGW in 750 kV transmission lines is focused on studying the variations of induced currents and induced voltages under different grounding methods [6, 7]. However, there is limited research on the impact of operating parameters such as grounding resistance and conductor transposition on induced currents and losses. This paper specifically investigates the variations of induced currents and currents into the earth in a typical single-circuit 750 kV tower under different grounding resistances, different spans, and conductor transpositions.

## 2 Data and Calculation Model

### 2.1 Mechanism of Ground Wire Induced Current Formation

When alternating current flows through high-voltage transmission lines, an alternating magnetic field is generated in space. The induced electromotive force (EMF) per kilometer of the ground wire can be calculated using Eqs. (1) and (2) [8]

$$E_1 = j0.145 \sum_{i=1}^n I_{iA} \left( \alpha^2 \lg \frac{d_{1ia}}{d_{1ib}} + \alpha \lg \frac{d_{1ia}}{d_{1ic}} \right) \quad (1)$$

$$E_2 = j0.145 \sum_{i=1}^n I_{iA} \left( \alpha^2 \lg \frac{d_{2ia}}{d_{2ib}} + \alpha \lg \frac{d_{2ia}}{d_{2ic}} \right) \quad (2)$$

where  $I_{iA}$  is the A-phase's conductor current of the  $i$ -line,  $n$  is the number of circuits,  $d_{1ia}, d_{1ib}, d_{1ic}, d_{2ia}, d_{2ib}, d_{2ic}$  are the distances between the ground wire and the  $i$ -line's three-phase conductor,  $\alpha = \angle 120^\circ$ ,  $E_1, E_2$  are the electromagnetic induction electromotive force per kilometer of ground wire.

The existing formula can only calculate the induced electromotive force generated on each section of the ground wire, but it still cannot directly calculate the induced current and current into the earth under the condition of all grounding.

## 2.2 Tower Model and Parameters

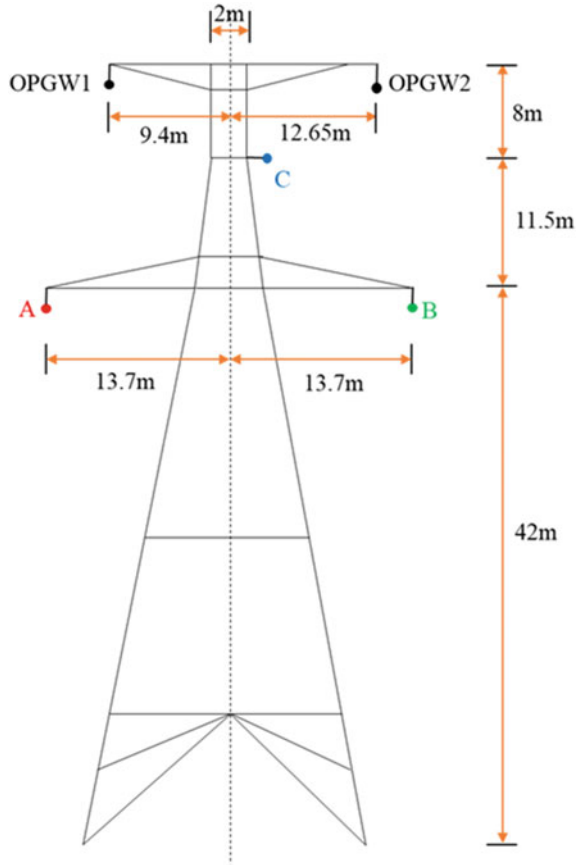
According to the 2010 edition of the "State Grid Corporation of China Transmission and Transformation Project Typical Design 750 kV Transmission Line Volume" [9], there are a total of 4 modules and 12 sub-modules in the typical design of the 750 kV transmission line. Among them, there are 8 sub-modules for single-circuit design and 4 sub-modules for double-circuit design. The 7A and 7B series are for single-circuit lines, while the 7C and 7D series are for double-circuit lines. The 7A and 7C modules are suitable for altitudes below 1000 m, while the 7B and 7D modules are suitable for altitudes above 1000 m and below 4000 m. The selected typical tower for this study is 7B1-JC1, as shown in Fig. 1 and Table 1. The conductors and ground wires used are listed in Table 2, with OPGW used for both ground wires on each side. The conductor's split spacing is set to 400 mm.

## 2.3 Line Model and Parameters

Based on the data provided in the previous section, the transmission line model is established in ATP-EMTP. The towers are modeled using the LCC model. The entire line consists of 40 towers, with a substation at each end. The substation grounding resistance is set to  $0.5 \Omega$ , and the tower grounding resistance is set to  $5 \Omega$ . The line load is chosen to be 2300 MVA at full load [10]. To simulate the transmission current, a current source of 1770 A is used. The load is set to  $244 \Omega$ .



**Fig. 1** Typical 750 kV transmission tower



**Table 1** 750 kV typical tower

Type	Feature	Wire	Span (m)	Height (m)
7B1-JC1	Single-circuit	6 × LGJ-500/45	450	48

**Table 2** Conductors and ground wires

Type	Calculation inside diameter (mm)	Calculation outside diameter (mm)	20 °C direct current resistance (Ω/km)
LGJ-500/45	2.8	30	0.05912
OPGW-2S1/2SB1	\	16	0.306

### 2.4 Operating Parameters of the Line

The operational parameters discussed in this paper include:

- (1) Grounding resistance, which is referred to the equivalent resistance between the ground wire and the tower grounding under power frequency, which is influenced by factors such as soil resistivity.
- (2) Span, which means the distance between adjacent towers. In typical designs, recommended span values are provided, but in practice, span design may be adjusted based on actual conditions.
- (3) Conductor transposition. The common ways of transposition can be divided into complete transposition and incomplete transposition: complete transposition means transposing the conductors at two thirds of the span, which in this line model is at towers 13 and 27; incomplete transposition means transposing the conductors only at the midpoint, which in this model is at tower 20. Ground wire transposition refers to exchanging the positions of two ground wires (Fig. 2).

## 3 The Induced Current Along the Line

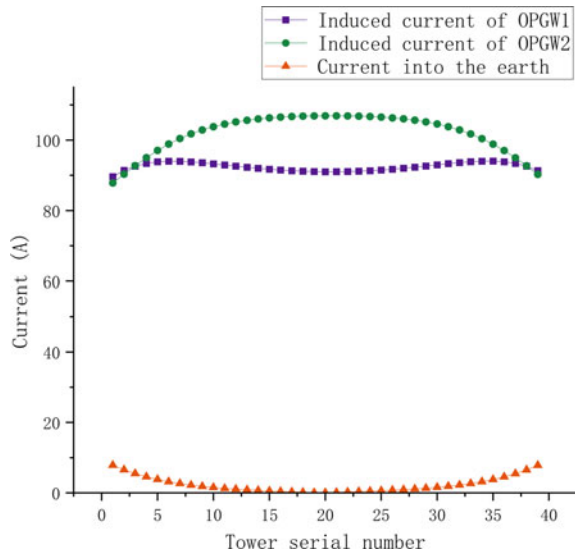
In this section, a recommended spacing of 450 m is used for all spans, and a grounding resistance of  $5 \Omega$  is assumed. Wire transposition is not considered. Figure 3 illustrates the magnitudes of the induced current and the grounding current along the single-circuit line.

As shown in Fig. 3, due to the asymmetry of the three-phase conductors, the induced current along the ground lines on the left and right sides differs. The induced current along OPGW2 increases from both ends towards the center, reaching a maximum value of approximately 106 A. In the middle section, the induced current remains relatively constant, at around 106 A. Similarly, the induced current along OPGW1 also increases from both ends towards the center, with a slight decrease in the middle section. The maximum value is around 94 A, while the middle section stabilizes at approximately 91 A. The grounding current at the tower exhibits the highest value at both ends, reaching about 8 A, gradually decreasing from the ends towards the center, and approaching zero at several towers near the midpoint.



**Fig. 2** Schematic diagram of conductor transposition **a** incomplete transposition, **b** complete transposition

**Fig. 3** Distribution of induced voltage on ground wire of 35 kV typical tower



## 4 The Influence of Operating Parameters on Induced Current

This chapter discusses the influence of three operational parameters on the induced current and grounding current: span length, grounding resistance, and conductor transposition.

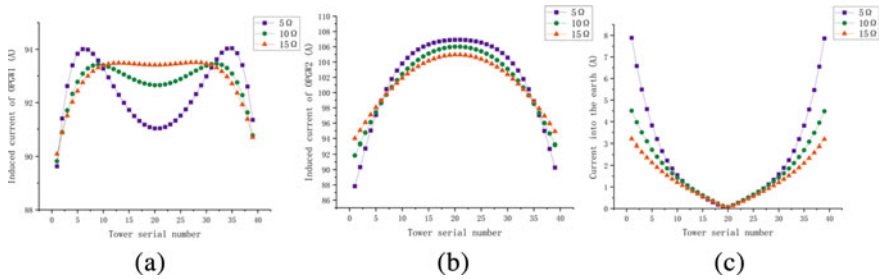
### 4.1 The Influence of Grounding Resistance on Induced Current

When the environment varies, the soil resistivity changes, resulting in variations in grounding resistance. This section discusses the changes in induced current and grounding current for grounding resistances of 5  $\Omega$ , 10  $\Omega$ , and 15  $\Omega$ , respectively.

Figure 4 illustrates the distribution of induced current along the ground wire and current into the earth for grounding resistances of 5  $\Omega$ , 10  $\Omega$ , and 15  $\Omega$ , respectively.

According to Fig. 4, the induced current along the OPGW increases with an increase in grounding resistance for the first 8 and last 8 tower locations at both ends of the line. However, at approximately the 24th tower location in the middle of the line, the induced current along the OPGW decreases with an increase in grounding resistance.

As the grounding resistance of the towers increases, the grounding current at the tower locations generally decreases. In comparison, the variation is more significant at the ends of the line and smaller in the middle of the line.



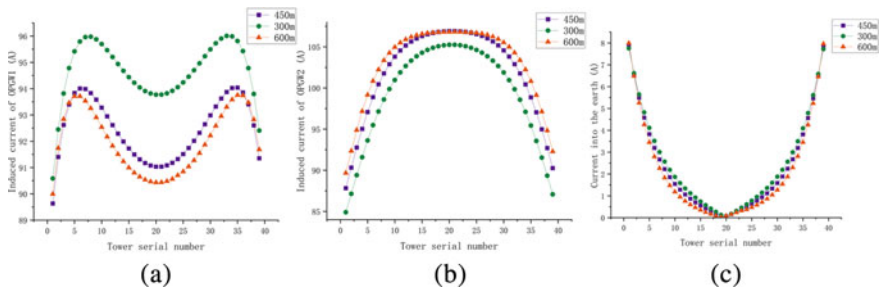
**Fig. 4** The influence of grounding resistance **a** induced current of OPGW1, **b** induced current of OPGW2, **c** current into the earth

### 4.2 The Influence of Span on Induced Current

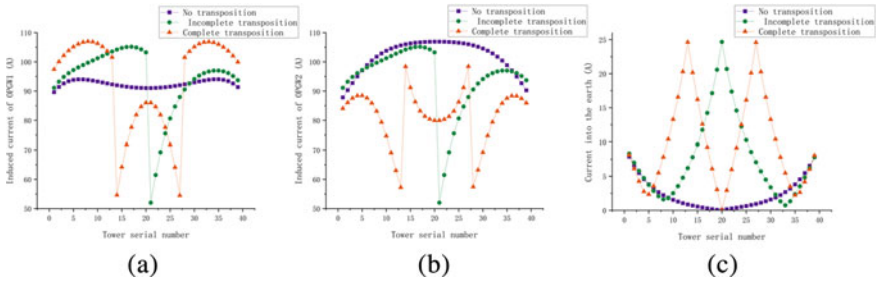
This section analyzed the distribution of induced currents along the ground wire and current into the earth for three common spans of 300 m, 450 m, and 600 m in 750 kV towers.

Figure 5 shows the distribution of induced currents along the ground wire and current into the earth for spans of 300 m, 450 m, and 600 m.

According to Fig. 5, as the span increases, the magnitude of induced currents along the ground wire slightly decreases in the middle tower section and slightly increases in the side tower sections. In the case of OPGW1, the induced current in the middle section decreases more compared to OPGW2, while the increase in the side sections is less significant. The current into the earth also show a decrease in the middle tower section and remain relatively constant in the side tower sections.



**Fig. 5** The influence of span **a** induced current of OPGW1, **b** induced current of OPGW2, **c** current into the earth



**Fig. 6** The influence of conductor transposition **a** induced current of OPGW1, **b** induced current of OPGW2, **c** current into the earth

### 4.3 The Influence of Conductor Transposition on Induced Current

This section analyzed the impact of incomplete and complete conductor transposition on induced currents.

Figure 6 shows the distribution of induced currents and currents into the earth along the line under three conditions: no transposition, incomplete transposition, and complete transposition.

According to Fig. 6, after the transposition of the conductors, significant changes can be observed in the induced currents and earth currents along the line. Overall, the induced current on OPGW1 reaches a minimum at the transposition point and shows a significant decrease around the transposition point, while it increases in other sections. On the other hand, the induced current on OPGW2 exhibits a general decreasing trend, reaching a minimum at the transposition point. The currents into the earth show a noticeable increase, reaching a maximum at the transposition point.

## 5 Conclusion

This study established a model of a 750 kV single-circuit transmission line with two OPGW installed on typical towers. The analysis focused on the distribution of induced currents along the line under the condition of all grounding, as well as the impact of grounding resistance, span length, and conductor transposition on induced currents.

The simulation results indicate that under the condition of complete grounding, these three operating parameters have an impact on induced currents. Among them, the span length and grounding resistance have a relatively small effect on induced currents in the ground wire, while grounding resistance has a more significant impact

on currents into the earth. On the other hand, conductor transposition has a considerable impact on both induced currents along the ground wire and currents into the earth.

**Acknowledgements** This work was supported by the Science and Technology Project of State Grid Limited Headquarters (Project 5108-202218280A-2-418-XG).

## References

1. Snider WC, Moore RC, Erdman AJ, Doucet D, Charlton D (2021) Lightning-induced state of polarization change in OPGW using a transmission line model. In: Optical fiber communication conference. Optica Publishing Group, pp M3C-8
2. Santos JA, Moore RC, Snider WC, Doucet D, Charlton D (2022) Lightning-related ELF transients as a potential source of rapid state of polarization changes in shielded OPGW. In: 2022 Optical fiber communications conference and exhibition (OFC). IEEE, pp 01–03
3. Ding ZW, Zhang XP, Zou NM, Xiong F, Song JY, Fang X, Zhang YX et al (2021) Phi-OTDR based on-line monitoring of overhead power transmission line. *J Lightwave Technol* 39(15):5163–5169
4. Zhang L, Zheng H, Gao J, Li Y, Li Y, Kong X (2022) Fault diagnosis method for relay protection channel based on semantic web. In: International conference on electronic information engineering and computer communication (EIECC 2021), vol 12172. SPIE, pp 416–420
5. Wang J, Wang Y, Peng X, Li X, Xu X, Mao X (2014) Induced voltage of overhead ground wires in 500-kV single-circuit transmission lines. *IEEE Trans Power Deliv* 29(3):1054–1062
6. Liu K, Wu T, Shi R, Xiao B, Liu T (2011) Loss analysis of 750 kV transmission line optical ground wire. *High Voltage Eng* 37(2):497–504 (in Chinese)
7. Li Y, Meng L, Wang D, Liu Q (2015) Analysis and research on grounding methods of overhead ground wires in 750 kV double-circuit transmission lines. *Electr Eng* 16(05):82–84 (in Chinese)
8. Diansheng Z (1999) Design handbook for high voltage power supply circuit of electric power engineering. China Electr Power Press 156–161 (in Chinese)
9. Liu Z (2012) Typical design of state grid corporation's transmission and transformation projects: 750 kV transmission lines. China Electr Power Press (in Chinese)
10. Qin W, Xiao Y, Wang J (2007) Overview of relay protection principles in 750 kV transmission lines. *Shanxi Electr Power* 1:9–11 (in Chinese)

# Analysis of Electromagnetic Field Distribution of Aircraft Lightning Strike



Qin Feng, Duan Denglei, Chen Jiaer, Wang Tong, Zhou Mi, Cai Li, Wang Jianguo, and Fan Yadong

**Abstract** The common lightning strikes in nature can threaten the flight safety of aircraft directly. In order to investigate the lightning environment of aircrafts and improve the lightning protection ability, a three-dimensional, full-size electromagnetic calculation model is established here. According to the static charge distribution, the lightning attachment points are determined, and several lightning paths are designed. Calculation results of the electromagnetic field on the aircraft surface under different paths show that the electric field distribution is uniform, but the magnetic field distribution is significantly different. Inside the aircraft, however, the variation characteristics of the electromagnetic field is related to the lightning path. The electromagnetic field tends to show the highest value in the area close to the lightning current flow. This study can determine the intensity of lightning current in each area, and help to find the weak point, which has important reference significance for the lightning protection design of the aircraft.

**Keywords** Aircraft · Lightning path · Simulation model · Electromagnetic environment

---

Q. Feng

Northwest Institute of Nuclear Technology, Xi'an 710024, Shaanxi, China

D. Denglei · C. Jiaer · W. Tong · Z. Mi (✉) · C. Li · W. Jianguo · F. Yadong

School of Electrical Engineering and Automation, Wuhan University, Wuhan 430072, Hubei, China

e-mail: [zhoumi927@whu.edu.cn](mailto:zhoumi927@whu.edu.cn)

D. Denglei · C. Jiaer · Z. Mi · C. Li · W. Jianguo · F. Yadong

Engineering Research Center of Ministry of Education for Lightning Protection and Grounding Technology, Wuhan 430072, China

© Beijing Paiké Culture Commu. Co., Ltd. 2024

X. Dong and L. Cai (eds.), *The Proceedings of 2023 4th International Symposium on Insulation and Discharge Computation for Power Equipment (IDCOMPU2023)*, Lecture Notes in Electrical Engineering 1103, [https://doi.org/10.1007/978-981-99-7413-9\\_61](https://doi.org/10.1007/978-981-99-7413-9_61)

# 1 Introduction

Lightning is a natural phenomenon occurring in the atmosphere, featured with a long distance, a high-intensity current and a strong electromagnetic radiation. Unfortunately, it has a serious threat to aircraft, power systems, electronics, and communications systems, etc. As an aircraft can become a path of the electric storm discharge either through a triggering mechanism process or through interception, the direct and indirect effects associated with lightning pose severe threats to the flight safety. These threats are heightened further with the upgrading of airframe manufacturing technology, as well as the updating of the on-board numerical control, communication and command systems [1]. Therefore, in order to minimize the loss caused by lightning, it is necessary to study the lightning environment of aircraft.

Regarding lightning protection measures for aircraft, the determination of lightning adhesion area is a basic step. In general, it can be determined by the scaled model test, the full-scale test or the electric field simulation. According to the distribution of lightning attachment points, the lightning strike area can be divided [2]. For the study of the lightning attachment area on the surface of Airbus A320-200, Song et al. [3], who, from a method of numerical simulation, obtained the results basically consistent with SAE ARP5414, proved the feasibility of their simulation method. Wen et al. [4], from a lightning attachment test on a scaled aircraft model, showed that lightning attachment points were mainly distributed in the wing, the tip of the horizontal tail, the tip of the vertical tail, and the front cone and other parts.

The combination of different lightning “entry” points and “exit” points can form a variety of lightning paths, under which the electromagnetic field distribution characteristics of the fuselage are different. Nevertheless, until recently, it is difficult to measure the current distribution and electromagnetic field characteristics directly and accurately. Compared with the experimental approach, the aircraft lightning strike calculation is flexible, efficient and of low cost. For instance, Apra et al. [5], according to the lightning zoning standard, designed six lightning paths for C-27J aircraft model, and simulated indirect effects under different lightning paths. Zhang et al. [6] analyzed the transient current burst induced in cable harness of aircraft through two lightning paths. The above work shows that, under different lightning conditions, the electromagnetic characteristics of aircraft vary significantly. In order to improve the lightning protection ability of aircraft, it is necessary to investigate the impact of lightning on the electromagnetic environment inside and outside the aircraft.

In this work, P100EV commercial airliner with a high market share is selected as the research object. A three-dimensional electromagnetic simulation model is adopted here. Firstly, the static charge distribution of the aircraft fuselage is analyzed to determine the lightning paths. Then the electromagnetic field distribution characteristics of the aircraft surface under different lightning paths are calculated and compared. The variation of electromagnetic field intensity in some typical positions inside aircraft is also analyzed. Our results here can provide data reference for the aircraft lightning coupling effect, which is of great significance for the subsequent lightning protection design.



## 2 Determination of Different Lightning Paths of Aircraft

Figure 1 is a schematic diagram of P100EV commercial aircraft, whose full-size calculation model is built in 3D modeling software. The fuselage is 12.82 m in length, the wingspan of the wing is 12.30 m, and the wingspan of the tail is 5.34 m. For the modeling, the wingspan direction is taken as the X axis direction, the height direction as the Y axis direction, and the fuselage longitudinal direction as the Z axis direction, as given in Fig. 1a. A full demonstration of the model is shown in Fig. 1b for a better view.

The model is then imported into the electromagnetic simulation software. A charge of 1 C is designed to the fuselage, and the infinity of space is set as the zero point of potential. The electrostatic field solver is used to calculate the electric field distribution, whose results are shown in Fig. 2. The electric field intensity of nose, the tip of wing and the tip of tail is  $3.5 \times 10^9$  V/m,  $6.3 \times 10^9$  V/m and  $7.5 \times 10^9$  V/m, respectively. For other parts, the electric field intensity is significantly smaller, indicating that there is a relatively concentrated charge distribution, resulting, probably, in more attached lightning leaders.

Combined with the recommendation of SAE ARP 5416 [7], as is shown in Table 1, the nose, the wing and the tail are selected as possible lightning attachment points. Accordingly, we set four typical lightning paths as shown in Fig. 3. They are “nose in–tail out”, “nose in–wing out”, “wing in–wing out” and “wing in–tail out”. When the lightning current passes through these paths, the electromagnetic field distribution is calculated.

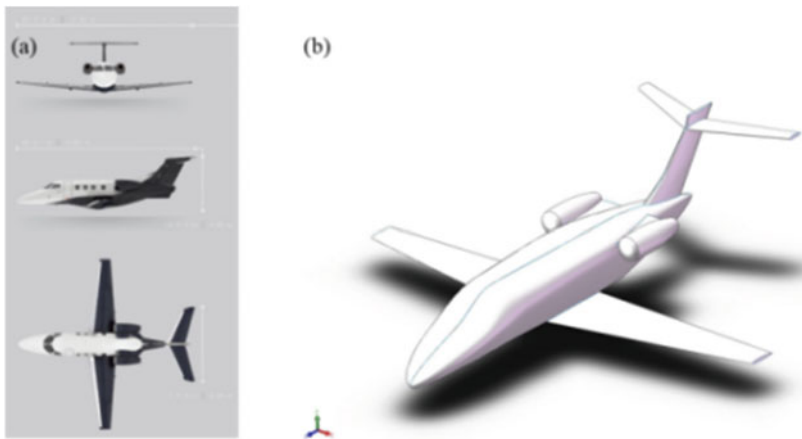
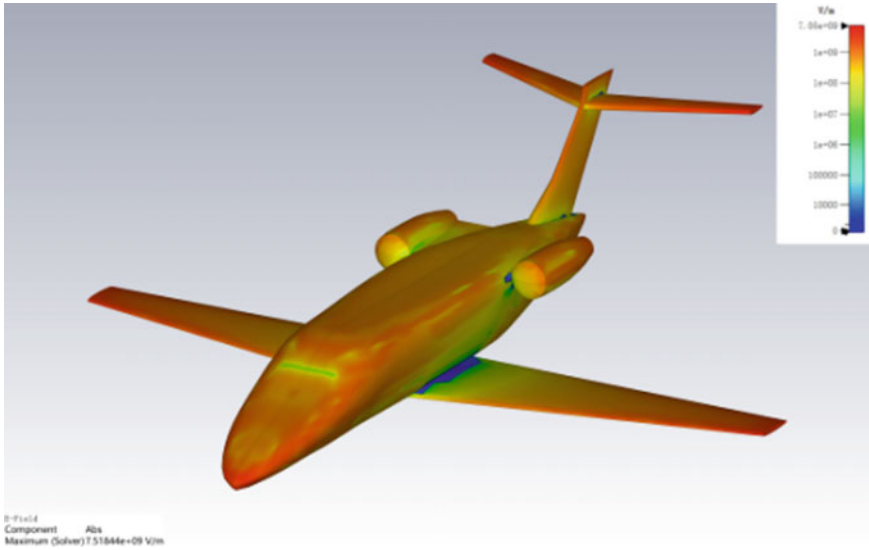


Fig. 1 Schematic diagram of P100EV and the overall picture of the model



**Fig. 2** Calculation results of fuselage electric field intensity distribution

**Table 1** Typical lightning attachment points recommended in SAE ARP5416A

Connection point of impulse current generator	Reflux conductor connection point
Nose	Tail
Wind shield	Tail
Nose	Wing tip
Nose	Engine
Nose	Landing gear
Nose	Vertical tail
Wing tip	Tail wing
Wing tip	Wing tip
Engine inlet	Engine exhaust
Engine inlet	Tail wing

### 3 Electromagnetic Field Distribution of Aircraft

In the evaluation of airborne electronic equipment and cables, SAE ARP 5412B [8] recommends the lightning current component A, with a risetime of 6.4  $\mu$ s, a tail time of 69  $\mu$ s, and a current amplitude of 200 kA. In the electromagnetic simulation software, the excitation is set as a double exponential function, whose waveform is seen in Fig. 4.

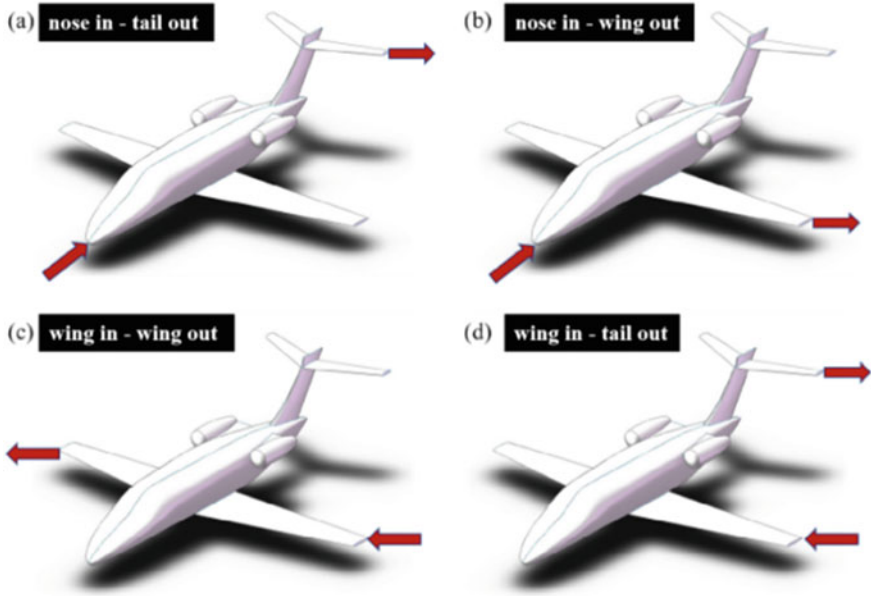


Fig. 3 Schematic diagram of four typical lightning paths

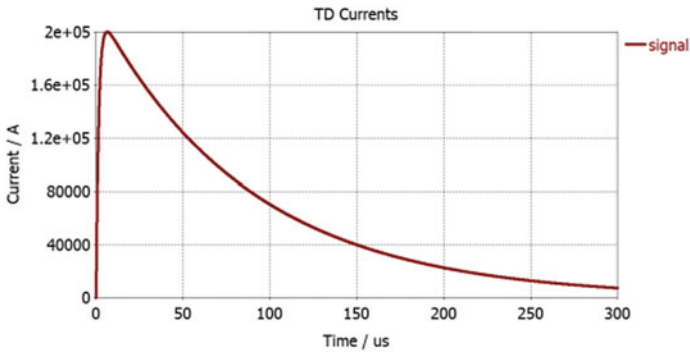


Fig. 4 Waveform of lightning current component A used in the simulation calculation

### 3.1 Electromagnetic Field Distribution on Aircraft Surface Under Different Lightning Paths

The electromagnetic field distribution on the aircraft surface is obtained for four different lightning paths shown in Fig. 4. Since the rise time and tail time of the excitation current are  $6.4 \mu\text{s}$  and  $69 \mu\text{s}$ , respectively, we focus on the calculation results of these two instants.

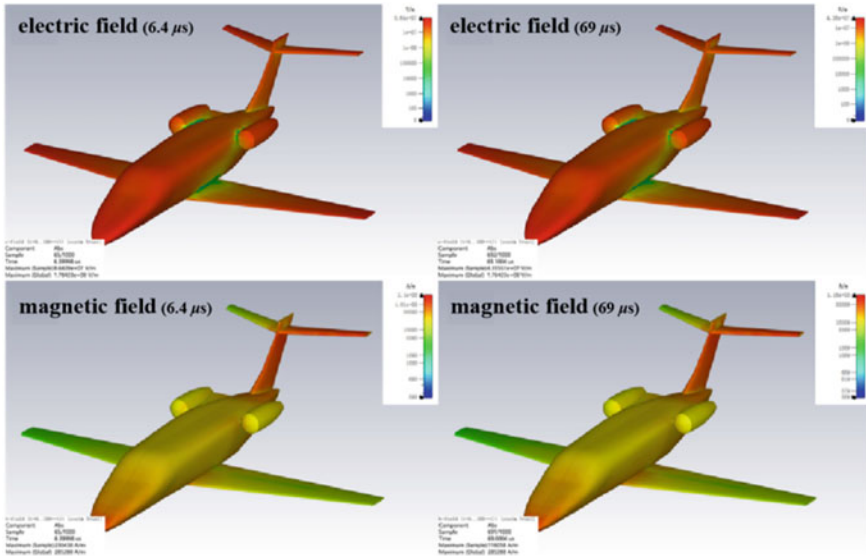


Fig. 5 Electromagnetic field distribution on aircraft surface for “nose in–left tail out”

### 3.1.1 Nose In–Left Tail Out

For the lightning strikes from the nose to the left tail, the calculation result is given in Fig. 5, showing that the fuselage electric field distribution is relatively uniform, and that there is no obvious structural differences. Moreover, the maximum electric field intensity at  $6.4 \mu\text{s}$  is  $8.6 \times 10^7 \text{ V/m}$ , and that at  $69 \mu\text{s}$  is  $4.4 \times 10^7 \text{ V/m}$ . As the two end points of the lightning path, the magnetic field intensity reaches maximum at the nose and the left tail.

### 3.1.2 Nose In–Left Wing Out

Figure 6 shows the distribution of the electromagnetic field when lightning strikes from the nose to the left wing. For this case, the electric field distribution is still relatively uniform, with no obvious structural differences. The magnetic field intensity becomes the highest at the nose and the left wing. Because other locations are not in the main path of lightning current, the magnetic field intensity of those is significantly weakened.

### 3.1.3 Right Wing In–Left Wing Out

Under the path of “Right wing in–Left wing out”, the calculation result is shown in Fig. 7. The magnetic field intensity of the left wing and the right wing is the highest,

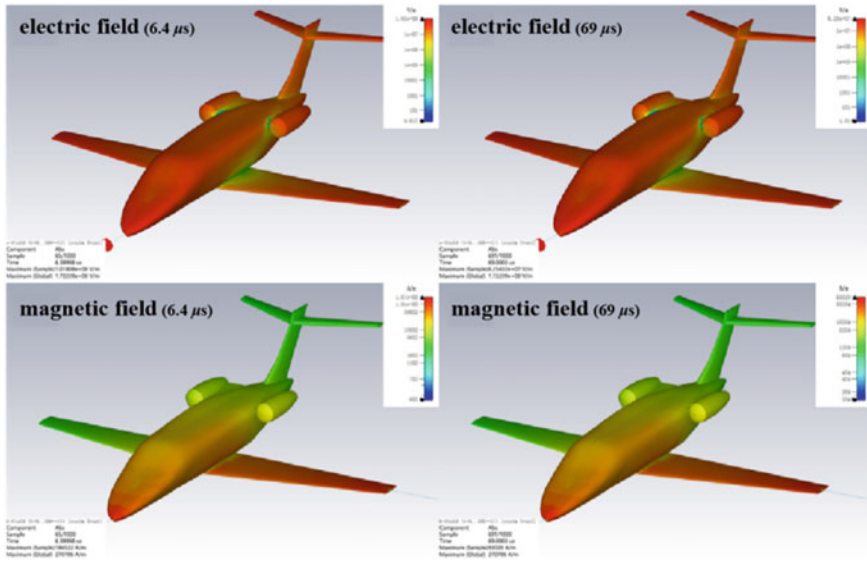


Fig. 6 Electromagnetic field distribution on aircraft surface for “nose in–left wing out”

being 158 kA/m at 6.4 μs and 80 kA/m at 69 μs, respectively. It is worth noting that, as a whole, the magnetic field intensity has an increasing trend, being most obvious at the tail. The distribution of the electric field remains uniform, but its maximum value exceeds those for other cases.

### 3.1.4 Left Wing In–Left Tail Out

Obviously, the fuselage electric field distribution characteristics are similar to the condition of other three lightning paths, but the magnetic field is the highest at the left wing and the left tail, followed by the fuselage near tail, as shown in Fig. 8. On the aircraft surface, the electric field distribution is almost unaffected by the lightning path, always uniformly distributed without obvious structural differences. However, the magnetic field distribution is significantly affected by the lightning path, and the intensity often gets a high value near the path, reaching maximum at the lightning “entry” points and “exit” points.

## 3.2 Electromagnetic Field Intensity in Aircraft Interior Space

Section 2.1 focuses on the electromagnetic field distribution on the surface of the aircraft, but the variation inside the aircraft is still not clear enough. Therefore, keeping the simulation conditions unchanged, by taking the lightning path “nose

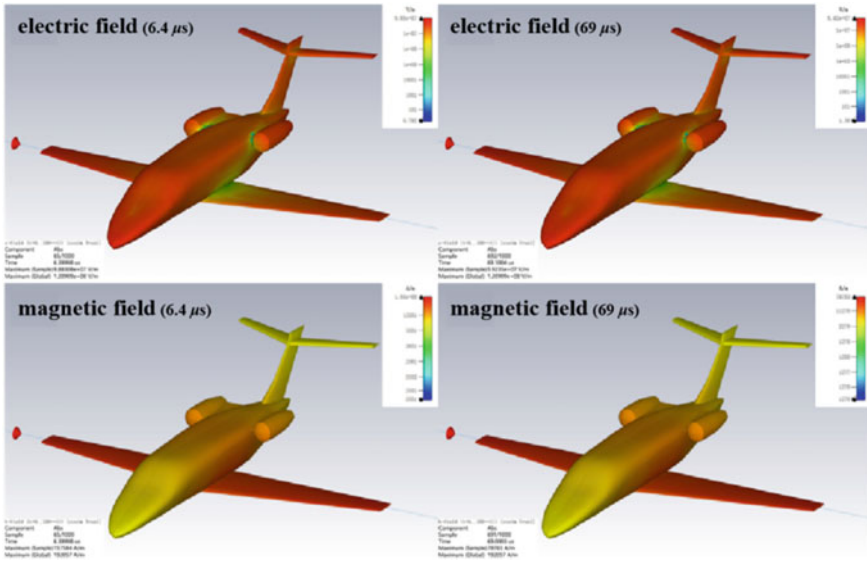


Fig. 7 Electromagnetic field distribution on aircraft surface for “right wing in-left wing out”

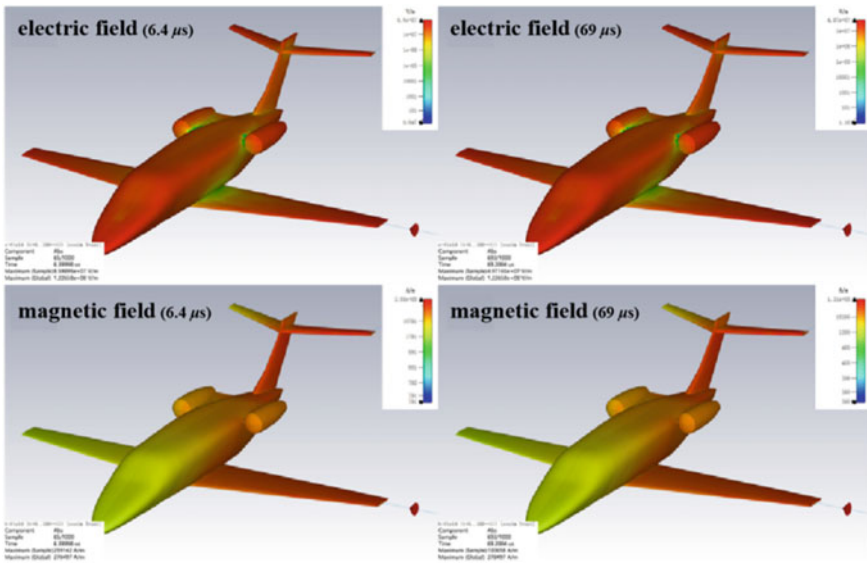


Fig. 8 Electromagnetic field distribution on aircraft surface for “left wing in-left tail out”

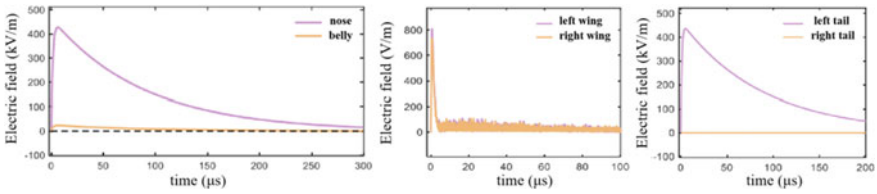


Fig. 9 Variation of electric field intensity inside the aircraft

in–left tail out” as the research object, an analysis will be given to the variation of electromagnetic field in the typical positions inside the aircraft.

### 3.2.1 Variation of Electric Field Intensity

Figure 9 shows the variation of electric field intensity at each typical position with time. Compared with Sect. 3.1.1, the electric field distribution inside the aircraft shows obvious differences and no longer maintains a uniform feature. The electric field intensity at the belly is weakened significantly, whose value is only 1/10 of that at the nose. At the left wing and the right wing, the intensity is several orders of magnitude lower. In particular, the electric field intensity at the right tail is close to zero. This can be interpreted as the fact that, although the right tail is close to the left tail, it is not in the lightning path and most of the lightning current flows out from the left tail.

### 3.2.2 Variation of Magnetic Field Intensity

The distribution of the magnetic field at each location, also related to the lightning path, is shown in Fig. 10. As the two positions with the highest electric field intensity, the magnetic field intensity becomes the highest at the nose and the left tail as well. For the left wing and the right wing, the magnetic field intensity is not large, but the variation trend is very similar. Compared with the left tail, although the magnetic field intensity curve of the right tail is very low, a small peak can be observed throughout the variation.

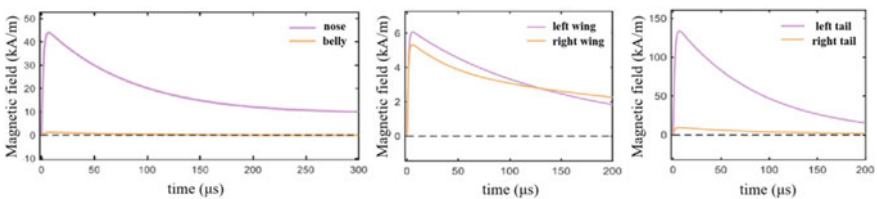


Fig. 10 Variation of magnetic field intensity inside the aircraft

## 4 Conclusion

In this paper, the main lightning attachment points of aircraft are analyzed, and the electromagnetic field distribution of aircraft under different lightning paths is calculated through a full size three-dimensional electromagnetic simulation model of aircraft. The main conclusions are as follows:

- (1) Lightning “entry” points and “exit” points are mostly concentrated at the nose area, the wing area and the tail area. These points can be combined into a variety of lightning paths.
- (2) On the surface of the aircraft, the lightning path has no significant effects on the electric field distribution. Under different lightning paths, the electric field distribution is relatively uniform, with no obvious structural differences.
- (3) The distribution of magnetic field has a strong relationship with the lightning path. Its intensity often gets a high value near the path and reaches maximum at the “entry” points and “exit” points.
- (4) For the interior of the aircraft, the distribution of electromagnetic field is uneven. At the position close to the lightning path, the transient electromagnetic field intensity tends to reach its maximum, while the intensity of other positions decreases by orders of magnitude, even close to zero.

## References

1. Hoole P, Hoole S (2022) Introduction to lightning and lightning protection. In: *Lightning engineering: physics, computer-based test-bed, protection of ground and airborne systems*. Springer, Cham
2. SAE ARP5414A (2005) Aircraft lightning zoning. Society of Automotive Engineers, Warrendale
3. Song S, Gao C, Guo Y et al (2011) Study of numerical simulation of aircraft lightning zoning based on CST software. In: *2011 second international conference on mechanic automation and control engineering*, Hohhot
4. Wen H, Hou X, Wang H (2006) Experimental study on aircraft model lightning attachment point. *High Voltage Technol* 32(7):90–92
5. Apra M, D’Amore M, Gigliotti K et al (2008) Lightning indirect effects certification of a transport aircraft by numerical simulation. *IEEE Trans Electromagn Compat* 50(3):513–523 (in Chinese)
6. Zhang M, Huang Z (2010) Transient current burst analysis induced in cable harness due to direct lightning strike on aircraft. *Asia Pac Int Symp Electromagne Compat* 1197–1200
7. SAE ARP5416A (2013) Aircraft lightning test methods
8. SAE ARP5412B (2013) Aircraft lightning environment and related test waveforms



# Study of the Effect of Oblique Photography Route Overlap Rate on 3D Reconstruction



Cong Hu, Fuhua Xie, Xian Zhou, Li Cai, Xin Yang, Jianguo Wang, and Yadong Fan

**Abstract** The side overlap rate and heading overlap rate of the oblique photographic route are an important factor affecting the 3D reconstruction. The heading overlap rate and the side overlap rate determine the number of images and thus affect the model accuracy and modeling time. In this paper, in order to investigate the influence of oblique photographic route overlap rate on 3D reconstruction, oblique photographic images of substations with different combinations of overlap rates were acquired by using DJI Mavic 2 Enterprise for oblique photography at 40 m height, and then 3D reconstruction was performed to obtain 3D models of substations. The final experimental results proved that as the overlap rate increased, the number of acquired images increased, and the 3D model obtained by the three reconstructions had higher accuracy, but the data acquisition time and modeling time also increased greatly. Considering the model accuracy and modeling work efficiency, it is more appropriate to use about 80% of the heading overlap rate and the side overlap rate for the 3D reconstruction of general substations.

**Keywords** Oblique photography · 3D reconstruction · Route overlap rate

## 1 Introduction

Oblique photography is one of the common methods used for 3D reconstruction, with low cost and simple operation [1]. It has contributed to map mapping [2], urban construction [3], and power patrol [4]. The main factors affecting the 3D

---

C. Hu · X. Yang

Foshan Power Supply Bureau, Guangdong Power Grid Co., Ltd., Foshan, China

F. Xie · X. Zhou · L. Cai (✉) · J. Wang · Y. Fan

Engineering Research Center of Ministry of Education for Lightning Protection and Grounding Technology, School of Electrical Engineering and Automation, Wuhan University, Wuhan, China  
e-mail: [2580968099@qq.com](mailto:2580968099@qq.com)

School of Electrical Engineering and Automation, Wuhan University, Wuhan, China

© Beijing Paiké Culture Commu. Co., Ltd. 2024

X. Dong and L. Cai (eds.), *The Proceedings of 2023 4th International Symposium on Insulation and Discharge Computation for Power Equipment (IDCOMPU2023)*, Lecture Notes in Electrical Engineering 1103, [https://doi.org/10.1007/978-981-99-7413-9\\_62](https://doi.org/10.1007/978-981-99-7413-9_62)

651

reconstruction by tilt photography are the number of images and the accuracy of the images. The number of images is mainly related to the route flight height, heading overlap rate and side overlap rate. And the image accuracy is mainly related to the flight height of the route and the UAV lens.

Wu et al. [5] proposed a method to process oblique images using a combination of automatically matching features and combined beams, and finally applied it to 3D modeling; Tang et al. [6] used oblique photography to model rocks in complex areas in 3D, which alleviated the difficulties of measuring rocks by traditional methods; Zhang [7] used oblique photogrammetry to achieve 3D reconstruction technology research for airports, and found out a suitable method for large-scale 3D modeling of airports. Li et al. [8] used circular photography-assisted technology to solve the problem of detail loss in 3D models, and effectively compensate for the loss caused by occlusion, deformation or airflow during UAV flight.

In recent years, oblique photographic 3D modeling has also started to be applied in power inspection. Rao et al. [9] compared oblique and vertical photographic methods and concluded that oblique photography is more suitable for 3D reconstruction of transmission lines. Zheng et al. [10] used oblique photography to effectively calculate and measure the oblique angle of power poles to improve the inspection efficiency of transmission and distribution lines.

## **2 Data Acquisition and Parameter Setting**

### **2.1 Study Area**

The experimental study area was practically modeled at the 220 kV substation of Wuhan University, which includes several types of high-voltage electrical equipment such as oil-immersed transformers, current transformers, voltage transformers, Y-type circuit breakers, and disconnect switches on the substation premises. The panoramic view of the study area is shown in Fig. 1.

### **2.2 UAV Selection**

The UAV selected for the substation oblique photography in this paper is the DJI Mavic 2 Enterprise, which has a high-definition, smooth thermal imaging sensor and a higher pixel visible light sensor. It is equipped with RTK (Real-time kinematic) module for centimeter-level positioning, portable, reliable, and efficient insight into the details of the work site. The UAV parameters are shown in Table 1.



**Fig. 1** The panoramic view of the study area

**Table 1** The parameters of UAV

Parameter	Value
Wheelbase	354 mm
weight	909 g
Maximum flight time	31 min
Maximum flight altitude	6000 m
Maximum flight speed	50 km/h
Maximum ascent speed	4 m/s

### 2.3 Route Parameters

The drone requires flight control software for tilt photography aerial photography tasks, and the DJI Pilot, which is the appropriate model, is selected as the flight control software. Before the flight, you need to set the route parameters such as flight height, heading and side overlap rate, gimbal pitch angle, etc.

The flight height is the basis of the route flight. When setting the flight height, care should be taken not to go below the highest height of the studied area to avoid economic loss or personnel safety problems caused by collision. At the same time, the flight height should not be too high, otherwise the GSD is too high will also affect

the model accuracy. Satisfy the equation:

$$H = \frac{f \times GSD}{\alpha}$$

where,  $H$  is the height of the UAV relative to the mean elevation;  $GSD$  is the image spatial resolution;  $f$  is the camera focal length;  $\alpha$  is the image element size. When the flight altitude is set to 40 m, the  $GSD$  reaches 1.10 cm/pixel, which meets the modeling accuracy requirement.

The highest point of this experimental study area is about 12 m, and the experimental navigation height is set to 40 m to ensure safety.

The overlap rate is divided into heading overlap rate and side overlap rate, considering that various electrical equipment in substations are relatively closely spaced and the electrical equipment is mostly slender columnar structure. In addition, it is challenging to model the complete insulator strings and slender transmission lines. Therefore, the heading overlap rate and the side overlap rate should preferably be set above 60%.

Setting the proper pan/tilt angle can reduce the blind spot in the image where buildings block the view. The pitch angle adjustment range is  $-85^\circ$  to  $-40^\circ$ . In principle, the higher the flight altitude or the flatter the elevation, the lower the tilt angle, and the lower the flight altitude, the higher the tilt angle. In this article, the head pitch angle is set to  $-45^\circ$ .

This experiment uses the foreign developed ContextCapture. ContextCapture software is Bentley Software's real-world modeling software, which can generate ultra-high density point clouds based on real images, and process simple and continuous image data to generate lifelike real-world 3D models.

## 3 3D Reconstruction

### 3.1 Aerial Triangulation

The main purpose of aerial triangulation, also known as air triangulation, is to find the coordinates of the image connection points and multiple elements based on the position information of the image points measured on the captured images and the actual coordinate information of a small number of control points in the real scene. There are three main methods for aerial triangulation solution: air strip method, independent model method and beam method. The most commonly used method is the beam method. The principle of the beam method is to extract the coordinates of the target point from the image and calculate the outer orientation elements of each photographic center. First, the error equation is listed according to the three-point co-linearity condition, and the external orientation element of the center of photography is calculated for each image, and then the specific ground coordinates

of the encrypted point of the photographed object are calculated according to the rendezvous of the same points in multiple images.

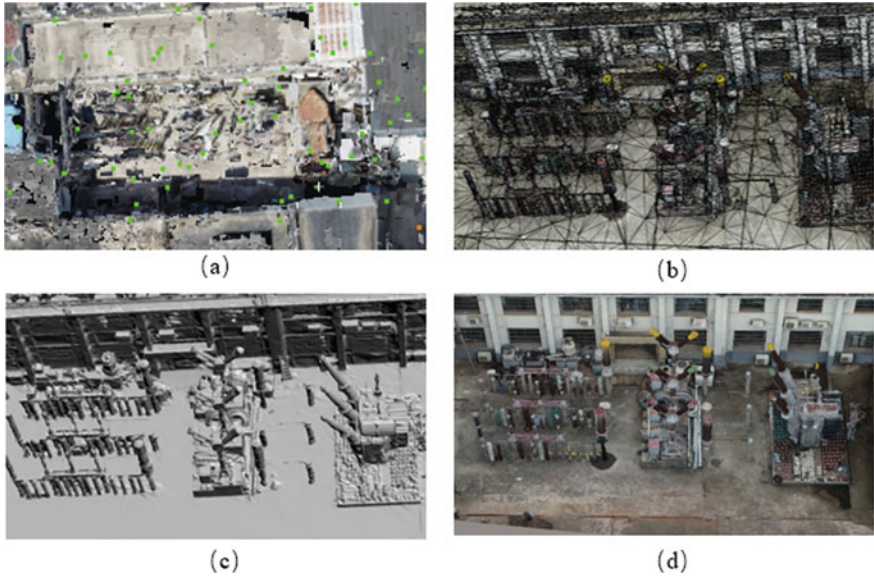
### 3.2 Multi-vision Image Intensive Matching

The purpose of dense matching of multi-view images is to extract the same objects with the same name points from the photos taken by UAV at different locations. In tilt photography, the images are taken from different viewpoints, and these images have wide coverage and high resolution, but there are also many duplicate image information, so it is necessary to accurately obtain the coordinates of the same name points of multi-view images to eliminate redundant information. The algorithm of image matching is divided into three categories: grayscale matching, feature matching and relationship matching, and the most common one is the SIFT algorithm based on feature matching, which is mainly divided into five steps, firstly, constructing multi-scale space, calculating gradient, detecting extreme points as main feature points, eliminating unstable feature points, giving direction to the remaining ones, and finally generating descriptors for the subsequent matching of feature points between images. The remaining ones are given directions, and finally descriptors are generated for the subsequent matching of feature points between images.

### 3.3 Mesh Construction and Texture Mapping

After completing the dense matching of multi-view images, a high-density point cloud is generated, and then the adjacent point clouds are connected to each other to form a continuous triangular surface to obtain the irregular triangular network (TIN). After getting the irregular triangle network, the white body model is filled, and finally the surface texture mapping is carried out based on this model to map the information contained in the 2D image such as image color and geometric texture to the surface of the 3D model, and the 3D model of the substation is obtained as shown in Fig. 2. Texture mapping is essentially a conversion of the correspondence between the 3D model and the 2D image, establishing the corresponding mapping function relationship between points  $(u, v)$  in 2D space and points  $(x, y, z)$  in 3D space, with the following equation:

$$\begin{bmatrix} u \\ v \\ 1 \end{bmatrix} = \frac{1}{Z_c} \begin{bmatrix} f_x & 0 & u_0 \\ 0 & f_y & v_0 \\ 0 & 0 & 1 \end{bmatrix} \begin{bmatrix} R & T \\ 0 & 1 \end{bmatrix} \begin{bmatrix} x \\ y \\ z \\ 1 \end{bmatrix} \quad (1)$$



**Fig. 2** **a** The result of aerial triangulation; **b** TIN model; **c** white body model; **d** 3D model of substation

where  $u_0$ ,  $v_0$  represent the two-dimensional coordinates of the image center pixel in the image coordinate system,  $Z_c$  is the camera depth,  $f_x$ ,  $f_y$  are the focal lengths in the  $x$ ,  $y$  directions,  $R$  is the rotation matrix, and  $T$  is the camera photography center.

## 4 Model Accuracy Analysis

After the aerial image acquisition is completed, the 3D reconstruction is carried out by ContextCapture. The coordinates can be measured on the model. 10 significant feature points are selected in the modeling area, which can be clearly found in the site and the model, and the actual coordinates of these points are measured and taken as the real values. The reference system chosen for both the site and the model is WGS-84 coordinate system, and the coordinates of the points are latitude and longitude, which are calculated according to the error formula, and then the difference of latitude and longitude is converted into length error, and finally the geometric accuracy of the model is evaluated according to the error. The error formula is as follows:

$$m_w = \sqrt{\frac{1}{n} \sum_{i=1}^n (dw_i)^2} \quad (2)$$

**Table 2** The experimental results

Side/heading	Error	Flight time	Images	Modeling time
90/90	0.25	9:36	127	35:43
80/80	0.34	6:12	94	23:06
80/70	1.04	6:07	66	20:51
80/60	3.26	5:58	67	21:28
70/80	2.26	5:13	66	20:41
70/70	5.81	4:53	47	12:43
70/60	7.10	4:52	47	12:01
60/80	8.33	3:53	43	11:19
60/70	8.52	3:47	33	7:03
60/60	6.05	3:43	33	7:19

$$m_j = \sqrt{\frac{1}{n} \sum_{i=1}^n (dj_i)^2} \quad (3)$$

$$\sigma = \sqrt{m_w^2 + m_j^2} \quad (4)$$

After determining the UAV model, flight altitude and modeling software, we analyzed and compared the effects of different bypass overlap rates and heading overlap rates on the accuracy of the model, and the experimental results are shown in Table 2. From the table, it can be learned that the lower the overlap rate of bypass and heading overlap rate, the less time is spent on flight photography, the less images are acquired, and the less time is needed for modeling, but the accuracy of the established 3D model is also worse. It can be seen that when the overlap rate increases from 60 to 80%, the accuracy increases more but the time spent does not increase much. However, when the overlap rate rises from 80% to 90, the accuracy is not improved much. Therefore, for the substation site in this paper, we choose a higher overlap rate of 80% in the side direction and the overlap rate in the heading direction, and spend more time on tilt photography and 3D reconstruction to obtain a more accurate 3D model of the substation.

## 5 Conclusion

In this paper, we study the influence of route overlap rate on UAV oblique photography 3D modeling, and carry out experiments of oblique photography 3D modeling under different overlap rates for the 220 kV substation site in this paper, and get the following conclusions: the lower the overlap rate of side direction and heading overlap rate, the less time used for flight shooting, the less images obtained, and the less time needed for modeling, but the accuracy of the established 3D model will

also be worse. It can be seen that when the overlap rate increases from 60 to 80%, the accuracy increases more but the time spent does not increase much. But from 80 to 90%, the accuracy is not much compared to the increase. So for general substation oblique photography 3D modeling, choose 80% overlap rate can be.

**Acknowledgements** This study was supported by the technology project of China Southern Power Grid (Project No. 030600KK52220016).

## References

1. Huang X, Yang J, Liu X, Zhang Z, Cui L (2021) Research and application of rapid 3D modeling technology based on UAV. In: 2021 IEEE 12th international conference on software engineering and service science (ICSESS), pp 109–112. <https://doi.org/10.1109/ICSESS52187.2021.9522226>
2. Huang C, Zhang H, Zhao J (2020) High-efficiency determination of coastline by combination of tidal level and coastal zone DEM from UAV tilt photogrammetry. *Remote Sens* 12(14):2189
3. Zhou T, Lv L, Liu J et al (2021) Application of UAV oblique photography in real scene 3d modeling. *Int Arch Photogrammetry Remote Sens Spat Inf Sci* 43:413–418
4. Liang LH, Yang ZG, Wang YG et al (2022) Accuracy analysis of oblique photogrammetry measurement in 3D modeling of power line selection design. *J Phys Conf Ser IOP Publishing* 2400(1):012013
5. Wu B, Xie L, Hu H et al (2018) Integration of aerial oblique imagery and terrestrial imagery for optimized 3D modeling in urban areas. *ISPRS J Photogramm Remote Sens* 139:119–132
6. Tang F, Ruan Z, Li L (2018) Application of unmanned aerial vehicle oblique photography in 3D modeling of crag. Shanghai, China
7. Zhang ZY (2022) Research on 3D reconstruction technology of airports based on tilt photogrammetry technology. Civil Aviation Flight Academy of China (in Chinese)
8. Li J, Yao Y, Duan P et al (2018) Studies on three-dimensional (3D) modeling of UAV oblique imagery with the aid of loop-shooting. *ISPRS Int J Geo Inf* 7(9):356
9. Rao CC, Xu ZH, Liao RC (2018) Comparative analysis of image shooting methods based on UAV photogrammetry. *IOP Conf Ser Earth Environ Sci IOP Publishing* 199(3):032095
10. Zheng Y, Yu X, Zhu Q, Ren Z, Zhang J (2021) Application of UAV tilt photography technology in accurate measurement of transmission tower slope. *Rural Electrification* 11:39–42. <https://doi.org/10.13882/j.cnki.ncdqh.2021.11.012> (in Chinese)



# Design and Thrust Output Analysis of Linear Induction Motor for Electromagnetic Ejection of Fixed-Wing UAV



Xijun Liu, Xianchun Huang, and Peifeng Zhao

**Abstract** According to the requirements of the fixed-wing UAV's ejection acceleration take-off index, based on the T-type equivalent circuit model of the linear induction motor, the electromagnetic thrust output value of the linear induction motor required for acceleration and driving is deduced and analyzed. Design a long primary unilateral linear induction motor for take-off of fixed-wing UAV to meet the electromagnetic ejection acceleration requirements of UAV. The equivalent circuit of the motor considering the side effect is established, and the mathematical model of the linear induction motor is established according to the design parameters of the linear induction motor. Simulation and analysis of the influence of the slip frequency on the electromagnetic thrust output of the linear induction motor under different operating speeds and different influencing factors. The constant current-slip frequency control method is used to control the electromagnetic thrust output of the linear motor, seek the optimal slip frequency of the linear induction motor, and optimize the design parameters and control methods to meet the accelerated take-off requirements of the fixed-wing UAV.

**Keywords** Fixed wing UAV · Electromagnetic ejection · Linear induction motor · Electromagnetic thrust · Slip frequency

---

X. Liu (✉) · X. Huang · P. Zhao

Institute of Electronic and Electrical Engineering, Civil Aviation Flight University of China, Guanghan 618307, China  
e-mail: [Edwiin850617@163.com](mailto:Edwiin850617@163.com)

X. Liu

Sichuan Province Engineering Technology Research Center of General Aircraft Maintenance, Guanghan 618307, China

© Beijing Paiké Culture Commu. Co., Ltd. 2024

X. Dong and L. Cai (eds.), *The Proceedings of 2023 4th International Symposium on Insulation and Discharge Computation for Power Equipment (IDCOMPU2023)*, Lecture Notes in Electrical Engineering 1103, [https://doi.org/10.1007/978-981-99-7413-9\\_63](https://doi.org/10.1007/978-981-99-7413-9_63)

659

## 1 Introduction

With the development of science and technology, fixed-wing UAVs have been widely used in agriculture, forestry, military, fire protection and other fields. Fixed-wing UAVs usually have three modes of accelerated take-off: rocket booster, hydraulic jet and pneumatic jet. Rocket-assisted energy consumption is high, the danger is high, and the impact on the environment is large, and the UAV's accelerated take-off is greatly affected by fluctuations. Hydraulic injection and pneumatic injection require a large number of pipelines, valves and accumulators and other devices. The equipment system is complex and occupies a large space, and the equipment maintenance work is cumbersome.

Electromagnetic ejection technology is an accelerated driving method that is developing rapidly at present. Electromagnetic ejection uses a linear motor as a driving device to convert electrical energy into the electromagnetic thrust output of the linear motor. The magnitude of the electromagnetic thrust is related to the current. By controlling the power supply current, the motor energy output is controlled, and then the light or heavy fixed-wing UAV is controlled to complete the accelerated ejection take-off. Task. The thrust output of the electromagnetic ejection system is easy to control, with low energy loss, light weight, small space, easy maintenance, and superior performance. For the electromagnetic ejection of UAVs, there are mainly two methods: coil ejection and linear motor. Compared with the two methods, the linear induction motor is used as the electromagnetic drive device, and the electromagnetic thrust output can be changed by changing the design parameters, and the thrust output is larger. More stable, high precision, strong controllability, and the equipment is easier to maintain.

Some scholars have studied the linear induction motor for electromagnetic ejection. Cai et al. [1] and Lu et al. [2] analyzed the electromagnetic influence of the end effect of the linear induction motor, and simulated the influence of the end effect on the magnetic field of the motor; [3, 4] verified the feasibility of electromagnetic drive; [5] analyzed the low frequency. The secondary structure of the linear induction motor is optimized to improve the electromagnetic thrust; [6–8] model and simulate the linear induction motor.

In this paper, according to the T-type equivalent circuit of the unilateral linear motor, considering the loss of the end effect on the motor, the output expression of the electromagnetic thrust of the linear induction motor is deduced, and the relationship between the slip frequency and the thrust output is found, and the slip frequency is optimized. Induction motor thrust output, and then meet the requirements of fixed-wing UAV ejection acceleration index.

## 2 Kinematics Analysis of UAV Takeoff

The electromagnetic acceleration system is used to instantly accelerate the UAV within a predetermined length of distance, and make its speed value meet the prescribed standard for take-off. The simplified force model of UAV launch is shown in Fig. 1.

Assuming that the accelerated light fixed-wing UAV and its payload mass do not exceed 40 kg, the length of the ejection track is 5 m, and the UAV should accelerate from 0 to 100 km/h within 0.36 s. During the acceleration process, the UAV's own power system No work is done, and the linear induction motor provides a constant electromagnetic thrust output for the UAV's acceleration and take-off traction power.

The kinematic process is expressed by Newton's second law as:

$$a = \frac{v_t^2}{2L_s} \tag{1}$$

$$t = \frac{2L_s}{v_t} \tag{2}$$

$$F = \frac{Mv_t^2}{2L_s} \tag{3}$$

In the formula,  $v_t$ ,  $L_s$  and  $t$  are the acceleration terminal speed, orbit length, and acceleration time of the fixed-wing UAV, respectively;  $F$ ,  $M$ , and  $a$  are the resultant force, the UAV and the motion of the UAV along the orbit, respectively. The total mass of the sub-slider, and the acceleration of the drone.

Among them, the resultant force of the UAV along the trajectory ejection direction is:

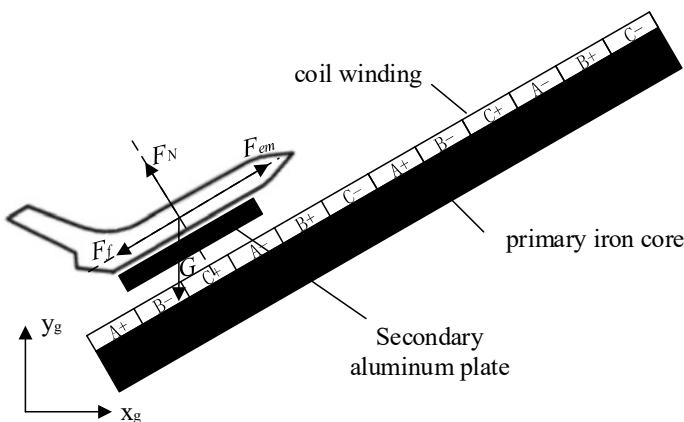


Fig. 1 Human-machine electromagnetic ejection model diagram

$$F = F_{em} - (F_f + G \sin(\theta)) \tag{4}$$

$F_{em}$  is the electromagnetic thrust generated by the linear motor;  $F_f$  is the resistance during the ejection of the drone;  $G$  is the total weight of the drone and the mover slider;  $\theta$  is the launch angle, which can be adjusted if the launch angle is less than  $60^\circ$ .

During the acceleration of the take-off and ejection of the fixed-wing UAV, due to the compression of the front air, the air friction on both sides of the fuselage, and the partial vacuum of the tail space, the air resistance during the acceleration process is caused.

The air resistance of the drone is proportional to the square of its speed. The greater the speed, the greater the air resistance. The air resistance of the drone is:

$$F_f = \frac{1}{2} C \rho S_0 v^2 \tag{5}$$

In the formula,  $C$ —drag coefficient, the value of which is mainly related to the shape and smoothness of the moving object, as well as the area of the object on the windward side, the wind resistance coefficient of the UAV is about 0.2–0.4;  $\rho$ —air density, dry air density is 1.293 g/l;  $S_0$ —the area of the windward side of the object;  $v$ —the relative velocity of the object and the air.

Calculated with a fixed-wing UAV and its load mass of 40 kg and a launch angle of  $30^\circ$ , the air resistance is smaller than the electromagnetic thrust, which is ignored for the time being. To accelerate the UAV to 100 km/h within 5 m, the linear induction The motor provides at least 3.09 KN of electromagnetic thrust. The specific indicators of the acceleration process of the fixed-wing UAV are shown in Table 1.

**Table 1** Fixed-wing UAV acceleration technical requirements

Parameter	Value	Parameter	Value
Acceleration track length $L_s$ (m)	5	Load mass $M$ (kg)	< 40
Initial velocity $V_0$ (m/s)	0	Final velocity $V_t$ (m/s)	27.78
Acceleration time $t$ (s)	0.36	Acceleration $a$ (m/s <sup>2</sup> )	128.62
Launch angle $\theta$ ( $^\circ$ )	< 60	Average electromagnetic thrust $F_{em}$ (KN)	3.09
Linear motor power $P$ (KW)	0.62	Linear motor power supply $E$ (KJ)	15.45

### 3 Establishment of Mathematical Model of Linear Induction Motor

The stator winding of the linear induction motor for electromagnetic ejection-driven fixed-wing UAV has no cogging, and the cogging structure can reduce the influence of the tooth harmonic magnetic field on the electromagnetic thrust output. The secondary of the linear induction motor is made of aluminum material, which is conducive to generating electromagnetic thrust output. The secondary is aluminum plate or copper plate, which reduces mass, reduces manufacturing and operating costs, and is conducive to high-speed and high-thrust motion.

Because the primary iron core and winding ends of the linear induction motor are disconnected, this special structure makes the linear motor have the problem of side effect, which affects the air gap magnetic field and attenuates the thrust output. The influence of the side effect on the output of electromagnetic thrust cannot be ignored. During the acceleration process of the UAV, the current and slip frequency of the stator of the linear induction motor can be controlled to complete the optimal control of the electromagnetic thrust output of the motor.

Considering the influence of the edge effect on the long primary linear induction motor, a T-type equivalent circuit of the linear induction motor is established, and the electromagnetic thrust output expression of the motor is deduced. The relevant mechanical characteristics of the linear induction motor can be calculated through the equivalent circuit. The equivalent circuit of the long primary linear induction motor considering the side effect is shown in Fig. 2.

$\dot{U}_1, \dot{E}_1$  are the phase voltage and winding electromotive force of the linear induction motor;  $\dot{I}_1, \dot{I}_2, \dot{I}_0,$  and  $\dot{I}_e$  are the primary winding current, secondary reduced current, excitation current and terminal current of the motor;  $x_1, r_1$  are the primary leakage reactance of the motor and the corresponding resistance of the primary;  $x'_2, r'_2$  are the secondary Leakage reactance of stage, corresponding resistance of secondary;  $x_0$  excitation reactance;  $R_{ed}$  end effect resistance;  $s$  slip rate.

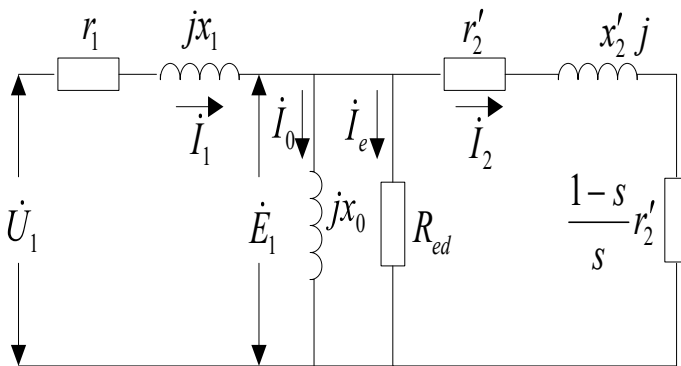


Fig. 2 Equivalent circuit diagram of linear motor considering side effect

## 4 Analysis of Thrust Force of Linear Induction Motor

Analysis of the electromagnetic thrust output of fixed-wing UAV driving acceleration According to the T-type equivalent circuit and Kirchhoff's law, the synchronous power calculation method is used to derive the output electromagnetic thrust of the linear induction motor. According to the equivalent circuit of the linear induction motor considering the end effect and Kirchhoff's law, the electromagnetic thrust output of the linear motor for the take-off drive of the UAV is deduced:

$$F_{em} = \frac{m_1}{v_s} I_2^2 \frac{r'_2}{s} \quad (6)$$

In the formula,  $m_1$  is the number of motor phases;  $v_s$  is the synchronous speed,  $v_s = 2\tau \cdot f_1$ , and  $f_1$  is the rated frequency of the winding. The relationship between the primary winding current  $\dot{I}_1$  and the secondary reduced current  $\dot{I}_2$  is:

$$\dot{I}_2 = \frac{R_{ed} j x_0}{2R_{ed} j x_0 + \frac{r'_2 R_{ed}}{s} + \frac{r'_2}{s} j x_0 - x'_2 x_0} \dot{I}_1 \quad (7)$$

The electromagnetic thrust output can be obtained by finishing Formulas 8:

$$F_{em} = \frac{m_1}{2\tau f_1} I_1^2 \frac{R_{ed}^2 x_0^2 r'_2 s}{(R_{ed}^2 + x_0^2) r_2'^2 + (R_{ed}^2 + x_2'^2) x_0^2 s^2} \quad (8)$$

## 5 Linear Motor Parameter Design and Simulation Analysis

In order to meet the electromagnetic thrust requirements required by the electromagnetic ejection index of the fixed-wing UAV, the design parameters of the linear induction motor are shown in Table 2.

According to the linear induction motor model for ejection drive, the influence of slip frequency on electromagnetic thrust output is simulated and analyzed, and the optimal slip frequency is sought. Figure 3 shows the relationship between ejection speed and electromagnetic thrust output under the condition of constant linear induction motor stator current and different slip frequencies.

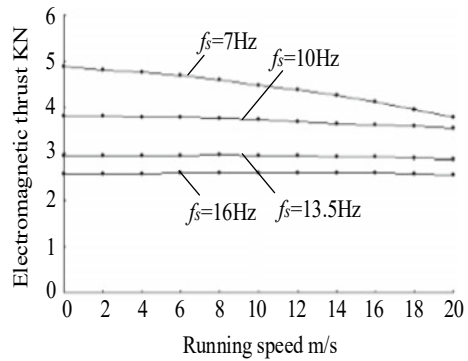
Simulation analysis of the relationship between the slip frequency and the electromagnetic thrust output under the condition of constant current and constant slip frequency and different operating speeds is shown in Fig. 4.

The slip frequency is fixed. When the slip frequency is large, the electromagnetic thrust output of the linear induction motor is basically constant with the change of the running speed; when the slip frequency is small, the electromagnetic thrust output generated by the motor is large, but with the operation as the speed increases,

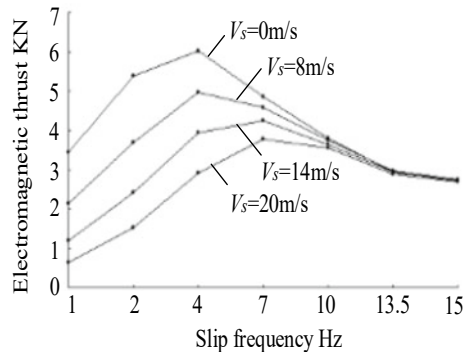
**Table 2** Design parameters of unilateral linear induction motor

Parameter	Value	Parameter	Value
Motor pole pairs $p$	4	Number of slots per pole per phase $q_1$	3
Number of motor phases $m_1$	3	Number of turns in series per phase $\omega_1$	72
Primary length $l_0/m$	3	Winding half turn length $l_{av}/m$	0.55
Mechanical air gap $\delta_0/mm$	5	Electromagnetic air gap $\delta_e/mm$	13
Motor pole pitch $\tau/mm$	250	Rated voltage $U_1/V$	220
Rated current $I_1/A$	340	Rated frequency $f_1/Hz$	50
Core stack thickness $l_\delta/mm$	220	Conductor cross-sectional area $S_1/mm^2$	90
Aluminum plate thickness $d_a/mm$	4.5	Aluminum plate width $l_a/mm$	220

**Fig. 3** The relationship between speed and thrust under different slip frequencies



**Fig. 4** Relationship between slip frequency and thrust output at different speeds



the electromagnetic thrust output decreases, which is easily affected by the running speed.

When the running speed is a certain value, with the increase of the slip frequency, the electromagnetic thrust output of the motor increases first and then decreases. When the slip frequency is small, the electromagnetic thrust output fluctuates greatly.

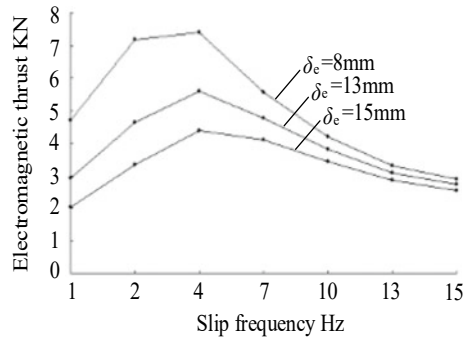
When the slip frequency increases to 13.5 Hz, the electromagnetic thrust. The output is basically constant and basically not affected by the running speed.

When the slip frequency is 13.5 Hz, with the change of the operating speed, the electromagnetic thrust output is basically constant, basically constant at 3.0–3.1 KN, which meets the demand of the electromagnetic thrust output value required by the UAV ejection and is sufficient to meet the fixed. The wing UAV can complete the acceleration drive. This design uses a slip frequency of 13.5 Hz to complete the accelerated ejection.

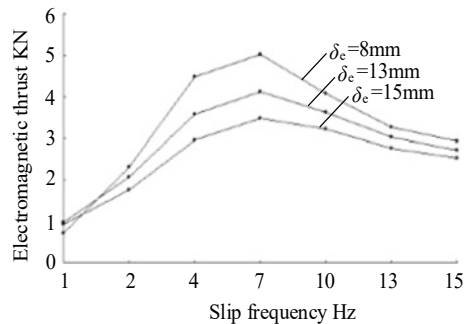
The suspended air gap of the linear induction motor used for the ejection acceleration of the fixed-wing UAV is the key factor for the electromagnetic thrust output of the motor. It is difficult to realize the processing process of the air gap that is too small, and the large air gap is not enough to generate the electromagnetic thrust output required for the ejection. The simulation analysis shows that when the operating speed is 4 and 16 m/s, under different electromagnetic air gaps, the effect of slip rate on the electromagnetic thrust output is shown in Figs. 5 and 6.

It can be verified from the electromagnetic air gap and electromagnetic thrust simulation analysis diagram that the larger the electromagnetic air gap is, the smaller the electromagnetic thrust output of the motor is, and the two are in an inversely proportional relationship. The smaller the air gap, the more obvious the thrust output fluctuation, especially at low speed, this fluctuation is more obvious.

**Fig. 5** At 4 m/s, the relationship between slip frequency and electromagnetic thrust output under different electromagnetic air gaps



**Fig. 6** The relationship between slip frequency and electromagnetic thrust output under different electromagnetic air gaps at 16 m/s





The acceleration process of the fixed-wing UAV is a uniform acceleration process, and it is necessary to keep the electromagnetic thrust output of the motor from fluctuating due to changes in speed. Therefore, the electromagnetic air gap of the motor is selected as 13 mm, the slip frequency is 13.5 Hz, and the electromagnetic thrust output is basically constant under different operating speeds., enough to meet the electromagnetic thrust output requirements of electromagnetic ejection.

## 6 Conclusion

In this paper, according to the requirements of the ejection acceleration index of fixed-wing UAV, a linear induction motor for ejection drive is designed, and the influence of slip frequency on the electromagnetic thrust output is simulated and analyzed. Based on the specific motor design parameters, a simulation analysis model is established to analyze the influence of the slip frequency on the electromagnetic thrust output under different electromagnetic air gaps and different operating speeds. The design finally determines that the slip frequency is 13.5 Hz, and the electromagnetic thrust output Basically constant at 3.0–3.1 KN, control the slip frequency value, and then control the output of the electromagnetic thrust, realize the optimal control of the thrust output, and then complete the accelerated ejection index requirements of the fixed-wing UAV.

## References

1. Cai J, Wang S, Pang C (2021) A linear induction motor electromagnetic design method considering the influence of the lateral end effect. *J Northwestern Polytechn Univ* 10:1114–1121 (in Chinese)
2. Lu J, Ma W, Li L (2008) Research on longitudinal end effect of high speed long primary linear induction motor. *Proc Chin Soc Electr Eng* 28(30):73–78 (in Chinese)
3. Lin Z, Chen G, Xu L (2021) Finite element simulation and analysis of missile electromagnetic catapult. *Aerospace Control* 39(2):57–60 (in Chinese)
4. Lu J, Ma W, Xu J (2008) Modeling and simulation of high-speed long-stator linear induction motor. *Proc Chinese Soc Electr Eng* 28(27):89–94 (in Chinese)
5. Wu S, Lu Q (2014) Design and analysis of the secondary structure of low-frequency linear induction motor. *Proc Chinese Soc Electr Eng* 41:324–331 (in Chinese)
6. Han Y, Nie Z, Xu J et al (2020) Mathematical model and vector control of a six-phase linear induction motor with the dynamic end effect. *J Power Electron* 20(3):698–709
7. Bazghaleh AZ, Naghashan MR (2010) Optimum design of single sided linear induction motors for improved motor performance. *IEEE Trans Magn* 46(11):3939–3947
8. Kim D, Kwon B (2006) A novel equivalent circuit model of linear induction motor based on finite element analysis and its coupling with external circuits. *IEEE Trans Magn* 42(10):3407–3409

# A Variable Frequency Voltage Injection Method for Modular Multilevel Converter in Variable Speed Driver



Guanlong Jia, Mingshuo Li, Dawei Feng, Binhao Shi, Xiaoming Liu, and Jun Huang

**Abstract** Modular Multilevel Converter (MMC) is a common multilevel topology for medium voltage motor drives. However, the voltage fluctuation of the sub-module (SM) capacitor is the main obstacle when motor runs at low speed. A variable frequency voltage injection method is recommended in this paper, in which the frequency of the injection voltage changes synchronously with the speed (output frequency) and is permanently guaranteed to be  $K$  times of the frequency. The optimal voltage suppression can be achieved at low frequency operation and overmodulation can be effectively avoided. Finally, the availability of the recommended variable frequency voltage injection method is checked with simulation and experimental results.

**Keywords** Modular multilevel converter (MMC) · Improved high-frequency injection · Voltage ripples · Variable-speed drives

## 1 Introduction

Modular multilevel converter (MMC) has obtained extensive interest in motor drive on account of its scalability and high efficiency [1]. However, the obstacle for motor drives is the heavy ripple in capacitor voltage when the motor is started or running at low frequency. Many strategies have been introduced to solve this problem.

In [2], the method of combining second and fourth-order circulation injection is discussed. An injection method combining third-harmonic voltage with second-harmonic current is presented in [3, 4]. However, the above methods need to be calculated offline, which is relatively complex. The method of decreasing voltage fluctuation by lowering the reference voltage of the SM is proposed in [5, 6]. However, reducing the SM reference voltage means that more SMs is required, which will

---

G. Jia (✉) · M. Li · D. Feng · B. Shi · X. Liu · J. Huang  
State Key Lab of Reliability and Intelligence of Electrical Equipment, HeBei University of Technology, Tianjin, China  
e-mail: [jjagl@hebut.edu.cn](mailto:jjagl@hebut.edu.cn)

cause greater system loss. In [7, 8], the methods of injecting variable amplitude high-frequency voltage and circulating current are proposed. And the above method ignores the impact of the inductor voltage on the arm voltage modulation waveform. Overmodulation of the arm voltage is caused when the injection frequency is too high. In this paper, to avoid overmodulation in low frequency operation, the frequency of the injected amounts is dynamically revised with the operating frequency. Simulation and experimental results indicate that the improved approach is effective for variable speed drives in the low frequency range.

## 2 Proposed Variable Frequency Injection Method

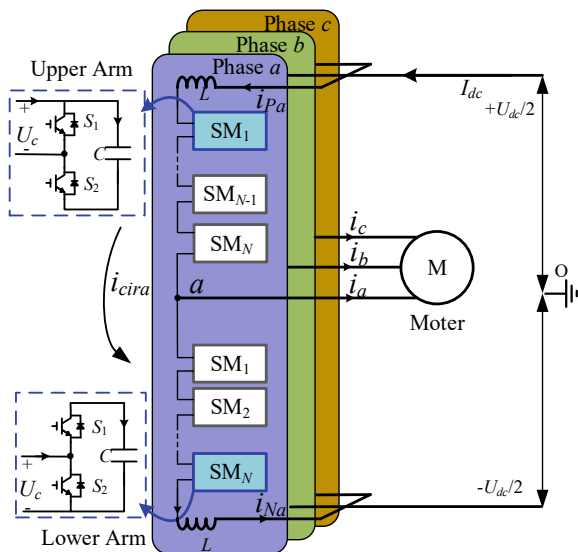
### 2.1 Circuit Configuration

The traditional three-phase MMC topology is displayed in Fig. 1. Each phase has two duplicate arms, and every arm contains an inductor and N half-bridge SM. The output voltage of SM is decided by switch  $S_1$  and  $S_2$ . The control strategy of MMC can be found in [9–11], this section will focus on the improved injection method. Due to the symmetry of three-phase MMC, it is reasonable to analyze phase  $a$  separately.

Ignoring the inductor voltage, the output voltage  $e_a$  and current  $i_a$  are as follows:

$$\begin{cases} e_a = E_a \sin(\omega t) \\ i_a = I_a \sin(\omega t - \varphi) \end{cases} \quad (1)$$

Fig. 1 MMC topology configuration with motor



where  $E_a$  and  $I_a$  are amplitude of the output voltage and current,  $\varphi$  is the power factor angle, and  $\omega$  is the output frequency. The circulating current through phase  $a$  is

$$i_{cira} = \frac{e_a i_a}{U_{dc}} \quad (2)$$

## 2.2 Analysis of SM Capacitor Voltage Ripples

The arm voltages  $u_{Pa}$  and  $u_{Na}$  are defined as

$$\begin{cases} u_{Pa} = \frac{U_{dc}}{2} - e_a \\ u_{Na} = \frac{U_{dc}}{2} + e_a \end{cases} \quad (3)$$

The arm currents  $i_{Pa}$  and  $i_{Na}$  can be derived as

$$\begin{cases} i_{Pa} = i_{cira} + \frac{i_a}{2} \\ i_{Na} = i_{cira} - \frac{i_a}{2} \end{cases} \quad (4)$$

The powers of the arm are gained from the arm voltage and the current. Based on (3) and (4), the instantaneous powers can be obtained as

$$\begin{cases} p_{Pa} = u_{Pa} i_{Pa} = I_a \sin(\omega t - \varphi) \left( \frac{U_{dc}}{4} - \frac{E_a^2 \sin^2(\omega t)}{U_{dc}} \right) \\ p_{Na} = -u_{Na} i_{Na} = -I_a \sin(\omega t - \varphi) \left( \frac{U_{dc}}{4} - \frac{E_a^2 \sin^2(\omega t)}{U_{dc}} \right) \end{cases} \quad (5)$$

The power ripple is negatively correlated to the operating frequency  $\omega$ , and the lower the operating frequency, the greater the voltage fluctuations [12]. According to (5), low frequency part ( $\omega$ ) is the main cause of capacitor voltage fluctuation. And the low frequency component of power can be converted into high frequency component to markedly reduce voltage fluctuation.

## 2.3 Proposed Injection Method

For the convenience of analysis, sine waveform is selected as the high-frequency injection quantity. The high-frequency voltage  $u_{oh}$  is

$$u_{oh} = U_{oh} \sin(\omega_h t) \tag{6}$$

where  $U_{oh}$  and  $\omega_h$  are the magnitude and frequency of  $u_{oh}$ . Then, the arms voltage and currents in (3) and (4) are rewritten as

$$\begin{cases} u_{Pa}^* = \frac{U_{dc}}{2} - e_a - u_{oh} \\ u_{Na}^* = \frac{U_{dc}}{2} + e_a + u_{oh} \end{cases} \tag{7}$$

$$\begin{cases} i_{Pa}^* = i_{cira} + \frac{i_a}{2} + i_{inja} \\ i_{Na}^* = i_{cira} - \frac{i_a}{2} - i_{inja} \end{cases} \tag{8}$$

where  $i_{inja}$  is the high-frequency current. And the change of arms voltage and current leads to the change of arm power [13]. By multiplying (7) and (8), the power of arms after injecting high frequency can be rewritten as

$$\begin{cases} P_{Pa}^* = u_{Pa}^* i_{Pa}^* = \frac{U_{dc} I_a \sin(\omega t - \varphi)}{4} [1 - m^2 \sin^2(\omega t)] \\ \quad - U_{oh} i_{inja} \sin(\omega_h t) + i_{inja} E_a \sin(\omega t) \\ \quad - \frac{m I_a U_{oh} \sin(\omega t - \varphi) \sin(\omega_h t) \sin(\omega t)}{2} \\ \quad - \frac{(I_a U_{oh} \sin(\omega t - \varphi) \sin(\omega_h t) - U_{dc} i_{inja})}{2} \\ P_{Na}^* = -u_{Na}^* i_{Na}^* = -\frac{U_{dc} I_a \sin(\omega t - \varphi)}{4} [1 - m^2 \sin^2(\omega t)] \\ \quad + U_{oh} i_{inja} \sin(\omega_h t) - i_{inja} E_a \sin(\omega t) \\ \quad + \frac{m I_a U_{oh} \sin(\omega t - \varphi) \sin(\omega_h t) \sin(\omega t)}{2} \\ \quad - \frac{(I_a U_{oh} \sin(\omega t - \varphi) \sin(\omega_h t) - U_{dc} i_{inja})}{2} \end{cases} \tag{9}$$

where  $m$  is the voltage modulation index. In order to eliminate the voltage fluctuations in (9), the injection current can be obtained as

$$i_{inja} = \frac{U_{dc} I_a (1 - m^2 \sin^2(\omega t)) \sin(\omega t - \varphi) \sin(\omega_h t)}{2 U_{oh}} \tag{10}$$

The injected high-frequency voltage is usually set as [14]

$$u_{oh} = \frac{(1 - m) U_{dc}}{2} \sin(\omega_h t) \tag{11}$$

Substituting (10) and (11) into (9) yields low frequency components have been transferred to high frequency components. The injected current is usually generated by adjusting the inductor voltage.

$$u_{inja} = l \frac{di_{inja}}{dt} \approx \frac{l(1 - m^2 \sin^2(\omega t)) [\omega_h i_a \cos(\omega_h t) + \frac{di_a}{dt} \sin(\omega_h t)]}{1 - m} \quad (12)$$

Consequently, the arms voltage in (7) can be rewritten as

$$\begin{cases} u_{paref}^* = \frac{U_{dc}}{2} - e_a - u_{oh} - u_{inja} \\ u_{Naref}^* = \frac{U_{dc}}{2} + e_a + u_{oh} - u_{inja} \end{cases} \quad (13)$$

It can be seen from (12) and (13) that  $u_{inja}$  will increase with  $\omega_h$ , and  $u_{inja}$  is directly superimposed on the arm voltage modulation wave. The high injection frequency at low frequency operation will inevitably lead to overmodulation of the modulated wave. In this paper, a method is used to realize that the frequency of the injected high-frequency amounts varies with the fundamental frequency. And the high-frequency voltage and current are redefined as

$$\begin{cases} u_{oh} = \frac{(1 - m)U_{dc}}{2} \sin[g(\omega)t] \\ i_{inj} = \frac{U_{dc}i_a(1 - m^2 \sin^2(\omega t))}{2U_{oh}} \sin[g(\omega)t] \end{cases} \quad (14)$$

In formula (14),  $g(\omega)$  will change with  $\omega$ , which is guaranteed to be  $K$  times of  $\omega$ , avoiding overmodulation caused by excessive injection frequency at low frequency.

### 3 Simulation and Experimental Results

#### 3.1 Simulation Results

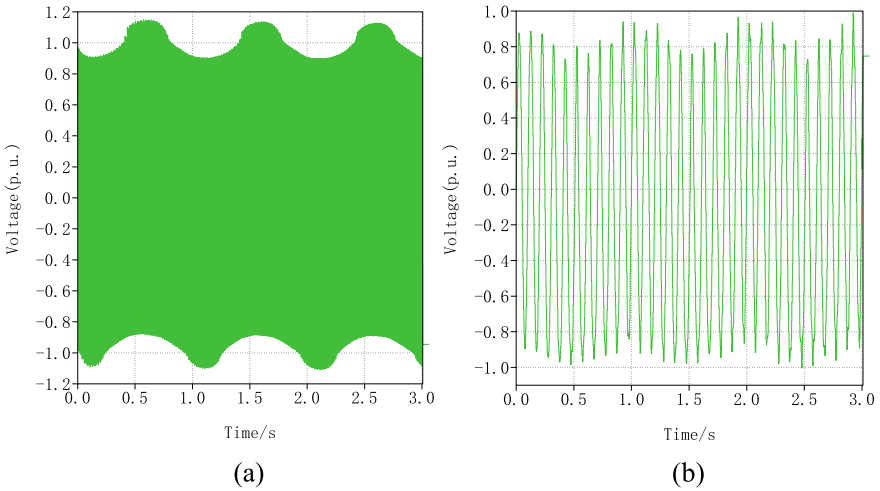
To prove the validity of the suggested strategy in the low-frequency conditions, the simulation results on PLECS are presented. Constant-torque load was adopted for simulation, and the parameters are displayed in Table 1.

Figure 2 compares the voltage modulation wave of the fixed injection frequency method and the improved method in low-speed operation. SM voltage ripple of traditional MMC and improved MMC operating at 5–10 Hz is shown in Fig. 3.

The transient process of load change when operating at 10 Hz is displayed in Fig. 4. At  $t = 2$  s, the load increases from 10 to 20 N. At  $t = 3$  s, the load decreases from 20 to 10 N. As can be seen, there is no overshoot in the capacitor voltage

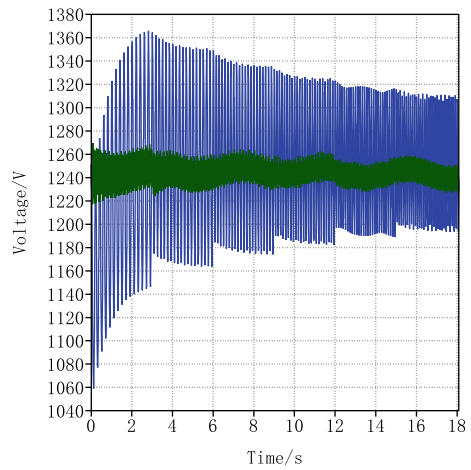
**Table 1** The simulation parameters

Symbol	Parameter	Value
$U_{dc}$	DC-side voltage	5 kV
$N$	SMs per arm	4
$C$	SM capacitance	1.36 mF
$L$	Arm inductance	9 mH
$f$	Output frequency	5–10 Hz
$T$	Load torque	20 N

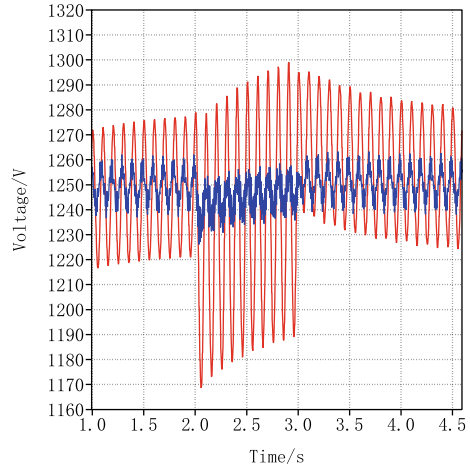


**Fig. 2** Voltage modulation wave. **a** Fixed injection frequency. **b** Improved method

**Fig. 3** SM voltage ripple at 5–10 Hz



**Fig. 4** SM voltage ripple when load changes



when the load changes and a steady state can be reached quickly, which indicates the validity of the recommended variable voltage injection method.

### 3.2 Experiment Results

To further validate the feasibility of the suggested approach, a single-phase MMC experimental platform is constructed. The concrete parameters are presented in Table 2.

(1) Experimental comparison at fundamental frequency  $f = 10$  Hz

Figure 5a illustrates the SM voltage fluctuation without high-frequency amounts injected into the MMC, and the magnitude is about 21.2 V. For comparison, when the injected voltage and current frequency  $f_h = 100$  Hz, the voltage waveform of capacitor is presented in Fig. 5b, with an amplitude of about 8.9 V.

(2) Experimental comparison at fundamental frequency  $f = 5$  Hz

**Table 2** The experiment parameters

Symbol	Parameter	Value
$U_{dc}$	DC-side voltage	400 V
$N$	SMs per arm	4
$C$	SM capacitance	1.36 mF
$L$	Arm Inductance	9 mH
$R$	Resistance of RL load	12.6 $\Omega$
$L_o$	Inductance of RL load	2 mH



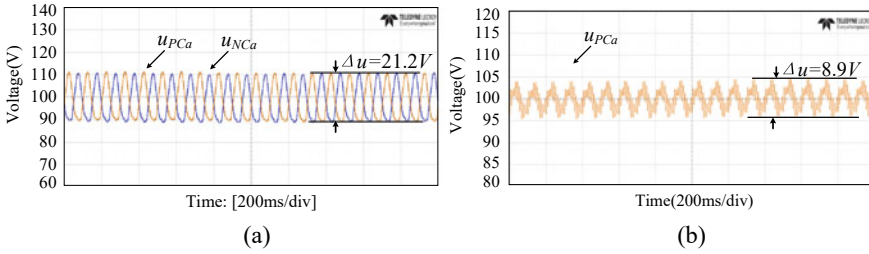


Fig. 5 SM capacitor voltage at 10 Hz. a Conventional MMC. b Improvement method

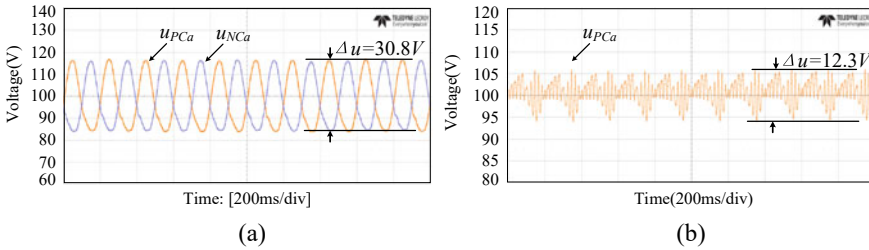


Fig. 6 SM capacitor voltage at 5 Hz. a Conventional MMC. b Improvement method

Figure 6a depicts the SM voltage fluctuation of the basic MMC without the injected amounts, and the fluctuation value is about 30.8 V. When the injected high-frequency components frequency  $f_h = 100$  Hz, the SM voltage waveform is listed in Fig. 6b, and its ripple value is about 12.3 V.

Based on the above simulation and experimental results, the suggested MMC control method with variable frequency voltage and current injection can dramatically reduce the capacitor voltage ripple.

### 4 Conclusion

This paper discusses the suppression method of SM capacitor voltage fluctuation when the motor runs at low-speed operation and proposes a high-frequency voltage injection method. In contrast to conventional MMC, the suggested method allows the frequency of the injected components to be dynamically adjusted as the operating frequency varies. The proposed method avoids overmodulation caused by high injection frequency at low frequencies. With this method, SM voltage fluctuation can be significantly reduced, so that the motor can operate normally in the low frequency stage. Simulation and experimental results verify the feasibility of the suggested control method.

**Acknowledgements** This work is sponsored by National Natural Science Foundation of China Grant (52307199), Natural Science Foundation of Hebei Province of China under grant E2022202065 and Science and Technology Research Projects for Universities in Hebei (QN2019041).

## References

1. Jia G, Chen M, Tang S, Zhang C, Zhao B (2020) A Modular multilevel converter with active power filter for submodule capacitor voltage ripples and power losses reduction. *IEEE Trans Power Electron* 35(11):11401–11417
2. Engel SP, De Doncker RW (2011) Control of the modular multi-level converter for minimized cell capacitance. In: *Proceedings of the 2011 14th European conference on power electronics and applications*, pp 1–10
3. Huang M, Kang Z, Li W, Zou J, Ma X et al (2021) Modified modular multilevel converter with third-order harmonic voltage injection to reduce submodule capacitor voltage ripples. *IEEE Trans Power Electron* 36(6):7074–7086
4. Guo G, Song Q, Yang W, Wang Y (2018) Application of third-order harmonic voltage injection in a modular multilevel converter. *IEEE Trans Industr Electron* 65(7):5260–5271
5. Zhao F, Xiao G, Zhu T, Zheng X, Wu Z et al (2020) A coordinated strategy of low-speed and start-up operation for medium-voltage variable-speed drives with a modular multilevel converter. *IEEE Trans Power Electron* 35(1):709–724
6. Wang K, Li Y, Zheng Z, Xu L (2013) Voltage balancing and fluctuation-suppression methods of floating capacitors in a new modular multilevel converter. *IEEE Trans Industr Electron* 60(5):1943–1954
7. Bao L, Yang H, Gu X, Zhao R (2020) An improved low-frequency ripple suppression method for modular multilevel converter in variable-speed motor drive application. In: *2020 23rd international conference on electrical machines and systems (ICEMS)*, pp 593–596
8. Li B, Zhou S, Xu D, Yang R, Xu D (2016) An improved circulating current injection method for modular multilevel converters in variable-speed drives. *IEEE Trans Industr Electron* 63(11):7215–7225
9. Zhao X, Zhao C, Li G (2011) Submodule capacitance voltage balancing of modular multi-level converter based on carrier phase shifted SPWM technique. *Proc CSEE* 31(21):48–55 (in Chinese)
10. Sau S, Fernandes BG (2019) Modular multilevel converter based variable speed drive with reduced capacitor ripple voltage. *IEEE Trans Industr Electron* 66(5):3412–3421
11. Espinoza-B M, Cárdenas R, Oberto JC, Soto-Sanchez D (2019) An integrated converter and machine control system for MMC-based high-power drives. *IEEE Trans Ind Electron* 66(3):2343–2354
12. Yu Q, Deng F, Liu C, Wang Z, Li B et al (2022) Advanced 2N+1 submodule unified PWM with reduced DC-link current ripple for modular multilevel converters. *IEEE Trans Power Electron* 37(4):4261–4274
13. Xu J, Deng W, Gao C (2021) Dual harmonic injection for reducing the submodule capacitor voltage ripples of hybrid MMC. *IEEE J Emerg Sel Topics Power Electron* 9(3):3622–3633
14. Kong Z, Huang X, Wang Z, Xiong J, Zhang K (2018) Active power decoupling for submodules of a modular multilevel converter. *IEEE Trans Power Electron* 33(1):125–136

# A 24-Pulse Aviation Rectifier Based on Auto-Fed Half-Bridge Auxiliary Circuit



Wenhao Tu, Yongshuai Wang, Hongjuan Ge, Yichen Pan, and Yanbo Shi

**Abstract** In order to suppress input current harmonics and output voltage ripple and simplify the configuration of linear aero AC-DC converters, this paper proposes a 24-pulse rectifier based on an auto-fed half-bridge auxiliary circuit. It consists of a 12-pulse transformer, a rectifier bridge and an auxiliary circuit. The auxiliary circuit is simple in structure and its output is connected in parallel with the load. It injects AC voltage ripple into the DC bus, which is six times the frequency of the power supply. Thus, a 24-pulse DC output is obtained, and pulse multiplication is achieved. In this paper, the circuit structure, operating mode and harmonic suppression principle of the proposed 24-pulse rectifier are analyzed. The output current and output current ripple functions are derived, the parameter optimization study of the autotransformer is carried out, and the KVA rating of the autotransformer is discussed. The simulation and experimental results verify the correctness of the theoretical analysis and the feasibility of the proposed method.

**Keywords** 24-pulse · Harmonic suppression · Half-bridge auxiliary circuit

---

W. Tu · H. Ge (✉) · Y. Shi

College of Civil Aviation, Nanjing University of Aeronautics and Astronautics, Nanjing 210016, China

e-mail: [allenge@nuaa.edu.cn](mailto:allenge@nuaa.edu.cn)

W. Tu

e-mail: [twh2000@nuaa.edu.cn](mailto:twh2000@nuaa.edu.cn)

Y. Shi

e-mail: [shiyambo@nuaa.edu.cn](mailto:shiyambo@nuaa.edu.cn)

Y. Wang · Y. Pan

College of Automation Engineering, Nanjing University of Aeronautics and Astronautics, Nanjing 210016, China

e-mail: [wangyongshuai@nuaa.edu.cn](mailto:wangyongshuai@nuaa.edu.cn)

Y. Pan

e-mail: [shirleychen@nuaa.edu.cn](mailto:shirleychen@nuaa.edu.cn)

© Beijing Paiké Culture Commu. Co., Ltd. 2024

X. Dong and L. Cai (eds.), *The Proceedings of 2023 4th International Symposium on Insulation and Discharge Computation for Power Equipment (IDCOMPU2023)*, Lecture Notes in Electrical Engineering 1103, [https://doi.org/10.1007/978-981-99-7413-9\\_65](https://doi.org/10.1007/978-981-99-7413-9_65)

## 1 Introduction

For aircraft AC power systems, the large number of power electronics and other non-linear components can cause harmonic pollution to the aircraft grid. Harmonics injected into the aircraft power system can have a bad effect on the quality of the aircraft power supply and the stability of the system [1, 2]. The DO160E/F/G test standard for airborne equipment specifies that the Total Harmonic Distortion (THD) of the input current should not exceed 10% [3]. The traditional 12-pulse transformer rectifier unit (TRU) has a theoretical THD of 15.2%, which does not meet the harmonic content limitation standard for airborne equipment. Series-connected LC passive filter circuit on the AC side makes the THD less than 10%, which can meet the harmonic content limit standard of airborne equipment [4]. However, the filtering effect of the LC filter circuit varies greatly under different load conditions, and the harmonic suppression capability is unstable. Since the multi-pulse TRU can simply and effectively suppress harmonics of the on-board input current and ripple of the output voltage. This TRU is widely used in the aviation field [5]. Increasing the number of pulses by increasing the number of output phases of the phase shift transformer is a common and effective method [6]. The traditional isolated 24-pulse TRU is implemented through a combination of two 12-pulse TRUs offset by  $15^\circ$  from each other, or through a phase shift transformer with 12 secondary phase shift windings connected to four rectifier bridges. However, these two structures have large transformer capacities and complex winding structures, resulting in large system size and weight. The autotransformer is smaller in size and capacity than the isolation transformers for the same power conditions. A P-type asymmetric 24-pulse autotransformer rectifier (ATRU) without balance reactor was proposed by Jiang et al. [7] and Zhang et al. [8]. However, its four sets of rectifier bridges are divided into primary and secondary. The output voltage of the rectifier bridges is asymmetrical, which limits the expansibility of the ATRU. It is difficult to achieve pulse multiplication by adding small power auxiliary circuits. References [9–11] proposed a method to increase the number of TRU pulses by increasing the number of taps of the interphase reactor (IPR), thus reducing the input current THD. References [12, 13] proposes a 6-phase output phase shift transformer connected to a double-tap IPR for increasing the number of TRU pulses to 24. However, IPR causes TRU to become complicated.

To simplify the structure and size of the TRU and further reduce the harmonic current injected into the system. This paper proposes a highly reliable and practical 24-pulse TRU based on an auto-fed half-bridge auxiliary circuit. Its structure is simple. The harmonics injected into the rectifier are modulated by an auxiliary auto-fed half-bridge circuit to give the TRU a 24-pulse characteristic. At the same time, it effectively reduces the harmonic and ripple content in the rectifier system to meet the limit standard of harmonic content of on-board equipment.

## 2 Proposed 24-Pulse TRU

### 2.1 The Proposed 24-Pulse TRU Topology Analysis

Figure 1 shows the topology of the 24-pulse TRU proposed in this paper. The auto-fed half-bridge auxiliary circuit is simple. The circuit consists of two equalization capacitors ( $C_1, C_2$ ), an auxiliary autotransformer ( $T_M$ ), and a ripple injection bridge arm ( $D_1, D_2$ ). The primary winding of the auxiliary single-phase autotransformer is connected to the midpoint of two three-phase rectifier bridges. The common point of the primary and secondary windings is connected to the midpoint of the two equalizing capacitors. The secondary winding is connected to the midpoint of the ripple injection bridge arm.

Neglecting the leakage inductance of the 12-pulse phase shift transformer is convenient for the principle analysis. The power electronics operates only in the on and off states, ignoring the on and off processes. The detailed analysis and design procedure is shown below.

The ratio of the input and output line voltages of this 12-pulse phase shift transformer is defined as  $K$ .

$$K = U_i / U \tag{1}$$

where  $U_i$  and  $U$  are the RMS value of the input and output line voltages of the 12-pulse phase shift transformer, respectively.

The turns ratio  $\beta$  of the auxiliary single-phase autotransformer is defined as:

$$\beta = \frac{N_p}{N_s} \tag{2}$$

where  $N_p$  and  $N_s$  are the turns number of the primary and secondary windings of the autotransformer, respectively.

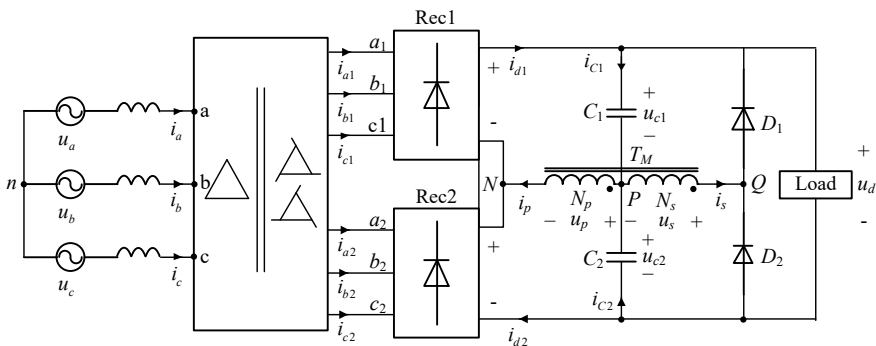


Fig. 1 Circuit of the 24-pulse TRU based on auto-fed half-bridge auxiliary circuit

Assume the three-phase input line voltages of the 24-pulse TRU as:

$$\begin{cases} u_a = U_{in} \sin(\omega t) \\ u_b = U_{in} \sin(\omega t - 2\pi/3) \\ u_c = U_{in} \sin(\omega t + 2\pi/3) \end{cases} \quad (3)$$

Then the three-phase input current of the 24-pulse TRU can be defined as:

$$\begin{cases} i_a = I_i \sin(\omega t + \varphi) \\ i_b = I_i \sin(\omega t + \varphi - 2\pi/3) \\ i_c = I_i \sin(\omega t + \varphi + 2\pi/3) \end{cases} \quad (4)$$

where  $\varphi$  is the phase difference between the three-phase AC voltage and the three-phase AC current, respectively.

From Fig. 2 and Eq. (4), the output current  $i_{d1}$  and  $i_{d2}$  of the two three-phase rectifier bridge are equal amplitude 6-pulse DC currents with a  $30^\circ$  phase shift, which can be expressed as:

$$\begin{aligned} i_{d1} &= \begin{cases} \frac{\sqrt{3}}{K} I_i \sin\left(\omega t + \varphi + \frac{11\pi}{12} - \frac{\pi}{3}k\right), \omega t \in \left(\frac{\pi}{3}k - \varphi - \frac{\pi}{12}, \frac{\pi}{3}k - \varphi + \frac{\pi}{12}\right] \\ \frac{\sqrt{3}}{K} I_i \sin\left(\omega t + \varphi - \frac{11\pi}{12} - \frac{\pi}{3}k\right), \omega t \in \left(\frac{\pi}{3}k - \varphi + \frac{\pi}{12}, \frac{\pi}{3}k - \varphi + \frac{\pi}{12}\right] \end{cases} \\ i_{d2} &= i_{d1} \angle -\frac{\pi}{6} \end{aligned} \quad (5)$$

## 2.2 Operation Modes Analysis

Considering the relation between the current  $i_{d1}$  and  $i_{d2}$ , the proposed 24-pulse TRU has two operation modes, which are analyzed in detail as follows.

As shown in Fig. 3, when the 24-pulse TRU is in operation mode I,  $i_{d1} > i_{d2}$ ,  $i_p > 0$ ,  $i_s > 0$ , the diode  $D_1$  is ON, the diode  $D_2$  is OFF.

The voltage  $u_p$  is expressed in Eq. (6).

$$u_p = \beta u_s = \frac{1}{2} \beta u_d \quad (6)$$

The current  $i_d$  is expressed in Eq. (7).

$$i_d = i_{d1} + \frac{\beta - 1}{2} (i_{d1} - i_{d2}) \quad (7)$$



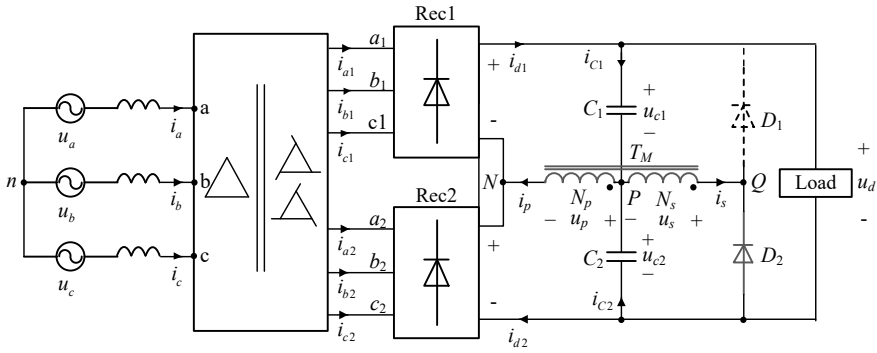


Fig. 4 The operation mode II

$$i_d = i_{d2} + \frac{1 - \beta}{2} (i_{d1} - i_{d2}) \tag{9}$$

### 2.3 Output Current and Optimal Turns Ratio $\beta$

The performance of the proposed 24-pulse TRU for ripple suppression will be analyzed below.

From Eqs. (5), (7), and (9), the output current  $i_d$  can be expressed as:

$$i_d = \begin{cases} \frac{\sqrt{\beta^2 + 7 - 4\sqrt{3}N_1}}{2N_3} I_i \sin\left(\omega t + \varphi + \pi - \theta - \frac{k\pi}{6}\right), & \omega t \in \left[\frac{k\pi}{6} - \varphi - \frac{\pi}{12}, \frac{k\pi}{6} - \varphi\right] \\ \frac{\sqrt{\beta^2 + 7 - 4\sqrt{3}N_1}}{2N_3} I_i \sin\left(\omega t + \varphi + \theta - \frac{k\pi}{6}\right), & \omega t \in \left[\frac{k\pi}{6} - \varphi, \frac{k\pi}{6} - \varphi + \frac{\pi}{12}\right] \end{cases} \tag{10}$$

$$0 < \theta = \arctan\left(\frac{2 - \sqrt{3}}{\beta}\right) < 90^\circ$$

When the output current is composed of 24 current vectors with equal amplitude and  $15^\circ$  phase shift, the output current ripple is the smallest. Analyzing Eq. (10), we can get the value of  $\beta$  at this time, as shown in Eq. (11).



$$\begin{aligned} \theta &= 11\pi / 24 \\ \beta &= \sqrt{6} - \sqrt{2} - 1 \approx 0.035 \end{aligned} \tag{11}$$

The calculation formula of ripple factor  $\gamma_{i_d}$  as follows:

$$\gamma_{i_d} = \frac{I_{d \max} - I_{d \min}}{2I_{dav}} \tag{12}$$

where  $I_{d \max}$  is the maximum output current,  $I_{d \min}$  is the minimum output current,  $I_{dav}$  is the average output current. From Eq. (10), they can be calculated as Eqs. (13), (14), (15).

$$I_{d \max} = \frac{\sqrt{\beta^2 + 7 - 4\sqrt{3}N_1}}{2N_3} I_i \tag{13}$$

$$I_{d \min} = \frac{(2 - \sqrt{3})N_1}{2N_3} I_i \tag{14}$$

$$I_{dav} = \frac{[9\sqrt{6} - 15\sqrt{2} - (3\sqrt{6} + 3\sqrt{2} - 12)\beta]N_1}{2\pi N_3} I_i \tag{15}$$

From Eqs. (12), (13), (14), (15), when the turns ratio  $\beta$  is 0.035, the ripple factor  $\gamma_{i_d}$  is minimal, 0.0043.

### 3 kVA of the Auxiliary Single-Phase Autotransformer

When the proposed 24-pulse TRU operates under the optimal parameters,  $\beta = 0.035$ , from Eq. (5), the current  $i_p$  can be expressed as:

$$i_p = \begin{cases} \frac{N_1}{N_3} I_i \sin\left(\omega t + \varphi + \pi - \frac{k\pi}{3}\right), & \omega t \in \left[\frac{k\pi}{3} - \varphi - \frac{\pi}{12}, \frac{k\pi}{3} - \varphi + \frac{\pi}{12}\right] \\ \frac{N_1}{N_3} I_i \sin\left(\omega t + \varphi - \frac{\pi}{6} - \frac{k\pi}{3}\right), & \omega t \in \left[\frac{k\pi}{3} - \varphi + \frac{\pi}{12}, \frac{k\pi}{3} - \varphi + \frac{3\pi}{12}\right] \end{cases} \tag{16}$$

From Eq. (16), the RMS value of the currents  $i_p$  can be expressed as:

$$I_p = \sqrt{\frac{\pi - 3}{2\pi}} \frac{N_1}{N_3} I_i \tag{17}$$

From Eqs. (6) and (8), the RMS value of the output voltage  $U_p$  can be expressed as:

$$U_p = 0.0175U_d \tag{18}$$

The RMS value of current  $I_d$  can be calculated as:

$$I_d \approx 0.13475 \frac{N1}{N3} I_i \tag{19}$$

Therefore, The kVA rating  $P$  of the auxiliary single-phase autotransformer can be calculated as:

$$P = (U_p I_p + U_s I_s) / 2 = 1.948\% U_d I_d \tag{20}$$

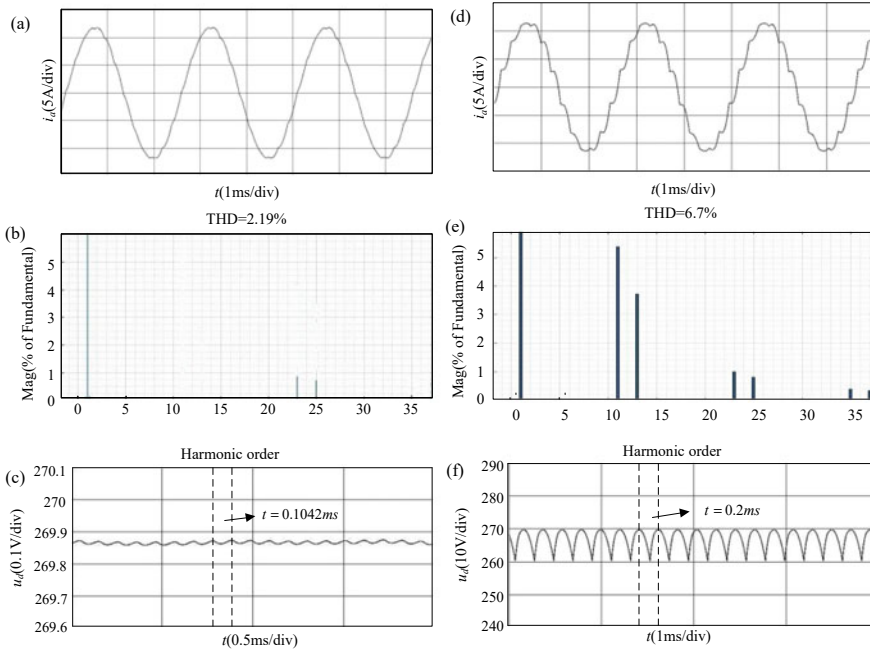
### 4 Simulation and Experiments

The correctness and effectiveness of the proposed 24-pulse TRU are verified below. In this paper, a simulation model is built for simulation analysis. In addition, a 24-pulse TRU principle prototype was built for experimental verification. The experimental equipment includes: Chroma 61704 programmable AC power supply, Tektronix 5 series MSO56 mixed signal oscilloscope, etc. The parameters of the simulation model and the experimental prototype are shown in Table 1. In the experimental prototype, the autotransformer is BOD16/25-5, the three-phase rectifier bridge is MDS series, and the diode is STPSC406B-TR.

When the TRU is connected to the auxiliary circuit, the simulation waveform is shown in Fig. 5a–c. The input current  $i_a$  contains 24 step waves in one cycle, of which the THD is 2.19%. And the output voltage contains 24 pulses in one cycle, of which the RMS value is 269.98 V.

**Table 1** The parameters of simulation model and prototype

Parameters	Value
Rated power	2.7 kW
System input three-phase power	115 V/400 Hz
Primary side turns $N_p$	15
Secondary side turns $N_s$	409
Autotransformer winding turns ratio $\beta$	0.035
Equalization capacitor $C_1, C_2$	68 $\mu$ F
Output resistance	27 $\Omega$
Phase shift transformer turns ratio $K$	2



**Fig. 5** Simulation waveforms **a** Input current  $i_a$  with auxiliary circuit, **b** THD with auxiliary circuit, **c** Output voltage  $u_d$  with auxiliary circuit, **d** Input current  $i_a$  without auxiliary circuit, **e** THD without auxiliary circuit, **f** Output voltage  $u_d$  without auxiliary circuit

When the TRU is not connected to the auxiliary circuit, it presents a 12-pulse characteristic, and the simulation waveform is shown in Fig. 5d–f. The input current  $i_a$  contains 12 step waves in one cycle, of which the THD is 6.7%. And the output voltage contains 12 pulses in one cycle, is not smooth enough, of which the RMS value is 266 V. It can be seen that the auxiliary circuit has an obvious effect, and the THD of the input current of the 24-pulse TRU directly drops from 6.7 to 2.19%.

Therefore, with the auto-feeding half-bridge auxiliary circuit, the TRU can output 24 pulses, effectively suppressing harmonics.

When the proposed 24-pulse TRU is not connected to the auto-fed half-bridge auxiliary circuit, the experimental waveforms are shown in Figs. 6a, 7a, and 8a. At this time, the system is a 12-pulse TRU. The TRU output current and voltage are fluctuating and unsmooth without adding output capacitor. There are 12 pulse waves in one cycle, the output voltage RMS value is 268.8 V, the output current RMS value is 9.95 A, the input current RMS value is 8.22 A, there are 12 step waves in one cycle, and the THD experimental value is 10.82%.

When the proposed 24-pulse wave TRU is connected to the auto-fed half-bridge auxiliary circuit, the experimental waveforms are shown in Figs. 6b, 7b, and 8b. It can be observed that the output voltage and output current waveforms of TRU are relatively stable and close to constant values, showing 24 pulse wave characteristics.

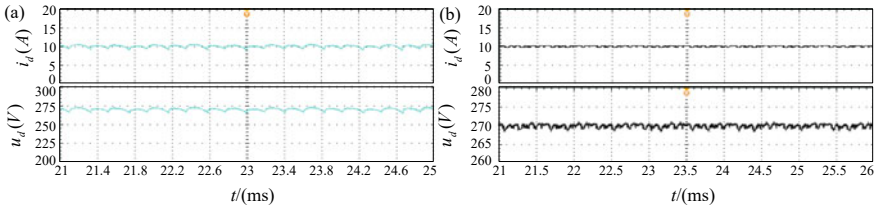


Fig. 6 Output current and voltage test a 12 pulse TRU, b 24 pulse TRU

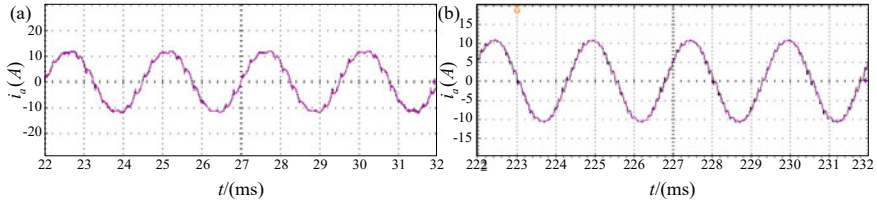


Fig. 7 Input current test a 12 pulse TRU, b 24 pulse TRU

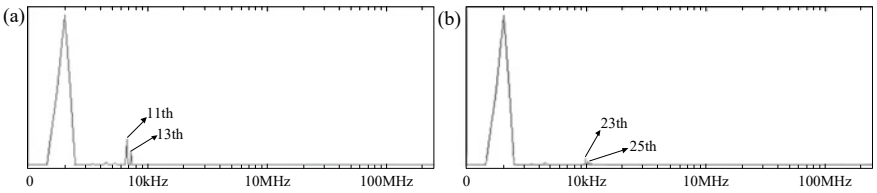


Fig. 8 Input current FFT analysis a 12 pulse TRU, b 24 pulse TRU

The output voltage RMS value is 269.7 V and the output current RMS value is 9.99 A. The TRU input current consists of a 24-step waveform, which approximates a sine wave, with a THD experimental value of 4.02% and an input current RMS value of 8.22 A. It can be seen that the effect of the auto-fed auxiliary half-bridge circuit is obvious. It changes the TRU from 12 to 24 pulses and achieves pulse multiplication, thus improving the system’s ability to suppress harmonics as well as the ability to suppress ripple. It makes the TRU input current THD drop from 10.82 to 4.02%, meeting the airline harmonic standard of less than 10%, without the need for additional LC filter circuit design, and improves the efficiency of the system.

## 5 Conclusion

This paper proposes a 24-pulse TRU based on an auto-fed half-bridge auxiliary circuit. It has a simple structure and is composed of a 12-pulse phase-shifting transformer, two sets of rectifier bridges and auxiliary circuits. It can simultaneously reduce the input current harmonic content and output voltage ripple content, achieve 24-pulse DC output, and does not require a control circuit, and is robust.

In this paper, the proposed 24-pulse TRU circuit topology, operating mode and 24-pulse waveform principle are analyzed in detail. The output current expression is derived and the output current ripple content is theoretically derived as 0.0043. The optimum turns ratio of the auxiliary autotransformer is designed as 0.035. At the optimum turns ratio, the rated kVA of the autotransformer is only 1.948% Po. The autotransformer has a high winding utilization and a simple structure. Simulation and experimental results show that the TRU increases from 12 to 24 pulses with the auxiliary circuit, the input current THD decreases, and the output voltage is sufficiently smooth. The 24-pulse TRU topology method proposed in this paper is correct and feasible.

**Acknowledgements** This work was supported by the National Science Foundation of China (NSFC) under grant U1933115.

## References

1. Madonna V, Giangrande P, Galea M (2018) Electrical power generation in aircraft: review, challenges, and opportunities. *IEEE Trans Transp Electrification* 4(3):646–659
2. Bozhko S, Yang T, Le Peuedic J et al (2018) Development of aircraft electric starter-generator system based on active rectification technology. *IEEE Trans Transportation Electrification* 4(4):985–996
3. Chen J, Shen J, Chen J, Shen P et al (2019) Investigation on the selection and design of step-up/down 18-pulse ATRUs for more electric aircrafts. *IEEE Trans Transportation Electrification* 5(3):795–811
4. Swamy M, Kume TJ, Takada N (2010) A hybrid 18-pulse rectification scheme for diode front-end rectifiers with large DC-bus capacitor. *IEEE Trans Ind Appl* 46(6):2484–2494
5. Wen J, Qin H, Wang S et al (2012) Basic connections and strategies of isolated phase-shifting transformers for multipulse rectifiers: a review. In: 2012 Asia-Pacific symposium on electromagnetic compatibility, pp 105–108. IEEE, Singapore
6. Kalpana R, Singh B, Bhuvaneshwari G (2018) A 20-pulse asymmetric multiphase staggering autoconfigured transformer for power quality improvement. *IEEE Trans Power Electron* 33(2):917–925
7. Jiang F, Ge H, Dong X, Zhang L (2018) Research on a new 12-pulse step-up and step-down aviation auto-transformer rectifier. *J Power Electron* 18(1):266–276
8. Zhang L, Ge H, Jiang F et al (2018) Step-up and step-down asymmetrical 24-pulse autotransformer rectifier. *J Power Electron* 18(5):1536–1544
9. Shih D, Young C, Whiteley C (2016) A passive auxiliary circuit with interphase transformer applied in 12-pulse converters to provide clean power utility interface. *J Chin Instit Eng* 39(8):986–996

10. Lian Y, Yang S, Yang W (2019) Optimum design of 48-pulse rectifier using unconventional interphase reactor. *IEEE Access* 7:61240–61250
11. Choi S, Lee B, Enjeti PN (1997) New 24-pulse diode rectifier systems for utility interface of high-power AC motor drives. *IEEE Trans Ind Appl* 33(2):531–541
12. Lian Y, Yang S, Xu K, Li Y, Yang W (2017) Harmonic reduction mechanism at DC link of two different 24-pulse rectifiers. In: 2017 IEEE transportation electrification conference and expo, Asia-Pacific (ITEC Asia-Pacific). IEEE, Harbin, pp 1–6
13. Meng F, Xu X, Gao L (2017) A simple harmonic reduction method in multipulse rectifier using passive devices. *IEEE Trans Ind Inf* 13(5):2680–2692

# Study on Analysis Method of Zinc Oxide Line Arrester Fracture



Qi Yang, Yang Tian, Haixiang Chen, Lei Gao, Zhiyong Deng,  
and Zhuohong Pan

**Abstract** The operation experience shows that the zinc oxide line arrester fracture is a common fault due to instantaneous large current. In view of the difficulties in the fracture analysis of zinc oxide line arresters, a highly reliable, objective, scientific and practical fracture prediction method for zinc oxide line arresters is proposed. Calculate that maximum pulse power of the zinc oxide valve plate by operate a nonlinear time domain method according to the waveform data of the obtained lightning current and the nonlinear resistance model of the lightning arrester; According to the internal crack defect data of the zinc oxide varistor and the calculated maximum pulse power, the fracture of the zinc oxide line arrester is predicted. Finally, a case study is given to illustrate the effectiveness of the proposed method. The work of this paper can provide an effective reference for the operation and maintenance of line arrester.

**Keywords** Zinc oxide arrester · Nonlinear volt-ampere characteristic · Instantaneous power · Fracture

---

Q. Yang

Hunan Province Key Laboratory of Intelligent Live Working Technology and Equipment (Robot),  
Changsha, China

Y. Tian (✉) · L. Gao · Z. Pan

School of Electrical and Electronic, North China Electric Power University, Baoding, China  
e-mail: [2585824441@qq.com](mailto:2585824441@qq.com)

Z. Pan

e-mail: [panzhuohong@ncepu.edu.cn](mailto:panzhuohong@ncepu.edu.cn)

H. Chen

Live Inspection and Intelligent Operation Technology, State Grid Corporation Laboratory,  
Changsha, China

Z. Deng

State Grid Hunan Extra High Voltage Transmission Company, Hengyang, China

© Beijing Paiké Culture Commu. Co., Ltd. 2024

X. Dong and L. Cai (eds.), *The Proceedings of 2023 4th International Symposium on Insulation and Discharge Computation for Power Equipment (IDCOMPU2023)*, Lecture Notes in Electrical Engineering 1103, [https://doi.org/10.1007/978-981-99-7413-9\\_66](https://doi.org/10.1007/978-981-99-7413-9_66)

## 1 Introduction

With the development of economic technology and the improvement of people's living standards, electrical energy has become an essential secondary energy source for people's production and life, bringing endless convenience to people's production and life. Therefore, ensuring the stable and reliable supply of electrical energy has become one of the most important tasks of the power system.

Lightning strikes that cause transmission lines to trip are still one of the reasons for endangering the safe and stable operation of the lines [1–4]. The installation of line surge arresters is the most direct and effective means to improve the level of line lightning resistance, and can effectively reduce the rate of lightning trips [5–8]. Zinc oxide line arrester is an important part of the power system, its application in the power system, mainly used to release the system in the operation process of various inrush current and absorb energy, limit the system operation process of normal operation shock, lightning strikes, etc. caused by overvoltage and so on [9–11].

Under various types of shocks, the varying magnitudes of the shock energy make the ZnO varistors absorb different amounts of energy under different shocks, thus causing various kinds of destruction and damage to the valve, mainly thermal collapse [12–14], perforation [15–18], fracture [19–21]. Thermal collapse is due to the effect of leakage currents, which increases the temperature of the valve sheet, thus leading to a disruption of the thermal equilibrium relationship of the valve sheet. Perforation is due to a relatively high current density in a region where the temperature rise causes the grains to be melted resulting in the formation of small holes through the valve sheet, while fracture is a physical damage caused by excessive energy absorption generating a large thermal stress [22–24]. Operational experience has shown that all three failure modes occur when AC or DC regulated voltage is applied to the ZnO valve disc [25–27]. However, if only an inrush voltage or fault current is applied to the zinc oxide valve disc, the line arrester will only perforate or fracture. The failure mode is dominated by fracture under short duration high pulse currents, which is exactly what lightning currents are.

At present, the replacement of zinc oxide line surge arresters is generally a direct replacement after breakage, or an early replacement by virtue of manual experience. Direct replacement after breakage may lead to problems with grid outages, while early replacement based on manual experience may produce problems such as wasted components. Currently, there is a lack of predictive research specifically for zinc oxide line arrester fracture caused by the thermal stress generated by lightning; therefore, the grid system is also unable to predict the zinc oxide line arrester fracture caused by the thermal stress generated by lightning, so that the zinc oxide line arrester can be replaced in advance, or the zinc oxide line arrester can be targeted for testing and overhaul [28].

In view of this, this paper proposes a highly reliable, objective and scientifically practical method for predicting the fracture of zinc oxide line arresters. Firstly, the volt-ampere characteristic curve of the zinc oxide valve in the zinc oxide line arrester is obtained to form a non-linear resistance model of the arrester; the maximum pulse



power of the zinc oxide valve is calculated based on the waveform data curve of the lightning current obtained; the fracture of the zinc oxide line arrester is predicted based on the crack defect data within the zinc oxide valve itself and the maximum pulse power calculated. The work in the thesis can provide an effective reference for the operation and maintenance of line surge arresters.

## 2 Calculate the Maximum Impulse Power of the Arrester Under Lightning Current Impact

### 2.1 Volt-Ampere Characteristics of Zinc Oxide Valve Plates

Zinc oxide grain boundary barrier has Schottky effect, which shows high resistance at low voltage and low resistance when it exceeds critical voltage. The typical nonlinear volt-ampere characteristics of zinc oxide valve plate are shown in Fig. 1.

According to the data provided by the manufacturer or the test can determine the voltammetry characteristic curve of the zinc oxide valve disc, that is

$$f = E(J) \tag{1}$$

where,  $f$  is the voltammetry characteristic curve of zinc oxide valve disc, electric field intensity is expressed by  $E$  (V/mm), current density is expressed by  $J$  (A/mm<sup>2</sup>).

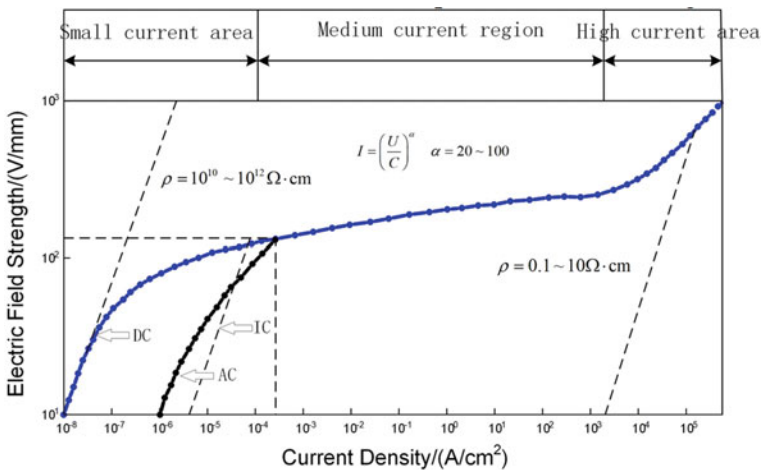


Fig. 1 Typical volt-ampere characteristics of zinc oxide valve

## 2.2 Double Exponential Function Lightning Current Waveforms

A double exponential function waveform is used to simulate the lightning current, with  $T_1$  being the wave head time;  $T_2$  being the half-amplitude time, at which point the waveform can be recorded as  $T_1/T_2$ , as shown in Fig. 2.

The lightning current rises approximately exponentially with time to a peak and then falls approximately exponentially again as a double exponential function of the lightning current waveform, expressed as follows:

$$i(t) = I_m k (e^{-\alpha t} - e^{-\beta t}) \tag{2}$$

with the peak value of lightning current  $I_m$ , instantaneous value of lightning current  $i$ , wavefront coefficient  $\alpha$ , wave tail coefficient  $\beta$ , and waveform correction coefficient  $k$ .

The volt-ampere characteristic curve of the zinc oxide valve sheet can be determined from data provided by the manufacturer or from tests, i.e. (Table 1).

Users can choose their own parameters according to their needs.

The empirical expression for the probability distribution of the lightning current amplitude is

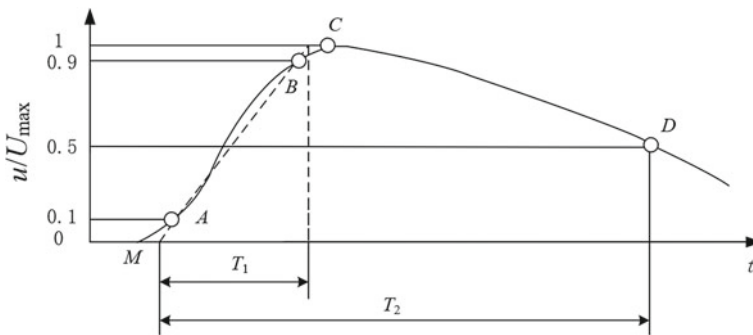
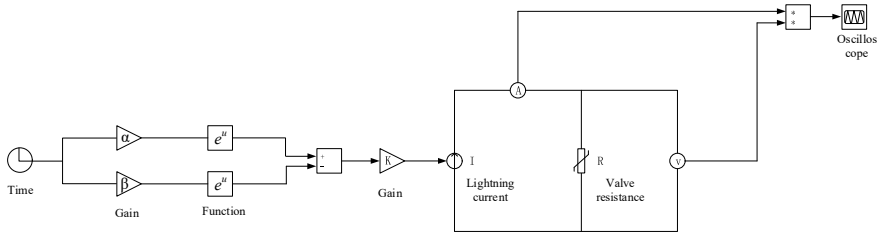


Fig. 2 Standard waveforms and parameters of lightning impulse voltage

Table 1 Parameter values corresponding to standard waveforms

Lightning waveform ( $\mu\text{s}$ )	$\alpha$	$\beta$	k
80/20	$7.713 \times 10^4$	$2.484 \times 10^5$	2.32
10/200	$3.913 \times 10^3$	$2.301 \times 10^5$	1.09
10/350	$2.125 \times 10^3$	$2.456 \times 10^5$	1.05
1.2/50	$1.471 \times 10^4$	$2.074 \times 10^6$	1.04
0.25/100	$6.984 \times 10^3$	$1.081 \times 10^7$	1.01



**Fig. 3** Matlab simulation module of arrester pulse power under lightning current impact

$$\lg P = -\frac{I_m}{88} \tag{3}$$

where the probability that the lightning current amplitude is greater than or equal to  $I_m$  is  $P$ ;  $I_m$  is the lightning current amplitude, kA. Typically, a nominal discharge current of 20 kA or 10 kA rating is used to test line surge arresters.

### 2.3 Matlab Simulation of Lightning Arrester Pulse Power Under Lightning Current Impact

The instantaneous power  $p$  is expressed as

$$p(t) = u(t)i(t) \tag{4}$$

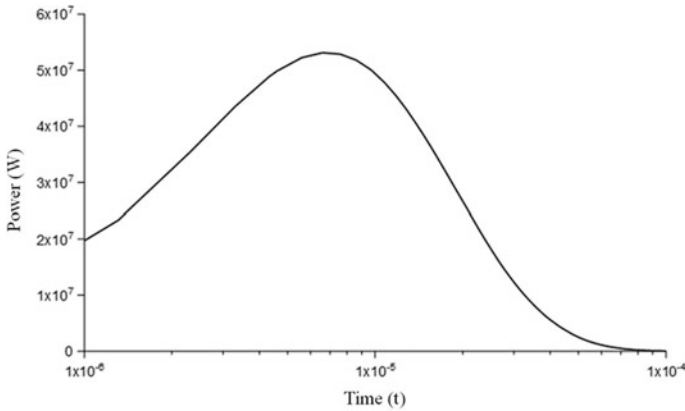
with the voltage applied to the valve plate  $u$  and the current through the valve plate  $i$ .

The maximum pulse power  $p_c = \max(p(t))$ . The solution model is carried out via matlab and the model is schematically shown as follows (Fig. 3).

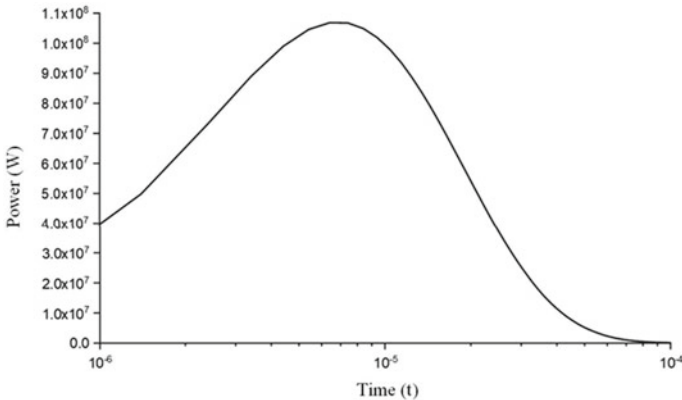
The simulations are based on a 23 mm thick and 63 mm diameter arrester valve sheet as an example, and the non-linear resistance of the valve sheet can be found from the collated zinc oxide volt-ampere characteristic curve. The matlab simulation results for the valve and lightning current parameters are shown in Figs. 4, 5, 6 and 7, with the highest point value being the maximum pulse power  $p_c$ .

## 3 Valve Break Determination and Case Studies Based on Griffith Standards

Zinc oxide valves, like other ceramics, are subject to microscopic defects that are invisible to the naked eye during the manufacturing process. Presumably, when subjected to large stresses, these small defects can develop into cracks and thus lead to fracture failure. However, to determine the boundary conditions for fracture



**Fig. 4** Pulse power of valve plate under 10 kA impact of 8/20  $\mu$ s lightning waveform ( $p_c = 5.31 \times 10^7$ )



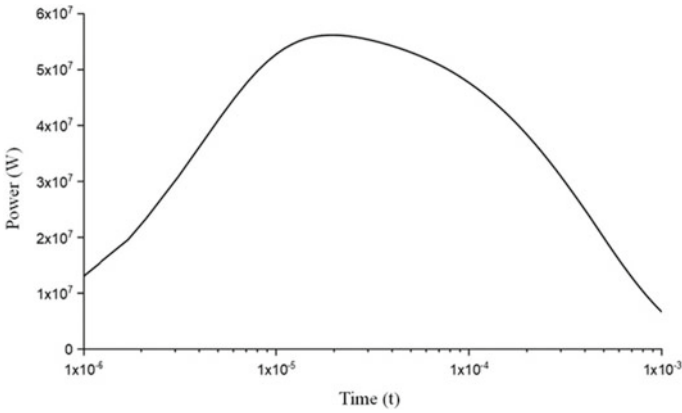
**Fig. 5** Pulse power of valve plate under 20 kA impact of 8/20  $\mu$ s lightning waveform ( $p_c = 1.06866 \times 10^8$ )

of the arrester valve piece, we need to consider the most serious internal defect, i.e. a small crack perpendicular to the cylindrical axis and the application field.

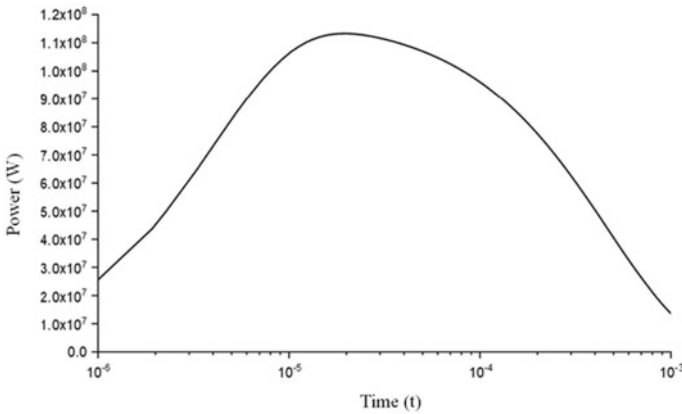
Assuming that the valve has a height of  $L$  and a diameter of  $d$ , and all the electrical energy it consumes is converted to heat energy, the increment of temperature rise from the reference temperature  $T_0$  is approximately

$$T(t) - T_0 = \frac{1}{mC_V} \int_0^t (x)V(x)dx \tag{5}$$

where,  $I$  is current,  $V$  is voltage,  $m$  is mass, and specific heat is expressed by  $C_V$ .



**Fig. 6** Pulse power of valve plate under 10 kA impact of 10/350  $\mu$ s lightning waveform ( $p_c = 5.61873 \times 10^7$ )



**Fig. 7** Pulse power of the valve plate under 20 kA impact of 10/350  $\mu$ s lightning waveform ( $p_c = 1.13284 \times 10^8$ )

We can think of the horizontal elongation of a cylinder as a one-dimensional problem:

$$\frac{\partial f}{\partial x} = \rho \frac{\partial^2 u}{\partial t^2} \tag{6}$$

with stress  $f$ , displacement  $u$ , and the density  $\rho$ . According to Hooke’s law, the relationship between stress and displacement can be expressed as follows

$$f = E \frac{\partial u}{\partial x} - E\alpha(T - T_0) \tag{7}$$

with the coefficient of thermal expansion  $\alpha$  and the modulus of elasticity  $E$ .

For convenience, the dissipation of elastic energy caused by the damping is ignored. Ultimately, the elastic displacement  $u$  can be expressed by the following partial differential equation

$$E \frac{\partial^2 u}{\partial x^2} = \rho \frac{\partial^2 u}{\partial t^2} \tag{8}$$

Although electrode is usually connected to the end of valve piece, and likely impact we ignore them, and that at the end of the cylinder without traction, namely when the  $x = 0$ , and  $x = L, f = 0$ . So if I plug in (7)

$$E \frac{\partial u}{\partial x} = E\alpha T \tag{9}$$

Besides, the displacement of all cross sections of the varistor has an initial constraint of  $u(x, 0) = 0$ . Substituting the relative displacement parameter  $v(x, t)$ , we can get:

$$u(x, t) = v(x, t) + x\alpha(T(t) - T_0) \tag{10}$$

In this way, the nonhomogeneous partial differential equation about  $v$  can be obtained.

$$\frac{E}{\rho} \frac{\partial^2 v}{\partial x^2} - \frac{\partial^2 v}{\partial t^2} = x\alpha \frac{\partial^2 T}{\partial t^2} \tag{11}$$

Using Green function method to solve Eq. (7), it can be obtained

$$v = \frac{4\alpha}{L} \sqrt{\frac{\rho}{E}} \sum_{\substack{n=1 \\ n=2j-1}}^{\infty} \frac{\cos \frac{n\pi}{L}x}{(n\pi/L)^3} \int_0^t dt' \ddot{T}(t') \sin \omega_n(t-t') - \frac{\alpha L}{2} \int_0^t dt' \ddot{T}(t')(t-t') \tag{12}$$

According to the expression of relative displacement, the stress can be found from Eqs. (7) and (10) as follows.

$$f = -4\alpha L \sqrt{E\rho} \sum_{\substack{n=1 \\ n=2j-1}}^{\infty} \frac{\sin \frac{n\pi}{L}x}{(n\pi)^2} \int_0^t dt' \ddot{T}(t') \sin \omega_n(t-t') \tag{13}$$

The final result is approximated by the first term of the expanded polynomial, so

$$|f_{\max}| \leq \frac{4\alpha L\sqrt{E\rho}}{\pi^2} \int_0^t |\ddot{T}(t')| dt' \tag{14}$$

Simultaneous equations (5):

$$|f_{\max}| \leq \frac{4\alpha L\sqrt{E\rho}}{\pi^2 m C_V} P_{\max} \tag{15}$$

With reference to the mechanics of materials, the stress required to cause fracture naturally by a defect of size  $a$  in the interior of a lightning arrester, i.e. the Griffith relationship, is

$$f_c = \frac{K_C}{\sqrt{\frac{2}{\pi} a_C}} \tag{16}$$

where the fracture toughness is expressed in  $K_C$ , for zinc oxide lightning arrester,  $K_C$  is generally taken as 2.

Typically, fracture occurs if the local tensile stresses exceed the Griffith criterion for crack-like defects within the valve disc. Fracture naturally results when the valve diameter  $d$ , the maximum pulse power  $P_c$ , the crack size  $a$  in the valve and the material properties of the valve are in the full range of the following equation.

$$P_c \geq F K_c \frac{d^2}{\sqrt{a}} \sqrt{\frac{\rho C_v}{\alpha Y}} \tag{17}$$

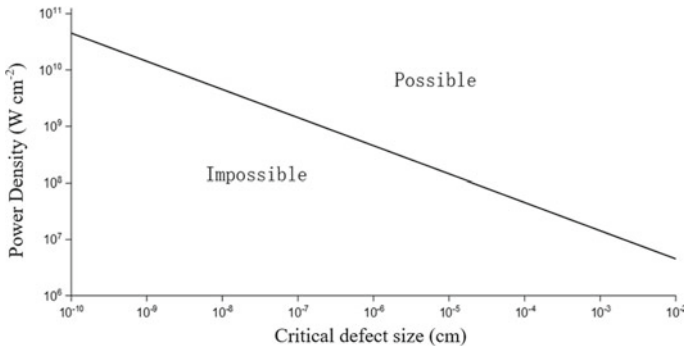
where  $F$  is the geometric constant,  $F = 32\sqrt{2}/\pi^{3.5}$ ;  $d$  is the diameter of the valve piece;  $\rho$  is the density of the valve piece,  $\rho = 5.5 \text{ g/cm}^3$ ;  $C_v$  is the specific heat,  $C_v = 0.6 \text{ J/(gK)}$ ;  $\alpha$  denotes the coefficient of thermal expansion,  $\alpha = b_1 + b_2 T + b_3 \ln T$ , where  $b_1 = -2.375 \times 10^{-5}$ ,  $b_2 = -3.76 \times 10^{-9}$  and  $b_3 = 5.11 \times 10^{-6}$ ; The Kelvin temperature is expressed in  $T$ , usually taken as 293 K; the Young’s modulus of the material is expressed in  $Y$ , usually taken as  $1.7 \times 10^7 \text{ psi}$ .

Collation gives

$$\sqrt{a} \geq \frac{F K_c d^2 \sqrt{\frac{\rho C_v}{\alpha Y}}}{P_c} = \frac{C_0 d^2}{P_c} \tag{18}$$

where  $C_0$  is a constant,  $3.5518 \times 10^5$ .

Substituting for the power density  $\varphi$ , the above equation can become



**Fig. 8** The relationship between power density and critical defect size

$$\sqrt{a} \geq \frac{C_0 d^2}{P_c} = \frac{C_0 d^2}{\varphi \pi \frac{d^2}{4}} = \frac{4C_0}{\pi \varphi} = \frac{C_1}{\varphi} \tag{19}$$

where  $\varphi$  is the power density,  $W\text{ cm}^{-2}$ ;  $C_1$  is the constant,  $4.5223 \times 10^5$ .

The relationship between the power density and the critical defect size can be obtained from Eq. (19) as shown in Fig. 8.

NDT techniques allow the size of defects within the valve piece to be determined, and where the pulse current waveform is known, the relationship between power density and critical defect size can be used to determine the likelihood of fracture occurring.

## 4 Conclusion

For the failure mode of zinc oxide line arrester absorbing lightning current leading to fracture, the thesis proposes a thermal stress leading to the evaluation method of zinc oxide line arrester fracture, through the relevant research to form the conclusion as follows.

- (1) Based on the lightning current waveform, a matlab simulation model of the arrester pulse power under lightning current impact is built, and the change in power after the valve piece is impacted by the lightning current can be clearly observed through the simulation results.
- (2) Based on the conclusion (1) can be known, the valve piece by the lightning current impact after the maximum power, and then based on Griffith standard can determine the valve piece in a given maximum power fracture critical defect size, iteration can be obtained many times between the power density and critical defect size relationship graph. Based on this graph, a determination is made as to whether fracture is likely to occur given the pulse current waveform.



## References

1. Wang Z, Liu K, Li M et al (2020) Co-simulation and analysis of “three transformers” for UHV transformer under DC-bias. *High Voltage Eng* 46(12):4097–4105
2. Munukutla K, Vittal V, Heydt GT et al (2010) A Practical evaluation of surge arrester placement for transmission line lightning protection. *IEEE Trans Power Delivery* 25(3):1742–1748
3. Zheng Z, Boggs SA, Imai T et al (2010) Computation of arrester thermal stability. *IEEE Trans Power Delivery* 25(3):1526–1529
4. Valsalal P, Usa S, Udayakumar K (2011) Importance of capacitance on metal oxide arrester block model for VFTO applications. *IEEE Trans Power Delivery* 26(2):1294–1295
5. Atefi MA, Sanaye-Pasand M, Bahari S (2013) Preventing transformer energizing resonant overvoltages using surge arrester temperature rise index and controlled closing method. *IEEE Trans Power Delivery* 28(2):998–1006
6. Lira GRS, Costa EG (2013) MOSA monitoring technique based on analysis of total leakage current. *IEEE Trans Power Delivery* 28(2):1057–1062
7. Xu Z, Zhao L, Ding A et al (2013) A current orthogonality method to extract resistive leakage current of MOSA. *IEEE Trans Power Delivery* 28(1):93–101
8. Zeinoddini-Meymand H, Vahidi B, Naghizadeh RA et al (2013) Optimal surge arrester parameter estimation using a PSO-based multiobjective approach. *IEEE Trans Power Delivery* 28(3):1758–1769
9. Tuzcek MN, Hinrichsen V (2014) Recent experimental findings on the single and multi-impulse energy handling capability of metal-oxide varistors for use in high-voltage surge arresters. *IEEE Trans Power Delivery* 29(5):2197–2205
10. Prasad V (2015) Possible measures to enhance the performance of metal-oxide arresters in the EHV network under very fast transients. *IEEE Trans Power Delivery* 30(2):783–790
11. Tuzcek MN, Bröker M, Hinrichsen V et al (2015) Effects of continuous operating voltage stress and AC energy injection on current sharing among parallel-connected metal-oxide resistor columns in arrester banks. *IEEE Trans Power Delivery* 30(3):1331–1337
12. Han Y, Li Z, Zheng H et al (2016) A decomposition method for the total leakage current of MOA based on multiple linear regression. *IEEE Trans Power Delivery* 31(4):1422–1428
13. Li ST, He JQ, Lin JJ et al (2016) Electrical-thermal failure of metal-oxide arrester by successive impulses. *IEEE Trans Power Delivery* 31(6):2538–2545
14. He J, Lin J, Liu W et al (2017) Structure-dominated failure of surge arresters by successive impulses. *IEEE Trans Power Delivery* 32(4):1907–1914
15. Tsukamoto N, Ishii M (2017) Repetitive impulse withstand performance of metal-oxide varistors. *IEEE Trans Power Delivery* 32(4):1674–1681
16. Bokoro P, Doorsamy W (2018) Reliability analysis of low-voltage metal-oxide surge arresters using accelerated failure time model. *IEEE Trans Power Delivery* 33(6):3139–3146
17. Brito VS, Lira GRS, Costa EG et al (2018) A Wide-range model for metal-oxide surge arrester. *IEEE Trans Power Delivery* 33(1):102–109
18. Fu Z, Wang J, Bretas A et al (2018) Measurement method for resistive current components of metal oxide surge arrester in service. *IEEE Trans Power Delivery* 33(5):2246–2253
19. Zhang Y, Wang Y, Han B et al (2018) Mechanism and mitigation of power fluctuation over-voltage for ultrahigh voltage half-wave length transmission system. *IEEE Trans Power Delivery* 33(3):1369–1377
20. An Z, Hu S, Cai H et al (2021) Research on the improvement of multiple lightning strike action characteristics of arrester discharge counter. *Electric Porcelain Arrester* 05:25–29+35
21. Li H, He Z, Chen S et al (2021) Transient overvoltage modeling analysis of transmission towers and grounding systems based on EMTP. *Electric Porcelain Arrester* 05:107–114
22. Li Y, Liu Y, Yu D (2021) Lightning arrester defect classification technology based on small samples and Bayesian reasoning. *New Technol Electr Eng* 40(11):56–63
23. Liu L, Zhao T, Yang L et al (2021) Analysis of lightning protection capability of distribution transformers under different base towers under lightning strikes. *Electric Porcelain Arrester* 05:1–8

24. Liu S, Hou Y, Sheng M et al (2021) Research on the selection of arresters for high-altitude AC overhead lines. *Electric Porcelain Arrester* 05:9–15+24
25. Wang Y, Zhang L, Xi Z et al (2021) Effect of porosity and grain size inhomogeneity coefficient on failure of high potential gradient zinc oxide ceramics under square wave pulse and high current. *Electric Porcelain Arrester* 05:149–155+163
26. Wang Z, Li T, Wang S et al (2021) Evaluation of shielding protection performance of arresters for high-voltage AC transmission lines in Zhejiang Ford. *Electric Porcelain Arrester* 05:61–65
27. Xu P (2021) Analysis and countermeasures of abnormal leakage current of 220 kV zinc oxide surge arrester. *Electric Ceramic Surge Arrester* 05:36–40
28. Yu D, Liu Y, Ding J et al (2021) Design of a leakage current sensor against strong power frequency magnetic field interference. *Electric Ceramic Surge Arrester* 05:48–53
29. Zhang Z, Tao F, Chen S et al (2021) Research on the thermal dissipation characteristics and influencing factors of MOA under transient shock load. *Electric Ceramic Surge Arrester* 04:112–117

# Multiphysics Coupling Simulation and Analysis of Influencing Factors on Temperature Rise Characteristics of Tri-Post Insulator GIL



F. F. Wu, S. Y. Xie, X. Lin, M. H. Chen, and C. H. Zhang

**Abstract** In this paper, a 1100 kV GIL thermal–mechanical–electrical multi-physics coupling simulation model was established, the evolution characteristics of the internal temperature field of the tri-post insulator GIL with external factors were investigated. The results show that the temperature of the GIL tri-post insulator gradually decreases from the conductor to the enclosure, and the internal temperature is slightly lower than the surface; the maximum thermal stress occurs at the edge of the insulator wrapped around the conduct. Under rated conditions, the maximum stress inside the insulator can be up to 180 MPa, and the thermal expansion difference between the upper and lower surfaces of the enclosure hardly changes with temperature. This study provides an important guarantee for the safe operation of GIL.

**Keywords** Gas insulated transmission lines · Tri-post insulator · Temperature rise characteristics

## 1 Introduction

Gas insulated metal-enclosed transmission line (GIL) has the advantages of high reliability, small transmission loss, low failure rate, and is not affected by external factors such as climate change [1]. It is an advanced power transmission method with great development prospects, and has gradually become an important direction for the construction of future power transmission networks.

The temperature rise effect caused by conductor Joule heat, enclosure induced current and eddy current heat loss causes the temperature of GIL conductor, enclosure

---

F. F. Wu · S. Y. Xie · X. Lin

Zhejiang Key Laboratory for Protection Technology of High-Rise Operation, Hangzhou, China

M. H. Chen (✉) · C. H. Zhang

Department of Electrical Engineering, Nanjing University of Aeronautics and Astronautics, Nanjing, China

e-mail: [tomzhumin@163.com](mailto:tomzhumin@163.com)

© Beijing Paiké Culture Commu. Co., Ltd. 2024

X. Dong and L. Cai (eds.), *The Proceedings of 2023 4th International Symposium on Insulation and Discharge Computation for Power Equipment (IDCOMPU2023)*, Lecture Notes in Electrical Engineering 1103, [https://doi.org/10.1007/978-981-99-7413-9\\_67](https://doi.org/10.1007/978-981-99-7413-9_67)

703

and insulating gas to rise [2], which leads to changes in the insulating properties, and endangers the operation safety of GIL. Therefore, the research on the temperature rise characteristics of GIL can provide a reference for the structural design of GIL equipment and provide guarantee for the safe operation of GIL equipment.

At present, numerical simulation methods are mainly used at home and abroad to study the temperature rise characteristics of GIL. Literature [3–5] established a two-dimensional model of GIL, and studied the transient temperature rise curve, the influence of different insulating gases and conductor diameters on the internal temperature distribution of GIL. Reference [2] carried out the research on the influence of external wind speed and solar radiation on the temperature field distribution of GIL in the 3D simulation model of GIL. Reference [6] carried out an experimental study on the temperature rise characteristics of GIL expansion joints, and compared with the simulation results. The temperature rise of GIL will cause the strain field and electric field of GIL to change. For multi-physics coupling, corresponding research has been carried out at home and abroad. Reference [7] used SF<sub>6</sub>-N<sub>2</sub> mixed gas to carry out related research on the electric field distribution under the temperature rise of GIL. It can be seen from the research status that the temperature rise characteristics of three-post insulators are important factors affecting the safe operation of GIL. However, at present, there is still a lack of relevant studies on the influence of GIL temperature rise on the internal stress of three-post insulators and the thermal expansion characteristics of the envelope.

Therefore, this paper builds a three-dimensional simulation model of GIL, and studies the factors affecting the temperature rise of GIL for the tri-post insulator GIL, as well as the effect of temperature rise on the strain field of GIL. The goal of clarifying the temperature rise characteristics of GIL and clarifying the factors affecting the local temperature rise of GIL has been achieved.

## 2 GIL Multiphysics Simulation Model

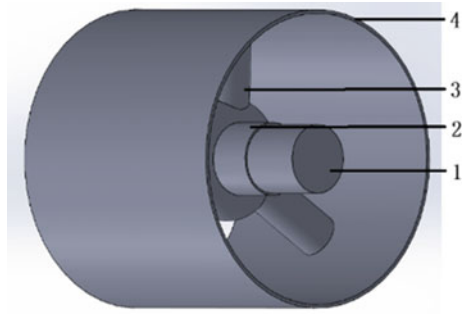
This research uses the COMSOL finite element simulation software to create a three-dimensional GIL model, and conducts simulation research on the internal temperature field, strain field and electric field of the GIL.

### 2.1 Geometric Model

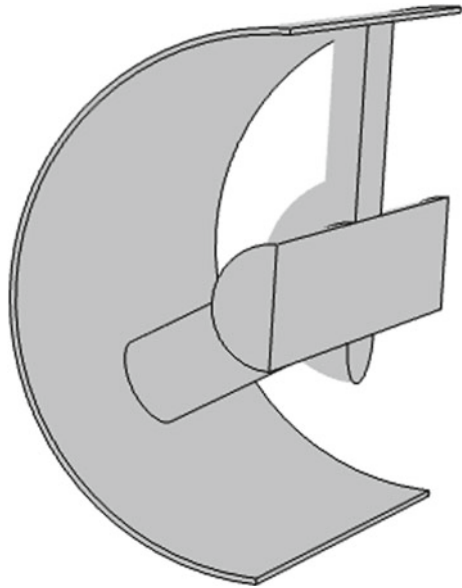
The research object of this paper is the 1100 kV tri-post insulator GIL. Its basic structure is shown in Fig. 1, which can be divided into a central conductor (1), a connecting cylinder (2), an epoxy resin insulator (3), and an aluminum alloy enclosure (4).

In order to prevent the asymmetry of the simulation results caused by meshing, the 3D geometric model of the GIL is simplified, as shown in Fig. 2.

**Fig. 1** Schematic diagram of tri-post insulator GIL, central conductor (1), connecting cylinder (2), an epoxy resin insulator (3), aluminum alloy enclosure (4)



**Fig. 2** GIL tri-post insulator simulation model



## 2.2 Flow Field-Temperature Field Mathematical Model

At the initial ambient temperature of 20 °C, the physical parameters of insulating gas, enclosure and insulator are shown in Table 1.

Under the set rated working conditions, the rated current is 6000 A, the ambient temperature is 20 °C, and the insulating gas pressure is 0.4 MPa. The insulating gas inside the GIL is set to SF<sub>6</sub>. The parameters of the influencing factors of the temperature rise characteristics used in the simulation are shown in Table 2.

**Table 1** Physical parameters of insulating gas, enclosure and insulator

	Destiny/(kg/m <sup>3</sup> )	Thermal Conductivity/[W/(m K)]	Dynamic viscosity/(Pa s)	Constant pressure heat capacity/[J/(kg K)]	Specific heat rate
SF <sub>6</sub>	6.52	0.01206	1.42e-5	665.18	1.09
Aluminum alloy	2680	156	/	942	/
Epoxy resin	1200	0.35	/	550	/

**Table 2** GIL external influence factor settings

Parameter	Selected value
Load current/A	4000, 5000, 6000, 7000, 8000
Ambient temperature/°C	0, 10, 20, 30, 40
Insulating gas pressure/MPa	0.1, 0.2, 0.3, 0.4, 0.5, 0.6, 0.7

### 2.3 Temperature-Strain Field Mathematical Model

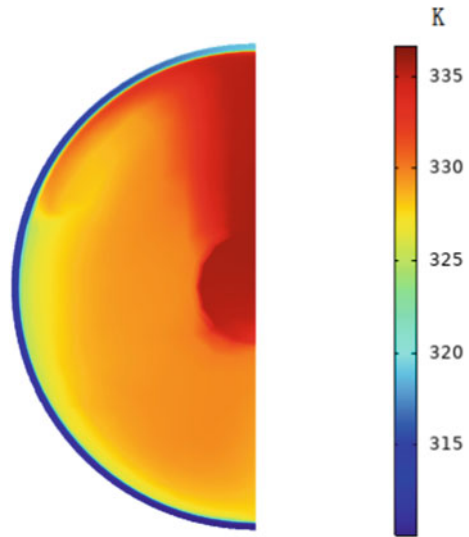
On the basis of inputting the thermal physical properties of the material in the coupled flow-heat analysis, in the thermal stress analysis, the mechanical properties of the material should also be input. The mechanical properties of the material required for the simulation are shown in Table 3.

First, fixing the two ends of the enclosure and the conductor, and the thermal-mechanical coupling analysis of the GIL is carried out. Then, fixing one end of the enclosure, and symmetrical boundaries are imposed on the inner and outer sides of the enclosure to explore the axial thermal expansion characteristics of the GIL enclosure.

**Table 3** Mechanical parameters of enclosure and insulator materials

	Elastic modulus/Pa	Poisson's ratio	Thermal expansion coefficient/(1/K)
Aluminum alloy	7e10	0.33	2.3e-5
Epoxy resin	2.5e10	0.38	6.24e-5

**Fig. 3** GIL temperature distribution



### 3 Results and Analysis

#### 3.1 GIL Temperature Field

The temperature distribution is shown in Fig. 3, and the gas flow rate distribution is shown in Fig. 4. It can be seen from the figure that the temperature of the insulating gas inside the GIL presents a distribution law of high above and low below. The maximum gas velocity is about 0.09 m/s.

The temperature distribution of the GIL tri-post insulator is shown in Fig. 5. It can be seen from the figure that the temperature of the insulator gradually decreases from the conductor to the enclosure. The internal temperature of the insulator is slightly lower than the surface temperature.

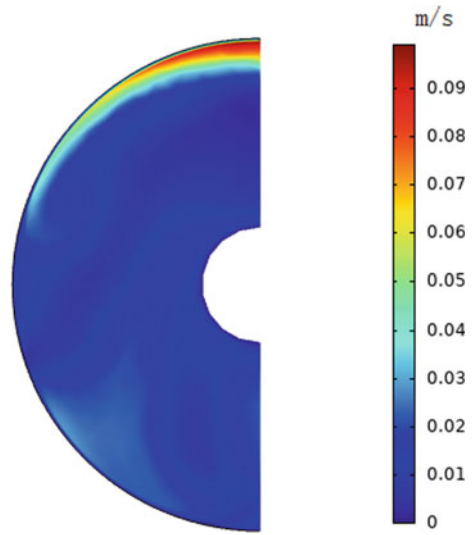
The temperature distribution of the GIL enclosure is shown in Fig. 6. The temperature of the upper surface of the enclosure is the highest and the temperature of the lower surface is the lowest. The temperature on both sides of the upper surface of the enclosure is higher than that of the middle part.

#### 3.2 Effect of Different Factor on GIL Temperature Field

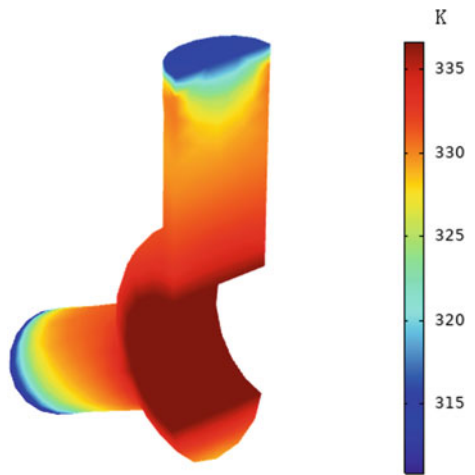
Figure 7a–c are GIL temperature rise curves obtained by changing load current, ambient temperature or gas pressure.

It can be seen from Fig. 7a that the relationship between the temperature of the GIL conductor and the enclosure is a nonlinear positive correlation. Figure 7b shows

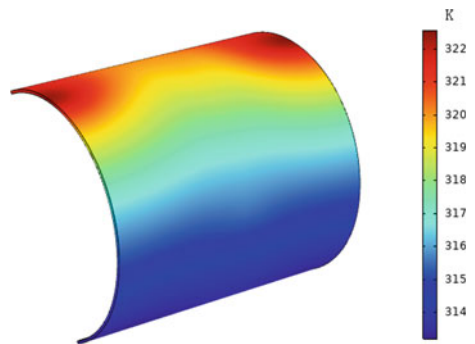
**Fig. 4** GIL gas flow velocity distribution



**Fig. 5** Temperature distribution of GIL insulator

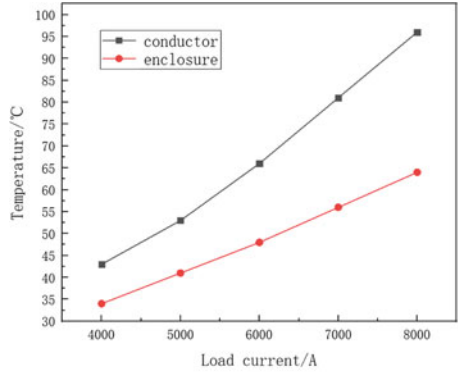


**Fig. 6** Temperature distribution of GIL enclosure

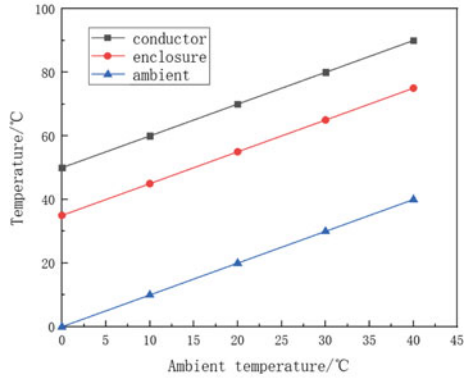




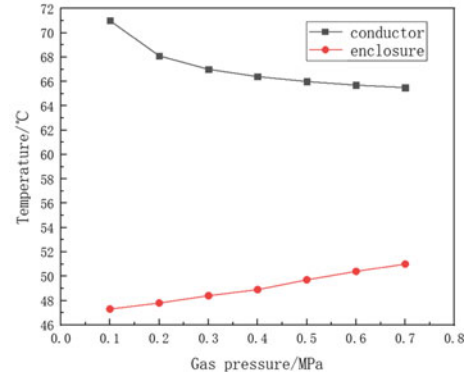
**Fig. 7** Influence of load current **a**, ambient temperature **b**, and gas pressure on GIL temperature distribution



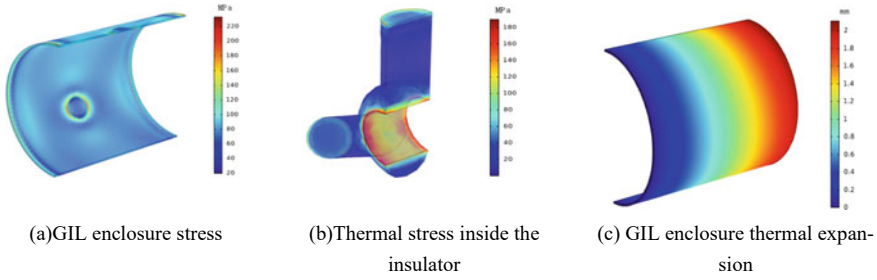
(a)



(b)



(c)



**Fig. 8** GIL thermal strain simulation results

that the GIL conductor and enclosure temperature are positively correlated with the ambient temperature. The temperature difference between the enclosure and the ambient temperature does not change with the change of the ambient temperature. Figure 7c shows that the GIL conductor temperature is more sensitive to the change of insulating gas pressure at lower air pressure, but remains basically unchanged when the air pressure reaches about 0.4 MPa.

### 3.3 Effect of Different Factor on GIL Thermal Strain

The simulation results of GIL enclosure stress (a), insulator stress (b) and GIL enclosure thermal expansion (c) are shown in Fig. 8. It can be seen from the figure that the thermal stress of the GIL enclosure is axisymmetric. The thermal stress at both ends is the largest and decreases in the middle of the pipeline. The maximum stress inside the insulator occurs at the junction of the conductor and the insulator, because the temperature of the insulator part close to the conductor is the highest. There is also a large stress distribution at the junction between the two ends and the enclosure.

Under rated conditions, the GIL enclosure with a length of 1 m thermally expands axially, with an upper surface of 2.11 mm and a lower surface of 1.83 mm.

## 4 Conclusion

In this paper, the temperature rise of the tri-post insulator GIL is calculated by the method of finite element simulation, and some related factors affecting the temperature rise and the strain field of tri-post insulator GIL are quantitatively analyzed. Based on the temperature rise results, the conclusions are as follows:

- (1) The temperature of the insulating gas inside the GIL presents a distribution law of high above and low below, and the temperature above the enclosure is higher than the temperature below the enclosure. The relationship between the

- influencing factors and the temperature rise effect of GIL was quantitatively analyzed.
- (2) The thermal stress of the GIL enclosure is axisymmetric, and the maximum stress of the insulator occurs at the junction of the conductor and the insulator. The maximum stress of the insulator increases with increasing temperature. The thermal expansion of the enclosure increases linearly with temperature, and the difference between the upper and lower surfaces is basically unchanged.

**Acknowledgements** This work is supported by Leading innovation and entrepreneurship team in Zhejiang Province (Project No.: 2019R01014).

## References

1. Qin Z et al (2017) Insulation properties of SF<sub>6</sub>/N<sub>2</sub> gas mixtures under high pressure and low ratio. In: 2017 IEEE electrical power and energy conference (EPEC), pp 1–4
2. Qiao Y et al (2020) Research on the distribution characteristics of GIL temperature field under different environmental factors. *Electr Power Eng Technol* 39(03):136–143+150 (in Chinese)
3. Wu X et al (2013) Temperature rise numerical calculation and correlative factors analysis of gas-insulated transmission lines. *Trans China Electrotechnical Soc* 28(01):65–72 (in Chinese)
4. Chen J et al (2020) Numerical calculation of temperature rise of gas insulated transmission lines and heat transfer capability of insulating gases. *High Voltage Eng* 46(11):4042–4051 (in Chinese)
5. Dong JN et al (2022) Effects of transient voltages on discharge inception of tri-post Insulator in DC-GIL. In: 2022 IEEE 4th international conference on dielectrics (ICD), pp 126–129
6. Liu Y et al (2020) Measurement and analysis of temperature distribution of UHV GIL expansion joints. *High Voltage Apparatus* 56(12):1–6 (in Chinese)
7. Li W et al (2021) The 3D accumulation characteristics of surface charges on actual 550 kV GIL tri-post insulator under AC voltage in SF<sub>6</sub>. In: 2021 IEEE conference on electrical insulation and dielectric phenomena (CEIDP), pp 359–362

# Influence Mechanism of Hot-Press Setting Time and Winding Tension on the Performance of Metallized Film Capacitors



Huize Cui , Zhaoliang Xing, and Chong Zhang 

**Abstract** Metallized film capacitors are key power equipment in flexible direct transmission systems, pulse power systems and electric vehicles, and their application performance directly affects the stability and reliability of power grid systems and users. This article investigates the effects of hot-press setting time and winding tension control on capacitor performance during the manufacturing process of capacitor elements in durability tests. At a certain temperature, the setting of the hot-press setting time of the capacitor element and the winding tension setting of the element can eliminate the residual stress inside the metallized film element, make the dielectric film produce irreversible heat shrinkage, eliminate the moisture and air in the metallized film element through the film shrinkage and physical compression force to compress the element, reduce the probability of air discharge inside the metallized film, and improve the internal breakdown strength and partial discharge starting voltage of the element. Therefore, according to different performance requirements, choosing a certain hot-press setting time and winding tension is conducive to improving the service life of metallized film capacitor.

**Keywords** Metallized film capacitors · Breakdown strength

## 1 Introduction

The main properties of metallized film capacitors are determined by their winding process and the polymer film material inside. At present, biaxially oriented polypropylene thin (BOPP) is widely used in the manufacture of capacitors with metallized films under different application conditions because of its good mechanical properties, electrical properties and processing properties [1–5]. The main factors influencing the performance of capacitors are polypropylene resin, polypropylene

---

H. Cui (✉) · Z. Xing · C. Zhang  
State Key Laboratory of Advanced Power Transmission Technology, State Grid Smart Grid Research Institute Co., Ltd., Beijing, China  
e-mail: [jameschz@126.com](mailto:jameschz@126.com)

© Beijing Paiké Culture Commu. Co., Ltd. 2024  
X. Dong and L. Cai (eds.), *The Proceedings of 2023 4th International Symposium on Insulation and Discharge Computation for Power Equipment (IDCOMPU2023)*, Lecture Notes in Electrical Engineering 1103, [https://doi.org/10.1007/978-981-99-7413-9\\_68](https://doi.org/10.1007/978-981-99-7413-9_68)

film, metallization coating process and capacitor winding process. Under normal circumstances, due to the difference in isotactic and impurity, the withstand voltage level of capacitors prepared from domestic polypropylene raw materials is about 20% lower than that of imported capacitors, which cannot meet the complex working conditions such as DC superposition of multiple AC, overvoltage, and high operating temperature in UHVDC systems, resulting in the high-end capacitor market being monopolized by foreign companies such as Vishay and Epcos. In addition, the use of high-voltage metallized film capacitors is huge, according to statistics, the number of capacitors for the 500 kV Zhangbei Roushi and  $\pm 800$  kV Wudongde hybrid DC engineering  $\pm 500$  kV is more than 45,000, resulting in the investment cost of capacitors as high as more than 10% of the total cost of converter stations. In addition, the capacitor winding process is an important factor affecting the performance of the capacitor, with the increase of IGBT voltage level for UHV converter valve from 5.2 to 6.5 kV and the development trend of equipment miniaturization. The matching capacitor voltage level needs to be increased from 2.8 to 4 kV, which puts forward higher requirements for capacitor manufacturing process and material performance, especially during the capacitor winding process to control the winding tension and pressure to maximize the pressure between the film layers, reduce the self-healing energy, and reduce the volume of the capacitor element [6–8]. The winding process of polypropylene film capacitors directly affects the performance of the capacitor and is a key problem that needs to be solved urgently. Therefore, it is urgent to explore the winding process suitable for high-voltage metallized film capacitors and improve the performance of metallized film capacitors, which is of great significance for improving the independent innovation ability of high-end power equipment and ensuring the national energy strategic security [9, 10].

The winding process of capacitor elements seriously affects its self-healing performance, and the air gap between the films during winding will affect the power density of arc extinguishing, and the power density is closely related to the interlayer voltage during winding, only when the power density of the arc is less than the critical power density, effective self-healing will occur, and vice versa. At present, the self-healing failure of polypropylene film capacitors is an important factor that leads to the breakdown of capacitor insulation and heating, resulting in frequent capacitor failures. In this paper, two components made of the same hot-press time and different winding pressures will be experimentally studied.

## 2 Samples and Tests

### 2.1 Sample Preparation

Polypropylene (PP) is a long-chain polymer, and the properties of polypropylene resin were calibrated by testing the melt index, oxidation induction period, yellowness index, tacticity and impurity content of polypropylene resin. The properties of

polypropylene resin are shown in Table 1, with a tacticity of 99.1 at 200 °C, a melt mass flow rate of 3.6 g/10 min, a yellowness index of − 4.9, an oxidation induction time of 45.5/min, and impurity content of 18 ppm.

For the polypropylene resin produced in this batch, in the film production process, the longitudinal stretching temperature adjustment range is 141–143 °C, in the film production process, the sampling test is completed at each stage of film production, according to the film performance test data, only need to adjust the longitudinal stretching temperature in the film production process to finally get sample A, and obtain the test data of the film sample as shown in Table 2.

The safety metallization film with segmented metallized electrode used in this paper is composed of three segmented series metal layers, as shown in Figs. 1 and 2, and the square resistance test results are between 3.4 Ω/□ and 12.5 Ω/□. The pp film produced is metallized with zinc and aluminum and used in the production of metallized film capacitors. The capacitors are produced in 5 kV/1.2 uF and are sealed with N<sub>2</sub>+SF<sub>6</sub> to ensure the insulation distance between the capacitor elements and shells. Secondly, using the same hot setting time, as shown in Fig. 3, adjusting different winding pressures finally obtains two capacitor elements with diameters of 71 and 78 mm [4].

**Table 1** Polypropylene resin properties

Product	Melt mass-flow rate/g/10 min	Oxidation induction time (200 °C)/min	Yellowness index	Tacticity/%	Impurity content
PP	3.6	45.5	− 4.9	99.1	18

**Table 2** Film properties

Sample				A
No.	Test item		Unit	Average value
1	Tensile strength	MD	MPa	184.1
		TD		349.2
2	Percentage of breaking elongation	MD	%	188.8
		TD		64.4
3	Elastic modulus	MD	MPa	2373
		TD		3858.6
4	Thermal shrinkage (120 °C, 15 min)	MD	%	3.33
		TD		0.5
5	Wetting tension		mN/m	39
6	Surface roughness	AK	μm	0.052
		CR		0.055
7	DC breakdown strength		V/um	589
8	Thickness		um	7.5

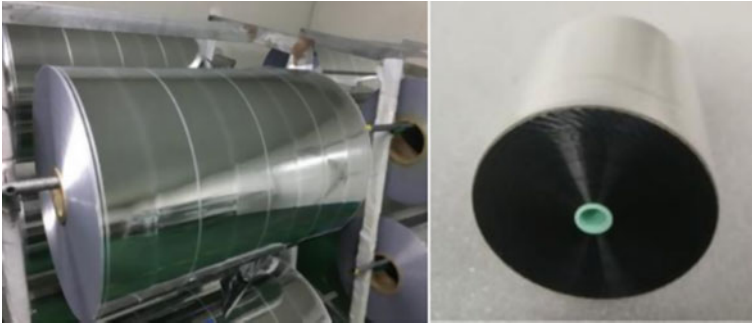


Fig. 1 Metallized film and capacitor elements

Fig. 2 Safety metallization film with segmented metallized electrode

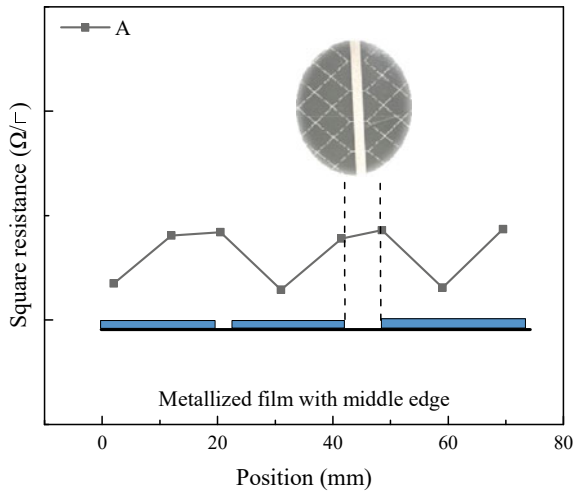
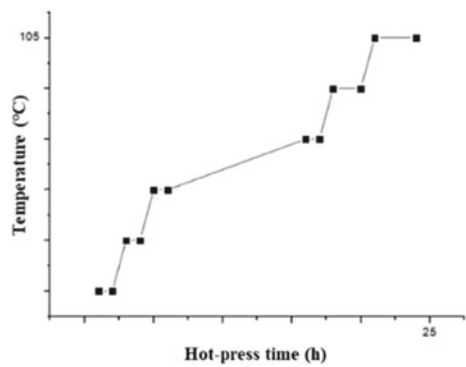


Fig. 3 Metallized film and capacitor elements



**Table 3** Capacitor properties

Model	Thickness	Sealing materials	Diameter (mm)	
			1	2
5 kV/1.2 uF	$7.5 \pm 1 \mu\text{m}$	$\text{N}_2+\text{SF}_6$	71	78

The main technical parameters of capacitors include rated capacity, AC voltage rms, AC voltage peak, maximum voltage, dielectric loss, inrush current, operating temperature, life expectancy and air gap, etc., as shown in Table 3, the capacitors developed in this paper can meet the engineering application requirements of capacitors for snubber circuits in UHV converter valves.

### 2.2 Test Method

A capacitor with a film thickness of  $7.5 \mu\text{m}$  was selected for the inter-terminal short term withstand voltage test, and the inter-terminal test voltage:  $1.75U_{\text{NDC}} = 8.75 \text{ kV}$ ; Test temperature:  $20 \text{ }^\circ\text{C}$ ; Test time: 1 min, as shown in Fig. 4. Moreover, the samples 71 and 78 mm were put into the electrothermal aging oven for a durability test of 500 h, of which, when completing the durability test of the first stage of 250 h, it was necessary to complete the 1000 times of surge current test of  $1.4I$ , and then the durability test of 250 h in the second stage, the voltage of long-term durability test was set to 3.4 kV, the temperature was  $65 \text{ }^\circ\text{C}$ , and the capacitance and dielectric loss were finally tested.



**Fig. 4**  $7.5 \mu\text{m}$  capacitor withstand voltage test diagram



### 3 Results and Discussion

The experimental results show that the dielectric loss of all samples is basically unchanged after the withstand voltage test, the capacitance attenuation of the metalized film capacitor with a diameter of 71 mm is greater, about 0.001  $\mu\text{F}$ , and the capacitance of the 78 mm thick capacitor remains unchanged, and its performance is better, so the test verification of this type of capacitor is carried out (Table 4).

After the long term electrical-thermal test, it was found that the capacitance of the 78 mm sample had the least capacitance attenuation and the smallest dielectric loss change (Table 5).

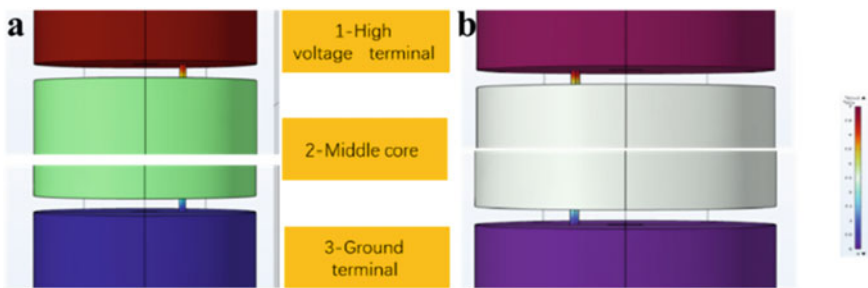
In addition, taking a 5 kV, 1.2  $\mu\text{F}$  capacitor for snubber circuits as an example, the element diameter is 71 mm, the rated working voltage is set to 4.5 kV, and the peak voltage is 5 kV, and the specific structure of the capacitor is shown in Fig. 5, which is composed of 3 capacitor elements inside, and the 3 elements are connected in series to form the overall capacitor. The upper ends of the three element terminals connected in series with capacitors are connected with high and low electric potentials.

**Table 4** Short term withstand voltage test results of different capacitors

Diameter (mm)	Original sample properties	Sealing materials	After test	
	Capacitance $\mu\text{F}$	Dielectric loss * $10^{-4}$	Capacitance $\mu\text{F}$	Dielectric loss * $10^{-4}$
71	1.224	2	1.223	2
78	1.228	2	1.228	2

**Table 5** Long term withstand voltage test results of different capacitors

Test voltage: 3.54 kV	Samples	
Properties	71 (mm)	78 (mm)
Capacitance $\mu\text{F}$	1.195	1.21
Dielectric loss %	0.037	0.032



**Fig. 5** Electric surface potential of pp film capacitor at **a** 5 kV, **b** 4.5 kV

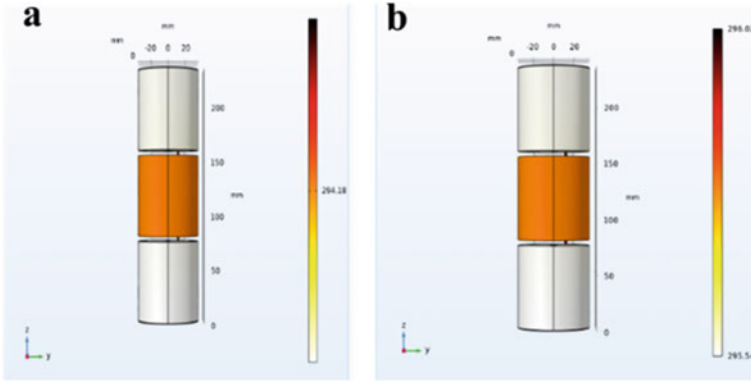
As shown in Fig. 5, at 5 kV, the maximum potential is 5 kV at the high-voltage electrode position, and the lowest potential at the lowest element gold injection ground is about 0.2 V. The potential of the three series elements decreases from top to bottom, with the potential difference between the first element and the middle element being about 2.3 kV, and the end element and the middle element about 2.15 kV. Therefore, the amplitude of potential decline at the series element wire is large. The highest potential of the connected high-voltage electrode element is 5 kV, the lowest potential is 4.82 kV, and the potential difference is 0.18 kV; The highest potential of the center element is 2.7 kV, the lowest potential is 2.3 kV, and the potential difference is 0.4 kV. The connecting ground element has a maximum potential of 0.162 kV, a minimum potential of 0.2 V, and a potential difference of approximately 0.16 kV.

At 4.5 kV, the maximum potential is 4.5 kV at the high-voltage electrode position, and the lowest potential at the lowest element gold injection ground is about 0.2 V. The potential of the three series elements decreases from top to bottom, with the potential difference between the first end element and the middle element being about 1.94 kV, and the end element and the middle element about 1.95 kV. Therefore, the amplitude of potential decline at the series element wire is large. The highest potential of the connected high-voltage electrode is 4500 V, the lowest potential is 4.34 kV, and the potential difference is 0.16 kV; The highest potential of the center element is 2.4 kV, the lowest potential is 2.1 kV, and the potential difference is 0.3 kV. The connecting ground element has a maximum potential of 0.14 kV and a minimum potential of 0.2 V, with a potential difference of approximately 0.138 kV.

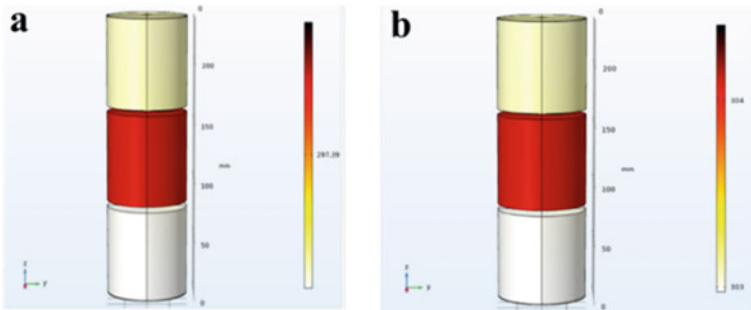
According to the typical  $\pm 800$  kV/5000 A UHV converter valve operation condition, a peak capacitor voltage is of  $\pm 4.2$  kV under long-term operation, a peak capacitance voltage is of 5 kV at a trigger angle of  $90^\circ$ , and a peak current is of 40 A/100 A, up to 70 A/140 A. Therefore, the average number of current peaks is selected for the simulation parameters in this paper is 70 A, 110 A, respectively, and the overall parameters of the capacitor are set to the parameters of the equivalent pp film, and the conductivity of the pp film is about  $3.0 \times 10^{-6}$  S/m, the dielectric constant is 2.2, the thermal conductivity is 0.2, and the initial temperature is 293.15 K.

Figures 6 and 7 show the surface temperature field distribution of pp film capacitors under different operating conditions. It can be seen from the figures that the temperature of the middle element is the highest, the temperature of the ground end element is the lowest, because the wire connection between the elements is not completely axisymmetric distribution, so the temperature field distribution generated by the electric field is not uniform, and the temperature difference of the same element is basically controlled within 1 K due to the small size.

When the 71 mm diameter film capacitor element operates at a 70 A current peak, the maximum temperature is located on the middle element, the maximum temperature of the element from top to bottom is 294.18, 294.24, 294.17 K, the lowest temperature is 294.09, 294.19, 294.09 K, and the maximum temperature rise is 1.09 K. When a current of 105 A is applied, the maximum temperature of the element from top to bottom is 295.77, 295.94, 295.75 K, the lowest temperature is 295.54, 295.81, 295.54 K, and the maximum temperature rise is 2.79 K.



**Fig. 6** Surface temperature distribution of a 71 mm diameter element at **a** 70 A, **b** 110 A



**Fig. 7** Surface temperature distribution of 78 mm diameter elements at **a** 70 A, **b** 110 A

When the 78 mm diameter film capacitor element operates at a 70 A current peak, the maximum temperature is located on the middle element, the maximum temperature from top to bottom is 294.07, 294.14, 294.07 K, the lowest temperature is 293.99, 294.09, 293.99 K, and the maximum temperature rise is 0.94 K. When a current of 105 A is applied, the maximum temperature of the element from top to bottom is 295.55, 295.67, 295.50 K, and the lowest temperature is 295.28, 295.54, 295.29 K, and the maximum temperature difference is 2.52 K. The temperature rise inside a element with a diameter of 78 mm is lower than that of a element with a diameter of 71 mm.

## 4 Conclusion

From the above results, it can be seen that different winding pressures at the same hot-press time will affect the thermal and electrical properties of the capacitor. The simulation results show that through simulation calculation, after the diameter of the capacitor element made of pp film is increased from 71 to 78 mm, the thermal effect generated by the element during operation is improved, the temperature rise is reduced at the same current level, and the difference is more significant under the high-current operating conditions, which can be attributed to the fact that the heat generated by the film after structural optimization is more easily dissipated. The adjustment of winding pressure in the structural optimization method of capacitor proposed in this paper can improve the heat generation problem of capacitor during normal operation, control the heat generation, reduce the change value of capacitance and dielectric loss after endurance test under long-term electrothermal action, and help improve the stability and safety of capacitor and converter valve.

**Acknowledgements** This work was funded by the State Grid Corporation of China Headquarters Science and Technology Project (No. 5500-202255488A-2-0-KJ).

## References

1. Bo P, Fuchuan L, Hua L, Yaohong C, Miao Z, Fei L (2010) Calculation and measurement of metalized film capacitor's inner pressure and its influence on self-healing characteristics. *IEEE Trans Dielectr Electr Insul* 17:1612–1618
2. Tortai JH, Bonifaci N, Denat A, Lesaint O (2002) Self-healing of aluminium metallized polypropylene films: a spectroscopic investigation. In: International conference on dielectric liquids (ICDL). IEEE, Graz, Austria, pp 190–193
3. Lei J, Lu C, Wenfeng L, Zhe X, Shengtao L (2020) Self-healing properties of metalized polypropylene film with elevated sheet resistance. In: International conference on high voltage engineering and application (ICHVE). IEEE, Beijing, China, pp 1–4
4. Huize C, Zhaoliang X, Chong Z, Shaowei G, Yaotian Su, Zhang H (2023) Characteristic evaluation of BOPP capacitor after winding process with mechanical stress. In: 4th International conference on electrical materials and power equipment (ICEMPE). IEEE, Shanghai, China, pp 1–4
5. Lu C, Zhiyuan L, Jingran W, Wenfeng L, Shengtao L (2023) Degradation behavior and mechanism of metalized film capacitor under ultrahigh field. *IEEE Trans Dielectr Electr Insul* 30:509–517
6. Lu C, Wenfeng L, Xiaowei L, Chengming L, Shengtao L, Xing Z (2019) Online degradation of biaxial-orientated polypropylene film from HVDC filter capacitors. *IEEE Trans Dielectr Electr Insul* 26:26–33
7. Chunlin L, Jinjun L, Yan Z, Jinpeng Y, Rui C, Yang L, Xue L (2023) A method to characterize the shrinking of safe operation area of metallized film capacitor considering electrothermal coupling and aging in power electronics applications. *IEEE Trans Dielectr Electr Insul* 70:1993–2002
8. Zhaoyu R, Boxue D, Meng X, Haoliang L (2022) Breakdown performance of polypropylene and its long-chain branched blending for metalized film capacitors. *IEEE Trans Dielectr Electr Insul* 29:145–152

9. Taylor DF (1984) On the mechanism of Al corrosion in metalized film AC capacitors. *IEEE Trans Electr Insul* 19:288–293
10. Janet H, Richard JT, Steven AB (2008) Implications of advanced capacitor dielectrics for performance of metallized film capacitor windings. *IEEE Trans Dielectr Electr Insul* 15:1754–1760

# Multivariate Model Predictive Control for High Permeability Photovoltaic Microgrid



Jipeng Gu, Binjie Wang, Sheng Zheng, Xuguang Wu, Youbing Zhang, and Weijie Zhang

**Abstract** In order to improve the efficiency of photovoltaic (PV) grid-connected response and reduce the total harmonic distortion rate, a multivariate model predictive control (MPC) strategy for PV inverter grid-connected system is proposed. Firstly, the maximum power point tracking (MPPT) of DC/DC converter is designed according to the output power curve of PV. Then, based on the mathematical model of the inverter in rotating coordinate system, MPC method is used to determine the predicted value of the output current at  $k + 2$  time. The current error and DC bus voltage error are taken as the control factors of the value function. The aim is to minimize the value function and achieve optimal control. Finally, MATLAB/Simulink simulation verifies the effectiveness of this strategy in improving the voltage stability of DC bus and reducing the total harmonic distortion of current on the grid side.

**Keywords** Photovoltaic · Grid-connected inverter · Maximum power point tracking · Model predictive control · Harmonic suppression

## 1 Introduction

The rapid development of economy leads to the increasing demand for energy. However, traditional fossil fuels, which are non-renewable resources, cause significant environmental damage [1, 2]. Therefore, countries are prioritizing reducing the consumption of traditional fossil fuels and accelerating the development of sustainable energy sources, including wind, solar, and biomass. This focus has led to a

---

J. Gu · B. Wang · Y. Zhang (✉) · W. Zhang  
College of Information Engineering, Zhejiang University of Technology, Hangzhou 310023,  
China  
e-mail: [youbingzhang@zjut.edu.cn](mailto:youbingzhang@zjut.edu.cn)

S. Zheng · X. Wu  
Pingyang Power Supply Company of State Grid Zhejiang Power Co., Ltd., Wenzhou 325000,  
China

significant growth in PV power projects [3–5]. In recent years, scholars both domestically and internationally have conducted extensive research on PV inverter grid-connected system. The aim of the researches is to enhance the stability and reliability of power supply to the grid. Prominent approaches include proportional integral (PI), proportional resonant (PR) [6], slip film control (SMC) [7], linear active disturbance rejection control (LADRC), and MPC [8].

In [9], it is described that traditional PI control lacks sufficient immunity in the face of interference (power grid failure, irradiance mutation). In [10], a voltage controller using LADRC is proposed to enhance the robustness of PV inverter grid-connected system. In [11], it is proved that the introduction of PR control at the resonant frequency can reduce the total harmonic distortion in the grid-connected current. However, the design process of the above control strategies is more complicated and requires higher calculation accuracy. MPC offer various advantages in inverter control, such as flexible control capabilities, eliminating the need for pulse-width modulator (PWM) and decoupling operations, multi-objective nonlinear control, and reduced switching losses. These advantages have garnered significant attention in the field. In [12], MPC is introduced into the PV inverter grid-connected system, but the MPPT state of PV does not considered, so it is difficult to accurately evaluate the overall performance improvement of system. In [13], finite set MPC is introduced into a single-stage T-type three-phase inverter to improve the dynamic response, but the algorithm has certain delay errors. If the PV inverter adopts a two-step predictive control strategy to compensate for the delay in the one-step predictive control, the fast response ability of the current reference amplitude will be enhanced.

Based on the above content, this paper proposes a multivariate MPC strategy for two-stage PV inverter grid-connected system. The pre-stage DC/DC converter adopts disturbance observation method to realize the MPPT of PV, and the post-stage DC/AC converter adopts multi-variable MPC to realize efficient grid-connection. Furthermore, two control factors of current error and DC bus voltage error are considered in the value function of MPC, which further enhances the anti-interference ability of the system.

## 2 Structure of the PV Inverter Grid-Connected System

PV inverter grid-connected system is composed of PV panels, DC/DC converter, DC/AC inverter, filter module, AC power grid and related control equipment. The structure of the two-stage PV inverter grid-connected system is shown in Fig. 1. This design segregates the MPPT and unit power factor grid connection functions, contributing to enhanced system stability.

In Fig. 1,  $C_{pv}$ ,  $C$  are the filter capacitance;  $R$ ,  $L$  are the resistance and inductance in the filter module;  $i_a$ ,  $i_b$ ,  $i_c$  are the output current of the inverter;  $u_{ga}$ ,  $u_{gb}$ ,  $u_{gc}$  are the voltage of the AC power grid;  $i_{abc}$  is the filtered grid-connected current;  $U_{pv}$ ,  $i_{pv}$  are the output voltage and current of the PV panels;  $U_{dc}^*$ ,  $U_{dc}$  are the reference voltage

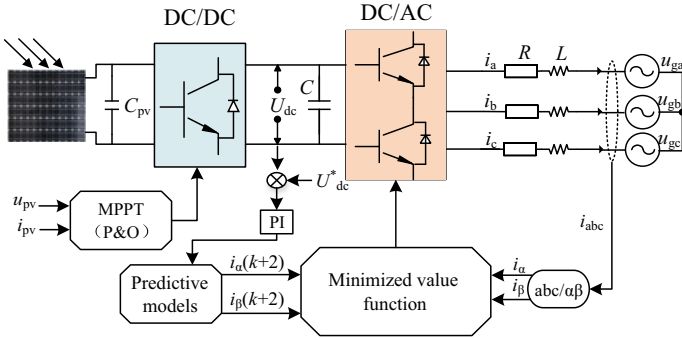


Fig. 1 The structure of two-stage PV inverter grid-connected system

and actual voltage of the DC bus;  $i_\alpha, i_\beta$  are the corresponding value of  $i_{abc}$  in the  $\alpha\beta$  coordinate system;  $i_\alpha(k + 2), i_\beta(k + 2)$  are the predicted value of  $k + 2$  step.

### 3 Control Strategy of the PV Inverter Grid-Connected System

#### 3.1 MPPT Control of DC/DC Converter

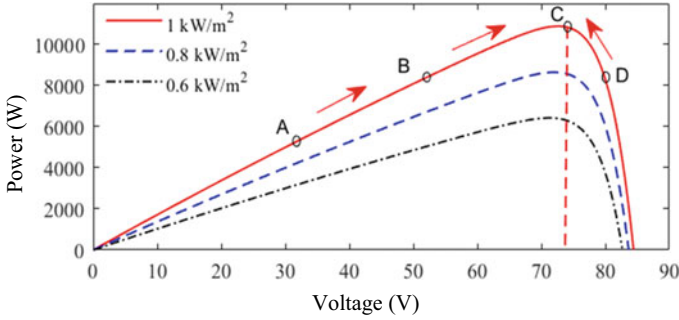
Considering the changes of the external environment in actual situation [14], the relevant parameters of the PV cell are shown in Eq. (1).

$$\begin{cases} \Delta T = T - T_{ref} \\ \Delta S = S - S_{ref} \\ U_{oc-n} = U_{oc}(1 - c\Delta T) \ln(e + b\Delta S) \\ I_{sc-n} = I_{sc} \frac{S}{S_{ref}}(1 + a\Delta T) \\ U_{m-n} = U_m(1 - c\Delta T) \ln(e + b\Delta S) \\ I_{m-n} = I_m \frac{S}{S_{ref}}(1 + a\Delta T) \end{cases} \quad (1)$$

where,  $\Delta T$  is the difference between the actual temperature and the standard temperature;  $\Delta S$  is the difference between the actual irradiance and the standard irradiance;  $I_{sc-n}, I_{m-n}, U_{oc-n}, U_{m-n}$  are the short circuit current, maximum operating point current, open circuit voltage, maximum power point voltage under any temperature and irradiance;  $a, b, c$  are the compensation coefficients,  $a = 0.0025, b = 0.5, c = 0.00288$ ;  $e$  is the natural base number,  $e = 2.71828$ .

According to the model, the output characteristic curve of PV cell under different irradiance and temperature can be obtained. In this paper, the P-U characteristic curve





**Fig. 2** P-U characteristic curve of PV cell under different irradiance

can be obtained by studying different irradiance at 25 °C operating conditions, as shown in Fig. 2.

The MPPT algorithm can be designed according to the P-U characteristic curve. Initially, the PV cell operates at point A to the left of the maximum power point (MPP), by applying a positive perturbation to move the PV cell to work at point B, which is still to the left of the MPP. Subsequently, another positive perturbation is applied to make the PV cell work at point D on the right side of the MPP. However, as point C (MPP) exhibits a higher voltage than point D, it becomes necessary to adjust the perturbation direction to decrease the output voltage ( $\Delta U$ ) and guide the PV cell back to the MPP. The flow chart of the perturbation observation method is shown in Fig. 3.

### 3.2 Model Predictive Control of DC/AC Inverter

Due to the limited number of switching states available for DC/AC inverter, specific guidelines must be followed to determine the optimal switching state. Through the design of the value function in MPC, the optimal switching state satisfying the control target can be selected, and the efficient control of DC/AC inverter can be realized.

The inverter output currents  $i_a$ ,  $i_b$  and  $i_c$  are transformed by Clack to obtain the currents  $i_\alpha$  and  $i_\beta$  in the static coordinate system.

$$\begin{bmatrix} i_\alpha \\ i_\beta \end{bmatrix} = C_{abc/\alpha\beta} \begin{bmatrix} i_a \\ i_b \\ i_c \end{bmatrix} = \frac{2}{3} \begin{bmatrix} 1 & -\frac{1}{2} & -\frac{1}{2} \\ 0 & \frac{\sqrt{3}}{2} & \frac{\sqrt{3}}{2} \end{bmatrix} \begin{bmatrix} i_a \\ i_b \\ i_c \end{bmatrix} \tag{2}$$

where,  $i_\alpha$ ,  $i_\beta$  are the current components in  $\alpha\beta$  coordinate.

Based on the forward difference theorem and derivation of current components  $i_\alpha$  and  $i_\beta$ , the discrete mathematical model of inverter output current can be obtained.

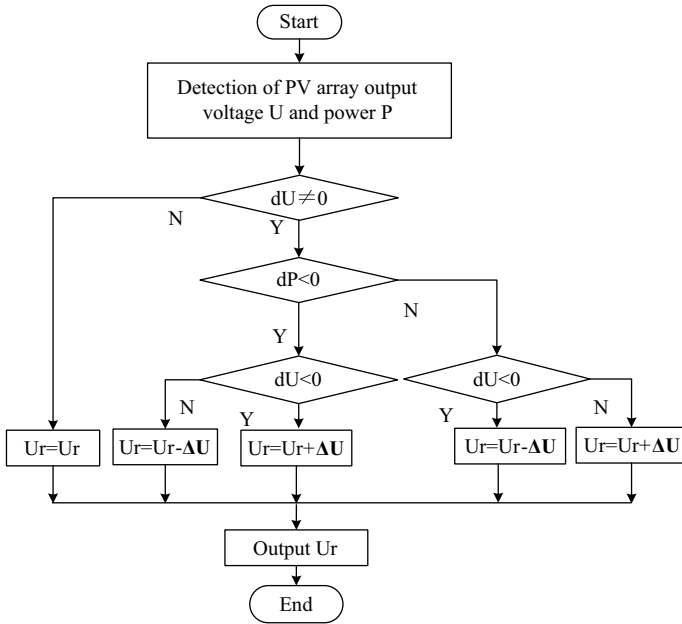


Fig. 3 Perturbed observation method flow chart

$$\frac{d}{dt} \begin{bmatrix} i_\alpha \\ i_\beta \end{bmatrix} = \frac{1}{T_s} \begin{bmatrix} i_\alpha(k+1) - i_\alpha(k) \\ i_\beta(k+1) - i_\beta(k) \end{bmatrix} \quad (3)$$

The voltage and current vector equations of the inverter are brought into Eq. (3) and combined with the derivative approximation principle, the discrete time model of the predicted current of the DC/AC inverter at  $k + 1$  moment can be obtained by correlation calculation.

$$\begin{bmatrix} i_\alpha(k+1) \\ i_\beta(k+1) \end{bmatrix} = \frac{T_s}{L} \begin{bmatrix} V_\alpha - E_\alpha \\ V_\beta - E_\beta \end{bmatrix} + \left(1 - \frac{RT_s}{L}\right) \begin{bmatrix} i_\alpha(k) \\ i_\beta(k) \end{bmatrix} \quad (4)$$

where,  $i_\alpha(k + 1)$ ,  $i_\beta(k + 1)$  are the predicted current components at moment  $k + 1$  in  $\alpha\beta$  coordinate;  $V_\alpha$ ,  $V_\beta$  are the inverter output voltage components in  $\alpha\beta$  coordinate;  $E_\alpha$ ,  $E_\beta$  are the grid voltage components in  $\alpha\beta$  coordinate;  $T_s$  is the sampling time.

The design of minimum value function  $g$  is an important part of MPC. The current reference value is derived through static-free tracking of the DC bus voltage command, which involves the error between  $V_{dc}^*(k)$  and  $V_{dc}(k)$  modulated by a PI controller, as illustrated in Eq. (5) and Eq. (6). The designed value function represents the dynamic response error between the discretized current predicted value and the reference value, as shown in Eq. (7).

$$\begin{bmatrix} i_d^*(k) \\ i_q^*(k) \end{bmatrix} = \left( K_p + \frac{K_i}{S} \right) \begin{bmatrix} V_{dc}^*(k) - V_{dc}(k) \\ 0 \end{bmatrix} \quad (5)$$

$$\begin{bmatrix} i_\alpha^*(k+1) \\ i_\beta^*(k+1) \end{bmatrix} = C_{dq/\alpha\beta} \begin{bmatrix} i_d^*(k) \\ i_q^*(k) \end{bmatrix} \quad (6)$$

$$g = |i_\alpha^*(k+1) - i_\alpha(k)| + |i_\beta^*(k+1) - i_\beta(k+1)| \quad (7)$$

where,  $i_d^*(k), i_q^*(k)$  are the reference current components at moment  $k$  in  $dq$  coordinate;  $V_{dc}^*(k)$  is the DC reference voltage at moment  $k$ ;  $V_{dc}(k)$  is the DC sampling voltage at moment  $k$ ;  $i_\alpha^*(k+1), i_\beta^*(k+1)$  are the reference current components at moment  $k+1$  in  $\alpha\beta$  coordinates;  $K_p$  and  $K_i$  are the proportionality and integration coefficients of the PI controller respectively.

Equation (7) is the value function established based on the current prediction at moment  $k+1$ . To further improve the control accuracy of the inverter, the value function is modified using the current prediction value at moment  $k+2$ . Considering that  $T_s$  is sufficiently small, the future value of the current reference quantity is generally considered to be approximately equal to the current value, as shown in Eq. (8).

$$\begin{bmatrix} i_\alpha^*(k+2) \\ i_\beta^*(k+2) \end{bmatrix} \approx \begin{bmatrix} i_\alpha^*(k+1) \\ i_\beta^*(k+1) \end{bmatrix} \quad (8)$$

where,  $i_\alpha^*(k+2), i_\beta^*(k+2)$  are the reference current components at moment  $k+2$  in  $\alpha\beta$  coordinate.

Since the power grid potential does not change much significantly in a short time, the next predicted value can be predicted by Eq. (9).

$$\begin{bmatrix} E_\alpha(k+1) \\ E_\beta(k+1) \end{bmatrix} = \begin{bmatrix} V_\alpha \\ V_\beta \end{bmatrix} - \frac{L}{T_s} \begin{bmatrix} i_\alpha(k+1) \\ i_\beta(k+1) \end{bmatrix} - \left( R - \frac{L}{T_s} \right) \begin{bmatrix} i_\alpha(k) \\ i_\beta(k) \end{bmatrix} \quad (9)$$

where,  $E_\alpha(k+1), E_\beta(k+1)$  are the power grid potential prediction components at moment  $k+1$  in  $\alpha\beta$  coordinate.

The model prediction controller of the inverter at moment  $k+2$  can be expressed as Eqs. (10) and (11).

$$\begin{bmatrix} i_\alpha(k+2) \\ i_\beta(k+2) \end{bmatrix} = \frac{T_s}{L} \begin{bmatrix} V_\alpha(k+1) - E_\alpha(k+1) \\ V_\beta(k+1) - E_\beta(k+1) \end{bmatrix} + \left( 1 - \frac{RT_s}{L} \right) \begin{bmatrix} i_\alpha(k+1) \\ i_\beta(k+1) \end{bmatrix} \quad (10)$$

$$g = |i_\alpha^*(k+2) - i_\alpha(k+2)| + |i_\beta^*(k+2) - i_\beta(k+2)| \quad (11)$$

To enhance the robustness of the system and account for the DC bus voltage fluctuation, the DC bus voltage error is multiplied by a specific weighting factor and

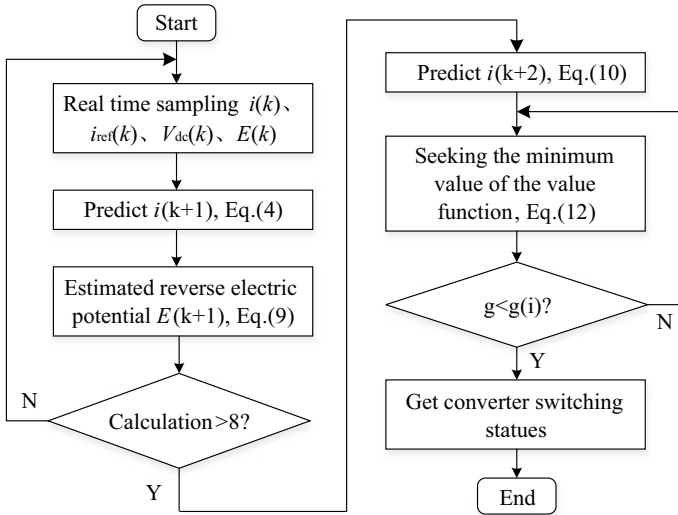


Fig. 4 Flow chart of multivariate MPC for PV inverter

incorporated into the value function presented in Eq. (11). The weighting factor  $\lambda$  is selected as 0.03. The final reconstructed value function is shown in Eq. (12).

$$g = |i_{\alpha}^*(k + 2) - i_{\alpha}(k + 2)| + |i_{\beta}^*(k + 2) - i_{\beta}(k + 2)| + \lambda |V_{dc}^* - V_{dc}| \quad (12)$$

The flow chart of multivariate MPC for PV grid-connected inverter proposed in this paper is shown in Fig. 4.

## 4 MATLAB/Simulink Simulation Experiment

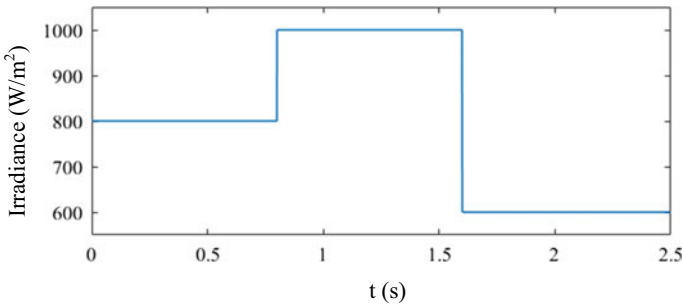
### 4.1 Testing Parameters

The PV inverter grid-connected system shown in Fig. 1 is built based on MATLAB/Simulink software. The setting of simulation parameters are shown in Table 1.

The initial irradiance is set to 800 W/m<sup>2</sup>. It suddenly increases to 1000 W/m<sup>2</sup> at 0.8 s and decreases to 600 W/m<sup>2</sup> at 1.6 s. The irradiance curve is depicted in Fig. 5. In this case, the two control strategies are compared and analyzed: the conventional PI control and the proposed multivariate MPC. The analysis focuses on various aspects, including PV power generation efficiency, DC bus voltage, power grid voltage and current, as well as current THD.

**Table 1** Parameters setting

Parameter	Describe	Value
$V_{dc}$	DC voltage	800 V
$V_{abc}$	AC voltage	220 V
$f$	Rated frequency	50 Hz
$T_s$	Sampling time	1e-6 s
$L$	Power grid-side filter inductance	20 mH
$R$	Power grid-side equivalent resistance	0.1 $\Omega$
$f_s$	IGBT switching frequency	5000 Hz



**Fig. 5** Irradiance variation curve

### 4.2 Test 1: PI Control

Figure 6 shows the results of simulation experiment considering the specified irradiance change curve under the PI control. The results from Fig. 6 are as follows: (a) Comparison between the theoretical maximum power and the actual power; (b) Calculated PV power generation efficiency; (c) DC bus voltage variation; (d) Current total harmonic distortion (THD); (e) and (f) AC current variation before and after the sudden change of irradiance at 0.8 s or 1.6 s; (g) and (h) Power grid side voltage and current variation before and after the sudden change of irradiance at 0.8 s or 1.6 s.

Combined with Fig. 6a, b, it can be seen that the oscillation time after the system is started is 0.38 s. The PV power generation efficiency reached 98.8% at 0.57 s, but the efficiency suddenly dropped 10.8% at 1.6 s. Figure 6c shows that the PI-controlled DC bus voltage exhibits an overshoot of 12.1% (896.8 V) at 0.13 s. It subsequently decreases to 789.3 V at 0.408 s, then gradually rises and stabilizes at 800 V within an approximate start-up time of 0.57 s. When the irradiance suddenly increases to 1000 w/m<sup>2</sup> at 0.8 s, the DC bus voltage rises to 814.6 V. When the irradiance suddenly drops to 600 w/m<sup>2</sup> at 1.6 s, the DC bus voltage drops to 758.2 V. However, after a short transition process, the DC bus voltage is restored to 800 V.

Figure 6d shows a current THD of 1.24%, indicating compliance with the grid connection requirements. Combined with Fig. 6e, f, we can observe the response

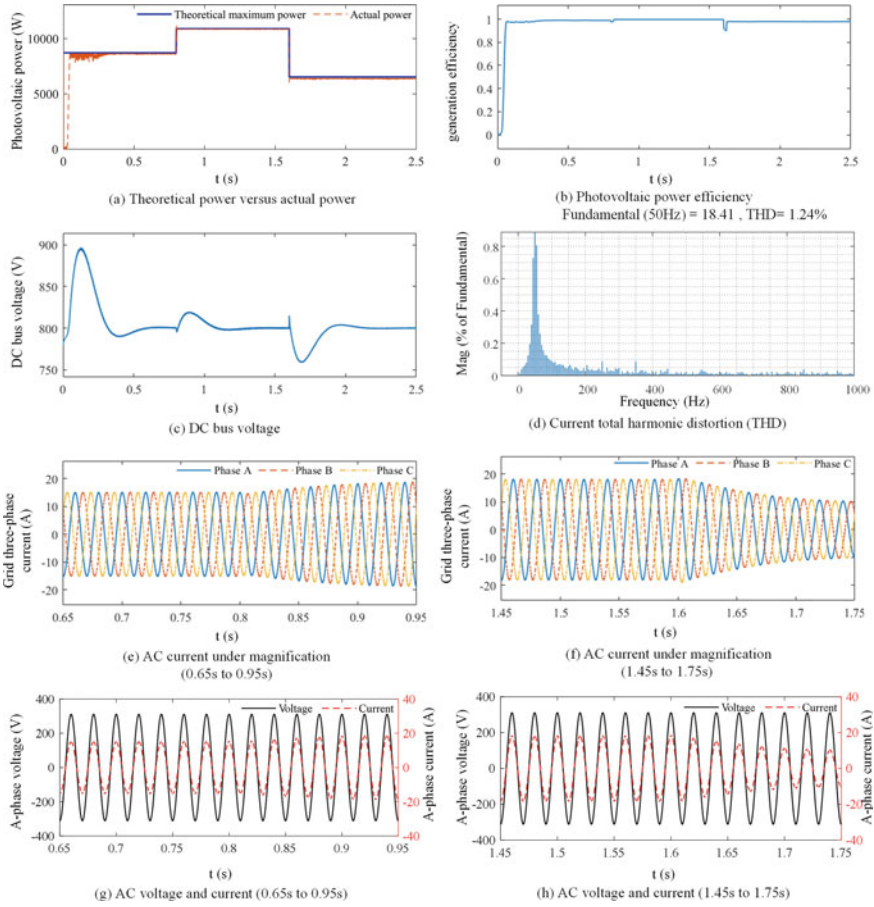


Fig. 6 Simulation results by PI control

speed of the PI control system when the irradiance changes, which is convenient to compare with the effect of the control strategy proposed in this paper. Combined with Fig. 6g, h, it can be seen that even if the irradiance changes, the PV inverter grid-connected system can run stably. It is worth noting that the voltage and current of the grid exhibit the same frequency and phase, that is, a power factor of 1, thus indicating a successful grid-connection.

### 4.3 Test 2: Multivariate MPC Control

Under the same simulation test conditions as above PI control, the simulation experiment results under multivariate MPC control are shown in Fig. 7.

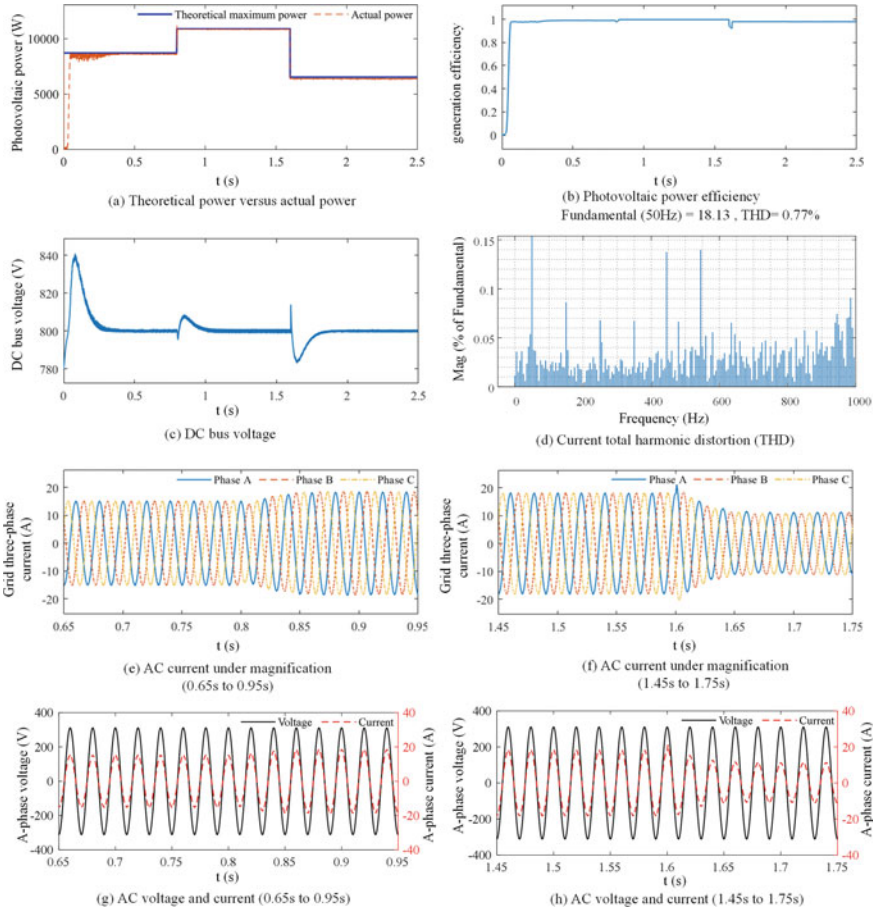


Fig. 7 Simulation results by multivariate MPC

Combined with Fig. 7a, b, it can be seen that the oscillation time after the system is started is 0.32 s. The PV power generation efficiency reached 98.8% at 0.53 s, but the efficiency suddenly dropped 8.8% at 1.6 s. Notably, the multivariate MPC control enhances the PV system’s efficiency and resilience to sudden environmental changes. Under multivariate MPC control, the DC bus voltage overshoots by 5% (840 V) at 0.079 s, then drops and stabilizes at 800 V for about 0.256 s, as shown in Fig. 7c. When the irradiance suddenly increases to 1000 w/m<sup>2</sup> at 0.8 s, the DC bus voltage rises to 807.8 V. When the irradiance suddenly drops to 600 w/m<sup>2</sup> at 1.6 s, the DC bus voltage drops to 784.1 V, and then stabilized at 800 V at 1.807 s.

Figure 7d demonstrates a current THD of 0.77%, indicating a lower value compared to the PI control. Combination with Fig. 7e, f, the response speed of multivariate MPC control can be observed when irradiance changes. Combined with Fig. 7g, h, it can be seen that under the condition of sudden changes in irradiance, the

PV inverter grid-connected system gradually realizes stable operation. Notably, the grid voltage and current exhibit the same frequency and phase, resulting in a power factor of 1, thereby accomplishing grid connection with unit power factor.

In summary, the AC current under multivariate MPC control exhibits reduced overshoot, peak time, and stability time compared to the corresponding values under PI control, resulting in a remarkable control effect. Numerical comparisons between the response speeds before and after the mutation demonstrate that multivariate MPC exhibits a smaller overshoot and faster response speed compared to PI control. Moreover, it successfully controls the THD at 0.77%, representing a significant reduction compared to the THD under PI control.

## 5 Conclusion

To enhance the response efficiency, minimize the total harmonic distortion rate of grid-connected PV, and mitigate the impact of large-scale grid-connected PV on the existing power system, this paper proposes a multivariate MPC for grid-connected PV inverter, which is then compared with PI control to assess the effectiveness and feasibility. The simulation test case analysis yields the following conclusions:

- (1) Multivariate MPC exhibits reduced overshoot and faster response in the DC bus voltage during sudden changes in irradiance, demonstrating improved resilience to interference and enhanced stability compared to PI control.
- (2) Although the AC voltage trends under PI control and multivariate MPC are comparable, multivariate MPC control achieves a smaller THD in the AC current, complying with the distortion rate requirement of less than 5% for grid connection in the national network and demonstrating practicality.
- (3) Incorporating the control factor derived from multi-step prediction into the value function yields improved control effectiveness, offering valuable insights for MPC applications in other domains.

**Acknowledgements** This work was supported by Zhejiang Electric Power Industry Corporation Technology Project (2020-YF-PYCT-01).

## References

1. Ullah B, Ullah H, Khalid S (2022) Direct model predictive control of noninverting buck-boost dc-dc converter. *CES Trans Electr Mach Syst* 6(3):332–339
2. Haghghat M, Niroomand M, Dehghani Tafti H (2022) An adaptive power ramp rate control method for photovoltaic systems. *IEEE J Photovoltaics* 12(2):557–564
3. Arsalan Khan M, Islam N, Khan MAM et al (2022) Experimental and simulation analysis of grid-connected rooftop photovoltaic system for a large-scale facility. *Sustain Energy Technol Assessments* 53(1):73–87



4. Song Y, Mu H et al (2023) Multi objective optimization of large-scale grid-connected photovoltaic-hydrogen-natural gas integrated energy power station based on carbon emission priority. *Int J Hydrogen Energy* 48(10):4087–4103
5. Zhang Y, Ma T, Yang H (2022) Grid-connected photovoltaic battery systems: a comprehensive review and perspectives. *Appl Energy* 328(1):82–97
6. Yanarates C, Wang Y, Zhou Z (2021) Unity proportional gain resonant and gain scheduled proportional (PR-P) controller-based variable perturbation size real-time adaptive perturb and observe (P&O) MPPT algorithm for PV systems. *IEEE Access* 9(1):138468–138482
7. Kumar N, Saha TK, Dey J (2016) Sliding-mode control of PWM dual inverter-based grid-connected PV system: modeling and performance analysis. *IEEE J Emerg Sel Topics Power Electron* 4(2):435–444
8. Ahmed M, Harbi I, Kennel R et al (2022) Model-based maximum power point tracking algorithm with constant power generation capability and fast DC-link dynamics for two-stage PV systems. *IEEE Access* 10(1):48551–48568
9. Sosa JL, Castilla M, Miret J et al (2016) Control strategy to maximize the power capability of PV three-phase inverters during voltage sags. *IEEE Trans Power Electron* 31(4):3314–3323
10. Zhou X, Liu Q, Ma Y et al (2021) DC-link voltage research of photovoltaic grid-connected inverter using improved active disturbance rejection control. *IEEE Access* 9(1):9884–9894
11. Mahfuz-Ur-Rahman AM, Rabiul Islam Md, Muttaqi KM et al (2023) An advanced modulation technique for transformer less grid connected inverter circuits used in solar photovoltaic systems. *IEEE Trans Ind Electron* 70(4):3878–3887
12. Jin N, Hu S, Cui G et al (2015) Finite state model predictive current control of grid-connected inverters for PV systems. *Proc CSEE* 35(1):190–196 (in Chinese)
13. Li Y, Gao X (2019) Fast finite set model predictive control of T-type three-phase three-level PV grid-connected inverters with power feedforward. *J Solar Energy* 40(11):3062–3070 (in Chinese)
14. Xu K, Zhang Z, Liu H et al (2020) Study on fault characteristics and its related impact factors of photovoltaic generator. *Trans China Electrotech Soc* 35(2):359–371 (in Chinese)